INEEL-EXT-98-00834

Revision 2.3

December 2004

ATHENA Code Manual Volume IV: Models and Correlations

The RELAP5-3D© Code Development Team

Idaho National Engineering and Environmental Laboratory
Bechtel BWXT Idaho, LLC

INEEL-EXT-98-00834
Volume IV
Revision 2.3

ATHENA CODE MANUAL
VOLUME IV: MODELS AND CORRELATIONS

The RELAP5-3D© Code Development Team

Original Manuscript Completed:
February 1999
Revision 2.3 Completed:
December 2004

Idaho National Engineering and Environmental Laboratory
Idaho Falls, Idaho 83415

Prepared Under DOE/NE Idaho Operations Office
Contract No. DE-AC07-99ID13727

The ATHENA manuals are living documents and are being corrected and updated continuously. A printed version of the manuals is frozen and archived when a code version is released. This version of the manual corresponds to ATHENA version 2.3, released December 2004.

ABSTRACT

The ATHENA code has been developed for best-estimate transient simulation of light water reactor coolant systems during postulated accidents. The code models the coupled behavior of the reactor coolant system and the core for loss-of-coolant accidents and operational transients such as anticipated transient without scram, loss of offsite power, loss of feedwater, and loss of flow. A generic modeling approach is used that permits simulating a variety of thermal hydraulic systems. Control system and secondary system components are included to permit modeling of plant controls, turbines, condensers, and secondary feedwater systems.

ATHENA code documentation is divided into six volumes: Volume I presents modeling theory and associated numerical schemes; Volume II details instructions for code application and input data preparation; Volume III presents the results of developmental assessment cases that demonstrate and verify the models used in the code; Volume IV discusses in detail ATHENA models and correlations; Volume V presents guidelines that have evolved over the past several years through the use of the ATHENA code; and Volume VI discusses the numerical scheme used in ATHENA.

CONTENTS

FIGURES

TABLES

EXECUTIVE SUMMARY

The RELAP5 series of codes has been developed at the Idaho National Engineering and Environmental Laboratory (INEEL) under sponsorship of the U.S. Department of Energy, the U.S. Nuclear Regulatory Commission, members of the International Code Assessment and Applications Program (ICAP), members of the Code Applications and Maintenance Program (CAMP), and members of the International RELAP5 Users Group (IRUG). Specific applications of the code have included simulations of transients in light water reactors (LWR) systems such as loss of coolant, anticipated transients without scram (ATWS), and operational transients such as loss of feedwater, loss of offsite power, station blackout, and turbine trip. ATHENA, the latest in the RELAP5 series of codes, is a highly generic code that, in addition to calculating the behavior of a reactor coolant system during a transient, can be used for simulating of a wide variety of hydraulic and thermal transients in both nuclear and nonnuclear systems involving mixtures of vapor, liquid, noncondensable gases, and nonvolatile solute.

The mission of the ATHENA development program was to develop a code version suitable for the analysis of all transients and postulated accidents in fusion reactor transient applications. Additional capabilities include space reactor simulation, gas cooled reactor modeling, fast breeder reactor modeling, and cardiovascular bloodflow modeling.

The ATHENA code is based on a nonhomogeneous and nonequilibrium model for the two-phase system that is solved by a fast, partially implicit numerical scheme to permit economical calculation of system transients. The objective of the ATHENA development effort from the outset was to produce a code that included important first-order effects necessary for accurate prediction of system transients but that was sufficiently simple and cost effective so that parametric or sensitivity studies are possible.

The code includes many generic component models from which general systems can be simulated. The component models include pumps, valves, pipes, heat releasing or absorbing structures, reactor point kinetics, electric heaters, jet pumps, turbines, separators, annuli, pressurizers, feedwater heaters, ECC mixers, accumulators, and control system components. In addition, special process models are included for effects such as form loss, flow at an abrupt area change, branching, choked flow, boron tracking, and noncondensable gas transport.

The system mathematical models are coupled into an efficient code structure. The code includes extensive input checking capability to help the user discover input errors and inconsistencies. Also included are free-format input, restart, renodalization, and variable output edit features. These user conveniences were developed in recognition that generally the major cost associated with the use of a system transient code is in the engineering labor and time involved in accumulating system data and developing system models, while the computer cost associated with generation of the final result is usually small.

The development of the models and code versions that constitute ATHENA has spanned more than two decades from the early stages of ATHENA numerical scheme development (circa 1976) to the present. ATHENA represents the aggregate accumulation of experience in modeling core behavior during severe

accidents, two-phase flow process, and LWR systems. The code development has benefitted from extensive application and comparison to experimental data in the LOFT, PBF, Semiscale, ACRR, NRU, and other experimental programs.

The ATHENA code contains several important enhancements over previous versions of the code. Enhancements include a new matrix solver, new thermodynamic properties for water, and improved time advancement for greater robustness. The new Border Profiled Lower Upper (BPLU) matrix solver is used to efficiently solve sparse linear systems of the form AX = B. BPLU is designed to take advantage of pipelines, vector hardware, and shared-memory parallel architecture to run fast. BPLU is most efficient for solving systems that correspond to networks, such as pipes, but is efficient for any system that it can permute into border-banded form.

The ATHENA code manual consists of six separate volumes. The modeling theory and associated numerical schemes are described in Volume I, to acquaint the user with the modeling base and thus aid in effective use of the code. Volume II contains more detailed instructions for code application and specific instructions for input data preparation.

Volume III presents the results of developmental assessment cases run with ATHENA to demonstrate and verify the models used in the code. The assessment matrix contains phenomenological problems, separate-effects tests, and integral systems tests.

Volume IV contains a detailed discussion of the models and correlations used in ATHENA. It presents the user with the underlying assumptions and simplifications used to generate and implement the base equations into the code so that an intelligent assessment of the applicability and accuracy of the resulting calculations can be made. Thus, the user can determine whether ATHENA is capable of modeling a particular application, whether the calculated results will be directly comparable to measurement, or whether they must be interpreted in an average sense, and whether the results can be used to make quantitative decisions.

Volume V provides guidelines that have evolved over the past several years from applications of the RELAP5 code at the Idaho National Engineering and Environmental Laboratory, at other national laboratories, and by users throughout the world.

Volume VI discusses the numerical scheme in ATHENA.

ACKNOWLEDGMENTS

Development of a complex computer code such as ATHENA is the result of team effort and requires the diverse talents of a large number of people. Special acknowledgment is given to those who pioneered in the development of the RELAP5 series of codes, in particular, V. H. Ransom, J. A. Trapp, and R. J. Wagner. A number of other people have made and continue to make significant contributions to the continuing development of the ATHENA code. Recognition and gratitude is given to the other current members of the ATHENA team:

P. D. Bayless	N. S. Larson	R. A. Riemke
V. T. Berta	M. A. Lintner	A. S-L. Shieh
K. E. Carlson	G. L. Mesina	R. R. Schultz
C. B. Davis	C. S. Miller	R. W. Shumway
J. E. Fisher	G. A. Mortensen	C. E. Slater
C. D. Fletcher	P. E. Murray	S. M. Sloan
E. C. Johnsen	C. E. Nielson	J. E. Tolli
G. W. Johnsen	R. B. Nielson	W. L. Weaver
H-H. Kuo	S. Paik	

The list of contributors is incomplete, as many others have made significant contributions in the past. Rather than attempt to list them all and risk unknowingly omitting some who have contributed, we acknowledge them as a group and express our appreciation for their contributions to the success of the ATHENA effort.

Finally, acknowledgment is made of all the code users who have been very helpful in stimulating timely correction of code deficiencies and suggesting improvements.

NOMENCLATURE

A	cross-sectional area (m^2), coefficient matrix in hydrodynamics, coefficient in pressure and velocity equations
A_1	coefficient in heat conduction equation at boundaries
A_t	throat area (m^2)
a	speed of sound (m/s), interfacial area per unit volume (m^{-1}), coefficient in gap conductance, coefficient in heat conduction equation, absorption coefficient
B	coefficient matrix, drag coefficient, coefficient in pressure and velocity equations
B_1	coefficient in heat conduction equation at boundaries
B_x	body force in x coordinate direction (m/s^2)
C	coefficient of virtual mass, general vector function, coefficient in pressure and velocity equations, delayed neutron precursors in reactor kinetics, concentration, pressure-dependent coefficient in Unal's correlation (1/k•s)
C_o	coefficient in noncondensable specific internal energy equation (J/kg•K)
C_0, C_1	constants in drift flux model
C_p	specific heat at constant pressure (J/kg•K)
C_D	drag coefficient
c	coefficient in heat conduction equation, coefficient in new time volume-average velocity equation, constant in CCFL model
D	coefficient of relative Mach number, diffusivity, pipe diameter or equivalent diameter (hydraulic diameter) (m), heat conduction boundary condition matrix, coefficient in pressure and velocity equations
D_o	coefficient in noncondensable specific internal energy equation ($J/kg•K^2$)
D_1	coefficient of heat conduction equation at boundaries
d	coefficient in heat conduction equation, droplet diameter (m)
DISS	energy dissipation function (W/m^3)
E	specific total energy ($U + v^2/2$) (J/kg), emissivity, Young's modulus, term in iterative heat conduction algorithm, coefficient in pressure equation
e	interfacial roughness
F	term in iterative heat conduction algorithm, gray-body factor with subscript, frictional loss coefficient, vertical stratification factor
FI	interphase drag coefficient ($m^3/kg•s$)
FWF, FWG	wall drag coefficients (liquid, vapor/gas) (s^{-1})
f	interphase friction factor, vector for liquid velocities in hydrodynamics

G	mass flux (kg/m^2-s), shear stress, gradient, coefficient in heat conduction, vector quantity, fraction of delayed neutrons in reactor kinetics
Gr	Grashof number
g	gravitational constant (m/s^2), temperature jump distance (m), vector for vapor/gas velocities in hydrodynamics
H	elevation (m), volumetric heat transfer coefficient (W/K•m^3), head (m)
HLOSSF, HLOSSG	form or frictional losses (liquid, vapor/gas) (m/s)
h	specific enthalpy (J/kg), heat transfer coefficient (W/m^2•K), energy transfer coefficient for Γ_g, head ratio
h_L	dynamic head loss (m)
I	identity matrix, moment of inertia (N-m-s^2)
i	$\sqrt{-1}$
J	junction velocity (m/s)
j	superficial velocity (m/s)
K	energy form loss coefficient
Ku	Kutateladze number
k	thermal conductivity (W/m•K)
k_B	Boltzmann constant
L	length, limit function, Laplace capillary length
M	Mach number, molecular weight, pump two-phase multiplier, mass transfer rate, mass (kg)
m	constant in CCFL model
N	number of system nodes, number density (#/m^3), pump speed (rad/s), nondimensional number
Nu	Nusselt number
n	unit vector, order of equation system
P	pressure (Pa), reactor power (W), channel perimeter (m), turbine power (J/s)
P_f	relates reactor power to heat generation rate in heat structures
p	wetted perimeter (m), particle probability function
Pr	Prandtl number
Q	volumetric heat addition rate (W/m^3), space dependent function, volumetric flow rate (m^3/s)
q	heat transfer rate (W), heat flux (W/m^2)

R	radius (m), surface roughness in gap conductance, radiation resistance term, nondimensional stratified level height
Ra	Rayleigh number
Re	Reynolds number
Re_p	the particle Reynolds number
r	reaction fraction for turbine, radial position
S	Chen's boiling suppression factor, stress gradient, specific entropy (J/kg•K), shape factor, real constant, source term in heat conduction or reactor kinetics (W)
T	temperature (K), trip
T_c	critical temperature (K)
T_R	reduced temperature (K)
t	time (s)
U	specific internal energy (J/kg), vector of dependent variables, velocity (m/s)
u	radial displacement in gap conductance (m)
V	volume (m^3), specific volume (m^3/kg), control quantity
VIS	numerical viscosity terms in momentum equations (m^2/s^2)
VISF, VISG	numerical viscosity terms in momentum equations (liquid, vapor/gas) (m^2/s^2)
v	mixture velocity (m/s), phasic velocity (m/s), flow ratio, liquid surge line velocity (m/s)
v_c	choking velocity (m/s)
W	weight of valve disk, weighting function in reactor kinetics, relaxation parameter in heat conduction, shaft work per unit mass flow rate, mass flow rate
We	Weber number
w	humidity ratio
X	quality, static quality, mass fraction, conversion from MeV/s to watts
x	spatial coordinate (m), vector of hydrodynamic variables
Y	control variable
Z	two-phase friction correlation factor, function in reactor kinetics

Symbols

α	void fraction, subscripted volume fraction, angular acceleration (rad/s^2), coefficient for least-squares fit, speed ratio, thermal diffusivity (m^2/s), Unal's term
β	coefficient of isobaric thermal expansion (K^{-1}), effective delayed neutron fraction

	in reactor kinetics, constant in CCFL model
Γ	volumetric mass exchange rate (kg/m^3•s)
γ	exponential function in decay heat model
ΔP_f	dynamic pressure loss (Pa)
ΔT	temperature difference
Δt	increment in time variable (s)
Δx	increment in spatial variable (m)
δ	area ratio, truncation error measure, film thickness (m), impulse function, Deryagin number
ε	coefficient, strain function, emissivity, tabular function of area ratio, surface roughness, wall vapor generation/condensation flag
η	efficiency, bulk/saturation enthalpy flag
θ	relaxation time in correlation for Γ, angular position (rad), discontinuity detector function
κ	coefficient of isothermal compressibility (Pa^{-1})
Λ	prompt neutron generation time, Baroczy dimensionless property index
λ	eigenvalue, interface velocity parameter, friction factor, decay constant in reactor kinetics
μ	viscosity (kg/m•s)
ν	kinematic viscosity (m^2/s), Poisson's ratio
ξ	exponential function, RMS precision
π	3.141592654
ρ	density (kg/m^3), reactivity in reactor kinetics (dollars)
Σ_f	fission cross-section
Σ'	depressurization rate (Pa/s)
σ	surface tension (J/m^2), stress, flag used in heat conduction equations to indicate transient or steady-state
τ	shear stresses (N), torque (N-m)
υ	specific volume (m^3/kg)
ϕ	donored property, Lockhart-Martinelli two-phase parameter, neutron flux in reactor kinetics, angle of inclination of valve assembly, elevation angle, velocity-dependent coefficient in Unal's correlation
χ	Lockhart-Martinelli function
ψ	coefficient, fission rate (number/s)

ω	angular velocity, constant in Godunov solution scheme

Subscripts

AM	annular-mist to mist flow regime transition
a	average value
ann	liquid film in annular-mist flow regime
BS	bubbly-to-slug flow regime transition
b	bubble, boron, bulk
bub	bubbles
bundle	value appropriate for bundle geometry
CHF	value at critical heat flux condition
CONV	value for convective boiling regime
c	vena contract, continuous phase, cladding, critical property, cross-section, condensation
cond	value for condensation process
core	vapor/gas core in annular-mist flow regime
cr,crit	critical property or condition
cross	value for crossflow
cyl	cylinder
D	drive line, vapor/gas dome, discharge passage of mechanical separator
DE	value at lower end of slug to annular-mist flow regime transition region
d	droplet, delay in control component
drop	droplets
drp	droplet
e	equilibrium, equivalent quality in hydraulic volumes, valve ring exit, elastic deformation, entrainment
F	wall friction, fuel
f	liquid phase, flooding, film, force, flow
fc	forced convection flow regime
fg	phasic difference (i.e., vapor/gas term-liquid term)
flow	flow
fr	frictional

GS	gas superficial
g	vapor/gas phase, gap
gj	drift velocity
H	head
HE	homogeneous equilibrium
h, hy, hydro	hydraulic
high	value at upper limit of transition region
I	interface
IAN	inverted annular flow regime
i	interface, index
j, j+1, j-1	spatial noding indices for junctions
K	spatial noding index for volumes
k	iteration index in choking model
L	spatial noding index for volume, laminar, value based on appropriate length scale
LS	liquid superficial
l	left boundary in heat conduction
lev, level	value at two-phase level
lim	limiting value
low	value at lower limit of transition region
m	mixture property, motor, mesh point
min	minimum value
n	noncondensable component of vapor/gas phase
o	reference value
POOL	value for pool boiling regime
p	partial pressure of vapor, particle, phase index
pipe	cross-section of flow channel
R	rated values
REG	flow regime identifier
r	relative Mach number, right boundary in heat structure mesh
S	suction region
SA	value at upper end of slug to annular-mist flow regime transition

s	vapor component of vapor/gas phase, superheated, superficial
sat	saturated quality, saturation
sb	small bubble
sm	Sauter mean value
spp	value based on vapor partial pressure
sppb	value based on vapor partial pressure in the bulk fluid
spt	value based on vapor/gas total pressure
sr	surface of heat structure
st	stratified
std	standard precision
T	point of minimum area, turbulent
TB	transition boiling
Tb	Taylor bubble
t	total pressure, turbulent, tangential, throat
tt	value for turbulent liquid and turbulent vapor/gas
up	upstream quantity
v	mass mean Mach number, vapor/gas quantity, valve
w	wall, liquid
1	upstream station, multiple junction index, vector index
1ϕ	single-phase value
2	downstream station, multiple junction index, vector index
2ϕ	two-phase value
τ	torque
μ	viscosity
∞	infinity

Superscripts

B	bulk liquid
f	value due to film flow process
e	value due to entrainment precess
exp	old time terms in velocity equation, used to indicate explicit velocities in choking

max	maximum value
min	minimum value
n, n+l	time level index
o	initial value
R	real part of complex number, right boundary in heat conduction
s	saturation property, space gradient weight factor in heat conduction
W	wall
2	vector index
*	total derivative of a saturation property with respect to pressure, local variable, bulk/saturation property
′	derivative
.	donored quantity
″	flux quantity, i.e. value per unit area per unit time
~	unit momentum for mass exchange, intermediate time variable
^	linearized quantity, quality based on total mixture mass

1 Introduction

Volume IV is intended to enhance the information presented in Volumes I and II of this document, which provide a detailed explanation of the code contents and its structure, its input requirements, and the interpretation of the code output. The purpose of this document is to provide the user with quantitative information addressing the physical basis for the ATHENA computer code, not only as documented in the other code manuals but also as actually implemented in the FORTRAN coding. The specific version of the code being discussed is ATHENA.

The information in this document allows the user to determine whether ATHENA is capable of modeling a particular application, whether the calculated result will directly compare to measurements or whether they must be interpreted in an average sense, and whether the results can be used to make quantitative decisions. Wherever possible, the other code manual volumes are referenced rather than repeat the discussion in this volume.

This introduction briefly describes the ATHENA code, presenting some of the history of the RELAP5 development leading to the current code capabilities and structure. The code structure is then discussed. The structure is significant, for it affects the time at which each of the calculated parameters is determined and gives the reader an understanding of the order in which a calculation proceeds and the manner in which transient parameters are passed from one portion of the calculational scheme to the next. The scope of the document is presented followed by a description of the document structure, which closely relates to the code structure.

1.1 Development of ATHENA

The ATHENA code is a successor to the RELAP5/MOD3 code[1.1-1] which was developed for the Nuclear Regulatory Commission. Department of Energy sponsors of the code extensions in ATHENA include the DOE Office of Fusion Energy Sciences, Savannah River Laboratory, Bettis Atomic Power Laboratory, the International RELAP5 Users Group (IRUG), and the Laboratory Directed Research and Development Program at the INEEL. The ATHENA version contains several important enhancements over previous versions of the code. Enhancements include a new matrix solver, new thermodynamic properties for water, and improved time advancement for greater robustness. The new Border Profiled Lower Upper (BPLU) matrix solver is used to efficiently solve sparse linear systems of the form AX = B. BPLU is designed to take advantage of pipelines, vector hardware, and shared-memory parallel architecture to run fast. BPLU is most efficient for solving systems that correspond to networks, such as pipes, but is efficient for any system that it can permute into border-banded form.

1.1.1 References

1.1-1. The RELAP5 Development Team, *RELAP5/MOD3 Code Manual, Volumes 1 and 2,* NUREG/CR-5535, INEL-95/0174, Idaho National Engineering Laboratory, August 1995.

1.2 Code Organization

ATHENA is coded in a modular fashion using top-down structuring. The various models and procedures are isolated in separate subroutines. The top level structure is shown in **Figure 1.2-1** and consists of input (INPUTD), transient/steady-state (TRNCTL), and stripping (STRIP) blocks.

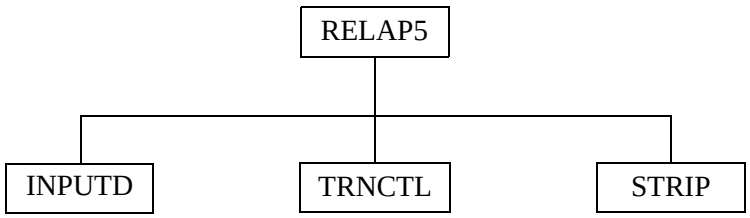

Figure 1.2-1 ATHENA top level structure.

The input (INPUTD) block processes input, checks input data, and prepares required data blocks for all program options.

Input processing has three phases. The first phase reads all input data, checks for punctuation and typing errors (such as multiple decimal points and letters in numerical fields), and stores the data keyed by card number such that the data are easily retrieved. A list of the input data is provided, and punctuation errors are noted.

During the second phase, restart data from a previous simulation is read if the problem is a RESTART type, and all the input data are processed. Some processed input is stored in fixed common blocks, but the majority of the data are stored in dynamic data blocks that are created only if needed by a problem and sized to the particular problem. Input is extensively checked, but at this level, checking is limited to new data from the cards being processed. Relationships with other data cannot be checked because the latter may not yet be processed.

The third phase of processing begins after all input data have been processed. Since all data have been placed in common or dynamic data blocks during the second phase, complete checking of interrelationships can proceed. Examples of cross-checking are the existence of hydrodynamic volumes referenced in junctions and heat structure boundary conditions; entry or existence of material property data specified in heat structures; and validity of variables selected for minor edits, plotting, or used in trips and control systems. As the cross-checking proceeds, the data blocks are cross-linked so that it need not be repeated at every time step. The initialization required to prepare the model for the start of the transient advancement is done at this level.

The transient/steady-state block (TRNCTL) handles both the transient option and the steady-state option. The steady-state option determines the steady-state conditions if a properly posed steady-state problem is presented. Steady-state is obtained by running an accelerated transient (i.e., null transient) until

the time derivatives approach zero. Thus, the steady-state option is very similar to the transient option but contains convergence testing algorithms to determine satisfactory steady-state, divergence from steady-state, or cyclic operation. If the transient technique alone were used, approach to steady-state from an initial condition would be identical to a plant transient from that initial condition. Pressures, densities, and flow distributions would adjust quickly, but thermal effects would occur more slowly. To reduce the transient time required to reach steady-state, the steady-state option artificially accelerates heat conduction by reducing the heat capacity of the conductors. **Figure 1.2-2** shows the second-level structures for the transient/steady-state blocks or subroutines.

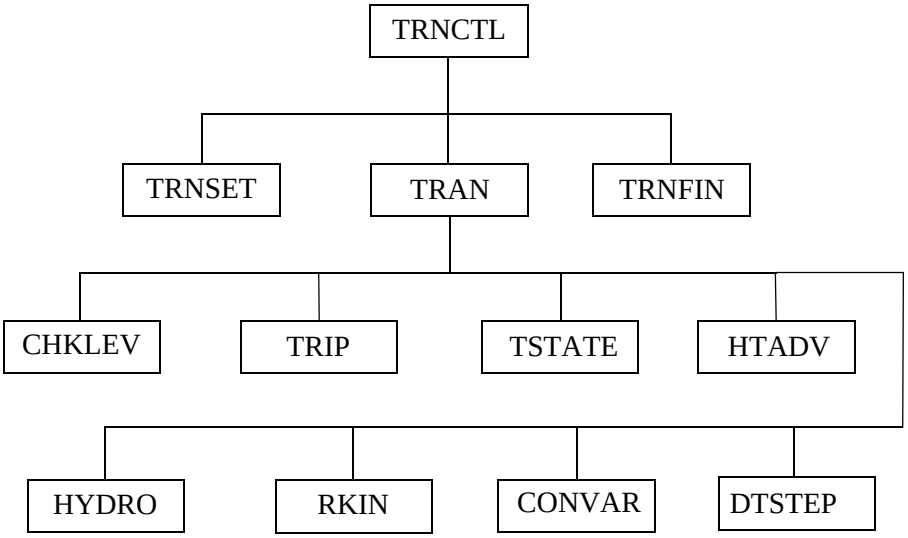

Figure 1.2-2 ATHENA transient/steady-state structure.

The subroutine TRNCTL consists only of the logic to call the next lower level routines. Subroutine TRNSET brings dynamic blocks required for transient execution from disk into memory, performs final cross-linking of information between data blocks, sets up arrays to control the sparse matrix solution, establishes scratch work space, and returns unneeded memory. Subroutine TRAN controls the transient advancement of the solution. Nearly all the execution time is spent in this block, and this block is the most demanding of memory. The subroutine TRNFIN releases space for the dynamic data blocks that are no longer needed.

Figure 1.2-2 also shows the structure of the TRAN block. CHKLEV controls movement of two-phase levels between volumes. TSTATE applies hydrodynamic boundary conditions by computing thermodynamic conditions for time-dependent volumes and velocities for time-dependent junctions. The remaining blocks perform or control the calculations for major models within ATHENA: trip logic (TRIP), heat structure advancement (HTADV), hydrodynamic advancement (HYDRO), reactor kinetics advancement (RKIN), control system advancement (CONVAR), and time step size (DTSTEP). The blocks are executed in the order shown in the figure from left to right, top to bottom. Although implicit techniques

are used within some of the blocks (HTADV and HYDRO), data exchange between blocks is explicit, and the order of block execution dictates the time levels of feedback data between models. Thus, HTADV advances heat conduction/convection solutions using only old-time reactor kinetics power and old-time hydrodynamic conditions. HYDRO, since it follows HTADV, can use both new- and old-time heat transfer rates to compute heat transferred into a hydrodynamic volume.

The strip block (STRIP) extracts simulation data from a restart-plot file for convenient passing of ATHENA simulation results to other computer programs.

1.3 Document Scope

This document is a revised and expanded version of the RELAP5/MOD2 models and correlations report.[1.3-1] This document is not all inclusive in that not every model and correlation is discussed. Rather, the information in Volumes I, II, and IV have been integrated and where a discussion of the correlations and implementation assumptions were necessary for an understanding of the model, it has been included in the other volumes and not repeated in this volume.

1.3.1 Reference

1.3-1. R. A. Dimenna et al., *RELAP5/MOD2 Models and Correlations*, NUREG/CR-5194, EGG-2531, Idaho National Engineering Laboratory, August 1988.

1.4 Document Structure

This document is structured around the field equations used in ATHENA. The field equations were chosen as the underlying thread because they provide the structure of the code itself; and using a common structure for the code and the description facilitates the use of this document in understanding the code. Section 2 lists the finite difference form of the basic field equations used in the two-fluid calculation. The finite difference field equations are derived in Volume I of the manual, and this derivation is not repeated in Section 2. References to other volumes are used where possible.

With the field equations identified, the next most pervasive aspect of the code calculation is probably the determination of the flow regime. Therefore, the flow regime map, or calculation, is discussed in Section 3. Sections 4, 5, and 6 then provide, in order, a discussion of the models and correlations used to provide closure for the energy, mass, and momentum balance equations. The closure models for the mass balance equations are closely related to those for the energy equations, so they were included before moving to the discussion of the models related to the momentum equations.

Section 7 describes the flow process models, such as the abrupt area change and the critical flow models. Section 8 describes selected component models, specifically, the pump and separator/dryer models. Section 9 describes the heat structure process models, including the solution of the heat conduction equations and the energy source term model as represented by the reactor kinetics equations.

Section 10 comments on the closure relations required by extra mass conservation fields, and Section 11 describes the steady-state model.

2 Field Equations

The ATHENA thermal-hydraulic model solves eight field equations for eight primary dependent variables. The primary dependent variables are pressure (P), phasic specific internal energies (U_g, U_f), vapor/gas volume fraction (void fraction) (α_g), phasic velocities (v_g, v_f), noncondensable quality (X_n), and boron density (ρ_b). The independent variables are time (t) and distance (x). Noncondensable quality is defined as the ratio of the noncondensable gas mass to the total vapor/gas phase mass, i.e., $X_n = M_n/(M_n + M_s)$, where M_n is the mass of noncondensable in the vapor/gas phase and M_s is the mass of the vapor in the vapor/gas phase. The secondary dependent variables used in the equations are phasic densities (ρ_g, ρ_f), phasic temperatures (T_g, T_f), saturation temperature (T^s), and noncondensable mass fraction in noncondensable gas phase (X_{ni}) for the i-th noncondensable species. Closure of the field equations is provided through the use of constitutive relations and correlations for such processes as interphase friction, interphase heat transfer, wall friction, and wall heat transfer. The field equations for the two phasic mass equations, two phasic momentum equations, and two phasic energy are presented in this section of Volume IV to show where the constitutive models and correlations apply to the overall ATHENA solution.

2.1 Differential Equations

The development of such equations for the two-phase process has been recorded in several references.[2.1-1,2.1-2,2.1-3] The one-dimensional, two-fluid phasic mass equations, phasic momentum equations, and phasic energy equations [Equations (8.12), (8.13), and (8.16) in **Reference 2.1-1**] by Ransom are referenced in Volume I of this manual, and the method used to obtain the differential equations used in ATHENA is presented in Volume I.

2.1.1 References

2.1-1. V. H. Ransom, *Course A-Numerical Modeling of Two-Phase Flows for Presentation at Ecole d'Ete d'Analyse Numerique*, EGG-EAST-8546, Idaho National Engineering Laboratory, May 1989.

2.1-2. M. Ishii, *Thermo-Fluid Dynamic Theory of Two-Phase Flow*, Collection de la Direction des Estudes d'Recherches of Electricute de France, 1975.

2.1-3. F. H. Harlow and A. A. Amsden, "Flow of Interpenetrating Material Phases," *Journal of Computational Physics, 18,* 1975, pp. 440-464.

2.2 Difference Equations

The one-dimensional difference equations are obtained by integrating the differential equations with respect to the spatial variable, dividing out common area terms, and integrating over time. The mass and energy equations are spatially integrated across the cells from junction to junction, while the momentum equations are integrated across the junctions from cell center to cell center. These were derived in Volume

I of this manual, and the final one-dimensional finite difference equations for the semi-implicit solution scheme are repeated here.

The semi-implicit scheme one-dimensional finite-difference equations for the mass, energy, and momentum are listed below. Some of the terms are intermediate time variables, which are written with a tilde (~).

The sum continuity equation is

$$\begin{aligned} V_L[\alpha^n_{g,L}(\tilde{\rho}^{n+1}_{g,L} - \rho^n_{g,L}) + \alpha^n_{f,L}(\tilde{\rho}^{n+1}_{f,L} - \rho^n_{f,L}) + (\rho^n_{g,L} - \rho^n_{f,L})(\tilde{\alpha}^{n+1}_{g,L} - \alpha^n_{g,L})] \\ + (\dot{\alpha}^n_{g,j+1}\dot{\rho}^n_{g,j+1}v^{n+1}_{g,j+1}A_{j+1} - \dot{\alpha}^n_{g,j}\dot{\rho}^n_{g,j}v^{n+1}_{g,j}A_j)\Delta t \\ + (\dot{\alpha}^n_{f,j+1}\dot{\rho}^n_{f,j+1}v^{n+1}_{f,j+1}A_{j+1} - \dot{\alpha}^n_{f,j}\dot{\rho}^n_{f,j}v^{n+1}_{f,j}A_j)\Delta t = 0 \ . \end{aligned} \tag{2.2-1}$$

The difference continuity equation is

$$\begin{aligned} V_L[\alpha^n_{g,L}(\tilde{\rho}^{n+1}_{g,L} - \rho^n_{g,L}) - \alpha^n_{f,L}(\tilde{\rho}^{n+1}_{f,L} - \rho^n_{f,L}) + (\rho^n_{g,L} + \rho^n_{f,L})(\tilde{\alpha}^{n+1}_{g,L} - \alpha^n_{g,L})] \\ + (\dot{\alpha}^n_{g,j+1}\dot{\rho}^n_{g,j+1}v^{n+1}_{g,j+1}A_{j+1} - \dot{\alpha}^n_{g,j}\dot{\rho}^n_{g,j}v^{n+1}_{g,j}A_j)\Delta t \\ - (\dot{\alpha}^n_{f,j+1}\dot{\rho}^n_{f,j+1}v^{n+1}_{f,j+1}A_{j+1} - \dot{\alpha}^n_{f,j}\dot{\rho}^n_{f,j}v^{n+1}_{f,j}A_j)\Delta t \\ = -\left(\frac{2}{h_g^* - h_f^*}\right)^n_L V_L \Delta t\left[\frac{P^n_{s,L}}{P^n_L}H^n_{ig,L}(\tilde{T}^{s,n+1}_L - \tilde{T}^{n+1}_{g,L}) + H^n_{if,L}(\tilde{T}^{s,n+1}_L - \tilde{T}^{n+1}_{f,L})\right] + 2V_L\Delta t\Gamma^n_{w,L} \ . \end{aligned} \tag{2.2-2}$$

The noncondensable continuity equation is

$$\begin{aligned} V_L[\rho^n_{g,L}X^n_{n,L}(\tilde{\alpha}^{n+1}_{g,L} - \alpha^n_{g,L}) + \alpha^n_{g,L}X^n_{n,L}(\tilde{\rho}^{n+1}_{g,L} - \rho^n_{g,L}) + \alpha^n_{g,L}\rho^n_{g,L}(\tilde{X}^{n+1}_{n,L} - X^n_{n,L})] \\ + (\dot{\alpha}^n_{g,j+1}\dot{\rho}^n_{g,j+1}\dot{X}^n_{n,j+1}v^{n+1}_{g,j+1}A_{j+1} - \dot{\alpha}^n_{g,j}\dot{\rho}^n_{g,j}\dot{X}^n_{n,j}v^{n+1}_{g,j}A_j)\Delta t = 0 \ . \end{aligned} \tag{2.2-3}$$

The vapor/gas thermal energy equation is

$$V_L[(\rho^n_{g,L}U^n_{g,L} + P^n_L)(\tilde{\alpha}^{n+1}_{g,L} - \alpha^n_{g,L}) + \alpha^n_{g,L}U^n_{g,L}(\tilde{\rho}^{n+1}_{g,L} - \rho^n_{g,L}) + \alpha^n_{g,L}\rho^n_{g,L}(\tilde{U}^{n+1}_{g,L} - U^n_{g,L})]$$
$$+ [\dot{\alpha}^n_{g,j+1}(\dot{\rho}^n_{g,j+1}\dot{U}^n_{g,j+1} + P^n_L)v^{n+1}_{g,j+1}A_{j+1} - \dot{\alpha}^n_{g,j}(\dot{\rho}^n_{g,j}\dot{U}^n_{g,j} + P^n_L)v^{n+1}_{g,j}A_j]\Delta t$$
$$= \left\{-\left(\frac{h^*_f}{h^*_g - h^*_f}\right)^n_L \frac{P^n_{s,L}}{P^n_L}H^n_{ig,L}(\tilde{T}^{s,n+1}_L - \tilde{T}^{n+1}_{g,L}) - \left(\frac{h^*_g}{h^*_g - h^*_f}\right)^n_L H^n_{if,L}(\tilde{T}^{s,n+1}_L - \tilde{T}^{n+1}_{f,L})\right. \tag{2.2-4}$$
$$\left. - \left(\frac{P^n_L - P^n_{s,L}}{P^n_L}\right)H^n_{gf,L}(\tilde{T}^{n+1}_{g,L} - \tilde{T}^{n+1}_{f,L}) + \left[\left(\frac{1+\varepsilon}{2}\right)h'^{,n}_{g,L} + \left(\frac{1-\varepsilon}{2}\right)h'^{,n}_{f,L}\right]\Gamma^n_{w,L} + Q^n_{wg,L} + DISS^n_{g,L}\right\}V_L\Delta t \ .$$

The liquid thermal energy equation is

$$V_L[-(\rho^n_{f,L}U^n_{f,L} + P^n_L)(\tilde{\alpha}^{n+1}_{g,L} - \alpha^n_{g,L}) + \alpha^n_{f,L}U^n_{f,L}(\tilde{\rho}^{n+1}_{f,L} - \rho^n_{f,L}) + \alpha^n_{f,L}\rho^n_{f,L}(\tilde{U}^{n+1}_{f,L} - U^n_{f,L})]$$
$$+ [\dot{\alpha}^n_{f,j+1}(\dot{\rho}^n_{f,j+1}\dot{U}^n_{f,j+1} + P^n_L)v^{n+1}_{f,j+1}A_{j+1} - \dot{\alpha}^n_{f,j}(\dot{\rho}^n_{f,j}\dot{U}^n_{f,j} + P^n_L)v^{n+1}_{f,j}A_j]\Delta t$$
$$= \left\{\left(\frac{h^*_f}{h^*_g - h^*_f}\right)^n_L \frac{P^n_{s,L}}{P^n_L}H^n_{ig,L}(\tilde{T}^{s,n+1}_L - \tilde{T}^{n+1}_{g,L}) + \left(\frac{h^*_g}{h^*_g - h^*_f}\right)^n_L H^n_{if,L}(\tilde{T}^{s,n+1}_L - \tilde{T}^{n+1}_{f,L})\right. \tag{2.2-5}$$
$$\left. + \left(\frac{P^n_L - P^n_{s,L}}{P^n_L}\right)H^n_{gf,L}(\tilde{T}^{n+1}_{g,L} - \tilde{T}^{n+1}_{f,L}) - \left[\left(\frac{1+\varepsilon}{2}\right)h'^{,n}_{g,L} + \left(\frac{1-\varepsilon}{2}\right)h'^{,n}_{f,L}\right]\Gamma^n_{w,L} + Q^n_{wf,L} + DISS^n_{f,L}\right\}V_L\Delta t \ .$$

The sum momentum equation is

$$(\alpha_g\rho_g)^n_j(v^{n+1}_g - v^n_g)_j\Delta x_j + (\alpha_f\rho_f)^n_j(v^{n+1}_f - v^n_f)_j\Delta x_j + \frac{1}{2}(\dot{\alpha}_g\dot{\rho}_g)^n_j[(v^2_g)^n_L - (v^2_g)^n_K]\Delta t$$
$$+ \frac{1}{2}(\dot{\alpha}_f\dot{\rho}_f)^n_j[(v^2_f)^n_L - (v^2_f)^n_K]\Delta t - \frac{1}{2}[(\dot{\alpha}_g\dot{\rho}_g)^n_j VISG^n_j + (\dot{\alpha}_f\dot{\rho}_f)^n_j VISF^n_j]\Delta t \tag{2.2-6}$$
$$= -(P_L - P_K)^{n+1}\Delta t + [(\rho_m)^n_j B_x - (\alpha_g\rho_g)^n_j FWG^n_j(v_g)^{n+1}_j - (\alpha_f\rho_f)^n_j FWF^n_j(v_f)^{n+1}_j$$
$$- (\Gamma_g)^n_j(v_g - v_f)^{n+1}_j]\Delta x_j\Delta t - [(\dot{\alpha}_g\dot{\rho}_g)^n_j HLOSSG^n_j v^{n+1}_{g,j} + (\dot{\alpha}_f\dot{\rho}_f)^n_j HLOSSF^n_j v^{n+1}_{f,j}]\Delta t \ .$$

The difference momentum equation is

$$\left(1+\frac{C\rho_m^2}{\rho_g\rho_f}\right)_j^n[(v_g^{n+1}-v_g^n)-(v_f^{n+1}-v_f^n)]_j\Delta x_j$$

$$+\frac{1}{2}\left(\frac{\dot{\alpha}_g\dot{\rho}_g}{\alpha_g\rho_g}\right)_j^n[(v_g^2)_L^n-(v_g^2)_K^n]\Delta t-\frac{1}{2}\left(\frac{\dot{\alpha}_g\dot{\rho}_g}{\alpha_g\rho_g}\right)_j^n VISG_j^n\Delta t$$

$$-\frac{1}{2}\left(\frac{\dot{\alpha}_f\dot{\rho}_f}{\alpha_f\rho_f}\right)_j^n[(v_f^2)_L^n-(v_f^2)_K^n]\Delta t+\frac{1}{2}\left(\frac{\dot{\alpha}_f\dot{\rho}_f}{\alpha_f\rho_f}\right)_j^n VISF_j^n\Delta t = -\left(\frac{\rho_f-\rho_g}{\rho_f\rho_g}\right)_j^n(P_L-P_K)^{n+1}\Delta t$$

$$-\left(FWG_j^n(v_g)_j^{n+1}-FWF_j^n(v_f)_j^{n+1}-\left[\frac{\Gamma_g^n(\rho_m^n v_I^{n+1}-\alpha_f^n\rho_f^n v_g^{n+1}-\alpha_g^n\rho_g^n v_f^{n+1})}{(\alpha_g\rho_g\alpha_f\rho_f)^n}\right]_j\right. \tag{2.2-7}$$

$$\left.-(f_x)_j^n\left(\frac{1}{\alpha_g\rho_g}+\frac{1}{\alpha_f\rho_f}\right)_j^n[(f_{wg})_j^n(v_g)_j^{n+1}-(f_{wf})_j^n(v_f)_j^{n+1}]\right.$$

$$\left.+(\rho_m FI)_j^n\{[1+f_x(C_1-1)]_j^n(v_g)_j^{n+1}-[1+f_x(C_0-1)]_j^n(v_f)_j^{n+1}\}\right)\Delta x_j\Delta t$$

$$-\left[\left(\frac{\dot{\alpha}_g\dot{\rho}_g}{\alpha_g\rho_g}\right)_j^n HLOSSG_j^n v_{g,j}^{n+1}-\left(\frac{\dot{\alpha}_f\dot{\rho}_f}{\alpha_f\rho_f}\right)_j^n HLOSSF_j^n v_{f,j}^{n+1}\right]\Delta t$$

$$+\left(\frac{\rho_m}{\rho_g\rho_f}\right)_j^n(\rho_f-\rho_g)_j^n B_y(y_L^n-y_K^n)\Delta t$$

In the coding of the finite difference form of the difference momentum equation, the difference momentum equation is programmed as the difference of the liquid and vapor/gas momentum equations instead of the difference of the vapor/gas and liquid momentum equations as is shown in Equation (2.2-7).

3 Flow Regime Maps

The constitutive relations include models for defining flow regimes and flow-regime-related models for interphase friction, the coefficient of virtual mass, wall friction, wall heat transfer, and interphase heat and mass transfer. Heat transfer regimes are defined and used for wall heat transfer. For the virtual mass, a formula based on the void fraction is used.

In RELAP5/MOD2, all constitutive relations were evaluated using volume-centered conditions; junction parameters, such as interfacial friction coefficients, were obtained as volume-weighted averages of the volume-centered values in the volumes on either side of a junction. The procedure for obtaining junction parameters as averages of volume parameters was adequate when the volumes on either side of a junction were in the same flow regime and the volume parameters were obtained using the same flow-regime map (i.e., both volumes were horizontal volumes or both volumes were vertical volumes). Problems were encountered when connecting horizontal volumes to vertical volumes.

These problems have been eliminated in ATHENA by computing the junction interfacial friction coefficient using junction properties so that the interfacial friction coefficient would be consistent with the state of the fluid being transported through the junction. The approach has been used successfully in the TRAC-B code.[3.0-1,3.0-3,3.0-3] As a result, it was necessary to define both volume and junction flow-regime maps. The flow regime maps for the volumes and junctions are somewhat different as a result of the finite difference scheme and staggered mesh used in the numerical scheme.

Four flow-regime maps in both volumes and junctions for two-phase flow are used in the ATHENA code: (a) a horizontal map for flow in pipes; (b) a vertical map for flow in pipes, annuli, and bundles; (c) a high mixing map for flow through pumps; and (d) an ECC mixer map for flow in the horizontal pipes near the ECC injection port. The volume flow regime calculations for interfacial heat and mass transfer and wall drag are found in subroutine PHANTV. The junction flow regime calculation for interphase friction and coefficient of virtual mass are found in subroutine PHANTJ. Wall heat transfer depends on the volume flow regime maps in a less direct way. Generally, void fraction and mass flux are used to incorporate the effects of the flow regime. Because the wall heat transfer is calculated before the hydrodynamics, the flow information is taken from the previous time step.

3.0.1 References

3.0-1. W. L. Weaver et al., *TRAC-BF1 Manual: Extensions to TRAC-BD1/MOD1*, NUREG/CR-4391, EGG-2417, Idaho National Engineering Laboratory, August 1986.

3.0-2. M. M. Giles et al., *TRAC-BF1/MOD1: An Advanced Best Estimate Computer Program for BWR Accident Analysis*, NUREG/CR-4356, EGG-2626, Idaho National Engineering Laboratory, June 1992 and August 1992.

3.0-3. S. Z. Rouhani et al., *TRAC-BF1/MOD1 Models and Correlations,* NUREG/CR-4391, EGG-2680, Idaho National Engineering Laboratory, August 1992.

3.1 Horizontal Volume Flow Regime Map

3.1.1 Map as Coded

The horizontal flow regime map is for volumes whose inclination (vertical) angle ϕ is such that $0 \leq |\phi| \leq 30$ degrees. An interpolation region between vertical and horizontal flow regimes is used for volumes whose absolute value of the inclination (vertical) angle is between 30 degrees and 60 degrees.

A schematic of the horizontal volume flow regime map as coded in ATHENA is illustrated in **Figure 3.1-1**. The map consists of bubbly, slug, annular mist, dispersed (droplets or mist), and horizontally stratified regimes. Transition regions used in the code are indicated. Such transitions are included in the map primarily to preclude discontinuities when going from one correlation to another in drag and heat and mass transfer. Details of the interpolating functions employed between correlations are given in those sections that describe the various correlations. **Figure 3.1-2** illustrates the geometry for horizontal stratification.

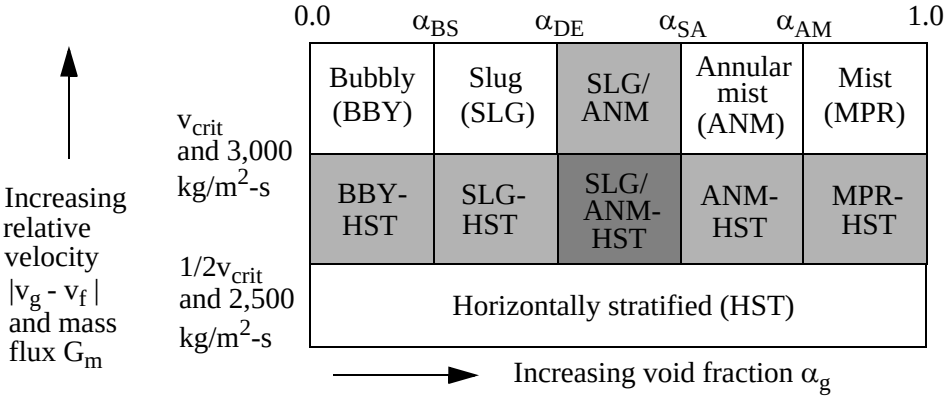

Figure 3.1-1 Schematic of horizontal flow regime map with hatchings, indicating transition regions.

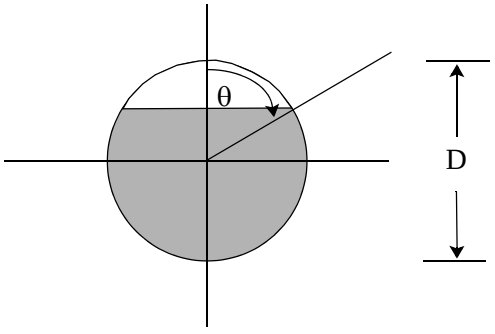

Figure 3.1-2 Schematic of horizontally stratified flow in a pipe.

Values for the parameters governing the flow-regime transitions are shown in **Figure 3.1-3** and listed below. G_m is the average mixture mass flux given by

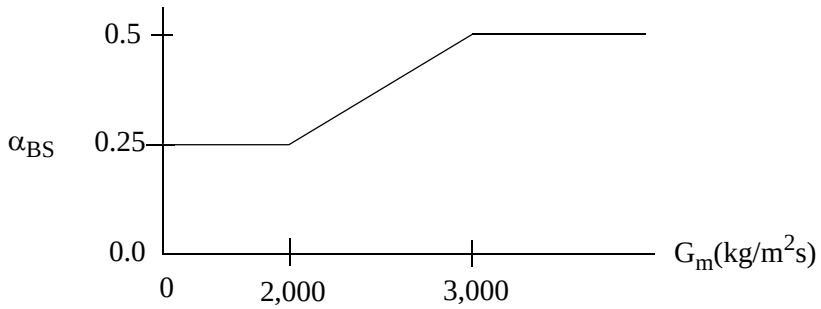

Figure 3.1-3 Horizontal bubbly-to-slug void fraction transition in ATHENA.

$$G_m = \alpha_g\rho_g|v_g| + \alpha_f\rho_f|v_f| \tag{3.1-1}$$

$\alpha_{BS} = 0.25 \qquad G_m \leq 2{,}000$ kg/m^2-s

$= 0.25 + 0.00025(G_m - 2{,}000) \qquad 2{,}000 < G_m < 3{,}000$ kg/m^2-s

$= 0.5 \qquad G_m \geq 3{,}000$ kg/m^2-s

$\alpha_{DE} = 0.75$

$\alpha_{SA} = 0.8$

$\alpha_{AM} = 0.9999$

and

$$v_{crit} = \frac{1}{2}\left[\frac{(\rho_f - \rho_g)g\alpha_g A}{\rho_g D \sin\theta}\right]^{1/2}(1 - \cos\theta) \tag{3.1-2}$$

where D is the pipe diameter or equivalent diameter (hydraulic diameter) and A is the cross-sectional area of the pipe, $A = \frac{\pi D^2}{4}$. Theta is the angle between the vertical and the stratified liquid level, as shown in **Figure 3.1-2**.

3.1.2 Map Basis and Assessment

The geometrical configuration of a two-phase flow regime is characterized by a combination of void fraction and interfacial area concentration and arrangement.[3.1-1] Traditionally, however, flow regime maps have been constructed using superficial velocities,[3.1-2,3.1-3] which, strictly speaking, do not uniquely define the flow regime. Ishii and Mishima[3.1-1] contend that while superficial velocities may provide for suitable flow regime mapping for steady, developed flow, the same is not true for transient or developing conditions such as arise frequently for nuclear reactor thermal-hydraulics. They recommend a direct geometric parameter, such as void fraction, for flow regime determination for unsteady and entrance flows where a two-fluid model (such as is used in ATHENA) is more appropriate than a more traditional mixture model. ATHENA uses the void fraction, α_g, to characterize the two-phase flow regimes. Taitel and Dukler[3.1-4] have devised a horizontal map from analytical considerations, albeit sometimes involving uncorroborated assumptions, that uses at least the void fraction for all regime transitions. Furthermore, in a later paper, they use the same flow-transition criteria to characterize transient two-phase horizontal flow.[3.1-5] Therefore, while void fraction does not uniquely determine the flow regime geometry, it appears to be a reasonable parameter for mapping the flow regimes expected in ATHENA applications and is consistent with the current state of the technology.

3.1.2.1 Transition from Bubbly Flow to Slug Flow. For high velocity flows ($|v_g - v_f| > v_{crit}$), the ATHENA horizontal flow map is an adaptation of the vertical map used in the code, which in turn is based on the work of Taitel, Bornea, and Dukler[3.1-6]. The bubbly-to-slug transition void fraction used in the code varies from 0.25 to 0.5 depending on the mass flux (see **Figure 3.1-3**). The lower limit of 0.25 is based on a postulate of Taitel, Bornea, and Dukler[3.1-6] that coalescence increases sharply when bubble spacing decreases to about half the bubble radius corresponding to about 25% void. Taitel, Bornea, and Dukler[3.1-6] then cite three references as supporting this approximate level. The first citation, Griffith and Wallis,[3.1-7] however, actually cites an unpublished source (Reference 6 in **Reference 3.1-7**), indicating that for $\alpha_g <$ 0.18 no tendency for slugs to develop was apparent. Griffith and Wallis were measuring the Taylor bubble rise velocity (air slugs) in a vertical pipe and admitted uncertainty about where the bubbly-slug transition should be. (Only two of their own data points fell into the region labeled bubbly flow on their flow-regime map.) Taitel, Bornea, and Dukler[3.1-6] also cite Griffith and Snyder,[3.1-8] suggesting that the bubbly-to-slug transition takes place between 0.25 and 0.30. Actually, Griffith and Snyder were studying slug flow using a novel technique. They formed a plastic “bubble” to simulate a Taylor bubble under which they injected air. Their setup allowed the bubble to remain stationary while the flow moved past it. While void fractions as low as 0.08 and no higher than 0.35 were obtained for “slug flow,” it seems inappropriate to use such information to set the bubbly-to-slug transition. The third reference cited by Taitel, Bornea, and Dukler[3.1-6] uses a semi-theoretical analysis involving bubble-collision frequency, which appears to

indicate a transition in the range α_g = 0.2 to 0.3.[3.1-9] A discussion by Hewitt,[3.1-10] however, points out some uncertainties and qualifications to the approach of **Reference 3.1-9**. Thus, the designation of α_g = 0.25 as the lower limit for a transition void fraction from bubbly-to-slug flow is somewhat arbitrary, although it does fall within the range suggested by the cited references.

Taitel, Bornea, and Dukler[3.1-6] further argue that the void fraction for bubbly flow could be at most 0.52 where adjacent bubbles in a cubic lattice would just touch. They then postulate that 0.52 represents the maximum attainable void fraction for bubbly flow, assuming the presence of vigorous turbulent diffusion. ATHENA uses a void fraction of 0.5 as an approximate representation of this condition for high mass flux.

The interpolation in ATHENA between α_g = 0.25 and 0.5 for the bubbly-to-slug transition is an attempt to account for an increase in maximum bubbly void fraction due to turbulence. The decision to base the transition on an average mixture mass flux increasing from 2,000 to 3,000 kg/m^2-s (Section 3.1.1) is from work by Choe, Weinberg, and Weisman[3.1-11] who show that at 2,700 kg/m^2-s, there is a transition between bubbly and slug flow. If, however, one plots the average mass fluxes on Figure 2 from Taitel, Bornea, and Dukler[3.1-6], the ATHENA transition for this special case (air-water at 25° C, 0.1 MPa in a vertical 5.0 cm diameter tube) appears reasonable. Figure 2 from Taitel, Bornea, and Dukler[3.1-6] is shown as **Figure 3.1-4**. Nevertheless, while the transition criterion based on G looks reasonable for the conditions of **Figure 3.1-4**, it is inappropriate to assume that it works well for all flow conditions found in reactor applications. A potentially better criterion for the variation of the bubbly-to-slug transition α_g would be based on dimensionless parameters. In **Figure 3.1-4**, the notation from Taitel, Bornea, and Dukler[3.1-6] is used, i.e., U_{LS} is liquid superficial velocity (j_f) and U_{GS} is vapor/gas superficial velocity (j_g).

3.1.2.2 Transition from Slug Flow to Annular Mist Flow. The coded transition from slug to annular mist flow takes place between void fractions of 0.75 and 0.80. This is based on a model by Barnea,[3.1-12] which implies that annular flow can occur for $\alpha_g > 0.76$. Barnea indicates that for cocurrent upflow, the transition criteria give reasonable agreement with atmospheric air-water data for a 2.5 and 5.1 cm diameter tube, and Freon-113 data for a 2.5 cm diameter tube.

3.1.2.3 Transition from Annular Mist Flow to Dispersed Flow. The void fraction upon which this transition is coded to take place simply corresponds to a very high vapor/gas fraction, α_g = 0.9999. This vapor/gas fraction was chosen to allow a smooth transition to single-phase vapor/gas flow.

3.1.2.4 Transition to Horizontal Stratification. The transition criterion from horizontally-stratified to nonstratified flow, Equation (3.1-2), is derived directly from Equations (23-24) of Taitel and Dukler[3.1-4], which are a statement of the Kelvin-Helmholtz instability. If $|v_g - v_f|$ is greater than v_{crit}, the flow is not stratified; if it is less, then a region of transition takes place (**Figure 3.1-1**) before the flow is considered to be completely stratified. The criterion holds that infinitesimal waves on the liquid surface will grow in amplitude if $|v_g - v_f| \geq v_{crit}$, transitioning from stratified flow as the waves bridge the gap to the top of the pipe. Taitel and Dukler[3.1-4] used $|v_g|$ rather than $|v_g - v_f|$, but the code was modified to

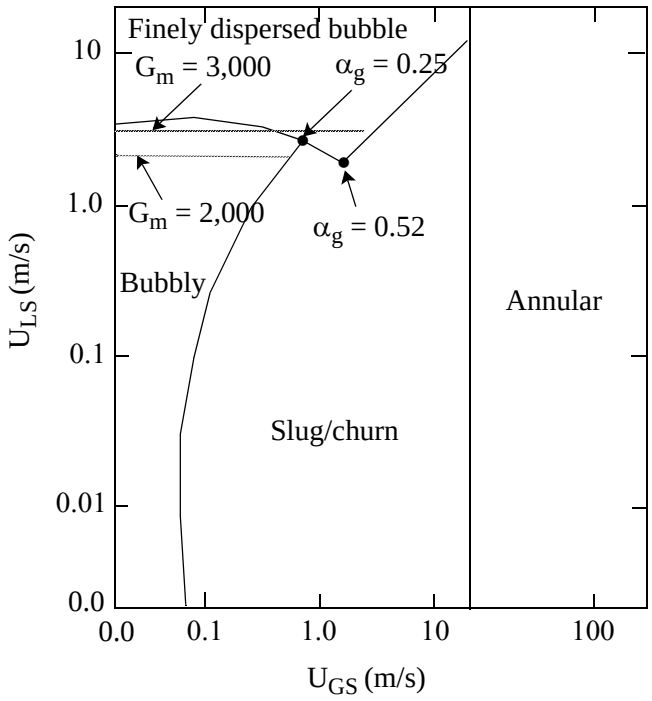

Figure 3.1-4 Flow-pattern map for air/water at 25 °C, 0.1 MPa, in a vertical 5.0-cm-diameter tube showing G_m = 2,000, 3,000 kg/m^2-s.

use $|v_g - v_f|$ based on TPTF experiment comparisons by Kukita et al.[3.1-13] (see Section 3.1.3). In addition, to disallow high flow cases, G must be less than 3,000 kg/m^2•s.

It is clear that the horizontal stratification criterion of Taitel and Dukler[3.1-4] requires some comparison with experiment to assess its validity. Taitel and Dukler[3.1-4] compare their transition criteria with the published map of Mandhane et al.[3.1-2] The comparison is quite favorable for the conditions of air-water at 25 °C and 1 atm in a 2.5-cm-diameter pipe. Choe et al.[3.1-11] show that the Taitel and Dukler[3.1-4] criterion works fairly well between intermittent and separated flow for liquids of low or moderate viscosity.

In summary, there is evidence that the Taitel and Dukler[3.1-4] horizontal stratification criterion works for low- and moderate-viscosity liquids, including water, at least in small-diameter pipes (up to 5 cm).

3.1.3 Effects of Scale

Experimental evidence reported by Kukita et al.[3.1-13] obtained at the JAERI TPTF separate-effects facility for horizontal flow of steam and water in an 18-cm-diameter pipe at high pressure (3 - 9 MPa) indicates that horizontally-stratified flow exists for conditions for which RELAP5/MOD2 predicted

unseparated flows. This failure of the stratification criterion [Equation (3.1-2)] was attributed by **Reference 3.1-13** largely to the fact that the code used the absolute vapor/gas velocity rather than relative velocity (v_g - v_f) to test for a stratification condition. Upon substituting relative velocity for vapor/gas velocity, which is what is used in ATHENA, it is shown that predictions for void fraction are significantly improved.[3.1-13]

3.1.4 References

3.1-1. M. Ishii and K. Mishima, *Study of Two-Fluid Model and Interfacial Area,* NUREG/CR-1873, ANL-80-111, Argonne National Laboratory, December 1980.

3.1-2. J. M. Mandhane, G. A. Gregory, and K. Aziz, "A Flow Pattern Map for Gas-Liquid Flow in Horizontal Pipes," *International Journal of Multiphase Flow, 1,* 1974, pp. 537-553.

3.1-3. J. Weisman, D. Duncan, J. Gibson, and T. Crawford, "Effects of Fluid Properties and Pipe Diameter on Two-Phase Flow Patterns in Horizontal Lines," *International Journal of Multiphase Flow, 5,* 1979, pp. 437-462.

3.1-4. Y. Taitel and A. E. Dukler, "A Model for Predicting Flow-Regime Transitions in Horizontal and Near Horizontal Gas-Liquid Flow," *AIChE Journal, 22,* 1, 1976, pp. 47-55.

3.1-5. Y. Taitel, N. Lee, and A. E. Dukler, "Transient Gas-Liquid Flow in Horizontal Pipes: Modeling Flow Pattern Transitions," *AIChE Journal, 24,* 5, 1978, pp. 920-934.

3.1-6. Y. Taitel, D. Bornea, and A. E. Dukler, "Modeling Flow Pattern Transitions for Steady Upward Gas-Liquid Flow in Vertical Tubes," *AIChE Journal, 26,* 3, 1980, pp. 345-354.

3.1-7. P. Griffith and G. B. Wallis, "Two-Phase Slug Flow," *Journal of Heat Transfer, 83,* 1961, pp. 307-318.

3.1-8. P. Griffith and G. A. Snyder, *The Bubbly-Slug Transition in a High Velocity Two-Phase Flow,* MIT Report 5003-29, TID-20947, July 1964.

3.1-9. N. A. Radovcich and R. Moissis, *The Transition from Two-Phase Bubble Flow to Slug Flow,* MIT Report 7-7673-22, June 1962.

3.1-10. G. F. Hewitt, "Two-Phase Flow Patterns and Their Relationship to Two-Phase Heat Transfer," *Two-Phase Flows and Heat Transfer, 1,* S. Kakac and F. Mayinger (eds.), Washington, D. C.: Hemisphere, 1977, pp. 11-35.

3.1-11. W. G. Choe, L. Weinberg, and J. Weisman, "Observation and Correlation of Flow Pattern Transition in Horizontal, Co-Current Gas-Liquid Flow," *Two-Phase Transport and Reactor Safety,* N. Veziroglu and S. Kakac (eds.), Washington, D. C.: Hemisphere, 1978.

3.1-12. D. Barnea, "Transition from Annular Flow and from Dispersed Bubble Flow - Unified Models for the Whole Range of Pipe Inclinations," *International Journal of Multiphase Flow, 12,* 1986, pp. 733-744.

3.1-13. Y. Kukita, Y. Anoda, H. Nakamura, and K. Tasaka, "Assessment and Improvement of RELAP5/MOD2 Code's Interphase Drag Models," *24th ASME/AIChE National Heat Transfer Conference, Pittsburgh, PA, August 9-12, 1987.*

3.2 Vertical Volume Flow Regime Map

3.2.1 Map as Coded

The vertical volume flow regime map is for upflow, downflow, and countercurrent flow in volumes whose inclination (vertical) angle ϕ is such that $60 < |\phi| \leq 90$ degrees. An interpolation region between vertical and horizontal flow regimes is used for volumes whose absolute value of the inclination (vertical) angle is between 30 and 60 degrees.

A schematic of the vertical flow regime map as coded in ATHENA is shown in **Figure 3.2-1**. The schematic is three-dimensional to illustrate flow-regime transitions as functions of void fraction α_g, average mixture velocity v_m, and boiling regime [pre-critical heat flux (CHF), transition, and post-dryout], where G_m is given by Equation (3.1-1), and

$$v_m = \frac{G_m}{\rho_m} \tag{3.2-1}$$

$$\rho_m = \alpha_g\rho_g + \alpha_f\rho_f \ . \tag{3.2-2}$$

The map consists of bubbly, slug, annular mist, and dispersed (droplet or mist) flows in the pre-CHF regime; inverted annular, inverted slug and dispersed (droplet or mist) flows in post-dryout; and vertically stratified for sufficiently low-mixture velocity v_m. Transition regions provided in the code are shown. Details of the interpolating functions employed for the transition regions are given in the sections dealing with the actual heat/mass transfer and drag correlations. Values for the parameters governing the flow-regime transitions are listed below and shown in **Figure 3.2-2**.

$$\alpha_{BS} = \alpha^*_{BS} \qquad \text{for } G_m \leq 2{,}000 \text{ kg/m}^2\text{-s} \tag{3.2-3}$$

$$\alpha_{BS} = \alpha^*_{BS} + \frac{(0.5 - \alpha^*_{BS})}{1{,}000}\ (G_m - 2{,}000) \qquad \text{for } 2{,}000 < G_m < 3{,}000 \text{ kg/m}^2\text{-s} \tag{3.2-4}$$

$$\alpha_{BS} = 0.5 \qquad \text{for } G_m \geq 3{,}000 \text{ kg/m}^2\text{-s} \tag{3.2-5}$$

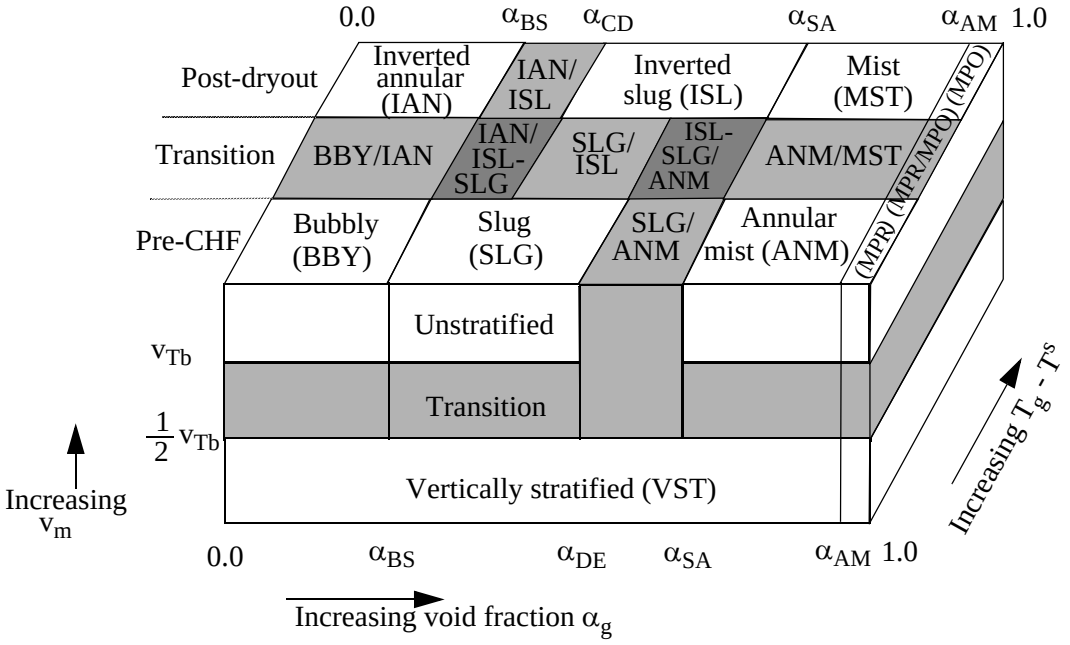

Figure 3.2-1 Schematic of vertical flow-regime map with hatchings indicating transitions.

$$\alpha^*_{BS} = \max \{0.25 \min [1, (0.045D^*)^8], 10^{-3}\} \quad (3.2\text{-}6)$$

where $D^* = D\left[\frac{g(\rho_f - \rho_g)}{\sigma}\right]^{1/2}$

$$\alpha_{CD} = \alpha_{BS} + 0.2 \quad (3.2\text{-}7)$$

$$\alpha_{SA} = \max [\alpha^{min}_{AM}, \min(\alpha^f_{crit}, \alpha^e_{crit}, \alpha^{max}_{BS})] \quad (3.2\text{-}8)$$

$$\alpha^f_{crit} = \min\left\{\frac{1}{v_g}\left[\frac{gD(\rho_f - \rho_g)}{\rho_g}\right]^{1/2}, 1.0\right\} \quad \text{for upflow} \quad (3.2\text{-}9)$$

$$\alpha^f_{crit} = 0.75 \quad \text{for downflow and countercurrent flow} \quad (3.2\text{-}10)$$

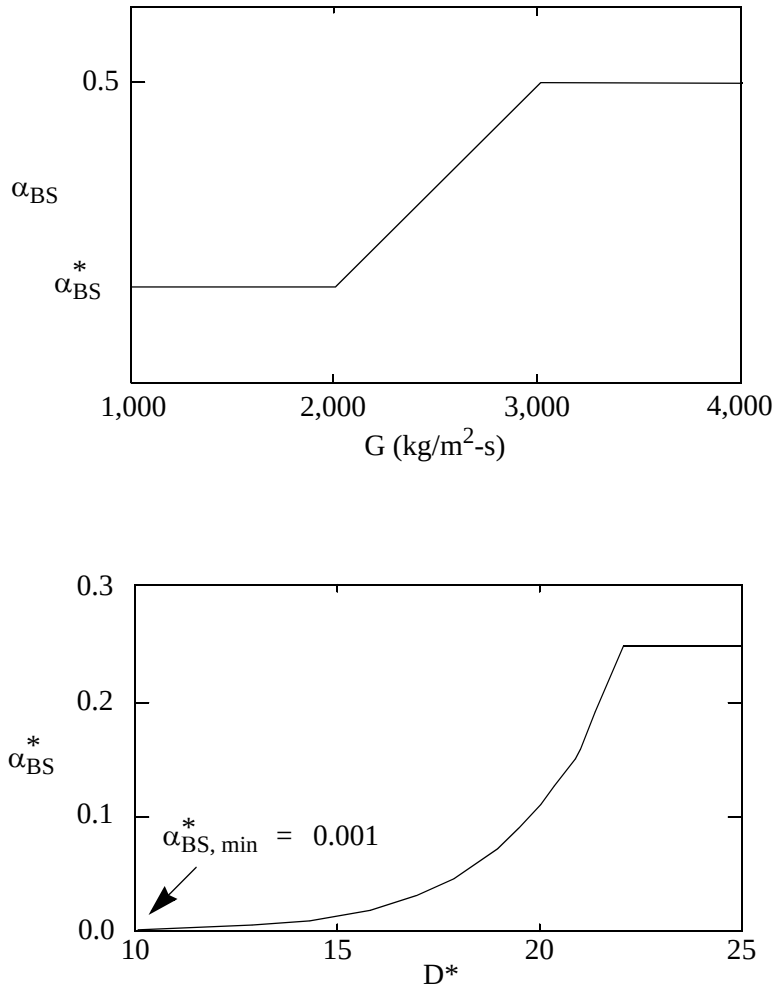

Figure 3.2-2 Vertical flow regime transition parameters in ATHENA.

$$\alpha^{e}_{crit} = \min\left\{\frac{3.2}{v_g}\left[\frac{g\sigma(\rho_f-\rho_g)}{\rho_g^2}\right]^{1/4}, 1.0\right\} \tag{3.2-11}$$

$$\alpha^{min}_{AM} = \begin{cases} 0.5 & \text{pipes} \\ 0.8 & \text{bundles} \end{cases} \tag{3.2-12}$$

$$\alpha^{max}_{BS} = 0.9 \tag{3.2-13}$$

$$\alpha_{DE} = \max(\alpha_{BS}, \alpha_{SA} - 0.05) \tag{3.2-14}$$

$$\alpha_{AM} = 0.9999 \tag{3.2-15}$$

$$v_{TB} = 0.35\left[\frac{gD(\rho_f - \rho_g)}{\rho_f}\right]^{1/2} . \tag{3.2-16}$$

The terms α^f_{crit} and α^e_{crit} will be discussed in Section 3.2.2.2.

Two further conditions must be satisfied for the flow to be considered vertically stratified. In the case of control volumes having only one inlet and one outlet, the void fraction of the volume above must be greater than 0.7. In addition, the void fraction difference between the volume above and the control volume or between the control volume and the volume below, must be greater than 0.2. If there are multiple junctions above and below the volume in question, the upper volume having the smallest α_g is compared to the lower volume having the largest α_g. Only connecting volumes that are vertically oriented are considered. The term v_{Tb} is the Taylor bubble rise velocity and will be discussed in Section 3.2.2.1 and Section 3.2.2.5.

3.2.2 Map Basis and Assessment

The vertical flow-regime map is mapped according to void fraction for nonstratified, wetted-wall regimes. This conforms to the recommendation of Ishii and Mishima,[3.1-1] as discussed for the horizontal map in Section 3.1.2. The dry-wall flow regimes (particularly inverted annular and inverted slug) are included[3.2-1] to account for post-dryout heat transfer regimes where a wetted wall is physically unrealistic. Heat and mass transfer and drag relations for the transition boiling region between pre-CHF and dryout are found by interpolating the correlations on either side (**Figure 3.2-1**). This means that for certain void fractions in the transition boiling region, two and sometimes three adjacent correlations are combined to obtain the necessary relations for heat/mass transfer and drag. The exact nature of these transition relations are found in the appropriate sections describing the correlations in question. The further configuration of vertical stratification includes a transition region, Section 3.2.1, wherein up to four correlations are combined to obtain the required constitutive relations.

3.2.2.1 Bubbly-to-Slug Transition. The transition from bubbly flow to slug flow is based on Taitel, Bornea, and Dukler[3.1-6]. The transition is the same as in the horizontal volume flow map, Section 3.1.2.1, except for the additional provision of the effect of small tube diameter.

When the rise velocity of bubbles in the bubbly regime, given by Taitel, Bornea, and Dukler[3.1-6] as

$$v_{sb} = 1.53\left[\frac{g(\rho_f - \rho_g)\sigma}{\rho_f^2}\right]^{1/4} \tag{3.2-17}$$

exceeds the Taylor bubble rise velocity, Equation (3.2-16), it is assumed that bubbly flow cannot exist, since the bubbles will approach the trailing edges of Taylor bubbles and coalesce. As shown in Equation (3.2-16), the rise velocity of Taylor bubbles is limited by the pipe diameter such that for sufficiently small D, $v_{Tb} < v_{sb}$, thereby precluding bubbly flow. Equating v_{Tb} and v_{sb} yields the critical pipe diameter,

$$D_{crit} = 19.11\left[\frac{\sigma}{g(\rho_f - \rho_g)}\right]^{1/2} \tag{3.2-18}$$

below which bubbly flow is theorized not to exist.

In ATHENA, the coefficient in Equation (3.2-18) has been modified to 1/0.045 = 22.22, precluding bubbly flow for a pipe diameter up to 16% greater than given by Equation (3.2-18). This criterion is observed down to a void fraction of 0.001 (**Figure 3.2-2**b). The designation of $\alpha_{BS,min}$ = 0.001 as the minimum void fraction at which slug flow may exist and the modification to use 22.22 were incorporated to obtain better agreement with data.[3.2-2]

In ATHENA for bundles, the transition from bubbly flow to slug flow (α_{BS}) is constrained from being less than 0.25, This was necessary to obtain good results in the developmental assessments.

3.2.2.2 Slug-to-Annular Mist Transition. The ATHENA vertical flow-regime map combines slug and churn flow regimes into a single regime called slug flow. Also, the annular flow regime and the annular mist regime are combined into a single regime called annular mist flow. (An exception to this occurs for the annulus component in which strictly annular flow exists with no droplets.) The transition from slug flow to annular mist flow is derived from the churn to annular flow transition of Taitel, Bornea, and Dukler[3.1-6] and Mishima-Ishii[3.2-3]

The analyses performed by Taitel et al.[3.1-6] and Mishima and Ishii[3.2-4] indicate that the annular flow transition is principally governed by criteria of the form

$$j_g^* = \frac{\alpha_g v_g}{\left[\frac{gD(\rho_f - \rho_g)}{\rho_g}\right]^{1/2}} \geq j_{g,crit}^* \tag{3.2-19}$$

$$Ku_g = \frac{\alpha_g v_g}{\left[\frac{g\sigma(\rho_f - \rho_g)}{\rho_g^2}\right]^{1/4}} \geq Ku_{g,crit} \tag{3.2-20}$$

with the first criterion (flow reversal) controlling the transition in small tubes and the second criterion (droplet entrainment) applying in large tubes. Unfortunately, the data comparisons reported by the authors

are not sufficient to make a judgment as to the most appropriate values of $j^*_{g,crit}$ and $Ku_{g,crit}$. However, McQuillan and Whalley[3.2-5,3.2-6] have compared these transition criteria against experimental flow-pattern data covering pipe diameters from 1 to 10.5 cm and a wide range of fluid conditions. They considered the above criteria using

$$j^*_{g,crit} = 1 \tag{3.2-21}$$

$$Ku_{g,crit} = 3.2 \tag{3.2-22}$$

and obtained good predictions of the annular flow boundary in each case, with the first criterion producing slightly more accurate predictions. On reexamining the flow-pattern data, however, Putney[3.2-7] found that better agreement can be obtained if annular flow is deemed to occur when either criteria is satisfied. It was also apparent that other values of $j^*_{g,crit}$ and $Ku_{g,crit}$ would not lead to transition criteria having better agreement with the data. The effect of applying both criteria together causes the transition to be controlled by the first criterion in tubes with diameters less than

$$D_{h,lim} = 10.24\left[\frac{\sigma}{g(\rho_f - \rho_g)}\right]^{1/2} \tag{3.2-23}$$

and by the second criteria in larger tubes. This is consistent with the theoretical analysis of Mishima and Ishii and also results in a transition boundary which is continuous in diameter. For steam-water conditions in the range 1 to 100 bars, $D_{h,lim}$ in Equation (3.2-23) varies from 2.6 to 1.4 cm.

The above criteria would therefore appear to be the most acceptable for predicting the annular flow transition in tubes. Although the experimental flow pattern data used in their assessment only covered tubes with diameters up to 10.5 cm, their theoretical basis makes it reasonable to apply them to pipes with larger diameters. In addition, there seems to be no reason why they should not provide an adequate approximation of the annular flow transition in rod bundles. However, there is no direct proof of this.

The two criterion can be expressed as

$$\alpha^f_{crit} = \min\left\{\frac{1}{v_g}\left[\frac{gD(\rho_f - \rho_g)}{\rho_g}\right]^{1/2}, 1.0\right\} \qquad \text{for upflow} \tag{3.2-24}$$

$$\alpha^f_{crit} = 0.75 \qquad \text{for downflow and countercurrent flow} \tag{3.2-25}$$

$$\alpha_{crit}^{e} = \min\left\{\frac{3.2}{v_g}\left[\frac{g\sigma(\rho_f-\rho_g)}{\rho_g^2}\right]^{1/4}, 1.0\right\} \quad . \tag{3.2-26}$$

The min function is needed to keep the values less than or equal to 1.0.

The term α_{crit}^{f} for upflow is from Equations (3.2-19) and (3.2-21), and the term α_{crit}^{e} is from Equations (3.2-20) and (3.2-22). These criteria have a reasonable physical basis and, in the case of cocurrent upflow, are well supported by a large body of experimental data. Insufficient data are available to perform comparisons for down and countercurrent flows. As discussed earlier in this section, the minimum of α_{crit}^{f} and α_{crit}^{e} is used based on Putney's analysis.

In formulating the criteria, an attempt was made to maintain as much consistency as possible between the various flow situations. The difference in α_{crit}^{f} between upflow and down and countercurrent flows is unavoidable because the film instability/flow reversal mechanism that can cause a breakdown of annular flow in upflow is not appropriate when the liquid flows downwards. The absence of this mechanism leads to more relaxed criteria, and this reflects the preponderance of annular flow in such situations. The two values of α_{crit}^{f} are smoothed using the same weighting function, w_j, based on the mixture superficial velocity that is used for the junction flow regime map (see Section 3.5), with 0.465 replaced by 0.3.

A possible weakness in the above criteria is that, at low vapor/gas velocities, transition to annular flow may not occur until an unphysically high void fraction is attained, or not at all. Likewise, at high vapor/gas velocities, the transition could occur at an unphysically low void fraction. To guard against these situations, the additional requirement is added that the annular flow transition can only occur in the void fraction range

$$\alpha_{AM}^{min} \le \alpha_g \le \alpha_{BS}^{max} \tag{3.2-27}$$

where α_{AM}^{min} is the minimum void fraction at which annular flow can exist, and α_{BS}^{max} is the maximum void fraction at which bubbly-slug flow can exist. The final transition criterion used in the code is then

$$\alpha_{SA} = \max[\alpha_{AM}^{min}, \min(\alpha_{crit}^{f}, \alpha_{crit}^{e}, \alpha_{BS}^{max})] \quad . \tag{3.2-28}$$

The code uses $\alpha_{AM}^{min} = 0.5$ and $\alpha_{BS}^{max} = 0.9$. For bundles in the code, the minimum void fraction for annular mist flow (α_{AM}^{min}) is 0.8. This was necessary to obtain good results in the developmental assessment.

The size of the transition region between slug and annular mist regimes ($\Delta\alpha_g = 0.05$) is based on engineering judgment.

3.2.2.3 Transition from Annular Mist Flow to Dispersed Flow. The void fraction (α_{AM}) upon which this transition is coded to take place corresponds to a very high vapor/gas fraction, $\alpha_g = 0.9999$. This vapor/gas fraction was chosen to allow a smooth transition to single-phase vapor/gas flow. In **Figure 3.2-1**, MPR stands for pre-CHF mist flow.

3.2.2.4 Post-Dryout Flow-Regimes (Inverted Annular, Inverted Slug, Dispersed Droplet). When surface temperatures and wall heat fluxes in confined boiling heat transfer situations are too high to allow surface wetting, inverted flow regimes occur. Inverted regimes are characterized by some form of liquid core surrounded by an annular vapor/gas blanket.[3.2-1]

A series of studies have begun an investigation into the nature and the controlling parameters of inverted flow-regimes including that of De Jarlais and Ishii[3.2-1]. They report that upon reaching CHF, bubbly flow transitions to inverted annular, slug/plug flow becomes inverted slug, and annular/annular-mist flow loses its annular liquid film and becomes dispersed droplet flow (**Figure 3.2-3**).

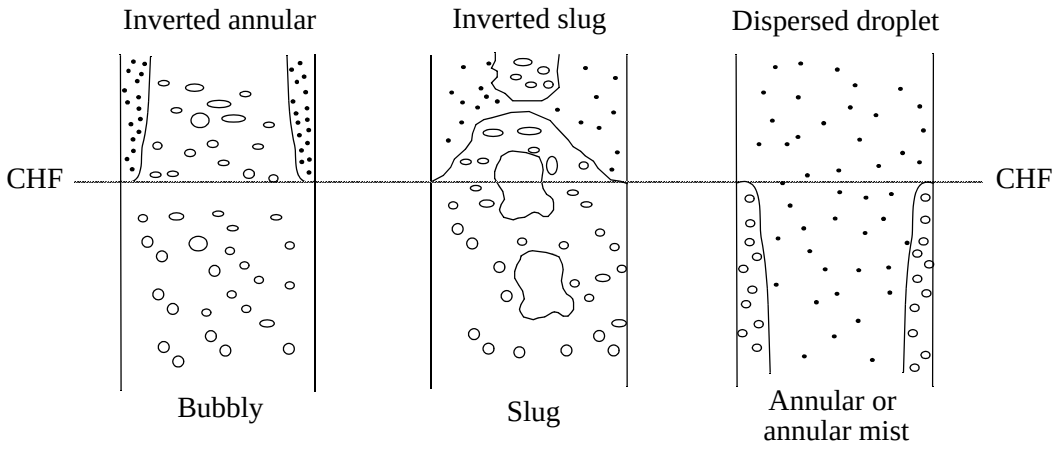

Figure 3.2-3 Flow-regimes before and after the critical heat flux (CHF) transition.

De Jarlais and Ishii[3.2-1] recommend that initially-inverted annular/initially-inverted slug and initially-inverted slug/initially-dispersed droplet transitions be based on the same criteria as their pre-CHF counterparts (bubbly-slug and slug-annular, respectively). The correspondence between pre- and post-CHF transitions is observed, as shown in **Figure 3.2-1**. In **Figure 3.2-1**, MPO stands for post-CHF mist flow.

A further transition region between pre-CHF and dryout where the surface is neither fully wet nor fully dry (analogous to transitional pool boiling) is present in the vertical flow-regime map. While boiling under flowing conditions is not the same as pool boiling, such a transitional regime seems appropriate.

3.2.2.5 Vertically Stratified Flow. The vertically stratified flow regime is designed to apply to situations where the flow in a vertical conduit is so slow that an identifiable vapor/gas-liquid interface is present. The vertical stratification model is not intended to be a mixture level model. The restriction that the average mixture velocity v_m be less than the Taylor bubble rise velocity represents the first requirement, since any large bubbles would have risen to the vapor/gas-liquid interface maintaining the stratified situation. This is given as follows:

$$v_m < v_{Tb}$$

or

$$\frac{\alpha_g \rho_g |v_g| + \alpha_f \rho_f |v_f|}{\rho_m} < 0.35 \left[g \frac{D(\rho_f - \rho_g)}{\rho_f} \right]^{1/2} . \qquad (3.2\text{-}29)$$

The second requirement consists of several criteria involving the axial void profile in three contiguous cells. Using **Figure 3.2-4**, the criteria are

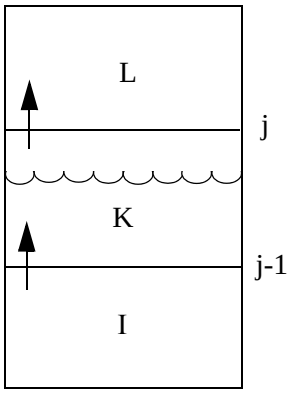

Figure 3.2-4 Three vertical volumes with the middle volume being vertically stratified.

$$\alpha_{g,L} > 0.7$$

and

$$\alpha_{g,L} - \alpha_{g,K} > 0.2 \text{ or } \alpha_{g,K} - \alpha_{g,I} > 0.2 . \qquad (3.2\text{-}30)$$

These two criteria are the default level-detection logic for a normal profile from TRAC-B.[3.0-1,3.0-3] A third criteria is

$$\alpha_{g,L} - \alpha_{g,I} > 0.2 \ . \tag{3.2-31}$$

In addition, the following two criteria, which were also present in RELAP5/MOD2, are used:

$$\alpha_{g,I} \leq \alpha_{f,K} \leq \alpha_{g,L} \tag{3.2-32}$$

and

$$10^{-5} < \alpha_{g,K} < 0.99999 \ . \tag{3.2-33}$$

The first criterion helps ensure that only one volume at a time in a stack of vertical volumes is vertically stratified. If the top volume (L) is dead end, a value of $\alpha_{g,L} = 1.0$ is used in the above logic. If the top volume (L) is horizontal, the void fraction $\alpha_{g,L}$ of this volume is used. The second criterion effectively precludes an essentially single-phase flow from inappropriately being labeled stratified.

If more than one junction is connected to the top, the volume above with the smallest void fraction will be treated as the "above volume;" if more than one junction is connected to the bottom, the volume below with the largest void fraction will be treated as the "below volume."

3.2.3 Effects of Scale

It has been postulated that a maximum diameter exists for vertical flow of individual dispersed phase drops/bubbles in a continuous phase, precluding the existence of slug flow as it is usually defined. Kocamustafaogullari, Chen, and Ishii[3.2-8] have derived a unified theory for the prediction of maximum fluid particle size for drops and bubbles. They developed a simple model based on the hypothesis that fluid particle breakup will occur if the rate of growth of a disturbance at the dispersed phase/continuous phase interface is faster than the rate at which it propagates around the interface. They show that the same theory is applicable to liquid in liquid, droplets in vapor/gas, and bubbles in liquid, and show a broad range of experimental data compared to their theoretical predictions with reasonably good results. This theory suggests that there will exist ranges where bubbles cannot coalesce to form slugs that are as large as the pipe diameter, thus preventing transition from bubbly to slug flow.

Some experimental evidence for large pipes also appears to support the above theory. Air-water flow experiments conducted by Science Applications Incorporated Corporation (SAIC) indicated that slug flow was unable to form in a 0.305-cm vertical pipe; rather, a transition from bubbly to bubbly/churn-type flow with strong local recirculation patterns took place.[3.2-9] The criteria used for pipe correlations for interphase

drag in the code is 0.08 m, i.e., for diameters greater than 0.08 m, slug flow correlations are not used in pipes. This is discussed in Section 6.

3.2.4 References

3.2-1. G. DeJarlais and M. Ishii, *Inverted Annular Flow Experimental Study,* NUREG/CR-4277, ANL-85-31, Argonne National Laboratory, April 1985.

3.2-2. V. H. Ransom et al., *RELAP5/MOD2 Code Manual, Volume 3: Developmental Assessment Problems,* EGG-TFM-7952, Idaho National Engineering Laboratory, December 1987.

3.2-3. K. Mishima and M. Ishii, "Flow Regime Transition Criteria for Upward Two-Phase Flow in Vertical Tubes," *International Journal of Heat and Mass Transfer, 27,* 1984, pp. 723-737.

3.2-4. K. Mishima and M. Ishii, *Flow Regime Transition Criteria Consistent with Two-Fluid Model for Vertical Two-Phase Flow,* NUREG/CR-3338, ANL-83-42, Argonne National Laboratory, April 1983.

3.2-5. K. W. McQuillan and P. D. Whalley, *Flow Patterns in Vertical Two-Phase Flow,* AERE-R 11032, 1983.

3.2-6. K. W. McQuillan and P. D. Whalley, "Flow Patterns in Vertical Two-Phase Flow," *International Journal of Multiphase Flow, 11,* 1985, pp. 161-175.

3.2-7. J. M. Putney, *An Assessment of the Annular Flow Transition Criteria and Interphase Friction Models in RELAP5/MOD2,* CERL Report RD/L/3451/R89, PWR/HTWG/A(88)653, February 1989.

3.2-8. G. Kocamustafaogullari, I. Y. Chen, and M. Ishii, *Unified Theory for Predicting Maximum Fluid Particle Size for Drops and Bubbles,* NUREG/CR-4028, ANL-84-67, Argonne National Laboratory, October 1984.

3.2-9. T. K. Larson, *An Investigation of Integral Facility Scaling and Data Relation Methods (Integral System Test Program),* NUREG/CR-4531, EGG-2440, Idaho National Engineering Laboratory, February 1987, p. 43.

3.3 High Mixing Volume Flow Regime Map

3.3.1 Map as Coded

The high mixing flow regime map is included in ATHENA to account for flow through pumps and compressors. **Figure 3.3-1** illustrates the map, which consists of bubbly and dispersed flow with a transition between them. The transition consists of weighted combinations of bubbly and dispersed correlations, which are described in detail in the sections above. The map is based purely on void fraction, with bubbly flow occurring below or equal to 0.5 and dispersed flow above or equal to 0.95.

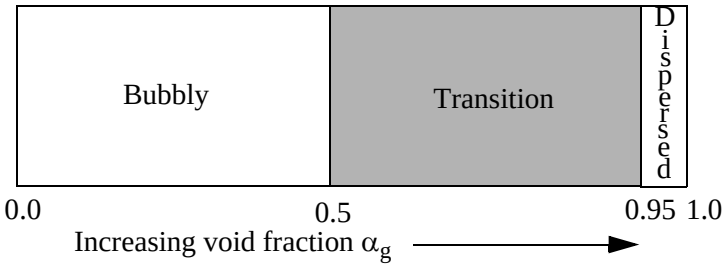

Figure 3.3-1 Schematic of high mixing flow regime map.

3.3.2 Map Basis and Assessment

The upper limit for bubbly flow of $\alpha_g = 0.5$ is based on Taitel, Bornea, and Dukler's[3.1-6] postulate discussed in Section 3.1.2.1. In the absence of definitive data, this is a reasonable postulate, since vigorous mixing takes place in the pumps and compressors. The transition to dispersed flow is consistent with Wallis,[3.3-1] who presents data indicating that only dispersed flow exists above $\alpha_g \approx 0.96$. (See Section 3.2.2.2 for further discussion.) The use of a transitional region between bubbly and dispersed flow rather than including a slug flow regime is appropriate, since the highly mixed nature of flow in the pump or compressor would disallow large vapor/gas bubbles from forming.

3.3.3 Reference

3.3-1. G. B. Wallis, *One-dimensional Two-phase Flow,* New York: McGraw-Hill, 1969.

3.4 ECC Mixer Volume Flow Regime Map

Prior to the introduction of the ECC mixer (ECCMIX) component, ATHENA included the three previously discussed flow regime maps, as described in the RELAP5/MOD2 manual[3.4-1] and in the RELAP5/MOD2 models and correlations report.[3.4-2] None of those, however, would apply specifically to the condensation process in a horizontal pipe near the emergency core coolant (ECC) injection point. A flow regime map for condensation inside horizontal tubes is reported by Tandon et al.,[3.4-3] and it was considered a more suitable basis for the interfacial heat transfer calculation in condensation for this geometry. According to **Reference 3.4-3**, the two-phase flow patterns during condensation inside a horizontal pipe may be identified in terms of the local volumetric ratios of liquid and vapor/gas, $\frac{1-\alpha_g}{\alpha_g}$, and the nondimensional vapor/gas velocity, $v_g^* = \left[\frac{X_{flow} G}{gD\rho_g(\rho_f - \rho_g)}\right]^{1/2}$. Here, X_{flow} = flow quality = $\frac{\alpha_g\rho_g v_g}{\alpha_g\rho_g v_g + \alpha_f\rho_f v_f}$ and G = mass flux = $\alpha_g\rho_g v_g + \alpha_f\rho_f v_f$. Thus $X_{flow}G = \alpha_g\rho_g v_g$. The term D is the diameter

of the channel. The flow pattern transition boundaries are presented in terms of the volumetric ratio on the abscissa and v_g^* on the ordinate. The condensation flow regime map of Tandon et al., **Reference 3.4-3**, does not include any zone for bubbly flow; the existence of a bubbly flow regime at very low void fractions cannot be logically excluded, particularly in a highly turbulent liquid flow. For this reason, a region of bubbly flow was included for void fractions less than 20% ($\alpha_g \leq 0.2$). Furthermore, to protect against failure of the numerical solution, it is necessary to specify some reasonable flow patterns for every combination of the volumetric ratios and v_g^*, and to include transition zones around some of the boundaries between different flow patterns. The transition zones are needed for interpolation between the calculated values of the correlations for the interfacial heat transfer and friction that apply for the different flow patterns. These interpolations prevent discontinuities that would exist otherwise and could make the numerical solutions very difficult. With these considerations, the flow regime map of **Reference 3.4-3** was modified, as shown in **Figure 3.4-1**. The modified condensation flow-regime map comprises eleven different zones that include six basic patterns and five interpolation zones. **Table 3.4-1** shows a list of the basic flow patterns and the interpolation zones for the ECCMIX component, with their acronyms and flow regime numbers, that are printed out in the ATHENA output.

Table 3.4-1 List of flow regimes in the ECCMIX component.

Flow regime number[1]	**Flow regime**	**Acronym**	**Remarks**
16[a]	Wavy	MWY	Basic pattern
17	Wavy/annular mist	MWA	Transition between wavy and annular mist flows
18	Annular mist	MAM	Basic pattern
19	Mist	MMS	Basic pattern
20	Wavy/slug	MWS	Transition between wavy and slug flows
21	Wavy/plug/slug	MWP	Transition between wavy, plug, and slug
22	Plug	MPL	Basic pattern
23	Plug/slug	MPS	Transition between plug and slug
24	Slug	MSL	Basic pattern
25	Plug/bubbly	MPB	Transition between plug and bubbly
26	Bubbly	MBB	Basic pattern

1. Flow regime numbers 1 through 15 are used in ATHENA for flow patterns in other components.

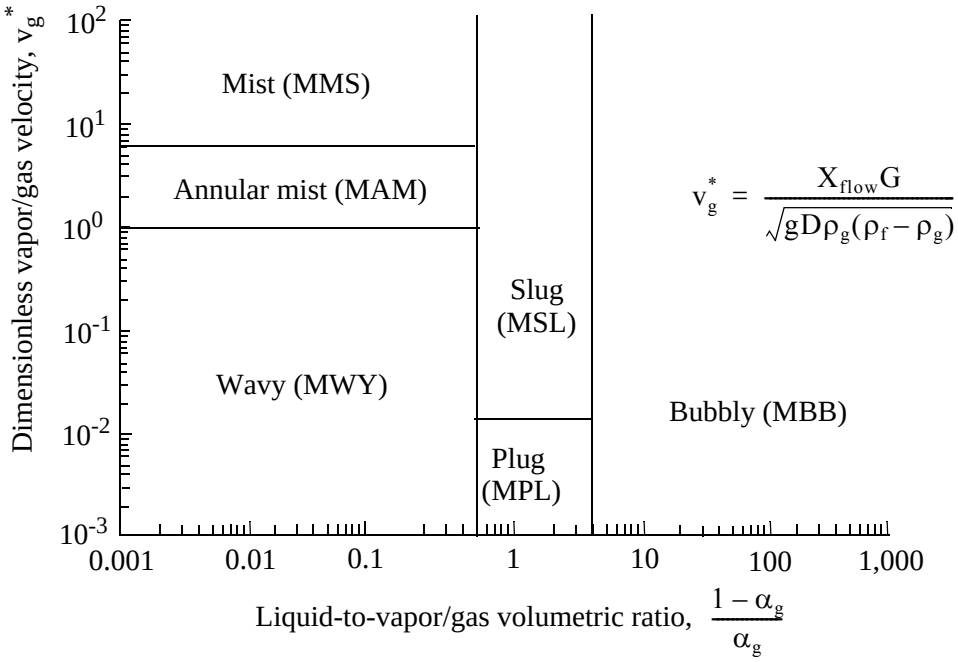

Figure 3.4-1 Schematic of ECC mixer volume flow regime map (modified Tandon et al.[3.4-3]).

The variable names that are used in the coding for the coordinates of the condensation flow regime map are

$$\text{voider} = \frac{1-\alpha_g}{\alpha_g} \tag{3.4–1}$$

$$\text{stargj} = v_g^* = \frac{X_{flow}G}{[gD\rho_g(\rho_f - \rho_g)]^{1/2}} \quad . \tag{3.4-2}$$

In the coding, $X_{flow}G$ is determined by averaging $\alpha_g\rho_g v_g$ for junctions 2 and 3, where it is assumed there is no vapor/gas in junction 1 (ECC injection junction).

In terms of these variables, the different zones of the flow regime map are

If voider > 4.0, bubbly flow, MBB

If 3.0 < voider $\leq$ 4.0 and stargj < 0.01, transition, MPB

If 0.5 < voider $\leq$ 4.0 and stargj > 0.0125, slug flow, MSL

If 0.625 < voider $\leq$ 4.0, and 0.01 < stargj $\leq$ 0.0125, transition, MPS

If 0.5 < voider $\leq$ 3.0, and stargj $\leq$ 0.01, plug flow, MPL

If 0.5 < voider $\leq$ 0.625, and 0.01 < stargj $\leq$ 0.0125, transition, MWP

If 0.5 < voider $\leq$ 0.625, and 0.0125 < stargj $\leq$ 1.0, transition, MWS

If voider $\leq$ 0.5 and stargj $\leq$ 1.0, wavy flow, MWY

If voider $\leq$ 0.5, and 1.0 < stargj $\leq$ 1.125, transition, MWA

If voider $\leq$ 0.5, and 1.125 < stargj $\leq$ 6.0, annular mist, MAM

If voider $\leq$ 0.5, and stargj > 6.0, mist flow, MMS.

In the coding, each one of these regions is identified by a flow pattern identification flag, MFLAG, whose value varies from 1 for wavy flow to 11 for bubbly flow. The flow regime number in **Table 3.4-1** is MFLAG + 15.

In addition to the transition zones that are shown in **Figure 3.4-1** and listed in **Table 3.4-1**, there are two other transitions, namely,

- Transition between wavy and plug flows.
- Transition between annular mist and mist (or droplet) flows.

Interpolations between the interfacial friction, interfacial heat transfer, and the wall friction rates for these transitions are performed through the gradual changes in the interfacial area in the first case and the droplet entrainment fraction in the second case. Hence, there was no need for specifying transition zones for these on the flow regime map.

3.4.1 References

3.4-1. V. H. Ransom et al., *RELAP5/MOD2 Code Manual*, NUREG/CR-4312, EGG-2396, Idaho National Engineering Laboratory, August 1985 and December 1985, revised March 1987.

3.4-2. R. A. Dimenna et al., *RELAP5/MOD2 Models and Correlations*, NUREG/CR-5194, EGG-2531, Idaho National Engineering Laboratory, August 1988.

3.4-3. T. N. Tandon, H. K. Varma, and C. P. Gupta, "A New Flow Regime Map for Condensation Inside Horizontal Tubes," *Journal of Heat Transfer, 104,* November 1982, pp. 763-768.

3.5 Junction Flow Regime Maps

The junction map is based on both junction and volume quantities. It is used for the interphase drag and shear, as well as the coefficient of virtual mass. The flow regime maps used for junctions are the same as used for the volumes and are based on the work of Taitel and Dukler,[3.1-4,3.1-5] Ishii,[3.1-1] and Tandon et al.[3.4-3]

Junction quantities used in the map decisions are junction phasic velocities, donored (based on phasic velocities) phasic densities, and donored (based on superficial mixture velocity) surface tension.

The junction void fraction, $\alpha^*_{g,j}$, is calculated from either of the volume void fractions of the neighboring volumes, $\alpha_{g,K}$ or $\alpha_{g,L}$, using a donor direction based on the mixture superficial velocity, j_m. A cubic spline weighting function is used to smooth the void fraction discontinuity across the junction when $|j_m| \leq 0.465$ m/s. The purpose of this method is to use a void fraction that is representative of the real junction void fraction. This is assumed to have the form

$$\alpha^*_{g,j} = w_j \bullet \alpha_{g,K} + (1 - w_j) \bullet \alpha_{g,L} \tag{3.5-1}$$

where

$$w_j = \begin{cases} 1.0 & j_m > 0.465 \text{ m/s} \\ x_1^2\,(3 - 2x_1) & -0.465 \text{ m/s} \leq j_m \leq 0.465 \text{ m/s} \\ 0.0 & j_m < -0.465 \text{ m/s} \end{cases} \tag{3.5-2}$$

$$x_1 = \frac{j_m + 0.465}{0.93} \tag{3.5-3}$$

$$j_m = \dot{\alpha}_{g,j} v_{g,j} + \dot{\alpha}_{f,j} v_{f,j}\,. \tag{3.5-4}$$

For horizontal stratified flow, the void fraction from the entrainment/pullthrough (or offtake) model is used. The case of vertical stratified flow will be discussed in Section 6.1.3.8. The junction mass flux is determined from

$$G_j = \dot{\alpha}_{g,j}\dot{\rho}_{g,j}|v_{g,j}| + \dot{\alpha}_{f,j}\dot{\rho}_{f,j}|v_{f,j}| \quad . \tag{3.5-5}$$

The methods for calculating $\alpha^*_{g,j}$ and G_j are the same ones that are used in TRAC-B.[3.5-1,3.5-3,3.5-3]

As with the volumes, four junction flow regime maps are used. They are a horizontal map for flow in pipes; a vertical map for flow in pipes/bundles; a high mixing map for flow in pumps and compressors; and an ECC mixer map. These will not be discussed in any detail because they are similar to the volumes flow regime maps. The decision of whether a junction is in the horizontal or vertical junction flow regime is done slightly differently than for a volume. The junction inclination (vertical) angle is determined from either of the volume inclination (vertical) angles, ϕ_K or ϕ_L, based on input by the user using a donor direction based on the mixture superficial velocity, j_m. The formula used is similar to that used for the junction void fraction; however, it uses the sine of the angle. It is given by

$$\sin \phi_j = w_j \sin \phi_K + (1 - w_j) \sin \phi_L \quad . \tag{3.5-6}$$

The vertical flow regime map is for junctions whose junction inclination (vertical) angle ϕ_j is such that $60 \leq |\phi_j| \leq 90$ degrees. The horizontal flow regime map is for junctions whose junction inclination (vertical) angle ϕ_j is such that $0 \leq |\phi_j| \leq 30$ degrees. An interpolation region between vertical and horizontal flow regimes is used for junctions whose junction inclination (vertical) angle ϕ_j is such that $30 < |\phi_j| < 60$ degrees. This interpolation region is used to smoothly change between vertical and horizontal flow regimes.

3.5.1 References

3.5-1. W. L. Weaver et al., *TRAC-BF1 Manual: Extensions to TRAC-BD1/MOD1,* NUREG/CR-4391, EGG-2417, Idaho National Engineering Laboratory, August 1986.

3.5-2. M. M. Giles et al., *TRAC-BF1/MOD1: An Advanced Best Estimate Computer Program for BWR Accident Analysis*, NUREG/CR-4356, EGG-2626, Idaho National Engineering Laboratory, June 1992 and August 1992.

3.5-3. S. Z. Rouhani et al., *TRAC-BF1/MOD1 Models and Correlations,* NUREG/CR-4391, EGG-2680, Idaho National Engineering Laboratory, August 1992.

4 Closure Relations for the Fluid Energy Equations

The one-dimensional nature of the field equations for the two-fluid model found in ATHENA precludes direct simulation of effects that depend upon transverse gradients of any physical parameter, such as velocity or energy. Consequently, such effects must be accounted for through algebraic terms added to the conservation equations. These terms should be based on correlations deduced from experimental data for their representation, or on models developed from sound physical principles. Some of the correlations used in ATHENA, however, are based on engineering judgment, due partly to the incompleteness of the science and partly to numerical stability requirements. A significant effort has gone into providing smooth transitions from correlation to correlation as conditions evolve to prevent numerical instability.

The assessment of the heat transfer correlations used to provide closure for the energy equations is complicated by the detailed nature of the correlations themselves. In general, each correlation is designed to represent energy transfer under a specific set of thermal-hydraulic and thermodynamic conditions, and each is typically measured for a fairly limited range of those conditions. A determination of accuracy may be available for the developmental range of parameters, but an extension of the accuracy estimate outside that range is difficult at best, and perhaps impossible mathematically. This situation is especially evident in Section 4.2, which addresses the wall heat transfer correlations. By treating each correlational model individually, a critical reviewer might generally conclude that the database over which the model was developed does not apply directly to reactor geometries or thermal-hydraulic conditions. If left at this stage, a conclusion of inadequacy could be reached. Yet the correlations have, in general, enjoyed a fairly widespread utilization and have shown at least a qualitative applicability outside the documented data range for which they were developed. The use of any given heat transfer correlation, either directly or in a modified form, then becomes an engineering judgment, and the application to reactor conditions becomes an approximation to the expected reactor behavior. When viewed in this context, the use of integral assessments, which inherently measure a global response rather than a local response, becomes more meaningful.

4.1 Bulk Interfacial Heat Transfer

In ATHENA, the interfacial heat transfer between the vapor/gas and liquid phases in the bulk actually involves both heat and mass transfer. Temperature-gradient-driven bulk interfacial heat transfer is computed between each phase and the interface. The temperature of the interface is assigned the saturation value for the local pressure. Heat transfer correlations for each side of the interface are provided in the code. Since both superheated and subcooled temperatures for each phase are allowed, the heat transfer may be either into or away from the interface for each phase. All of the thermal energy transferred to the interface from either side contributes to vaporization as it is used to compute the mass transfer Γ_{ig} to the vapor/gas phase. Conversely, all of the heat transfer away from the interface contributes to condensation, since it is used to compute the mass transferred to the liquid phase ($-\Gamma_{ig}$). In other words, the cases of superheated liquid and superheated vapor/gas contribute to vaporization, while both subcooled liquid and

subcooled vapor/gas contribute to condensation. The net rate of mass transfer is determined by summing the contributions, positive and negative, from each side of the interface.

The form used in defining the heat transfer correlations for superheated liquid (SHL), subcooled liquid (SCL), superheated vapor/gas (SHG), and subcooled vapor/gas (SCG) is that for a volumetric heat transfer coefficient (W/m^3K). Since heat transfer coefficients are often given in the form of a dimensionless parameter (usually Nusselt number, Nu), the volumetric heat transfer coefficients are coded as

$$H_{ip} = \frac{k_p}{L} Nu\ a_{gf} = h_{ip} a_{gf} \qquad (4.1\text{-}1)$$

where

H_{ip} = volumetric interfacial heat transfer coefficient for phase p ($W/m^3 \cdot K$)

k_p = thermal conductivity for phase p ($W/m \cdot K$)

L = characteristic length (m)

a_{gf} = interfacial area per unit volume (m^2/m^3)

h_{ip} = interfacial heat transfer coefficient for phase p ($W/m^2 \cdot K$)

p = phase p (either f for liquid for g for vapor/gas).

Individual correlations for heat/mass transfer are fully detailed in Appendix 4A. Expressions for the cases of SHL, SCL, SHG, and SCG are given for each flow regime recognized by the code. The flow regimes are those cataloged in Section 3. The following section discusses the relationship between the coded correlations and the literature, the stabilizing and smoothing features built into the code, and assessments (when possible) of the validity of the expressions for operating conditions typical to nuclear reactors. The methods employed to smooth transitions amongst flow regimes are given in Appendix 4A and are discussed herein. Furthermore, the techniques used to incorporate effects due to noncondensable gases are presented and discussed. Reference should be made to the flow-regime maps in Section 3 to help clarify Appendix 4A and the discussion to follow hereafter.

When one of the phases is superheated, the other phase is allowed to be either superheated or subcooled. Likewise, if one of the phases is subcooled, the other phase is allowed to be either superheated or subcooled.

4.1.1 Flow Regime Correlations

Flow regime correlations are shared amongst the four flow regime maps (horizontal, vertical, high mixing, and ECC mixer) for flow regimes identified by the same names.

4.1.1.1 Bubbly Flow. In bubbly flow, the bubbles are viewed as spheres. If the liquid temperature is between one degree K subcooled and one degree K superheated, the final liquid coefficient H_{if} is the result of a cubic spline interpolation between the superheated and subcooled result.

4.1.1.1.1 Bubbly Superheated Liquid (SHL, $T_f > T^s$)--

Model as Coded

$$H_{if} = \left\{ \max \left[\begin{array}{ll} -\frac{k_f}{d_b}\frac{12}{\pi}\Delta T_{sf}\frac{\rho_f C_{pf}}{\rho_g h_{fg}}\beta & \text{Plesset} - \text{Zwick} \\ \frac{k_f}{d_b}(2.0 + 0.74 Re_b^{0.5}) & \text{modified Lee} - \text{Ryley} \end{array} \right] + 0.4|v_f|\rho_f C_{pf} F_1 \right\} (a_{gf} F_2 F_3) \quad (4.1\text{-}2)$$

otherwise

$$= \quad 0.0 \qquad \text{if } \alpha_g = 0 \text{ and } \Delta T_{sf} \geq 0$$

where

ΔT_{sf} = $T^s - T_f$

Re_b = $\frac{(1-\alpha_{bub})\rho_f v_{fg} d_b}{\mu_f} = \frac{We\ \sigma(1-\alpha_{bub})}{\mu_f (v_{fg}^2)^{1/2}}$

$We\ \sigma$ = $\max(We\ \sigma, 10^{-10})$

d_b = average bubble diameter ($= \frac{1}{2} d_{max}$)

= $\frac{We\ \sigma}{\rho_f v_{fg}^2}$, We = 5,

β = 1.0 for bubbly flow

a_{gf} = interfacial area per unit volume

$$= \frac{3.6\alpha_{bub}}{d_b}$$

α_{bub} = $\max(\alpha_g, 10^{-5})$

v_{fg} = relative velocity = $v_g - v_f$ $\alpha_g \geq 10^{-5}$

= relative velocity = $(v_g - v_f)\,\alpha_g 10^5$ $\alpha_g < 10^{-5}$

$$v_{fg}^2 = \max\left[v_{fg}^2, \frac{We\,\sigma}{\rho_f \min(D'\alpha_{bub}^{1/3}, D)}\right]$$

D = hydraulic diameter

D′ = 0.005 m for bubbly flow

$$F_1 = \frac{\min(0.001, \alpha_{bub})}{\alpha_{bub}}$$

$$F_2 = \frac{\min(0.25, \alpha_{bub})}{\alpha_{bub}}$$

F_3 = 1 $\Delta T_{sf} \leq -1$

= $\max[0.0, F_4(1+\Delta T_{sf}) - \Delta T_{sf}]$ $-1 < \Delta T_{sf} < 0$

= $\max(0.0, F_4)$ $\Delta T_{sf} \geq 0$

F_4 = $\min[10^{-5}, \alpha_g(1 - X_n)](10^5)$

X_n = noncondensable quality.

Model Basis and Assessment

The Nusselt number upon which the volumetric heat transfer coefficient H_{if} is based for SHL bubbly flow is coded to be the maximum value produced by one of two correlations. The first correlation is derived from an equation determined analytically by Plesset and Zwick,[4.1-1] which represents the growth rate of a bubble radius, e.g.,

$$\dot{r}_b = \frac{\Delta T_{sat} k_f}{h_{fg}\rho_g\left(\frac{\pi\alpha_f t}{3}\right)^{-1/2}} \tag{4.1-3}$$

where

$\dot{r}_b$ = time rate of change of bubble radius (m/s)

ΔT_{sat} = liquid phase superheat (K) (= T_f - T^s)

α_f = thermal diffusivity of liquid (m^2/s)

k_f = thermal conductivity of liquid (W/m•K)

h_{fg} = latent heat of vaporization (J/kg)

ρ_g = vapor/gas density (kg/m^3)

C_{pf} = specific heat of liquid (J/kg•K).

According to Collier,[4.1-2] the solution to Equation (4.1-3) is

$$r_b = \frac{2\Delta T_{sat} k_f}{h_{fg}\rho_g}\left(\frac{3t}{\pi\alpha_f}\right)^{1/2} . \tag{4.1-4}$$

Upon replacing the thermal diffusivity by its definition, substituting Equation (4.1-4) in Equation (4.1-3), and rearranging, one obtains

$$\dot{r}_b = \frac{6k_f\rho_f C_{pf}}{\pi r_b}\left(\frac{\Delta T_{sat}}{h_{fg}\rho_g}\right)^2 . \tag{4.1-5}$$

As the bubble grows, there is positive mass transfer Γ_{ig} to the vapor/gas phase given by

$$\Gamma_{ig} = \frac{\rho_g 4\pi r_b^2 \dot{r}_b}{V} \tag{4.1-6}$$

where V is the volume.

Γ_{ig} can also be given in terms of a heat transfer coefficient as

$$\Gamma_{ig} = \frac{h_b \Delta T_{sat} (4\pi r_b^2)}{h_{fg} \bullet V} \tag{4.1-7}$$

where h_b is the heat transfer coefficient (W/m^2K). Defining a Nusselt number for heat transfer to the growing bubble,

$$Nu_b = \frac{2 r_b h_b}{k_f} \tag{4.1-8}$$

and combining Equations (4.1-5) through (4.1-7), one obtains

$$Nu_b = \frac{\frac{12}{\pi} \rho_f C_{pf} \Delta T_{sat}}{\rho_g h_{fg}} \quad . \tag{4.1-9}$$

The original bubble growth rate equation of Plesset and Zwick, Equation (4.1-3), and hence Equation (4.1-9) (which is used for H_{if}) is based on several assumptions. These are

1. The bubble remains spherical throughout its growth.
2. Radial acceleration and velocity of the interface are small.
3. Translational velocity of the bubble is negligible.
4. Compressibility and viscous effects are negligible.
5. The vapor within the bubble has a uniform temperature and pressure equal to those of the interface.

The authors, Plesset and Zwick,[4.1-1] indicate that for a superheat of 10 °C for bubble growth in water, negligible error in their theoretical estimate of bubble growth results from translational bubble velocity (due to buoyancy) for bubble radii up to 1 mm. They further indicate that the heat transfer coefficient to the bubble will increase for non-negligible bubble velocity. Since the study of Plesset and Zwick is apparently for pool boiling, it seems appropriate to use relative velocity (as ATHENA does) rather than absolute bubble velocity.

To account for the increase in Nu_b due to a significant bubble relative velocity, ATHENA employs a second correlation deduced by Lee and Ryley[4.1-3] (but modified in ATHENA); the original correlation from **Reference 4.1-3** is:

$$Nu_b = 2.0 + 0.74 Re_b^{0.5} Pr^{1/3} \quad . \tag{4.1-10}$$

The Prandtl number dependence has been dropped in ATHENA. At typical operating conditions (Appendix 4B), the Prandtl number is Pr = 0.98, which represents less than a 1% error for Equation (4.1-10).

Lee and Ryley derived their correlation, Equation (4.1-10), by observing the evaporation rate of a water droplet suspended from a glass fiber into a superheated steam flow. The ranges of variables for which the correlation is fitted are (a) droplet Reynolds number 64 - 250, (b) superheated steam pressure 14.7 - 29 psia, (c) superheat 5 - 61 °F, and (d) steam velocity 9 - 39 ft/s. The data, as plotted by **Reference 4.1-3**, fall within $\pm$ 20% of the correlation. The form of Equation (4.1-10) is not original with Lee and Ryley; Frossling[4.1-4] and Ranz and Marshall[4.1-5] each fitted similar equations to their respective data, obtaining coefficients of 0.552 and 0.6, respectively (as compared to 0.74). Kreith[4.1-6] compiles data from several sources for forced convective heat transfer to spheres ranging from 0.033 to 15 cm in diameter for droplet Reynolds numbers ranging from 20 to 10^5. For the range of Re above that employed by Lee and Ryley (250 - 10^5), Equation (4.1-10) is in excellent agreement with the data plotted in **Reference 4.1-6**. All of the data plotted by Kreith are for atmospheric or near-atmospheric pressures.

There are several additional limitations of the data upon which Lee and Ryley based their correlating equation. The most obvious is that they measured droplet evaporation and not bubble growth. Since their correlation also holds for forced convective heat transfer over a sphere,[4.1-6] however, it seems that it should apply to a spherical bubble. Bubbles in bubbly flow, of course, deform significantly, especially as they get bigger, raising questions as to the overall validity of Equation (4.1-10) for bubbly flow. A further significant complication is the presence of turbulence in the flow. This is not the case for the range of Re plotted in Kreith,[4.1-6] since laminar flow prevails below droplet Reynolds numbers of 10^5 and since, presumably, care was taken to minimize free stream turbulence from those flows. Finally, the pressures at which the aforementioned data were taken are far below typical reactor operating pressures, bringing additional doubt to the viability of Equation (4.1-10) for typical operating conditions.

Additional smoothing functions have been added to H_{if} for SHL bubbly, as indicated in Appendix 4A. The additive term $0.4|v_f|\rho_f C_{pf} F_1$ is included to represent enhanced nucleation effects at low void fraction following the pressure undershoot seen in experiments. This results in the pressure rise. Here, the Stanton number of 0.4 was arrived at during the developmental assessment[4.1-7] of RELAP5/MOD2 for test problems that exhibit an undershoot (i.e., Edwards Pipe, Marviken, GE Level Swell). F_1 decreases from 1.0 at a void fraction of 10^{-3} which reduces the effect of this term. Function F_2 serves to diminish H_{if} for a

void fraction between 0.25 and 0.5, although the opposite would seem to be in order since it is assumed (see Section 3.1.2.1) that bubbly flow can exist above α_g = 0.25 only if vigorous turbulent diffusion is present. Such diffusion should act to enhance the heat transfer. Function F_3 smoothly ramps on H_{if} during the first 1 degree K period of liquid superheat; there is no nucleation temperature criteria. The ramping of F_3 allows the pressure undershoot to occur. Function F_4 relates to effects of noncondensables at low void fraction. It is noted that no minimum bubble diameter is specified in the code, although a maximum one is ($d_{b\ max}$ = minimum of hydraulic diameter D and $0.005\alpha_{bub}^{1/3}$).

Interfacial Area

Specification of the volumetric heat transfer coefficients H_{if} and H_{ig} requires an estimate of the interfacial area per unit volume a_{gf}. Wallis[4.1-8] gives a detailed description of how the interfacial area per unit volume for a spray of droplets can be found. An adapted version of Wallis's discussion is given below, since ATHENA uses it for bubbly flow and dispersed (droplet, mist) flow.

A distribution for droplet diameter for a spray in the form of a probability density function and based on a model deduced by Nukiyama and Tanasawa[4.1-9] is given as

$$p^*(d^*) = 4d^{*2} e^{-2d^*} \qquad (4.1\text{-}11)$$

where

p^* = $d'p(d)$ is the dimensionless probability function

p = probability of a drop having diameter between d and d + δd

d^* = dimensionless droplet diameter = d/d'

d' = most probable droplet diameter (m)

d = droplet diameter (m).

The Sauter-mean diameter, d_{sm}, can be computed from $p^*(d^*)$. A droplet having the Sauter-mean diameter has the same area-to-volume ratio as the entire spray (that is, total surface area of the droplets versus the total volume of the droplets). One can write[4.1-8]

$$d_{sm} = \frac{\int_0^\infty d^3 p(d)dd}{\int_0^\infty d^2 p(d)dd} \quad . \tag{4.1-12}$$

Incorporating Equation (4.1-11) and writing in dimensionless form, one has

$$d^*_{sm} = \frac{\int_0^\infty d^{*5} e^{-2d^*} dd^*}{\int_0^\infty d^{*4} e^{-2d^*} dd^*} \quad . \tag{4.1-13}$$

The improper integrals in Equation (4.1-13) can be evaluated in terms of the gamma function giving

$$d^*_{sm} = \frac{\frac{\Gamma(6)}{2^6}}{\frac{\Gamma(5)}{2^5}} = \frac{5!2^5}{4!2^6} = \frac{5}{2} \quad . \tag{4.1-14}$$

The area-to-volume ratio for a droplet having a Sauter-mean diameter is

$$\left|\frac{A_{sm}}{V_{sm}}\right|_{drop} = \frac{\pi d_{sm}^2}{\frac{\pi}{6} d_{sm}^3} = \frac{6}{d_{sm}} \quad . \tag{4.1-15}$$

Now a_{gf} can be written

$$a_{gf} = \frac{A_{interfacial}}{\text{unit volume}} = \frac{A_{interfacial}}{\frac{V_{drops}}{\alpha_f}} \tag{4.1-16}$$

but

$$\left|\frac{A_{sm}}{V_{sm}}\right|_{drop} = \frac{A_{interfacial}}{V_{drops}}$$

from the definition of Sauter-mean diameter. Hence, one can rewrite Equation (4.1-16) as

$$a_{gf} = \frac{6\alpha_f}{d_{sm}} = \frac{6\alpha_f}{d'}\left(\frac{2}{5}\right) = \frac{2.4\alpha_f}{d'} \tag{4.1-17}$$

where Equation (4.1-14) has been used.

The dimensionless mean droplet diameter $d_o^* = d_o/d'$ can be found from[4.1-10]

$$d_o^* = \int_{-\infty}^{\infty} d^* p^*(d^*) dd^* \quad . \tag{4.1-18}$$

The lower limit of the integral in Equation (4.1-18) can be set to zero since a negative diameter is meaningless. Substituting p*(d*) from Equation (4.1-11) into Equation (4.1-18) and integrating, one obtains

$$d_o^* = 4\frac{\Gamma(4)}{2^4} = \frac{3}{2} \quad . \tag{4.1-19}$$

Combining Equations (4.1-17) and (4.1-19), one obtains

$$a_{gf} = \frac{3.6\alpha_f}{d_o} \quad . \tag{4.1-20}$$

It remains to specify the mean droplet diameter, d_o, in order to find a_{gf}. This is done by assuming that $d_o = (1/2)\, d_{max}$ and using the critical Weber number defined by

$$We_{crit} = \frac{\rho_c (v_g - v_f)^2 d_{max}}{\sigma} \tag{4.1-21}$$

where ρ_c is the density of the continuous phase.

Before a value for d_{max} can be calculated from Equation (4.1-21), the value for critical We for droplet break-up must be specified. A similar We_{crit} for maximum bubble size in bubbly flow can also be specified.[4.1-8]

The values used in ATHENA for We_{crit} for pre-CHF droplets, post-CHF droplets, and bubbles are 3, 12, and 10, respectively. (In the code itself, We_{crit} is given in terms of d_o rather than d_{max}, with values given as 1.5, 6.0, and 5.0, respectively.) Note that the relative velocity, v_{fg}, used to find the bubble size (d_b) results in a maximum bubble size (minimum of $0.005\alpha_{bub}^{1/3}$ and hydraulic diameter D).

Although Equation (4.1-20) for interfacial area has been derived for droplet flow, it is used in ATHENA for bubbly flow as well.

In assessing the determination of the volumetric interfacial area, a_{gf}, it must be remembered that the final result depends upon the fluid properties and three intermediate results: (a) the particle diameter distribution function used to compute the Sauter-mean diameter, (b) the relationship between d_{sm} and d_{max}, and (c) the values used for We_{crit}, which determine the maximum particle size. While the particle diameter distribution is based on Nukiyama and Tanasawa,[4.1-9] the choice of $d_o = \frac{d_{max}}{2}$ is an assumption. While there appears to be considerable variation in the parameters used to compute a_{gf}, the combination gives, for ATHENA,

$$\begin{aligned} a_{gf} &= \frac{3.6\alpha_g}{d_o} = 0.72\frac{\alpha_g\rho_f(v_g - v_f)^2}{\sigma}, \text{ bubbles} \\ &= \frac{3.6\alpha_f}{d_o} = 2.4\frac{\alpha_f\rho_g(v_g - v_f)^2}{\sigma}, \text{ pre-CHF droplets} \\ &= \frac{3.6\alpha_f}{d_o} = 0.6\frac{\alpha_f\rho_g(v_g - v_f)^2}{\sigma}, \text{ post-CHF droplets} \end{aligned} \tag{4.1-22}$$

In arriving at the combination of parameters that produces Equation (4.1-22) , RELAP5/MOD2 developers set the critical Weber number such that reasonable drag forces (which depend on drag coefficients and a_{gf}) would be predicted in order to simulate data from several separate effects tests.[4.1-7,4.1-11] Further discussion regarding these development efforts is given in the section on interfacial drag, Section 6.1.

In summary, the determination of volumetric interfacial area a_{gf} for ATHENA is based partly on published theory/experiment and partly on tuning related parameters to fit RELAP5/MOD2 simulations of separate-effects test data. One of the separate-effects tests used was the Edwards pipe blowdown, and comparisons of data and calculations for pressure and void fraction for this test are shown in **Reference 4.1-7**. This calculation uses the bubbly superheated liquid interfacial heat transfer coefficient H_{if}.

4.1.1.1.2 Bubbly Subcooled Liquid (SCL, $T_f < T^s$)--

Model as Coded

$$H_{if} = \frac{F_3 F_5 h_{fg} \rho_g \rho_f \alpha_{bub}}{\rho_f - \rho_g} \text{ (modified Unal and Lahey)} \qquad (4.1\text{-}23)$$

where

$\rho_f - \rho_g$ = $\max(\rho_f - \rho_g, 10^{-7}\ kg/m^3)$

F_3, α_{bub} as for bubbly SHL

F_5 = $0.075 \frac{1}{K \bullet s}$ $\alpha_{bub} \geq 0.25$

= $1.8\phi C \exp(-45\alpha_{bub}) + 0.075 \frac{1}{K \bullet s}$ $\alpha_{bub} < 0.25$

C = $65.0 - 5.69 \times 10^{-5} (P - 1.0 \times 10^5) \frac{1}{K \bullet s}$ $P \leq 1.1272 \times 10^6$ Pa

= $\frac{2.5 \times 10^9}{P^{1.418}} \frac{1}{K \bullet s}$ $P > 1.1272 \times 10^6$ Pa

P = pressure (Pa)

ϕ = 1.0 $|v_f| \leq 0.61$ m/s

= $(1.639344\ |v_f|)^{0.47}$ $|v_f| > 0.61$ m/s.

Model Basis and Assessment

Unal[4.1-12] gives the heat transfer coefficient for condensation at a bubble interface for subcooled nucleate flow boiling as

$$h = \frac{C\phi h_{fg} d}{2\left(\frac{1}{\rho_g} - \frac{1}{\rho_f}\right)} \qquad (4.1\text{-}24)$$

where

$$\phi = 1 \qquad v_f \le 0.61 \text{ m/s}$$

$$= \left|\frac{v_f}{0.61}\right|^{0.47} \qquad v_f > 0.61 \text{ m/s}$$

$$C = 65 - 5.69 \times 10^{-5} (P - 10^5) \frac{1}{K \bullet s} \qquad 10^5 \le P \le 10^6 \text{ Pa}$$

$$= 0.25 \times 10^{10} P^{-1.418} \frac{1}{K \bullet s} \qquad 10^6 < P \le 17.7 \times 10^6 \text{ Pa}$$

and d is the bubble diameter. The term ϕ is Unal's velocity dependent coefficient, and C is Unal's pressure dependent coefficient. The volumetric heat transfer coefficient H_{if} is found by multiplying h by the volumetric interfacial area, a_{gf}, Equation (4.1-22) . At the same time, Equation (4.1-22) provides an expression for the average bubble diameter that can be used for d in Equation (4.1-24).

Hence, one can write

$$H_{if} = h a_{gf} = \frac{C\phi h_{fg} d a_{gf}}{2\left(\frac{1}{\rho_g} - \frac{1}{\rho_f}\right)} = \frac{3.6\alpha_g C\phi h_{fg}}{2\left(\frac{1}{\rho_g} - \frac{1}{\rho_f}\right)} = \frac{1.8\alpha_g C\phi h_{fg}\rho_f\rho_g}{\rho_f - \rho_g} \quad . \tag{4.1-25}$$

Unal specifies the ranges for which his correlation fits the experimental data: (a) pressure, 0.1 - 17.7 MPa, (b) heat flux, 0.47 - 10.64 MW/m^2, (c) bulk liquid velocity, 0.08 - 9.15 m/s, (d) subcooling, 3 - 86 K, (e) maximum bubble diameter, 0.08 - 1.24 mm, and (e) maximum bubble growth time, 0.175 - 5 ms. The assumptions made by Unal appear to be quite reasonable and supportable, except that the function C has a discontinuity (factor of 2) at P = 1 MPa. Examination of Unal's paper[4.1-12] and discussions with Unal[1] indicated that the part $0.25 \times 10^{10} P^{-1.418}$ in the function C was obtained from Equation (12) in Unal's paper[4.1-12] by assuming Unal's term $\alpha^2 = 1$ for $1 \times 10^6 < P < 17.7 \times 10^6$ Pa. This was done because Unal indicates that the dry area under the bubble disappears at ~ 1 MPa. Unal also indicates that the part $65 - 5.69 \times 10^{-5} (P - 1.0 \times 10^{-5})$ in the function C is determined by linear interpolation and extrapolation using values found from C for experiments at 0.17 MPa and 1 MPa. If one uses both parts of the function C but assumes the dry area under the bubble disappears at 1.1272 MPa, then the function C is continuous to three significant places.[4.1-13] This referenced modification, which was approved by Unal, is used in ATHENA to remove the discontinuity.

1. Personal communication, H. C. Unal to R. A. Riemke, February 1992.

The 0.075 term in F_5 is the term used by Lahey[4.1-14] for the interfacial condensation in conjunction with his subcooled boiling model. The smoothing factor [$\exp(-45\alpha_{bub})$] between the modified Unal and the Lahey models was arrived at during the RELAP5/MOD2 developmental assessment.[4.1-7]

4.1.1.1.3 Bubbly Superheated Vapor/Gas (SHG, $T_g > T^s$)--

Model as Coded

$$H_{ig} = h_{ig} F_6 F_7 a_{gf} \tag{4.1-26}$$

where

h_{ig} = 10^4 W/m^2-K

a_{gf} as for bubbly SHL

F_6 = $[1 + \eta (100 + 25\eta)]$, $\eta = |\max(-2, \Delta T_{sg})|$

ΔT_{sg} = $T^s - T_g$

$$F_7 = \frac{\max(\alpha_g, 10^{-5})}{\max(\alpha_g, 10^{-9})} .$$

Model Basis and Assessment

The volumetric heat transfer coefficient, H_{ig}, for bubbly SHG is based on an empirical correlation. The vapor/gas interfacial heat transfer coefficient $h_{ig} = 10^4$ W/m^2-K, is chosen to be large in order to bring the vapor/gas temperature rapidly toward the saturation temperature. **Reference 4.1-15** indicates that a value of 10^4 W/m^2-K is a reasonable condensation heat transfer coefficient to use for bubbles. Reference **Reference 4.1-15** documents direct contact condensation experiments of saturated steam bubbles in quiesent subcooled water; thus, the value 10^4 W/m^2-K quoted in the reference would normally be used for the liquid interfacial heat transfer coefficient h_{if}. As discussed in Section 4.1.1.1.2, the code instead uses the modified Unal and Lahey models for h_{if}. The value 10^4 W/m^2-K is used in the code for h_{ig} since it is representative and it is large. Function F_6, Appendix 4A, enhances this tendency, especially as ΔT_{sg} increases in magnitude. Function F_7 improves numerical stability for low void fractions. The determination of volumetric interfacial area, a_{gf}, is discussed in Section 4.1.1.1.1. There is room for improving the determination of H_{ig} for this case, although to the best of our knowledge, this might require further experimental work.

4.1.1.1.4 Bubbly Subcooled Vapor/Gas (SCG, $T_g < T^s$)--

Model as Coded

H_{ig} as for bubbly SHG

Note that $\Delta T_{sg} > 0$ for this case (Function F_6).

Model Basis and Assessment

The expression used for bubbly SCG is the same as for bubbly SHG, Appendix 4A, except that the Nu enhancing function F_6 increases H_{ig} dramatically for large subcooled levels, pushing T_g more quickly toward saturation temperature. The fact that Nu for subcooled vapor/gas is much greater than for superheated vapor/gas, especially as the subcooling increases, seems appropriate in view of the unstable nature of the subcooled state. Nevertheless, a better basis for the correlation for bubbly SCG is needed.

4.1.1.2 Slug Flow. In slug flow, interfacial heat transfer can be divided into two distinct parts: (a) the heat transfer between the large Taylor bubbles and the liquid surrounding them, and (b) the heat transfer between the small bubbles in the liquid slug and their host liquid. The heat transfer for each part is summed to obtain the total. For the total bulk (superscript B, see Volume I) heat transfer rate per unit volume, Q_{ip}^B (W/m^3), between the interface and a given phase, p, one has

$$Q_{ip}^B = \frac{h_{Tb} A_{Tb} \Delta T}{V_{tot}} + \frac{h_{bub} A_{bub} \Delta T}{V_{tot}} \qquad (4.1\text{-}27)$$

where

h_{Tb}	=	heat transfer coefficient for Taylor bubble ($W/m^2 \cdot K$)
A_{Tb}	=	interfacial area of Taylor bubble (m^2)
h_{bub}	=	heat transfer coefficient for small bubbles ($W/m^2 \cdot K$)
A_{bub}	=	interfacial area of small bubbles (m^2)
V_{tot}	=	total volume of cell (m^3)
ΔT	=	difference between the saturation temperature and the temperature of the phase in question (K)
p	=	phase p (either f for liquid or g for vapor/gas).

Equation (4.1-27) can be rewritten

$$Q_{ip}^{B} = h_{Tb}\frac{A_{Tb}}{V_{Tb}}\frac{V_{Tb}}{V_{tot}}\Delta T + h_{bub}\frac{A_{bub}}{V_{bub}}\frac{V_{bub}}{V_{tot}}\Delta T \quad (4.1\text{-}28)$$

or finally

$$Q_{ip}^{B} = H_{ip,\,Tb}\Delta T + H_{ip,\,bub}\Delta T \quad . \quad (4.1\text{-}29)$$

Hence, the volumetric interfacial area for each part can be computed either based on the volume of that part (Taylor bubble or slug volume) or based on the total volume. The final volumetric interfacial area, a_{gf}, must be based on the total cell volume as implied by Equation (4.1-27). One can write

$$a_{gf,\,Tb} = \frac{A_{Tb}}{V_{Tb}}\frac{V_{Tb}}{V_{tot}} = a^{*}_{gf,\,Tb}f_{Tb} \quad (4.1\text{-}30)$$

where $a^{*}_{gf,\,Tb} = \frac{A_{Tb}}{V_{Tb}}$ and $f_{Tb} = \frac{V_{Tb}}{V_{tot}}$

and

$$a_{gf,\,bub} = \frac{A_{bub}}{V_{bub}}\frac{V_{bub}}{V_{tot}} = a^{*}_{gf,\,bub}f_{bub} \quad (4.1\text{-}31)$$

where $a^{*}_{gf,\,bub} = \frac{A_{bub}}{V_{bub}}$ and $f_{bub} = \frac{V_{bub}}{V_{tot}}$.

ATHENA recognizes the contributions from the two distinct divisions of slug flow toward the total heat transfer. The correlations for the contributions for the bubbles in the liquid slug are based on those computed for bubbly flow, but are exponentially diminished as α_g increases. The details of the coded correlations for slug flow heat/mass transfer appear in Appendix 4A. If the liquid temperature is between one degree K subcooled and one degree K superheated, the final liquid coefficient, H_{if}, is the result of a cubic spline interpolation between the superheated and subcooled result. If the vapor/gas temperature is between one degree K subcooled and one degree K superheated, the final vapor/gas coefficient, H_{ig}, is the result of a cubic spline interpolation between the superheated and subcooled result.

4.1.1.2.1 Slug Superheated Liquid (SHL, $T_f > T^S$)--

Model as Coded

$$H_{if} = H_{if,Tb} + H_{if,bub} \quad (4.1\text{-}32)$$

where

$H_{if,Tb}$ = $3.0 \times 10^6 \, a^*_{gf,\,Tb} \alpha_{Tb}$

$a^*_{gf,\,Tb}$ = volumetric interfacial area (m^2/m^3)

= $\frac{4.5}{D}(2.0)$, 2.0 being a roughness factor

α_{Tb} = Taylor bubble void fraction = $\frac{\alpha_g - \alpha_{gs}}{1 - \alpha_{gs}}$

= Taylor bubble volume/total volume

α_{gs} = the average void fraction in the liquid film and slug region

= $\alpha_{BS} F_9$

F_9 = $\exp\left[-8\left(\frac{\alpha_g - \alpha_{BS}}{\alpha_{SA} - \alpha_{BS}}\right)\right]$

α_{BS} = α_g for bubbly-to-slug transition

α_{SA} = α_g for slug-to-annular mist transition

and

$H_{if,bub}$ is as for H_{if} for bubbly SHL with the following modifications:

α_{bub} = $\alpha_{BS} F_9$

v_{fg} = $(v_g - v_f) F_9^2$

$a_{gf,bub}$ = $(a_{gf})_{bub} (1 - \alpha_{Tb}) F_9$

β = F_9

$(a_{gf})_{bub}$ is as for bubbly SHL.

Model Basis and Assessment

The coded two-part correlation for slug SHL is presented in detail in Appendix 4A. The contribution for the large Taylor bubbles, $H_{if,Tb}$, is an ad hoc correlation. It is given a large value to promote a rapid return of T_f toward the saturation temperature, since SHL is a metastable state. The roughness factor appears to be a tuning coefficient.

The Taylor bubble void fraction α_{Tb} is used to determine the fraction f_{Tb}, Equation (4.1-30), that comes from interfacial heat/mass transfer across the Taylor bubble boundary; f_{bub}, Equation (4.1-31), is set equal to $(1 - \alpha_{Tb})$. The term α_{Tb} is computed from simple geometric considerations and can be given in terms of α_g and the average void fraction in the portion of the flow where the liquid is the continuous phase, α_{gs}.[4.1-16] The expression used for α_{gs} causes it to drop exponentially from the bubbly-slug transition α_g to near zero as α_g approaches the slug-annular-mist transition.

The part of H_{if} that is used to account for the heat transfer in the continuous liquid portion of the flow is based directly on H_{if} for bubbly flow, SHL, Section 4.1.1.1.1, but with some modifications. These additional modifications to $H_{if,bub}$ serve to further reduce the contribution of $H_{if,bub}$ to the total volumetric coefficient.

In summary, the primary purpose of H_{if} for slug SHL is to drive the liquid temperature to the saturation value.

Interfacial Area

The expression used for the interfacial area for the Taylor bubble portion of slug flow, $a^*_{gf} = [4.5/D](2)$, is based on an argument of Ishii and Mishima.[4.1-16] If one computes the surface area per unit volume of a cylinder, one obtains

$$\frac{A_{cyl}}{V_{cyl}} = \frac{\pi D_{cyl} L_{cyl} + 2\frac{\pi}{4} D^2_{cyl}}{\frac{\pi}{4} D^2_{cyl} L_{cyl}} \quad . \tag{4.1-33}$$

As the length of the cylinder L_{cyl} increases, the surface area of the ends of the cylinder becomes negligible and the area-to-volume ratio becomes

$$\lim_{L_{cyl} \to \infty} \frac{A_{cyl}}{V_{cyl}} = \frac{4}{D_{cyl}} \quad . \tag{4.1-34}$$

Assuming that a Taylor bubble can be approximated by a cylinder and employing the relation[4.1-16] $D_{Tb} = 0.88\, D_{pipe}$, one has

$$\frac{4}{D_{cyl}} = \frac{4}{0.88D} = \frac{4.55}{D} \approx \frac{4.5}{D} \tag{4.1-35}$$

where D is the hydraulic diameter. Except for the factor of two, Equation (4.1-35) is the same result given by Ishii and Mishima for volumetric interfacial area. It is noted that it is appropriate to use the cylinder/bubble volume in Equation (4.1-33) for ATHENA, since the fraction of the computational cell used for $H_{if,Tb}$ is the ratio of the Taylor bubble volume to the cell volume (see Model Basis and Assessment above). Ishii and Mishima[4.1-16] insert a coefficient into the expression for a^*_{gf} to account for rippling of the Taylor bubble surface. A value of two is used in ATHENA for this coefficient.

4.1.1.2.2 Slug Subcooled Liquid (SCL, $T_f < T^S$)--

Model as Coded

$$H_{if} = H_{if,Tb} + H_{if,bub} \tag{4.1-36}$$

where

$$H_{if,Tb} = 1.18942\, Re_f^{0.5} Pr_f^{0.5} \frac{k_f}{D} a^*_{gf,\,Tb} \alpha_{Tb}$$

where

α_{Tb} and $a^*_{gf,\,Tb}$ are as for slug SHL

$$Pr_f = \frac{C_{pf}\mu_f}{k_f}$$

$$Re_f = \frac{\rho_f D \min(|v_f - v_g|,\, 0.8\text{m/s})}{\mu_f}$$

and

$H_{if,bub}$ is as for bubbly SCL.

Model Basis and Assessment

The volumetric heat transfer coefficient for the interfacial heat transfer for the Taylor bubble portion for slug SCL is based on a dependence of the Reynolds and Prandtl numbers.[1] The Nusselt number upon which $H_{if,Tb}$ is based varies as $Re^{0.5}$, Appendix 4A. This dependence lies between that for laminar flow, $Re^{0.3}$, and that for turbulent flow, $Re^{0.8}$, as reported by Kreith.**4.1-6** Also, the coefficient 1.18942 lies between the laminar Sieder-Tate correlation coefficient, 1.86, and the turbulent Dittus-Boelter coefficient, 0.023.**4.1-6** [The Sieder-Tate correlation is also a function of $\left(\frac{D}{L}\right)^{0.33}$.] Since the liquid flow past a Taylor bubble does not exhibit the full effects of turbulence but is probably not purely laminar, the correlation used in the code should give a result that is plausible, although it may still be significantly in error.

The expression used for the bubbly part of the volumetric coefficient $H_{if,bub}$, is the same as that used for bubbly SCL, Section 4.1.1.1.2. The apportionment of the two contributions to H_{if} is effected the same as for slug SHL, as is the determination of a_{gf}.

4.1.1.2.3 Slug Superheated Vapor/Gas (SHG, $T_g > T^s$)--

Model as Coded

$$H_{ig} = H_{ig,Tb} + H_{ig,bub} \tag{4.1-37}$$

where

$$H_{ig,Tb} = (2.2 + 0.82Re_g^{0.5})\frac{k_g}{D}a^*_{gf,\,Tb}\alpha_{Tb}$$

where

$a^*_{gf,\,Tb}$ and α_{Tb} are as for slug SHL

$$Re_g = \frac{\rho_g|v_f - v_g|D}{\mu_g}$$

1. The literature reference for this correlation is unknown as of this writing, and it is in the process of being researched.

and

$$H_{ig,bub} = h_{ig} F_6 (1 - \alpha_{Tb}) a_{gf,bub}$$

where

α_{Tb} and $a_{gf,bub}$ are as for slug SHL

and

h_{ig} and F_6 are as for bubbly SHG.

Model Basis and Assessment

The contribution to the volumetric heat transfer coefficient from the Taylor bubble interfacial heat transfer, Appendix 4A, is based on a modified form of the Lee-Ryley[4.1-3] correlation derived for laminar flow heat transfer to a sphere (Section 4.1.1.1.1). The coefficients have been augmented from the original, and the Prandtl number dependence has been dropped as is the case for interfacial heat transfer for bubbly flow. While the bullet-shaped cap on the Taylor bubble may approximate a sphere, it seems inappropriate to use the Lee-Ryley correlation for this case.

The heat transfer coefficient for the bubbly flow contribution is based on an empirical correlation[4.1-15] for $H_{if,bub}$ along with an enhancement function F_6. These are as for bubbly SHG and are discussed in Section 4.1.1.1.3. The apportionment of H_{if} between the two contributions is based on the same α_{Tb} as for slug SHL, Section 4.1.1.2.1.

4.1.1.2.4 Slug Subcooled Vapor/Gas (SCG, $T_g < T^S$)--

Model as Coded

$$H_{ig} = H_{ig,Tb} + H_{ig,bub} \qquad (4.1\text{-}38)$$

where

$$H_{ig,Tb} = h_{ig} F_6 \alpha_{Tb} a^*_{gf,Tb}$$

where α_{Tb} and $a^*_{gf,Tb}$ are as for slug SHL,

h_{ig} and F_6 are as for bubbly SHG,

and

$H_{ig,bub}$ is as for slug SHG.

Model Basis and Assessment

Both contributions to H_{ig} for slug SCG ($H_{ig,Tb}$ and $H_{ig,bub}$) are based on an empirical correlation[4.1-15] along with enhancement function F_6. Although the two parts look similar, the interfacial area is different for each. The large values for Nu used for slug SCG (F_6 increases dramatically for large subcooled levels) are apparently designed to drive the vapor/gas temperature toward the saturation value. This seems reasonable in view of the fact that subcooled vapor/gas is an unstable state.

4.1.1.3 Annular Mist Flow. For annular mist flow, the interfacial heat transfer results from two contributory sources: (a) the heat transfer between the annular liquid film and vapor/gas core, and (b) the heat transfer between the vapor/gas core and entrained liquid droplets. The correlations that are used to represent the overall volumetric heat transfer are constructed from the two contributing sources, as in the case for slug flow. Equations (4.1-27) through (4.1-31) for slug flow apply to annular mist flow as well, except for the identities of the two sources. One can write [see Equation (4.1-29)]

$$Q_{ip}^{B} = H_{ip,\,ann}\Delta T + H_{ip,\,drp}\Delta T\,, \tag{4.1-39}$$

where subscript ann refers to the annular film-vapor/gas core contribution and subscript drp refers to the droplet-vapor/gas core contribution. Further information regarding the correlations coded in ATHENA are recorded in Appendix 4A. If the liquid temperature is between one degree K subcooled and one degree K superheated, the final liquid coefficient H_{if} is the result of a cubic spline interpolation between the superheated and subcooled result. If the vapor/gas temperature is between one degree K subcooled and one degree K superheated, the final vapor/gas coefficient H_{ig} is the result of a cubic spline interpolation between the superheated and subcooled result.

4.1.1.3.1 Annular Mist Superheated Liquid (SHL, $T_f > T^s$)--

Model as Coded

$$H_{if} = H_{if,ann} + H_{if,drp} \tag{4.1-40}$$

where

$$H_{if,ann} = 3.0 \times 10^{6}\, a_{gf,ann}\, F_{10}$$

$a_{gf,ann} = \left(\frac{4C_{ann}}{D}\right)(1-\alpha_{ff})^{1/2}$

C_{ann} = $2.5\,(30\alpha_{ff})^{1/8}$, where 2.5 is a roughness factor

α_{ff} = $\max\,(0.0, \alpha_f F_{11})$

F_{11} = $\gamma^{*}\,\max\,[0.0, (1\text{-}G^{*})]\,\exp\,(-C_e \times 10^{-5}\,\lambda^{6})$

C_e = 4.0 horizontal

= 7.5 vertical

λ = $\frac{v_g^{*}}{v_{crit}}$ horizontal flow

= $\frac{\alpha_g v_g}{v_{crit}}$ vertical flow

v_g^{*} = $\max\,(|v_g - v_f|, 10^{-15}\,\text{m/s})$

$$v_{crit}\,(\text{horizontal}) = \max\left\{0.5\left[\frac{(\rho_f-\rho_g)g\alpha_g A_{pipe}}{\rho_g D\sin\theta}\right]^{1/2}(1-\cos\theta),\ |v_g-v_f|10^{-15},\ 10^{-30}\text{m/s}\right\}$$

[see Equation (3.1-2)]

$$v_{crit}(\text{vertical}) = 3.2\frac{[\sigma^{*}g(\rho_f-\rho_g)]^{1/4}}{\rho_g^{1/2}}$$ [see Equations (3.2-20) and (3.2-22)]

σ^{*} = $\max\,(\sigma, 10^{-7}\,\text{N/m})$

G^{*} = $10^{-4}\,Re_f^{0.25}$

Re_f = $\frac{\alpha_f\rho_f|v_f|D}{\mu_f}$

γ^{*} = γ $\alpha_g > \alpha_{SA}$ and $\alpha_f < \alpha_{EF}$

= 1 otherwise

$$\gamma = \frac{\alpha_f - \alpha_{AD}}{\alpha_{EF} - \alpha_{AD}}$$

$$\alpha_{AD} = 10^{-4}$$

$$\alpha_{EF} = \max\left[2\,\alpha_{AD}, \min\left(2.0 \times 10^{-3}\,\frac{\rho_g}{\rho_f}, 2 \times 10^{-4}\right)\right]$$

$$F_{10} = \min\left(1.0 + |\lambda|^{1/2} + 0.05\,|\lambda|, 6\right)$$

and

$$H_{if,drp} = \frac{k_f}{d_d}\,F_{12}\,F_{13}\,a_{gf,drp}$$

$$a_{gf,drp} = \frac{3.6\alpha_{fd}}{d_d}(1 - \alpha_{ff})$$

$$F_{13} = 2.0 + 7.0 \min\left[1.0 + \frac{C_{pf}\max(0, \Delta T_{sf})}{h_{fg}}, 8.0\right]$$

d_d = characteristic droplet diameter $\left(= \frac{1}{2} d_{max}\right)$

$$= \frac{We\,\sigma}{\rho_g \hat{v}_{fg}^2},\ We = 1.5,\ We\,\sigma = \max\left(We\,\sigma, 10^{-10}\ N/m\right)$$

$$\hat{v}_{fg}^2 = \max\left[v_{fg}^{**2}, \frac{We\,\sigma}{\rho_g \min(D'\alpha_{fd}^{1/3}, D)}\right]$$

$$v_{fg}^{**} = v_{fg}^{*}\,\alpha_f 10^6 \qquad \alpha_f < 10^{-6}$$

$$= v_{fg}^{*} \qquad \alpha_f \geq 10^{-6}$$

$$v_{fg}^{*} = v_{fg}\,(1 - F_{11}\gamma) \qquad \alpha_g > \alpha_{SA} \text{ and } \alpha_f < \alpha_{EF}$$

$$= v_{fg}\,(1 - F_{11}) \qquad \text{otherwise}$$

$$v_{fg} = v_g - v_f$$

$D' = 0.0025$ m

$\alpha_{fd} = \max\left(\frac{\alpha_f - \alpha_{ff}}{1 - \alpha_{ff}}, \alpha^*_{AD}\right)$

$\alpha^*_{AD} = \alpha_{AD}\gamma + 10^{-5}(1 - \gamma)$ $\quad \alpha_g > \alpha_{SA}$ and $\alpha_f < \alpha_{EF}$

$= \alpha_{AD}$ otherwise

$\alpha_{AD} = 10^{-4}$

$F_{12} = 1 + \xi(250 + 50\xi)$

$\xi = \max(0, -\Delta T_{sf})$.

For an annulus component, $\alpha_{ff} = \alpha_f$ and $\alpha_{fd} = 0$.

Model Basis and Assessment

The Nusselt number, upon which the annular film portion of the volumetric heat transfer coefficient is based, is simply a large number, designed to push T_f toward the saturation temperature. Function F_{10}, Appendix 4A, is a smoothing function that greatly decreases $H_{if,ann}$ as the velocity ratios parameter λ approaches zero.

The Nusselt number for the droplet to vapor/gas core is represented by a function, F_{12}, which grows quadratically as the magnitude of ΔT_{sf} increases (helps drive T_f toward T^s), and by a function of F_{13}, whose value is 9 for superheated liquid.

Interfacial Area

The interfacial areas per unit volume for the annular film-vapor/gas core interface contribution as well as that for the droplet-vapor/gas core are based on simple geometric considerations as given by Ishii and Mishima.[4.1-16] It is appropriate to give the derivation leading to the results of **Reference 4.1-16** and then show how these results are transformed into the coded version.

The volumetric interfacial area of the liquid annular film in a pipe is

$$a_{gf,\,ann} = \frac{\pi D' L}{\frac{\pi}{4} D^2 L} = \frac{4D'}{D^2} \qquad (4.1\text{-}41)$$

where

D' = inner diameter of liquid annulus

D = diameter of pipe

L = unit pipe length.

An expression for the ratio D'/D can be found in terms of volume fractions. First, one can write

$$\frac{V_{core}}{V_{tot}} = \frac{\left(\frac{\pi}{4}\right)D'^2L}{\left(\frac{\pi}{4}\right)D^2L} = \frac{D'^2}{D^2} \tag{4.1-42}$$

where

V_{core} = idealized volume of the vapor/gas core

V_{tot} = volume of control volume.

Also, one can write

$$\frac{V_{core}}{V_{tot}} = \frac{\frac{V_g}{V_{tot}}}{\frac{V_g}{V_{core}}} = \frac{\alpha_g}{\alpha_{gd}} = \frac{\alpha_g}{1-\alpha_{fd}} \tag{4.1-43}$$

where

V_g = volume of vapor/gas (all of which is assumed to be in the core)

α_{gd} = vapor/gas (void) fraction in the core [defined in Equation (4.1-43)]

α_{fd} = liquid fraction in the core [defined in Equation (4.1-43)].

Hence,

$$a_{gf,\,ann} = \frac{4}{D}\left(\frac{D'}{D}\right) = \frac{4}{D}\left(\frac{\alpha_g}{1-\alpha_{fd}}\right)^{1/2} \tag{4.1-44}$$

which is the expression given by **Reference 4.1-16**.

The coded expression for volumetric interfacial area is given in terms of α_{ff}, the liquid fraction of the annular film, or

$$\alpha_{ff} = \frac{V_{f,film}}{V_{tot}} = 1 - \frac{V_{core}}{V_{tot}} = 1 - \frac{\alpha_g}{1-\alpha_{fd}} \quad . \tag{4.1-45}$$

Rewriting, one obtains

$$\frac{\alpha_g}{1-\alpha_{fd}} = 1 - \alpha_{ff} \quad . \tag{4.1-46}$$

Applying this result to Equation (4.1-44) yields

$$a_{gf,ann} = \frac{4}{D}(1-\alpha_{ff})^{1/2} \quad . \tag{4.1-47}$$

This is the same as the coded version shown above, with the exception of the C_{ann} factor. C_{ann} contains a multiplier of 2.5 as a roughness factor to increase the surface area for mass transfer, and a term $(30\ \alpha_{ff})^{1/8}$ that gives a value near unity for α_{ff} between 0.01 and 0.1, yet ensures $\alpha_{gf,ann} \rightarrow 0$ as $\alpha_{ff} \rightarrow 0$.

The volumetric interfacial area for the droplets in the vapor/gas core is derived as detailed in Section 4.1.1.1.1 and is given by Equation (4.1-20). It is

$$a^*_{gf,drp} = \frac{3.6\alpha_{fd}}{d_d} \tag{4.1-48}$$

where d_d denotes a droplet diameter and α_{fd} is the liquid fraction in the vapor/gas core. In order to normalize $a^*_{gf,drp}$ to the total cell volume, it must be multiplied by the fraction of the total cell volume occupied by the core, Equation (4.1-43). Using Equation (4.1-46) one has

$$a_{gf,drp} = \frac{3.6\alpha_{fd}}{d_d}(1-\alpha_{ff}) \ , \tag{4.1-49}$$

which is the coded version as indicated in Appendix 4A. The liquid fraction of the annular film, α_{ff}, depends upon the amount of liquid entrained in the vapor/gas core. Using Equation (4.1-46), the variable α_{fd} can be shown to be

$$\alpha_{fd} = \frac{\alpha_f - \alpha_{ff}}{1 - \alpha_{ff}} \quad . \tag{4.1-50}$$

Liquid Droplet Entrainment Model and Assessment

This model is discussed in Section 6.3.

4.1.1.3.2 Annular Mist Subcooled Liquid (SCL, $T_f < T^s$)--

Model as Coded

$$H_{if} = H_{if,ann} + H_{if,drp} \tag{4.1-51}$$

where

$H_{if,ann}$ = $10^{-3}\ \rho_f C_{pf}\ |v_f|\ a_{gf,ann}\ F_{10}$ (modified Theofanous)

$a_{gf,ann}$ and F_{10} are as for annular mist SHL

and

$H_{if,drp}$ = $\frac{k_f}{d_d}\ F_{13}\ a_{gf,drp}$ (modified Brown)

where

$a_{gf,drp}$, F_{13}, and d_d are as for annular-mist SHL.

For an annulus component, $\alpha_{ff} = \alpha_f$ and $\alpha_{fd} = 0$.

Model Basis and Assessment

The volumetric heat transfer coefficient for annular mist SCL is comprised of two parts (Appendix 4A). The contribution from the interface between the liquid annular film and the vapor/gas core is based on a model given by Theofanous.[4.1-17] Theofanous makes reference to an earlier work (Brumfield, Houze, Theofanous[4.1-18]) wherein models are obtained for the mass transfer coefficient for vapor/gas absorption

by a turbulent, thin, falling liquid film. The mass transfer models are compared with data for water at 25 °C absorbing various gases for turbulent Reynolds number $Re_t << 500$. (Re_t is defined below.) The agreement with the data is very good. Theofanous[4.1-17] then writes the heat transfer analogues of the mass transfer correlations, using the same numerical coefficients and exponents. These are

$$Nu_t = 0.25\, Re_t^{3/4}\, Pr^{1/2} \qquad Re_t > 500$$

$$= 0.70\, Re_t^{1/2}\, Pr^{1/2} \qquad Re_t < 500 \tag{4.1-52}$$

where

$Nu_t = \frac{h\lambda}{k}$, λ = integral scale of turbulence

$Re_t = \frac{u\lambda}{\nu}$, u = turbulence intensity

and where a fully developed residence time is assumed. Introducing the Stanton number $St = \frac{Nu}{Re \bullet Pr}$ and approximating[4.1-17] $u \approx 5 \times 10^{-2} v$, where v is bulk liquid velocity, Equation (4.1-52) can be rewritten as

$$St = \frac{h}{\rho_f C_{pf} v_f} = 1.25 \times 10^{-2}\, Re_t^{-1/4}\, Pr^{-1/2} \qquad Re_t > 500$$

$$= 3.5 \times 10^{-2}\, Re_t^{-1/2}\, Pr^{-1/2} \qquad Re_t < 500\ . \tag{4.1-53}$$

Theofanous[4.1-17] then declares that the usual range for Re_t is 10^2 - 10^3 and chooses Pr = 3. Finally, he indicates that for either $Re_t > 500$ or $Re_t < 500$, one obtains for St, using the numbers indicated

$$St \sim 1 \times 10^{-3} \text{ to } 3 \times 10^{-3}\ . \tag{4.1-54}$$

Theofanous[4.1-17] goes on to develop an expression for the decay of St for a liquid jet flow where the turbulence decays with increasing distance from the initial orifice. He finally arrives at a correlation that compares favorably with experimental data[4.1-17] and is written as

$$St = 2 \times 10^{-2} \left(\frac{1}{d}\right)^{-1/2}\ . \tag{4.1-55}$$

Comparing Equation (4.1-55) to Equation (4.1-54) for a value of l = d (d = orifice diameter, l = streamwise distance), Theofanous[4.1-17] notes a difference in St of an order of magnitude for which he can only partly account. Theofanous indicates the correlation is based on data for l/d = 4 - 600, d = 0.02 - 1.5 cm, v = 0.2 - 38 m/s, and Re = 4.5×10^3 - 5×10^5.

The coded version for the heat transfer coefficient is (Appendix 4A)

$$h = 10^{-3}\rho_f C_{pf}|v_f| F_{10} \quad (4.1\text{-}56)$$

where it has been assumed that St = 10^{-3}, as given in Equation (4.1-54).

Several weaknesses in the coded correlations as it relates to the original mass transfer model of Brumfield et al.[4.1-18] can be identified:

1. The original correlation is based on a falling-liquid film surrounded by quiescent air, whereas annular-mist flow involves a flowing, possibly turbulent, possibly laminar vapor/gas core.

2. The original correlation is based on the liquid velocity against quiescent air. The liquid velocity in the code is a single bulk value representing both the liquid annular film and the liquid droplets in the core. As such, it is possible for the liquid velocity to be zero when the mass flow of droplets in one direction is balanced by an annular-film flow in the opposite direction. In such a case, the code would incorrectly predict zero for $H_{if,ann}$.

3. The original correlation is based on turbulent flow for the liquid film. In an actual reactor flow, the liquid film may be in laminar flow, or it may be stationary, as in vertical flow when just enough drag is imparted by the core flow to prevent downflow of the annular film.

4. The original mass transfer correlation is based on isothermal flow. The code attempts to simulate flows with boiling heat transfer where bubbles may form at the pipe wall and push their way toward the annular film-vapor/gas core interface, thereby dynamically enhancing the mass/heat transfer.

5. The original correlation for mass transfer[4.1-17] is valid for high values of Schmidt number, Sc, whereas the heat transfer analogue of Sc, the Prandtl number, is of order unity for most flows of thermal-hydraulic interest. This means that the heat transfer analogue of the original mass transfer correlation is not valid for small Re_t.[4.1-17]

6. Finally, there is the problem discussed above, that an order-of-magnitude difference exists between Equation (4.1-54) and Equation (4.1-55) for l/d ~ 1.

In summary, the weaknesses described above make the applicability of the correlation for $H_{if,ann}$ to reactor conditions unclear. It must be assessed against experiment to determine its validity.

The volumetric heat transfer coefficient for the vapor/gas core interface to liquid droplets is based on a paper by Brown.[4.1-19] Brown solves a classical transient-heat conduction problem for a sphere immersed suddenly in a uniform temperature bath. The boundary condition at the surface is simply that the surface temperature remains constant at the bath temperature, implying a very large heat transfer coefficient from the bath to the sphere. Brown then forms an internal energy balance in which an internal heat transfer coefficient is defined between the surface and internal mean temperature. This heat transfer is set equal to the increase in the thermal energy of the sphere. An unsteady, one-dimensional heat conduction problem has been linearized. A graph showing the variation of $Nu = \frac{hd}{k}$ versus $\frac{T_m}{T_s}$, or the ratio of mean to surface temperature, is shown in **Figure 4.1-1**. The mean temperature is, of course, a function of time. The coded version of $H_{if,drp}$ is based on the curve in **Figure 4.1-1**. The fact that Nu drops as $\frac{T_m}{T_s}$ increases follows from Fourier's law of conduction, which indicates that the heat transfer will decrease if the temperature gradient (related to T_s-T_m) decreases. The coded version of Nu for this case (Appendix 4A) is represented by Function F_{13}, which is

$$F_{13} = 2.0 + 7.0 \min \left[1.0 + \frac{C_{pf} \max(0.0, \Delta T_{sf})}{h_{fg}}, 8.0 \right] \quad . \tag{4.1-57}$$

F_{13} gives Nu = 9, compared to Nu = 10 in **Figure 4.1-1**, for $\frac{T_m}{T_s} = 1$ ($\Delta T_{sf} = 0$). It also gives the correct trend of Nu increasing as $\frac{T_m}{T_s}$ decreases (ΔT_{sf} increasing). It is not clear, however, how Brown arrived at the curve for Nu in **Figure 4.1-1**, since Nu is a complicated function of $\frac{T_m}{T_s}$ and involves specification of droplet diameter and length of time since initiation of heat transfer. Brown does not specify either of the above in arriving at the functional relationship, **Figure 4.1-1**.

In evaluating the validity of the model for Nu provided by Brown,[4.1-19] the following points are noted:

1. Brown's heat transfer problem does not address increasing droplet size due to condensation except in a correction applied to the mean temperature, T_m. It is not clear if this correction is incorporated in obtaining the curve in **Figure 4.1-1**. Furthermore, it appears that this correction is wrong, since it does not account for the relative masses of the original drop and the additional condensate. The correction is given as[4.1-19]

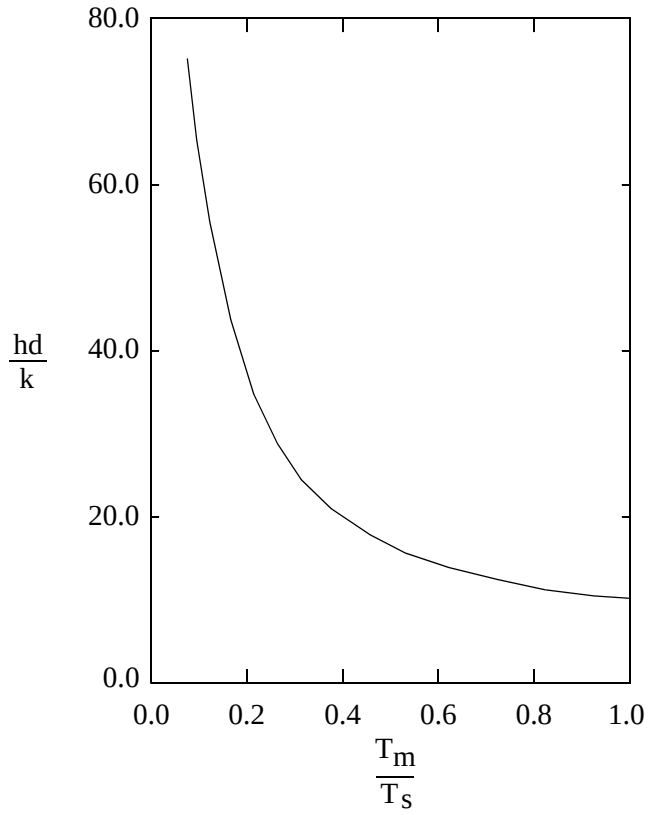

Figure 4.1-1 Nusselt number as a function of mean-to-surface-temperature ratio for heat conduction in a sphere.

$$T = \frac{T_f}{1 + \frac{C_{pf}\Delta T_{sf}}{h_{fg}}} \qquad (4.1\text{-}58)$$

where T_m is the mean temperature of the original drop and T_f that for the drop plus new condensate.

2. Brown assumes that the surface temperature of the drop remains constant; this same condition is assumed in ATHENA wherein the interface is assumed equal to the saturation temperature. Thus, the "convective" heat transfer between the interface and mean droplet temperature is actually based on conduction. True convection in the droplet is neglected. On the whole, this seems an appropriate simplification.

3. It is stated by Brown that this curve, **Figure 4.1-1**, is based on k = 0.38 Btu/hr•ft °F, the thermal conductivity of water at about 150 °F.

In summary, it seems that the correlation for $H_{if,drp}$ could be based on firmer ground by including the effects of condensation and comparing such with experimental data. An evaluation of this correlation requires assessment against experiment.

4.1.1.3.3 Annular Mist Superheated Vapor/Gas (SHG, $T_g > T^s$)--

Model as Coded

$$H_{ig} = H_{ig,ann} + H_{ig,drp} \tag{4.1-59}$$

where

$$H_{ig,ann} = \frac{k_g}{D} 0.023\ Re_g^{0.8}\ a_{gf,ann} F_{10}$$

$$Re_g = \frac{\alpha_g \rho_g |v_g - v_f| D}{\mu_g}$$

F_{10} and $a_{gf,ann}$ are as for annular mist SHL

and

$$H_{ig,drp} = \frac{k_g}{d_d}(2.0 + 0.5\ Re_d^{0.5}) a'_{gf,drp}$$

where

d_d is as for annular mist SHL

$$Re_d = \frac{(1-\alpha_{fd})^{2.5} \rho_g \hat{v}_{fg} d_d}{\mu_g} = \frac{We \bullet \sigma (1-\alpha_{fd})^{2.5}}{\mu_g \hat{v}_{fg}}\ ,\ We = 1.5,$$

$$We\ \sigma = \max (We\ \sigma, 10^{-10}\ N/m)$$

$$a'_{gf,drp} = a_{gf,drp} \qquad \alpha_f \geq \alpha^*_{AD}$$

$$= a_{gf,drp} \left[\frac{\alpha_f F_{14}}{a^*_{AD}} + (1 - F_{14}) \right] \qquad \alpha_f < \alpha^*_{AD}$$

$a_{gf,drp}$, α_{fd}, $\hat{v}_{fg}$, and α^*_{AD} are as for annular mist SHL

and

F_{14} = 1.0 - 5.0 min [0.2, max (0, ΔT_{sg})].

For an annulus component, $\alpha_{ff} = \alpha_f$ and $\alpha_{fd} = 0$.

Model Basis and Assessment

The coded correlation for the heat transfer between the vapor/gas and the liquid-vapor/gas interface for annular mist SHG consists of two parts.

The contribution to H_{ig} from the heat transfer from the vapor/gas to the liquid annular film is represented by a correlation obviously based on the Dittus-Boelter relation. While the Dittus-Boelter correlation is valid for turbulent flow, there is no test for turbulent flow in the code. An evaluation of this model requires an assessment against experiment.

The expression used to represent heat transfer from the vapor/gas core to the entrained liquid droplets is based on the correlation of Lee and Ryley,[4.1-3] except that the coefficient of the Reynolds number is changed from 0.74 to 0.5. A discussion of the Lee-Ryley model is given in Section 4.1.1.1.1.

The Reynolds number used for the modified Lee-Ryley correlation[4.1-3] employs a mixture viscosity defined as

$$\mu_m = \frac{\mu_c}{(1-\alpha_d)^{2.5}} \quad (4.1\text{-}60)$$

where c and d represent continuous and dispersed phases, respectively. This relationship is given by Ishii and Chawla[4.1-20] for use in a drag correlation for dispersed droplet flow. The Lee-Ryley correlation, however, employs Re based on the continuous phase $\left(\mathrm{Re} = U_\infty \frac{d}{\nu}\right)$, where U_∞ is the free-stream velocity and d is the droplet diameter. It seems inappropriate, therefore, to use a mixture viscosity.

Another significant limitation of the coded correlation appears to be that the liquid velocity, v_f, used in the Reynolds number is some average of the annular film and entrained droplets, rather than just the velocity of the droplets. The relative velocity computed, then, is not a true relative velocity for the droplets flowing in the vapor/gas core.

In summary, significant doubts remain about the validity of H_{ig} for annular mist SHG.

4.1.1.3.4 Annular Mist Subcooled Vapor/Gas (SCG, $T_g < T^s$)--

Model as Coded

$$H_{ig} = H_{ig,ann} + H_{ig,drp} \quad (4.1\text{-}61)$$

where

$$H_{ig,ann} = h_{ig} a_{gf,ann} F_{10} F_6$$

where h_{ig} and F_6 are as for bubbly SHG, and $a_{gf,ann}$ and F_{10} are as for annular mist SHL and

$$H_{ig,drp} = h_{ig} a'_{gf,drp} F_6$$

where

$a'_{gf,drp}$ is as for annular mist SHG.

For an annulus component, $\alpha_{ff} = \alpha_f$ and $\alpha_{fd} = 0$.

Model Basis and Assessment

Both parts of the volumetric heat transfer coefficient H_{ig} for annular mist SCG are based on large values which increase quadratically as ΔT_{sg} increases (Function F_6, Appendix 4A). This practice is clearly intended to push T_g toward the saturation temperature from its metastable subcooled state.

4.1.1.4 Inverted Annular Flow. The volumetric heat transfer coefficients for inverted annular flow, H_{if} and H_{ig}, are each based on the contributions from two sources: (a) the interfacial heat transfer between the bubbles and liquid in the liquid core (see **Figure 3.2-3**) and (b) the interfacial heat transfer between the liquid core and the annular vapor/gas film surrounding them. Equations (4.1-27) through (4.1-31) for slug flow apply to inverted annular flow with the annular contribution replacing that for the Taylor bubble (Tb). Hence, one can write for the total heat transfer:

$$Q_{ip}^{B} = H_{ip,bub}\Delta T + H_{ip,ann}\Delta T \quad . \quad (4.1\text{-}62)$$

If the liquid temperature is between one degree K subcooled and one degree K superheated, the final liquid coefficient H_{if} is the result of a cubic spline interpolation between the superheated and subcooled result.

4.1.1.4.1 Inverted Annular Superheated Liquid (SHL, $T_f > T^S$)--

Model as Coded

$$H_{if} = H_{if,bub} + H_{if,ann} \quad (4.1\text{-}63)$$

$H_{if,bub}$ is as for H_{if} for bubbly with the following modifications:

$$v_{fg} = (v_g - v_f)F_{16}^2 \quad (4.1\text{-}64)$$

where

F_{16} = $1 - F_{17}$

F_{17} = $\exp\left[\frac{-8(\alpha_{BS} - \alpha_{IAN})}{\alpha_{BS}}\right] F_{18}$

α_{IAN} = α_g Inverted annular

= α_{BS} IAN/ISLG transition (see **Figure 3.2-1**)

F_{18} = $\min\left(\frac{\alpha_g}{0.05}, 0.999999\right)$

β = F_{16}

α_g = α_{bub}

α_{bub} = $\max\left[\frac{(\alpha_{IAN} - \alpha_B)}{(1 - \alpha_B)}, 10^{-7}\right]$

α_B = $F_{17}\,\alpha_{IAN}$

$a_{gf,bub}$ = $\frac{3.6\alpha_{bub}}{d_b}(1 - \alpha_B)F_{16}$

d_b = average bubble diameter (see bubbly SHL)

and

$H_{if,ann}$ = $3 \times 10^6\, a_{gf,ann}$

where

$$a_{gf,ann} = \frac{4}{D} F_{15}(2.5)$$

$$F_{15} = (1 - \alpha_B)^{1/2}.$$

Model Basis and Assessment

The volumetric heat transfer coefficient, $H_{if,bub}$, for inverted annular SHL is based on that for pure bubbly flow SHL, Section 4.1.1.1.1, with some modifications to account for the fact that it only represents one part of the interfacial heat transfer. Function F_{16} (Appendix 4A) is an ad hoc function that accounts for the decrease in that portion of the void fraction related to the bubbles as α_g increases. Conversely, F_{17} (= 1 - F_{16}) represents the increasing portion of α_g due to the annular vapor/gas blanket. As such, the interfacial area, $a_{gf,bub}$, is correctly apportioned (see Section 4.1.1.3.1), as are α_B, the average vapor/gas volume of the annular vapor/gas blanket (analogous to α_{ff}), and α_{bub}, the void fraction of the bubbles in the liquid slugs.

The selection of the correlation to be used for $H_{if,bub}$, either Plesset-Zwick[4.1-1] or Lee-Ryley,[4.1-3] (Section 4.1.1.1.1), is affected, however, by diminishing the first (via parameter β) and increasing the second [via $v_{fg}(F_{16})^2$]. In forcing the selection of the Lee-Ryley correlation for larger α_g, which is appropriate, this logic also increases the magnitude of the Lee-Ryley correlation, which seems inappropriate.

The value used for $H_{if,ann}$ is simply a large number to drive T_f toward the saturation temperature, since this is a metastable state. The combination of the two parts of H_{if} amounts to an ad hoc correlation which must be assessed against experiment.

4.1.1.4.2 Inverted Annular Subcooled Liquid (SCL, $T_f < T^s$)--

Model as Coded

$$H_{if} = H_{if,bub} + H_{if,ann} \quad (4.1\text{-}65)$$

where

$H_{if,bub}$ is as for bubbly SCL

and

$$H_{if,ann} = \frac{k_f}{D} 0.023\ Re_{IAN}^{0.8}\ a_{gf,ann}\ F_3$$

where

$$Re_{IAN} = \frac{(1-\alpha_{IAN})\rho_f |v_f - v_g| D}{\mu_f}$$

$a_{gf,ann}$ and α_{IAN} are as for inverted annular SHL and F_3 is as for bubbly SHL.

Model Basis and Assessment

The same expression is used to compute $H_{if,bub}$ for SCL as for bubbly SCL, Section 4.1.1.1.2. The expression used for $H_{if,ann}$ is obviously based on the Dittus-Boelter correlation for turbulent flow in a duct. While the relative velocity is appropriately used in computing the Reynolds number for the Dittus-Boelter correlation, the correctness of the values it gives is unknown and must be assessed against experiment.

4.1.1.4.3 Inverted Annular Superheated Vapor/Gas (SHG, $T_g > T^s$)--

Model as Coded

$$H_{ig} = H_{ig,bub} + H_{ig,ann} \qquad (4.1\text{-}66)$$

where

$$H_{ig,bub} = h_{ig}\ F_6\ a_{gf,bub}$$

where

h_{ig} and F_6 are as for bubbly SHG and $a_{gf,bub}$ is as for inverted annular SHL

and

$$H_{ig,ann} = \frac{k_g}{D}\ F_{19}\ a'_{gf,ann}$$

where

$$F_{19} = 2.5 - \Delta T_{sg}\ (0.20 - 0.10\ \Delta T_{sg})$$

$$a'_{gf,ann} = \frac{a_{gf,ann}}{F_{20}}$$

$$F_{20} = 0.5 \max (1.0 - F_{15}, 0.04).$$

F_{15} and $a_{gf,ann}$ are as for inverted annular SHL.

Model Basis and Assessment

Both contributions to H_{ig} for inverted annular SHG are clearly ad hoc correlations and must be compared to experiments for evaluation purposes.

4.1.1.4.4 Inverted Annular Subcooled Vapor/Gas (SCG, $T_g < T^s$)--

Model as Coded

H_{ig} is as for inverted annular SHG.

Note that $\Delta T_{sg} > 0$ for this case (Function F_{19}).

Model Basis and Assessment

The same expression is used for this case as for inverted annular SHG with the minor variation of F_{19} for $\Delta T_{sg} > 0$ versus $\Delta T_{sg} < 0$, as noted in Appendix 4A. Since the expression used gives increasingly large values for Nu as $|\Delta T_{sg}|$ increases, the treatment is consistent with those for metastable SCG for other flow regimes.

4.1.1.5 Inverted Slug Flow. The inverted slug flow regime as envisioned by DeJarlais and Ishii[4.1-21] consists of bubble impregnated liquid slugs flowing in a pipe core surrounded by a vapor/gas blanket containing liquid droplets (see **Figure 3.2-3**). The coded volumetric heat transfer coefficients recognize the liquid droplets, vapor/gas blanket and liquid slugs, but not the presence of bubbles in the slugs. Contributions to the interfacial heat/mass transfer in the bulk are recognized, then, as coming from two sources: (a) the liquid droplet interfaces in the vapor/gas annulus and (b) the liquid slug/annulus interface. It is assumed, apparently, that the liquid slugs are so long that any contributions to interfacial heat transfer at their ends are negligible. One can write for the heat transfer as coded

$$Q^B_{ip} = H_{if,ann}\Delta T + H_{if,drp}\Delta T \quad . \tag{4.1-67}$$

If the liquid temperature is between one degree K subcooled and one degree K superheated, the final liquid coefficient H_{if} is the result of a cubic spline interpolation between the superheated and subcooled result.

4.1.1.5.1 Inverted Slug Superheated Liquid (SHL, $T_f > T^s$)--

Model as Coded

$$H_{if} = H_{if,ann} + H_{if,drp} \tag{4.1-68}$$

where

$$H_{if,ann} = \frac{k_f}{D} F_{12} F_{13} a_{gf,ann}$$

$$a_{gf,ann} = \frac{4.5}{D}\alpha_B(2.5)$$, where 2.5 is a roughness factor

$$\alpha_B = \frac{\alpha_f - \alpha_{drp}}{1 - \alpha_{drp}}$$

$$\alpha_{drp} = (1 - \alpha_{SA}) F_{21}$$

$$F_{21} = \exp\left(-\frac{\alpha_{SA} - \alpha_g}{\alpha_{SA} - \alpha_{BS}}\right)$$

F_{12} is as for annular mist SHL

and

$$H_{if,drp} = \frac{k_f}{d_d} F_{12} F_{13} a_{gf,drp}$$

where

$$a_{gf,drp} = \frac{3.6\alpha_{drp}}{d_d}(1 - \alpha_B)$$

$$d_d = \text{characteristic droplet diameter } (= \frac{1}{2}d_{max})$$

$$= \frac{We\ \sigma}{\rho_g v_{fg}^2}$$, We = 6.0, We σ = max (We σ, 10^{-10} N/m)

$$v_{fg} = \max [(v_g - v_f) F_{21}^2, 0.001 \text{ m/s}], We = 6.0.$$

The drop diameter is the maximum of d_d and d_{min}, where d_{min} = 0.0025 m for P* < 0.025 and 0.0002 m for P* > 0.25, $P^* = \frac{P}{P_{critical}}$. Between P* = 0.025 and P* = 0.25, linear interpolation is used. The drop diameter is the minimum of d_d, D, and 0.0025 m. Also, above a thermodynamic equilibrium quality of -0.02, the inverted slug interfacial heat transfer coefficient H_{if} is linearly interpolated with respect to equilibrium quality to a dispersed (droplet, mist) flow value at a thermodynamic equilibrium quality of zero.

Model Basis and Assessment

The expressions for $H_{if,ann}$ and $H_{if,drp}$ are both based on large values for the Nusselt number as provided by function F_{12} (see Appendix 4A). This tends to drive T_f toward the saturation temperature and is consistent with other treatments in the code for metastable states.

Interfacial Area

The interfacial areas for the annulus/droplet portion and the slug/annulus portion are derived analogously to those for slug flow, Section 4.1.1.2. The void fraction of the liquid slug, α_B, is analogous to that for a Taylor bubble, α_{Tb}, and the average droplet void in the vapor/gas blanket, α_{drp}, is analogous to the average void fraction, α_{gs}, in the liquid annulus for slug flow. That is, the interfacial areas are computed for inverted slug flow by simply reversing the liquid and vapor/gas phases from slug flow. The droplet void fraction, α_{drp}, in the vapor/gas annulus is based on an ad hoc expression which exponentially increases the portion of α_f due to droplets as α_g increases until the transition void fraction, α_{SA}, is reached, at which point all of the liquid is appropriately assumed to be in droplet form. The larger minimum drop size at low pressure was put in to allow more vapor/gas superheat during reflood.

4.1.1.5.2 Inverted Slug Subcooled Liquid (SCL, $T_f < T^S$)--

Model as Coded

$$H_{if} = H_{if,ann} + H_{if,drp} \tag{4.1-69}$$

where

$$H_{if,ann} = \frac{k_f}{D} F_{13}\, a_{gf,ann}$$

F_{13} is as for annular mist SCL, $a_{gf,ann}$ is as for inverted slug SHL

and

$$H_{if,drp} = \frac{k_f}{d_d} F_{13} a_{gf,drp}$$

where

$a_{gf,drp}$ is as for inverted slug SHL.

Also, above a thermodynamic equilibrium quality of -0.02, the inverted slug interfacial heat transfer coefficient H_{if} is linearly interpolated with respect to equilibrium quality to a dispersed (droplet, mist) flow value at a thermodynamic equilibrium quality of zero.

Model Basis and Assessment

The expressions for $H_{if,ann}$ and $H_{if,drp}$ for inverted slug SCL are both based on Brown's[4.1-19] model for droplets condensing in vapor/gas. The weaknesses of this model are discussed in Section 4.1.1.3.2. While Brown's model may be appropriate for $H_{if,drp}$, it clearly is not appropriate for the heat transfer between the liquid slug and vapor/gas interface. An evaluation of the expressions for inverted slug SCL for H_{if} requires assessment against experiment. Not allowing inverted slug flow when the liquid is saturated seems appropriate, because the water globes do not hold together well when they do not have the momentum forces of condensing vapor/gas on their boundaries.

4.1.1.5.3 Inverted Slug Superheated Vapor/Gas (SHG, $T_g > T^s$)--

Model as Coded

$$H_{ig} = H_{ig,ann} + H_{ig,drp} \tag{4.1-70}$$

where

$$H_{ig,ann} = \frac{k_g}{D} \frac{F_{19}}{F_{22}} a_{gf,ann}$$

F_{19} is as for inverted annular SHG, $a_{gf,ann}$ is as for inverted slug SHL

$$F_{22} = \max\left\{0.02, \min\left[\frac{\alpha_g}{4}\left(1 - \frac{\alpha_g}{4}\right), 0.2\right]\right\}$$

and

$$H_{ig,drp} = \frac{k_g}{d_d}(2.0 + 0.5\ Re_{drp}^{0.5})a_{gf,drp}$$

where

d_d and $a_{gf,drp}$ are as for inverted slug SHL

and

$$Re_{drp} = \frac{\rho_g v_{fg} d_d}{\mu_g}$$

where We = 6.0 and We σ = max (We σ, 10^{-10} N/m).

Above a thermodynamic equilibrium quality of -0.02, the inverted slug interfacial heat transfer coefficient H_{ig} is linearly interpolated with respect to equilibrium quality to a dispersed (droplet, mist) flow value at a thermodynamic equilibrium quality of zero.

Model Basis and Assessment

The Nusselt number upon which $H_{ig,ann}$ for inverted slug SHG is based (F_{19}/F_{22}, Appendix 4A) is ad hoc and requires comparison with experiments for evaluation.

The correlation used in the code for Nu for $H_{ig,drp}$ is a modified version of the Lee-Ryley[4.1-3] model for heat transfer to a droplet (see Section 4.1.1.1.1) in the process of evaporation. While the coded version of the Lee-Ryley correlation is within experimental uncertainty for Pr = 1, Section 4.1.1.1.1, the complications of turbulence in the vapor/gas blanket combined with the fact that liquid velocity is some average of the droplet and slug fields must be considered. Thus, a complete validation for H_{ig} for this case must include comparisons with experiments.

4.1.1.5.4 Inverted Slug Subcooled Vapor/Gas (SCG, $T_g < T^s$)--

Model as Coded

H_{ig} is as for inverted slug SHG.

Model Basis and Assessment

The same expressions are used for inverted slug SCG as for SHG for H_{ig}, Section 4.1.1.5.3. This is not consistent with the practice used for similar metastable states for other flow regimes, wherein Nu is set

to a large value to push T_f toward T^s. Comparison with experiment is required for an assessment of the validity of the model used here.

4.1.1.6 Dispersed (Droplet, Mist) Flow. In dispersed (droplet, mist) flow, the droplets are viewed as spheres. If the liquid temperature is between one degree K subcooled and one degree K superheated, the final liquid coefficient H_{if} is the result of a cubic spline interpolation between the superheated and subcooled result.

4.1.1.6.1 Dispersed Superheated Liquid (SHL, $T_f > T^s$)--

Model as Coded

$$H_{if} = \frac{k_f}{d_d} F_{12} F_{13} F_{23} a_{gf} \qquad (4.1\text{-}71)$$

where

F_{12} and F_{13} are as for annular mist SHL

F_{23} = $\frac{\alpha_{drp}}{\max(\alpha_f, 10^{-10})}$ for pre-CHF

= $\frac{\alpha_{drp}}{\max(\alpha_f, 10^{-12})}$ for post-CHF

a_{gf} = $\frac{3.6\alpha_{drp}}{d_d}$

α_{drp} = $\max(\alpha_f, 10^{-3})$ $X_n \neq 0.0$ and $\alpha_g = 1.0$ for pre-CHF

= $\max(\alpha_f, 10^{-4})$ $X_n = 0.0$ or $\alpha_g \neq 1.0$ for pre-CHF

= $\max(\alpha_f, 10^{-4})$ post-CHF

d_d = characteristic drop diameter $(=\frac{1}{2} d_{max})$

= $\frac{We\ \sigma}{\rho_g v_{fg}^2}$, We = 1.5 for pre-CHF and 6.0 for post-CHF,

We σ = max (We σ, 10^{-10} N/m)

$$v_{fg} = v_g - v_f$$

$$v_{fg}^2 = \begin{cases} \max\left[v_{fg}^2, \dfrac{We\ \sigma}{\rho_g \min(D'\alpha_{drp}^{1/3}, D)} \right] & \text{pre-CHF} \\ \max(v_{fg}^2, 10^{-6} m^2/s^2) & \text{post-CHF} \end{cases}$$

$$D' = \begin{cases} 0.0025\ m & \text{pre-CHF} \\ 0.0002\ m & \text{post-CHF} \end{cases} .$$

For post-CHF, the minimum drop diameter is as shown for inverted slug flow and the maximum drop diameter is the minimum of D and 0.0025 m.

Model Basis and Assessment

The volumetric heat transfer coefficient, H_{if}, for dispersed SHL is based on an ad hoc expression for Nusselt number which increases quadratically as $|\Delta T_{sf}|$ increases (function F_{12}, Appendix 4A), thus driving T_f toward T^s. Another function, F_{23}, is incorporated to improve numerical stability for high void fractions (i.e., low liquid volume fractions).

The volumetric interfacial area is based on the same derivation as that for bubbly flow (which is, in fact, based on the interfacial area of a droplet spray, see Section 4.1.1.1.1).

4.1.1.6.2 Dispersed Subcooled Liquid (SCL, $T_f < T^s$)--

Model as Coded

$$H_{if} = \frac{k_f}{d_d} F_{13}\ F_{23}\ a_{gf} \qquad (4.1\text{-}72)$$

where

F_{13} is as for annular mist SCL, F_{23} and a_{gf} are as for dispersed SHL.

Model Basis and Assessment

The volumetric heat transfer coefficient for dispersed SCL is based on the model of Brown,[4.1-19] which is discussed in detail in Section 4.1.1.3.2 for annular mist SCL. The same conclusions apply here.

4.1.1.6.3 Dispersed Superheated Vapor/Gas (SHG, $T_g > T^s$)--

Model as Coded

$$H_{ig} = \frac{k_g}{d_d}(2.0 + 0.5\ Re_{drp}^{0.5})F_{24}\ a_{gf} \qquad (4.1\text{-}73)$$

where d_d and a_{gf} are as for dispersed SHL

$$Re_{drp} = \frac{(1-\alpha_{drp})^{2.5}\rho_g v_{fg} d_d}{\mu_g} = \frac{We \bullet \sigma(1-\alpha_{drp})^{2.5}}{\mu_g v_{fg}} \quad \text{pre-CHF and post-CHF}$$

$$F_{24} = \max [0.0, F_{26}(F_{25} - 1) + 1]$$

$$F_{25} = 10^5 \min (\alpha_f, 10^{-5})$$

$$F_{26} = 1.0 - 5.0 \min [0.2, \max (0.0, \Delta T_{sg})].$$

Model Basis and Assessment

The Nusselt number correlation upon which H_{ig} for dispersed SHG is based is a modified form of the Lee-Ryley[4.1-3] model, where 0.5 has replaced 0.74 as the coefficient of $Re^{0.5}$ and the Prandtl number dependence has been dropped. A detailed discussion of the Lee-Ryley correlation is given in Section 4.1.1.1.1.

4.1.1.6.4 Dispersed Subcooled Vapor/Gas (SCG, $T_g < T^s$)--

Model as Coded

$$H_{ig} = h_{ig} F_6 F_{24} a_{gf} \qquad (4.1\text{-}74)$$

where

h_{ig} and F_6 are as for bubbly SHG, F_{24} and a_{gf} are as for dispersed SHG.

Model Basis and Assessment

The volumetric heat transfer coefficient as coded for dispersed droplet SCG is simply based on a large value for Nu (= $10^4 F_6$, Appendix 4A) which will push T_g toward the saturation temperature.

4.1.1.7 Horizontally Stratified Flow. In horizontally stratified flow, a flat interface is assumed to exist between the liquid and vapor/gas. If the liquid temperature is between one degree K subcooled and

one degree K superheated, the final liquid coefficient H_{if} is the result of a cubic spline interpolation between the superheated and subcooled result.

4.1.1.7.1 Horizontally Stratified Superheated Liquid (SHL, $T_f > T^s$)--

Model as Coded

$$H_{if} = \frac{k_f}{D_{hf}}\left[0.023 Re_f^{0.8} F_{12} - 3.81972 \frac{\Delta T_{sf} \rho_f C_{pf}}{\rho_g h_{fg} \max(4\alpha_g, 1)}\right] a_{gf} \qquad (4.1\text{-}75)$$

where

D_{hf} = liquid phase hydraulic diameter

= $\frac{\pi \alpha_f D}{\pi - \theta + \sin\theta}$ (see **Figure 3.1-2** for definition of θ)

Re_f = $\frac{\alpha_f \rho_f D |v_g - v_f|}{\mu_f}$

a_{gf} = $\left(\frac{4 \sin\theta}{\pi D}\right) F_{27}$

F_{27} = $1 + \left|\frac{v_g - v_f}{v_{crit}}\right|^{1/2}$.

F_{12} is as for annular mist SHL.

In the coding, D_{hf} is protected from being 0/0 when $\alpha_f = 0$, $\pi - \theta = 0$, and $\sin\theta = 0$.

Model Basis and Assessment

The expression used for the Nusselt number for H_{if} for horizontally stratified flow, while giving the appearance of modeling two processes [main interface (first term) plus entrained droplet interface (second term)], is effectively an ad hoc relationship which gives a large value. This is due to the presence of function F_{12}. This practice promotes the return of T_f toward T^s, which is generally used in the code for metastable states. The Nusselt number is converted to a heat transfer coefficient by use of a phasic hydraulic diameter defined as

$$D_{hf} = \frac{4 \text{ x phasic cross-sectional area}}{\text{phasic perimeter}} \quad . \qquad (4.1\text{-}76)$$

The expression for phasic hydraulic diameter given above incorporates the expression

$$\pi\alpha_f = \pi - \theta + \sin\theta\cos\theta \quad (4.1\text{-}77)$$

which can be derived from simple geometric considerations. (See **Figure 3.1-2** for the definition of angle θ).

Interfacial Area

The volumetric interfacial area is based on simple geometric considerations. It is easily shown that

$$a_{gf} = \frac{4\sin\theta}{\pi D} \quad (4.1\text{-}78)$$

for a smooth interface. A multiplicative parameter is applied to a_{gf} in the code to attempt to account for an increase in a_{gf} due to a wavy surface. This parameter is represented by function F_{27}, which appropriately increases as $\left|\frac{v_g - v_f}{v_{crit}}\right|$ increases. An evaluation of the validity of function F_{27} requires comparison with experiments.

4.1.1.7.2 Horizontally-Stratified Subcooled Liquid (SCL, $T_f < T^s$)--

Model as Coded

$$H_{if} = \frac{k_f}{D_{hf}}(0.023\ Re_f^{0.8})a_{gf} \quad (4.1\text{-}79)$$

where

D_{hf}, Re_f, and a_{gf} are as for horizontally-stratified SHL.

Model Basis and Assessment

The expression for the Nusselt number for horizontally stratified SCL is obviously based on the Dittus-Boelter correlation. The Reynolds number used for the correlation does not employ the phasic hydraulic diameter, as is the widely accepted practice for this correlation. Furthermore, the Dittus-Boelter correlation is valid for single-phase flow in solid-boundary ducts and not necessarily for a fluid-fluid boundary. Developmental assessment against Bankoff's stratified-flow condensation experiments[4.1-7,4.1-11] provided an indication of model acceptability. Comparison with further experiments is required for complete evaluation.

4.1.1.7.3 Horizontally Stratified Superheated Vapor/Gas (SHG, $T_g > T^s$)--

Model as Coded

$$H_{ig} = \frac{k_g}{D_{hg}}[0.023\ Re_g^{0.8} + 4h_{ig}F_6 max(0.0, 0.25 - \alpha_g)]a_{gf} \quad (4.1\text{-}80)$$

where

D_{hg} = vapor/gas phase hydraulic diameter

$$= \frac{\pi\alpha_g D}{\theta + \sin\theta}$$

$$Re_g = \frac{\alpha_g \rho_g D|v_g - v_f|}{\mu_g}.$$

h_{ig} and F_6 are as for bubbly SHG, and a_{gf} is as for horizontally stratified SHL.

Model Basis and Assessment

In the coding, D_{hg} is protected from being 0/0 when $\alpha_g = 0$, $\theta = 0$, and $\sin\theta = 0$.

The Nusselt number upon which the expression for H_{ig} for horizontally stratified SHG is based has two parts; the first part is the Dittus-Boelter correlation and the second part is a large number ($h_{ig} F_6$). The same criticisms pertaining to horizontally stratified SCL apply, including the fact that Re_g is not based on the phasic hydraulic diameter. Thus, H_{ig} is basically ad hoc for this thermodynamically stable state.

4.1.1.7.4 Horizontally Stratified Subcooled Vapor/Gas (SCG, $T_g < T^s$)--

Model as Coded

$$H_{ig} = h_{ig} F_6 a_{gf} \quad (4.1\text{-}81)$$

where

h_{ig} and F_6 are as for bubbly SHG, and

a_{gf} is as for horizontally stratified SHL.

Model Basis and Assessment

The expression for H_{ig} for this case is the same as for horizontally-stratified SHG (except for the difference in F_6 for a SCG, Appendix 4A). The use of a large Nu to drive T_g toward T^s is consistent with the treatment of other metastable states.

4.1.1.8 Vertically Stratified Flow and Transition. The two-phase flow in vertical control volumes can become vertically stratified for low mass fluxes. If the volume average mixture velocity is less than the Taylor bubble rise velocity, i.e.,

$$\frac{v_m}{v_{Tb}} < 1 \tag{4.1-82}$$

where v_m and v_{Tb} are given by Equations (3.2-1) and (3.2-16), respectively, transition to vertically stratified flow begins. If the criterion in Equation (4.1-82) is not met, the flow is completely unstratified. The vertical stratification model is not intended to be a mixture level model.

The correlations used for H_{if} and H_{ig} in the transition region (**Figure 3.2-1**) are combinations of those already computed for nonstratified flow and the stratified correlations (Appendix 4A). The transition region extends down to $\frac{v_m}{v_{Tb}} = 1/2$ for the stable states (SCL, SHG). The exceptions to this transition interval are for $\alpha_f < 0.01$ or $\Delta T_{sf} < 0$ for H_{if}, and $\Delta T_{sg} > 0$ for H_{ig}. If the liquid temperature is between one degree K subcooled and one degree K superheated, the final liquid coefficient H_{if} is the result of a cubic spline interpolation between the superheated and subcooled result.

4.1.1.8.1 Vertically Stratified Superheated Liquid (SHL, $T_f > T^s$)--

Model as Coded

$$H_{if} = Nu_f \frac{k_f}{D} a_{gf}(1 - F_{30}) + H_{if,REG} F_{30} \tag{4.1-83}$$

where

REG = flow regime of flow when not vertically stratified, which can be BBY, SLG, SLG/ANM, ANM, MPR, IAN, IAN/ISL, ISL, MST, MPO, BBY/IAN, IAN/ISL-SLG, SLG/ISL, ISL-SLG/ANM, ANM/MST, MPR/MPO (see flow regime maps, **Figure 3.2-1**).

F_{30} = max (F_{32}, F_{33}, F_{34})

F_{32} = $1.0 - \min(1.0, 100\alpha_f)$

F_{33} = $\max\left[0.0, 2.0\min\left(1.0, \frac{v_m}{v_{Tb}}\right) - 1.0\right]$

v_{Tb} = Taylor bubble rise velocity, Equation (3.2-16)

v_m = $\frac{G_m}{\rho_m}$

G_m = $\alpha_g\rho_g|v_g| + \alpha_f\rho_f|v_f|$

ρ_m = $\alpha_g\rho_g + \alpha_f\rho_f$

F_{34} = $\min(1.0, -0.5\,\Delta T_{sf})$

a_{gf} = $\frac{A_c}{V} = \frac{A_c}{A_c L} = \frac{1}{L}$

L = length of volume cell

A_c = cross-section area of cell.

Nu_f = $0.27\,(Gr_f Pr_f)^{0.25}$

Gr_f = $\frac{g\beta\rho_f^2 D^3 \max(|T_f - T^s|, 0.1K)}{\mu_f^2}$

β = $\max(\beta_f, 10^{-5}\,K^{-1})$

Pr_f = $\left(\frac{\mu C_p}{k}\right)_f$.

Model Basis and Assessment

Vertical stratification can occur for superheated liquid only in the interval $-2 < \Delta T_{sf} < 0$. Even then, it is considered to be in a transition state, since the partitioning function F_{30} is nonzero (Appendix 4A).

For both pressurizer and non-pressurizer components, the Nusselt number correlation[4.1-22,4.1-23] is for the lower surface of a heated horizontal plate or the upper surface of a cooled horizontal plate. It is recommended by McAdams as well as Incopera and DeWitt for laminar Grashof numbers in the range of 3

x 10^5 to 3 x 10^{10}. Data in the turbulent range are lacking. Use of this condition worked well for the MIT pressurizer problem (see Volume III of this manual), but wall condensation was dominant in that problem. Further validation is needed.

The pressurizer component input to ATHENA also allows the user to specify the liquid interfacial heat transfer coefficient. The Nusselt number for this case is given by

$$Nu_f = hif_{in}\frac{D}{k_f} \tag{4.1-84}$$

where hif_{in} is the user specified liquid interfacial heat transfer coefficient.

Interfacial Area

The interfacial area per unit volume for vertically stratified flow is simply the cross-sectional area of the control volume divided by its volume, which results in the reciprocal of cell-volume length, L.

4.1.1.8.2 Vertically Stratified Subcooled Liquid (SCL, $T_f < T^S$)--

Model as Coded

H_{if} is as for vertically stratified SHL.

Model Basis and Assessment

Fully vertically stratified flow can exist for SCL. The same expression is used for SCL as was used for SHL, except that the partition function allows fully stratified flow; that is, function $F_{34} = 0$ for all $\Delta T_{sf} > 0$, which allows the partition function F_{30} to be zero in low flow conditions and $\alpha_f > 0.01$.

4.1.1.8.3 Vertically Stratified Superheated Vapor/Gas (SHG, $T_g > T^S$)--

Model as Coded

$$H_{ig} = Nu_g\left(\frac{k_g}{D}\right)a_{gf}(1 - F_{35}) + H_{if,REG}F_{35} \tag{4.1-85}$$

where

F_{35} = max (F_{32}, F_{33}, F_{36}).

REG, F_{33}, Nu_g are as for vertically stratified SHL except that vapor/gas properties rather than liquid properties are used to calculate Nu_g,

$$F_{32} = \begin{cases} 1.0 - \min(1.0, 100\alpha_g) & \text{level model on} \\ 0.0 & \text{level model off} \end{cases}$$

$$F_{36} = \min (1.0, 0.5\ \Delta T_{sg})$$

a_{gf} is as for vertically stratified SHL.

Model Basis and Assessment

The transition H_{ig} is analogous to that for H_{if} with the function F_{35} linearly partitioning the contributions between stratified and unstratified models (Appendix 4A). The interfacial area is the same as for SHL. Comparison with experimental data is required to evaluate the model for H_{ig} for vertically stratified flow.

4.1.1.8.4 Vertically Stratified Subcooled Vapor/Gas (SCG, $T_g < T^s$)--

Model as Coded

H_{ig} is as for vertically stratified SHG.

Model Basis and Assessment

Fully stratified flow for SCG is not recognized; only a transition between stratified and unstratified flow is recognized (Appendix 4A). Otherwise, the model used for vertically stratified SCG is the same as for SHG.

4.1.2 Flow-Regime Transitions

A number of transitions between flow regimes are incorporated into ATHENA for purposes of interfacial heat and mass transfer. These transitions are illustrated schematically in **Figure 3.1-1**, **Figure 3.2-1**, and **Figure 3.3-1** (horizontal, vertical, and high mixing maps, respectively). Included are

Horizontal

1. Slug-annular mist

2. Horizontally stratified-nonstratified

Vertical

1. Slug-annular mist.

2. Vertically stratified-nonstratified.

3. Inverted annular-inverted slug.

4. Transition boiling regime (post-CHF, pre-dryout).

5. Bubbly-inverted annular.

6. (Inverted annular-inverted slug)-slug.

7. Slug-inverted slug.

8. Inverted slug-(slug-annular mist).

9. Annular mist-dispersed (droplet).

High Mixing Map

- Bubbly-dispersed (droplet)

These transitions are included in the code to prevent the numerical instability which can arise when abruptly switching from one flow regime to another. In most cases, the correlation from one regime is exponentially reduced, while that for the other is exponentially increased from a negligible amount to full value. Power law interpolation is used because the coefficients can often be orders of magnitude apart; linear interpolation would weight the large value too heavily. The power law interpolation has the form

$$c = c_1^f \bullet c_2^{1-f} \tag{4.1-86}$$

where c, c_1, and c_2 are the coefficients and f takes on values from 0 to 1. This interpolation is really the linear interpolation of the logarithms of the two coefficients, that is,

$$\ln c = f \ln c_1 + (1 - f) \ln c_2 \ . \tag{4.1-87}$$

The only exception is the transition from bubbly-to-dispersed flow for the high mixing map, which uses linear interpolation. In some cases, three and even four correlations/models are combined to obtain the volumetric heat transfer coefficients. For instance, the transitional boiling region between slug and the transition between inverted annular and inverted slug (IAN/ISL-SLG) can undergo transition to vertical stratification, combining four models to obtain H_{if} and H_{ig}.

The full details of the transition/combination logic used in the code are found in Appendix 4A.

4.1.3 Time-Smoothing

The constitutive models that are used in most two-phase models are formulated as algebraic functions of the dependent variables, and the models to be used are selected based on flow-regime considerations. This can result in discontinuous functions and/or very rapid change in the constitutive parameters. Naturally, such formulations impact the accuracy of the numerical scheme. An approach in wide usage to ameliorate the effect of such formulations is time-smoothing (sometimes also called under-relaxation). This process has been effective in permitting a larger time step and thus achieving faster running. However, this process can have significant effect on the computed results[4.1-24,4.1-25] unless it is implemented in a time-step insensitive manner.

The code implements time-smoothing of the interfacial heat transfer coefficients, H_{if} and H_{ig}, and the direct heating heat transfer coefficient, H_{gf}, by logarithmically weighting the old time-value of a parameter (denoted by n) with the new time-calculated value of a parameter (denoted by n+1). This is given by

$$f_{weight}^{n+1} = f_{calculated}^{n+1}\left(\frac{f_{weight}^{n}}{f_{calculated}^{n+1}}\right)^{\eta} \tag{4.1-88}$$

where f is the function to be smoothed and η is the weighting factor. The term f_{weight}^{n} is the old time-value of the function f, and the term $f_{calculated}^{n+1}$ is the new time-calculated value of the function f.

For H_{if}, the equation for η was developed by Chow and Bryce, documented in Feinauer at al.,[4.1-26] and assumes the form

$$\eta = \exp\left(-\min\left\{0.693, \max\left[\frac{\Delta t}{\tau_c}\max(0.01, \alpha_f), 1.0 - \min(1.0, \alpha_f \bullet 10^7), \min\left(\frac{\Delta t}{\tau_f}, \gamma_s\right)\right]\right\}\right) \tag{4.1-89}$$

where

$$\tau_c = \frac{\Delta x}{0.7\min(|v_g|, |v_f|)}$$

$$\tau_f = \frac{1.0}{\left[\frac{\max\left(g, \frac{gD^*}{19}\right)}{D}\right]^{1/2}}$$

$$D^* = D\left[\frac{g(\rho_f - \rho_g)}{\sigma}\right]^{1/2}$$

$$\gamma_s = \max\left\{\frac{0.10536, [\min(|v_g|, |v_f|) + 10^{-7}\,m/s]}{\max(|v_g|, |v_f|, 10^{-7}\,m/s)}\right\}.$$

In Equation (4.1-89), τ_c is a Courant-type of time constant. The term γ_s is large when there is a large slip velocity between the liquid and vapor/gas at low velocities. It is used (see p. 75 of Feinauer et al.,[4.1-26]) because of the dependence of the calculated H_{if} on the slip velocity for some regimes. The τ_f term is a gravity-related time constant to cover the cases when velocities are low.

If $H^{n+1}_{if,\,calculated} > H^n_{if}$, then η is modified to give

$$\eta = \eta \{1.0 + \max [-0.5, 0.25 \min (0.0, T^s - T_f)]\} \quad . \tag{4.1-90}$$

This reduces the time smoothing factor η by a factor of 2 over a 2.0-degree K range as the liquid enters the metastable (superheated) state. This helps keep H_{if} higher when in the metastable state and drives the liquid back to saturation.

For H_{ig}, Equation (4.1-89) is modified to use α_g instead of α_f and to use 10^5 instead of 10^7. If $H^{n+1}_{ig,\,calculated} > H^n_{ig}$, then η is modified to give

$$\eta = \eta \{1.0 - 2.5 \max [0.0, \min (0.2, T^s - T_g)]\} \quad . \tag{4.1-91}$$

This reduces the time smoothing factor η by a factor of 2 over a 0.2-degree K range as the vapor/gas enters the metastable (subcooled) state. This helps keep H_{ig} higher when in the metastable state and drives the vapor/gas back to saturation.

Ransom[4.1-24] and Ransom and Weaver[4.1-25] indicated that a time step insensitive procedure is obtained if η is of the exponential form

$$\eta = e^{-\Delta t/\tau} \tag{4.1-92}$$

where τ is a time constant associated with the physical process. Equation (4.1-89) will produce an equation like Equation (4.1-92) when the min/max logic results in η being $\exp\left(-\frac{\Delta t}{\tau_c}\right)$ or $\exp\left(-\frac{\Delta t}{\tau_f}\right)$. Otherwise, it

is time-step size dependent and nodalization dependent. Modifications are being tested so that the time-step size dependency and nodalization dependency will be removed in the future.

4.1.4 Modifications to Correlations--Noncondensable Gas

The presence of a noncondensable gas is represented by the mass fraction (X_n) of the combination of noncondensable and vapor which is attributable to the noncondensable gas. The effects of a noncondensable gas are represented by multipliers that modify and reduce the volumetric heat transfer coefficients, H_{if} and H_{ig}. Function F_4, which is embedded in function F_3, is an ad hoc modifier for H_{if} for bubbly SHL (Appendix 4A). Its influence is felt whenever H_{if} for bubbly flow is used to help define the overall H_{if} for a flow regime. Further modifications are applied to H_{if} and H_{ig} for all flow regimes or transition regimes depending on the thermodynamic state (SHL, SCL, SHG, SCG) as detailed in Appendix 4A, Modifications for Noncondensable Gas. All are ad hoc except the modification to H_{if} for SCL. This modification factor (F_{40}) is from the Vierow-Schrock correlation.[4.1-27].

4.1.5 Modifications to Correlations--Limits

An upper limit has been placed on the liquid interfacial heat transfer coefficient, H_{if}, in all the flow regimes when the liquid is subcooled. This limit is umbrella-shaped so as to force the coefficient to small values as the void fraction, α_g, approaches zero or one. The expression used is

$$H_{if} = \min \{H_{if}, 17539 \max [4.724, 472.4\, \alpha_g(1 - \alpha_g)] \bullet \max \left[0, \min\left(1, \frac{\alpha_g - 1.0\text{x}10^{-10}}{0.1 - 1.0\text{x}10^{-10}}\right)\right]\} \quad . \quad (4.1\text{-}93)$$

This limit was required to prevent code failures due to thermodynamic property errors caused by high condensation rates during N-Reactor simulations.[4.1-28] A similar umbrella limit has been used in the COBRA[4.1-29] and TRAC-BF[4.1-30] codes. The number 472.4 is from the COBRA code and was arrived at by making some assumptions on bubble/drop size, the number 4.724 is a lower limit (1% limit), and the number 17539 is the heat transfer coefficient used for this limit that was in the COBRA code at the time of the N-Reactor calculation.[1]

At pressures for a PWR primary loop, this umbrella limit can result in too low an interfacial condensation rate compared to the subcooled boiling model, which can result in some amounts of vapor/gas remaining in the primary loop. The small amount of vapor/gas is unphysical, and it can cause problems with other models in the code. As a result, a pressure-dependent linear ramp is used that begins

1. Personal communication, M. J. Thurgood to R. A. Riemke, September 1991.

ramping off the umbrella limit at 1,250 psia (8.618 x 10^6 Pa) and eventually turns it off at 1,500 psia (10.342 x 10^6 Pa).

A lower limit has been placed on both the liquid (H_{if}) and vapor/gas (H_{ig}) interfacial heat transfer coefficients. The limits are $H_{if,min} = H_{ig,min} = 0$. These values of zero correctly result in no mass transfer from the phase that is present in single-phase correlations. An upper limit has been placed on both H_{if} and H_{ig}. The limits are $H_{if,max} = H_{ig,max} = 10^{14}$ W/m^2·K.

Limits are also placed on the interfacial heat transfer coefficients based on a 50% vaporization/condensation limit. The limits are designed to reduce one of the interfacial heat transfer coefficients if more than 50% of the liquid would be vaporized on this time step or if more than 50% of the vpaor/gas would be condensed on this time step. This is used to help prevent code failure when a phase disappears. The method is as follows. First, the mass-per-unit volume from the mass transfer is calculated based on old temperatures from

$$\text{term} = \left[\Gamma_w^n - \frac{\frac{P_s^n}{P^n} H_{ig}^n (T^{s,n} - T_g^n) + H_{if}^n (T^{s,n} - T_f^n)}{h_g^{*,n} - h_f^{*,n}} \right] \Delta t \quad . \tag{4.1-94}$$

For vaporization (term > 0), if term > 0.5 $\alpha_f^n \rho_f^n$, the scaling factor AVELFG is computed from

$$\text{AVELFG} = \frac{0.5 \alpha_f^n \rho_f^n}{\text{term}} \quad . \tag{4.1-95}$$

For condensation (term < 0), if - term > 0.5 $\alpha_g^n \rho_g^n (1 - X_n^n)$, the scaling factor AVELFG is computed from

$$\text{AVELFG} = - \frac{0.5 \alpha_g^n \rho_g^n}{\text{term}} (1 - X_n^n)^n \quad . \tag{4.1-96}$$

For mostly liquid ($\alpha_g < 0.5$), H_{if} is modified to use

$$H_{if} = H_{if} \bullet \text{AVELFG} \tag{4.1-97}$$

and for mostly vapor/gas ($\alpha_g \geq 0.5$), H_{ig} is modified to use

$$H_{ig} = H_{ig} \bullet \text{AVELFG} \ . \tag{4.1-98}$$

4.1.6 Modifications to Correlations -- Smoothing Between Superheated and Subcooled

For the bubbly, slug, annular mist, inverted annular, inverted slug, dispersed (droplet), horizontally stratified, and vertically stratified flow regimes, if the liquid temperature is between one degree K subcooled and one degree K superheated, the final liquid coefficient H_{if} is the result of a cubic spline interpolation between the superheated and subcooled result. For the slug and annular-mist flow regimes, if the vapor/gas temperature is between one degree K subcooled and one degree K superheated, the final vapor/gas coefficient H_{ig} is the result of a cubic spline interpolation between the superheated and subcooled result. The interpolation for both the liquid and vapor/gas has the following form:

$$H_{ip} = H_{ip,\,subcooled}^{\eta} \bullet H_{ip,\,superheated}^{1-\eta} \tag{4.1-99}$$

where

$$\eta = \eta_1^2(3 - 2\eta_1)$$

$$\eta_1 = \max\left\{0.0, \min\left[1.0, \frac{1}{2}(T^s - T_p + 1.0\text{K})\right]\right\}$$

p is either liquid (f) or vapor/gas (g).

4.1.7 Modifications to Correlations -- Vertically Stratified Flow

If a volume is vertically stratified and more liquid is coming into the volume than there is vapor/gas available, then the liquid interfacial heat transfer coefficient H_{if} in the volume above the vertically stratified volume is modified in anticipation that the level will be appearing in the volume. The modification is of the form

$$H_{if,\,above}^{n+1} = H_{if,\,above,\,calculated}^{n} \bullet \text{AVEV} + H_{if,\,below,\,vertstrat}^{n+1}(1 - \text{AVEV}) \tag{4.1-100}$$

where

$$\text{AVEV} = \frac{\max(10^{-2}\text{K}, T_{above}^s - T_{f,\,above})}{\max(10^{-2}\text{K}, T_{below}^s - T_{f,\,below})}\left\{1.0 - \max\left[0.0, \min\left(1.0, 200.0\sqrt{\frac{V_{fin}}{V_{above}}}\right)\right]\right\}$$

V_{above} = volume of the volume above the vertically stratified volume

V_{fin} = volume of vapor/gas and liquid increase in the vertically stratified volume - volume of vapor/gas in the vertically stratified volume

$$= \sum_{j}^{N} (\dot{\alpha}_{fj}\dot{\rho}_{fj}v_{fj} + \dot{\alpha}_{gj}\dot{\rho}_{gj}v_{gj})A_j \bullet \frac{\Delta t}{\rho_f} - \alpha_{g,\,below} \bullet V_{below}$$

N = number of junctions connected to the vertically stratified volume

V_{below} = volume of the volume below in the vertically stratified volume.

4.1.8 Modifications to Vertically Stratified Flow or Level Model Caused from a Jet Junction

A junction at the bottom of a vertical volume, in which a subcooled liquid pool may exist, can be flagged as a "jet" junction. The fluid from the jet causes a stirring action in the pool to increase the condensation rate on the surface of the pool. The jet induced surface turbulence intensity is a function of the distance of the surface from the jet, the pool diameter, the jet Reynolds number, and fluid properties such as the Prandtl and Jacob numbers.

Thomas[4.1-31] obtained surface heat transfer experimental data for vertical geometries at pressures near ambient. Condensation rate measurements were made at six liquid levels, with either two or three nozzle diameters, and the inlet flow rate was varied to yield nozzle Reynolds numbers in the range from about 15,000 to 90,000. Thomas also ran an experiment (in a 1.2 m by 1.8 m tank) to evaluate the Kutateladze number at which "surface breakup" occurred. Surface breakup is defined as the point at which the surface is so disturbed by the liquid jet that vapor/gas entrainment occurs. Thomas found that the critical Kutateladze number was

$$\frac{\rho_f v_j^2}{[(\rho_f - \rho_g)g\sigma]^{0.5}} = \left(0.46\frac{z}{d}\right)^2 \qquad (4.1\text{-}101)$$

where

v_j = liquid jet velocity

σ = surface tension

d = liquid inlet diameter

z = height of liquid surface above inlet.

Some of his data was taken above the critical value. Surface heat transfer varied almost linearly with the jet Reynolds number below the critical value. All the data points taken at the lowest liquid level had a Kutateladze number above the critical value.

4.1.8.1 Surface Heat Transfer Model for Velocities Below the Critical Value. Pre-surface breakup correlations are grouped in high, medium, and low liquid level correlations.

<u>High Liquid Levels, z/D > 3.2:</u>

Brown-Khoo-Sonin[4.1-32] developed a high liquid level correlation in terms of the Stanton, Nusselt, Reynolds, Prandtl, Jacob, and Richardson numbers. It is given by

$$St = St_o\left(1 - \frac{Ja}{2}\right) \tag{4.1-102}$$

where

$$St = \frac{Nu_D}{Re_f Pr_f}$$

$$Nu_D = h_{if}\frac{D}{k_f}$$

$$Re_f = \frac{\rho_f v_b D}{\mu_f}$$

$$Pr_f = \frac{\mu_f C_{pf}}{k_f}$$

$$St_o = \frac{0.0198}{Pr_f^{0.33}}, \text{ for Ri less than 1}$$

$$= 0.136 - 0.00081Ri, \text{ for } 3.5 < Ri \le 15$$

$$\text{interpolate, for } 1 \le Ri \le 3.5$$

$$Ri = \min\left[\frac{\beta_f g(T^s - T_f)\Lambda}{v_b^2}, 15\right]$$

$$\Lambda = 0.24D$$

where D is the pool diameter.

The turbulent velocity, v_b, used in the Brown-Khoo-Sonin correlation was developed by Sonin-Shimko-Chun[4.1-33]

$$v_b = \Phi(Re)\left(\frac{Q}{Dd}\right)e^{-1.2\frac{z}{D}} \tag{4.1-103}$$

where

$\Phi(Re)$ = 21.1 for $Re_j > 25{,}000$

= 35 for $Re_j < 5{,}000$

interpolate for $5{,}000 \le Re_j \le 25{,}000$

Re_j = $\frac{\rho_b v_j A_j}{d\mu_b}$

Q = $v_j A_j$, the jet inlet liquid volumetric flow rate

A_j = jet inlet flow area

and d is the jet diameter and the subscript b represents pool bulk conditions.

Low Liquid Levels, z/D < 2.5:

Brown-Helmick-Sonin[4.1-34] obtained data and developed the correlation

$$St = 0.5\left(1 - \frac{Ja}{2}\right)\frac{\left[0.2\beta_2 - (0.14\beta_2 - 0.06\beta_1)\frac{z}{D}\right]}{Pr_f^{0.33}} \tag{4.1-104}$$

where

β_1 = 0.34

β_2 = 0.24

$$St = \frac{Nu}{Re_n Pr_f}$$

$$Nu = h_{if}\frac{D}{k_f}$$

Re_n = nozzle Reynolds number = $\frac{\rho_f v_j d}{\mu_f}$.

The 0.5 in front of the Brown-Helmick-Sonin correlation is not in the quoted literature. However, by closely examining the data upon which the correlation was based, it is evident that an error was made in the paper. This error was perpetuated from Brown's thesis[4.1-35] which contains the "raw" data.

Medium Liquid Levels, $2.5 < z/D < 3.2$:

Interpolate between Equations (4.1-102) and (4.1-104).

Final Interphase Liquid Heat Transfer Coefficient

The interphase liquid heat transfer coefficient used by the code (H_{if}) is then given by

$$H_{if} = h_{iflevel}\left(\frac{A_{level}}{V_{Total}}\right) \qquad (4.1\text{-}105)$$

where

$$A_{level} = \frac{\pi D^2}{4}$$

V_{Total} = volume of vapor/gas and liquid.

$h_{iflevel}$ is from Brown-Helmeck-Sonin, Sonin-Shimko-Chun, Brown-Khoo-Sonin, or interpolated. H_{if} used in the code has been multiplied by the area per unit volume.

4.1.8.2 Surface Heat Transfer Model for Velocities Above the Critical Value. Thomas[4.1-31] has given a method to predict the critical Kutateladze jet velocity at which breakup occurs for a given liquid level. No literature has been found that predicts post-surface breakup heat transfer. The approach used is to assume that the velocity head loss for "no surface break through" is predicted from the Kutateladze velocity and any remaining kinetic energy causes a fountain as shown in **Figure 4.1-2**. The fountain velocity is given by

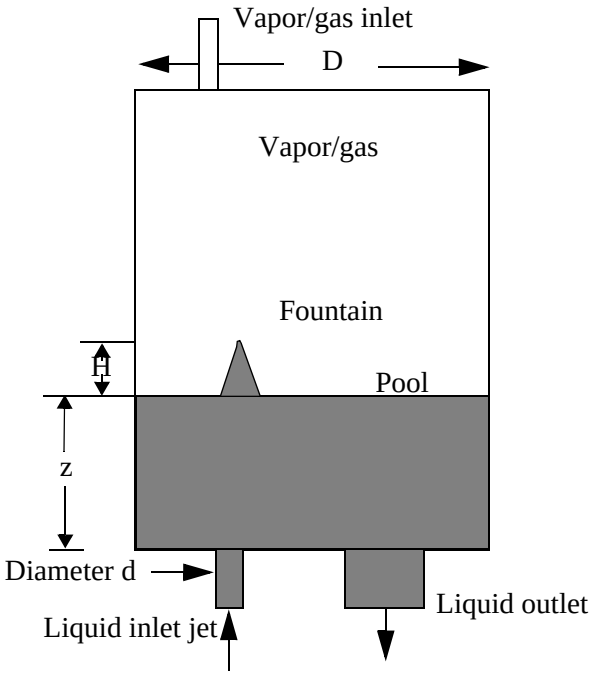

Figure 4.1-2 Pool with surface breakup.

$$v_{fountain}^2 = v_{jet}^2 - v_{critical}^2 \tag{4.1-106}$$

where from Equation (4.1-101)

$$v_{critical}^2 = \left(0.46\frac{z}{d}\right)^2 \frac{[(\rho_f - \rho_g)g\sigma]^{0.5}}{\rho_f} \quad . \tag{4.1-107}$$

The height of the liquid fountain above the surface, H, is approximated using the Bernoulli equation which equates the initial kinetic energy to the potential energy at the top of the fountain

$$\frac{v_{fountain}^2}{2} = gH \quad . \tag{4.1-108}$$

The Theofanous[4.1-17] jet equation is used to predict the additional heat transfer and is given by

$$St_{fountain} = 0.02\left(\frac{d}{H}\right)^{0.5} \quad . \tag{4.1-109}$$

Until data is found that gives the fountain diameter, the jet diameter, d, will be used. The total heat transfer when the inlet jet velocity is larger than the critical velocity is the sum of the heat transfer to the fountain and the heat transfer to the stratified level. Two heat transfer areas are involved. The energy from the two surfaces must be added and converted to an equivalent heat transfer coefficient. This is determined from

$$q_{total} = (h_{iflevel} A_{level} + h_{iffountain} A_{fountain}) (T^s - T_f) \quad (4.1\text{-}110)$$

$$H_{if} = \frac{q_{Total}}{A_{level}(T^s - T_f)}\left(\frac{A_{level}}{V_{Total}}\right) \quad (4.1\text{-}111)$$

where

$A_{level} = \frac{\pi D^2}{4}$

$A_{fountain} = 2\pi dH$

V_{Total} = volume of vapor/gas and liquid.

$h_{iflevel}$ is from Brown-Helmick-Sonin, Sonin-Shimko-Chun, Brown-Khoo-Sonin, or interpolated. $h_{iffountain}$ is from the Theofanous jet correlation. H_{if} is the value used in ATHENA. H_{if} used in the code has been multiplied by the area per unit volume.

The high liquid level data sources have some data points with inlet velocities which exceed the predicted critical value. However, experimenters such as Brown-Khoo-Sonin reported no breakthrough. Correlations such as Brown-Khoo-Sonin were developed to predict data without any fountain contribution. Consequently, the fountain contribution is arbitrarily linearly ramped to zero between a z/D of 0.5 and 1.0. The critical velocity correlation may not have a wide range data range of applicability.

4.1.9 Direct Heating

The direct (sensible) heating between the vapor/gas and liquid becomes important when there is noncondensable present (see Volume I). When $P_s < P$, this occurs. The value used for the direct heating heat transfer coefficient is

$H_{gf} = 0$ if $\alpha_f = 0$ and $[T^s \leq T_g$ or $P_s < P_{triplepoint}]$

$$H_{gf} = \begin{cases} H_{ig}(T_g > T^s) & T_g > T^s \\ H_{ig}(T_g = T^s) & T_g \le T^s \end{cases} \quad \text{otherwise.} \tag{4.1-112}$$

Thus, when the vapor/gas is subcooled, H_{gf} uses the value of H_{ig} at saturation. The term H_{gf} uses flow transitions and time smoothing like H_{ig}.

Using H_{ig} for the value of H_{gf} has the advantage that H_{gf} will depend upon the configuration of the interface (i.e. flow regime) between the liquid and the noncondensable vapor/gas. This is due to the presence of the interfacial area term a_{gf}.

4.1.10 Summary

Table 4.1-1 summarizes the interfacial area per unit volume (a_{gf}) and the interfacial heat transfer coefficient for phase p (h_{ip}) for the various flow regimes. The units for a_{gf} are m^{-1}, and the units for the interfacial heat transfer coefficinets are $W/m^2 \cdot K$. The superscript M indicates that the correlation has been modified from the literature value.

Table 4.1-1 Summary of interfacial areas and heat transfer coefficients[1].

Flow Type	$\mathbf{a_{gf}}$	$\mathbf{h_{if,SHL}}$	$\mathbf{h_{if,SCL}}$	$\mathbf{h_{ig,SHG}}$	$\mathbf{h_{ig,SCG}}$
Bubbly	$\frac{3.6\alpha_{bub}}{d_b}$	Lee-Ryley^M Plesset-Zwick or 0	Unal^M or 0	10^4 f(ΔT_{sg})	10^4 f(ΔT_{sg})
Slug:					
Bubbles	$\frac{3.6\alpha_{gs}(1-\alpha_{TB})}{d_b}$	Lee-Ryley^M Plesset-Zwick	Unal^M	10^4 f(ΔT_{sg})	10^4 f(ΔT_{sg})
Taylor bubble	$\frac{4.5}{D}\alpha_{Tb}(2.0)$	3 x 10^6 f(ΔT_{sf})	Sieder-Tate^M	Lee-Ryley^M	10^4 f(ΔT_{sg})
Annular mist:					
Drops	$\frac{3.6\alpha_{fd}(1-\alpha_{ff})}{d_d}$	$\frac{k_f}{d_d}$f(ΔT_{sf})	Brown^M xf(ΔT_{sf})	Lee-Ryley^M	10^4 f(ΔT_{sg})
Liquid film	$\frac{4}{D}(1-\alpha_{ff})^{1/2}(2.5)$	3 x 10^6	Theofanous^M	Dittus-Boelter^M	10^4 f(ΔT_{sg})
Inverted annular:					

Table 4.1-1 Summary of interfacial areas and heat transfer coefficients[1]. (Continued)

Flow Type	a_{gf}	$h_{if,SHL}$	$h_{if,SCL}$	$h_{ig,SHG}$	$h_{ig,SCG}$
Bubbles	$\frac{3.6\alpha_{bub}}{d_b}(1-\alpha_B)$	Lee-Ryley^M Plesset-Zwick	Unal^M	10^4 f(ΔT_{sg})	10^4 f(ΔT_{sg})
Vapor/gas film	$\frac{4}{D}(1-\alpha_B)^{1/2}(2.5)$	3×10^6	Dittus-Boelter^M	$\frac{k_g}{D}$f(ΔT_{sg})	$\frac{k_g}{D}$f(ΔT_{sg})
Inverted slug:					
Drops	$\frac{3.6\alpha_{drp}}{d_d}(1-\alpha_B)$	$\frac{k_f}{D}$f(ΔT_{sf})	Brown^M xf(ΔT_{sf})	Lee-Ryley^M	Lee-Ryley^M
Taylor drop	$\frac{4.5}{D}(\alpha_B)(2.5)$	$\frac{k_f}{D}$f(ΔT_{sf})	Brown^M xf(ΔT_{sf})	$\frac{k_g}{D}$f(ΔT_{sg})	$\frac{k_g}{D}$f(ΔT_{sg})
Dispersed (droplet, mist)	$\frac{3.6\alpha_{drp}}{d_d}$	$\frac{k_f}{D}$f(ΔT_{sf})	Brown^M xf(ΔT_{sf})	Lee-Ryley^M xf(ΔT_{sg}) or 0	10^4 f(ΔT_{sg}) or 0
Horizontally stratified	$\frac{4\sin\theta}{\pi D}$	Dittus-Boelter xf(ΔT_{sf})	Dittus-Boelter	Dittus-Boelter 10^4 f(ΔT_{sg})	10^4 f(ΔT_{sg})
Vertically stratified or level model	$\frac{A_c}{V}$	$h_{if,REG}$	McAdams or Incropera-DeWitt	McAdams or Incropera-De Witt	$h_{ig,REG}$
Vertical stratified or level model with a jet junction	$\frac{A_c}{V}$	$h_{if,REG}$	Brown-Khoo-Sonin, Brown-Helmick-Sonin, Sonin-Shimko-Chun, Theofanous	$h_{ig,REG}$	$h_{ig,REG}$

1. SCL = subcooled liquid; SHL = superheated liquid; SHG = superheated vapor/gas; SCG = subcooled vapor/gas; M = modified; f(ΔT_{sg}) = function of $\Delta T_{sg} = T^s - T_g$; f($\Delta T_{sf}$) = function of $\Delta T_{sf} = T^s - T_f$; REG = flow regime when not vertically stratified.

4.1.11 References

4.1-1. M. S. Plesset and S. A. Zwick, "The Growth of Vapor Bubbles in Superheated Liquids," *Journal of Applied Physics, 25,* 4, 1954, pp. 493-500.

4.1-2. J. G. Collier, *Convective Boiling and Condensation,* New York: McGraw-Hill, 1972.

4.1-3. K. Lee and D. J. Ryley, "The Evaporation of Water Droplets in Superheated Steam," *Transactions of the ASME, Journal of Heat Transfer*, November 1968, pp. 445-451.

4.1-4. N. Frossling, *The Gerlands Beitr. Geophys., 52,* 1938, p. 170.

4.1-5. W. E. Ranz and W. R. Marshall, Jr., *Chemical Engineering Progress, 48,* 1952, pp. 141-146, 173-180.

4.1-6. F. Kreith, *Principles of Heat Transfer,* 3rd Edition, New York: Intex Educational, 1973.

4.1-7. V. H. Ransom et al., *RELAP5/MOD2 Code Manual, Volume 3: Developmental Assessment Problems,* EGG-TFM-7952, Idaho National Engineering Laboratory, December 1987.

4.1-8. G. B. Wallis, *One-dimensional Two-phase Flow,* New York: McGraw Hill, 1969.

4.1-9. S. Nukiyama and Y. Tanasawa, *Transactions of the Society of Mechanical Engineers (Japan), 5,* 18, 1969, p. 63.

4.1-10. E. Kreyszig, *Advanced Engineering Mathematics,* 5th Edition, New York: Wiley, 1983, p. 918.

4.1-11. J. C. Lin et al., "Nonequilibrium Constitutive Models for RELAP5/MOD2," *ANS Topical Meeting on Anticipated and Abnormal Plant Transients in Light Water Reactors, Jackson, WY, September 26-29, 1983.*

4.1-12. H. C. Unal, "Maximum Bubble Diameter, Maximum Bubble-Growth Time and Bubble Growth Rate During the Subcooled Nucleate Flow Boiling of Water up to 17.7 MN/m^2," *International Journal of Heat and Mass Transfer, 19,* 1976, pp. 643-649.

4.1-13. R. A. Riemke, "Modification to Unal's Subcooled Flow Boiling Bubble Model," *Nuclear Technology, 102,* 1993, pp. 416-417.

4.1-14. R. T. Lahey, "A Mechanistic Subcooled Boiling Model," *Proceedings of the 6th International Heat Transfer Conference, Toronto, Canada, August 7-11, 1978,* Volume 1, pp. 293-297.

4.1-15. G. G. Brucker and E. M. Sparrow, "Direct Contact Condensation of Steam Bubbles in Water at High Pressure," *International Journal of Heat and Mass Transfer, 20,* 1977, pp. 371-381.

4.1-16. M. Ishii and K. Mishima, *Study of Two-Fluid Model and Interfacial Area,* NUREG/CR-1873, ANL-80-111, Argonne National Laboratory, December 1980.

4.1-17. T. G. Theofanous, "Modeling of Basic Condensation Processes," *The Water Reactor Safety Research Workshop on Condensation, Silver Springs, MD, May 24-25, 1979.*

4.1-18. L. K. Brumfield, R. N. Houze, and T. G. Theofanous, "Turbulent Mass Transfer at Free, Gas-Liquid Interfaces, with Applications to Film Flows," *International Journal of Heat and Mass Transfer, 18,* 1975, pp. 1077-1081.

4.1-19. G. Brown, "Heat Transmission of Condensation of Steam on a Spray of Water Drops," *Proceedings of the General Discussion on Heat Transfer, 11-13 September 1951*, published by the Institution of Mechanical Engineers, pp. 49-52.

4.1-20. M. Ishii and T. C. Chawla, *Local Drag Laws in Dispersed Two-Phase Flow*, NUREG/CR-1230, ANL-79-105, Argonne National Laboratory, December 1979.

4.1-21. G. DeJarlais and M. Ishii, *Inverted Annular Flow Experimental Study*, NUREG/CR-4277, ANL-85-31, Argonne National Laboratory, April 1985.

4.1-22. W. H. McAdams, *Heat Transmission*, 3rd Edition, New York: McGraw-Hill, 1954.

4.1-23. F. P. Incropera and D. P. DeWitt, *Introduction to Heat Transfer*, 3rd Edition, New York: Wiley, 1990.

4.1-24. V. H. Ransom, *Course A-Numerical Modeling of Two-Phase Flows for Presentation at Ecole d'Ete d'Analyse Numerique*, EGG-EAST-8546, Idaho National Engineering Laboratory, May 1989.

4.1-25. V. H. Ransom and W. L. Weaver, "Selective Review of LWR Thermal-Hydraulic Simulation Methods," *Proceedings of the International Topical Meeting on Advances in Reactor Physics, Mathematics, and Computation, Paris, France, 1987*, pp. 1813-1829.

4.1-26. L. R. Feinauer, W. M. Bryce, D. M. Kiser, R. A. Riemke, and C. C. Tsai, *Post-Release Improvements for RELAP5/MOD2*, EG&G Internal Report, SE-CMD-001, Idaho National Engineering Laboratory, August 1984.

4.1-27. K. M. Vierow and V. E. Schrock, "Condensation in a Natural Circulation Loop with Noncondensable Gas Present," *Japan - U. S. Seminar on Two-Phase Flow Dynamics, Berkeley, California, USA, 1992.*

4.1-28. R. W. Shumway, J. R. Larson, and J. L. Jacobson, *Applicability of RELAP5/MOD2 to N-Reactor Safety Analysis*, EGG-TFM-8026, Idaho National Engineering Laboratory, July 1988.

4.1-29. M. J. Thurgood et al., *COBRA/TRAC--A Thermal Hydraulic Code for Transient Analysis of Nuclear Reactor Vessels and Primary Coolant Systems*, NUREG/CR-2046, PNL-4385, Pacific Northwest Laboratory, March 1983.

4.1-30. W. L. Weaver et al., *TRAC-BF1 Manual: Extensions to TRAC-BD1/MOD1*, NUREG/CR-4391, EGG-2417, Idaho National Engineering Laboratory, August 1986.

4.1-31. R. M. Thomas, "Condensation of Steam on Water in Turbulent Motion," *International Journal of Multiphase Flow, 5*, 1979, pp. 1-15.

4.1-32. J. S. Brown, B. C. Khoo, and A. A. Sonin, "Rate Correlation for Condensation of a Pure Vapor on Turbulent, Subcooled Liquid," *International Journal of Heat and Mass Transfer, 33*, 9, 1990, pp. 2001-2018.

4.1-33. A. A. Sonin, M. A. Shimko, and J. Chun, "Vapor Condensation onto a Turbulent Liquid--I. The Steady Condensation Rate as a Function of Liquid-Side Turbulence," *International Journal of Heat and Mass Transfer, 29*, 9, 1986, pp. 1319-1332.

4.1-34. J. S. Brown, M. R. Helmick, and A. A. Sonin, "Vapor Condensation at a Turbulent Liquid Surface in Systems with Possible Space-Based Applications," *AIAA Paper 89-2846*, July 1989.

4.1-35. J. S. Brown, *Vapor Condensation on Turbulent Liquid*, Ph.D. Dissertation, Massachusetts Institute of Technology, May 1991.

4.2 Wall-to-Fluid Heat Transfer

This section describes the correlations and methods used to obtain the information necessary for the walls to exchange energy with the fluid where reflood is not activated. The modifications to the wall-to-fluid heat transfer for reflood are discussed in Section 4.4.

When a user flags a solid surface as having a convective boundary condition, the heat transfer coefficients must be calculated and passed to the conduction solution. The liquid and vapor/gas energy solutions include the wall heat flux to liquid or vapor/gas. The experimental coefficients used to develop correlations were determined by obtaining the experimental heat flux and dividing it by a wall-to-reference-temperature difference. Consequently, when the correlations are used to obtain the code-calculated heat flux, they use the same reference temperature as the correlation developer used. During boiling, the saturation temperature based on the total pressure is the reference temperature, and during condensation the saturation temperature based on the partial pressure is the reference temperature. There are three possible reference temperatures for each heat transfer coefficient, but for many cases there is only one coefficient that is nonzero. The general expression for the total wall heat flux is

$$q''_{total} = h_{wgg}(T_w - T_g) + h_{wgspt}(T_w - T_{spt}) + h_{wgspp}(T_w - T_{spp}) + h_{wff}(T_w - T_f) + h_{wfspt}(T_w - T_{spt}) \quad (4.2\text{-}1)$$

where

h_{wgg} = heat transfer coefficient to vapor/gas, with the vapor/gas temperature as the reference temperature ($W/m^2 \cdot K$)

h_{wgspt} = heat transfer coefficient to vapor/gas, with the saturation temperature based on the total pressure as the reference temperature ($W/m^2 \cdot K$)

h_{wgspp} = heat transfer coefficient to vapor/gas, with the saturation temperature based on the vapor partial pressure as the reference temperature ($W/m^2 \cdot K$)

h_{wff} = heat transfer coefficient to liquid, with the liquid temperature as the reference temperature ($W/m^2 \cdot K$)

h_{wfspt} = heat transfer coefficient to liquid, with the saturation temperature based on the total pressure as the reference temperature ($W/m^2 \cdot K$)

T_w = wall surface temperature (K)

T_g = vapor/gas temperature (K)

T_f = liquid temperature (K)

T_{spt} = saturation temperature based on the total pressure (K)

T_{spp} = saturation temperature based on the partial pressure of vapor in the bulk (K).

Only one or two of the heat transfer coefficients are nonzero in most flow regimes. For instance, during nucleate boiling, h_{wff} is equal to h_{mac} and h_{wfspt} is h_{mic} from the Chen correlation; all the others are zero except at high void fractions, where h_{wgg} has a value to smooth the transition to vapor/gas cooling.

The wall temperature is solved implicitly, and the reference temperature can also be the new time value if the user so chooses.

A boiling curve is used in ATHENA to govern the selection of heat transfer correlations. Much of the ATHENA boiling curve logic is based on the value of the heat slab surface temperature. If noncondensable gas is present, there is a window region when the wall temperature is too small for boiling and too high for condensation. This occurs when the temperature is less than the saturation temperature based on total pressure but greater than the saturation temperature based on vapor partial pressure. **Figure 4.2-1** illustrates the curve.

The heat transfer package in ATHENA uses heat transfer correlations that are based on fully developed steady-state flow, where entrance length effects are not considered except for the calculation of CHF.

ATHENA has a built-in capability to generate 3-D surface information to illustrate the boiling-condensing curves. An example of this is shown in **Figure 4.2-2**, where the void fraction is varied from zero to one, the wall superheat is varied from negative 35 K to a positive 35 K, and the resulting total heat flux is output. The plot shows that the heat flux smoothly transitions from condensation to boiling.

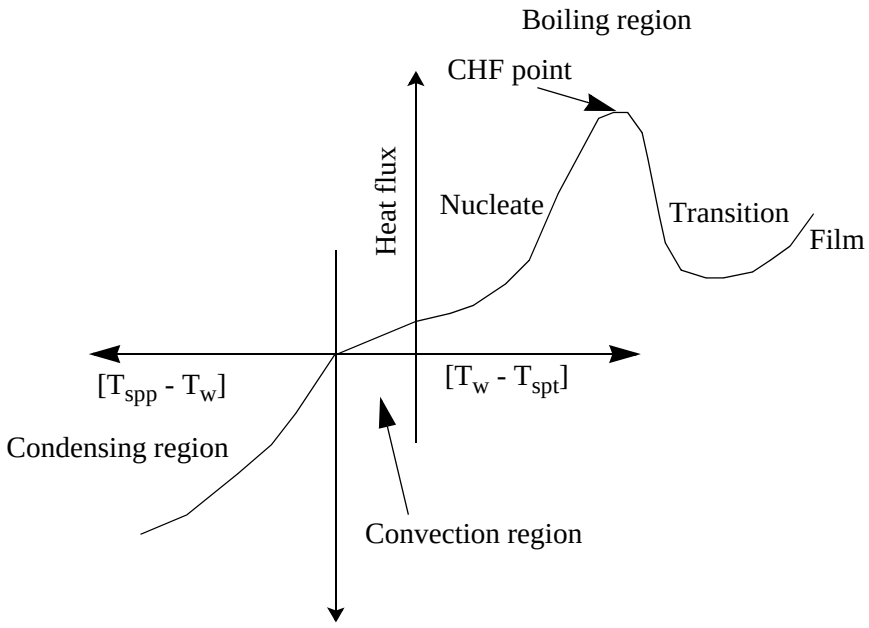

Figure 4.2-1 ATHENA boiling and condensing curves.

Condensation increases as the liquid film thickness increases. Boiling decreases as the liquid fraction increases. This data was generated for low mass flux and low pressure conditions.

4.2.1 Logic for Selection of Heat Transfer Modes

The following list gives the ATHENA heat transfer mode numbers. Mode numbers indicate which regime is being used to transfer heat between heat structure surfaces and the circulating fluid contained in the reactor primary and secondary systems. These mode numbers are printed on the major edits.

Mode 0 Convection to noncondensable-vapor-liquid mixture.

Mode 1 Convection at supercritical pressure or superheat wall with negative heat flux due to superheated vapor/gas.

Mode 2 Single-phase liquid convection at subcritical pressure, subcooled wall and low void fraction.

Mode 3 Subcooled nucleate boiling.

Mode 4 Saturated nucleate boiling.

Mode 5 Subcooled transition boiling.

Mode 6 Saturated transition boiling.

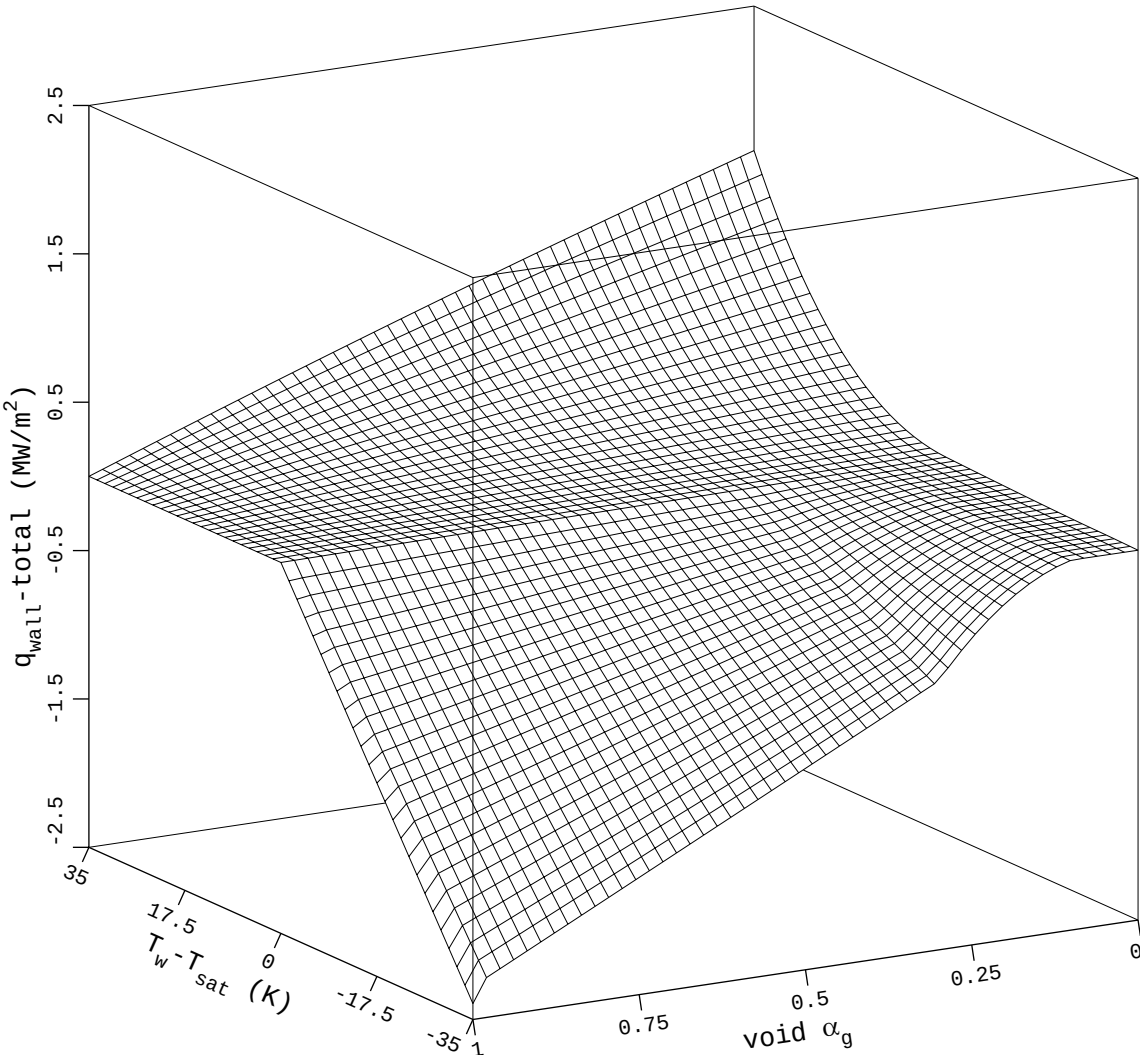

Figure 4.2-2 Heat flux surface plot.

Mode 7 Subcooled film boiling.

Mode 8 Saturated film boiling.

Mode 9 Single-phase vapor/gas or supercritical two-phase convection.

Mode 10 Condensation when void fraction is less than one. (For FWHTR heat slabs, a combination of condensation above the water level and liquid convection below it.)

Mode 11 Condensation when void fraction is one. (For FWHTR heat slabs, condensation on a heat slab completely above the water level.)

Mode 12 Nucleate boiling (non-positive heat flux)

If the noncondensable quality (based on vapor/gas mass) is greater than 0.000000001, then 20 is added to the mode number. Thus, the mode number could be 20 to 31. This number is increased by another 40 if the reflood flag is set. **Figure 4.2-3** is a schematic diagram showing the logic built into the code to select the appropriate heat transfer mode. The capitalized names in the boxes are names of subroutines. The variables are

T = TRUE

F = FALSE

P = total pressure

P_{crit} = critical pressure

X_n = noncondensable mass quality

X_e = equilibrium quality used in wall heat transfer (based on phasic specific enthalpies and mixture specific enthalpy, with the mixture specific enthalpy calculated using the flow quality)

$$= \frac{[X_{flow}h_g + (1 - X_{flow})h_f] - h_f^s}{h_g^s - h_f^s}$$

X_{flow} = flow quality

$$= \frac{\alpha_g \rho_g v_g}{\alpha_g \rho_g v_g + \alpha_f \rho_f v_f}$$

α_g = vapor/gas void fraction

T_w = wall temperature

T_{spt} = vapor saturation temperature based on total pressure

T_{spp} = vapor saturation temperature based on vapor partial pressure

T_f = liquid temperature

CHF = critical heat flux

q'' = heat flux

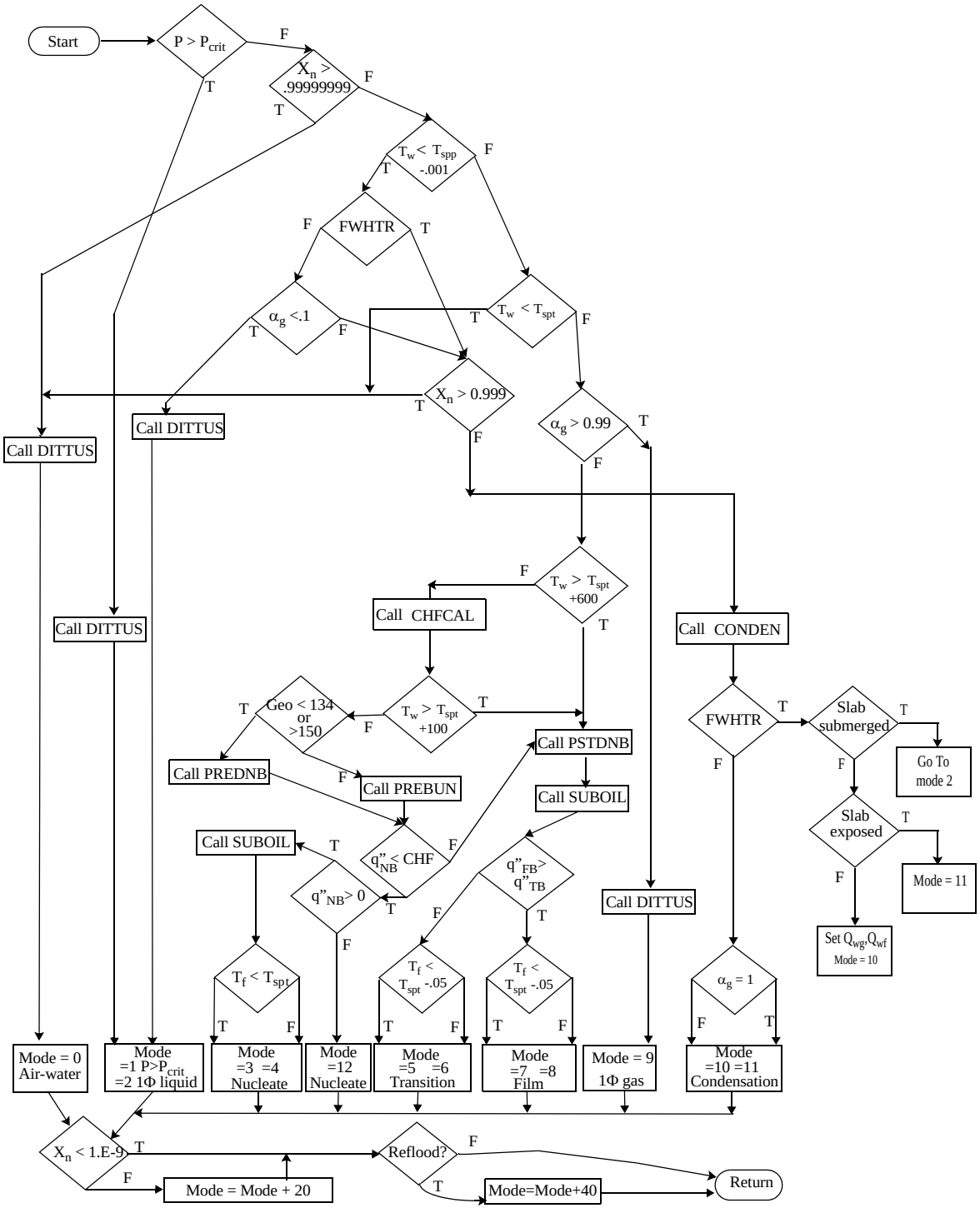

Figure 4.2-3 ATHENA wall heat transfer flow chart.

q''_{NB} = nucleate boiling heat flux

q''_{FB} = film boiling heat flux

q''_{TB} = transition boiling heat flux

Geom = type of hydraulic cell

1Φ = single-phase.

Most of this logic is built into the HTRC1 subroutine. The heat transfer coefficients are determined in one of five subroutines: DITTUS, PREDNB, PREBUN, PSTDNB, and CONDEN. Subroutine CONDEN calculates the coefficients when the wall temperature is below the saturation temperature based on the partial pressure of vapor. Subroutine DITTUS is called for the single-phase liquid or single-phase vapor/gas convection correlations. Subroutine PREDNB contains the nucleate boiling correlations for all surfaces except horizontal bundles and subroutine PREBUN is used for the outer surface of horizontal bundles of rods or tubes. Subroutine PSTDNB has the transition and film boiling correlations. Subroutine CHFCAL determines the critical heat flux. When reflood is on, subroutine CHFCAL has been called prior to the call to subroutine HRTC1, and thus is not called from subroutine HTRC1. Subroutine SUBOIL calculates the vapor generation rate in the superheated liquid next to a superheated wall when the bulk liquid is subcooled. The correlations, used for each of the 13 mode numbers, are given in **Table 4.2-1**.

Table 4.2-1 Wall convection heat transfer mode numbers .

Mode number	Heat transfer phenomena	Correlations
0	Noncondensable-vapor-liquid convection	Kays,[4.2-1] ORNL,[4.2-2] Dittus-Boelter,[4.2-3] Petukhov,[4.2-4] ESDU[1], Shah,[4.2-5] Churchill-Chu,[4.2-6] McAdams,[4.2-7] Elenbaas,[4.2-8] Seider-Tate/Lopina-Bergles[4.2-9,4.2-10], Gnielinski[4.2-11], Bishop[4.2-12], Koshizuka-Oka[4.2-13], Jackson[4.2-14], Jackson-Wu[4.2-15,4.2-16]
1	Supercritical or single-phase liquid convection	Same as mode 0
2	Single-phase liquid convection or subcooled wall with void fraction < 0.1	Same as mode 0
3	Subcooled nucleate boiling	Chen,[4.2-17] Bergles-Rohsenow[4.2-18]
4	Saturated nucleate boiling	Chen[4.2-17], Araki[4.2-19]
5	Subcooled transition boiling	Chen-Sundaram-Ozkaynak,[4.2-20] Marshall[4.2-21]

Table 4.2-1 Wall convection heat transfer mode numbers (Continued).

Mode number	Heat transfer phenomena	Correlations
6	Saturated transition boiling	Same as mode 5
7	Subcooled film boiling	Bromley,[4.2-22] Sun-Gonzalez-Tien,[4.2-23] and mode 0 Correlations
8	Saturated film boiling	Same as mode 7
9	Supercritical two-phase or single-phase vapor/gas convection	Same as mode 0
10	Filmwise condensation	Nusselt,[4.2-24] Shah,[4.2-25] Chato,[4.2-26] Colburn-Hougen[4.2-27]
10 (FWHTR)	Condensation above water level Liquid convection below water level	Chen[4.2-28] Same as mode 2
11	Condensation in vapor	Same as mode 10
11 (FWHTR)	Condensation	Chen[4.2-28]
12	Nucleate boiling ($q''_{NB} \leq 0$)	Same as modes 3,4
3,4 for horizontal bundles	Nucleate boiling	Forster-Zuber,[4.2-29] Polley-Ralston-Grant,[4.2-30] ESDU[a]

1. ESDU (Engineering Science Data Unit, 73031, Nov 1973; ESDU International Plc, 27, Corsham Street, London, N1 6UA)

The correlation set appropriate for a specific surface depends on the hydraulic geometry of the adjacent fluid. The following text discusses geometry and presents the correlations used to calculate the heat transfer for a specific mode. For each mode, the text provides the code model or correlation basis and model as coded.

4.2.2 Hydraulic Geometry

An important factor that effects the magnitude of heat transfer coefficients, besides obvious parameters such as velocity, is the flow field or hydraulic geometry surrounding the surface. The flow field next to the wall influences the velocity profile and turbulence. The two basic types of fields are internal and external as shown in **Table 4.2-2**. Pipes can be any shape, but ATHENA has correlations for only circular pipes. Parallel plates are a special case of annuli; i.e., in the limit as the annuli inner radius gets

large the flow field is the same as flow between parallel plates. Spheres are shown in the table, and ATHENA is capable of solving the conduction solution for spheres, but no convection correlations specifically for spheres are currently in the code.

Table 4.2-2 Hydraulic geometries.

Flow field	Hardware
Internal	Pipe: horizontal, vertical, helical
	Parallel plates: horizontal, vertical
	Annuli: horizontal, vertical; inner wall heated, outer wall heated
	Spheres: horizontal, vertical
External	Spheres: horizontal, vertical
	Single plate: horizontal, vertical; heated, cooled
	Single tube: horizontal, vertical; with crossflow, without crossflow
	Tube bundle: horizontal, vertical, helical; square pitch, staggered pitch; with crossflow, without crossflow

To help users communicate the flow field geometry types to the code, a numbering system has been set up for some of the possible geometries. The numbering scheme is

- Standard
  - 1, 100, or 101
- Vertical structures
  - 102 parallel plates (ORNL ANS geometry)
  - 103 infinite parallel plates
  - 104 single wall
  - 105 annuli with this wall unheated
  - 106 annuli with this outer wall heated
  - 107 annuli with this inner wall heated
  - 108 single rod

- 109 single rod with crossflow
- 110 bundle with in-line rods, parallel-flow only
- 111 bundle with in-line rods, parallel-flow and crossflow
- 112 bundle with staggered rods, parallel-flow only
- 113 bundle with staggered rods, parallel-flow and crossflow
- 114 helical pipe
- 151 annuli with aluminum walls heated and downflow (SRL geometry)

• Horizontal structures

- 121 annuli with this wall unheated
- 122 annuli with this outer wall heated
- 123 annuli with this inner wall heated
- 124 bundle (CANDU)
- 130 plate above fluid
- 131 plate below fluid
- 132 single tube
- 133 single tube with crossflow
- 134 bundle with in-line rods or tubes, crossflow and parallel-flow
- 135 bundle with in-line rods or tubes, crossflow only
- 136 bundle with staggered rods or tubes, crossflow and parallel-flow
- 137 bundle with staggered rods or tubes, crossflow only

• Alternate geometry and/or correlations

- 115 swirl tubes
- 160 Gnielinski for forced convection in a tube

- 161 Bishop for forced convection in a tube
- 162 Koshizuka-Oka for forced convection in a tube
- 163 Jackson for forced convection in a tube
- 164 Jackson for forced/mixed convection is a tube (upflow)
- 165 Jackson for forced/mixed convection is a tube (downflow)

Coding has been implemented for only a few of the numbers (i.e., 101, 102, 110, 111, 115, 130, 134, 160-165). For the other numbers, for which there are no special correlations implemented, these are associated and defaulted to a similar implemented correlation, In the future, it is planned to implement correlations for these numbers. Users normally run with a 1 or 100. These two values are still accepted so that old decks will run. They both default to 101. The other numbers are used to modify some of the standard correlations in 101. Churchill-Chu is usually used for natural convection; if the connecting hydrodynamic volume is horizontal or 121 - 133 is chosen, McAdams is used for natural convection. Except for feedwater heater components, Nusselt-Shah-Coburn-Hougen is used for condensation; if the connecting hydrodynamic volume is horizontal and not a feedwater heated component, Chato-Shah-Coburn-Hougen is used. For the right side (outside surface) of heat slabs associated with a feedwater heater component, Chen is used for condensation. The code currently gives specific consideration for only those geometry numbers underlined in **Table 4.2-3**. The other numbers in a table cell default to the underlined number. The name of the correlation is given for each mode of heat transfer and the correlations are discussed in the following sections. The alternate correlations implemented in heat structure geometries 160 through 165 are used for analysis of advanced reactors, including those cooled by supercritical light water or gas.

Table 4.2-3 Available ATHENA wall heat transfer correlations.

	Mode of heat transfer							
User geometry default value underlined	**Laminar**	**Natural**	**Turbulent**	**Conden-sation**	**Nucleate boiling**	**Transition boiling**	**Film boiling**	**CHF**
1, 100, <u>101</u>, 104-109, 114	Sellars Nu=4.36	Churchill-Chu or McAdams	Dittus-Boelter	Nusselt/ Chato-Shah-Colburn-Hougen	Chen	Chen	Bromley	Table

Table 4.2-3 Available ATHENA wall heat transfer correlations. (Continued)

	Mode of heat transfer							
User geometry default value underlined	**Laminar**	**Natural**	**Turbulent**	**Conden-sation**	**Nucleate boiling**	**Transition boiling**	**Film boiling**	**CHF**
102,103	ORNL ANS Nu = 7.63	Elenbaas	Petukhov or Dittus-Boelter	"	"	"	"	Table Gambill-Weatherhead
121-124, 130, 131-133	Sellars Nu = 4.36	McAdams	Dittus-Boelter	"	"	"	"	Table
110, 112	"	Churchill-Chu or McAdams	Dittus-Boelter-Inayatov	"	Chen-Inayatov	"	"	"
111, 113	"	"	Dittus-Boelter-Inayatov-Shah	"	"	"	"	"
115	"	"	Seider-Tate/ Lopina and Bergels	"	Bergles and Rohsenow	Marshall	"	Marshall
134, 135-137	"	Churchill-Chu	Dittus-Boelter-ESDU	" except Chen for FWHTR	Polley	Chen	"	Folkin
151	"	Churchill-Chu or McAdams	Dittus-Boelter	Nusslet/ Chato-Shah -Colburn-Hougen	Chen	"	"	Table SRL
160	"	"	Gnielinski	"	"	"	Chen	Table
161	"	"	Bishop	"	"	"	"	"
162	"	"	Koshizuka-Oka	"	"	"	"	"
163	"	"	Jackson	"	"	"	"	"
164	"	Jackson-Wu	Jackson-Wu	"	"	"	"	"
165	"	"	"	"	"	"	"	"

4.2.3 Geometry 101, Default Geometry

Geometry 1, 100, and 101 are the standard convective boundary types used by all previous input decks. The current number 101 yields the same results as 1, 100, or 101 used previously. The correlations for each heat transfer regime are presented below.

4.2.3.1 Geometry 101, Correlations for Single-Phase Liquid At Supercritical and Subcritical Pressure (Modes 1 and 2), Single-Phase Vapor/Gas (Mode 9), and Noncondensable-Vapor-Liquid Mixture (Mode 0). The DITTUS subroutine calculates heat transfer coefficients for single-phase and noncondensable-vapor-liquid mixtures. There are correlations for forced turbulent convection, forced laminar convection, and free (natural) convection. The code uses the maximum of the three correlations. Using the maximum value ensures a smooth transition between correlations and follows the suggestion by Raithby and Hollands in Handbook of Heat Transfer:[4.2-31]

$$Nu = \max (Nu_{\text{forced turbulent}}, Nu_{\text{forced laminar}}, Nu_{\text{free}}) \quad (4.2\text{-}2)$$

where

Nu = Nusselt number = $\frac{hD}{k}$

k = fluid thermal conductivity

h = surface heat transfer coefficient

D = heated equivalent diameter = $4 \bullet \frac{A_{cs}}{P_{heated}}$

A_{cs} = flow area

P_{heated} = perimeter of heated surface.

Liquid properties are used for supercritical liquid, and vapor/gas properties are used when the void fraction is above zero.

4.2.3.1.1 Geometry 101, Turbulent Forced Convection Model Basis--The Dittus-Boelter correlation[4.2-3] was originally derived for turbulent flow in smooth tubes for application to automobile radiators. It takes the form

$$Nu = C\, Re^{0.8} Pr^{n} \quad (4.2\text{-}3)$$

where

C = coefficient

Re = Reynolds Number = $\frac{GD}{\mu}$

Pr = Prandtl Number = $\frac{\mu C_p}{k}$

G = mass flux

μ = viscosity

C_p = specific heat.

The physical properties are evaluated at the bulk fluid temperature; n = 0.4 for heating and 0.3 for cooling.

The correlation was developed from data from the literature for heating water,[4.2-32, 4.2-33] heating and cooling water and oil,[4.2-34] and heating and cooling gases. The data obtained were for long tubes with an average conductance obtained using a log mean temperature difference. Some of the data were reported by Stanton in 1897. The conditions for the data are

- McAdams-Frost[4.2-32]
  - Fluid - water (heating)
  - Coefficient - 850 to 15,300 W/m^2•K
  - Tube ID - 0.0095, 0.0127, 0.0254 m
  - Velocity - 0.183 to 6.1 m/s
  - Data scatter ~40%
  - Data points - ~60
- McAdams-Frost[4.2-33]
  - Fluid - water (heating)
  - Tube ID - 0.0074 to 0.0145 m
  - Tube length - 0.44 to 1.24 m

- Fluid velocity - 0.065 to 4.9 m/s
- Coefficient - 840 to 20,700 $W/m^2 \cdot K$

• Morris-Whitman[4.2-34]

- Fluids - water, miscellaneous oils
- Tube ID - 0.0157 m
- Tube length - 2.74 m

• Heating parameters

- Velocity - 0.27 to 5.98 m/s
- Fluid temperature - 301 to 349 K
- Coefficient - 227 to 8,860 $W/m^2 \cdot K$
- Data points - 56

• Cooling parameters

- Velocity - 0.34 to 5.15 m/s
- Fluid temperature - 319 to 540 K
- Coefficient - 80 to 3,975 $W/m^2 \cdot K$
- Data points - 62
- Literature fluids - unspecified gases
- Pressure range - 10,342 to 1.31 x 10^6 Pa
- Temperature range - 289 to 1,033 K
- Mass velocity range - 0.98 to 32.2 $kg/s \cdot m^2$
- Tube ID range - 0.0127 to 0.152 m
- Number of data points - unspecified.

The correlation was obtained by drawing mean curves through the heating and cooling data of Morris and Whitman.[4.2-34] The data of **Reference 4.2-32** and **Reference 4.2-33**, and gas data were plotted against the mean curves to evaluate the applicability of the correlation to other data. Attempts were made to improve the correspondence of **Reference 4.2-34** data to the correlation based on using the wall, bulk fluid, or average film temperature for property evaluation, but no improvement was noted. Manipulation of the data also did not eliminate the need for separate curves for correlating heating and cooling. No mention was made concerning the deviation between the data and the correlation.

The value of the constant C = 0.023 is found in McAdams.[4.2-7]

As reported by Kreith,[4.2-35] Equation (4.2-3) has been confirmed experimentally for a variety of fluids to within $\pm$ 25% for uniform wall temperature as well as uniform heat flux conditions with moderate temperature differences between the wall and fluid (constant property conditions) within the following ranges of parameters:

$0.7 < Pr < 160$

$Re > 6{,}000$

$\frac{L}{D} > 60$.

At very small temperature differences (near adiabatic) in air and helium, results of Reynolds[4.2-36] were well correlated by the form of Equation (4.2-3) using a constant of 0.021 instead of 0.023. The test conditions were

- Tube ID - 0.00584 m
- Tube length - 0.635 m
- Pressure - 0.689 to 0.965 MPa
- Temperature - 298 K.

Sleicher and Rouse[4.2-37] indicate that the correlation likely overpredicts heat transfer coefficients for gases by 10-25% at moderate-to-high temperature differences.

The Dittus-Boelter equation was tested by Larsen and Ford[4.2-38] against water vapor data while being heated for the following conditions:

- Tube ID - 0.0127 m

- Tube length - 0.914 m
- Pressure - 0.17, 0.34, 0.51 MPa
- Inlet temperature - 422, 644, 867 K
- Mass velocity - 2.3 to 54.2 kg/s•m^2
- Re - 1,900 to 35,000
- Heat flux - 7,569 to 97,760 W/m^2
- Wall temperature - 478 to 1,256 K
- Vapor temperature - 422 to 1,089 K
- Pr - 0.7 - 1.1.

The data for Re > 6,000 fit the analysis within $\pm$ 5% when a thermal radiation model was included.

Heat transfer from a heated tube wall to superheated, single-phase vapor/gas during turbulent forced convection has been experimentally obtained and correlated by Heineman.[4.2-39] The data were taken for the conditions as follows:

- Tube ID - 0.00846 m
- Tube length - 0.3048 m
- Pressure - 2.07 to 10.34 MPa
- Temperature - 255 to 755 K
- Superheat - 296 to 334 K
- Wall temperature - 616 to 972 K
- Heat flux - 0.157 to 0.905 MW/m^2
- Mass velocity - 195 to 1,074 kg/s•m^2
- Re - 60,000 to 370,000.

Heineman used the data to develop a correlation having the same form as Equation (4.2-3), which fits the steam data within ± 10%.

4.2.3.1.2 Geometry 101, Turbulent Forced Convection Model as Coded--The model is coded as presented with n = 0.4 for all usage.

The mass flux used in the Reynolds number is increased in two-phase flow cases where the DITTUS subroutine is called with the mode flag set to 9 or greater, indicating a vapor/gas condition. This occurs when subroutines CONDEN, PREDNB, or PSTDNB call subroutine DITTUS. In these cases, the liquid mass flux times the vapor/gas-to-liquid density ratio is added to the vapor/gas mass flux. This effectively converts the Dittus-Boelter condition into the Dougall-Rohsenow[4.2-40] correlation, as is done in the TRAC codes.[4.2-41]

Deissler and Taylor's analysis[4.2-42] and experiments by Weisman[4.2-43] indicate that for turbulent forced convection of water exterior and parallel to a rod bundle, the heat transfer coefficients value is a function of the rod spacing to diameter ratio. For spacing/diameter ratios typical of PWRs, **Reference 4.2-43** indicates the increase in the heat transfer coefficients could be ~ 30%. Surfaces that are flagged as vertical rod bundles (discussed later) increase the turbulent heat transfer value by use of a pitch-to-diameter ratio multiplier developed by Inayatov.[4.2-44]

The assumption is made that the form of the equation for heating is satisfactory for cooling also. Therefore, the correlation is coded with the exponent on the Prandtl number n = 0.4. The use of n = 0.4 instead of 0.3 for cooling applications results in a 15% higher prediction for vapor/gas and 10% higher for liquid at 17.24 MPa (2,500 psia). For fluid at a lower saturation pressure or at a superheated temperature, the difference caused by n diminishes significantly.

There are other situations besides cooling that are not accounted for. These include entrance effects, laminar-turbulent transition and mixed forced, and free convection. The entrance effect can be important in the first 20 diameters. Fortunately, important reactor energy exchange surfaces such as the core and steam generator are hundreds of diameters long.

In the region between forced laminar and turbulent flow, the Dittus-Boelter equation will over-predict. However, helium flow in a small tube has been characterized by the form of the Dittus-Boelter equation with a constant of 0.021 to an accuracy of ± 4% at Re > 3,000.[4.2-37] For Re < 2,100, only a laminar flow coefficient would be correct. This transition is illustrated for air in **Reference 4.2-35**, p. 289. The code switches between laminar and turbulent at Re between 350 and 700. These values are obtained by equating the Nusselt numbers and solving for Re for the range of Pr likely for liquid and vapor/gas.

When equality of the Grashof (Gr) number and Re^2 exists, the buoyancy forces and drag forces affecting the velocity profile are of the same order of magnitude.[4.2-45] The transition encompasses a significant range in Gr and Re for various geometries. Specific transitional values are known for vertical

concurrent flow. The effects of combined free and forced convection are different for opposing flow and result in significant changes in the value of the heat transfer coefficient.

For liquid metals, the convective heat transfer coefficient is based on the correlation described by Bird, Stewart, and Lightfoot for constant wall temperature.

4.2.3.1.3 Geometry 101, Laminar Forced Convection Model Basis--The model is an exact solution for fully developed laminar flow in a tube with a uniform wall heat flux and constant thermal properties developed by Sellars, Tribus, and Klein.[4.2-46] The solution takes the form

$$Nu = 4.36 \qquad (4.2\text{-}4)$$

$Nu = h\frac{D}{k}$

h = heat transfer coefficient

D = equivalent diameter

k = fluid thermal conductivity based on bulk temperature.

Some data exist to indicate that the solution is correct. For example, Shumway[4.2-47] provides a comparison for helium flow in a tube. The solution is confirmed to within $\pm$ 10%.

4.2.3.1.4 Geometry 101, Laminar Forced Convection Model as Coded--The correlation is applied as presented.

The practice of using the hydraulic diameter in correlations to account for various geometries is not valid for laminar flow.[4.2-48] Thus, the exact solution for flow in a tube does not necessarily apply to rectangular or triangular ducts.

For laminar flow with small heat transfer coefficients (h), entrance effects become more important than for turbulent flow. Neglecting the entrance length for a developing parabolic velocity profile has a pronounced effect on the average h over the length. Based on information presented in Kreith[4.2-35] from the analytical solutions of Kays,[4.2-1] the h as modeled can be 30 to 75% low, depending on Pr over the several feet of length required to develop the profile. **Reference 4.2-49** also presents a correlation for viscous flow in tubes, which includes the effect of the entrance length and with h decreasing along the length.

The wall boundary condition is also important. For comparison, the average h for a constant wall temperature is ~ 80% of the h for the constant heat flux assumption. Neither ideal condition applies

directly to reactor conditions, but the constant heat flux assumption used in this correlation will result in the higher value of h.

The transition to natural (i.e., free) convection flow occurs over a range of conditions as a function of Re and Gr. The h is also a function of the forced and natural (free) convection component directions (same or opposite) and entrance length effects. Currently, ATHENA does not account for these factors.

4.2.3.1.5 Geometry 101, Natural Convection Model Basis--A user-input convective boundary type of 1, 100, or 101 uses one natural convection correlation if the connecting hydraulic cell is vertical and another if it is horizontal. When the connecting hydraulic cell is vertical, the Churchill and Chu correlation[4.2-6] is used. When the cell is horizontal, a McAdams correlation[4.2-7] is used.

The Churchill-Chu correlation was developed for a vertical flat plate, and it has the form

$$Nu_L = \left\{ 0.825 + \frac{0.387(Ra_L)^{\frac{1}{6}}}{\left[1 + \left(\frac{0.492}{Pr}\right)^{\frac{9}{16}}\right]^{\frac{8}{27}}} \right\}^2 \qquad (4.2\text{-}5)$$

where

Ra_L = Rayleigh number = $Gr_L \bullet Pr$

Pr = Prandtl number = $\frac{\mu C_p}{k}$

Gr_L = Grashof number = $\frac{\rho^2 g\beta(T_w - T_b)L^3}{\mu^2}$ (4.2-6)

μ = fluid viscosity

C_p = fluid specific heat at constant pressure

k = fluid thermal conductivity

ρ = fluid density

β = coefficient of thermal expansion

g	=	gravitational constant
L	=	the natural convection length
T_w	=	wall temperature
T_b	=	bulk temperature.

The Nusselt number correlation recommended by McAdams[4.2-7] as well as by Incopera and DeWitt is for the lower surface of a heated horizontal plate or the upper surface of a cooled horizontal plate, and it has the form

$$Nu_L = 0.27 Ra_L^{0.25} \quad . \tag{4.2-7}$$

The Churchill-Chu correlation is reported to be valid over the full laminar and turbulent Rayleigh number range. The authors show good comparisons with data over a wide range but do not quote accuracy values. The applicable range of the McAdams correlation is between a Rayleigh number of 10^5 and 10^{10}.

4.2.3.1.6 Geometry 101, Natural Convection Model as Coded--The model is coded as shown. The correlations are for flat plates, however the code is using them for pipes. The properties are evaluated at the bulk fluid temperature. The value of the natural convection length used in the correlations is controlled by the user on the 1CCCG801 through 1CCCG899 and 1CCCG901 through 1CCCG999 cards. If no values are entered or if zero is entered for the natural convection length, it defaults to the heat transfer hydraulic diameter (i.e., heated equivalent diameter). The Churchill-Chu correlation needs a plate height. Incropera and DeWitt[4.2-8] suggest length = surface area/perimeter for the McAdams correlation. Equation (4.2-7) does not apply to heat transfer inside of horizontal cylinders or for horizontal plates when the energy flow is vertically up. Additional correlations need to be implemented for pipes, tube bundles, and flat plates with energy flowing against the gravity vector. Use of the correlations in the code is not limited by the value of the Rayleigh number.

4.2.3.2 Geometry 101, Correlations for Saturated Nucleate Boiling (Mode 4) and Subcooled Nucleate Boiling (Mode 3). The Chen correlation[4.2-17] is used for saturated and subcooled nucleate boiling. Although the correlation was based on saturated liquid conditions, it is used for subcooled liquid conditions by using the bulk liquid temperature as the reference temperature for the convective part of the correlation. The wall is viewed as fully wetted by liquid except for vertically stratified conditions or, as the void fraction goes above 0.95, the heat transfer coefficient to liquid is ramped to zero at α_g = 0.99, and the heat transfer coefficient to vapor/gas is ramped up to the value obtained from the DITTUS subroutine.

4.2.3.2.1 Geometry 101, Saturated Nucleate Boiling Model Basis--The nucleate boiling correlation proposed by Chen has a macroscopic convection term plus a microscopic boiling term:

$$q'' = h_{mac}(T_w - T_{spt})F + h_{mic}(T_w - T_{spt})S \quad . \tag{4.2-8}$$

Chen chose Dittus-Boelter times a Reynolds number factor, F, for the convection part and Forster-Zuber[4.2-29] pool boiling times a suppression factor, S, for the boiling part, where h_{mac} is the Dittus-Boelter equation, Equation (4.2-3), and the Forster-Zuber equation is

$$h_{mic} = 0.00122\left(\frac{k_f^{0.79} C_{pf}^{0.45} \rho_f^{0.49}}{\sigma^{0.5} \mu_f^{0.29} h_{fg}^{0.24} \rho_g^{0.24}}\right)\Delta T_w^{0.24} \Delta P^{0.75} \tag{4.2-9}$$

where the subscript f means liquid, the subscript g means vapor/gas, and

ΔT_w = T_w minus T_{spt} (based on total pressure)

ΔP = pressure based on wall temperature minus total pressure.

A plot of the F factor is shown in **Figure 4.2-4**.

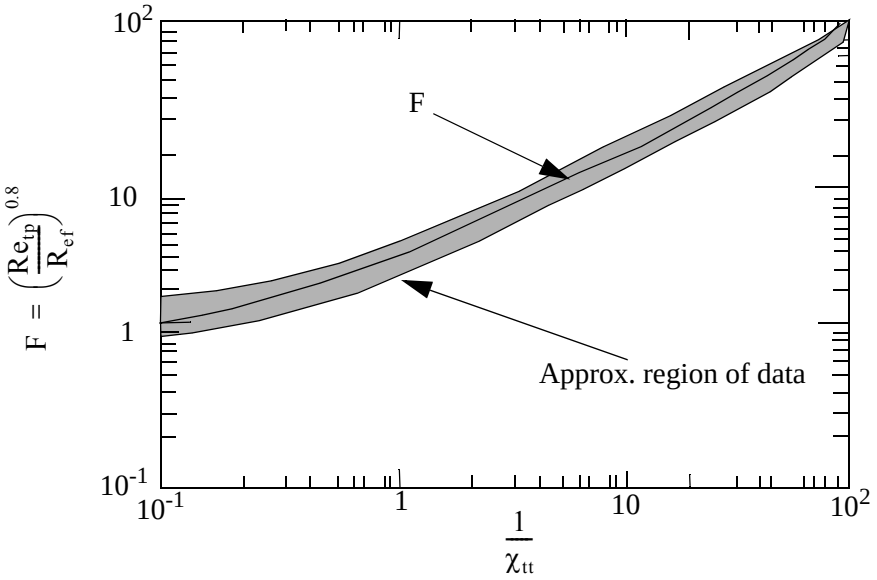

Figure 4.2-4 Reynolds number factor, F.

The suppression factor shown in **Figure 4.2-5**, is the ratio of effective superheat to wall superheat. The S factor accounts for decreased boiling heat transfer because the effective superheat across the boundary layer is less than the superheat based on a wall temperature.

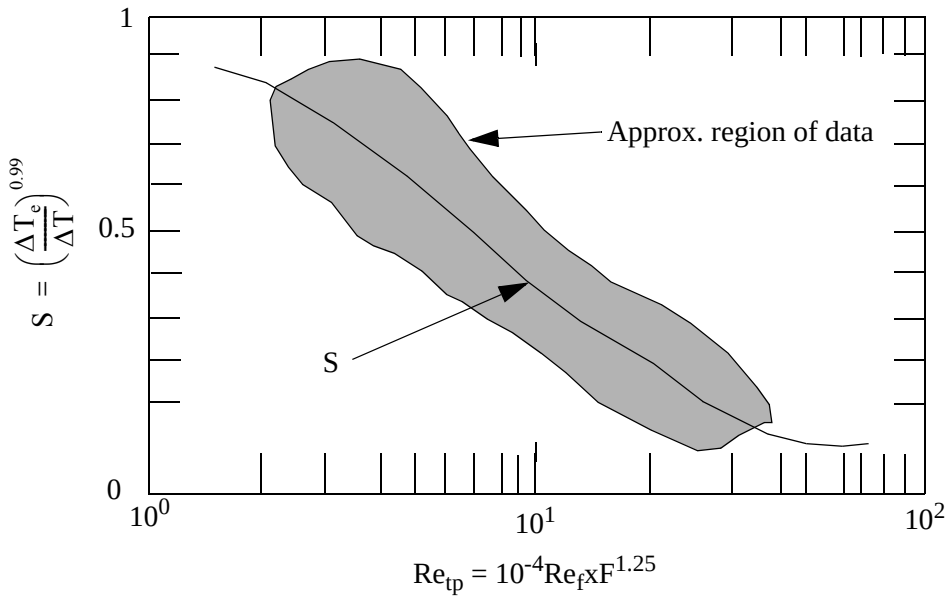

Figure 4.2-5 Suppression factor, S.

The F and S factors were determined by an iterative process. First, F was calculated assuming a functional relationship with the Martinelli flow parameter, χ_{tt}, and the ratio of the two-phase to liquid Reynolds numbers. With F determined, the convective component was extracted from the total heat transfer, leaving the boiling component. Then, S was determined assuming it to be a function of the local two-phase Re. The process was continued for 10 iterations. The solid lines drawn through the data ranges of **Figure 4.2-4** and **Figure 4.2-5** were taken as the values for F and S.

Table 4.2-4 indicates data for water, for which the correlation was developed and tested.[4.2-50 - 4.2-54] The mean percent deviations between the correlation and the data sets are presented in the last column. **Table 4.2-4** presents nonwater data used in development and testing of the Chen correlation.[4.2-55] The data ranges indicate that for little high-pressure data were used to develop and test the correlation. The mean deviation for all the data considered is stated as 11.6%.

Recent development[4.2-56] has extended the database over which the correlation has been exposed. The maximum pressure of the database was increased to 7.0 MPa for saturated water. The specific effect of this comparison was not noted.

Table 4.2-4 Range of conditions tested by Chen for water data .

Reference	Geometry	Flow direction	Pressure (MPa)	Liquid velocity (m/s)	Quality (%)	Heat flux (kW/m^2)	Average error (%)
Dengler-Addoms	Tube	Up	0.05 - 0.27	0.06 - 1.5	15 - 71	88 - 63	14.7
Schrock-Grossman	Tube	Up	0.29 - 3.48	0.24 - 4.5	3 - 50	205 - 240	15.1
Sani	Tube	Down	0.11 - 0.21	0.24 - 0.82	2 - 14	44 - 158	8.5
Bennett et al.	Annulus	Up	0.10 - 0.24	0.06 - 0.27	1 - 59	55 - 101	10.8
Wright	Tube	Down	0.11 - 0.47	0.54 - 3.41	1 - 19	41 - 278	15.4

Table 4.2-5 Range of conditions for nonwater data used in testing Chen correlation .

Fluid	Pressure (MPa)	Reduced pressure (MPa)	Liquid velocity (m/s)	Quality (%)	Heat flux (kW/m^2)	Average error (%)
Methanol	.1	0.013	0.3 - 0.76	1 - 4	22 - 56	11.3
Cyclohexane	.1	0.026	0.4 - 0.85	2 - 10	9 - 41	13.6
Pentane	.1	0.031	0.27 - 0.67	2 - 12	9 - 390	6.3
Heptane	.1	0.038	0.3 - 0.73	2 - 10	6 - 30	11.0
Benzene	.1	0.021	0.3 - 0.73	2 - 9	13 - 43	11.9

4.2.3.2.2 Geometry 101, Saturated Nucleate Boiling Model as Coded--The model is coded as expressed above, subject to the modifications as explained below.

Chen's original paper presented S and F in graphical form, and Butterworth made the curve fits given by Equations (4.2-10) and (4.2-12) as reported by Bjornard and Griffith.[4.2-57]

The suppression factor S makes use of the F factor and is given by

$$S = \begin{cases} (1 + 0.12 Re_{tp}^{1.14})^{-1} & Re_{tp} < 32.5 \\ (1 + 0.42 Re_{tp}^{0.78})^{-1} & 32.5 \le Re_{tp} < 70 \\ 0.0797 & Re_{tp} \ge 70 \end{cases} \quad (4.2\text{-}10)$$

where

$$Re_{tp} = \min (70, 10^{-4} Re_f F^{1.25}) \quad (4.2\text{-}11)$$

$$Re_f = \frac{G_f D}{\mu_f} .$$

G_f = liquid mass flux.

At Re_{tp} = 70, S is 0.0797, not 0.1, as given by Bjornard and Griffith.[4.2-57] This avoids a discontinuity.

The F factor comes from the inverse of the Lockhart-Martinelli[4.2-58] factor χ_{tt}; it is given by

$$F = 2.35(\chi_{tt}^{-1} + 0.213)^{0.736} \quad (4.2\text{-}12)$$

where

$$\chi_{tt}^{-1} = \left(\frac{G_g}{G_f}\right)^{0.9}\left(\frac{\rho_f}{\rho_g}\right)^{0.5}\left(\frac{\mu_g}{\mu_f}\right)^{0.1} . \quad (4.2\text{-}13)$$

The term χ_{tt}^{-1} is limited to 100 and, if it is less than 0.1, F is set to 1.0.

The mac term uses the Dittus-Boelter equation unless the liquid Reynolds number is less than one million, then it calls the DITTUS subroutine and uses the maximum of laminar forced convection, turbulent forced convection, and natural convection. Thus, when the liquid Reynolds number is zero, the mac term will be nonzero. Calling subroutine DITTUS at low Reynolds numbers helps smooth the transition between boiling and forced convection.

Where the code flow regime model indicates that vertical stratified flow exists or the level model is on in the cell connected to the heat structure, the code combines the coefficients above the level with those below the level. Below the level, the modified Chen model (discussed above) is used. Above the level, the maximum of the Dittus-Boelter equation [Equation (4.2-3)] and the Bayley natural convection equation are used. The Bayley equation is

$$Nu = 0.1\, Ra^{0.3333} . \quad (4.2\text{-}14)$$

It was developed for air with Grashof numbers above 10^9. When vertical stratified flow exists, the above level coefficient is reduced by the vapor/gas volume fraction and the modified Chen coefficients below the level are reduced by the liquid volume fraction. When the level model is on, the level fractional height

within the cell is used as the multiplier on the Chen coefficients instead of the liquid volume fraction, and one minus this value multiplies the vapor/gas region coefficient. Note that the level model does not have to be "on" in order for there to be a vertical stratified flow regime. The multiplier on the liquid coefficient is M_f, and the multiplier on the vapor/gas coefficient is $1\text{-}M_f$.

Between a wall superheat value of 0 and 1 K, the F factor is ramped between 1.0 and its full value. It is ramped to 1.0 at zero degrees superheat so that the mac term will match the mac term calculated in subroutine CONDEN as the wall temperature crosses the saturation value. Subroutine CONDEN values are also ramped as the wall subcooling disappears.

If the total heat flux is calculated to be less than or equal to zero, the mode is set to 12.

4.2.3.2.3 Geometry 101, Subcooled Nucleate Boiling Model Basis--The subcooled boiling model was developed to generate bubbles in the superheated liquid next to the wall. A special model was needed because ATHENA can only track the bulk liquid temperature. Actually, there is a superheated liquid layer next to the hot wall that is a source of vapor. The model basis is the same as for saturated nucleate boiling expressed by Equation (4.2-8), with changes proposed by Bjornard and Griffith;[4.2-57] set F to one and use the total mass flux in the Reynolds number.

The correlation has been tested with some water, ammonia, and n-butyl alcohol fluid data by Moles and Shah.[4.2-59] The data scatter was large (+180 to -60%), with the data generally being underpredicted.

4.2.3.2.4 Geometry 101, Subcooled Nucleate Boiling Model as Coded--The coding follows Collier and Butterworth's[4.2-60] suggestion for subcooled liquid conditions by using $T_w\text{-}T_{liquid}$ instead of $T_{wall} - T_{spt}$ as the driving potential for the convection term.

Using the model exactly as suggested could result in unacceptable discontinuities. Between a liquid subcooling of zero and 5 K, the Chen F factor is linearly modified from the correlation value to 1.0, as follows:

$$F' = F - 0.2(T_{spt} - T_f)(F - 1) \qquad T_{spt} > T_f \geq (T_{spt} - 5K)$$

$$F' = 1 \qquad T_f < (T_{spt} - 5K)\ . \qquad (4.2\text{-}15)$$

The functional relationship is shown in **Figure 4.2-6**. This procedure provides smoothing of F for the liquid forced convection h if the fluid temperature falls between T_{sat} and $T_{sat} - 5$. Also, under subcooled conditions, the mass flux in the Reynolds number continues to be the liquid mass flux.

The modification resulting in the F' factor can result in a larger multiplying factor than recommended for subcooling between 0 and an arbitrary 5 K. The modification does result in a smooth transition between subcooled and saturated forced convection as the subcooling goes to zero.

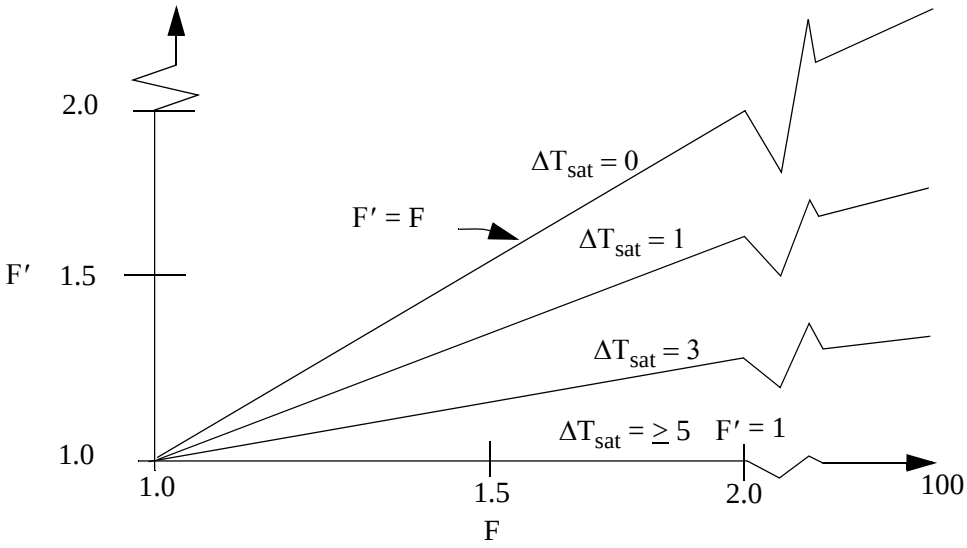

Figure 4.2-6 Modified Chen F factor F′ as a function of F and subcooling ($\Delta T_{sat} = T_{spt} - T_f$).

The modifications for vertical stratification/level for saturated nucleate boiling are also used for subcooled nucleat boiling.

If the total heat flux is calculated to be less than or equal to zero, the mode is set to 12.

4.2.3.3 Geometry 101, Correlations for Subcooled Transition Boiling (Mode 5) and Saturated Transition Boiling (Mode 6). The heat fluxes for both transition and film boiling are evaluated in subroutine PSTDNB. When transition boiling flux is the highest, the mode number is either 5 or 6. The same correlation is applied to saturated and subcooled flow. The calculated heat flux value for transition boiling is applied to post-CHF heat transfer if it is larger then the value for film boiling given in Section 4.2.3.4.

4.2.3.3.1 Geometry 101,Transition Boiling Model Basis--The Chen transition boiling model[4.2-20] considers the total transition boiling heat transfer to be the sum of individual components, one describing wall heat transfer to the liquid and a second describing the wall heat transfer to the vapor/gas. Radiative heat transfer from wall to fluid is not specifically described in the model, as it is estimated to be less than 10% of the total. Whatever radiation effects are present are lumped into the liquid and vapor/gas heat transfer components.

The development of the Chen transition boiling model is stated to be primarily applicable to a dispersed flow regime, where liquid droplets are suspended in a bulk vapor/gas stream. It is recognized that an inverse annular flow regime, where a vapor/gas film separates a bulk liquid core from the wall, may be present near the CHF point. Nonequilibrium phase states are treated through the apportioning of heat energy to the individual phases. The model is expressed as

$$q_{tb} = q_{wf}A_f + h_{wgg}(T_w-T_g)(1-A_f) \quad (4.2\text{-}16)$$

where

q_{tb} = transition boiling heat flux

A_f = fractional wall wetted area

h_{wgg} = heat transfer coefficient to vapor/gas (from DITTUS subroutine).

The q_{wf} term is a complex mechanistic relationship predicting the average heat flux during the time of contact between the liquid and the wall. The heat removal process is described by a three-step model considering a prenucleation period, a bubble growth period, and a film evaporation period.

A_f is dependent on the amount of liquid present at any instant at a particular section of the heated tube and on the probability of this liquid contacting the hot wall. A_f is empirically correlated as

$A_f = e^{-\lambda(T_w - T_{spt})^{0.5}}$

$\lambda = \max(\lambda_1,\lambda_2)$

$\lambda_1 = C_1 - \frac{C_2 G}{10^5}$ (G is mass flux in $lb_m/hr\text{-}ft^2$)

$\lambda_2 = \frac{C_3 G}{10^5}$

$C_1 = 2.4C_2$

$C_2 = \frac{0.05}{1-\alpha_g^{40}} + 0.075\alpha_g$

$C_3 = 0.2\ C_2$

α_g = vapor/gas volume fraction.

The C_1 and C_2 coefficients are correctly given above but are not correct in **Reference 4.2-20**[1]. The constant in C_1 is incorrectly given as 24 in **Reference 4.2-20** rather than the correct value of 2.4. The constants in C_2 are incorrectly given as 0.005 and 0.0075 in **Reference 4.2-20** rather than the correct values of 0.05 and 0.075.

The void fraction α_g is calculated assuming homogeneous flow.

The h_{wgg} term in Equation (4.2-16) is based on the Reynolds analogy for forced turbulent vapor/gas flow in a duct with the Colburn suggested $Pr^{2/3}$ factor multiplying the Stanton number. The analogy takes the form

$$StPr^{\frac{2}{3}} = \frac{f}{2} \tag{4.2-17}$$

where f is the Fanning friction factor. The model uses an explicit form for f, which approximates the work of Beattie**[4.2-61]** who developed friction factors for two-phase post-CHF conditions. The form is $f = 0.037\ Re^{-0.17}$. The coefficient for wall-to-vapo/gas heat transfer then takes the form

$$h_{wgg} = 0.0185\ Re^{0.83}\ Pr^{1/3}\ . \tag{4.2-18}$$

This h_{wgg} term is replaced in the code adaptation, which will be discussed in the next section, and thus it will not be described further here.

The Chen transition boiling model was compared to data (4167 points) from eight sources for water flowing in tubes with a mean deviation[2] of 16.0%. **Table 4.2-6** lists the parameter ranges.

Table 4.2-6 Chen transition boiling correlation database.

Geometry: **Flow:** **Experimental method:**		**Vertical tube** **Upward** **Heat flux controlled, uniform heat flux at the wall**				
Data source	**System pressure (MPa)**	**Tube diameter (cm)**	**Mass flux 10^3 (kg/m^2-s)**	**Equilibrium quality**	**Heat flux 10^5 (W/m^2)**	**Data points**
B&W	0.42 - 10.4	1.27	40.7 - 678	0.675 - 1.728	1.00 - 6.63	904

1. Personal communication, J. C. Chen to R. W. Shumway, May 1988.

Table 4.2-6 Chen transition boiling correlation database. (Continued)

Geometry: **Flow:** **Experimental method:**		**Vertical tube** **Upward** **Heat flux controlled, uniform heat flux at the wall**				
Data source	**System pressure (MPa)**	**Tube diameter (cm)**	**Mass flux 10^3 (kg/m^2-s)**	**Equilibrium quality**	**Heat flux 10^5 (W/m^2)**	**Data points**
Bennett	6.89	1.26	380 - 5,235	0.30 - 0.9	3.47 - 20.5	1111
Bennett & Kearsey	6.77 - 7.03	1.26	1,112 - 1,871	0.516 - 1.083	1.29 - 14.6	73
Bertoletti	6.89	0.488	1,085 - 3,946	0.383 - 0.90	1.36 - 15.8	65
Bishop	16.6 - 19.5	0.91 - 0.25	2,034 - 3,377	0.16 - 0.96	8.92 - 16.6	43
Era	6.89 - 7.28	0.60	1,098 - 3,024	0.456 - 1.238	2.09 - 16.5	576
Jansson	0.64 - 7.07	1.27	16.3 - 1,024	0.392 - 1.634	0.34 - 9.97	836
Herkenrath	14.0 - 19.5	1.0 - 2.0	693 - 3,526	0.151 - 1.270	2.58 - 16.6	559

4.2.3.3.2 Geometry 101, Transition Boiling Model as Coded--Total wall heat flux, q_{tb}, is obtained from components describing the wall-to-liquid heat flux and wall-to-vapor/gas heat flux, as follows:

$$q_{tb} = q_{CHF} A_f M_f + h_{wgg} (T_w - T_g) (1 - A_f M_f) \quad . \tag{4.2-19}$$

The term q_{CHF} corresponds to the boiling critical heat flux calculated for the current local conditions. This substitution simplifies the computational process. The CHF computational models are described in a later section. M_f is the vertical stratification/level model multiplier for the liquid.

The following modifications were made to the process for calculating A_f. The code used the actual void fraction below $\alpha_g = 0.99$ instead of the homogeneous value. To limit the possibility of dividing by zero during the evaluation of constant C_2, a limit was placed on α_g, as follows:

$$\alpha_g = \min (\alpha_g, 0.99) \quad . \tag{4.2-20}$$

---

2. The mean deviation is taken to be $M = \frac{1}{N}\sum_{1}^{N} \frac{|Q_{measured} - Q_{predicted}|}{Q_{measured}}$.

The minimum of 15 K and the square root of the temperature difference, $(T_w - T_{spt})^{1/2}$ is used in the equation for A_f. This procedure ensures that the computed wetted wall area fraction, A_f, remains bounded and protects against computer underflow.

If the flow regime has been identified as being vertically stratified, or if the level model is on in the cell, a reduction factor is applied (shown as M_f above; described in the nucleate boiling section where M_f is the liquid volume fraction when vertically stratified and M_f is the level fractional height within the cell when the level model is on). If stratified flow does not exist, M_f is 1.0.

The effective h_{wgg} for the wall-to-vapor/gas heat transfer component is obtained by a call to subroutine DITTUS with vapor/gas conditions (see the previous description of Mode 9 in Section 4.2.3.1). The call to subroutine DITTUS is used here to provide a smooth transition to film boiling which also calls subroutine DITTUS. Linear ramping is used between $\alpha_g = 0$ and $\alpha_g = 0.5$. The heat transfer to vapor/gas must ramp to zero at $\alpha_g = 0$ because heat transfer to a nonexisting mass causes code failures. The void fraction can go to zero, whereas a surface connected to a fluid cell is highly superheated if the fluid has enough subcooling to condense the vapor.

4.2.3.4 Geometry 101, Correlations for Subcooled Film Boiling (Mode 7) and Saturated Film Boiling (Mode 8). Film boiling is described by heat transfer mechanisms that occur during several flow patterns, namely inverted annular flow, slug flow, and dispersed flow. The wall-to-fluid heat transfer mechanisms are conduction across a vapor/gas film blanket next to a heated wall, convection to flowing vapor/gas and between the vapor/gas and droplets, and radiation across the film to a continuous liquid blanket or dispersed mixture of liquid droplets and vapor/gas. The liquid does not touch the wall because of a repulsive force generated by the evaporating liquid. The fluid environment may be stagnant or flowing, saturated or subcooled. The analytical models for conduction, convection, and radiation that form the basis for the code models are described below. The calculated heat flux from film boiling is applied to post-CHF heat transfer if it is larger than the value determined from transition boiling (Section 4.2.3.3).

4.2.3.4.1 Geometry 101, Film Boiling Model Basis for Conduction--The conductive mechanism can be attributed to the work of several investigators.[4.2-22,4.2-62,4.2-63] Bromley[4.2-22] developed an expression to describe the laminar conductive flow of heat energy from a horizontal tube to a stagnant fluid environment. The expression takes the form

$$h = C\left[\frac{g\rho_g k_g^2(\rho_f - \rho_g)h'_{fg}C_{pg}}{L(T_w - T_{spt})Pr_g}\right]^{0.25} \qquad (4.2\text{-}21)$$

where h'_{fg} is a correction to the heat of vaporization, h_{fg}, which additionally includes the energy absorbed by the vapor/gas surrounding the tube. Bromley took this additional energy to be determined by $C_{pg}(T_{film} - T_{spt})$, where the arithmetic average temperature of the vapor/gas film is given by

$$T_{film} = \frac{T_w + T_{spt}}{2} . \quad (4.2\text{-}22)$$

Thus, h'_{fg} is given by (4.2-23)

$$h'_{fg} = h_{fg} + 0.5\, C_{pg} (T_w - T_{spt}) . \quad (4.2\text{-}24)$$

The length term, L, for tubes is the tube diameter. A value for C = 0.62 was determined from fitting data. Test conditions are described below.[1]

Carbon tube diameter: 0.63, 0.95, 1.27 cm.

Stainless steel tube diameter: 0.476 cm.

Pressure: atmospheric.

Fluids: water, nitrogen, n-pentane, benzene, carbon tetrachloride, and ethyl alcohol.

The water data were somewhat overpredicted by Equation (4.2-21).

Essentially, all the data were correlated within $\pm$ 18%. The conductive portion of the total experimental heat flux was obtained by calculating and subtracting a radiation component based on a parallel plate model using an appropriate wall and liquid emissivity (not stated).

Berenson**[4.2-62]** performed a hydrodynamic stability analysis for laminar film boiling above a flat plate. A solution was obtained for the most dangerous wave length resulting in instability. The form of the solution was similar to that of Equation (4.2-21), with some differences. It is of the form

$$L = 2\pi \left[\frac{\sigma}{g(\rho_f - \rho_g)} \right]^{0.5} \quad (4.2\text{-}25)$$

where

σ = liquid surface tension

and

C = 0.425.

1. Data tables are on file with the American Documentation Institute, Washington, D.C.

The L of Equation (4.2-25) was observed to be the characteristic length for film boiling on a horizontal flat plate.

Breen and Westwater[4.2-63] compared data to Equation (4.2-21) and observed film boiling flow patterns. They determined that heat transfer from horizontal tubes in a stagnant fluid pool could be characterized by the ratio of the minimum critical hydrodynamic wave length, L (defined above), to the tube diameter, D. If $\frac{L}{D}$ was less than 0.8, the heat transfer rate exceeded that given by Equation (4.2-21). This limit marked the departure from viscous vapor/gas flow and a smooth liquid-vapor/gas interface to turbulentvapor/gas flow and a wavy interface. The data considered included that from horizontal tubes with diameters ranging from 0.185 to 1.85 in. and the fluids freon-113 and isopropanol boiling at atmospheric pressure and saturation temperature.

The relationship noted between the hydrodynamic wave length and horizontal tube diameter provides a reasonable rationale for the code correlation described in the next section.

4.2.3.4.2 Geometry 101, Film Boiling Conduction Model as Coded--The code model for energy transport to the vapor/gas film is that obtained by replacing the diameter of Equation (4.2-21) with the minimum critical wave length given by Equation (4.2-25). The equation is

$$hf_{spt} = 0.62\left[\frac{g\rho_g k_g^2(\rho_f - \rho_g)h'_{fg}C_{pg}}{L(T_w - T_{spt})Pr_g}\right]^{0.25} M_a \qquad (4.2\text{-}26)$$

where

M_a = void fraction factor.

The void fraction factor smooths h over the range of the void fraction likely seen from an inverted annular flow pattern (α_g = 0.2) to a dispersed flow film boiling pattern (α_g = 0.99). A spline fit is used between 0.2 and 0.99. M_a is one between α_g = 0 and α_g = 0.2. It is zero at α_g = 0.99. The property C_{pg} is evaluated at the vapor/gas temperature, T_g, while ρ_g, μ_g, and k_g are evaluated at the film temperature [Equation (4.2-22)].

The effect of liquid subcooling is included and is from Sudo and Murao.[4.2-64] It is given by

$$hf_{spt} = hf_{spt}\{1 + 0.025 \max[(T_{spt} - T_f), 0.0]\} \ . \qquad (4.2\text{-}27)$$

4.2.3.4.3 Geometry 101, Film Boiling Model Basis for Convection--As the liquid core for the inverted annular flow pattern shrinks, convection to thevapor/gas increases and becomes the predominant heat transfer mechanism for significant flow rates. The single-phase vapor/gas correlations previously presented in Section 4.2.3.1 become the model basis.

4.2.3.4.4 Geometry 101, Film Boiling Convection Model as Coded--The coefficient describing the convective portion of film boiling heat transfer to the vapor/gas is the value calculated by the DITTUS subroutine using vapor/gas properties (see the previous description of Mode 9 in Section 4.2.3.1). The coefficient is linearly ramped to zero as the void fraction decreases from 0.5 to zero. To calculate the heat flux, T_g is taken to be the maximum of T_g or T_{sat}. Convection between the vapor/gas and liquid is included in the interfacial heat transfer models.

4.2.3.4.5 Geometry 101, Film Boiling Model Basis for Radiation--The radiation mechanism for heat transfer is attributed to Sun, Gonzalez-Santalo, and Tien.[4.2-23] The main purpose of the reference is to develop an engineering method for calculating boiling water reactor (BWR) fuel rod heat transfer to the cooling medium during emergency core cooling (ECC) top spray injection. The report presents a method for estimating the radiation energy transfer between a vapor/gas-liquid-droplet mixture enclosed by a wall. Interchange between metal surfaces is not considered, which implies that all wall surfaces must be at equal temperatures, so no net energy transfer occurs between surfaces. The model considers the vapor/gas-liquid mixture as an optically thin medium, which means the vapor/gas and liquid do not self-absorb emitted radiation. Thus, the vapor/gas and liquid may be treated as simple nodes. Radiation energy exchange occurs between the liquid and the vapor/gas, between the liquid and the wall, and between the vapor/gas and the wall. The surface areas of the liquid and vapor/gas are both taken to be equal to the wall surface area with view factors of unity. The three "surfaces" are isothermal, radiosity is uniform, and the "surfaces" are diffuse emitters and reflectors. The radiation heat fluxes are expressed by Sun, Gonzalez-Santalo, and Tien as

$$\begin{aligned} q_{wf} &= F_{wf}\sigma(T_w^4 - T_{spt}^4) \\ q_{wg} &= F_{wg}\sigma(T_w^4 - T_g^4) \\ q_{gf} &= F_{gf}\sigma(T_g^4 - T_{spt}^4) \end{aligned} \qquad (4.2\text{-}28)$$

The subscripts wf, wg, and gf denote wall-to-liquid, wall-to-vapor/gas and vapor/gas-to-liquid heat transfer, respectively. The liquid is assumed to be at the saturation temperature corresponding to the total pressure. Also, the F's are the gray-body factors and σ is the Stefan-Boltzman constant, 5.670×10^{-8} $W/m^2 \cdot K$. The gray-body factors are defined as

$$F_{wf} = \frac{1}{R_f\left(1 + \frac{R_w}{R_g} + \frac{R_w}{R_f}\right)}$$

$$F_{wg} = \frac{1}{R_g\left(1 + \frac{R_w}{R_g} + \frac{R_w}{R_f}\right)}$$

$$F_{gf} = \frac{1}{R_f\left(1 + \frac{R_g}{R_f} + \frac{R_g}{R_w}\right)} \quad .$$

The R terms are given as

$$R_g = \frac{1 - \varepsilon_g}{\varepsilon_g(1 - \varepsilon_g\varepsilon_f)}$$

$$R_f = \frac{1 - \varepsilon_f}{\varepsilon_f(1 - \varepsilon_g\varepsilon_f)}$$

$$R_w = \frac{1}{1 - \varepsilon_g\varepsilon_f} + \frac{1 - \varepsilon_w}{\varepsilon_w} \quad .$$

The emissivities, ε, are given as

$$\varepsilon_g = 1 - \exp(-a_g L_m)$$

$$\varepsilon_f = 1 - \exp(-a_f L_m)$$

$$\varepsilon_w = 0.7.$$

L_m is a mean path length, and a_g and a_f are vapor/gas and liquid absorption coefficients, respectively. The variables L_m and a_f are defined as defined as

$$L_m = D$$

$$a_f = \frac{X_a \pi d^2 n}{4}$$

where

X_a = absorption efficiency

n = droplet number density

d = droplet diameter.

The number density is

$$n = \frac{6G_f}{\pi d^3 \rho_f v_f} = \frac{6\alpha_f}{\pi d^3} \quad . \tag{4.2-29}$$

The absorption efficiency, X_a, is 0.74 for drops of size range 0.01 to 0.2 cm diameter, where $\frac{\pi d}{\lambda} >> 1$ and λ is the characteristic wave length emitted by the heated wall ($\lambda = 2.3 \times 10^{-6}$ m for 1,255 K). From the above,

$$a_f = \frac{1.11\alpha_f}{d} \quad . \tag{4.2-30}$$

The vapor/gas absorption coefficient a_g and the emissivity ε_w of a zircaloy wall are taken directly from references for a fixed temperature.

The authors state that comparison of model calculations (which include convection from vapor/gas to droplets) with empirical FLECHT data shows the average droplet size in FLECHT is about 0.228 cm. This average drop size corresponds well to data in the literature. Thus, it is concluded that the model predicts the thermal behavior during ECC spray cooling. The drop diameter found also shows that the fluid mixture is optically thin for the assumed conditions.

4.2.3.4.6 Geometry 101, Film Boiling Radiation Model as Coded--The coded model applies the equations above with some changes as follows. The liquid droplet diameter is determined by two expressions, and the minimum is selected for application. This minimum is protected to be greater than or equal to 0.00001 m to prevent a divide by zero. The first expression calculates the diameter of a cylinder of liquid in a tube with diameter D. It assumes all the available liquid forms a cylinder of diameter d_{max} in the center of the tube, and it is given by

$$d_{max} = \alpha_f^{0.5} D \quad . \tag{4.2-31}$$

The second expression calculates the average droplet size based on a Weber number criterion of 7.5, and it is given by

$$d_{ave} = \frac{We\ \sigma}{\rho_g (v_g - v_f)^2} \quad , \tag{4.2-32}$$

where $(v_g - v_f)^2$ is protected to be greater than or equal to 0.005 m to prevent a divide by zero.

The liquid emissivity is calculated using the minimum d from Equation (4.2-31) and (4.2-32) (protected by 0.00001 m) and a mean path length of $L_m = 0.9$ D. The mean path length L_m is obtained from

Holman's[4.2-65] formula L_m = 3.6 V/A, where V is the total volume of the vapor/gas and A is the total surface area. For a cylindrical pipe, this gives L_m = 0.9 D. The final liquid emissivity used is taken to be the smaller of the calculated value and 0.75. The vapor/gas emissivity is assumed to be 0.02. The vapor/gas emissivity ε_g is obtained from Holman's[4.2-65] Figure 8-35, using FLECHT data. A value of ε_g = 0.02 is an average value over the range of this data. The wall emissivity is assumed to be 0.9. The emissivity ε_w used in the code (0.9) is slightly larger than the value (0.7) used by Sun, Gonzalez-Santalo, and Tien.[4.2-23] The radiative interchange between wall and vapor/gas and between vapor/gas and liquid is neglected; only the radiative interchange between wall and liquid is coded. The radiative interchange between wall and vapor/gas is neglected because during FLECHT experiments, the wall temperature and the vapor/gas temperature are similar; thus, q_{wg} is small. The radiative interchange between vapor/gas and liquid is neglected because representative calculations using FLECHT data indicate F_{gf} is much less than F_{wf}, thus implying q_{gf} is much less than q_{wf}.

4.2.3.5 Geometry 101, Correlations for Critical Heat Flux. The RELAP5/MOD2 computer program had been criticized for using the Biasi correlation[4.2-66] for predicting the CHF in rod bundles when the correlation is based on tube data.[4.2-67] The Royal Institute of Technology in Sweden[4.2-67] tested RELAP5/MOD2 against their tube data and found it to generally overpredict the value of CHF, particularly in the mid-mass flux range (1,500 - 3,000 kg/s•m^2). ATHENA uses the 1986 AECL-UO Critical Heat Flux Lookup Table[4.2-68] method by Groeneveld and co-workers. The table is made from tube data normalized to a tube inside diameter of 0.008 m but has factors that are applied to allow its use in other sized tubes or in rod bundles. In addition, it considers both forward and reverse flow, axial power shape, and the effect of boundary layer changes at both the bundle inlet and behind grid spacers.

***4.2.3.5.1 Geometry 101, Critical Heat Flux Model Basis*--Reference 4.2-68** compares the predictions of the Biasi correlation to some 15,000 data points in the Chalk River data bank. The comparison is tabulated in **Table 4.2-7**. The correlation is compared to two sets of data, (a) all the data and (b) only data within the correlation range from which it was developed. The data were compared by specifying the quality at CHF. The comparison indicates that the AECL-UO table is better than the Biasi correlation.

Table 4.2-7 AECL-UO table and Biasi correlation compared to Chalk River data bank .

	Data within the error bound (%)			
	Constant dryout quality			**No. of data points**
	+10%	**+20%**	**+50%**	
Biasi: all data	19.30	36.64	67.04	14,401
Biasi: validity only	21.32	41.12	73.04	9,936
AECL-UO	40.6	66.54	92.35	14,401

CHF correlations use analytical expressions to try to cover a wide range of flow conditions and geometries. For instance, if a coefficient is modified to give a better fit to one set of data in a new flow range, the fit for the original set is adversely impacted. This is not true of tables, because only the points around the new data need to be adjusted.

The lookup table was formulated from the 15,000 data points to make a three-dimensional table with 4,410 points in a three-dimensional array covering 15 pressures (P) from 0.1 to 20.0 MPa, 14 values of mass flux (G) from 0.0 kg/m^2-s to 7,500.0 kg/s•m^2, and 21 equilibrium qualities (X_e) from -0.5 to 1.0. After finding the CHF from the table, multiplying factors from Groeneveld et al.,[4.2-68] are used to modify the table value, i.e.,

$$CHF = CHF_{table} \bullet chfmul \tag{4.2-33}$$

$$chfmul = k1 \bullet k2 \bullet k3 \bullet k4 \bullet k5 \bullet k6 \bullet k8 \ . \tag{4.2-34}$$

Eight multipliers are given in **Table 4.2-8**, and the reason k7 is not in the above expression is explained later. If the mass flux or equilibrium quality are out of range, they are reset to the border value. The table can also be used for nonaqueous fluids by using property ratios.

Table 4.2-8 CHF table lookup multipliers .

k	Expression
k1 = hydraulic factor	$k1 = \left(\frac{0.008}{D}\right)^{0.33}$ for D < 0.016 m $k1 = \left(\frac{0.008}{0.016}\right)^{0.33}$ for D > 0.016 m D = heated equivalent diameter = $\frac{4A}{\text{heated perimeter}}$
k2 = bundle factor	k2 = min[.8,.8exp(-.5$X_e^{.33}$)] for rod bundles k2 = 1.0 for other surfaces
k3 = grid spacer factor	$k3 = 1 + A\exp\left(-B \bullet \frac{L_{sp}}{D}\right)$ $A = 1.5(Kloss)^{.5}(G \bullet 0.001)^{0.2}$; B = 0.1 Kloss = grid pressure loss coefficient L_{sp} = distance from grid spacer

Table 4.2-8 CHF table lookup multipliers (Continued).

k	Expression
k4 = heated length factor	$k4 = \exp\left\{\left(\frac{D}{L}\right)[\exp(2.alp)]\right\}$ $alp = \frac{xlim}{[xlim + (1 - xlim)]}\frac{\rho_g}{\rho_f}$ xlim = min[1, max (0,X_e)] L = heated length from entrance to point in question
k5 = axial power factor	k5 = 1. for $X_e < 0$ k5 = $\frac{qlocal}{qbla}$; qbla = average flux from start of boiling to point in question
k6 = horizontal factor	k6 = 1 if vertical k6 = 0 if horizontal stratified k6 = 1 if horizontal high flow k6 = interpolate if medium flow
k7 = vertical flow factor	a. for G < -400 or G > 100 kg/m^2-s, k7 = 1 b. for -50 < G < 10 kg/m^2-s k7 = (1-alp) for alp < 0.8 $k7 = (1 - alp)\frac{(0.8 + .2 \bullet denr)}{[alp + (1 - alp) \bullet denr]}$ $denr = \frac{\rho_f}{\rho_g}$ for alp > 0.8 table value of CHF is evaluated at G = 0, X_e = 0 c. for 10 < G < 100 kg/m^2-s or -400 < G < -50 kg/m^2-s interpolate
k8 = pressure out-of-range	$k8 = \frac{prop(out)}{prop(border)}$ prop = $rho_g^{.5} h_{fg}[sig(rho_f - rho_g)]^{.25}$

Figure 4.2-7 shows the strong hydraulic entrance length effect on k4 at two different void fractions. The importance of k4 diminishes rapidly with elevation. **Figure 4.2-8** illustrates the variation in CHF as the mass flux changes from -1,000 kg/m^2-s to 1,000 kg/m^2-s at a pressure of 0.1 MPa and a void fraction of 0.8.

Questions about the accuracy of the table lookup method under low pressure, low mass flux conditions have been raised. Groeneveld's[4.2-68] paper reports good agreement with 153 data points between 40 kg/m^2-s and 100 kg/m^2-s, as shown in **Figure 4.2-9**. The root-mean-squared (RMS) error at low pressure is about 40%. Its accuracy for rod bundles is uncertain.

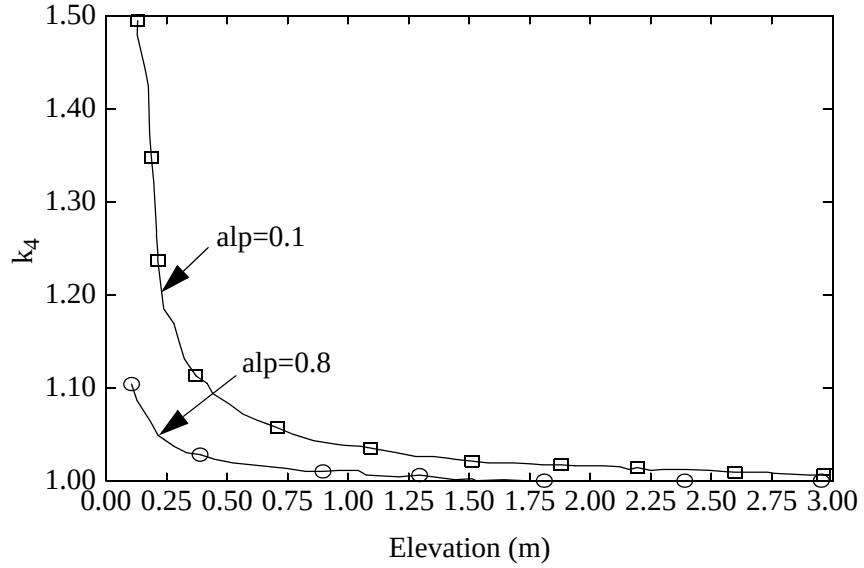

Figure 4.2-7 Effect of heated length on CHF k4 multiplier (D = 0.008 m).

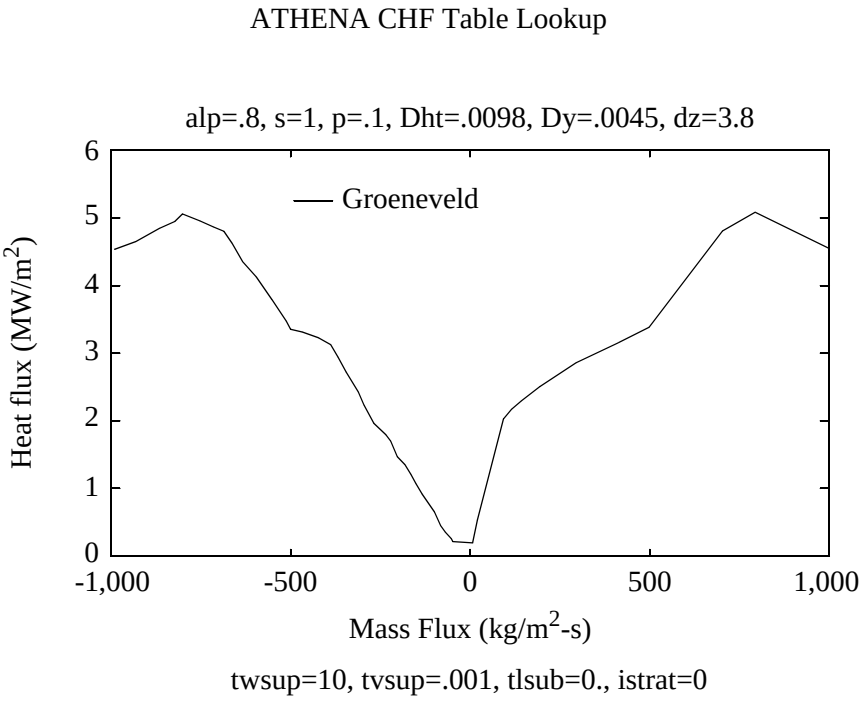

Figure 4.2-8 Variation of CHF with mass flux.

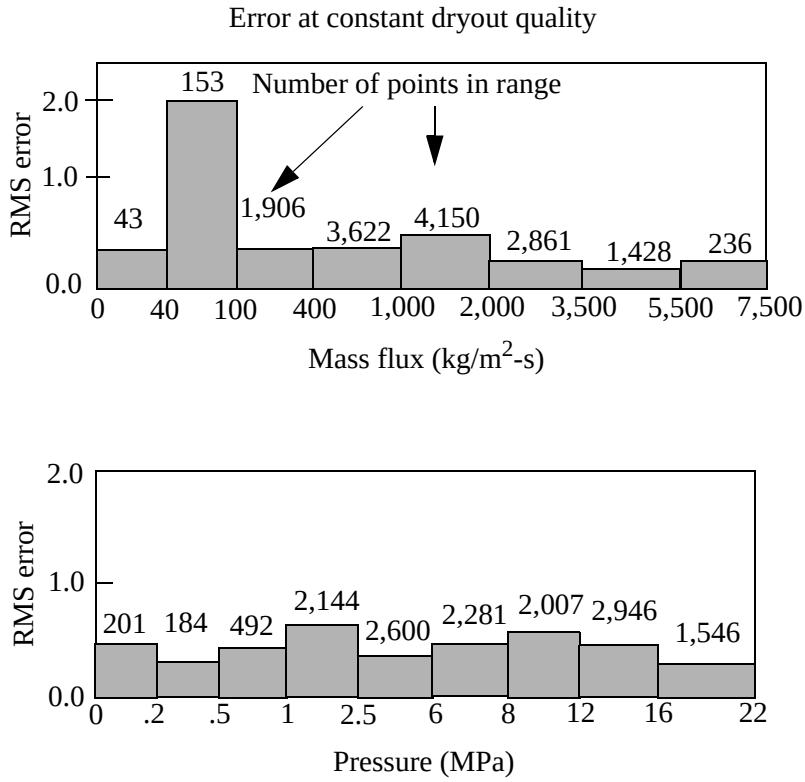

Figure 4.2-9 Groeneveld reported root-mean-squared CHF errors.

4.2.3.5.2 Geometry 101, CHF Model as Coded--The model coded is the same as described above except for the items discussed below.

The first difference is number of points in the table. Because G = 10 kg/m^2-s and G = 400 kg/m^2-s were not in the table but are used for interpolation, these two sets of points were found by interpolation and added to the table. This way, they would not need to be found at each heat slab at each time step under low mass flux conditions. The equilibrium quality (X_e) used in the code in wall heat transfer is based on phasic specific enthalpies and mixture specific enthalpy, with the mixture specific enthalpy calculated using the flow quality.

Reference 4.2-68 says to set G and X_e to zero when the mass flux is between 10.0 kg/m^2-s and -50.0 kg/m^2-s (reset method). Since CHF decreases with increasing quality, CHF is elevated and has a flat shape compared to using G and X_e at their actual values. This is illustrated in **Figure 4.2-10** at a pressure of 7 MPa and a void fraction of 0.9. To find out what the effect would be of using actual values of G and X_e, points were chosen out of the Groeneveld data in the INEEL data bank, which had a mass flux less than 100 kg/m^2-s. Of the 9,353 points, 133 were in this range. **Figure 4.2-11** shows the predicted-versus-measured CHF for these 133 data points, using the model as coded. The data are

scattered, as may be expected for low mass flux. The average error was -0.503, with a root-mean-square (RMS) value of 4.78. Comparing the same data using the actual values (measured G), the average error was -0.30, with an RMS error of 3.92. Based on this data set, it appears better not to use the G and X_e reset method recommended in **Reference 4.2-68**. However, Kyoto University data[4.2-69] suggest just the opposite. These data were taken in a vertical rectangular duct with one wall heated. **Figure 4.2-12** compares the data with the two methods of handling the low mass flux problem. **Figure 4.2-13** shows only the low mass flux region. The suggested reset method is obviously better in this case. The region between -50kg/m^2-s and 10 kg/s•m^2 is not flat, as it is in **Figure 4.2-10**, because of the void fraction variation built into k7. The net result of these comparisons is that the model has been coded with the reset method suggested by Groeneveld.[4.2-68]

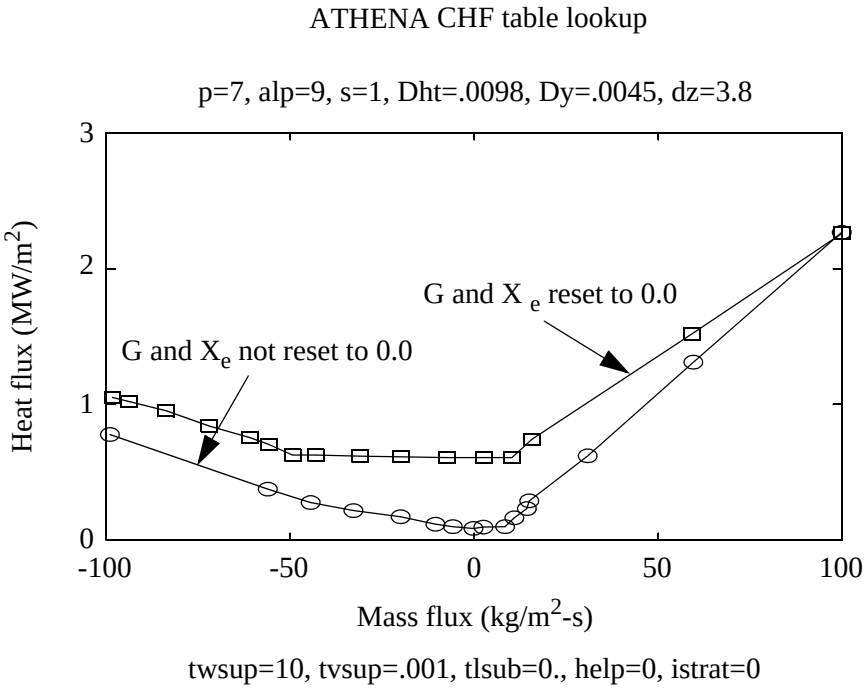

Figure 4.2-10 Low mass flux CHF with and without G and X_e reset to 0.0.

The average error for all 9,353 data points was -0.049 and the RMS error was 0.39 (i.e., 39.%).

After finding the correct point in the CHF table for a given P, G, and X_e, four pressure interpolations are made to find the value of CHF at C1, C2, C3, and C4. Next, two mass flux interpolations are made to find C5 and C6. Lastly, the quality interpolation is made. The interpolation box is illustrated in **Figure 4.2-14**. In order to have a smooth CHF curve as the mass flux changes from high to low, the k7 multiplier is treated differently than the other multipliers. In the low mass flux range, k7 is applied only to the CHF values obtained in the mass flux range of G = 10 kg/m^2-s to -50 kg/s•m^2. In other words, when

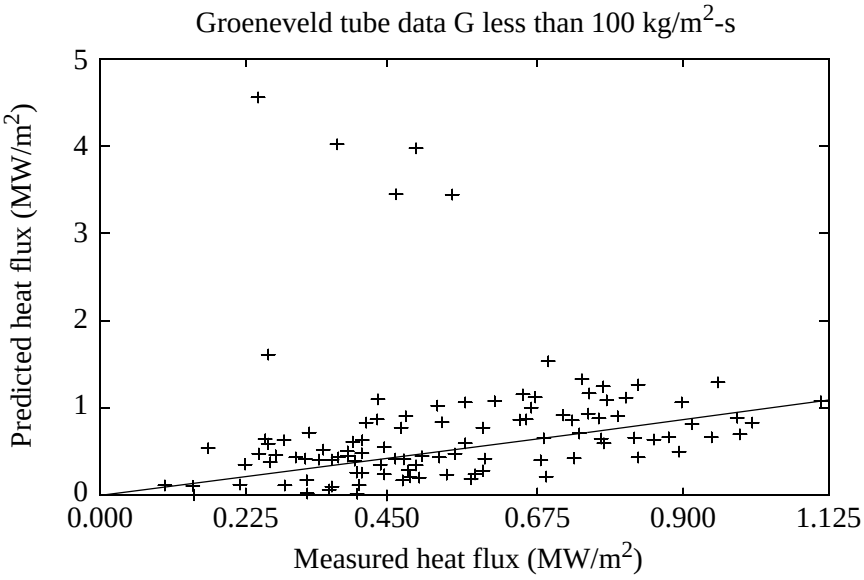

Figure 4.2-11 Low mass flux data comparison with G and X_e reset to 0.0.

interpolation is required, the low mass flux ends of the interpolation box are multiplied times k7, but the high mass flux ends (100 kg/m^2-s and -400 kg/m^2-s) are not.

The horizontal multiplicative factor k6 used in the code is different than that of the original model. The original model sets k6 = 0 if horizontal stratified flow, k6 = 1 if horizontal high flow, and k6 is interpolated if medium flow. The interpolation region is between mass fluxes G_1 and G_2 (see **Reference 4.2-68**). This was originally implemented in the code useing a modified method. The method uses 1.0 minus the horizontal stratification factor (FSTRAT in Appendix 4A of this volume of the manual). This method caused problems with a ROSA test facility cold leg break calculation where a pressure spike was traced to k6 changing from 0 (perfect horizontally stratified) to 0.5 (non-perfect horizontially stratified). To avoid sudden changes, k6 is now defined as the ratio of the wetted perimeter devided by the total perimeter, where the wetted perimeter is found from geometry considerations using the void fraction and the diameter.

4.2.3.6 Geometry 101, Correlations for Condensation (Modes 10 for $\alpha_g < 1$ and 11 for $\alpha_g = 1$). Wall condensation is the process of changing a vapor near a cold wall to a liquid on the wall by removing heat. In many postulated light water reactor accident conditions there may be noncondensable (NC) gases mixed with vapor. The noncondensable gases have an insulating effect on the heat transfer between the vapor/gas and the wall. The rate of the condensation process and heat transfer to the wall depends on the degree of wall subcooling relative to the saturation temperature based on the partial

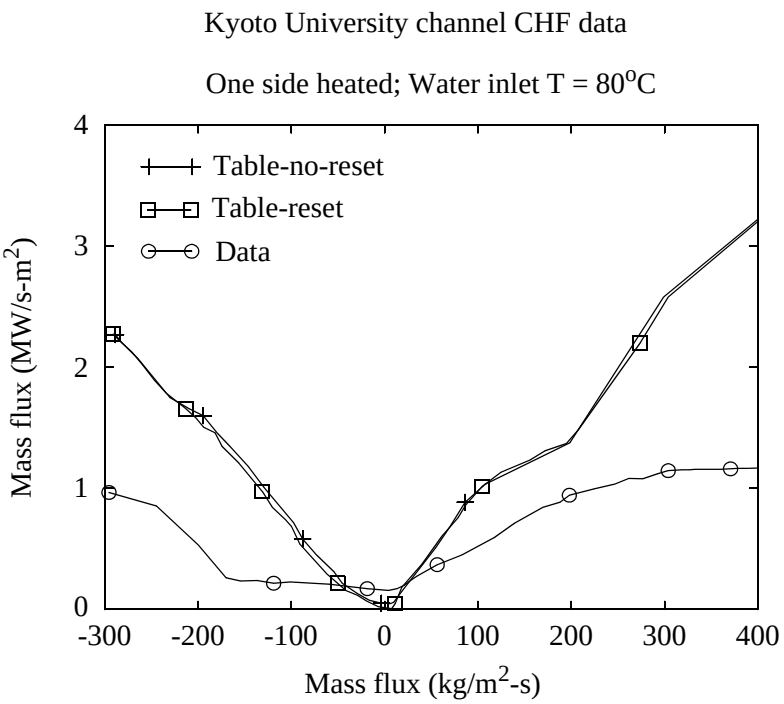

Figure 4.2-12 Kyoto University data comparison with and without G and X_e reset to 0.0.

pressure of the vapor and other factors such as the liquid film thickness, turbulence, vapor/gas shear, etc. The heat released at the vapor/gas-liquid interface is transferred through the liquid film and into the wall.

Two general classifications of wall condensation are “film” and “dropwise.” Film condensation has been studied experimentally more than dropwise condensation because metal tubes are easily wetted. Special coating materials are sometimes applied to metals to increase the surface areas over which beads of water drops exist because dropwise condensation rates can be an order of magnitude larger than filmwise rates. A schematic of film condensation on a vertical surface is shown in **Figure 4.2-15**. Radial flow of vapor toward the cold wall transports the noncondensables to the wall, where they accumulate due to condensation of the vapor. The resulting noncondensable concentration gradient causes noncondensable diffusion back toward the mainstream counter to the vapor flow direction. The vapor partial pressure and temperature are lower in the noncondensable buffer layer than in the mainstream, as shown in the figure. The effect of the noncondensible gas is to make a reduced temperature difference (T_{gi}-T_w) and reduced heat flux through the liquid film.

Figure 4.2-15 also shows that as the condensate layer thickness increases it can undergo a transition from laminar to turbulent flow. McAdams[4.2-7] suggests that transition occurs at a condensate Reynolds number of 1,800, where the Reynolds number (Re) is defined as

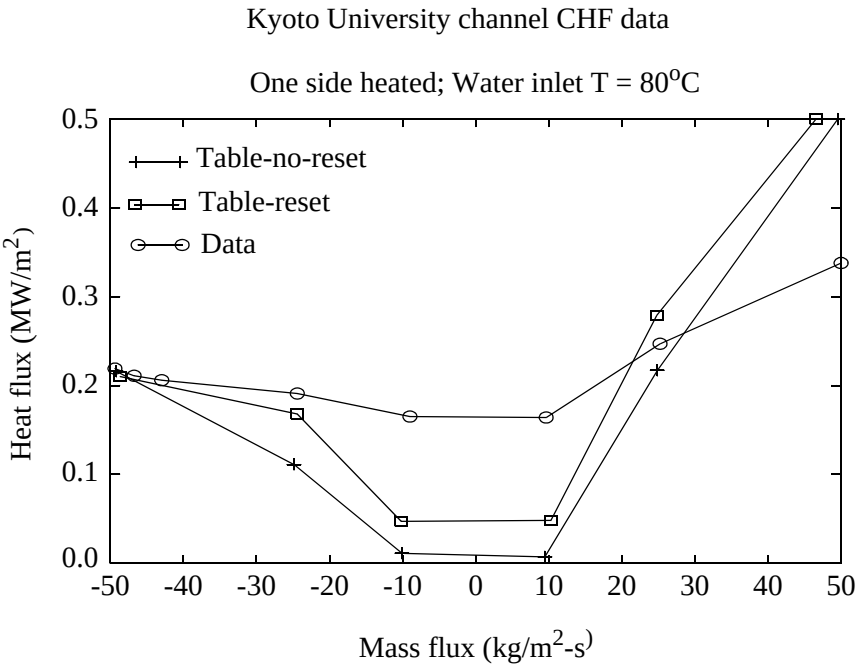

Figure 4.2-13 Kyoto University data comparison at low mass flux.

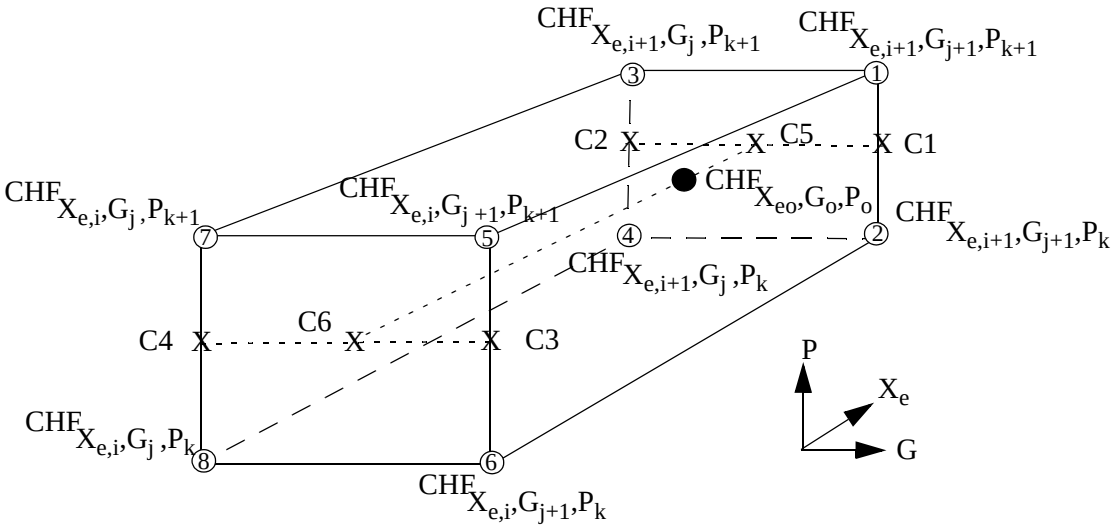

Figure 4.2-14 Illustration of CHF interpolation technique.

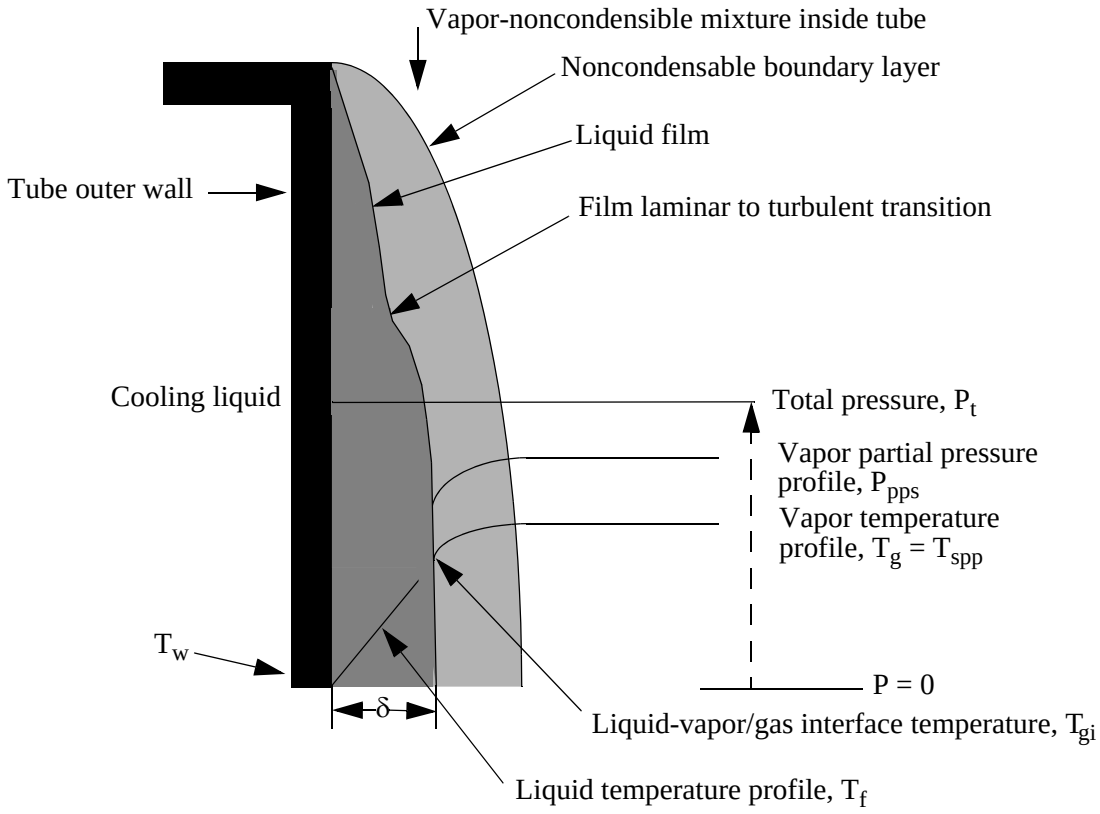

Figure 4.2-15 Film condensation schematic.

$$Re = \frac{4\Gamma}{\mu_f} \tag{4.2-35}$$

where

μ_f = liquid viscosity

Γ = liquid mass flow rate per unit periphery

$$\Gamma = \frac{\dot{m}_f}{\pi D_i} \tag{4.2-36}$$

$\dot{m}_f$ = liquid mass flow rate

D_i = inner diameter of the tube.

However, at high values of the vapor/gas shear stress, Carpenter and Colburn[4.2-70] found transition Reynolds number values as low as 200 to 300.[4.2-71]

For inclined surfaces, the model uses the maximum of the Nusselt[4.2-24] (laminar) and Shah[4.2-25,4.2-72] (turbulent) correlations with a diffusion calculation based on the Colburn-Haugen[4.2-27] method when noncondensable gases are present. For horizontal surfaces, the model uses the maximum of the Chato[4.2-26] (laminar) and Shah[4.2-25,4.2-72] (turbulent) correlations with a diffusion calculation based on the Colburn-Haugen[4.2-27] method when noncondensable gases are present. A new condensation model is being developed which will use the diffusion method for both the wall and vapor/gas-liquid interfacial heat transfer rates. Currently the wall and interfacial heat transfer are partially uncoupled. The mass transfer rate calculated in the wall heat transfer section of the code is used in the energy and mass continuity equations. However, the bulk interfacial part of the code does not recognize a unique film condensation mode where, in steady-state, energy from the vapor/gas must equal energy to the wall.

The ATHENA condensation heat transfer routines model laminar film condensation on an inclined or vertical surface and laminar film condensation inside a horizontal tube with a stratified liquid surface. ATHENA calculates a wall heat transfer coefficient based on condensation logic under the following conditions:

1. The wall temperature is below the saturation temperature based on the bulk partial pressure of vapor minus 0.001 K. The small subtraction was made because, when noncondensables are present and the default diffusion method (by Colburn-Hougen) is being applied, the code could not converge on a liquid-vapor/gas interface temperature if the temperature difference was insignificant.

2. The liquid temperature is above the wall temperature. The model is a film condensation model where the liquid is heating the wall.

3. The liquid volume fraction is greater than 0.1. As the liquid volume fraction approaches zero, transition to forced convection occurs.

4. The bulk noncondensable quality is less than 0.999.

5. The pressure is below the critical pressure.

Several other factors are considered for smoothing, physical arguments, and the presence of a noncondensable gas. When the wall temperature is less than one degree subcooled, the liquid coefficient is ramped to the Dittus-Boelter value and the vapor/gas coefficient is ramped to zero, so that transition will occur smoothly between the condensation mode and boiling mode. Besides the temperature ramp, there is a void fraction ramp. At void fractions less than 0.1, the HTRC1 subroutine goes to subroutine DITTUS to get the coefficients. Therefore, in the CONDEN subroutine, between a void fraction of 0.3 and 0.1, h_{wff} is

ramped to the Dittus-Boelter value, and h_{wgg} is ramped to zero. When the void fraction is 1.0, subroutine DITTUS is called to obtain the convection-to-vapor/gas ratio, and this contribution is added to the condensation term. The direct vapor/gas mass transfer term, Γ_w, is computed from the vapor/gas heat flux and the vapor/gas-to-saturated liquid specific enthalpy difference.

The method calculates heat transfer coefficients based on filmwise condensation. The method of calculating the heat transfer coefficient is given below. Once it is known, it is used to calculate the total heat flux, and it is given by

$$q_t'' = h_c(T_w - T_{sppb}) \tag{4.2-37}$$

where

q_t'' = total heat flux

h_c = predicted condensation heat transfer coefficient

T_w = wall temperature

T_{sppb} = saturation temperature based on vapor partial pressure in the bulk.

Because ATHENA is a two-fluid code, the liquid and the vapor/gas can both theoretically exchange energy with the wall. Although film condensation is the only condensation mode considered, currently ATHENA allows both a heat flux to liquid and one to vapor/gas. The heat flux to liquid is

$$q_f'' = h_c(T_w - T_f) \tag{4.2-38}$$

where

T_f = bulk liquid temperature.

The vapor/gas to wall heat flux is the difference between the total wall heat flux and the liquid to wall heat flux. The vapor/gas to wall heat transfer is required to be less than or equal to zero. The interfacial mass transfer term used in the continuity equation consists of mass transfer near the wall and mass transfer in the bulk. The term for mass transfer near the wall is computed from the heat flux from the vapor/gas to the wall.

One abnormal condensation situation the code considers is when the wall is subcooled but the liquid temperature is below the wall temperature. This occurs when subcooled liquid is injected into a cold tank with a vapor/gas source at the top of the tank. The problem is that the code only has one liquid temperature to work with and it needs two; one for the liquid film on the wall and another for the entering liquid. In this

situation the heat flux to the vapor/gas is the condensation coefficient times the wall-to-saturation temperature difference and the heat flux to the liquid is the coefficient obtained by a call to the DITTUS subroutine times the wall-to-liquid temperature difference.

4.2.3.6.1 Geometry 101, Inclined Surface Condensation Model Basis--The wall condensation heat transfer coefficient for an inclined surface in ATHENA is the maximum of the Nusselt[4.2-24] (laminar) correlation and the Shah[4.2-25,4.2-72] (turbulent) correlation. The original work for laminar condensation was accomplished by Nusselt.[4.2-24] The Nusselt expression for vertical surfaces uses the film thickness, δ, as the key parameter instead of the temperature difference, and it is given by

$$h_{Nusselt} = \frac{k_f}{\delta} \tag{4.2-39}$$

where from Nusselt's[4.2-24] derivation the film thickness is

$$\delta = \left[\frac{3\mu_f\Gamma}{g\rho_f(\rho_f-\rho_g)}\right]^{\frac{1}{3}} \tag{4.2-40}$$

or, in terms of the film Reynolds number defined by Equation (4.2-35),

$$\delta = \left[\frac{3\mu^2_f Re_f}{4g\rho_f(\rho_f-\rho_g)}\right]^{\frac{1}{3}} = 0.9086\left[\frac{\mu^2_f Re_f}{g\rho_f(\rho_f-\rho_g)}\right]^{\frac{1}{3}} . \tag{4.2-41}$$

This derivation is also given in Collier[4.2-60].

Assumptions in the analysis for the top of an inclined surface include

1. Constant fluid properties.
2. Vapor/gas exerts no drag on liquid surface.
3. Liquid subcooling is neglected.
4. Momentum changes in the laminar liquid annular film are negligible.
5. Heat transfer is by conduction through the laminar liquid annular film.

The Genium Handbook (previously the GE handbook) in Section 506.3 on film condensation with turbulent flow reports that "perhaps the most-verified predictive general technique available is the following correlation of Shah", which is given by

$$h_{Shah} = h_{sf}\left(1 + \frac{3.8}{Z^{0.95}}\right) \quad (4.2\text{-}42)$$

where

$$Z = \left(\frac{1}{X} - 1\right)^{0.8} P_{red}^{0.4} \quad (4.2\text{-}43)$$

and

X = static quality = (mass vapor + mass noncondensable)/(mass vapor + mass noncondensable + mass liquid)

P_{red} = reduced bulk pressure, $\frac{P}{P_{critical}}$

h_{sf} = superficial heat transfer coefficient

$$h_{sf} = h_1 (1 - X)^{0.8} \quad (4.2\text{-}44)$$

and

h_1 = Dittus-Boelter coefficient assuming all fluid is liquid

$$h_1 = 0.023\left(\frac{k_1}{D_h}\right) Re_1^{0.8} Pr_1^{0.4} \quad (4.2\text{-}45)$$

where the Reynolds number is given by $Re_1 = G_{total}\frac{D_h}{\mu_f}$. The data base for the Shah correlation includes both horizontal and vertical data.

In ATHENA, the wall condensation heat transfer coefficient for inclined surfaces is

$$h_c = \max (h_{Shah}, h_{Nusselt}) \ . \quad (4.2\text{-}46)$$

Thus, the maximum of a turbulent correlation and a laminar correlation is used.

4.2.3.6.2 Geometry 101, Inclined Surface Condensation Model as Coded--No analytical improvements have been incorporated. The laminar model in the code is Equations (4.2-39) and (4.2-41)

with the ρ_f - ρ_g term approximated by ρ_f and the gravity term modified for inclined surfaces. For inclined surfaces the gravity term is replaced by the fluid cell elevation rise times the gravity constant divided by the length of the cell. The gravity constant, g, is taken as 9.80665 m/s^2. The minimum film thickness allowed in ATHENA is 10 microns. Thus, if a volume had a void fraction of 1.0, a high rate of condensation would be predicted to simulate the beginning of dropwise condensation. The basis for this less-precise model is the short-lived existance of dropwise condensation[4.2-65]. The coefficient value from Equation (4.2-39) is compared with the value obtained from assuming a minimum laminar Nusselt number of 4.36, and the larger of the two is accepted.

Experiments indicate that the $h_{Nusselt}$ value can be 40 to 50% too low[4.2-60]. The increased heat transfer (from the experiments) is attributed to vapor/gas velocity and ripples changing the film thickness, or turbulence. Collier[4.2-60] recommends that the computed value be increased by 20%.

The turbulent model in the code for inclined surfaces condensation is Equations (4.2-42) through (4.2-45).

Where the code flow regime indicates that vertical stratified flow exists or the level model is on in the cell connected to the heat structure, the code combines the coefficients above the level with those below the level. Above the level, the laminar (Nusselt) model discussed above is used. Below the level, the code uses the maximum of laminar forced convection, turbulent forced convection, and natural convection. Similar to saturated nucleate boiling, subcooled nucleate boiling, and transition boiling, the same vertical stratification/level model multiplier M_f for the liquid is used. For the vapor/gas, the multiplier 1-M_f is used.

4.2.3.6.3 Geometry 101, Horizontal Surface Condensation Model Basis-- The wall condensation heat transfer coefficient in ATHENA is the maximum of the Chato modification[4.2-26] to the Nusselt[4.2-24] (laminar) correlation and the Shah[4.2-25,4.2-72] (turbulent) correlation. Chato's modification[4.2-26] to the Nusselt[4.2-24] formulation applies to laminar condensation on the inside of a horizontal tube. It is assumed that the liquid film collects on the upper surfaces, drains to the tube bottom, and collects with negligible vapor/gas shear. The condensate drains out one end because of a hydraulic gradient.

The correlation takes the form

$$h_{Chato} = F\left[\frac{g\rho_f(\rho_f - \rho_g)h_{fgb}k_f^3}{D_h\mu_f(T_{sppb} - T_w)}\right]^{\frac{1}{4}} \qquad (4.2\text{-}47)$$

where

k_f = liquid thermal conductivity

μ_f = liquid viscosity

ρ_f = liquid density

g = gravitational constant

h_{fgb} = $h_{fgsat}(P_{vb})$ = vapor minus liquid saturation specific enthalpy based on the vapor partial pressure in the bulk

P_{vb} = vapor partial pressure in the bulk

T_{sppb} = saturation temperature based on vapor partial pressure in the bulk.

The F term corrects for the liquid level in the tube bottom with the form

$$F = \left(1 - \frac{\Phi}{\pi}\right) F' \quad . \tag{4.2-48}$$

The angle 2Φ corresponds to the angle subtended from the tube center to the chord forming the liquid level. The values for F′ range in magnitude upward from 0.725, where 2Φ = zero. F corrects for the condensing area fraction as well as the heat transfer coefficient. The development by Chato[4.2-26] indicates that a value of 0.296 for F is an average value appropriate for free flow from a horizontal tube, with the liquid level controlled by the critical depth at the exit.

The angle 2Φ changes if the tube drains because of inclination or fills up because of a pressure gradient. The angle is determined from

$$\alpha_f = \frac{\Phi - 0.5 \sin 2\Phi}{\pi} \quad . \tag{4.2-49}$$

The development determined that, for the parameter range of concern, the bottom liquid layer was in laminar flow. The analytical work indicates that the heat transfer through the bottom layer was less than 2.5% of the total for angles of 2Φ between 90 and 170 degrees and was therefore neglected in the correlation. Chato suggests a mean value of F = 0.296 which corresponds to Φ = 120 degrees.

Data were taken for the conditions as follows:

- Tube material copper
- Tube length 0.718 m

- Tube ID 1.45 cm
- Fluid refrigerant 113
- Tube inclination 0 to 37 degrees
- vapor/gas inlet Re 0 to 35,000.

The bulk of data points were within +8 to -16% of the correlation for level flow. The Chato correlation was tested to an inclined angle of about 37 degrees with reasonable results. It is not valid for vertical flow.

For turbulent flows, the Shah[4.2-25,4.2-72] correlation is used as the model basis for a horizontal surface just as it is for an inclined surface [Equations (4.2-42) through (4.2-45)]. As mentioned before, the data base for the Shah correlation includes both horizontal and vertical data.

In ATHENA, the wall condensation heat transfer coefficient for horizontal surfaces is

$$h_c = \max(h_{Shah}, h_{Chato}) \ . \qquad (4.2\text{-}50)$$

Thus, the maximum of a turbulent correlation and a laminar correlation is used.

4.2.3.6.4 Geometry 101, Horizontal Condensation Model as Coded--The laminar model in the code is Equation (4.2-47), with F = 0.296.

The Chato correlation form is not strictly valid for superheated vapor/gas. The heat capacity between the actual and saturated temperature must be accounted for, as illustrated by Jakob.[4.2-73] The solution form including the superheat effect is much more complex, but the change in h_{Chato} may be less than the uncertainty of the basic correlation.

The Chato correlation is valid only after a film has been established, but when the wall is bare, some coefficient must be applied to get a film started. The correlation is valid only for a laminar film.

The turbulent model in the code for horizontal surface condensation is Equations (4.2-42) through (4.2-45).

4.2.3.6.5 Geometry 101, Condensation with Noncondensable Model Basis--The Colburn-Hougen[4.2-27] diffusion method is used to solve for the liquid/gas interface temperature in the presence of noncondensables. The Colburn-Hougen diffusion calculation involves an iterative process to solve for the temperature at the interface between the vapor/gas and liquid film.

The model for the influence of noncondensables on condensation was developed by B&W for the RELAP5/MOD2 code[4.2-74] and is based on the work of Colburn and Hougen.[4.2-27] The model is developed under the following assumptions:

1. The sensible heat transfer through the diffusion layer to the interface is negligible.

2. Stratification of the noncondensable gas in the vapor/gas region by buoyancy effects is negligible.

3. Required mass transfer coefficients can be obtained by applying the analogy between the heat and mass transfer.

4. The noncondensable gas is not removed from the vapor/gas region by dissolving it in the condensate.

The formulation is based on the principle that the amount of heat transferred by condensing vapor to the liquid-vapor/gas interface by diffusing through the noncondensable gas film is equal to the heat transferred through the condensate. From this energy conservation principle, the interface pressure and interface temperature (see **Figure 4.2-15**) will be determined by iteration. The heat transfer rate then will be known.

The heat flux due to condensation of vapor mass flux, j_v, flowing toward the liquid-vapor/gas interface is

$$q''_v = j_v \bullet h_{fgb} \tag{4.2-51}$$

where

h_{fgb} = $h_{fgsat}(P_{vb})$ = vapor minus liquid saturation specific enthalpy based on the vapor partial pressure in the bulk

P_{vb} = vapor partial pressure in the bulk.

The mass flux is given by

$$j_v = h_m \rho_{vb} \ln\left(\frac{1 - \frac{P_{vi}}{P}}{1 - \frac{P_{vb}}{P}}\right) \tag{4.2-52}$$

where

P = total pressure

P_{vi} = vapor partial pressure at the liquid-vapor/gas interface

h_m = mass transfer coefficient

ρ_{vb} = saturation vapor density at P_{vb}

= $(1 - X_n)\rho_{mb}$

ρ_{mb} = combined vapor and gas density in the bulk at the bulk vapor/gas temperature.

The heat flux due to mass flux, q''_v, then, is

$$q''_v = h_m h_{fgb} \rho_{vb} \ln\left(\frac{1 - \frac{P_{vi}}{P}}{1 - \frac{P_{vb}}{P}}\right) \quad . \tag{4.2-53}$$

The value of the mass transfer coefficient, h_m, is the maximum value predicted from a laminar forced convection correlation, a turbulent forced convection correlation, and a natural convection correlation. For turbulent vapor/gas flow, the mass transfer coefficient is obtained from the Gilliand[4.2-75] correlation

$$Sh = 0.023(Re_v^{0.83})(Sc^{0.44}) \tag{4.2-54}$$

where

Sh = Sherwood number = $\frac{h_m D}{D_{vn}}$

Re_v = vapor/gas Reynolds number = $\frac{\rho_{mb}|v_g|D}{\mu_{mb}}$

Sc = Schmidt number = $\frac{\mu_{mb}}{\rho_{mb} D_{vn}}$

D = hydraulic diameter

D_{vn} = mass diffusivity

μ_{mb} = combined vapor and gas viscosity in the bulk.

For laminar flow, the mass transfer coefficient is derived from the Rohsenow-Choi[4.2-75] heat transfer correlation

$$\frac{h_m D}{D_{vn}} = 4.0 \quad . \tag{4.2-55}$$

The correlation used for natural convection is the Churchill-Chu correlation[4.2-6] cast in mass transfer terms. It is given by

$$Nu_{LD} = \left\{ 0.825 + \frac{0.387(Ra_{LD})^{\frac{1}{6}}}{\left[1 + \left(\frac{0.492}{Sc}\right)^{\frac{9}{16}}\right]^{\frac{8}{27}}} \right\}^2 \tag{4.2-56}$$

where

Nu_{LD} = $h_m L/D_{vn}$

Ra_{LD} = Rayleigh number = $Gr_{LD} \bullet Sc$

Gr_{LD} = Grashof number

= $\dfrac{\rho_{mb}^2 g |\rho_{mw} - \rho_{mb}| L^3}{\mu_{mb}^2 \rho_{mw}}$

ρ_{mw} = combined vapor and gas density at the wall temperature.

A thermodynamic property table call determines the vapor density and the vapor partial pressure based on the wall temperature. The gas density is found from the ideal gas equation. The combined density at the wall is the sum of the vapor and gas densities at the wall.

The mass diffusivity of noncondensable gas in the vapor is calculated using the equation of Fuller, Scettler, and Giddings.[4.2-74] It is given by

$$D_{vn} = 0.0101325 \frac{\left(\frac{1}{M_v} + \frac{1}{M_n}\right)^{\frac{1}{2}} T_g^{1.75}}{P\left[(\varepsilon_v)^{\frac{1}{3}} + (\varepsilon_n)^{\frac{1}{3}}\right]^2} \quad (4.2\text{-}57)$$

where

M_v = molecular weight of vapor

M_n = molecular weight of noncondensable

T_g = bulk vapor/gas temperature

ε_v = atomic diffusion volume of vapor

ε_n = atomic diffusion volume of noncondensable.

The atomic diffusion volume, ε, values for different gases and liquids are given in **Reference 4.2-76**.

The heat flux from the liquid film to the wall is calculated by

$$q''_l = h_c(T_{vi} - T_w) \quad (4.2\text{-}58)$$

where

T_{vi} = interface $T_{sat}(P_{vi})$ saturation temperature corresponding to the interface vapor pressure (same as T_{gi} in **Figure 4.2-15**).

The condensation heat transfer coefficient, h_c, is calculated based on the correlations given in the previous section. Once an interface saturation temperature (T_{vi}) corresponding to the liquid-vapor/gas interface partial pressure (P_{vi}) is assumed, the energy balance equation can be checked by

$$q''_l = q''_v \quad (4.2\text{-}59)$$

or

$$h_c(T_{vi} - T_w) = h_m h_{fgb} \rho_{vb} \ln\left(\frac{1 - \frac{P_{vi}}{P}}{1 - \frac{P_{vb}}{P}}\right) \quad . \tag{4.2-60}$$

Although the condensation heat transfer coefficient is known, the heat flux (needed by the hydrodynamics) is not known until the T_{vi} is determined.

Two bounding initial guesses for the interface saturation temperature (T_{vi}) are used. The guesses are the wall temperature and the saturation temperature corresponding to the vapor partial pressure in the bulk. An iteration[4.2-74] is used to find the interfacial saturation temperature (T_{vi}) that satisfies Equation (4.2-60). If convergence is not obtained after 20 iterations, liquid convection heat transfer (mode 2) is used instead (see **Figure 4.2-3**).

4.2.3.6.6 Geometry 101, Condensation with Noncondensable Model as Coded--The model is coded as presented.

4.2.4 Geometry 102, Correlations for Vertical Parallel Plates

Only those regimes that use different heat transfer coefficient correlations than Geometry 101 are discussed.

ORNL has had special correlations put into ATHENA for their Advanced Neutron Source (ANS) reactor design. The correlations are activated by a user flag. The ANS core design has parallel plates with an aspect ratio of 68.11.[4.2-2] New correlations were implemented for laminar, natural, and turbulent convection, and for CHF. As with Geometry 101, the maximum of laminar, natural, and turbulent convection is used as the resultant convection correlation.

4.2.4.1 Geometry 102, Turbulent Forced Convection Model Basis. During liquid turbulent forced convection, the Petukhov[4.2-4] correlation is used in place of the Dittus-Boelter correlation for all cases including nucleate boiling. The correlation is

$$Nu = \frac{\left(\frac{f}{8} \times Re_f \times Pr_f\right) \bullet \left(\frac{\mu_f}{\mu_{ws}}\right)^{0.11}}{(1. + 3.4f) + \left(11.7 + \frac{1.8}{Pr_f^{\frac{1}{3}}}\right) \bullet \left(\frac{f}{8}\right)^{0.5} \bullet \left(Pr_f^{\frac{2}{3}} - 1.0\right)} \quad . \tag{4.2-61}$$

Pr is the Prandtl number, and the subscript f represents liquid properties. The subscript ws on the viscosity means that the viscosity is evaluated at the minimum of the wall and the saturation temperature.

The correlation is mainly from air or water data, with Re = 9,000-35,000. The Darcy-Weisbach friction factor, f, comes from the Filonenko[4.2-77] expression

$$f = \frac{1.0875 - 0.1125\left(\frac{Gap}{S}\right)}{(1.82 \log_{10} Re_f - 1.64)^2} \quad (4.2\text{-}62)$$

where

Gap = distance between the side walls (short length, pitch)

S = span (distance from one end wall to the other, long length).

During turbulent vapor/gas forced convection, the Dittus-Boelter correlation is still used.

4.2.4.2 Geometry 102, Turbulent Forced Convection Model as Coded. The model is coded as shown above.

4.2.4.3 Geometry 102, Laminar Forced Convection Model Basis. The ORNL laminar forced convection correlation from **Reference 4.2-2** is

$$Nu = 7.63 \ . \quad (4.2\text{-}63)$$

4.2.4.4 Geometry 102, Laminar Forced Convection Model as Coded. The model is coded as shown.

4.2.4.5 Geometry 102, Natural Convection Model Basis. With geometry 102, the Elenbaas[4.2-8] correlation is used, and it is given by

$$Nu = Ra\left(\frac{Gap}{24L}\right) \quad (4.2\text{-}64)$$

where

Ra = Rayleigh number = Gr • Pr

Gr = Grashof number defined by Equation (4.2-6), with the plate spacing for the length term

Gap = distance between plates (short length, pitch)

L = plate length in the direction of flow.

The length is read into ATHENA on the heat slab 1CCCG801 through 1CCCG899 and 1CCCG901 through 1CCCG999 cards, and the spacing is read in by

1. Setting b=2 in the volume control flag to obtain ORNL ANS narrow channel interphase friction. This is on the CCC1001 through CCC1009 cards for pipes and the CCC0101 through CCC0109 cards for single-volumes and branches.

2. Setting the gap (pitch) as Word 1 and the span as Word 2 on the CCC3101 through CCC3199 cards for pipes and the CCC0111 card for single-volumes and branches.

4.2.4.6 Geometry 102, Natural Convection Model as Coded. The model is coded as shown. RELAP5/MOD2 and early versions of ATHENA compared the Grashof number with the Reynolds number squared to decide whether or not natural convection was appropriate. This criterion results in discontinuities in the heat transfer coefficient. By using the maximum of the forced turbulent, forced laminar, and free convection coefficients [see Equation (4.2-2)], there are no discontinuities in the coefficient.

4.2.4.7 Geometry 102, CHF Model Basis. The normal ATHENA critical heat flux (CHF) calculation using the Groeneveld table is used for plate type fuel adjacent to narrow channels for medium/low flow conditions and the Gambill-Weatherhead model is used for plate type fuel adjacent to narrow channels for high flow conditions. The Gambill-Weatherhead model[4.2-78,4.2-79] makes use of the following equations:

$$q''_{CHF} = q''_{POOL} + q''_{CONV} \tag{4.2-65}$$

$$q''_{POOL} = 0.18 h_{fg} \rho_g \bullet \left[\sigma g \bullet \frac{(\rho_f - \rho_g)}{\rho_g^2} \right]^{0.25} \bullet \left\{ 1. + \left[\left(\frac{\rho_f}{\rho_g} \right)^{0.75} \bullet C_{pf} \left(\frac{T_{sat} - T_f}{9.8 h_{fg}} \right) \right] \right\} \tag{4.2-66}$$

$$q''_{CONV} = \frac{k_f}{D} Nu \bullet (T_w - T_f) \tag{4.2-67}$$

$$T_w = [47.7 - 0.127 \bullet (T_{sat} - 273.16)] \bullet \left(\frac{q''_{CHF}}{3154.6} \right)^{0.25} + T_{sat} \tag{4.2-68}$$

where

Nu is the Nusselt number defined by Petukhov[4.2-4] [Equation (4.2-61)].

If the mass flux is less than 7,500 kg/m^2-s, the normal ATHENA Groeneveld CHF table value is used, and if the mass flux is greater than 10,000 kg/m^2-s, the Gambill-Weatherhead CHF [set of Equations

(4.2-65) through (4.2-68) is solved iteratively] is used. For mass flux values between 7,500 kg/m^2-s and 10,000 kg/m^2-s , linear interpolation yields the CHF value.

The ORNL database and Gambill-Weatherhead correlation are designed to be used under subcooled conditions. Therefore, ORNL decided to have ATHENA print a warning message when the subcooling is less than 8 degrees Kelvin. The message says “Blue Flag from CHFCAL Subroutine,” and the value of the subcooling and mass flux are printed. If the quality is positive, the message says “Red Flag from CHFCAL Subroutine,” and the value of the quality and mass flux are printed.

4.2.4.8 Geometry 102, CHF Model as Coded.

The model is coded as shown.

4.2.5 Geometry 103, Correlations for Vertical Infinite Parallel Plates

No ATHENA coding changes have been made for this geometry. Refer to Geometry 102. When this geometry is implemented in the code, the laminar flow Nusselt number for uniform heat flux should be set to 8.23[4.2-80]. For a constant wall temperature boundary condition, the Nusselt number is 7.54, but uniform heat flux is generally a more useful boundary condition for reactor simulation.

4.2.6 Geometry 104, Correlations for Single Vertical Wall

Refer to Geometry 101. This is the geometry to which the Churchill-Chu natural convection correlation applies.

4.2.7 Geometry 105, 106, 107, Correlations for Vertical Annuli

Currently, annuli are treated as pipes. Refer to Geometry 101. Annuli have some correlations available that are different from pipe correlations. Laminar flow is one of these situations. As identified by Reynolds, Lundburg, and McCuen[4.2-81] there are four “fundamental solutions” for laminar heat transfer in an annulus:

- Fundamental solution of the first kind
  - Wall 1: step change in temperature
  - Wall 2: maintained at inlet temperature
- Fundamental solution of the second kind
  - Wall 1: step change in heat flux
  - Wall 2: insulated
- Fundamental solution of the third kind

- Wall 1: step change in temperature
- Wall 2: insulated

• Fundamental solution of the fourth kind

- Wall 1: step change in heat flux
- Wall 2: maintained at inlet temperature.

Since wall 1 can be either the inner wall or the outer wall, there are a total of eight sets of boundary conditions. In cases of single-phase flow with constant thermodynamic properties, superposition of results from the fundamental solutions may be used to obtain results for other boundary conditions. The fully developed Nusselt number for fundamental solution number 2 is probably of most interest for ATHENA.

4.2.8 Geometry 108, Correlations for Single Vertical Rod

Refer to the Geometry 101.

4.2.9 Geometry 109, Correlations for Vertical Single Rod with Crossflow

Refer to the Geometry 101.

4.2.10 Geometry 110, Correlations for Vertical Bundles with In-Line Rods, Parallel Flow Only

4.2.10.1 Geometry 110, Parallel Flow Model Basis. The correlations for this geometry differs from Geometry 101 only in the implementation of a turbulent flow multiplier developed by Inayatov,[4.2-44] based on the rod pitch to rod diameter ratio. The pitch is the distance between the centers of the adjacent rods. Inayatov correlated data for 4 in-line and 30 staggered tube bundles in air, water and superheated vapor/gas with pitch-to-diameter ratios between 1.1 and 1.5. He recommends that the McAdams coefficient (0.023) to the Dittus-Boelter equation be replaced by C, where C is given by

$$C = 0.023\left(\frac{P_1 P_2}{D^2}\right)^{0.5} \tag{4.2-69}$$

where P_1 and P_2 are the "pitches of the tubes in the bundle" and D is the tube diameter. If the bundle consists of in-line tubes on a square pitch or staggered tubes on an equilateral triangle pitch, C becomes

$$C = \frac{0.023P}{D} \quad . \tag{4.2-70}$$

Morgan and Hassan[4.2-82] used a $\frac{P}{D}$ multiplier developed by Weisman[4.2-43] and showed improved ATHENA predictions of once-through steam generator data. The Inayatov formulation has a broader data base than Weisman's form. The largest pitch/diameter ratio in Weisman's data is about 1.27.

4.2.10.2 Geometry 110, Parallel Flow Model as Coded. The Inayatov equation is implemented in ATHENA. The $\frac{P}{D}$ multiplier is used in both forced turbulent convection and nucleate boiling. The pitch-to-diameter ratio for bundles is input as Word 10 on the 1CCCG801 through 1CCCG899 and 1CCCG901 through 1CCCG999 cards. A warning message is printed during input processing if $\frac{P}{D}$ is input greater than 1.6. The term $\frac{P}{D}$ is then reset to 1.6. If $\frac{P}{D}$ is not entered, or less than 1.1, a default value of 1.1 is used and a warning message is printed.

Forced laminar and natural (free) convection correlations specifically for vertical bundles have not been implemented into ATHENA. This is an area where more investigation is needed.

For liquid metals, the convective heat transfer coefficient for vertical bundles, with and without crossflow is based on the Westinghouse correlation described by Todreas and Kazimi.

4.2.11 Geometry 111, Correlations for Vertical Bundles with In-Line Rods, Parallel Flow and Crossflow

Users can chose which flow direction is the dominant direction parallel to the tubes on Word 1 of cards 1CCCG501 through 1CCCG599 or 1CCCG601 through 1CCCG699. The form of Word 1 is CCCXX000F, where F is the direction parallel to the tubes. If F is 0 or 4, the x-direction is the parallel direction. If F is 2 or 1, the parallel direction is the y- or z-direction, respectively. An input error occurs if a 1 or 2 is chosen and the directions have not been activated with hydraulic input.

4.2.11.1 Geometry 111, Crossflow Model Basis. With these geometries, the heat transfer coefficient is the average coefficient caused by flow parallel to the tubes and flow perpendicular to the tubes. The method of averaging uses the square root of the sum of the squares in order to weight the answers more toward the larger of the two values. It is given by

$$h = (h_{parallel}^2 + h_{cross}^2)^{0.5} \quad (4.2\text{-}71)$$

where

$h_{parallel}$ = heat transfer coefficient from a call to subroutine DITTUS using the parallel mass flux shown in **Table 4.2-9**

DITTUS = a subroutine that outputs the maximum of forced turbulent, forced laminar convection, and natural convection as previously discussed.

h_{cross} = crossflow heat transfer coefficient from Equation (4.2-72) developed by Shah.[4.2-5]

$$Nu_{cross} = 0.21\left(G\frac{D_o}{\mu}\right)^{0.62} Pr^{0.4} \quad (4.2\text{-}72)$$

where

Nu = Nusselt Number

D_o = tube outer diameter

μ = liquid viscosity

Pr = Prandtl number

G = crossflow mass flux shown in **Table 4.2-9** at minimum area.

The sum of the squares method of Equation (4.2-71) has been suggested by Kutateladze.[4.2-83]

4.2.11.2 Geometry 111, Crossflow Model as Coded. The only nonstandard ATHENA parameter is the mass flow at the minimum area. To obtain G at the minimum area for the above equation, the code's volume average value from **Table 4.2-9** is multiplied times the area ratio of volume average area divided by the gap area and is given by

$$Aratio = \frac{1-\frac{\pi}{4}\left(\frac{D}{P}\right)^2}{1-\frac{D}{P}} \quad . \quad (4.2\text{-}73)$$

Table 4.2-9 Mass flux values for geometry 111.

Bundle is aligned with	**G for $h_{parallel}$**	**G for h_{cross}**
x-axis	G_x	$(G_y^2+G_z^2)^{0.5}$
y-axis	G_y	$(G_x^2+G_z^2)^{0.5}$
z-asis	G_z	$(G_x^2+G_y^2)^{0.5}$

This equation is derived by setting the average area to

$$\overline{A} = \frac{\text{Volume}}{\text{Length}} = \frac{P \bullet P \bullet Z - \frac{\pi D^2}{4} Z}{P} \qquad (4.2\text{-}74)$$

where Length = P because it is desired to derive the average area in the crossflow direction, and the gap area to

$$Agap = (P - D)\, Z \qquad (4.2\text{-}75)$$

where

P = rod pitch (distance between the centers of adjacent rods)

D = rod diameter

Z = length along the rods.

Inayatov's enhancement coefficients are applied to the parallel flow heat transfer coefficient before it is added to the crossflow value. The macroscopic part of the Chen correlation is increased by the Inayatov coefficient as well as the single-phase forced-flow coefficient.

The existing Groeneveld table lookup method is used for the critical heat flux with the mass flux from the parallel direction.

For liquid metals, the convective heat transfer coefficient for vertical bundles, with and without crossflow is based on the Westinghouse correlation described by Todreas and Kazimi.

4.2.12 Geometry 112-113, Correlations for Vertical Bundles with Staggered Rods

Geometry 112 defaults to Geometry 110, and Geometry 113 defaults to Geometry 111.

4.2.13 Geometry 114, Correlations for Helical Pipe

Refer to the Geometry 101. Flow inside helical pipes is not considered.

4.2.14 Geometry 121, 122, 123, Correlations for Horizontal Annuli

Refer to Geometry 130. When this Geometry is implemented, stratification can drive the surfaces out of nucleate boiling easier than it does with vertical surfaces.

4.2.15 Geometry 124, Correlations for Horizontal Bundle (CANDU)

The CANDU reactor core has horizontal fuel rods in horizontal pipes. No coding specific to CANDU reactors has been implemented.

4.2.16 Geometry 130, Correlations for Horizontal Plate Above Fluid

There is one correlation in the code specifically for a horizontal plate with natural convection. The correlation is for energy flow in the direction of gravity. Since the correlation for energy up-flow is not in the code, the code does not check the direction of energy flow. For condensation, the code uses a value of F = 0.296 in Equation (4.1-55), as suggested by Chato.[4.2-26] A multiplier, k6, is applied to the CHF value from the Groeneveld table.

4.2.16.1 Geometry 130, Correlations for Natural Convection Model Basis. The following McAdams[4.2-7] natural convection correlation is used:

$$Nu_L = 0.27 Ra_L^{0.25} \quad \text{for } 10^5 \le Ra_L < 10^{10} \quad . \tag{4.2-76}$$

This same correlation is used for Geometry 101 and is based on flat plate data. Incropera and DeWitt[4.2-8] suggest length = surface area/perimeter for the McAdams correlation. The Rayleigh number range for Equation (4.2-76) is between 10^5 and 10^{10} and is applicable when the direction of energy transfer is in the direction of the gravity vector, i.e., the lower surface of a heated plate or the upper surface of a cooled plate. This yields considerably smaller coefficients than the McAdams correlation for energy flow upward, as shown in **Figure 4.2-16**. Also shown are the Churchill-Chu values. The McAdams correlation for energy upflow is

$$Nu_L = 0.54 Ra_L^{0.25} \quad \text{for } 10^4 \le Ra_L > 10^7 \tag{4.2-77}$$

$$Nu_L = 0.15 Ra_L^{0.333} \quad \text{for } 10^7 \le Ra_L > 10^{11} \quad . \tag{4.2-78}$$

4.2.16.2 Geometry 130, Natural Convection Model as Coded. The model is coded as shown.

4.2.17 Geometry 131, Correlations for Horizontal Plate Below Fluid

This Geometry defaults to Geometry 130.

4.2.18 Geometry 132, Correlations for Horizontal Single Tube

This Geometry defaults to Geometry 130.

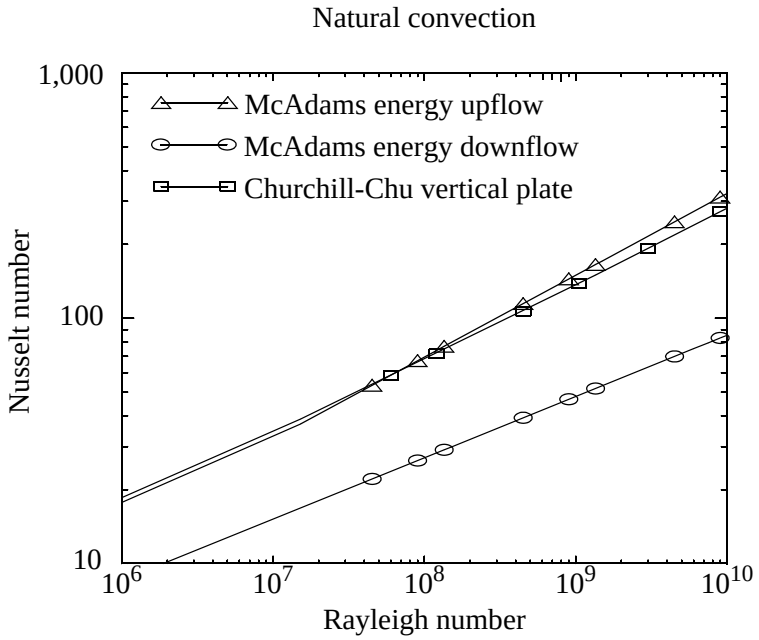

Figure 4.2-16 Natural convection correlation comparison.

4.2.19 Geometry 133, Correlations for Horizontal Single Tube with Crossflow

This Geometry defaults to Geometry 130. The only crossflow logic that has been implemented is for bundles.

4.2.20 Geometry 134, Correlations for Horizontal Bundles with In-Line Rods or Tubes, Crossflow and Parallel Flow

Calculating the performance of horizontal tube bundles is important in some heat exchangers such as condensers and feedwater heaters.

This geometry differs from Geometry 101 only in the nucleate boiling, CHF, natural convection, and condensation correlations. There are no changes for the transition boiling or film boiling correlations. Khalil[4.2-84] and Palen, Yarden, and Taborek[4.2-85] found reasonable agreement with their horizontal bundle film boiling data and the Bromley correlation used in ATHENA. For all but FWHTR components, condensation is the same as Geometry 101. For the right side (outside surface) of heat slabs representing tube walls in a FWHTR component Chen[4.2-28] is used for condensation.

An illustration from **Reference 4.2-85** (see **Figure 4.2-17**) shows the horizontal bundle boiling curve is shifted to the left compared to a single horizontal tube. The peak is also lowered. These curves are based on a “common hydrocarbon liquid.”

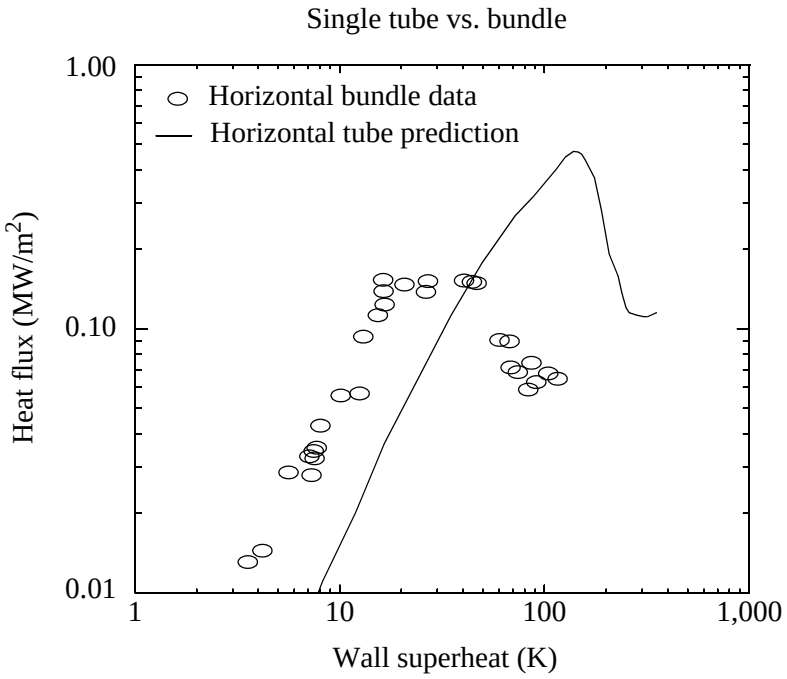

Figure 4.2-17 Boiling curve for horizontal tubes (**Reference 4.2-85**).

There are considerable difficulties in obtaining best-estimate heat transfer coefficients and critical heat flux values for horizontal bundles. **Table 4.2-10** shows the range of some of the available data. Very few water data are available. Palen and Small[4.2-86] were studying reboiler applications in the petroleum industry; Slesarenko, Rudakova, and Zakharov[4.2-87] were interested in desalinization evaporators; and Polley, Ralston, and Grant[4.2-30] performed experiments for the United Kingdom Department of Industry.

Table 4.2-10 Horizontal bundle data sources .

Variable	Palen and Small	Slesarenko, Rudakova, and Zakharov	Polley, Ralston, and Grant
Pressure (MPa)	0.25 - 0.69	0.006 - 0.101	0.101
Mass flux (kg/m^2-s)	?	?	90 - 450
Heat flux (MW/m^2)	0.003 - 0.59	0.022 - 0.135	0.01 - 0.06
Quality	?	?	0 - 0.17
Pitch/diameter	1.25 - 2.0	1.25 - 2.0	1.244
Tube diameter (m)	0.019 - 0.0254	0.018	0.0254
Tube layout	triangular, square, and rotated square	?	square

Table 4.2-10 Horizontal bundle data sources (Continued).

Variable	Palen and Small	Slesarenko, Rudakova, and Zakharov	Polley, Ralston, and Grant
Bundle diameter (m)	0.5 - 1.3	(6 rows)	(6 rows)
Liquid subcooling (K)	7.8 - 30.5	?	0
Fluids	hydrocarbons	water	R113
Tube material	carbon steel	MZS copper	stainless

Cornwell, Duffin, and Schuller;[4.2-88] Cornwell and Schuller;[4.2-89] Nakajima;[4.2-90] Chan and Shoukri;[4.2-91] Leong and Cornwell;[4.2-92] Brisbane, Grant, and Whalley;[4.2-93] and Slesarenko, Rudakova, and Zakharov[4.2-87] show that the heat transfer coefficient increases with increasing vertical position in the bundle. Bubbles from below cause increased turbulence higher in the bundle. Average bundle heat transfer coefficients can be several times larger than single-tube coefficients. **Figure 4.2-18** shows lines of constant heat transfer coefficient from kettle reboiler data taken by Leong and Cornwell. However, Palen and Small[4.2-86] show that the critical heat flux decreases as the bundle height increases.

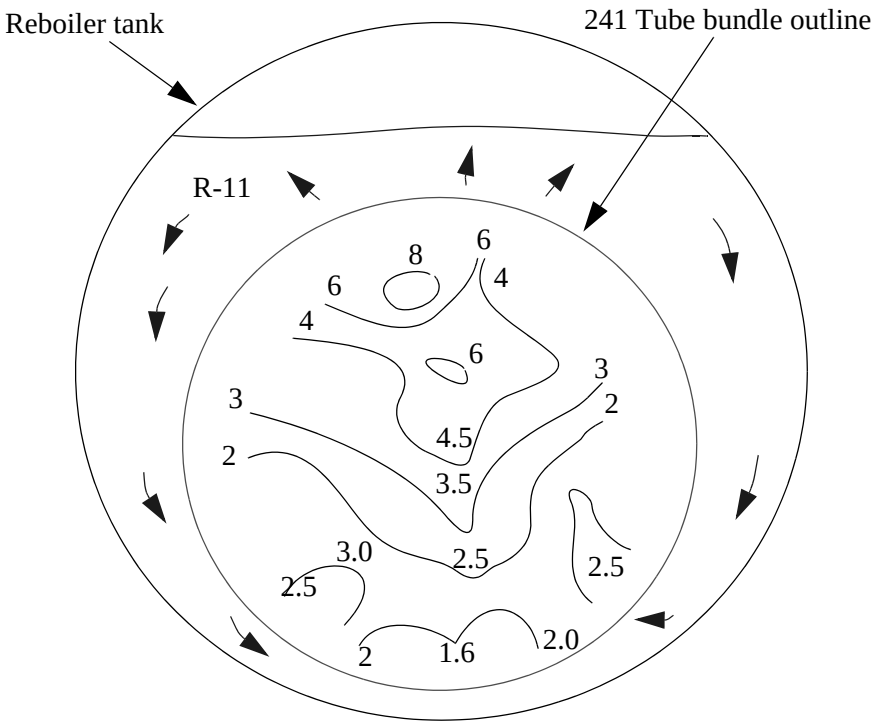

Figure 4.2-18 Iso-heat transfer coefficient lines from Leong and Cornwell reboiler (kW/m^2-K).

4.2.20.1 Geometry 134, Horizontal Tube Bundles Nucleate Boiling Model Basis. A literature search has shown several possibilities. Polley, Ralston, and Grant tested a 36-tube horizontal bundle with vertical flow in refrigerant 113 and recommend an equation like the Chen equation on the outside of the tubes. It is given by

$$h = Sh_{pb} + Fh_{fc} \tag{4.2-79}$$

where

h_{pb} = pool boiling heat transfer coefficient

h_{fc} = forced convection heat transfer coefficient

S = suppression factor

F = two phase multiplier.

For horizontal bundles under investigation, they say,

"However, S may not be a suppression factor."

In other words, convection may not suppress nucleate boiling in a horizontal bundle. They further say,

> "In the case of forced flow boiling in tube bundles we do not have sufficient information to provide any means of evaluating the factor S. Until such information is available we shall assume a value of unity."

The authors also say that the F factor cannot be obtained in the same manner Chen used because the pressure loss is dominated by form loss instead of wall friction. They assume that the liquid flowing through the gap between the tubes does so as a film on the tubes. They further assume that the ratio of the two-phase heat transfer coefficient to the single-phase coefficient is inversely proportional to the ratio of the liquid volumetric flow to the total volumetric flow. Thin films have less resistance to energy transfer than thick films. They finally assume a 1/7 power velocity profile in the films and arrive at

$$h = h_{pb} + h_f\left(\frac{1}{1-\alpha_g}\right)^{0.744} \tag{4.2-80}$$

where

h_f = single-phase liquid heat transfer coefficient

α_g = local void fraction.

The liquid h_f was evaluated using an ESDU (Engineering Science Data Unit, London, 1973) equation. It is given by

$$Nu_f = 0.211 Re_f^{0.651} Pr_f^{0.34} F_4 \quad (4.2\text{-}81)$$

where

Re_f = Reynolds number based on the liquid velocity in the gap between the tubes

Pr_f = liquid Prandtl number

F_4 = a factor that depends on which row the tube of interest is in.

The authors report that for the upper tubes (row 6) in their experiment, F_4 is 1.06.

The Heat Transfer and Fluid Service Handbook (HTFS) insert BM13 presents a 1969 ESDU crossflow correlation for a single horizontal tube as

$$Nu_f = \exp[-0.186 + 0.338 \ln Re + 0.362 \ln Pr + 0.0131(\ln Re)^2 - 0.00926(\ln Pr)^2] \; . \quad (4.2\text{-}82)$$

Figure 4.2-19 shows three crossflow correlations along with the Dittus-Boelter equation. The line marked ESDU bundle is from Equation (4.2-81) with $F_4 = 1$, and the line marked ESDU tube is from Equation (4.2-82).

Polley, Ralston, and Grant used the following Voloshko[4.2-94] correlation for pool boiling, which is given by

$$Nu_B = 0.236 \, Kt^{0.588} \, Pe^{0.706} \quad (4.2\text{-}83)$$

where

$$Nu_B = \frac{hL}{k_f} \quad (4.2\text{-}84)$$

k_f = liquid thermal conductivity

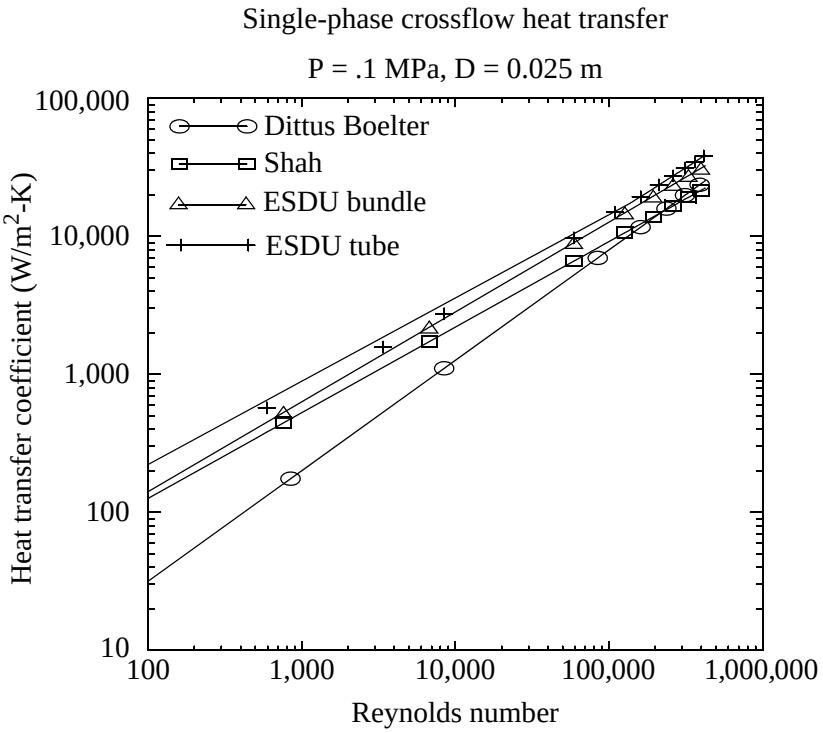

Figure 4.2-19 Liquid crossflow correlations compared to Dittus-Boelter.

$$L = \left[\frac{\sigma}{g(\rho_f - \rho_g)}\right]^{0.5}$$

σ = surface tension

$$Kt = \frac{L(h_{fg}\rho_g)^2}{\rho_f C_{pf} T_{spt} \sigma}$$

h_{fg} = vapor minus liquid saturated specific enthalpy

C_{pf} = liquid specific heat

$$Pe = \frac{q'' C_{pf} \rho_f L}{h_{fg} k_f \rho_g}.$$

All the Polley-Ralston-Grant data agree within 30% of Equation (4.2-80), and 310 of their 330 points agree within 20%.

The problem with using the Voloshko correlation in ATHENA is that it was developed specifically for pool boiling of refrigerant 113 on a stainless steel surface. **Figure 4.2-20** shows data from the bundles of Slesarenko, Rudakova, and Zakharov and Polley, Ralston, and Grant. The former tested with water and the later used refrigerant 113. ATHENA does not have freon fluid properties. Even though the Voloshko correlation was evaluated with water properties, it agrees with the freon data from the top tube in the Polley-Ralston-Grant experiment. No data were reported for the bottom row (Row 1).

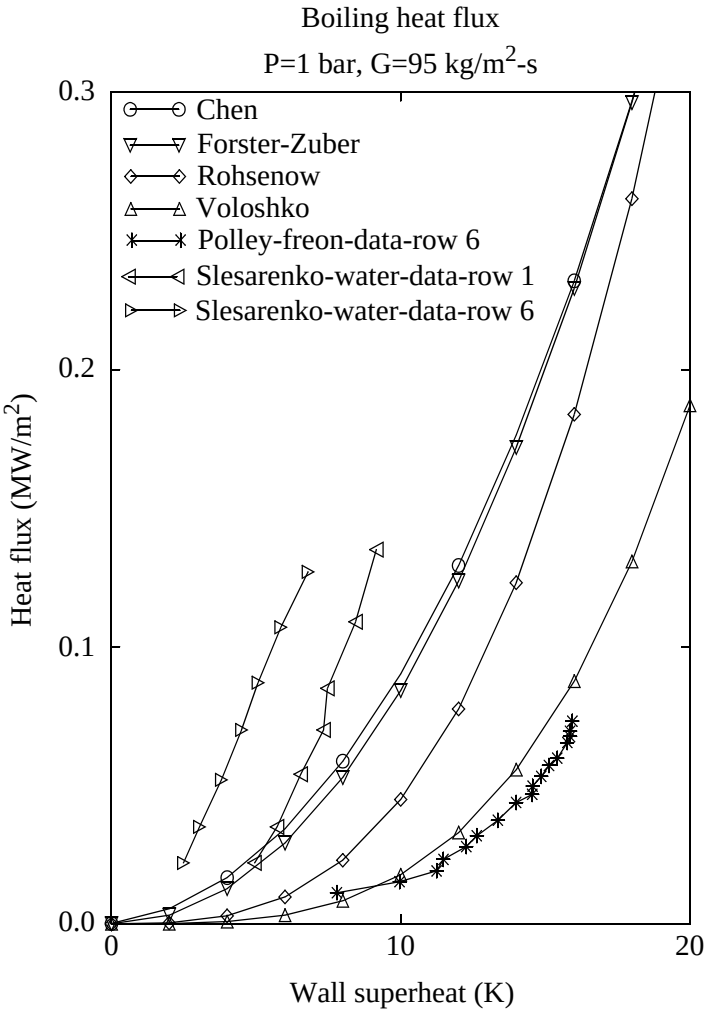

Figure 4.2-20 Horizontal bundle data and correlations.

The Rohsenow[4.2-35] pool boiling equation is

$$h_{pb} = 4.55\times10^{5}\left(\frac{\mu_f C_{pf}^3}{h_{fg}Pr_f^{5.1}}\right)\left[\frac{g(\rho_f-\rho_g)}{\sigma}\right]^{0.5}\Delta T_{sup}^2 \qquad (4.2\text{-}85)$$

where

μ_f = liquid viscosity

C_{pf} = liquid specific heat at constant pressure

h_{fg} = saturated enthalpy difference between vapor and liquid

Pr_f = liquid Prandtl number

g = gravitational constant

$\Delta\rho$ = liquid- vapor/gas density difference

ΔT_{sup} = wall superheat (T_{wall} - T_{spt}).

The coefficient 4.55 x 10^5 is $\left(\frac{1}{C_{sf}}\right)^3$, where C_{sf} is a Rohsenow parameter, which depends on the surface material and liquid type. Rohsenow lists three surfaces on which data were taken with boiling water, copper, platinum, and brass. The reported C_{sf} coefficient for the first two materials is 0.013; for brass it is 0.006. The former value is used here. The Rohsenow prediction will cross the Forster-Zuber prediction at larger wall superheats.

Based on **Figure 4.2-20** results, it appears unwise to strictly follow the Polley-Ralston-Grant method developed for freon to predict light water reactors. However, the void fraction effect may be acceptable for predicting bundles submerged in liquid. Since the void fraction increases in the vertical direction, Equation (4.2-80) predicts increased heat transfer at the top of the bundle compared to the bottom. Although Polley-Ralston-Grant propose the void fraction weighted convection term, they do not report void fraction profiles.

Shah[4.2-95] developed a correlation for horizontal bundles but says it has only been verified up to a Prandtl number of 0.051. Water has a Prandtl number in the range of 1 to 10. He recommends the superposition method of Kutateladze[4.2-83] for higher Prandtl numbers, which is given by

$$h = \left[h_{pb}^2 + h_l^2\left(1 + \frac{\Delta T_{sub}}{\Delta T_{sup}}\right)^2\right]^{0.5} \quad (4.2\text{-}86)$$

where

ΔT_{sub} = liquid subcooling relative to saturation.

Equation (4.2-86) will yield the effect of subcooling on the convection term, but if used as is, it would predict decreasing heat transfer with increasing elevation. Equation (4.2-80) will yield increasing heat transfer with increasing elevation but does not have an explicit subcooling term.

4.2.20.2 Geometry 134, Horizontal Tube Bundles Nucleate Boiling Model as Coded. Equation (4.2-80) was coded with Forster-Zuber[4.2-29] for pool boiling, and the subcooling effect is obtained by using the liquid temperature as the reference temperature for the forced convection part of Equation (4.2-80), just as is done on the Chen correlation for other surfaces. Equation (4.2-81) without the F_4 factor is used for the liquid convection term.

Later, if assessment using the Polley-Ralston-Grant method proves unsatisfactory, the Nakajima approach will be examined, which is given by

$$q'' = \alpha_g q''_{film} + (1 - \alpha_g) q''_{pb} \tag{4.2-87}$$

where

α_g = vapor/gas void fraction

q''_{film} = heat flux across the thin film of liquid on the tubes

q''_{pb} = pool boiling heat flux on a single tube.

The film referred to consists of water wetting the heated tubes in a two-phase upflow environment.

4.2.20.3 Geometry 134, Horizontal Tube Bundles CHF Model Basis. The critical heat flux on horizontal bundles can be similar to a single tube at the bottom of the bundle. At the top of the bundle, the tubes can become *circulation limited* if their liquid is being supplied from below, or *flooding limited* if their water is supplied from above.

Cumo et al.[4.2-96] performed a forced convection experiment using a nine-rod horizontal bundle and found that CHF did not degrade with increasing fluid quality. However, the Palen-Small data are from natural circulation experiments with large diameter bundles and represent reactor heat exchanges better than the Cumo data. Shah[4.2-72] correlated the Palen-Small data to obtain

$$CHF_{bundle} = CHF_{pb} 6.2 \left(\frac{D_B}{\pi D_o N} \right)^{0.975} \tag{4.2-88}$$

where

CHF_{pb} = pool boiling critical heat flux for a single tube

D_B = bundle diameter

D_o = outer tube diameter

N = number of tubes.

Increasing the tube density for a given heat flux would raise the bundle average quality, yet the equation predicts a decrease in bundle critical heat flux.

The Zuber[4.2-97] correlation for the pool boiling CHF developed for a flat plate is

$$CHF_{pb} = Kh_{fg} [\sigma g (\rho_f - \rho_g)]^{0.25} \rho_g^{0.5} \quad (4.2\text{-}89)$$

where

K = hydrodynamic boiling stability number

σ = liquid surface tension

g = gravitational constant

h_{fg} = difference between saturated vapor and saturated liquid enthalpy.

The value of K suggested by Zuber is $\pi/24 \approx 0.13$. Kutateladze[4.2-98] independently developed the same equation and recommended K = 0.16; Rohsenow[4.2-31] recommends K = 0.18.

Sun and Lienhard[4.2-99] extended this correlation to a horizontal cylinder by using a multiplier that depends on a radius factor, which is given by

$$Mul = \begin{cases} 0.89 + 2.27\exp(-3.44R'^{0.5}) & \text{for } 0.15 < R' \le 3.47 \\ 0.89 & \text{for } R' > 3.47 \end{cases} \quad (4.2\text{-}90)$$

where

$$R' = \frac{R}{\left[\frac{\sigma}{g(\rho_f - \rho_g)}\right]^{0.5}} \quad (4.2\text{-}91)$$

R = tube outer radius.

R' is about 3.8 for a 2 cm tube; therefore, the reduction from a flat plate to a tube of this size is 11%.

Hassan, Eichorn and Lienhard[4.2-100] studied CHF during vertical crossflow over a horizontal heated cylinder and found that an unheated cylinder directly in front of the heated cylinder reduced CHF to as low as 10% of the single cylinder value. If the pitch to diameter ratio $\frac{P}{D}$ was larger than 4 the unheated cylinder had no effect. Shah[4.2-101] correlated the data between a $\frac{P}{D}$ of 2.1 and 3.8 with

$$CHF = h_{fg}\rho_g\mu_\infty v_f\left[2.58\left(\frac{P}{D}\right) - 4.13\right] \quad . \tag{4.2-92}$$

The term v_f is the free stream liquid velocity.

The important factor causing bundle CHF is liquid starvation. When the escaping vapor/gas occupies too much of the space between tubes, nucleate boiling can no longer be supported on the upper tubes. Folkin and Goldberg[4.2-102] bubbled air across tubes in a pool of water to simulate boiling and report that

$$CHF_{bundle} = CHF_{tube}(1 - 1.175\alpha_g) \tag{4.2-93}$$

where α_g is the void fraction around the heated tube. According to this correlation, the bundle CHF is zero at a void fraction of 0.851. The pressure, temperature, and flow enter the correlation implicitly through the void fraction.

Crossflow is used for surfaces in the correlations. The mass flux values used are shown in **Table 4.2-11**. In cells without crossflow, the parallel mass flux is used in the correlations with the assumption that the bundle is at right angles to the flow direction.

Table 4.2-11 Mass flux values for geometry 134.

Bundle is aligned with	**G for $h_{parallel}$**	**G for h_{cross}**
x-axis	G_x	$(G_y^2 + G_z^2)^{0.5}$
y-axis	G_y	$(G_x^2 + G_z^2)^{0.5}$
z-axis	G_z	$(G_x^2 + G_y^2)^{0.5}$

4.2.20.4 Geometry 134, Horizontal Tube Bundles CHF Model as Coded. The Shah correlation of the Palen and Small data was not implemented because it was developed for design rather than best estimate. The Shah correlation is more of a criterion to prevent CHF on any of the tubes. It does

not give users the capability to nodalize horizontal bundles in the vertical direction and obtain nucleate boiling on the bottom tubes and film boiling on the top tubes. Equation (4.2-93) was implemented in ATHENA without the Sun-Lienhard extension of the Zuber correlation for a single tube. Folkin and Goldberg used Equation (4.2-89) with K = 0.14. The coding follows Folkin and Goldberg. Equation (4.2-80) predicts an increasing heat flux with an increasing void fraction during nucleate boiling, but Equation (4.2-93) predicts a decreasing CHF with a void fraction. Film or transition boiling will be predicted by ATHENA when the two equations cross.

Three researchers report a subcooling effect on CHF. Two of them are in the form

$$Fsub = 1 + m\left(\frac{\rho_f}{\rho_g}\right)^n \left[\frac{C_{pf}(T_{spt} - T_f)}{h_{fg}}\right] \quad . \tag{4.2-94}$$

Ivey and Morris[4.2-103] give a value of m and n of 0.1 and 0.75, respectively, whereas Kutateladze[4.2-104] gives values of 0.065 and 0.8.

A similar factor was developed by Zuber, Tribus, and Westwater,[4.2-105] which is given by

$$Fsub = 1 + \left\{\frac{5.32L^{0.5}(\rho_f C_{pf} k_f)^{0.5}}{\rho_g h_{fg}\left[\frac{g\sigma(\rho_f - \rho_g)}{\rho_g^2}\right]^{0.125}}\right\}(T_{spt} - T_f) \tag{4.2-95}$$

where

$$L = \left[\frac{g(\rho_f - \rho_g)}{\sigma}\right]^{0.5} \quad . \tag{4.2-96}$$

Figure 4.2-21 compares these two equations at two pressures. At 100 K subcooling and 0.1 MPa, the later equation is higher by about 8%. Since this is smaller than the uncertainties involved, the computer time savings is defensible. Since the two equations give similar results, the simplest one has been implemented. The final equation for CHF in horizontal bundles is

$$CHF_{bundle} = CHF_{tube}\,(1 - 1.175\alpha_g)\,Fsub \tag{4.2-97}$$

where Fsub is determined from Equation (4.2-94), (with Ivey and Morris constants), and CHF_{tube} uses a K factor [in Equation (4.2-89)] of 0.14 as recommended by Folkin and Goldberg.

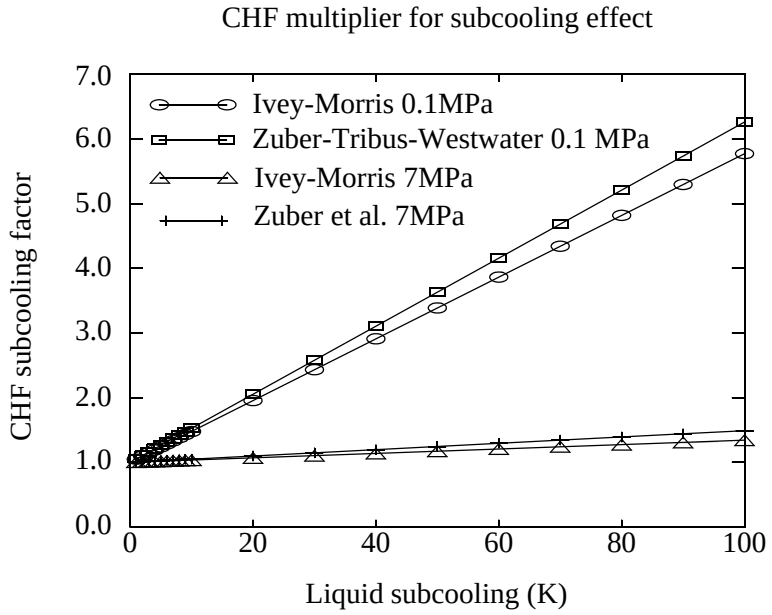

Figure 4.2-21 Comparison of subcooled boiling factors for CHF.

The textbook by Carey[4.2-106] evaluates Equation (4.2-89) at saturation conditions before applying the subcooling factor. This appears logical but the other literature is not clear on this point. A check was made to determine if additional calls to the thermodynamic property tables could be avoided by not using the subcooling factor and by simply evaluating CHF at the local temperature. **Figure 4.2-22** is a result of this investigation. At low pressure, the CHF with liquid properties evaluated at the liquid temperature only rises by about 7.5% between 0 and 100 K subcooling, but the multiplier at low pressure is 600% (see **Figure 4.2-21**) over this same subcooling range. At high pressure, the CHF based on the liquid temperature rises about 29%, but the high pressure subcooling multiplier only rises about 9%. The code evaluates CHF at saturation conditions, and the subcooling multiplier is then applied.

4.2.20.5 Geometry 134, Horizontal Tube Bundles Natural Convection Model Basis. No correlation for horizontal bundles is known. A correlation by Churchill-Chu[4.2-107] (discussed in Incropera and DeWitt[4.2-8]) for a long horizontal cylinder is employed where the pertinent length can be input by the code user as a bundle diameter. The correlation is

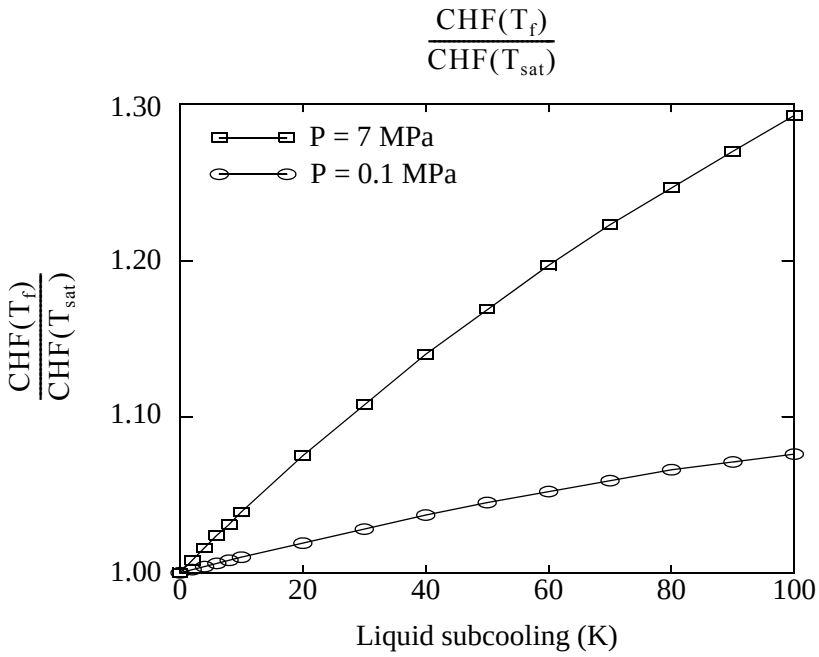

Figure 4.2-22 Effect of property evaluation temperature on CHF.

$$Nu_L = \left\{ 0.6 + \frac{0.387(Ra_L)^{\frac{1}{6}}}{\left[1 + \left(\frac{0.559}{Pr}\right)^{\frac{9}{16}}\right]^{\frac{8}{27}}} \right\}^2 . \qquad (4.2\text{-}98)$$

This correlation is valid for Rayleigh numbers of 10^{-5} to 10^{12}.

4.2.20.6 Geometry 134, Horizontal Tube Bundles Natural Convection Model as Coded. The model is coded as presented above.

4.2.20.7 Geometry 134, Horizontal Tube Bundles Condensation Model Basis. The correlations for condensation differ from those described in Section 4.2.3.6 for the right side of heat slabs representing tube bundle outside walls associated with the feedwater heater (FWHTR) component. **Figure 4.2-23** shows a diagram of a typical tube-in-shell feedwater heater.

Condensation of steam occurs within the shell on the outside of the tubes that carry the cooler feedwater. Condensate pools in the bottom of the shell, covering some fraction of the tube bundle. Typically, a control system is used to control the level of the condensate to expose enough tube surface

.

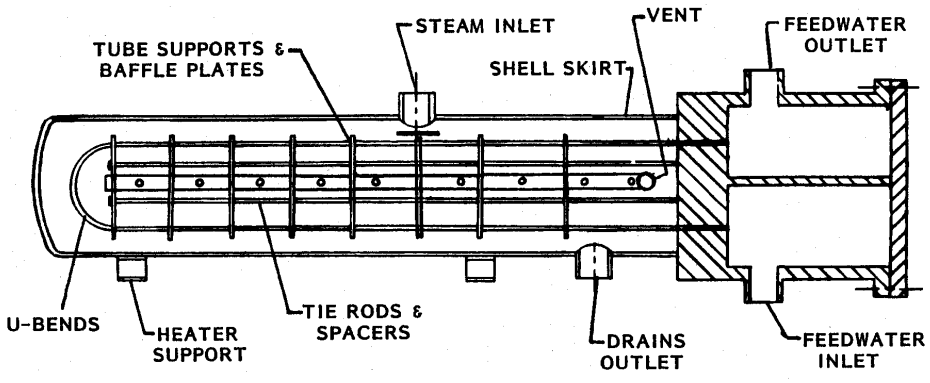

Figure 4.2-23 Typical low-pressure feedwater heater (from **Reference 4.2-109**)

area to maintain a desired outlet temperature. Heat transfer from the shell to the tubes is therefore a combination of condensation above the level and convection below the level.

When a FWHTR component is specified, the heat transfer logic for the right side of heat slabs associated with the FWHTR computes the heat transfer based on the fractional surface area of the heat slabs above and below the water level of the pool. **Figure 4.2-24** illustrates a version of a nodalization of a feedwater heater.

.

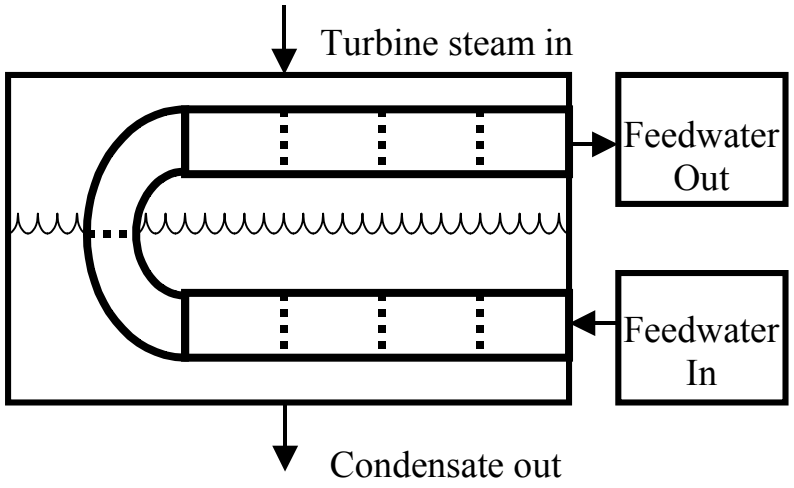

Figure 4.2-24 Typical feedwater heater nodalization

The shell is represented by the FWHTR component and the tube bundle by three interconnected pipes. Two-sided heat slabs that represent the tube walls are defined that thermally connect the shell to the pipes. The analyst may specify any number of parallel pipes to represent the tube bundle. The code logic determines the fractional surface area exposed to steam (above the water level) and the fractional surface area exposed to liquid (below the water level) based on input data for the FWHTR (relationship between

void fraction and water level) and the heat slabs (elevation of the top and bottom of the bundle above the bottom of the shell). **Figure 4.2-25** shows the relevant levels.

.

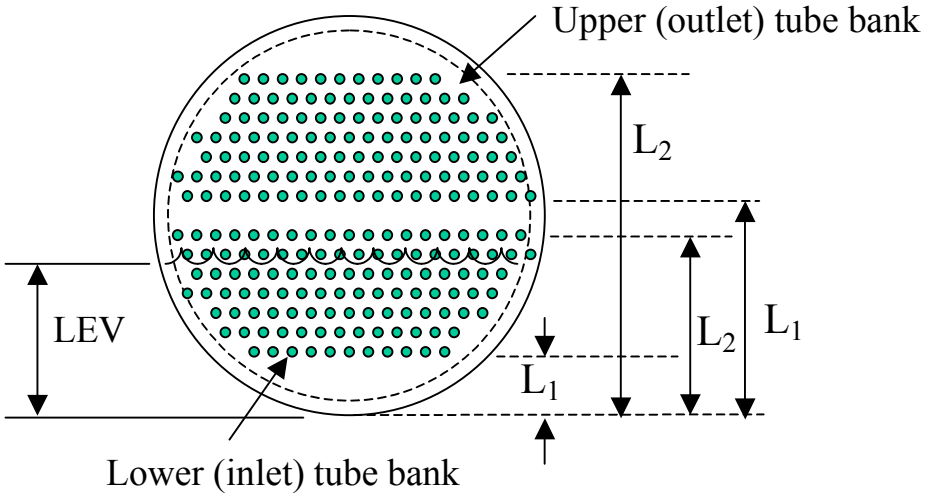

Figure 4.2-25 Depiction of levels in a feedwater heater

For each heat slab i, the heat flux is calculated as

$$q_{iw} = q_{iwg} + q_{iwf}$$

where q_{iwg} is the heat flux to the vapor in the shell volume and q_{iwf} is the heat flux to the liquid in the shell volume.

The respective fluxes are given by

$$q_{iwg} = \phi_i h_{iwg}(T_{iw} - T_{sat})$$
$$q_{iwf} = (1 - \phi_i) h_{iwf}(T_{iw} - T_f)$$

where ϕ_i is the fractional area of the slab above the water level, h_{iwg} is the condensation heat transfer coefficient, and h_{iwf} is the liquid convection heat transfer coefficient, and T_{sat} is T_{sppb} (see Section 4.2.3.6). Referring to **Figure 4.2-25**, ϕ_i is computed as

$$\phi_i = \max\left\{0.0, \min\left[1.0, \left(1.0 - \frac{LEV - L_1}{L_2 - L_1}\right)\right]\right\}$$

The condensation mechanism on the exterior of the tubes is like that on an inclined surface. **Figure 4.2-26** depicts an idealization of the process in which condensate originating in the upper tubes flows down to tubes beneath in a cascading fashion.

.

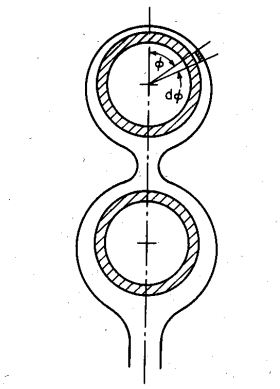

Figure 4.2-26 Depiction of condensation process (from **Reference 4.2-31**)

ATHENA uses a correlation by Chen[4.2-28], given by

$$h_{iwg} = 0.728\left[1.0 + 0.2\frac{c_{pf}\Delta T}{h_{fg}}(n-1)\right]\left[\frac{g\rho_f(\rho_f-\rho_g)k_f^3 h'_{fg}}{nD_h\mu_f\Delta T}\right]^{\frac{1}{4}}$$

The variable n is the number of tubes in vertical alignment, the variable ΔT is T_{sppb} - T_{iw}, and the variable h'_{fg} is $h_{fg} + 0.375C_{pf}\Delta T$. This expression is a modification of one proposed by Nusselt[4.2-24], which is given by the second bracketed term. Nusselt's form under-predicts most horizontal tube bundle data. Chen proposed that condensation on the liquid film between tubes was an enhancing mechanism, which explains the effect of the first bracketed term. The liquid convection heat transfer coefficient h_{iwf} is obtained as described in Section 4.2.20. These heat transfer correlations are utilized only when the flow regime in the FWHTR component is horizontally stratified. Otherwise, the correlations presented in Section 4.2.20 are used.

4.2.20.8 Geometry 134, Horizontal Tube Bundles Condensation Model as Coded. The model is coded as presented above. The correlation is coded as

$$h_{iwg} = 0.728\left[1.0 + 0.2\frac{c_{pf}\Delta T}{h_{fg}}(\max(1, \varphi_i n)-1)\right]\left[\frac{g\rho_f(\rho_f-\rho_g)k_f^3 h'_{fg}}{\max(1, \varphi_i n)D_h\mu_f\Delta T}\right]^{\frac{1}{4}} \quad (4.2\text{-}99)$$

The appearance of n being multiplied by φ_i accounts for the fractional number of tubes exposed to steam.

4.2.21 Geometry 135, Correlations for Horizontal Bundles with In-Line Rods or Tubes, Crossflow Only

This geometry defaults to Geometry 134.

4.2.22 Geometry 136, Correlations for Horizontal Bundles with Staggered Rods or Tubes, Crossflow and Parallel Flow

The geometry defaults to Geometry 134.

4.2.23 Geometry 137, Correlations for Horizontal Bundles with Staggered Rods or Tubes, Crossflow Only

This geometry defaults to Geometry 134.

4.2.24 Geometry 151, Correlations for Vertical Annuli with Aluminum Walls Heated and Downflow

This geometry differs from Geometry 101 only in the CHF correlation. The correlation is from the Savannah River Laboratory and is applicable to vertical annuli with aluminum walls heated and downflow.

4.2.24.1 Geometry 151, Vertical Annuli with Aluminum Walls CHF Model Basis.

The critical heat flux in vertical annuli with aluminum walls was determined using an aluminum heater with fluid flowing in the downward direction[4.2-108]. The correlation is of the form

$$CHF = \max(CHF_1, CHF_2) \tag{4.2-100}$$

$$CHF_1 = 5.93x10^5(1.0 + 0.169|v_f|)[1.0 + 0.124(T_{sat} - T_f)] \tag{4.2-101}$$

$$CHF_2 = 12.87x10^5(1.0 + 0.348|v_f|)[1.0 + 0.005(T_{sat} - T_f)] \tag{4.2-102}$$

These are in SI units, where the CHF units are W/m^2, the velocity units are m/s, and the temperature units are K.

4.2.24.2 Geometry 151, Vertical Annuli with Aluminum Walls CHF Model as Coded.

The model is coded as presented above (the coding uses British units) except that the final CHF correlation for this Geometry 151 is obtained from the maximum of Equation (4.2-100) and the Groeneveld Table Lookup[4.2-68] (see Section 4.2.3.5.2).

4.2.25 Geometry 115, Swirl Tubes

The heat transfer correlations applied for swirl tubes are based on the thesis of Marshall[4.2-21] and are based on experiments supporting fision reactors. This geometry uses alternate correlations for turbulent

convection, nucleate boiling, transition boiling, and CHF. The default correlations are applied in the other heat transfer regimes.

The correlations for turbulent convection is based on the Seider-Tate[4.2-9] correlation with enhancements for swirl tubes based on the correlation of Lopina and Bergles[4.2-10]. The nucleate boiling model is based on four correlations: Sieder-Tate[4.2-9] for turbulent convection, Bergles and Rohsenow[4.2-18] for the onset of nucleate boiling, Bergles and Rohsenow[4.2-18] for partial nucleate boiling, and Araki et. al.[4.2-19] for fully developed nucleate boiling. The transition boiling model is based on Marshall's modification to the Berenson correlation. The CHF model is based on Marshall's[4.2-21] modification to the Tong[4.2-111] correlation to represent the enhancement in CHF due to a swirl tape insert.

4.2.26 Geometries 160 - 165, Alternate Correlations for Tubes

Several correlations have been added to the code to support the analysis of advanced reactors cooled by supercritical fluids, including light water, helium, and carbon dioxide. The correlations primarily simulate turbulent convection.

The Gnielinski[4.2-11] correlation (Geometry 160) utilizes different equations for heat transfer to liquid and to gas. The correlation simulates entrance and heated wall effects.

Geometries 161 through 165 support the analysis of reactors cooled by supercritical light water and are described in detail by MacDonald et. al[4.2-112].. The correlation of Bishop et al.[4.2-12] (Geometry 161) is based on experiments in supercritical light water. The correlation of Koshizuka and Oka [4.2-13](Geometry 162) is based on numerical analysis of heat transfer to supercritical water in a 10-mm diameter tube. The correlation of Jackson [4.2-14](Geometry 163) simulates turbulent convection heat transfer from tubes to supercritical water and supercritical carbon dioxide.

Geometries 164 and 165 modify the correlation of Jackson[4.2-14] to account for the effects of buoyancy on mixed convection based on the semi-empirical model of Jackson [4.2-15]as described by Wu et al.[4.2-16] for a tube. The correlations represent the transition from turbulent to natural convection. Consequently, the code's default natural convection correlations are not applied for these geometries. The correlations account for the effect of buoyancy on the heat transfer. The heat transfer is enhanced for downwards flow compared to upwards flow. Geometry 164 should be applied when the positive flow direction is defined upwards. Geometry 165 should be applied when the positive flow direction is defined downwards. The code correctly accounts for both positive and negative flows within the tube.

For liquid metals, the convective heat transfer coefficient for vertical bundles, with and without crossflow is based on the Westinghouse correlation described by Todreas and Kazimi[4.2-114]. For liquid metals, the convective heat transfer coefficient is based on the correlation described bu Bird, Stewart, and Lightfoot[4.2-113] for constant wall temperature.

4.2.27 References

4.2-1. W. M. Kays, "Numerical Solution for Laminar Flow Heat Transfer in Circular Tubes," *Transactions of the ASME, 77,* 1955, pp. 1265-1274.

4.2-2. *ORNL Monthly Progress Report,* ORNL/ANS/INT-5/V19, Oak Ridge National Laboratory, October, 1989.

4.2-3. F. W. Dittus and L. M. K. Boelter, "Heat Transfer in Automobile Radiators of the Tubular Type," *Publications in Engineering, 2,* University of California, Berkeley, 1930, pp. 443-461.

4.2-4. B. S. Petukhov, "Heat Transfer and Friction in Turbulent Pipe Flow with Variable Physical Properties," *Advances in Heat Transfer,* New York: Academic Press, 1970, pp. 503-565.

4.2-5. M. M. Shah, *Heat Transfer and Fluid Flow Data Books,* Genium Publishing, January 1992, Section 507.6, p. 7.

4.2-6. S. W. Churchill and H. H. S. Chu, "Correlating Equations for Laminar and Turbulent Free Convection From a Vertical Plate," *International Journal of Heat and Mass Transfer, 18,* 1975, pp. 1323-1329.

4.2-7. W. H. McAdams, *Heat Transmission,* 3rd Edition, New York: McGraw-Hill, 1954.

4.2-8. F. P. Incropera and D. P. DeWitt, *Introduction to Heat Transfer,* New York: Wiley, 1990.

4.2-9. E. N. Sieder, and G. E. Tate, "Heat Transfer and Pressure Drop of Liquids in Tubes," Industrial and Engineering Chemistry, 28, No. 12, pp. 1429-1435, 1936.

4.2-10. R. F. Lopina and A. E. Bergles, "Heat Transfer and Pressure Drop in Tape-Generated Swirl Flow of Single-Phase Water," Transactions of the ASME, Journal of Heat Transfer, 91, No. 8, pp. 434-442, 1969.

4.2-11. V. Gnielinski, "New Equations for Heat and Mass Transfer in Turbulent Pipe and Channel Flow," *International Chemical Engineering, 16,* No. 2, pp. 359-368, 1976.

4.2-12. A. A. Bishop, R. O. Sandberg, and L. S. Tong, *Forced Convection Heat Transfer to Water near Critical Temperature and Supercritical Pressures,* WCAP-2056-P, Part-III-B, February 1964.

4.2-13. S. Koshizuka and Y. Oka, "Computational Analysis of Deterioration Phenomena and Thermal-hydraulic Design of SCR," *Proceedings of the First International Symposium on Supercritical Water-cooled Reactors, Design and Technology, University of Tokyo, SCR-2000, pp. 169-179, November 6-9, 2000.*

4.2-14. J. D. Jackson, "Consideration of the Heat Transfer Properties of Supercritical Pressure Water in Connection with the Cooling of Advanced Nuclear Reactors," *Proceedings of the 13th Pacific Basin Nuclear Conference, Shenzhen, China, October 21-25, 2002*.

4.2-15. J. D. Jackson, "Mixed Forced and Free Convection - The Influence of Buoyancy on Turbulent Forced Flow in Vertical Pipes," *The Euromech Meeting on Boundary Layers and Turbulence in Internal Flows, Session 5, University of Salford, England, 1979.*

4.2-16. T. H. Wu, Z. Xu and J. D. Jackson, "Mixed Convection Heat Transfer to Water Flowing Through a Vertical Passage of Annular Cross Section," *Transactions of the Institution of Chemical Engineers, Chemical Engineering Research and Design, 80,* Part A, pp. 239-245, 2002.

4.2-17. J. C. Chen, "A Correlation for Boiling Heat Transfer to Saturated Fluids in Convective Flow," *Process Design and Development, 5,* 1966, pp. 322-327.

4.2-18. A. E. Bergles and W. M. Rohsenow, "The Determination of Forced Convection Surface Boiling Heat Transfer," *Transactions of the ASME, Journal of Heat Transfer, 86,* pp. 365-372, 1964.

4.2-19. M. Araki, M. Ogawa, T. Kunugi, S. Ikeda, K. Satoh, and S. Suzuki, "Experiment on Heat Transfer of Smooth and Swirl Tubes Under One-Sided Heating Conditions," I*nternational Journal of Heat and Mass Transfer, 39,* No. 14, pp. 3045-3055, 1996.

4.2-20. J. C. Chen, R. K. Sundaram, and F. T. Ozkaynak, *A Phenomenological Correlation for Post-CHF Heat Transfer*, NUREG-0237, June 1977.

4.2-21. T. D. Marshall, *Experimental Examination of the Post-Critical Heat Flux and Loss of Flow Accident Phenomena for Prototypical ITER Divertor Channels*, Ph.D. Thesis, Rensselaer Polytechnic Institute, Nuclear Engineering, 1998.

4.2-22. L. A. Bromley, "Heat Transfer in Stable Film Boiling," *Chemical Engineering Progress, 46,* 1950, pp. 221-227.

4.2-23. K. H. Sun, J. M. Gonzalez-Santalo, and C. L. Tien, "Calculations of Combined Radiation and Convection Heat Transfer in Rod Bundles Under Emergency Cooling Conditions," *Transactions of the ASME, Journal of Heat Transfer, 98,* 1976, pp. 414-420.

4.2-24. W. Nusselt, "Die Oberflachenkondensation des Wasserdampfes," *Zeitschrift Ver. Deutsch. Ing., 60,* 1916, pp. 541-546 and 569-575.

4.2-25. M. M. Shah, "A General Correlation for Heat Transfer during Film Condensation Inside Pipes," *International Journal of Heat and Mass Transfer, 22,* 1979, pp. 547-556.

4.2-26. J. C. Chato, "Laminar Condensation Inside Horizontal and Inclined Tubes," *American Society of Heating, Refrigeration, and Air Conditioning Journal, 4,* 1962, pp. 52-60.

4.2-27. A. P. Colburn and O. A. Hougen, "Design of Cooler Condensers for Mixtures of Vapors with Noncondensing Gases," *Industrial and Engineering Chemistry, 26,* 1934, pp. 1178-1182.

4.2-28. M. M. Chen, "An Analytical Study of Laminar Film Condensation: Part 2 - Single and Multiple Horizontal Tubes," *Transactions of the ASME, Journal of Heat Transfer, 83,* 1961, pp. 55-60.

4.2-29. H. K. Forster and N. Zuber, "Dynamics of Vapor Bubbles and Boiling Heat Transfer," *AIChE Journal, 1,* No. 4, December 1955, pp. 531-535.

4.2-30. G. T. Polley, T. Ralston, and I. D. R. Grant, "Forced Crossflow Boiling in an Ideal In-line Tube Bundle," *ASME 80-HT-46,* 1981.

4.2-31. W. M. Rohsenow and H. P. Hartnett (ed.), *Handbook of Heat Transfer,* New York: McGraw-Hill, 1973.

4.2-32. W. H. McAdams and T. H. Frost, "Heat Transfer by Conduction and Convection," *Industrial and Engineering Chemistry, 14,* 1922, p. 1101.

4.2-33. W. H. McAdams and T. H. Frost, "Heat Transfer for Water Flowing Inside Pipes," *Refrigerating Engineering, 10,* 1924, p. 23.

4.2-34. F. H. Morris and W. G. Whitman, "Heat Transfer for Oils and Water in Pipes," *Industrial and Engineering Chemistry, 20,* 1928, p. 234.

4.2-35. F. Kreith and M. S. Bohn, *Principles of Heat Transfer,* 4th Edition, New York: Harper and Row, 1986.

4.2-36. H. C. Reynolds, Jr., *Internal Low Reynolds Number Turbulent Heat Transfer,* University of Arizona, EMMT Lab TR 2, January 1968.

4.2-37. C. A. Sleicher and M. W. Rouse, "A Convenient Correlation for Heat Transfer to Constant and Variable Property Fluids in Turbulent Pipe Flow," *International Journal of Heat and Mass Transfer, 18,* 1975, pp. 677-683.

4.2-38. P. S. Larsen and H. A. Lord, *Convective and Radiative Heat Transfer to Superheated Steam in Uniformly and Nonuniformly Heated Tubes,* Westinghouse Electric Corporation, Atomic Power Division, 08742-1-F, February 1969.

4.2-39. J. B. Heineman, *An Experimental Investigation of Heat Transfer to Superheated Steam in Round and Rectangular Channels,* ANL-6213, Argonne National Laboratory, 1960.

4.2-40. M. S. Dougall and W. M. Rohsenow, *Film Boiling on the Inside of Vertical Tubes with Upward Flow of a Fluid at Low Qualities,* MIT-ME 9079-26, 1963.

4.2-41. D. D. Taylor et al., *TRAC-BD1/MOD1: An Advanced Best Estimate Computer Program for Boiling Water Reactor Transient Analysis, Vol. 1,* NUREG/CR-3633, EGG-2294, Idaho National Engineering Laboratory, April 1984, p. 65.

4.2-42. R. G. Deissler and M. F. Taylor, *Reactor Heat Transfer Conference of 1956,* TID-7529, November 1957, pp. 416-461.

4.2-43. J. Weisman, "Heat Transfer to Water Flowing Parallel to Tubes," *Nuclear Science and Engineering, 6,* 1959, pp. 78-79.

4.2-44. A. Y. Inayatov, "Correlation of Data on Heat Transfer Flow Parallel to Tube Bundles at Relative Tube Pitches of 1.1 < s/d < 1.6," *Heat Transfer-Soviet Research, 7,* 3, May-June 1975.

4.2-45. B. Gebhart, *Heat Transfer,* 2nd Edition, New York: McGraw-Hill, 1971.

4.2-46. J. R. Sellars, M. Tribus, and J. S. Klein, "Heat Transfer to Laminar Flows in a Round Tube or Flat Conduit: The Graetz Problem Extended," *Transactions of the ASME, 78,* 1956, p. 441.

4.2-47. R. W. Shumway, *Variable Properties Laminar Gas Flow Heat Transfer and Pressure Drop in Annuli***,** University of Arizona, EMMT Lab TR 3, August 1969.

4.2-48. L. C. Burmeister, *Convective Heat Transfer,* New York: Wiley, 1983.

4.2-49. Y. S. Touloukian, G. A. Hawkins, and M. Jakob, "Heat Transfer by Free Convection from Heated Vertical Surfaces to Liquids," *Transactions of the ASME, 70,* January 1948, pp. 13-18.

4.2-50. G. E. Dengler and J. N. Addoms, *Chemical Engineering Progress Symposium Series, 52,* 18, 1956, pp. 95-103.

4.2-51. V. E. Schrock and L. M. Grossman, "Forced Convection Boiling in Tubes," *Nuclear Science and Engineering, 12,* 1962, pp. 474-481.

4.2-52. R. L. Sani, *Downflow Boiling and Nonboiling Heat Transfer in a Uniformly Heated Tube,* UCRL-9023, 1960.

4.2-53. J. A. R. Bennett et al., *Heat Transfer to Two-Phase Gas Liquid Systems,* AERE-R3159, 1959.

4.2-54. R. M. Wright, *Downflow Forced-Convection Boiling of Water in Uniformly Heated Tubes,* UCRL-9744, August 1961.

4.2-55. S. A. Guerrieri and R. D. Talty, *Chemical Engineering Progress Symposium Series, 52,* 18, 1956, pp. 69-77.

4.2-56. K. E. Gungor and R. H. S. Winterton, "A General Correlation for Flow Boiling in Tubes and Annuli," *International Journal of Heat and Mass Transfer, 29,* 1986, pp. 351-356.

4.2-57. T. A. Bjornard and P. Griffith, "PWR Blowdown Heat Transfer," *Thermal and Hydraulic Aspects of Nuclear Reactor Safety, 1,* American Society of Mechanical Engineers, New York, 1977, pp. 17-41.

4.2-58. R. W. Lockhart and R. C. Martinelli, "Proposed Correlation of Data for Isothermal Two-Phase, Two-Component Flow in Pipes," *Chemical Engineering Progress, 45,* 1, 1949, p. 39-48.

4.2-59. F. D. Moles and J. R. G. Shah, "Boiling Heat Transfer to Subcooled Liquids Under Conditions of Forced Convection," *Transactions of the Institution of Chemical Engineers, 50,* 1972, pp. 76-84.

4.2-60. J. G. Collier, *Convective Boiling and Condensation,* 2nd Edition, New York: McGraw-Hill, 1981.

4.2-61. D. R. H. Beattie and P. B. Whalley, "A Simple Two-Phase Frictional Pressure Drop Calculational Method," *International Journal of Multiphase Flow, 8,* 1982, pp. 83-87.

4.2-62. P. J. Berenson, "Film Boiling Heat Transfer from a Horizontal Surface," *Journal of Heat Transfer,* 1961, pp. 351-358.

4.2-63. B. P. Breen and J. W. Westwater, "Effect of Diameter of Horizontal Tubes on Film Boiling Heat Transfer," *Chemical Engineering Progress, 58,* 1962, p. 67.

4.2-64. Y. Sudo and Y. Murao, *Study on Film Boiling Heat Transfer During Reflood Process,* JAERI Report, JPNRSR-15, August 1975.

4.2-65. J. P. Holman, *Heat Transfer,* 6th Edition, New York: McGraw-Hill, 1986, p. 492.

4.2-66. L. Biasi et al., "Studies on Burnout Part 3 - A New Correlation for Round Ducts and Uniform Heating and Its Comparison with World Data," *Energia Nucleare, 14,* 1967, pp. 530-536.

4.2-67. A. Sjoberg and D. Caraher, *Assessment of RELAP5/MOD2 Against 25 Dryout Experiments Conducted at the Royal Institute of Technology,* NUREG/IA-0009, October 1986.

4.2-68. D. C. Groeneveld, S. C. Cheng, and T. Doan, "1986 AECL-UO Critical Heat Flux Lookup Table," *Heat Transfer Engineering, 7,* 1-2, 1986, pp. 46-62.

4.2-69. K. Mishima and H. Nishihara, "The Effect of Flow Direction and Magnitude on the CHF for Low Pressure Water in Thin Rectangular Channels," *Nuclear Engineering and Design,* 1985, pp. 165-181.

4.2-70. E. F. Carpenter and A. P. Colburn, "The Effect of Vapor Velocity on Condensation Inside Tubes," *Proceedings of General Discussion on Heat Transfer, Institute Mechanical Engineering/American Society of Mechanical Engineers,* 1951, pp. 20-26.

4.2-71. W. H. Rohsenow, J. H. Webber, and A. T. Ling, "Affect of Vapor Velocity on Laminar and Turbulent-Film Condensation," *Transactions of the ASME, 78,* 1956.

4.2-72. M. M. Shah, *Heat Transfer and Fluid Flow Data Books,* Genium Publishing, January 1992, Sec. 507.6, p. 8.

4.2-73. M. Jakob, *Heat Transfer, Vol. 1,* New York: Wiley, 1949, p. 666.

4.2-74. C. K. Nithianandan et al., "RELAP5/MOD2 Model for Surface Condensation in the Presence of Noncondensable Gases," *Proceedings of 8th International Heat Transfer Conference, San Francisco, CA, August 17-22, 1986,* Vol. 4, pp. 1627-1633.

4.2-75. W. M. Rohsenow and Y. H. Choi, *Heat Mass and Momentum Transfer,* Englewood Cliffs, NJ: Prentice-Hall, 1961.

4.2-76. R. C. Reid, J. M. Prausnitz, and B. E. Poling, *The Properties of Gases and Liquids,* New York: McGraw-Hill, 1987.

4.2-77. G. K. Filonenko, "Hydraulic Resistance in Pipes (in Russian)," *Teploenergetika, 1,* 4, 1954, pp. 40-44.

4.2-78. W. R. Gambill and T. Mochizuki, "ANS Design: Burnout Heat Flux Correlation Development," *Transactions of the American Nuclear Society, 57,* 298, October 1988.

4.2-79. M. Siman-Tov et al., "Thermal-Hydraulic Correlation for the ANS Reactor Fuel Element Design and Analysis," *Proceedings of the 1991 ASME Winter Annual Meeting, Atlanta, GA, December, 1991.*

4.2-80. R. Viskanta and A. K. Mohanty, *TMI-2 Accident: Postulated Heat Transfer Mechanisms and Available Data Base,* NUREG/CR-2121, ANL-81-26, Argonne National Laboratory, April 1981.

4.2-81. W. C. Reynolds, R. E. Lundburg, and P. A. McCuen, "Heat Transfer in Annular Passages. General Formulation of the Problem for Arbitrary Prescribed Wall Temperatures and Heat Fluxes," *International Journal of Heat and Mass Transfer, 6,* 1963, p. 483.

4.2-82. C. D. Morgan and Y. A. Hassan, "On the Use of the Chen Boiling Heat Transfer Correlation in Once-Through Steam Generator Analysis," *Transactions of the American Nuclear Society, 53,* 1986, pp. 332-334.

4.2-83. S. S. Kutateladze, "Boiling Heat Transfer," *International Journal of Heat and Mass Transfer, 4,* 1961, pp. 31-45.

4.2-84. A. Khalil, "Steady-State Heat Transfer of Helium Cooled Cable Bundles," *Cryogenics,* June 1983, pp. 277-281.

4.2-85. J. W. Palen, A. Yarden, and J. Taborek, "Characteristics of Boiling Outside Large-Scale Horizontal Tube Bundles," *AIChE Symposium Series, 68,* 118, 1972, pp. 50-61.

4.2-86. J. W. Palen and W. M. Small, "Kettle and Internal Reboilers," *Hydrocarbon Processing, 43,* 11, November 1964, pp. 199-208.

4.2-87. V. N. Slesarenko, A. Y. Rudakova, and G. A. Zakharov, "Effect of Operating Conditions and Tube Bundle Geometry on Boiling Heat Transfer," *Heat Transfer-Soviet Research, 14,* 2, March-April 1982.

4.2-88. K. Cornwell, N. W. Duffin, and R. B. Schuller, *An Experimental Study of the Effects of Fluid Flow on Boiling within a Kettle Reboiler Tube Bundle,* ASME 80-HT-45, 1980.

4.2-89. K. Cornwell and R. B. Schuller, "A Study Outside a Tube Bundle Using High Speed Photography," *International Journal of Heat and Mass Transfer, 25,* 5, 1982, pp. 683-690.

4.2-90. K. Nakajima, "Boiling Heat Transfer Outside Horizontal Multitube Bundles," *Heat Transfer Japanese Research, 7,* 1978, pp. 1-24.

4.2-91. A. M. C. Chan and M. Shoukri, "Boiling Heat Transfer and Burnout Around Horizontal Tube Bundles, Fundamentals of Phase Change: Boiling and Condensation," *ASME Winter Annual Meeting, New Orleans, LA, December 9-14, 1984, HTD, Vol. 38.*

4.2-92. L. S. Leong and K. Cornwell, "Heat Transfer Coefficients in Reboiler Tube Bundle," *Chemical Engineering, No. 343,* 1979, pp. 219-221.

4.2-93. T. W. C. Brisbane, I. D. R. Grant, and P. B. Whalley, *A Prediction Method for Kettle Reboiler Performance,* ASME, 80-HT-42, 1980.

4.2-94. A. A. Voloshko, "Free Convection Boiling of Freons," *Heat Transfer-Soviet Research, 4,* No. 4, 1972, pp. 60-66.

4.2-95. M. M. Shah, *Heat Transfer and Fluid Flow Data Books,* Genium Publishing, January 1992, Section 507.6, , p. 7.

4.2-96. M. Cumo et al., "Quality Influence on the Departure from Nucleate Boiling in Crossflows Through Bundles," *Nuclear Technology, 49,* August 1980, pp. 337-346.

4.2-97. N. Zuber, *Hydrodynamic Aspects of Boiling Heat Transfer,* AECU-4439, U. S. Atomic Energy Commission, 1959.

4.2-98. S. S. Kutateladze, "A Hydrodynamic Theory of Changes in the Boiling Process under Free Convection," *Izv. Akad. Nauk. S. S. S. R. Otd. Tekh. Nauk., 4,* 1951.

4.2-99. K. H. Sun and J. H. Lienhard, "The Peak Pool Boiling Heat Flux on Horizontal Cylinders," *International Journal of Heat and Mass Transfer, 13,* 1970, pp. 1425-1439.

4.2-100. M. M. Hassan, R. Eichorn, and J. H. Lienhard, "Burnout During Flow Across a Small Cylinder Influenced by Parallel Cylinders," *Proceedings of the Seventh International Heat Transfer Conference,* 1982, pp. 285-290.

4.2-101. M. M. Shah, *Heat Transfer and Fluid Flow Data Books,* Genium Publishing, January 1992, Section 507.6, , p. 9.

4.2-102. B. S. Folkin and Y. N. Goldberg, "Simulation of Free Convection Boiling Crisis in Vapor Blanketing of a Horizontal Tube Bundle," *Heat Transfer Soviet Research, 12,* 3, 1980, pp. 77-81.

4.2-103. H. J. Ivey and D. J. Morris, *On the Relevance of the Vapor Liquid Exchange Mechanism for Subcooled Boiling Heat Transfer at High Pressures*, AEEW-R137, Atomic Energy Establishment Winfrith, 1962.

4.2-104. S. S. Kutateladze, *Heat Transfer During Condensation and Boiling*, Translation AEC-tr-3770, 1952.

4.2-105. N. Zuber, M. Tribus, and J. W. Westwater, "The Hydrodynamic Crisis in Pool Boiling of Saturated and Subcooled Liquids," *Proceedings of the 1961-62 Heat Transfer Conference, Boulder, CO, August 28-September 1, 1961 and London, UK, January 8-12, 1962, International Developments in Heat Transfer, ASME, New York, 1963*, pp. 230-236.

4.2-106. V. P. Carey, *Liquid-Vapor Phase-Change Phenomena,* Philadelphia and London: Hemisphere, 1992.

4.2-107. S. W. Churchill and H. H. S. Chu, "Correlating Equations for Laminar and Turbulent Free Convection from a Horizontal Cylinder," *International Journal of Heat and Mass Transfer, 18,* 1975, p.1049-1053.

4.2-108. D. H. Knoebel, S. D. Harris, B. Crain, Jr., and R. M. Biderman, *Forced-Convection in Subcooled Critical Heat Flux*, DP-1306, Savannah River Laboratory, February 1973.

4.2-109. Heat Exchanger Systems, "Nuclear Plant Feedwater Heater Handbook, Volume I: Primer," EPRI Report NP-4057, June 1985.

4.2-110. P. J. Berenson, "Experiments on Pool-Boiling Heat Transfer," International Journal of Heat and Mass Transfer, 5, pp. 985-999, 1962.

4.2-111. L. S. Tong, "A Phenomenological Study of Critical Heat Flux," Proceedings of the American Institute of Chemical Engineers - American Society of Mechanical Engineers Heat Transfer Conference, San Francisco, California, ASME Paper 75-HT-68, 1975.

4.2-112. P. MacDonald, J. Buongiorno, C. Davis, and R. Witt, Feasibility Study of Supercritical Light Water Cooled Reactors for Electric Power Production, Nuclear Energy Research Initiative Project 2001-001, Westinghouse Electric Co. Award Number: DE-FG-07-02SF22533, 2nd Annual Report, 8th Quarterly Report, INEEL/EXT-03-01277, 2003.

4.2-113. R. B. Bird, W. E. Stewart, and E. N. Lightfoot, Transport Phenomena, New York: Wiley, 1960.

4.2-114. N. E. Todreas and M. S. Kazimi, Nuclear Systems I, London: Taylor & Francis, 1990.

4.3 PG-CHF Correlations

ATHENA users may activate a new set of CHF correlations which were developed by the Nuclear Research Institute Rez in the Czech Republic.[4.3-1,4.3-2] These correlations replace the "CHF Table

Look-up" method. They are activated by the user on the heat structure 1CCCG800 and 1CCCG801 through 1CCCG899 cards or 1CCCG900 and 1CCCG901 through 1CCCG999 cards.[4.3-3]

The correlations are based on data in the Czech Republic data bank from 173 different sets of tube data, 23 sets of annular data, and 153 sets of rod bundle data. **Table 4.3-1** shows the range of the experimental data.

Table 4.3-1 Range of experimental data for development of the PG-CHF correlation.

Data base geometry	**Tube**	**Rod bundle**	**Annulus**
Test geometries/Total points	**173/9,547**	**153/7,616**	**23/713**
Exit pressure p (MPa) (min/max)	0.26/17.95	0.28/18.73	6.89/6.89
Mass flux G (kg/m^2-s)	102.3/7,491.0	34.1/7,478.0	189.87/6,740.0
Inlet quality X_i	-1.73/0.0	-1.14/0.44	-0.63/0.0
Local quality X_1	-0.49/0.99	-0.34/1.0	-0.23/0.61
CHF (MW/m^2)	0.07/7.0	0.12/6.0	0.49/8.96
Heated length L (m)	0.22/6.05	0.4/7.0	0.61/2.74
Equivalent diameter d (m)	0.00384/0.03747	0.00241/0.07813	0.00322/0.02223
Heated length/equivalent diameter L/d	20.06/756.25	12.29/1,422.36	36.9/584.5
Rod diameter D (m)	-	0.005/0.01905	0.00952/0.09647
Pitch/Diameter t	-	1.02/2.48	-
Peak/Average heat flux k_a	1.0/3.1	1.0/1.9	1.0/1.0
Maximum to radial average rod power ratio k_r	-	1.0/1.95	-

The correlation of the critical heat flux divided by the local heat flux, R, has the general form

$$R = \frac{(k1)(fg)f(P, G)f(P, X)}{f(p)(dTr)^{k2}f(Q, G, h_{fg}, X_i, X_1)f(P, G, h_{fg}, X_i, X_1)f(P, X_i, X_1)} \quad . \qquad (4.3\text{-}1)$$

Another name for the ratio is the departure from nucleate boiling ratio (DNBR) used to evaluate margins. However, this is a "loose" definition for the term since it can not be used to specify power margins as will be explained below.

There are four different formulations of the correlations (basic, flux, geometry, and power) with three different internal coefficient sets which are chosen by the user on Word 12 of the 1CCCG801 through 1CCCG899 or 1CCCG901 through 1CCCG999 cards. The “basic” form uses the local equilibrium quality and the local heat flux. The “flux” form uses the local heat flux and the heated length including the axial power peaking factor. The “geometry” form uses the local equilibrium quality and the heated length including the axial power peaking factor. The “power” form comes from a heat balance method and can be used to calculate the critical power ratio (CPR). When the first three forms are used, the resulting ratio represents the departure from nucleate boiling ratio (DNBR).

Reference 4.3-4 discusses two type of methods to obtain the DNBR. They are the direct substitution method (DSM) (also called the constant dryout quality approach) and the heat balance method (HBM) (also called the constant inlet subcooling approach). The DSM uses the available thermal-hydraulic and geometry information and predicts the DNBR at each point along the channel based on the input heat flux at each point. This method is used in the “Table Lookup” approach as well as the first three PG-CHF approaches. The HBM is more computer intensive because it uses iteration to adjust the power level so that the local quality at the point in question is just equal to the critical quality. Then the channel total power is the power which results in a critical heat flux at the point in question. The critical power ratio (CPR) is the ratio of the power which first causes critical conditions to exist at any axial location divided by the operating power. The DSM yields the correct CPR only when the DNBR is 1.0. The DNBR calculated by the DSM are generally higher than those calculated by the HBM and are, therefore, of only relative value when used to evaluate power margins. The “power” form of the PG-CHF correlations should be used when a critical power ratio is desired.

The HBM generally yields better statistical agreement with data than does the DSM. The PG correlations were assessed using the DSM on the Czech data base. Moreover, the PG correlations were verified on Westinghouse (WEC) and Combustion Engineering (CE) rod bundle data bases.[4.3-1] Statistical results are shown in **Table 4.3-2**. $\overline{R}$ is the mean value of R and S_R is the standard deviation. These results do not involve use of any favorable feedback from the rod bundle statistical error factor, fg, (described later), i.e., fg was set to 1.0. The rod bundle error statistics are based on an isolated (no crossflow) subchannel model. The mean error and standard deviation are defined by

Table 4.3-2 Statistical error analysis results of the PG correlations for five data bases.

Correlation type	**$\overline{R}/S_R$ (mean error value/standard deviation)**				
Basic form or flux form or geometry form	1.001/0.056	0.998/0.052	0.987/0.081	0.947/0.06	1.021/0.08
Power form	1.003/0.103	0.999/0.126	0.993/0.145	0.959/0.111	1.064/0.258
Total points	9,547	713	7,616	2,485	4,689
Data base	Czech	Czech	Czech	WEC	CE
Geometry	Tube	Annulus	Rod-bundle-isolated subchannel		

$$\bar{R} = \frac{1}{n}\sum_{i=1}^{n} R_i \qquad (4.3\text{-}2)$$

$$S_R = \left[\frac{1}{n-1}\sum_{i=1}^{n}(R_i - \bar{R})^2\right]^{0.5} . \qquad (4.3\text{-}3)$$

Some ATHENA users may model reactor cores which include radial crossflow and axial stacks of heat slabs with differing hydraulic inlet cells. This type of modeling is more realistic than isolated subchannel modeling for open lattice cores but the statistical errors will not apply under these conditions.

The documentation of the correlations can be best described in terms of user options. Word 12 on the 1CCCG801 through 1CCG899 or 1CCCG901 through 1CCCG999 cards is a two-digit word. The left digit indicates one of four PG-CHF correlations as shown in **Table 4.3-3**. The right digit specifies the geometry type as shown in **Table 4.3-4**. Use of right digit values 4 and 5 for rod bundles is also possible but is not discussed here.

Table 4.3-3 User PG-CHF correlation form.

Correlation type	Subroutine name	Word 12 left digit
Basic form	CHFPG	1
Flux form	CHFPGF	2
Geometry form	CHFPGG	3
Power form	CHFPGP	4

Table 4.3-4 User PG-CHF geometry type.

Geometry type	Word 12 right digit
Tube	1
Internally heated annulus	2
Rod bundle	3

This two-digit word forms a key word known as kg in the subroutines and the equations presented below. If the mass flux is in the range from -100 to +100 kg/m^2-s, the value of 100 kg/m^2-s is used in the PG correlations and the final value of CHF is mass flux interpolated between the PG-CHF and the modified Zuber value (the next section of reflood gives the Zuber expression). Use of the PG-CHF method

requires users to specify which volume is the bundle inlet volume for both forward and reverse flow. Inlet volume information is needed for ATHENA to obtain the channel inlet quality.

There are at least three distinct type of hydraulic models used to model reactor cores. The modeling terminology needs to be addressed to help readers understand the following paragraphs dealing with how to best use the PG-CHF correlations.

- Isolated subchannel model - Code users are using an “isolated subchannel model” when they use one heat structure connected to a hydraulic flow channel with no crossflow. The contiguous stack of hydraulic volumes could represent a heated pipe or annulus, a fuel rod subchannel, a rod bundle, or a complete core. Local coolant parameters in the “isolated subchannel model” are determined in ATHENA by applying conservation equations in an isolated (radially closed) stack of coolant cells.

- Bundle mean parameters model - This model has multiple heat structures connected to each hydraulic cell but, again the cells do not allow crossflow. Use of the word “mean” is appropriate because the hydraulic conditions are the result of the integral of the heat flux from all the heat structures connected to a cell.

- Subchannel mixing model - This model uses mixing coefficients among adjacent coolant cells to determine local coolant parameters in every rod cell. The model is used in subchannel codes (COBRA, VIPRE, etc.). Determined local parameters depend on mixing coefficient values. If the mixing coefficient is zero the model transforms into the isolated subchannel model and if the mixing coefficient is infinite the model transforms into the bundle mean parameters model.

Normally, users would choose the basic form of the correlation for the heated channel representing a tube, an internally heated annulus, or a rod bundle. However, depending on the nodalization used to model the heated channel, the choice of the flux form can be recommended. Here is an example. When modeling the core region, the modeling practice is to place the hydraulic node boundaries at the position of grid spacers. The user may still need more detailed axial nodalization of the heat structure representing a fuel rod, e.g., two or more axial segments over one axial hydraulic node. If the basic form of the correlation is used in this case, local information for the bottom node is lost to some extent, because the code calculates volume averaged thermodynamic quality. If the flux form of the correlation is used in this case, local information is retained, because the heated length including the axial peaking factor is used instead of the thermodynamic equilibrium quality. When modeling rod bundles, the flux form of the correlation can be used only if the isolated subchannel thermal-hydraulic model is applied. The geometry form of the correlation may be of interest if the user prefers its combination of local parameters. Again, when modeling rod bundles, the geometry form of the correlation can be used only if the isolated subchannel thermal-hydraulic model is applied.

The power form of the correlation would be chosen if the thermal-hydraulic analysis is performed to calculate the critical power ratio. For example, if a heated channel is operated in steady-state, the maximum power to avoid boiling crisis can be determined in a single ATHENA run. Note that a series of

trial and error runs would be needed if the other forms of correlations are used to solve this problem. Again, when modeling rod bundles, the power form of the correlation can be used only if the isolated subchannel thermal-hydraulic model is applied.

4.3.1 PG-CHF Basic Form

When the user sets Word 12 (kg) to 11, 12, or 13 on the 1CCCG801 through 1CCCG899 or 1CCCG901 through 1CCCG999 cards, subroutine CHFPG is called. This form of the correlation set calculates the ratio of the critical heat flux to the local heat flux. This ratio, R, is printed on the output in place of the CHF multiplier. The expression for the flux ratio is

$$R = \frac{(k1)(fg)(f1)(f2)}{(fp)(dTr)^{k2}(fxx)(f3)(f4)(f5)} \tag{4.3-4}$$

where

$$k1 = \begin{cases} 70.9 & \text{if kg = 11} \\ 102.1 & \text{if kg = 12} \\ 109.8 & \text{if kg = 13} \end{cases}$$

fg = Word 4 or 5 on the 1CCCG801 through 1CCCG899 or 1CCCG901 through 1CCCG999 cards. The value of fg is 1.0 unless the code user has statistical error data from the PG correlation based on experimental CHF data of an examined fuel design.

$$fg = \begin{cases} 1.0 & \text{if kg = 11, 12} \\ \dfrac{1}{\bar{R}} & \text{if kg = 13} \end{cases}$$

use fg = 1 if statistical data is not available

$$f1 = W^{(0.126 + 0.22P_{red})}$$

W = max (absolute value of total mass flux G, 50 kg/m^2-s)

P_{red} = pressure/critical pressure

f2 = $1.9 + 8P_{red}^{10} - P_{red} - X_i$

X_i = thermodynamic equilibrium quality at the channel inlet

fp = $\begin{cases} 0.17 + P_{red} + 1.82P_{red}^2 + 17.7P_{red}^{12} & \text{if kg = 11} \\ 0.2 + P_{red} + 1.2P_{red}^2 + 14.4P_{red}^{11} & \text{if kg = 12, 13} \end{cases}$

dTr = hydraulic equivalent diameter (d) times Tr. Tr is the radial heat flux distribution parameter defined in Word 6 on the 1CCCG801 through 1CCCG899 or 1CCCG901 through 1CCCG999 cards

d = equivalent hydraulic diameter. Set Word 1 = 0 on the 1CCCG801 through 1CCCG899 or 1CCCG901 through 1CCCG999 cards

Tr = $Q\left(\frac{\sum_i \text{Perimeter}_i}{\sum_i Q_i \text{Perimeter}_i}\right)$

i = one of all surfaces adjacent to the hydraulic channel

Q = local heat flux on surface (Q has units of MW/m^2)

k2 = $\begin{cases} 0.15 & \text{if kg = 11} \\ 0.04 & \text{if kg = 12, 13} \end{cases}$

yta = Word 2 or 3 on the 1CCCG801 through 1CCCG899 or 1CCCG901 through 1CCCG999 cards

fx = $0.25\ W\ h_{gf} \max [1 \times 10^{-9}, (X_1 - X_i)]$

fxx = $\max\left[fx, 0.5 \bullet yta\frac{Q}{dTr}\right]$

h_{gf} = difference between saturated vapor and liquid specific enthalpy divided by one million

X_1 = local thermodynamic equilibrium quality

$$f3 = 1 + \frac{40}{30 + \frac{fx}{Q + 1x10^{-9}}}$$

$$f4 = 1 + \frac{400 + \frac{10}{0.016 + P_{red}^{1.8}}}{30 + fx}$$

$$f5 = \left(1 + \frac{1.8}{h1}\right)\left(1 + \frac{1x10^{-3}}{6x10^{-3} + h_2^3}\right)$$

$$h1 = \max\left(1 \times 10^{-9}, 1.6 + 4P_{red} - h11\right)$$

$$h11 = \max\left(X_i, X_1\right)$$

$$h2 = h11 - X_i.$$

The correlation has no explicitly defined axial position or axial shape factor. Axial information is represented by the change in quality from the inlet to the point in question.

Note that on the first time step, the local heat flux, Q, is unknown. For this reason subroutine CHFPG is not initially called. The power form of the correlation, subroutine CHFPGP, is called first. This calling sequence is used even if the CHF subroutines are not called until sometime after the first time step.

4.3.2 PG-CHF Flux Form

When the user sets Word 12 (kg) to 21, 22, or 23 on the 1CCCG801 through 1CCCG899 or 1CCCG901 through 1CCCG999 cards, subroutine CHFGF is called. This form of the correlation set also calculates the ratio of the critical heat flux to the local heat flux. It requires additional geometry information (pertaining to the distance from the inlet and the axial power distribution). The additional geometry information effectively replaces local quality as a correlating parameter. The expression for the flux ratio is

$$R = \frac{(k1)(fg)(f1)(f2)}{(fp)(dTr)^{k2}(Q + 1x10^{-9})(fgg)(f3)(f4)(f5)} \qquad (4.3\text{-}5)$$

where

$$k1 = \begin{cases} 70.9 & \text{if kg} = 21 \\ 102.1 & \text{if kg} = 22 \\ 109.8 & \text{if kg} = 23 \end{cases}$$

$$fg = \begin{cases} 1.0 & \text{if kg} = 21, 22 \\ \dfrac{1}{\bar{R}} & \text{if kg} = 23 \end{cases}$$

use fg = 1 if statistical data is not available

yta = Word 2 or 3 on the 1CCCG801 through 1CCCG899 or 1CCCG901 through 1CCCG999 cards

$$fgg = \frac{yta}{dTr}$$

$$fp = \begin{cases} 0.17 + P_{red} + 1.82P_{red}^2 + 17.7P_{red}^{12} & \text{if kg} = 21 \\ 0.2 + P_{red} + 1.2P_{red}^2 + 14.4P_{red}^{11} & \text{if kg} = 22, 23 \end{cases}$$

$$f3 = 1 + \frac{40}{30 + fgg}$$

$$f4 = 1 + \frac{400 + \dfrac{10}{0.016 + P_{red}^{1.8}}}{30 + Q \bullet fgg}$$

$$f5 = \left(1 + \frac{1.8}{h1}\right)\left(1 + \frac{1x10^{-3}}{6x10^{-3} + h_2^3}\right)$$

$$h1 = \max\left(1 \times 10^{-9}, 1.6 + 4\,P_{red} - X_i - h_2\right)$$

$$h2 = \frac{4Q \bullet fgg}{W \bullet fgg}.$$

For Q, W, h_{gf}, P_{red}, X_1, X_i, dTr, f1, f2, and k2 see Section 4.3.1.

4.3.3 PG-CHF Geometry Form

When the user sets Word 12 (kg) to 31, 32, or 33 on the 1CCCG801 through 1CCCG899 or 1CCCG901 through 1CCCG999 cards, subroutine CHFPGG is called. This form of the correlation set also calculates the ratio of the critical heat flux to the local heat flux. The expression for the flux ratio is

$$R = \frac{(k1)(fg)(f1)(f2)}{(fp)(dTr)^{k2}(fxx)(f3)(f4)(f5)} \tag{4.3-6}$$

where

$$k1 = \begin{cases} 70.9 & \text{if } kg = 31 \\ 102.1 & \text{if } kg = 32 \\ 109.8 & \text{if } kg = 33 \end{cases}$$

$$fg = \begin{cases} 1.0 & \text{if } kg = 31, 32 \\ \dfrac{1}{\bar{R}} & \text{if } kg = 33 \end{cases}$$

use fg = 1 if statistical data is not available

$$fp = \begin{cases} 0.17 + P_{red} + 1.82P_{red}^2 + 17.7P_{red}^{12} & \text{if } kg = 31 \\ 0.2 + P_{red} + 1.2P_{red}^2 + 14.4P_{red}^{11} & \text{if } kg = 32, 33 \end{cases}$$

$$f4 = 1 + \frac{40}{30 + fx}$$

$$fx = 0.25\, W\, h_{fg} \max\left[1 \times 10^{-9}, (X_1 - X_i)\right]$$

$$fxx = \max(fx, 0.07\, fgg)$$

$$f3 = 1 + \frac{40}{30 + fgg}$$

$$f4 = 1 + \frac{400 + \dfrac{10}{0.016 + P_{red}^{1.8}}}{30 + fx}$$

$$f5 = \left(1 + \frac{1.8}{h1}\right)\left(1 + \frac{1x10^{-3}}{6x10^{-3} + h_2^3}\right)$$

$$h1 = \max(1 \times 10^{-9}, 1.6 + 4\,P_{red} - h11)$$

$$h11 = \max(X_i, X_1)$$

$$h2 = h11 - X_i.$$

For W, h_{fg}, P_{red}, X_1, X_i, dTr, f1, f2, and k2, see Section 4.3.1. For fgg, see Section 4.3.2.

4.3.4 PG-CHF Power Form

The power form is used, at least initially, for all heat structures. It is applicable to a tube, annulus, or an isolated subchannel in a rod bundle. When the user sets Word 12 (kg) to 41, 42, or 43 on the 1CCCG801 through 1CCCG899 or 1CCCG901 through 1CCCG999 cards, subroutine CHFPGP is called. This form of the correlation set predicts the critical heat flux in units of MW/m^2. An iterative procedure is used to find the root of a non-linear correlation. The root z represents the heat flux at the critical power level, i.e., CHF = z. This non-linear equation for CHF(z) is

$$z = \frac{fq4}{\left\{1 + \frac{1.8}{[h1 - (h2)(z)]}\right\}\left[1 + \frac{0.001}{0.006 + (x13)(z)^3}\right]}\left[\frac{30 + (fgg)(z)}{f4 + (fgg)(z)}\right] \qquad (4.3\text{-}7)$$

where

$$fq4 = \frac{(k1)(fg)(f1)(f2)}{(fp)(dTr)^{k2}(fgg)(f3)}$$

$$k1 = \begin{cases} 70.9 & \text{if } kg = 41 \\ 102.1 & \text{if } kg = 42 \\ 109.8 & \text{if } kg = 43 \end{cases}$$

$$fg = \begin{cases} 1.0 & \text{if } kg = 41, 42 \\ \frac{1}{\bar{R}} & \text{if } kg = 43 \end{cases}$$

use fg = 1 if statistical data is not available

$$fp = \begin{cases} 0.17 + P_{red} + 1.82P_{red}^2 + 17.7P_{red}^{12} & \text{if kg} = 41 \\ 0.2 + P_{red} + 1.2P_{red}^2 + 14.4P_{red}^{11} & \text{if kg} = 42, 43 \end{cases}$$

$$f4 = 430 + \frac{10}{0.016 + P_{red}^{1.8}}$$

$$h1 = 1.6 + 4\,P_{red} - X_i$$

$$h2 = 4\,\frac{fgg}{W\ h_{fg}}$$

$$x13 = h2^3.$$

For W, h_{fg}, P_{red}, X_i, dTr, f1, f2, and k2, see Section 4.3.1. For fgg and f3, see Section 4.3.2.

A guess of CHF(z) is made and the variable f(z) estimates the error. It is given by

$$f(z) = z - fq4\left\{\frac{1}{1 + \frac{1.8}{[h1 - (h2)(z)]}}\right\}\left[\frac{30 + (fgg)(z)}{f4 + (fgg)(z)}\right]\left[\frac{1}{1 + \frac{0.001}{0.006 + (x13)(z)^3}}\right] \quad (4.3\text{-}8)$$

The solution sequence is begun by calling the f(z) function twice; once with z = amin, and once with z = bmax, where

$$amin = 0.$$

$$bmax = 0.9999\,\frac{h_1}{h_2}$$

$$fa = f(amin)$$

$$fb = f(bmax).$$

Iteration is then used to find the root of f(z).

4.3.5 Boiling Surface Plots

Differences in the output of the PG and the table lookup method can be significant. Surface heat flux plots quickly reveal differences in the point wall temperatures that exceed the critical value. **Figure 4.3-1**

and **Figure 4.3-2** were generated for the two correlation types under low flow and low pressure conditions. The PG formulation uses the void weighted Zuber correlation at low flow. It shows a decreasing peak heat flux and decreasing critical temperature as the void fraction increases. The table lookup method shows an increasing critical temperature with increasing void fraction but the magnitude of the CHF (peak total heat flux) remains about the same. More data comparisons are needed under low flow, low pressure conditions.

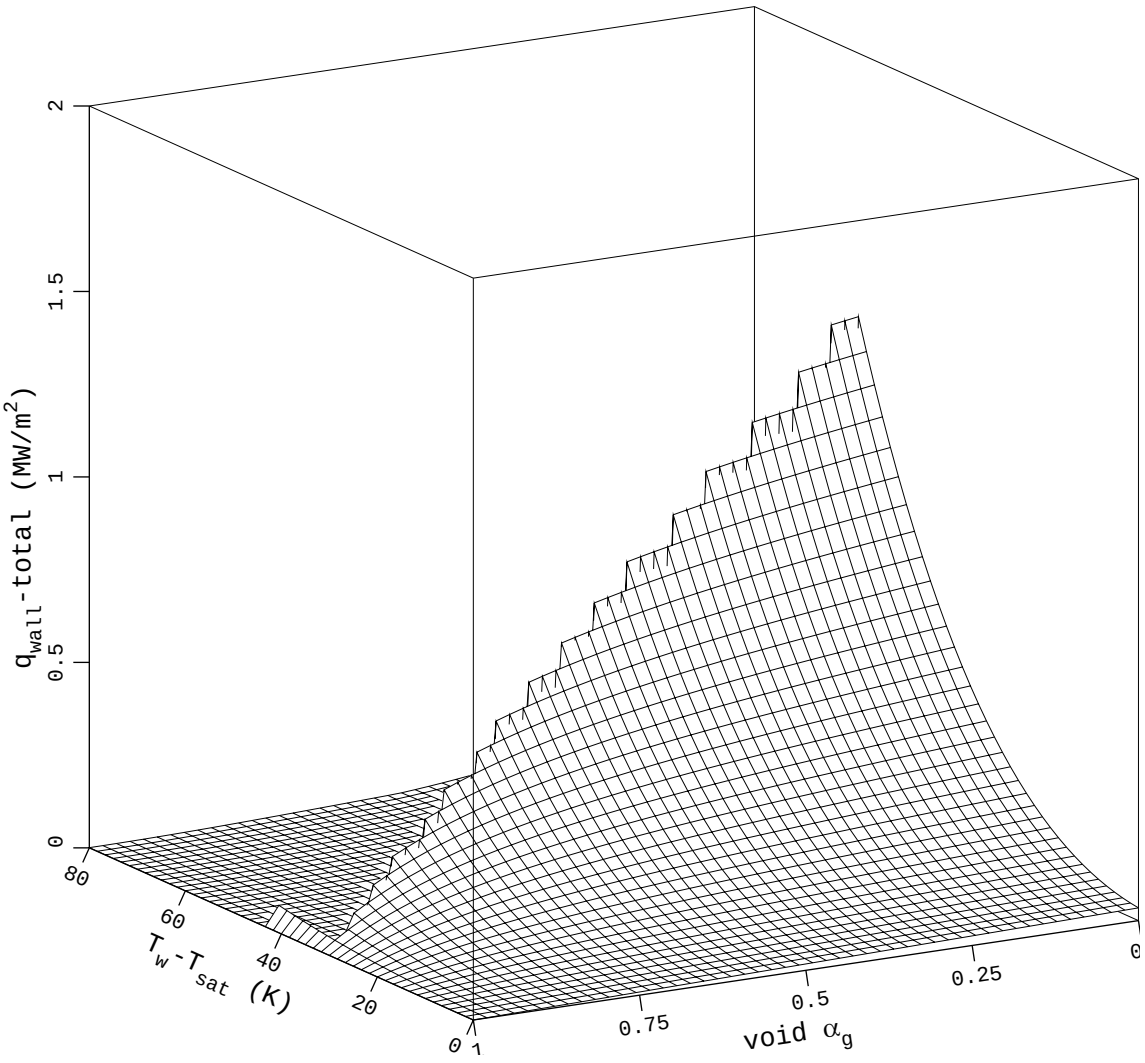

Figure 4.3-1 Boiling heat flux using PG-CHF.

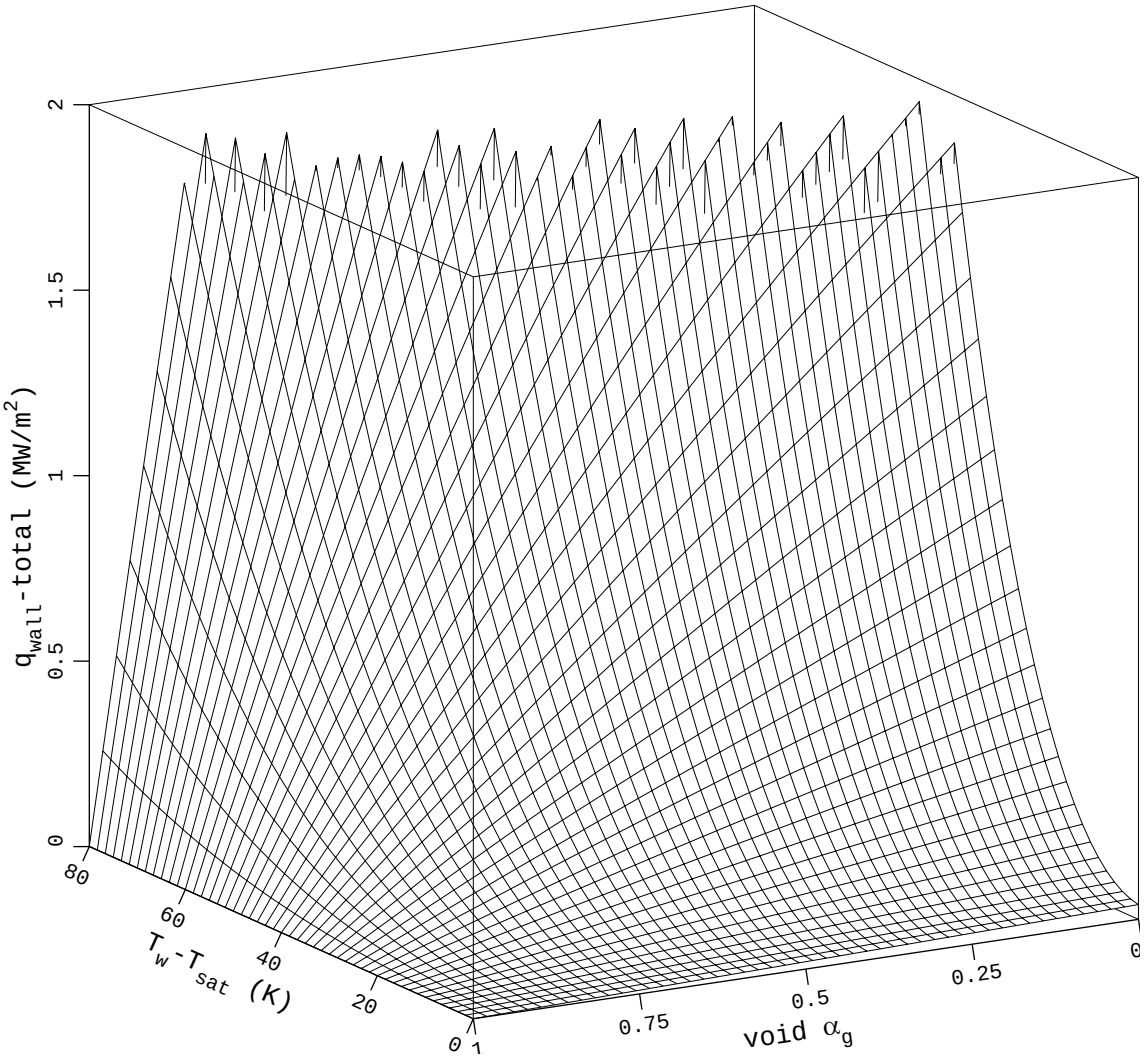

Figure 4.3-2 Boiling heat flux using table lookup of CHF.

4.3.6 References

4.3-1. R. Pernica and J. Cizek, "General Correlation for Prediction of Critical Heat Flux Ratio," *Proceedings of the 7th International Meeting on Nuclear Reactor Thermal-Hydraulics, NURETH-7, Saratoga Springs, NY, September 10 - 15, 1995*, NUREG/CP-0142, Vol. 4.

4.3-2. R. Pernica and J. Cizek, *PG General Correlation of CHFR and Statistical Evaluation Results*, NRI Report, UJV-10156-T, February 1994.

4.3-3. M. Kyncl, *Implementation of PG CHFR Correlation into RELAP5/MOD3.2*, NRIR Report, UJV-10739-T, August 1996.

4.3-4. P. Hejzlar and N. E. Todreas, “Consideration of Critical Heat Flux Margin Prediction by Subcooled or Low Quality Critical Heat Flux Correlations,” *Nuclear Engineering and Design, 163*, 1996, pp. 215-223.

4.4 Reflood Model

A reflood heat transfer model has been designed specifically for the reflood process which normally occurs at low flow and low pressure. The reflood model (which includes wall mesh rezoning and axial conduction) is activated in one of three ways as controlled by Word 6 on the first line of the general heat structure data (see Appendix A, Volume II). If users omit Word 6, or input as 0, no reflood occurs. If users input a trip number, reflood begins following trip activation. Users may also input a 1 or 2 which allows reflood to begin at pressures less than 1.2 MPa if the average core void fraction is greater than 0.9 or 0.1, respectively. The fine mesh rezoning scheme is described in Volume I. The modifications to the wall heat transfer coefficients when reflood is active are discussed here. Interfacial heat transfer and interfacial drag are also modified when reflood is active, and these modifications are also discussed here.

4.4.1 Introduction

The Paul Scherrer Institute (PSI) in Switzerland developed updates[4.4-1] to improve the quench front behavior during the reactor core reflood process. A modified version of these updates was incorporated into ATHENA along with a new quench front plotting capability.

4.4.2 Major Features of the Model

Changes were made to interfacial heat transfer, interfacial drag, and wall heat transfer. The changes to these models refer to the original models; the original models are discussed in Sections 4.1, 6.1 and 4.2 respectively, of this volume of the manual. Whenever a code user activates the reflood model (see Appendix A, Volume II of the manual), the code uses these model changes. Parts of the PSI model which were not implemented were: (1) disabling interfacial time smoothing, and (2) using TRAC’s interpolation method for transition boiling (used for non-reflood heat structures). PSI found that disabling time smoothing gave smoother results in an older RELAP5 version. This feature is not needed in the current ATHENA code version.

4.4.3 Interfacial Heat Transfer

The interfacial area is changed in a control volume next to a heat structure with reflood activated. Both the wet and dry wall interfacial areas were changed in subroutine FIDISV. The wet wall droplet diameter (d_d) maximum (D’) was reduced from 2.5 mm to 1.5 mm. The dry wall Weber number was reduced from 12 to 3.

The logic for deciding whether the wall was wet or dry was also changed in subroutine PHANTV. A variable, tgsat, was reduced by 30 K for a rod bundle. Tgsat was previously T_g - T^s - 1. This variable affects both the value of the variables poschf and pfinrg. Poschf is a logical variable that is set true when a

heat structure transfers positive heat flux to the vapor/gas and tgsat is greater than zero. If reflood is on and poschf is true, then

$$\text{pfinrg} = \max\{0.0,\min[1.0,(1. - e^{-0.5\text{tgsat}})1.0000454]\} \quad (4.4\text{-}1)$$

for a bundle and

$$\text{pfinrg} = \max[0.0, \min(1, \text{twindo} \bullet \text{tgsat})] \quad (4.4\text{-}2)$$

for a non-bundle.

Twindo is pressure dependent and is given by

$$\text{twindo} = \begin{cases} 0.06666667 & P_{red} \le 0.025 \\ 0.01666667 & P_{red} \ge 0.25 \\ \text{Interpolate} & 0.025 < P_{red} < 0.25 \end{cases} \quad (4.4\text{-}3)$$

where

$$P_{red} = \frac{\text{pressure}}{\text{critical-pressure}}.$$

When pfinrg is equal to 1, the dry wall variable posdry is true, and the dry wall Weber number and drop size are used instead of the wet wall values. Pfinrg is also used as an interfacial heat transfer coefficient interpolating value between wet and dry conditions. When poschf is false, pfinrg is zero.

When reflood is not active and poschf is true, pfinrg is given by

$$\text{pfinrg} = \max[0.0, \min(1, \text{twindo} \bullet \text{tgsat})] \quad . \quad (4.4\text{-}4)$$

The purpose of reducing tgsat and changing the definition of pfinrg for reflood in a bundle was to force the code to use wet wall interfacial values close to the quench front. The 30 degree tgsat reduction was developed by comparing calculations with data.

4.4.4 Interfacial Drag

Subroutines FIDIS2 and PHANTJ (used for interfacial drag calculations) were changed in the same manner as were subroutines FIDISV and PHANTV. In addition, subroutine FIDISJ was changed when reflood and the bundle flag are active adjacent to a hydraulic junction. The modified Bestion correlation

(by Analytis[4.4-1]) is used for interfacial drag in vertical bubbly-slug flow at pressures below 10 bars in place of the EPRI correlation. Above 20 bars the EPRI correlation is used. Between 10 and 20 bars the interfacial drag is interpolated. The modified Bestion correlation for the code interfacial drag coefficient, C_i, is coded in subroutine FIDISJ as

$$C_i = \frac{65\alpha_g\rho_g(1-\alpha_g)^3}{D} \tag{4.4-5}$$

where

C_i = interfacial drag coefficient (the variable name is fic in subroutine FIDISJ)

α_g = junction vapor/gas void fraction (see Section 6.1)

ρ_g = donored junction vapor/gas density

D = junction hydraulic diameter.

The void distribution parameter C_0 is set to 1.2.

4.4.5 Wall Heat Transfer

Changes occur in transition and film boiling heat transfer coefficients, both with and without the hydraulic bundle flag activated, when reflood is active.

Quenching can occur at both ends of rod bundles. Quench front advancement is determined in subroutine QFHTRC and keys off the mode number. The current fine mesh is considered to be wetted when the mode number is less than 5. Quench fronts can also recede if dryout reoccurs. **Figure 4.4-1** illustrates a bottom wetted region (wetbot) and top wetted region (wettop) along with distance variables used by the code and variables used in this section of the manual.

Some of the ideas for the empirical methods described below were taken from the CATHARE code by PSI.

4.4.5.1 Bottom Quench Front Model. The magnitude of the transition or film boiling heat transfer coefficient may be altered if the point in question is close to the bottom quench position and either the bundle option or non-bundle option is on.

A modified Weisman[4.4-2] correlation replaces the Chen-Sundaram-Ozkaynak[4.4-3] transition boiling correlation. The modified Weisman correlation is

.

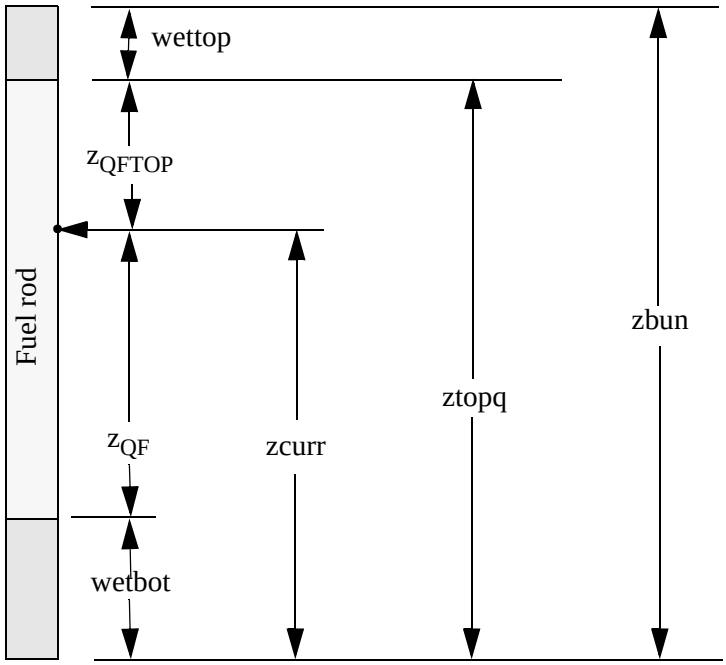

Figure 4.4-1 Fuel rod showing variables used by the reflood model.

$$h_w = h_{max}(e^{-0.02\Delta T_{wchf}}) + 4500\left(\frac{G}{G_R}\right)^{0.2}(e^{-0.012\Delta T_{wchf}}) \quad (4.4\text{-}6)$$

where

h_{max} = $\frac{0.5\ CHF}{\Delta T_{chf}}$

CHF = critical heat flux

ΔT_{chf} = max[3 K, min (40 K, T_w - T_{spt})]

ΔT_{wchf} = max (0, T_w - T_{wchf})

G = total mass flux

G_R = 67.8 kg/m^{2}s

T_{wchf} = wall temperature at critical heat flux.

The original Weisman correlation used 0.04 in place of 0.02. The 0.5 multiplier in h_{max} was not in the PSI updates as received but was added to reduce the magnitude of the spike in heat flux to the fluid which occurs near the critical heat flux temperature. Reducing this spike is the whole motivation behind the reflood model. The reduction is physically justified because of the hysteresis in going from nucleate boiling to transition boiling and back.[4.4-4] The magnitude of the peak flux is much less on the return trip.

Code use of the modified Weisman correlation depends on the distance from the point in question to the quench front position. The transition boiling heat transfer coefficient to liquid, h_{fTB}, is given by

$$h_{fTB} = \begin{cases} h_{high} & z_{QF} \le 0.1 \text{ m} \\ h_{low} & z_{QF} \ge 0.2 \text{ m} \\ \text{Interpolate} & 0.1 \text{ m} < z_{QF} < 0.2 \text{ m} \end{cases} \quad (4.4\text{-}7)$$

where

h_{high} = $\min(h_{max},h_w)$

z_{QF} = distance from the point in question to the bottom quench front

h_{low} = 0.0001 W/m^2K.

As the void fraction goes above 0.95, the value of h_{fTB} is ramped to zero at a void fraction of 0.99. The transition boiling heat flux to liquid, q_{fTB}, is h_{fTB} $(T_w - T_{spt})$.

The transition boiling heat transfer coefficient to vapor/gas, h_{gTB}, comes from the single-phase vapor/gas correlations previously discussed in Section 4.2.3.1. This is calculated from a call to the DITTUS subroutine using vapor/gas properties. The coefficient, h_{Ditt}, calculated by this routine is then void fraction ramped so that it goes to zero as the void fraction goes to zero and is given by

$$h_{gTB} = h_{Ditt}\,\alpha_g \ . \quad (4.4\text{-}8)$$

The transition boiling heat flux to vapor/gas, q_{gTB}, is h_{gTB} $(T_w - T_g)$.

The film boiling heat transfer coefficient to liquid, h_{fFB}, uses the maximum of a film coefficient, h_{FBB}, the modified Forslund-Rohsenow[4.4-5] correlation coefficient, h_{FR}, and the normal ATHENA Bromley[4.4-6] correlation. The film coefficient, h_{FBB}, is given by

$$h_{FBB} = \{1{,}400 - [1{,}880 \max(0.005\text{m}, z_{QF})]\}\min(0.99 - \alpha_g, 0.5) + h_{FBGR}(0.99 - \alpha_g)^{0.5} \quad . \tag{4.4-9}$$

The first part of h_{FBB} is an empirical length dependent expression, and the second part includes a modified Bromley correlation coefficient, h_{FBGR}, which uses z_{QF} for the length in the denominator instead of the wave length as does the normal ATHENA Bromley correlation. The modified Bromley correlation coefficient used here is given by

$$h_{FBGR} = 0.62\left\{\frac{gk_g^3\rho_g(\rho_f - \rho_g)[h_{fg} + 0.5C_{pg}(T_w - T_{spt})]}{\max(0.005\text{m}, z_{QF})\mu_g(T_w - T_{spt})}\right\}^{0.25} \quad . \tag{4.4-10}$$

The modified Forslund-Rohsenow correlation coefficient is given by

$$h_{FR} = h1\left[\frac{g\rho_g\rho_f h_{fg}k^3}{(T_w - T_{spt})\mu_g d\left(\frac{\pi}{6}\right)^{\frac{1}{3}}}\right]^{0.25} \tag{4.4-11}$$

where

$$h1 = 0.4\left(\frac{\pi}{4}\right)\left[\frac{6(0.99 - \alpha_g)}{\pi}\right]^{\frac{2}{3}}.$$

$$d = \min\left[0.003\text{m}, \max\left(0.0001\text{m}, \frac{3\sigma}{\rho_g\{\max[0.01\text{m}^2/\text{s}^2, (v_g - v_f)^2]\}}\right)\right] \tag{4.4-12}$$

where

v_g = vapor/gas velocity

v_f = liquid velocity.

The normal ATHENA Bromley correlation used in the maximum for the reflood film boiling heat transfer coefficient to liquid, h_{fFB}, is the same as Equation (4.2-26), except that the void factor M_a linearly smooths the h over the void fraction range 0.0 to 0.99 rather than over the range 0.02 to 0.99.

Radiation to droplets (Sun, Gonzalez-Santalo, and Tien[4.4-7]) is added to the final film boiling coefficient to liquid, h_{fFB}, which is the maximum of Equation (4.4-9), Equation (4.4-11), and the normal ATHENA Bromley correlation discussed above. The final value is multiplied times T_w - T_{spt} to get the film boiling heat flux to liquid.

The film boiling heat flux to vapor/gas is the same as the transition boiling value.

4.4.5.2 Top Quench Front Model. The magnitude of the transition or film boiling heat transfer coefficient may be altered if the point in question is close to the top quench position and the bundle option is used. This is a new model not described in any other literature. This model is only used for a bundle.

The transition boiling heat transfer coefficient to liquid is

$$h_{fTB} = \begin{cases} h_{high} & z_{QFTOP} \le 0.1 \text{ m} \\ \max[h_{low}(\text{from above}), h_{fTB}(\text{from above})] & z_{QFTOP} \ge 0.2 \text{ m} \\ \text{Interpolate} & 0.1 \text{ m} < z_{QFTOP} < 0.2 \text{ m} \end{cases} \quad (4.4\text{-}13)$$

where

h_{high} = $\min(h_{max}, h_w)$

z_{QFTOP} = distance from the point in question to the top quench front

h_{max} = $\dfrac{0.5 \text{ CHF}}{\Delta T_{chf}}$

CHF = ctitical heat flux

ΔT_{chf} = $\max[1 \text{ K}, \min(40 \text{ K}, T_w - T_{spt})]$

h_w = $h_{max}(e^{-0.05\Delta T_{wchf}}) + 4500\left(\dfrac{G}{G_R}\right)^{0.2}(e^{-0.012\Delta T_{wchf}})$

ΔT_{wchf} = $\max(0, T_w - T_{wchf})$

G = total mass flux

G_R = 67.8 kg/m^{2}s

T_{wchf} = wall temperature at critical heat flux.

As the void fraction goes above 0.95, the value of h_{high} is ramped to zero at a void fraction of 0.99.

The derivation of the film boiling heat transfer coefficient to liquid, h_{fFB}, is similar to that of the bottom quench front. The modified Bromley coefficient [similar to Equation (4.4-10)] here uses z_{QFTOP} for the length term and is given by

$$h_{FBGR} = 0.62\left\{\frac{gk_g^3\rho_g(\rho_f-\rho_g)[h_{fg}+0.5C_{pg}(T_w-T_{spt})]}{\max(0.005m, z_{QFTOP})\mu_g(T_w-T_{spt})}\right\}^{0.25} . \quad (4.4\text{-}14)$$

This value is multiplied times $(0.99 - \alpha_g)^{0.5}$ and is added to an empirical length dependent expression as in Equation (4.4-9) to give

$$h_{FBB} = \{600-[5{,}000\ \max(0.005m, z_{QFTOP})]\}\min(0.99-\alpha_g, 0.5) + h_{FBGR}(0.99-\alpha_g)^{0.5} . \quad (4.4\text{-}15)$$

The maximum of Equation (4.4-15), the modified Forslund-Rohsenow correlation Equation (4.4-11), and the final bottom quench value of h_{fFB} (see Section 4.4.5.1) is used to obtain the top quench value of h_{fFB}. The values of 600 and 5,000 in Equation (4.4-15) have not been assessed. They were chosen to demonstrate the feasibility of the model.

For the top quench front model, Equation (4.4-8) is used for the vapor/gas heat transfer coefficient in both transition and film boiling. Thus, the top quench and bottom quench front models are the same for this coefficient.

4.4.5.3 Low Flow CHF. The reflood model uses a modified Zuber[4.4-8] CHF correlation instead of the Groeneveld Table Lookup[4.4-9] at low values of mass flux.

ATHENA calculates a wall heat flux for both liquid and vapor/gas and computes a heat flux in both film boiling and transition boiling. This is done in subroutine PSTDNB. Before calling subroutine PSTDNB, subroutine CHFCAL has been called to obtain the critical heat flux. The critical heat flux value from the Groeneveld Table Lookup is returned unless the mass flux is less than 200 kg/m^{2}s. Below a mass flux of 100 kg/m^{2}s, the modified Zuber correlation is used and is given by

$$CHF = \max[0.04, (1-\alpha_g)]0.13h_{fg}[\sigma g(\rho_f-\rho_g)]^{0.25}\rho_g^{0.5} \quad (4.4\text{-}16)$$

where

h_{fg} = saturation specific enthalpy difference between vapor and liquid

σ = surface tension

g = gravitational constant.

The term $(1-\alpha_g)$ is the Griffith[4.4-10] modification to the Zuber correlation. Between a mass flux of 100 and 200 kg/m^2-s interpolation is used.

4.4.6 Reflood Summary

ATHENA capability has been enhanced by the addition of a new reflood model. **Table 4.4-1** is presented to help clarify the correlation use differences with/without reflood activated and with/without the bundle flag set.

Table 4.4-1 Reflood correlation usage.

Non-reflood slabs		**Reflood slabs**	
Bundle	**Non-bundle**	**Bundle**	**Non-bundle**
Interface flow regime: original	Interface flow regime: original	Interface flow regime: modified	Interface flow regime: modified
Film boiling: Bromley	Film boiling: Bromley	Film boiling: modified Bromley and modified Forslund-Rohsenow	Film boiling: modified Bromley and modified Forslund-Rohsenow
Transition boiling: Chen	Transition boiling: Chen	Transition boiling: modified Weisman	Transition boiling: modified Weisman
Critical Heat Flux: Groeneveld	Critical Heat Flux: Groeneveld	Critical Heat Flux: Groeneveld and modified Zuber	Critical Heat Flux; Groeneveld and modified Zuber
Interface drag: EPRI and others	Interface drag: less EPRI and more others	Interface drag: modified Bestion, EPRI and modified others	Interface drag: less EPRI and more modified others

4.4.7 References

4.4-1. G. Th. Analytis, "Developmental Assessment of RELAP5/MOD3.1 with Separate Effect and Integral Test Experiments: Model Changes and Options," *Nuclear Engineering and Design, 163,* 1996, pp. 125-148.

4.4-2. J. Weisman, *Studies of Transition Boiling Heat Transfer at Pressure from 1-4 Bar*, EPRI NP-1899, 1981.

4.4-3. J. C. Chen, R. K. Sundaram, and F. T. Ozkaynak, *A Phenomenological Correlation for Post-CHF Heat Transfer*, NUREG-0237, June 1977.

4.4-4. R. W. Shumway, "Return to Nucleate Boiling," *ANS Proceedings, 1985 National Heat Transfer Conference, Denver, CO, August 4 - 7, 1985.*

4.4-5. R. P. Forslund and W. M. Rohsenow, "Dispersed Flow Film Boiling," *Transactions of the ASME, Journal of Heat Transfer, 90*, 1968, pp. 399-407.

4.4-6. L. A. Bromley, "Heat Transfer in Stable Film Boiling," *Chemical Engineering Progress, 46*, 1950, pp. 221-227.

4.4-7. K. H. Sun, J. M. Gonzalez-Santalo, and C. L. Tien, "Calculations of Combined Radiation and Convection Heat Transfer in Rod Bundles Under Emergency Cooling Conditions," *Transactions of the ASME, Journal of Heat Transfer, 98*, 1976, pp. 414-420.

4.4-8. N. Zuber, M. Tribus, and T. W. Westwater, "The Hydrodynamic Crisis in Pool Boiling of Saturated and Subcooled Liquids," *Proceedings of the 1961-1962 Heat Transfer Conference, Boulder, CO, August 28-September 1, 1961, and London, UK, January 8-12, 1962, International Developments in Heat Transfer, ASME, New York, 1963*, pp. 230-236.

4.4-9. D. C. Groeneveld, S. C. Cheng, and T. Doan, "1968 AECL-UO Critical Heat Flux Lookup Table," *Heat Transfer Engineering, 7*, 1-2, 1986, pp. 46-62.

4.4-10. P. Griffith, C. T. Avedissian, and J. F. Walkush, "Countercurrent Flow Critical Heat Flux," *Annual Heat Transfer Conference, San Francisco, CA, August 1975.*

4.5 Wall-to-Wall Radiation

ATHENA has a model that calculates wall-to-wall radiation heat transfer directly, whereas RELAP5/MOD2 did not. The model is presented in Volume I of this code manual and is not repeated here. One weakness of the model is that it does not include absorption by the fluid between the surfaces.

4.6 Energy Source Term

Volumetric heat sources can be placed into any heat structure in ATHENA. The power for the heat source can be determined from the reactor kinetics package that calculates the time-dependent power response, or from a table, or a control system. The internal power source can be partitioned by the use of three factors.

The first factor is applied to indicate the internal heat source generated in the heat structure. The other two factors provide for direct heating of the fluid in the hydrodynamic volumes communicating with the heat structure surface. A user-specified multiplicative factor times the internal power in the heat structure is added directly to the energy source term in the associated control volume to provide the direct moderator heating. The energy transferred is partitioned between the liquid and vapor/gas phases by means

of the static quality. The sum of all the factors multiplying the source power should be unity to conserve energy in the calculation.

The direct heating model is simply a portioning of energy and is clearly applicable in any situation where the application of direct heating has been justified. No scaling dependence or uncertainties past those associated with the determination of the input are introduced by the model itself.

4.7 Near Wall and Bulk Interfacial Heat Transfer

The heat transfer correlations described above determine a heat transfer coefficient which relates an energy transfer rate to a temperature difference. Two distinct cases were discussed: (a) interfacial heat transfer through an assumed interface as a result of differences in the bulk temperature of the liquid and vapor/gas phases, and, (b) wall heat transfer, providing energy to either the liquid or vapor/gas phase, or both. A special case of wall heat transfer occurs when the wall is communicating with a two-phase mixture, for then boiling or condensation can occur as a direct result of the wall heat transfer. This heat transfer is referred to as near wall interfacial heat transfer and is similar to the bulk interfacial heat transfer described in (a), but it is treated separately in the code because it is not a result of differences between bulk phase temperatures. The following discussion will address the various heat transfer conditions by identifying those terms in the energy equation used to account for them and by showing the relationship of each term to the overall mass and energy balance. Because the interpretation of each of these terms in the energy equation is nontrivial, they will also be related to the heat transfer output information typically contained in a ATHENA major edit. The discussion to follow will address primarily the boiling model. The condensation model will be discussed briefly. The case of one wall connected to the fluid will be addressed initially, and Section 4.7.1.4 will contain a discussion of multiple walls connected to the fluid.

4.7.1 Interfacial Heat Transfer Terms in the Energy Equation

The phasic energy equations stated in Volume I of this manual, are

$$\frac{\partial}{\partial t}(\alpha_g \rho_g U_g) + \frac{1}{A}\frac{\partial}{\partial x}(\alpha_g \rho_g U_g v_g A) = -P\frac{\partial \alpha_g}{\partial t} - \frac{P}{A}\frac{\partial}{\partial x}(\alpha_g v_g A) + Q_{wg} + Q_{ig} + \Gamma_{ig} h_g^* + \Gamma_w h_g' - Q_{gf} + DISS_g \quad (4.7\text{-}1)$$

[I] [J] [K] [L]

$$\frac{\partial}{\partial t}(\alpha_f \rho_f U_f) + \frac{1}{A}\frac{\partial}{\partial x}(\alpha_f \rho_f U_f v_f A) = -P\frac{\partial \alpha_f}{\partial t} - \frac{P}{A}\frac{\partial}{\partial x}(\alpha_f v_f A) + Q_{wf} + Q_{if} - \Gamma_{ig} h_f^* - \Gamma_w h_f' + Q_{gf} + DISS_f \; . \quad (4.7\text{-}2)$$

[I] [J] [K] [L]

See Volume I for the meaning of these terms. The identification of the terms of interest here is

I	wall heat transfer
J	interphase heat transfer
K	interphase latent heat in the bulk
L	interphase latent heat near the wall.

Terms J (Q_{ig}, and Q_{if}) are interfacial heat transfer terms resulting from both bulk energy exchange due to phasic temperature differences and near wall energy exchange due to wall heat transfer in the form of boiling or condensing. They relate to both terms K and L, which are Γ_{ig}, the interfacial mass transfer resulting from a difference in phasic temperatures, and Γ_w, the mass transfer resulting from wall heat transfer.

These four terms relate the wall heat transfer to the fluid energy, and they relate each of the phases through the interfacial heat transfer. Terms I and L refer to wall heat transfer. Term I is the total wall heat transfer to the given phase, either liquid or vapor/gas, so the sum of Q_{wf} and Q_{wg} is the total wall heat transfer to the fluid space, Q, as shown in Volume I. The terms Q_{if}^W and Q_{ig}^W are the fraction of Q_{wf} and Q_{wg} resulting in mass transfer. Terms I and L are related through Γ_w. The association between heat and mass transfer near the wall is given in Equation (4.7-3) (boiling) and (4.7-4) (condensing), that is

$$\Gamma_w = \frac{-Q_{if}^W}{h_g' - h_f'} \qquad \Gamma_w > 0 \tag{4.7-3}$$

$$\Gamma_w = \frac{-Q_{ig}^W}{h_g' - h_f'} \qquad \Gamma_w < 0 \quad . \tag{4.7-4}$$

The relationships among terms I, J, K, and L are algebraically complete and correct in Volume I, so the derivations will not be repeated here. It is useful, however, to summarize the assumptions used to determine those relationships.

1. The phasic specific enthalpies, h_g^* and h_f^*, associated with bulk interphase mass transfer in Equations (4.7-1) and (4.7-2) are defined such that $h_g^* = h_g^s$ and $h_f^* = h_f$ for vaporization, and $h_g^* = h_g$ and $h_f^* = h_f^s$ for condensation. This is tantamount to the bulk fluid being heated or cooled to the saturation condition at the interface and the phase change taking place at saturation conditions. The same is true for the phasic specific enthalpies, h'_g and h'_f, associated with near wall interphase mass transfer.

2. It is assumed that the summation of terms J, K, and L in Equations (4.7-1) and (4.7-2) vanishes, i.e., the sum of the interface transfer terms vanishes. This is because the interface contains no mass and energy storage.

3. Assumption 2 is satisfied by requiring that the near wall interface heat transfer terms and the bulk interface heat transfer terms sum to zero independently.

The ramifications of these assumptions and their implementation in the code will be discussed next.

4.7.1.1 Near Wall Interphase Heat Transfer. Near wall interphase heat transfer is directly in only one term in the energy equation, Q_{wf} or Q_{wg}. During nucleate boiling, Q_{wg} is zero and the code treats Q_{wf} in two parts, that is

$$Q_{wf} = Q_{conv} + Q_{boil} \tag{4.7-5}$$

where Q_{conv} is that portion of the wall heat transfer treated as a convective heat flux and Q_{boil} is that portion which results in the saturated pool boiling from the liquid phase. The term Q_{boil} is the same as $-Q_{if}^{w}$ in Equation (4.7-3); this is the near wall interphase heat transfer. When boiling exists, a fraction of the energy is accumulated in the variable Γ_w.

Because ATHENA has just one liquid temperature in a volume and does not calculate thermal gradients in the wall boundary layer, another model must be used for Γ_w. This is especially true for subcooled boiling. In this case, the bulk liquid can be subcooled while liquid in the boundary layer is warmer and is flashing to vapor, resulting in a net vapor generation. To capture this effect, the mechanistic method proposed by Lahey,[4.7-1] as implemented in the TRAC-B code,[4.7-2] is used in ATHENA during nucleate, transition, and film boiling. Furthermore, the model for Γ_{ig} will not result in positive Γ_{ig} for subcooled bulk liquid temperature.

The Saha-Zuber[4.7-3] method of predicting the conditions necessary for net voids to exist is calculated; then Lahey's method of assigning a fraction of the total heat flux to liquid, which causes flashing at the wall, is applied. The Saha-Zuber correlation uses the Peclet number to decide whether the heat flux should be related to the Nusselt number (low flow) or Stanton number (high flow). At some point, as the liquid flows axially past a heated wall, the specific enthalpy may become close enough to the saturation specific enthalpy that bubbles generated at the wall will not be condensed. The specific enthalpy necessary is the critical specific enthalpy given by

$$\begin{aligned} h_{cr} &= h_{f,sat} - \frac{St'C_{pf}}{0.0065} \qquad \text{for Pe} > 70{,}000 \\ &= h_{f,sat} - \frac{Nu'C_{pf}}{455} \qquad \text{for Pe} \le 70{,}000 \end{aligned} \tag{4.7-6}$$

where

$$St' = \frac{Nu'}{Pe} \tag{4.7-7}$$

$$Nu' = \frac{q_f'' D}{k_f} \tag{4.7-8}$$

$$Pe = \frac{G_t D C_{pf}}{k_f} \tag{4.7-9}$$

q_f'' = wall heat flux to the liquid. (4.7-10)

If the minimum of the bulk liquid specific enthalpy, h_f, and the saturation liquid specific enthalpy, $h_{f,sat}$ is greater than the critical specific enthalpy, h_{cr}, then the direct wall flashing term, Γ_w, is a fraction of the wall heat flux to liquid. From Lahey,[4.7-1] the fraction is

$$Mul = \frac{\min(h_f, h_f^s) - h_{cr}}{(h_f^s - h_{cr})(1 + \varepsilon_P)} \tag{4.7-11}$$

where

ε_P = the pumping term

$$= \frac{\rho_f [h_f^s - \min(h_f, h_f^s)]}{\rho_g h_{fg}} \; . \tag{4.7-12}$$

The final expression for the wall vapor generation rate per unit volume during boiling is

$$\Gamma_w = \frac{q_f'' A_w}{V\left[\max\left(h_g^s - h_f, 10^4 \frac{J}{kg}\right)\right]} Mul \tag{4.7-13}$$

where V is the cell volume. A lower limit on the specific enthalpy difference in the denominator was found to be needed in a test problem which included noncondensables. A value of 10^4 J/kg was chosen.

During condensation, there is also a Γ_w term, but for partitioning it uses all the heat flux from the vapor/gas q_g''. The difference between the actual vapor/gas specific enthalpy and the saturated liquid specific enthalpy is used in the equation for the condensation rate, given by

$$\Gamma_w = \frac{q_g'' A_w}{V\left[\max\left(h_g - h_f^s,\ 10^4 \frac{J}{kg}\right)\right]} \quad . \tag{4.7-14}$$

A boiling condition is checked to ensure that Γ_w does not represent a greater mass of liquid than is available to boil in 90% of the current time step. For the boiling situation,

$$\Gamma_w = \min\left(\Gamma_w,\ \frac{0.9\alpha_f\rho_f}{\Delta t}\right) \quad . \tag{4.7-15}$$

In the event this test shows Γ_w greater than 90% of the remaining liquid in the control volume, the value of Γ_w is reset to the 90% limiting value. A similar test is performed for a condensation calculation to allow no more than 90% of the available vapor/gas in a given control volume to condense in a single time step. This test results in less vaporization (or condensation) for a system calculation when the void fraction in a control volume is close to either unity or zero.

4.7.1.2 Bulk Interphase Heat Transfer. The relationship between bulk interfacial heat and mass transfer is similar in the use of $(h_g^* - h_f^*)$ to determine the mass transfer associated with the interfacial heat transfer. The code includes no specific variable to represent interfacial heat transfer. Instead, it is incorporated into the energy equation in terms of an interfacial heat transfer coefficient, H_{ig} or H_{if}, and a calculated temperature difference, $(T^s - T_g)$ or $(T^s - T_f)$, respectively.

4.7.1.3 Total Interphase Heat Transfer. The reduction of the energy equation from its basic form in Equation (4.7-2) (liquid phase) to the following equations (see Volume I):

$$\begin{aligned} &\frac{\partial}{\partial t}(\alpha_f\rho_f U_f) + \frac{1}{A}\left[\frac{\partial}{\partial x}(\alpha_f\rho_f U_f v_f A) + P\frac{\partial}{\partial x}(\alpha_f v_f A)\right] \\ &= P\frac{\partial\alpha_g}{\partial t} + \left(\frac{h_f^*}{h_g^* - h_f^*}\right)\left(\frac{P_s}{P}\right)H_{ig}(T^s - T_g) + \left(\frac{h_g^*}{h_g^* - h_f^*}\right)H_{if}(T^s - T_f) + \left(\frac{P - P_s}{P}\right)H_{gf}(T_g - T_f) \\ &\quad - \left[\left(\frac{1+\varepsilon}{2}\right)h_g' + \left(\frac{1-\varepsilon}{2}\right)h_f'\right]\Gamma_w + Q_{wf} + DISS_f \end{aligned} \tag{4.7-16}$$

from which the numerical form is derived, requires an assumption for the interface transfer terms described in Section 4.7.1. Combining the phasic energy equations, Equations (4.7-1) and (4.7-2), into a mixture form by adding results in the following collection of terms representing the total interface energy transfer:

$$Q_{ig} + Q_{if} + \Gamma_{ig}(h_g^* - h_f^*) + \Gamma_w(h_g' - h_f') \quad . \tag{4.7-17}$$

Assumption 2 in Section 4.7.1 is a requirement that the sum of these terms vanish, i.e.,

$$Q_{ig} + Q_{if} + \Gamma_{ig}(h_g^* - h_f^*) + \Gamma_w(h_g' - h_f') = 0 \quad . \tag{4.7-18}$$

Assumption 3 in Section 4.7.1 goes on to assume further that the bulk transfer terms and the near wall transfer terms vanish separately. Thus,

$$\frac{P_s}{P}H_{ig}(T^s - T_g) + H_{if}(T^s - T_f) + \Gamma_{ig}(h_g^* - h_f^*) = 0 \tag{4.7-19}$$

and

$$Q_{ig}^W + Q_{if}^W + \Gamma_w(h_g' - h_f') = 0 \quad . \tag{4.7-20}$$

Equation (4.7-20) is rewritten in the form

$$\Gamma_w = \frac{-Q_{if}^W}{h_g' - h_f'}, \; Q_{ig}^W = 0, \qquad \Gamma_w > 0 \tag{4.7-21}$$

and

$$\Gamma_w = \frac{-Q_{ig}^W}{h_g' - h_f'}, \; Q_{if}^W = 0, \qquad \Gamma_w < 0 \tag{4.7-22}$$

and is evaluated in the heat transfer correlation when boiling or condensing is calculated. The energy associated with Γ_w is never deposited in the associated fluid space, but rather is carried in the calculational scheme as a mass generation rate. The energy is accounted for in terms of Γ_w and is converted into an energy form in the energy equation itself, as seen in Equation (4.7-1) or (4.7-2). Note that the saturation

specific enthalpy multiplying Γ_w in both phasic energy equations properly incorporates the latent heat such that the energy contribution (positive or negative) from Γ_w is correct.

The other mass transfer term arises from bulk exchange between the liquid and vapor/gas spaces. Equation (4.7-19) is the essential defining equation and is rewritten as

$$\Gamma_{ig} = -\frac{\frac{P_s}{P}H_{ig}(T^s - T_g) + H_{if}(T^s - T_f)}{h_g^* - h_f^*} \quad . \tag{4.7-23}$$

The actual coding for Γ_{ig} is included in its final form in subroutine EQFINL, where the back substitution following the implicit pressure solution is completed. The term Γ_{ig} is not calculated directly, but its contribution to the energy equation is determined exactly as shown above in Equation (4.7-23). **Figure 4.7-1** provides an overview of the energy partitioning used in ATHENA. **Figure 4.7-2** provides another view of this energy partitioning.

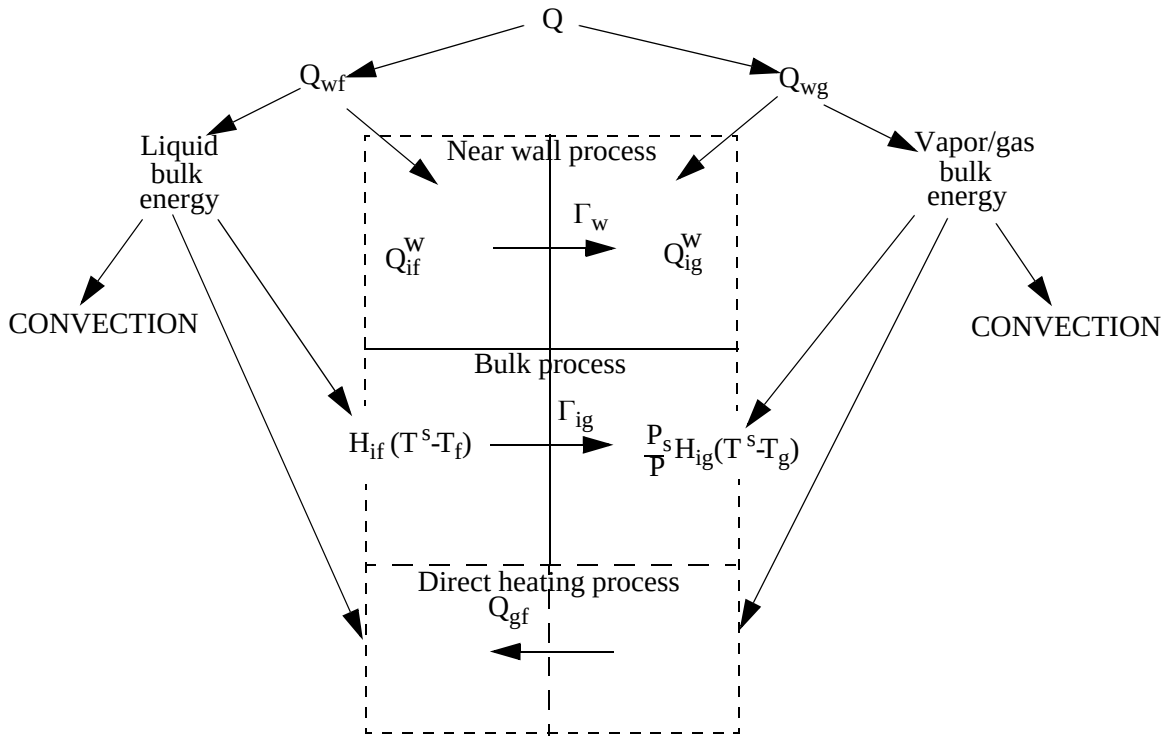

Figure 4.7-1 Energy partitioning in ATHENA.

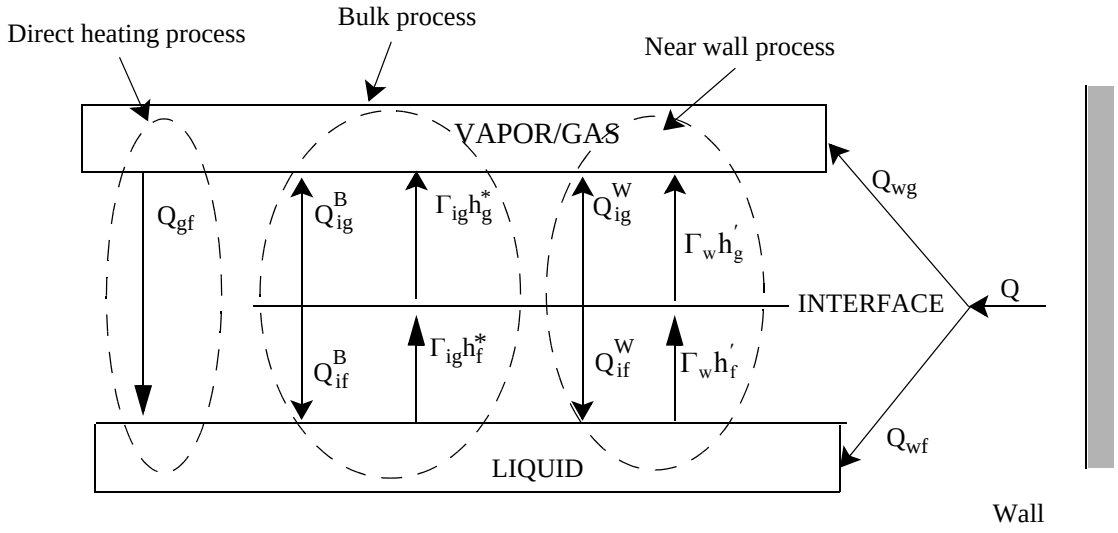

Figure 4.7-2 Energy partitioning in ATHENA (another view).

The term Q is the sum of Q_{wg} and Q_{wf}. The term Γ_{ig} is the mass transfer associated with bulk energy exchange, and specifically does not include any direct effects of mass transfer from wall heat transfer. The terms Q_{if} and Q_{ig}, on the other hand, include the energy associated with both forms of mass transfer, as shown in Equations (4.7-24) and are given by

$$Q_{ig} = Q_{ig}^{B} + Q_{ig}^{W} = \frac{P_s}{P} H_{ig}(T^s - T_g) + Q_{ig}^{W} , \qquad (4.7\text{-}24)$$

and

$$Q_{if} = Q_{if}^{B} + Q_{if}^{W} = H_{if}(T^s - T_f) + Q_{if}^{W} \quad . \qquad (4.7\text{-}25)$$

The sum of Q_{ig} and Q_{if} represents the net energy exchange between the phases.

4.7.1.4 Further Description of Interphase Heat Transfer. As discussed in Volume I, there is the possibility of multiple heat slabs connected to the fluid. To accurately model multiple heat slabs, the mass transfer near the wall (Γ_w) is split into a boiling part (Γ_w) and condensing part (Γ_c). For this option, Γ_w is the near wall mass transfer for all the heat slabs that are in the boiling mode, and Γ_c is the near wall mass transfer for all the heat slabs that are in the condensing mode. Thus the total mass transfer consists of mass transfer in the bulk fluid (Γ_{ig}) and mass transfer in the boundary layers near the walls (Γ_w and Γ_c); that is,

$$\Gamma_g = \Gamma_{ig} + \Gamma_w + \Gamma_c \ . \tag{4.7-26}$$

The Γ_w and Γ_c terms are the mass transfers from flashing and condensation associated with wall heat transfer and both are determined from the wall heat transfer computation.

Using this Γ_w and Γ_c notation, a more detailed description of the energy partitioning process is next described.

Using somewhat different notation in the source terms, the phasic energy Equations (4.7-1) and (4.7-2) have the form

$$\frac{\partial}{\partial t}(\alpha_g \rho_g U_g) + \frac{1}{A}\frac{\partial}{\partial x}(\alpha_g \rho_g U_g v_g A) = -P\frac{\partial \alpha_g}{\partial t} - \frac{P}{A}\frac{\partial}{\partial x}(\alpha_g v_g A) + Q_{ig}^B + \Gamma_{ig} h_g^* + Q_{wg} - Q_{cond} + \Gamma_w h'_{wg} + \Gamma_c h'_{cg} - Q_{gf} + DISS_g \tag{4.7-27}$$

$$\frac{\partial}{\partial t}(\alpha_f \rho_f U_f) + \frac{1}{A}\frac{\partial}{\partial x}(\alpha_f \rho_f U_f v_f A) = -P\frac{\partial \alpha_f}{\partial t} - \frac{P}{A}\frac{\partial}{\partial x}(\alpha_f v_f A) + Q_{if}^B - \Gamma_{ig} h_f^* + Q_{wf} - Q_{flash} - \Gamma_w h'_{wf} - \Gamma_c h'_{cf} + Q_{gf} + DISS_f \ . \tag{4.7-28}$$

The term Q_{flash} corresponds to $-Q_{if}^w$ for boiling (flashing), and the term Q_{cond} corresponds to $-Q_{ig}^w$ for condensation.

Figure 4.7-3 illustrates terms in the energy Equations (4.7-27) and (4.7-28). The top and bottom rectangles represent vapor/gas and liquid regions of a hydrodynamic volume and have nonzero volumes to indicate that the time derivatives represent the accumulation of energy in the two regions. The horizontal line between the two volumes represents the liquid-vapor/gas interface and the fact that the line has no volume indicates that the interface cannot accumulate mass or energy. Arrows show mass and energy entering or leaving the liquid and vapor/gas regions and the interface. The direction of the arrow shows the positive flow direction and most quantities can have positive or negative values. The arrows marked with convection ($\alpha\rho Uv$) and 'work' are from fluid flow into and out of the regions. The work terms are PV work terms in the energy Equations (4.7-1) and (4.7-2). The use of inward and outward pointing arrows anticipate the development of numerical approximations to these equations. In those approximations, inlet and outlet surfaces to the volumes are assumed and inward arrows point to an inlet and outward arrows leave an outlet surface. The arrow points in the direction of positive flow. If the flow is reversed, the signs simply change. Quote signs are used with the work term since this is a thermal energy equation and only part of the work term is present.

The wall heat transfer computation (Section 4.2) computes phasic heat fluxes. The heat transfer rates per unit volume to each phase, Q_{wf} and Q_{wg}, are given by

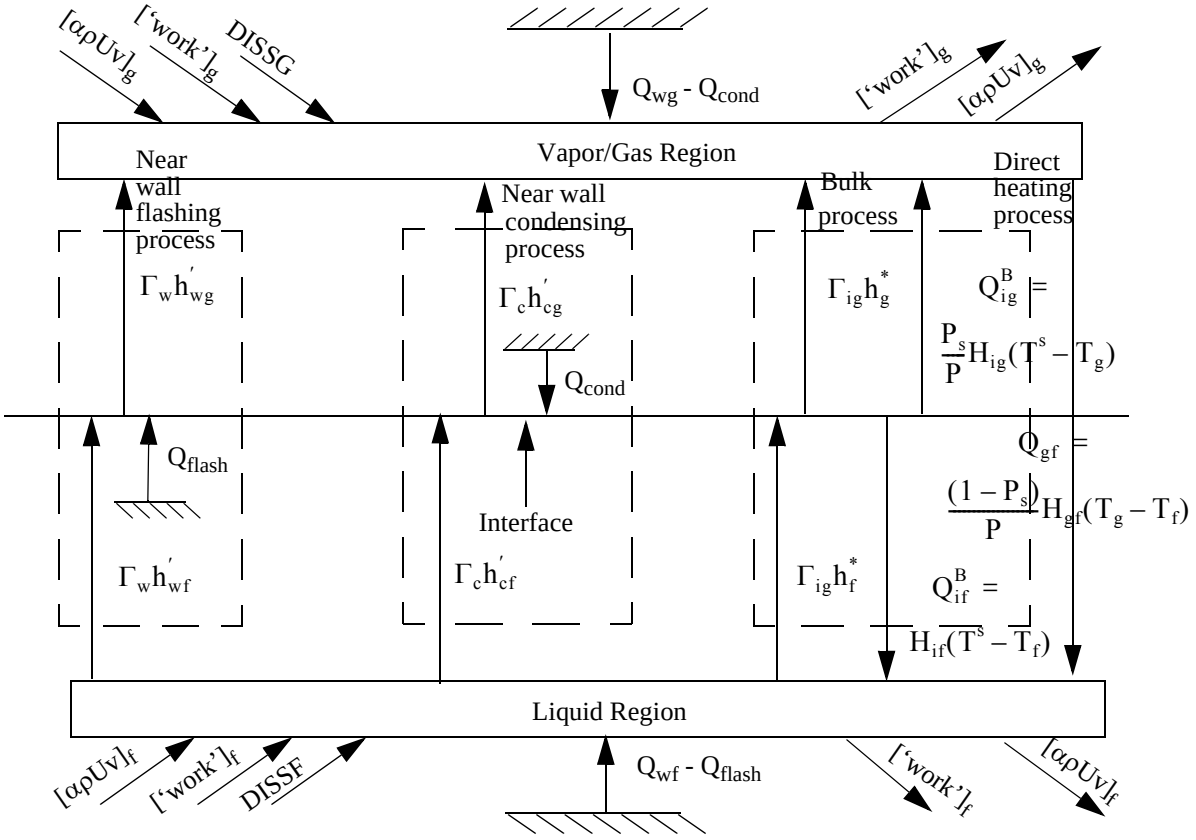

Figure 4.7-3 Energy partitioning in ATHENA (detailed view).

$$Q_{wf} = \frac{1}{V}\sum_{i} q_{fi} A_{hi} \tag{4.7-29}$$

$$Q_{wg} = \frac{1}{V}\sum_{i} q_{gi} A_{hi} \tag{4.7-30}$$

where q_{fi} and q_{gi} are phasic heat fluxes for surface i, A_{hi} is the wall heat transfer surface area for surface i, V is the volume of the hydrodynamic volume, and the summation is over all heat structures attached to the volume. These phasic wall heat transfer rates satisfy the equation $Q = Q_{wf} + Q_{wg}$ where Q is the total wall heat transfer rate to the fluid per unit volume. For some modes of heat transfer, the heat transfer correlation package divides the phasic wall heat transfer into two parts, one part going to the phase, the other part going to the interface where it causes mass and energy transfer. For flashing, a portion of the heat transfer

to the liquid from each heat structure (i) goes to the interface where it generates a change of phase with mass and energy transfer from liquid to vapor/gas The wall heat transfer correlation package determines the factor m_{fi} for each heat structure (i) such that

$$\Gamma_{wi} = m_{fi} q_{fi}, \tag{4.7-31}$$

where Γ_{wi} is the wall associated flashing mass transfer for heat structure i.

For condensation, a portion of the heat transfer to the vapor/gas from each heat structure (i) goes to the interface where it generates a change of phase with mass and energy transfer from vapor/gas to liquid. The wall heat transfer correlation package determines the factor m_{gi} for each heat structure (i) such that

$$\Gamma_{ci} = m_{gi} q_{gi}, \tag{4.7-32}$$

where Γ_{ci} is the wall associated condensing mass transfer for heat structure i.

The contributions of wall associated mass transfer are summed over all heat transfer surfaces to obtain the totals within a volume, that is

$$\Gamma_w = \sum_i \Gamma_{wi} \tag{4.7-33}$$

$$\Gamma_c = \sum_i \Gamma_{ci} \quad . \tag{4.7-34}$$

The flashing process portion of **Figure 4.7-3** shows Q_{flash} as that portion of the wall transfer to liquid going directly to the interface, causing mass transfer from liquid to vapor/gas. Similarly, the condensation process shows Q_{cond} as that portion of the wall transfer to vapor/gas going to the interface, causing mass transfer from vapor/gas to liquid. The directions of the arrows for flashing and condensation mass flows are the same even though condensation is in the reverse direction. Γ_w is always greater than or equal to zero; Γ_c is always less than or equal to zero.

Using the principle that no mass or energy accumulates at the interface, the following is true:

$$Q_{flash} = \Gamma_w (h'_{wg} - h'_{wf}) \tag{4.7-35}$$

$$Q_{cond} = \Gamma_c (h'_{cg} - h'_{cf}) \quad . \tag{4.7-36}$$

Comparing to the notation used in Section 4.7.1, the term Q_{flash} corresponds to $-Q_{if}^{W}$ for boiling, and the term Q_{cond} corresponds to $-Q_{ig}^{W}$ for condensation. The heat from the wall going directly to the interface must be subtracted from the wall heat transfer rates. As illustrated in **Figure 4.7-3**, the liquid energy Equation (4.7-28) includes the terms Q_{wf} - Q_{flash} for energy entering the liquid from the walls and the terms, $\Gamma_w h'_{wf}$ and $\Gamma_c h'_{cf}$ for energy leaving the liquid due to change of phase. The vapor/gas energy Equation (4.7-27) includes the terms Q_{wg} - Q_{cond} for energy entering the vapor/gas from the walls and terms $\Gamma_w h'_{wg}$ and $\Gamma_c h'_{cg}$ for energy entering the vapor/gas due to change of phase.

4.7.2 Interpreting ATHENA Output of the Energy Equation

The three variables printed in a major edit are macroscopic terms related to the entire control volume. These variables are the total wall heat transfer to the control volume, Q, the total wall heat transfer to the vapor/gas space in the control volume, QWG, and the total vapor generation, VAPGEN. In the major edit, these are labeled TOT.HT.INP, VAP.HT.INP, and VAPOR-GEN. In terms of variables discussed above, Q is straightforward and includes all wall energy from (or to) the heat structure. The term Q can be interpreted as consisting of two terms, QWF and QWG, the total wall energy transferred to each of the phases. These two terms include wall energy convected to the particular phase and energy associated with the mass transfer. The term QWG is printed in the major edits; the term QWF must be inferred from QWF = Q - QWG. The term QWF includes the convective heat flux term, noted in Section 4.7.1.1 as Q_{conv}, and the Γ_w term associated with boiling. From Equation (4.7-3), the energy associated with Γ_w is

$$Q_{if}^{W} = -\Gamma_w (h'_g - h'_f) \quad . \tag{4.7-37}$$

Note that in this form, Q_{if}^{W} is a negative contribution to the liquid phase, for the net result on the phase is a removal of mass and its internal energy. Note also that a test is performed such that a given heat structure will contribute to either Q_{if}^{W} or Q_{ig}^{W}, depending on the thermal-hydraulic conditions of the associated fluid space, but it will not contribute to both in the same time step. Thus, the energy terms for each phase in the control volumes are identified. The term VAPGEN, noted as vapor generation in the output, is the total interphase mass transfer and includes both the bulk and near wall terms.

4.7.3 References

4.7-1. R. T. Lahey, "A Mechanistic Subcooled Boiling Model," *Proceedings Sixth International Heat Transfer Conference, Toronto, Canada, August 7-11, 1978, Volume 1*, pp. 293-297.

4.7-2. D. D. Taylor et al., *TRAC-BD1/MOD1: An Advanced Best Estimate Computer Program for Boiling Water Reactor Transient Analysis, Volume 1*, NUREG/CR-3633, EGG-2294, Idaho National Engineering Laboratory, April 1984, p. 65.

4.7-3. P. Saha and N. Zuber, “Point of Net Vapor Generation and Vapor Void Fraction in Subcooled Boiling,” *Proceedings Fifth International Heat Transfer Conference, Tokyo, Japan, September 3-7, 1974, Volume 4*, pp. 175-179.

Appendix 4A--Correlations for Interfacial Heat and Mass Transfer in the Bulk Fluid for ATHENA

Bubbly Flow

SHL (superheated liquid, $\Delta T_{sf} < 0$)

$$H_{if} = \left\{ \max \left[\begin{array}{l} -\frac{k_f}{d_b}\frac{12}{\pi}\Delta T_{sf}\frac{\rho_f C_{pf}}{\rho_g h_{fg}}\beta \\ \frac{k_f}{d_b}(2.0 + 0.74 Re_b^{0.5}) \end{array} \right] + 0.4|v_f|\rho_f C_{pf} F_1 \right\} a_{gf} F_2 F_3 \qquad \text{otherwise} \qquad (4A\text{-}1)$$

$$= 0.0 \qquad \text{if } \alpha_g = 0.0 \text{ and } \Delta T_{sf} \geq 0$$

where

ΔT_{sf} = $T^s - T_f$

Re_b = $\frac{(1-\alpha_{bub})\rho_f v_{fg} d_b}{\mu_f} = \frac{We\ \sigma(1-\alpha_{bub})}{\mu_f (v_{fg}^2)^{1/2}}$

$We\ \sigma$ = max ($We\ \sigma$, 10^{-10} N/m)

d_b = average bubble diameter ($= \frac{1}{2} d_{max}$)

= $\frac{We\ \sigma}{\rho_f v_{fg}^2}$, We = 5

β = 1.0 for bubbly flow

a_{gf} = interfacial area per unit volume

= $\frac{3.6\alpha_{bub}}{d_b}$

α_{bub} = max (α_g, 10^{-5})

v_{fg} = relative velocity = $v_g - v_f$ $\qquad \alpha_g \geq 10^{-5}$

$= (v_g - v_f)\,\alpha_g 10^{-5} \qquad \alpha_g < 10^{-5}$

$v_{fg}^2 = \max\left[v_{fg}^2, \dfrac{We\ \sigma}{\rho_f \min(D' \alpha_{bub}^{1/3}, D)}\right]$

D = hydraulic diameter

D' = 0.005 m for bubbly flow

$F_1 = \dfrac{\min(0.01, \alpha_{bub})}{\alpha_{bub}}$

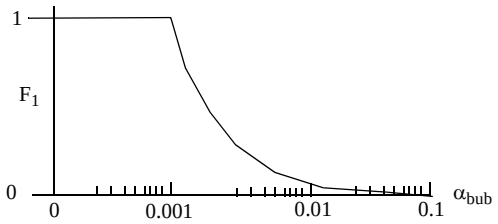

$F_2 = \dfrac{\min(0.25, \alpha_{bub})}{\alpha_{bub}}$

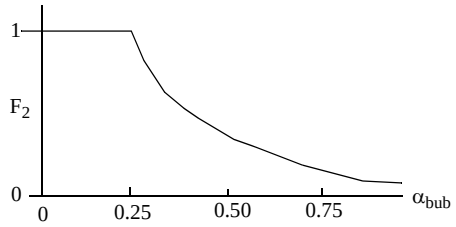

$F_3 = 1 \qquad \Delta T_{sf} \le -1$

$= F_4\,(1 + \Delta T_{sf}) - \Delta T_{sf} \qquad -1 < \Delta T_{sf} < 0$

$= F_4 \qquad \Delta T_{sf} \ge 0$

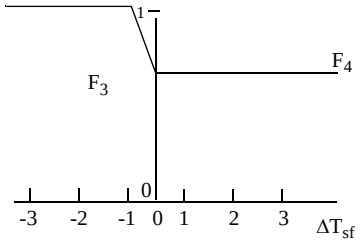

F_4 = $\min [10^{-5}, \alpha_g (1 - X_n)] (10^5)$

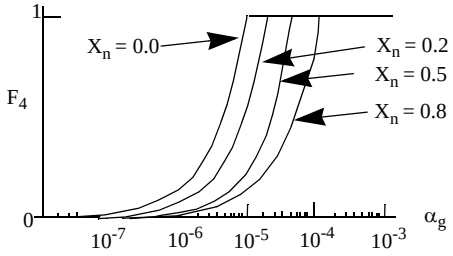

X_n = noncondensable quality.

SCL (subcooled liquid, $\Delta T_{sf} > 0$)

$$H_{if} = \frac{F_3 F_5 h_{fg} \rho_g \rho_f \alpha_{bub}}{\rho_f - \rho_g} \qquad \alpha_g > 0.0$$
$$= 0.0 \qquad \alpha_g = 0.0 \qquad \text{(4A-2)}$$

where

$\rho_f - \rho_g$ = $\max (\rho_f - \rho_g, 10^{-7}\ kg/m^3)$

F_3, α_{bub} as for bubbly SHL

F_5 = $0.075 \frac{1}{K \cdot s}$ $\alpha_{bub} \geq 0.25$

= $1.8\phi C \exp(-45\alpha_{bub}) + 0.075 \frac{1}{K \cdot s}$ $\alpha_{bub} < 0.25$

C = $65.0 - 5.69 \times 10^{-5} (P - 1.0 \times 10^5) \frac{1}{K \cdot s}$ $P \leq 1.1272 \times 10^6$ Pa

= $\frac{2.5 \times 10^9}{P^{1.418}} \frac{1}{K \cdot s}$ $P > 1.1272 \times 10^6$ Pa

P = Pressure (Pa)

ϕ = 1.0 $|v_f| \leq 0.61$ m/s

= $(1.639344\ |v_f|)^{0.47}$ $|v_f| > 0.61$ m/s

SHG (superheated vapor/gas, $\Delta T_{sg} < 0$)

$$H_{ig} = h_{ig} F_6 F_7 a_{gf} \quad \text{(4A-3)}$$

where

h_{ig} = 10^4 W/m^2-K

a_{gf} as for bubbly SHL

F_6 = $[1 + \eta (100 + 25\eta)]$, $\eta = |\max(-2, \Delta T_{sg})|$

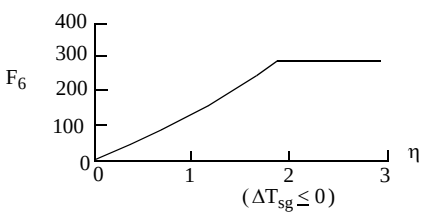

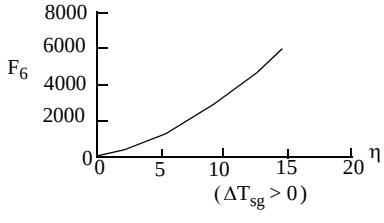

ΔT_{sg} = $T^s - T_g$

$$F_7 = \frac{\max(\alpha_g, 10^{-5})}{\max(\alpha_g, 10^{-9})} .$$

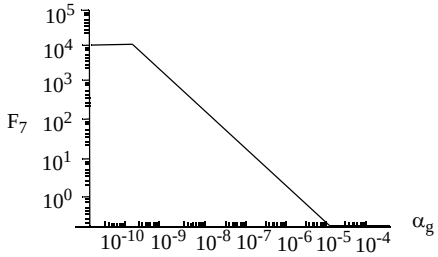

SCG (subcooled vapor/gas, $\Delta T_{sg} > 0$)

H_{ig} as for bubbly SHG

Note that $\Delta T_{sg} > 0$ for this case (function F_6).

Slug Flow

SHL (superheated liquid, $\Delta T_{sf} < 0$)

$$H_{if} = H_{if,Tb} + H_{if,bub}$$

where

$$H_{if,\,Tb} = 3.0 \times 10^{6} a^{*}_{gf,\,Tb} \alpha_{Tb} \qquad \text{(4A-4)}$$

where

$a^{*}_{gf,\,Tb}$ = volumetric interfacial area = $\frac{4.5}{D}$ (2.0)

D = hydraulic diameter

α_{Tb} = Taylor bubble void fraction = $\frac{\alpha_g - \alpha_{gs}}{1 - \alpha_{gs}}$

= Taylor bubble volume/total volume

α_{gs} = the average void fraction in the liquid film and slug region

= $\alpha_{BS} F_9$

F_9 = $\exp\left(-8 \frac{\alpha_g - \alpha_{BS}}{\alpha_{SA} - \alpha_{BS}}\right)$

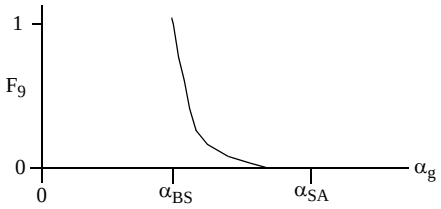

α_{BS} = α_g for bubbly-slug transition

α_{SA} = α_g for slug-annular mist transition

and

$H_{if,bub}$ is as for H_{if} for bubbly SHL with the following modifications:

α_{bub} = $\alpha_{BS} F_9$

$$v_{fg} = (v_g - v_f)\, F_9^2$$

$$a_{gf,bub} = (a_{gf})_{bub}(1 - \alpha_{Tb})F_9$$

$$\beta = F_9$$

$(a_{gf})_{bub}$ is a_{gf} for bubbly SHL.

SCL (subcooled liquid, $\Delta T_{sf} > 0$)

$$H_{if} = H_{if,Tb} + H_{if,bub}$$

where

$$H_{if,Tb} = 1.18942\ Re_f^{0.5} Pr_f^{0.5} \frac{k_f}{D} a^*_{gf,\,Tb} \alpha_{Tb}$$

where

α_{Tb} and $a^*_{gf,\,Tb}$ are as for slug SHL

$$Pr_f = \frac{C_{pf}\mu_f}{k_f}$$

$$Re_f = \frac{\rho_f \min(|v_f - v_g|, 0.8\ m/s) D}{\mu_f}$$

and

$H_{if,bub}$ is as for bubbly SCL.

SHG (superheated vapor/gas, $\Delta T_{sg} < 0$)

$$H_{ig} = H_{ig,Tb} + H_{ig,bub} \qquad (4A\text{-}5)$$

where

$$H_{ig,Tb} = (2.2 + 0.82\ Re_g^{0.5}) \frac{k_g}{D} a^*_{gf,\,Tb} \alpha_{Tb}$$

where

$a^*_{gf,\,Tb}$ and α_{Tb} are as for slug SHL

$$Re_g = \frac{\rho_f |v_f - v_g| D}{\mu_g}$$

and

$$H_{ig,bub} = h_{ig} F_6 (1 - \alpha_{Tb}) a_{gf,bub}$$

where

α_{Tb} and $a_{gf,bub}$ are as for slug SHL

and

h_{ig} and F_6 are as for bubbly SHG.

SCG (subcooled vapor/gas, $\Delta T_{sg} > 0$)

$$H_{ig} = H_{ig,Tb} + H_{ig,bub} \qquad (4A\text{-}6)$$

where

$$H_{ig,Tb} = h_{ig} F_6 \alpha_{Tb} a^*_{gf,\,Tb}$$

where

α_{Tb} and $a^*_{gf,\,Tb}$ are as for slug SHL

h_{ig} and F_6 are as for bubbly SHG

and

$H_{ig,bub}$ is as for slug SHG.

Annular Mist Flow

SHL (superheated liquid, $\Delta T_{sf} < 0$)

$$H_{if} = H_{if,ann} + H_{if,drp} \tag{4A-7}$$

where

$H_{if,ann}$ = $3.0 \times 10^{6}\, a_{gf,ann}\, F_{10}$

where

$a_{gf,ann}$ = $\left(\frac{4C_{ann}}{D}\right)(1-\alpha_{ff})^{1/2}$

C_{ann} = $(30\alpha_{ff})^{1/8}\,(2.5)$

D = hydraulic diameter

α_{ff} = $\max(0.0, \alpha_f F_{11})$

F_{11} = $\gamma^{*} \max[0.0, (1 - G^{*})] \exp(-C_e \times 10^{-5}\lambda^{6})$

C_e = 4.0 horizontal

= 7.5 vertical

λ = $\frac{v_g^{*}}{v_{crit}}$ horizontal flow

= $\frac{\alpha_g v_g}{v_{crit}}$ vertical flow

v_g^{*} = $\max(|v_f - v_g|, 10^{-15}\ \text{m/s})$

v_{crit} = $\max\left(0.5\left\{\frac{\max\left[(\rho_f-\rho_g), 10^{-7}\frac{kg}{m^3}\right] g\alpha_g A_{pipe}}{\rho_g D \sin\theta}\right\}^{1/2}(1-\cos\theta),\ |v_g - v_f|10^{-15},\ 10^{-30}\text{m/s}\right)$

(horizontal) [see Equation (3.1-2)]

$$= \frac{3.2\left\{\sigma^* g \max\left[(\rho_f - \rho_g), 10^{-7}\frac{kg}{m^3}\right]\right\}^{1/4}}{\rho_g^{1/2}}$$ (vertical) [see Equation (3.2-20) and (3.2-22)]

σ^* = max (σ, 10^{-7}N/m)

G^* = $10^{-4}\ Re_f^{0.25}$

Re_f = $\frac{\alpha_f \rho_f |v_f| D}{\mu_f}$

γ^* = γ $\alpha_g > \alpha_{SA}$ and $\alpha_f < \alpha_{EF}$

= 1 otherwise

γ = $\frac{\alpha_f - \alpha_{AD}}{\alpha_{EF} - \alpha_{AD}}$

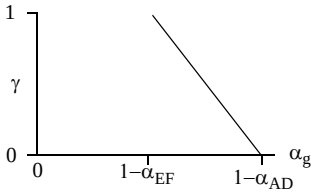

α_{AD} = 10^{-4}

α_{EF} = max [2 α_{AD}, min (2.0 x 10^{-3} $\frac{\rho_g}{\rho_f}$, 2 x 10^{-4})]

F_{10} = min (1.0 + $|\lambda|^{1/2}$ + 0.05 $|\lambda|$, 6)

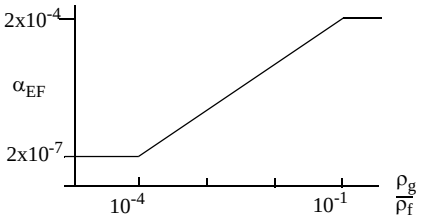

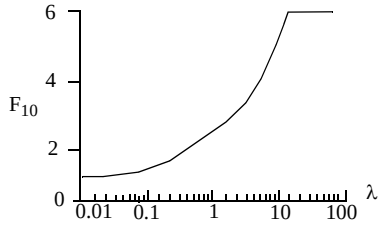

and

$H_{if,drp}$ = $\frac{k_f}{d_d} F_{12} F_{13} a_{gf,drp}$

d_d = characteristic droplet diameter $\left(= \frac{1}{2} d_{max} \right)$

= $\frac{We\ \sigma}{\rho_g \hat{v}_{fg}^2}$, We = 1.5, We σ = max (We σ, 10^{-10} N/m)

$\hat{v}_{fg}^2$ = $\max\left[v_{fg}^{**2}, \frac{We\ \sigma}{\rho_g \min(D' \alpha_{fd}^{1/3}, D)} \right]$

v_{fg}^{**} = $v_{fg}^{*}\ \alpha_f 10^6$ $\alpha_f < 10^{-6}$

= v_{fg}^{*} $\alpha_f \geq 10^{-6}$

v_{fg}^{*} = $v_{fg} (1 - F_{11}\gamma)$ $\alpha_g > \alpha_{SA}$ and $\alpha_f < \alpha_{EF}$

= $v_{fg} (1 - F_{11})$ otherwise

v_{fg} = $v_g - v_f$

D' = 0.0025 m

α_{fd} = $\max\left(\frac{\alpha_f - \alpha_{ff}}{1 - \alpha_{ff}}, \alpha_{AD}^{*} \right)$

α_{AD}^{*} = $\alpha_{AD}\gamma + 10^{-5} (1 - \gamma)$ $\alpha_g > \alpha_{SA}$ and $\alpha_f < \alpha_{EF}$

= α_{AD} otherwise

F_{12} = $1 + \xi (250 + 50\xi)$

ξ = $\max (0, - \Delta T_{sf})$

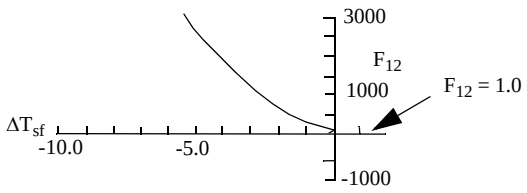

$$F_{13} = 2.0 + 7.0 \min\left[1.0 + \frac{C_{\rho f}\max(0.0, \Delta T_{sf})}{h_{fg}}, 8.0\right]$$

$$a_{gf,drp} = \frac{3.6\alpha_{fd}}{d_d}(1 - \alpha_{ff}) .$$

For an annulus component , $\alpha_{ff} = \alpha_f$ and $\alpha_{fd} = 0$.

SCL (subcooled liquid, $\Delta T_{sf} > 0$)

$$H_{if} = H_{if,ann} + H_{if,drp} \quad (4A\text{-}8)$$

where

$$H_{if,ann} = 10^{-3}\, \rho_f C_{pf} |v_f|\, a_{gf,ann}\, F_{10}$$

where

$a_{gf,ann}$ and F_{10} are as for annular mist SHL

and

$$H_{if,drp} = \frac{k_f}{d_d}\, F_{13}\, a_{gf,drp}$$

where

$a_{gf,drp}$, F_{13}, and d_d are as for annular mist SHL.

For an annulus component, $\alpha_{ff} = \alpha_f$ and $\alpha_{fd} = 0$.

SHG (superheated vapor/gas, $\Delta T_{sg} < 0$)

$$H_{ig} = H_{ig,ann} + H_{ig,drp}$$

where

$$H_{ig,ann} = \frac{k_g}{D} 0.023\ Re_g^{0.8} a_{gf,ann} F_{10}$$

where

$$Re_g = \alpha_g \rho_g |v_g - v_f| \frac{D}{\mu_g}$$

F_{10} and $a_{gf,ann}$ are as for annular mist SHL, and

$$H_{ig,drp} = \frac{k_g}{d_d}(2.0 + 0.5\ Re_d^{0.5}) a'_{gf,\,drp}$$

where

d_d is as for annular mist SHL

$$Re_d = \frac{(1-\alpha_{fd})^{2.5}\rho_g \hat{v}_{fg} d_d}{\mu_g} = \frac{We \bullet \sigma (1-\alpha_{fd})^{2.5}}{\mu_g \hat{v}_{fg}}$$

$$We = 1.5,\ We\sigma = \max(We\sigma,\ 10^{-10}\ N/m)$$

$$a'_{gf,\,drp} = a_{gf,drp} \qquad \alpha_f \geq \alpha^*_{AD}$$

$$= a_{gf,\,drp}\left[\frac{\alpha_f F_{14}}{\alpha^*_{AD}} + (1 - F_{14})\right] \qquad \alpha_f < \alpha^*_{AD}$$

$a_{gf,drp}$, α_{fd}, $\hat{v}_{fg}$, and α^*_{AD} are as for annular mist SHL, and

F_{14} = 1.0 - 5.0 min [0.2, max (0, ΔT_{sg})].

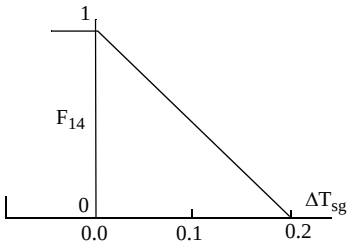

For an annulus component, $\alpha_{ff} = \alpha_f$ and $\alpha_{fd} = 0$.

SCG (subcooled vapor/gas, $\Delta T_{sg} > 0$)

$$H_{ig} = H_{ig,ann} + H_{ig,drp} \qquad (4A\text{-}9)$$

where

$H_{ig,ann} = h_{ig} a_{gf,ann} F_{10} F_6$

where

h_{ig} and F_6 are as for bubbly SHG and $a_{gf,ann}$ and F_{10} are as for annular-mist SHL

and

$H_{ig,drp} = h_{ig} a'_{gf,drp} F_6$

where

$a'_{gf,drp}$ is as for annular mist SHG,

and h_{ig} is as for bubbly SHG.

For an annulus component, $\alpha_{ff} = \alpha_f$ and $\alpha_{fd} = 0$.

Inverted Annular Flow

SHL (superheated liquid, $\Delta T_{sf} < 0$)

$$H_{if} = H_{if,bub} + H_{ig,ann} \quad (4A\text{-}10)$$

where

$H_{if,bub}$ is as for H_{if} for bubbly with the following modifications:

$$v_{fg} = (v_g - v_f) F_{16}^2$$

where

$F_{16} = 1 - F_{17}$

$$F_{17} = \exp\left[\frac{-8(\alpha_{BS} - \alpha_{IAN})}{\alpha_{BS}}\right] F_{18}$$

α_{IAN} = α_g for inverted annular

= α_{BS} for IAN/ISLG transition (see **Figure 3.2-1**)

F_{18} = $\min\left(\frac{\alpha_g}{0.05}, 0.999999\right)$

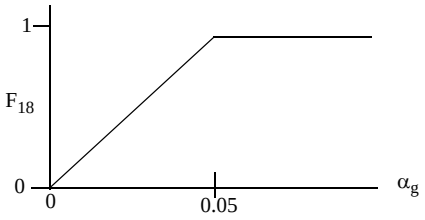

β = F_{16}

α_g = α_{bub}

α_{bub} = $\max\left[\frac{(\alpha_{IAN} - \alpha_B)}{(1 - \alpha_B)}, 10^{-7}\right]$

α_B = $F_{17}\,\alpha_{IAN}$

$a_{gf,bub}$ = $\frac{3.6\alpha_{bub}}{d_b}(1 - \alpha_B)F_{16}$

d_b = average bubble diameter (see bubbly SHL)

and

$H_{if,ann}$ = $3 \times 10^6\, a_{gf,ann}$

where

$a_{gf,ann}$ = $\frac{4}{D}F_{15}(2.5)$

D = hydraulic diameter

F_{15} = $(1 - \alpha_B)^{1/2}$.

SCL (subcooled liquid, $\Delta T_{sf} > 0$)

$H_{if} = H_{if,bub} + H_{if,ann}$ (4A-11)

where

$H_{if,bub}$ is as for bubbly SCL

and

$$H_{if,ann} = \frac{k_f}{D} 0.023\ Re_{IAN}^{0.8} a_{gf,ann} F_3$$

where

$$Re_{IAN} = (1 - \alpha_{IAN}) \frac{\rho_f |v_f - v_g|}{\mu_f} D\ .$$

$a_{gf,ann}$ and α_{IAN} are as for inverted annular SHL and F_3 is as for bubbly SHL.

SHG (superheated vapor/gas, $\Delta T_{sg} < 0$)

$$H_{ig} = H_{ig,bub} + H_{ig,ann} \qquad (4A\text{-}12)$$

where

$$H_{ig,bub} = h_{ig}\, F_6\, a_{gf,bub}$$

where

h_{ig} and F_6 are as for bubbly SHG and $a_{gf,bub}$ is as for inverted annular SHL

and

$$H_{ig,ann} = \frac{k_g}{D} F_{19} a'_{gf,ann}$$

where

$$F_{19} = 2.5 - \Delta T_{sg}\,(0.20 - 0.10\,\Delta T_{sg})$$

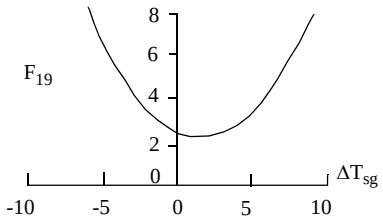

$$a'_{gf,ann} = \frac{a_{gf,ann}}{F_{20}}$$

F_{20} = 0.5 max (1.0 - F_{15}, 0.04).

F_{15} and $a_{gf,ann}$ are as for inverted annular SHL.

SCG (subcooled vapor/gas, $\Delta T_{sg} > 0$)

H_{ig} is as for inverted annular SHG.

Note that $\Delta T_{sg} > 0$ for this case (Function F_{19}).

Inverted Slug Flow

SHL (superheated liquid, $\Delta T_{sf} < 0$)

$$H_{if} = H_{if,ann} + H_{if,drp} \quad (4A\text{-}13)$$

where

$$H_{if,ann} = \frac{k_f}{D} F_{12} F_{13} a_{gf,ann}$$

where

$a_{gf,ann}$ = $\frac{4.5}{D}\alpha_B(2.5)$ (2.5 is a roughness factor)

D = hydraulic diameter

$$\alpha_B = \frac{\alpha_f - \alpha_{drp}}{1 - \alpha_{drp}}$$

α_{drp} = $(1 - \alpha_{SA})\, F_{21}$

$$F_{21} = \exp\left(-\frac{\alpha_{SA} - \alpha_g}{\alpha_{SA} - \alpha_{BS}}\right)$$

F_{21} is as for annular-mist SHL

and

$$H_{if,drp} = \frac{k_f}{d_d} F_{12} F_{13} a_{gf,drp}$$

where

$$a_{gf,drp} = \left(\frac{3.6\alpha_{drp}}{d_d}\right)(1-\alpha_B)$$

$$d_d = \text{characteristic droplet diameter } (\frac{1}{2} d_{max})$$

$$= \frac{We\,\sigma}{\rho_g v_{fg}^2},\ We = 6.0,\ We\,\sigma = \max(We\,\sigma, 10^{-10}\ N/m)$$

$$v_{fg} = \max[(v_g - v_f)F_{21}^2, 0.001 m/s],\ We = 6.0 .$$

The drop diameter is the maximum of d_d and d_{min}, where

$$d_{min} = 0.0025 \text{ m for } P^* < 0.025$$

$$= 0.0002 \text{ m for } P^* > 0.25$$

$$P^* = \frac{P}{P_{critical}} .$$

The drop diameter is the minimum of d_d, D, and 0.0025 m.

Between $P^* = 0.025$ and $P^* = 0.25$, linear interpolation is used. However, above an equilibrium quality of -0.02, the inverted slug interfacial heat transfer coefficient, H_{if}, is linearly interpolated with respect to equilibrium quality to a dispersed (droplet, mist) flow value at an equilibrium quality of zero.

SCL (subcooled liquid, $\Delta T_{sf} > 0$)

$$H_{if} = H_{if,ann} + H_{if,drp} \qquad (4A\text{-}14)$$

where

$$H_{if,ann} = \frac{k_f}{D} F_{13} a_{gf,\,ann}$$

where

F_{13} is as for annular mist SCL

$a_{gf,ann}$ is as for inverted slug SHL

and

$$H_{if,drp} = \frac{k_f}{d_d} F_{13} a_{gf,\,drp}$$

where

$a_{gf,drp}$ is as for inverted slug SHL.

However, above an equilibrium quality of -0.02, the inverted slug interfacial heat transfer coefficient, H_{if}, is linearly interpolated with respect to equilibrium quality to a dispersed (droplet, mist) flow value at an equilibrium quality of zero.

SHG (superheated vapor/gas, $\Delta T_{sg} < 0$)

$$H_{ig} = H_{ig,ann} + H_{ig,drp} \qquad (4A\text{-}15)$$

where

$$H_{ig,ann} = \frac{k_g}{D} \frac{F_{19}}{F_{22}} a_{gf,\,ann}$$

where

F_{19} is as for inverted annular SHG

$a_{gf,ann}$ is as for inverted slug SHL

$$F_{22} = \max\left\{0.02, \min\left[\frac{\alpha_g}{4}\left(1-\frac{\alpha_g}{4}\right), 0.2\right]\right\}$$

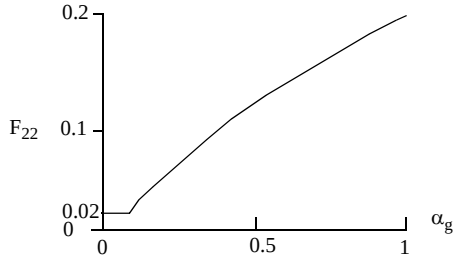

and

$$H_{ig,drp} = \frac{k_g}{d_d}(2.0 + 0.5\ Re_{drp}^{0.5})a_{gf,\,drp}$$

where

d_d and $a_{gf,drp}$ are as for inverted slug SHL

and

$$Re_{drp} = \frac{\rho_g v_{fg} d_d}{\mu_g}$$

where

We = 6.0, We σ = max (We σ, 10^{-10} N/m),

v_{fg}^2 is as for inverted slug SHL.

However, above an equilibrium quality of -0.02, the inverted slug interfacial heat transfer coefficient H_{ig}, is linearly interpolated with respect to equilibrium quality to a dispersed (droplet, mist) flow value at an equilibrium quality of zero.

SCG (subcooled vapor/gas, $\Delta T_{sg} > 0$)

H_{ig} is as for inverted slug SHG.

Dispersed (Droplet, Mist) Flow

SHL (superheated liquid, $\Delta T_{sf} < 0$)

$$H_{if} = \frac{k_f}{d_d} F_{12} F_{13} F_{23} a_{gf} \qquad (4A\text{-}16)$$

where

F_{12} and F_{13} are as for annular mist SHL.

F_{23} = $\dfrac{\alpha_{drp}}{\max(\alpha_f, 10^{-10})}$ pre-CHF

= $\dfrac{\alpha_{drp}}{\max(\alpha_f, 10^{-12})}$ post-CHF

a_{gf} = $\dfrac{3.6\alpha_{drp}}{d_d}$.

α_{drp} = $\max(\alpha_f, 10^{-3})$ $X_n \neq 0.0$ and $\alpha_g = 1.0$ pre-CHF

= $\max(\alpha_f, 10^{-4})$ $X_n = 0.0$ or $\alpha_g \neq 1.0$ pre-CHF

= $\max(\alpha_f, 10^{-4})$ post-CHF

d_d = characteristic drop diameter $(\frac{1}{2} d_{max})$

= $\dfrac{We\ \sigma}{\rho_g v_{fg}^2}$, We = 1.5 for pre-CHF and 6.0 for post-CHF,

We σ = max (We σ, 10^{-10} N/m)

v_{fg} = $v_g - v_f$,

v_{fg}^2 = $\begin{cases} \max\left(v_{fg}^2, \dfrac{We\ \sigma}{\rho_g \min(D'\alpha_{drp}^{1/3}, D)}\right) & \text{pre-CHF} \\ \max(v_{fg}^2, 10^{-6} m^2/s^2) & \text{post-CHF} \end{cases}$

D' = $\begin{cases} 0.0025\ m & \text{pre-CHF} \\ 0.0002\ m & \text{post-CHF} \end{cases}$.

For post-CHF, the minimum and maximum drop size is as for inverted slug flow.

SCL (subcooled liquid, $\Delta T_{sf} > 0$)

$$H_{if} = \frac{k_f}{d_d} F_{13} F_{23} a_{gf} \qquad \text{(4A-17)}$$

where

F_{13} is as for annular mist SCL.

F_{23} and a_{gf} are as for dispersed SHL.

SHG (superheated vapor/gas, $\Delta T_{sg} < 0$)

$$H_{ig} = \frac{k_g}{d_d}(2.0 + 0.5\ Re_{drp}^{0.5}) F_{24} a_{gf} \qquad \alpha_f > 0.0$$
$$= 0.0 \qquad \alpha_f = 0.0 \qquad \text{(4A-18)}$$

where

d_d and a_{gf} are as for dispersed SHL

$$Re_{drp} = \frac{(1-\alpha_{drp})^{2.5} \rho_g v_{fg} d_d}{\mu_g} = \frac{We \bullet \sigma (1-\alpha_{drp})^{2.5}}{\mu_g v_{fg}} \quad \text{pre-CHF and post-CHF}$$

$$F_{24} = \max [0.0, F_{26} (F_{25} - 1) + 1]$$

$$F_{25} = 10^5 \min (\alpha_f, 10^{-5})$$

$$F_{26} = 1.0 - 5.0 \min [0.2, \max (0.0, \Delta T_{sg})].$$

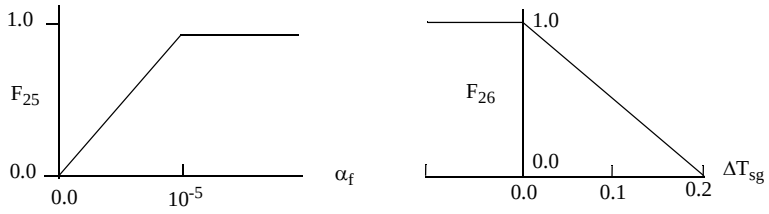

SCG (subcooled vapor/gas, $\Delta T_{sg} > 0$)

$H_{ig} = h_{ig} F_6 F_{24} a_g$ otherwise

$= 0$ $\alpha_f = 0.0$ and $P_s < P_{triple\ point}$ (4.7-19)

where

h_{ig} and F_6 are as for bubbly SHG,

F_{24} and a_{gf} are as for dispersed SHG.

Horizontally Stratified Flow

SHL (superheated liquid, $\Delta T_{sf} < 0$)

$$H_{if} = \frac{k_f}{D_{hf}}\left[0.023\ Re_f^{0.8} F_{12} - 3.81972 \frac{\Delta T_{sf} \rho_f C_{pf}}{\rho_g h_{fg} \max(4\alpha_g, 1)}\right] a_{gf} \qquad \alpha_g > 0 \text{ or } \Delta T_{sf} < -1 \qquad (4A\text{-}20)$$

$= 0$ otherwise

where

D_{hf} = liquid phase hydraulic diameter

= $\frac{\pi \alpha_f D}{\pi - \theta + \sin\theta}$ (see **Figure 3.1-2** for definition of θ)

Re_f = $\frac{\alpha_f \rho_f |v_g - v_f| D}{\mu_f}$

a_{gf} = $\left(\frac{4 \sin\theta}{\pi D}\right) F_{27}$

F_{27} = $1 + \left|\frac{v_g - v_f}{v_{crit}}\right|^{1/2}$.

SCL (subcooled liquid, $\Delta T_{sf} > 0$)

$$H_{if} = \frac{k_f}{D_{hf}}(0.023\ Re_f^{0.8}) a_{gf} \qquad \alpha_g > 0 \text{ or } \Delta T_f < -1 \qquad (4A\text{-}21)$$

$= 0$ otherwise

where

D_{hf}, Re_f, and a_{gf} are as for horizontally stratified SHL.

SHG (superheated vapor/gas, $\Delta T_{sg} < 0$)

$$H_{ig} = \frac{k_g}{D_{hg}}[0.023\ Re_g^{0.8} + 4h_{ig}\ F_6 \max(0.0, 0.25 - \alpha_g)]a_{gf} \qquad \alpha_f > 0 \text{ or } \Delta T_g > 0.2K \qquad (4A\text{-}22)$$

$= 0$ otherwise

where

D_{hg} = vapor phase hydraulic diameter

$$= \frac{\pi \alpha_g D}{\theta + \sin\theta}$$ (see **Figure 3.1-2** for definition of θ)

$$Re_g = \frac{\alpha_g \rho_g |v_g - v_f| D}{\mu_g}$$

h_{ig} and F_6 are as for bubbly SHG and a_{gf} is as for horizontally stratified SHL.

SCG (subcooled vapor/gas, $\Delta T_{sg} > 0$)

$$H_{ig} = h_{ig} F_6 a_{gf} \qquad \alpha_f > 0 \text{ or } \Delta T_g > 0.2K \qquad (4A\text{-}23)$$

$= 0$ otherwise

where

h_{ig} and F_6 are as for bubbly SHG.

a_{gf} is as for horizontally stratified SHL.

Vertically Stratified Flow

SHL (superheated liquid, $\Delta T_{sf} < 0$)

$$H_{if} = Nu\frac{k_f}{D}a_{gf}(1 - F_{30}) + H_{if,REG}F_{30} \quad (4A\text{-}24)$$

where

REG = flow regime of flow when not vertically stratified, which can be BBY, SLG, SLG/ANM, ANM, MPR, IAN, IAN/ISL, ISL, MST, MPO, BBY/IAN, IAN/ISL-SLG, SLG/ISL, ISL-SLG/ANM, ANM/MST, MPR/MPO (see flow regime map, **Figure 3.2-1**)

F_{30} = max (F_{32}, F_{33}, F_{34})

F_{32} = 1.0 - min (1.0, $100\alpha_f$)

$$F_{33} = \max\left[0.0, 2.0\min\left(1.0, \frac{v_m}{v_{Tb}}\right) - 1.0\right]$$

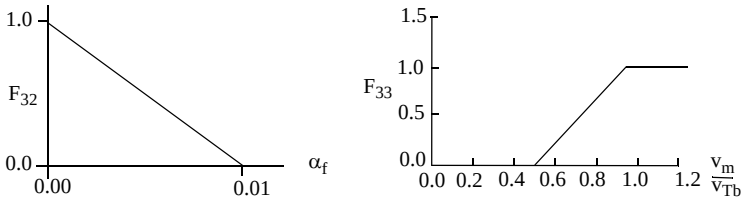

v_{Tb} = Taylor bubble rise velocity, Equation (3.2-16)

$$v_m = \frac{G_m}{\rho_m}$$

G_m = $\alpha_g\rho_g |v_g| + \alpha_f\rho_f |v_f|$

ρ_m = $\alpha_g\rho_g + \alpha_f\rho_f$

F_{34} = max[0.0, min (1.0, -0.5 ΔT_{sf})]

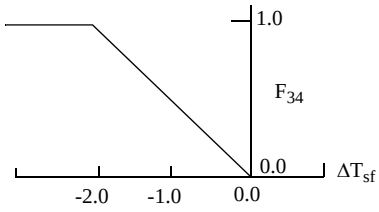

D = hydraulic diameter

$$Nu = 0.27\,(Gr_f Pr_f)^{0.25}$$

where

$$Gr = \frac{g\beta\rho_f^2 D^3 \max(|T_f - T^s|, 0.1K)}{\mu_f^2}$$

$$\beta = \max(\beta_f, 10^{-5}\,K^{-1})$$

$$Pr = \left(\frac{\mu C_p}{k}\right)_f$$

$$a_{gf} = \frac{A_c}{V} = \frac{A_c}{A_c L} = \frac{1}{L}$$

where L = length of volume cell and A_c = cross-sectional area of cell.

SCL (subcooled liquid, $\Delta T_{sf} > 0$)

H_{if} is as for vertically stratified SHL.

SHG (superheated vapor/gas, $\Delta T_{sg} < 0$)

$$H_{ig} = Nu\left(\frac{k_g}{D}\right) a_{gf}(1 - F_{35}) + H_{ig,\,REG} F_{35} \qquad (4A\text{-}25)$$

where

$$F_{35} = \max(F_{32}, F_{36}, F_{33})$$

REG, F_{33}, and Nu are as for vertically stratified SHL, and Nu uses vapor/gas properties instead of liquid properties

$$F_{32} = \begin{cases} 1.0 - \min(1.0, 100\alpha_g) & \text{level model on} \\ 0.0 & \text{level model off} \end{cases}$$

F_{36} = min (1.0, 0.5 ΔT_{sg})

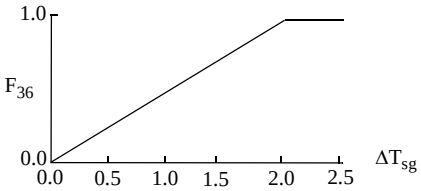

a_{gf} is as for vertically stratified SHL.

SCG (subcooled vapor/gas, $\Delta T_{sg} > 0$)

H_{ig} is as for vertically stratified SHG.

Transitions

Notes:

1. The abbreviations for flow regimes are defined in **Figure 3.1-1** and **Figure 3.2-1**.
2. Subscript "p" represents both f for liquid and g for vapor/gas phases.
3. Transition void fractions are illustrated in **Figure 3.1-1** and **Figure 3.2-1**.
4. These are transitions between flow regimes shown in **Table 4.1-1**.

Horizontal Flow

Slug-Annular-Mist Transition

$$H_{ip_{SLG-ANM}} = [H_{ip_{SLG}}]^{FSLUG}[H_{ip_{ANM}}]^{FANM} \quad (4A\text{-}26)$$

where

FANM = max {0.0, min [20 (α_g - α_{DE}), 1.0]}

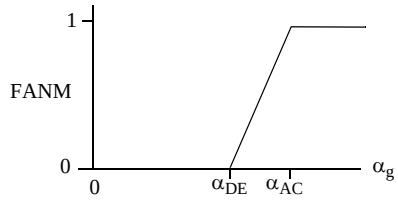

FSLUG = max [0.0, min(1.0 - FANM, 1.0)].

Transition to Horizontally Stratified Flow

$$H_{ip_{REG-HS}} = H_{ip_{REG}}\left(\frac{H_{ip_{HS}}}{H_{ip_{REG}}}\right)^{FSTRAT} \quad (4A\text{-}27)$$

where

REG = BBY, SLG, SLG/ANM, ANM, or MPR, as appropriate

FSTRAT = $F_{28}\,F_{29}\,F_{31}$

$$F_{28} = \min\left\{1.0, \max\left[0.0, 2\left(1 - \frac{|v_g - v_f|}{v_{crit}}\right)\right]\right\}$$

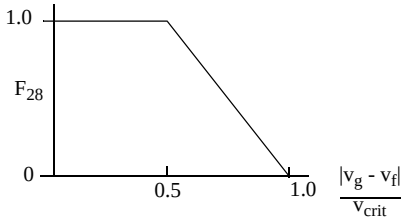

v_{crit} is as for annular mist SHL (horizontal)

$$F_{29} = \min\left[1.0, \frac{\alpha_f}{\alpha_{EF}}, \max(0.0, 10^5\alpha_g - 1)\right] \min\left[1.0, \frac{\alpha_f}{\alpha_{EF}}, \max(0.0, 10^5\alpha_g - 1)\right]$$

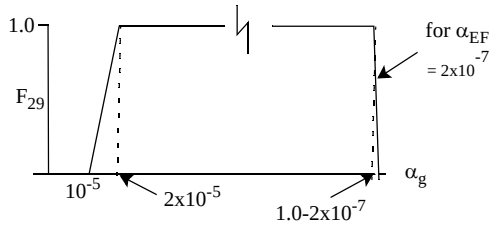

α_{EF} is as for annular mist SHL

F_{31} = min {1.0, max[0.0, 0.002(3,000 - G)]}

G is as for vertically stratified SHL.

Vertical Flow

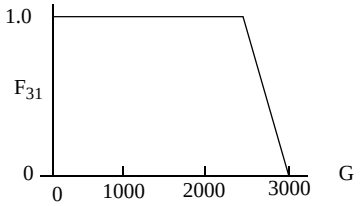

Slug-Annular Mist Transition

$H_{ip_{SLG/ANM}}$ is as for $H_{ip_{SLG/ANM}}$ for horizontal flow.

Transition from Nonstratified to Vertically Stratified

See vertically stratified flow herein.

Inverted Annular-Inverted Slug Transition

$$H_{ip_{IAN-ISL}} = (H_{ip_{IAN}})^{FIAN}(H_{ip_{ISL}})^{FISLG} \quad (4A\text{-}28)$$

where

FIAN = max {0.0, min [5(α_{AB} + 0.2 - α_g), 1.0]}

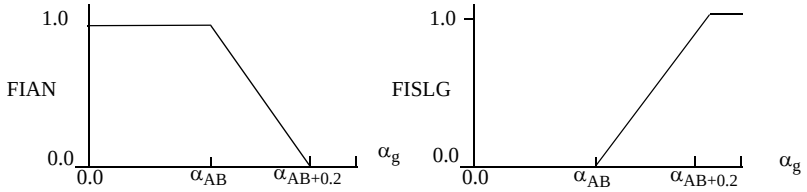

FISLG = max [0.0, min (1.0 - FIAN, 1.0)].

Transitional Boiling Regimes

$$H_{ip_{REG1-REG2}} = H_{ip_{REG2}} \bullet (1 - Z) + H_{ip_{REG2}} \bullet Z \quad (4A\text{-}29)$$

where

REG1-REG2 can represent BBY-IAN, IAN/ISL-SLG, SLG-ISL, ISL-SLG/ANM, ANM/MST, MPR/MPO (see **Figure 3.2-1**)

Z = max (0.0, min {1.0, 10.0 [min (1.0, $T_{windo} \bullet T_{gsat}$)] (0.4 - α_{AB})})

α_{AB} = transition from bubbly-to-slug flow (see **Figure 3.2-1** and **Figure 3.2-2**)

T_{gsat} = $T_g - T^s - 1.0$

T_{windo} = 0.06666667 for $\frac{P}{P_{crit}} < 0.025$

= $\frac{1}{15 + 200\left(\frac{P}{P_{crit}} - 0.025\right)}$ $0.025 \le \frac{P}{P_{crit}} < 0.25$

= 0.016666667 $\frac{P}{P_{crit}} \ge 0.25$.

High Mixing Map

Bubbly-Mist Transition

$$H_{ip_{CTB-CTM}} = FBUB \bullet H_{ip_{CTB}} + FDIS \bullet H_{ip_{ctm}} \quad (4A\text{-}30)$$

where

FDIS = $\max\left\{0.0, \min\left[\left(\frac{\alpha_g - \alpha^*}{1 - \alpha^* - \alpha^{**}}\right), 1.0\right]\right\}$

α^* = $0.5 \exp [-10.0 (\alpha_g - 0.5)]$

α^{**} = $0.05 \exp [-10.0 (0.95 - \alpha_g)]$

FBUB = 1 - FDIS.

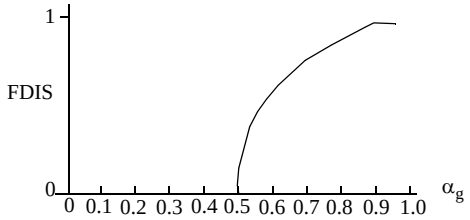

Modifications for Noncondensable Gas

Note: Function F_4, which is part of Function F_3, represents a modification to H_{if} for bubbly and inverted annular SHL based on the noncondensable quality, X_n (fraction of α_g which is noncondensable). The modifications below are applied to all volumetric heat transfer coefficients H_{if} and H_{ig} for all flow regimes as described.

SHL (superheated liquid, $\Delta T_{sf} < 0$)

H_{if} remains unchanged (except as noted above).

SCL (subcooled liquid, $\Delta T_{sf} > 0$)

$$H_{if} = H_{if_{REG}}[F_{40}F_{39} + (1 - F_{39})] \tag{4A-31}$$

where

REG = flow regime or transition regime in question

F_{39} = $\min(10^{-5}, \alpha_g)\, 10^5$

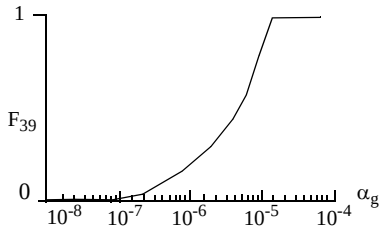

F_{40} = $1 - 10\, X_n$ $\quad X_n < 0.063$

= $1 - 0.938 X_n^{0.13}$ $\quad 0.063 \leq X_n \leq 0.60$

= $1 - X_n^{0.22}$ $\quad X_n > 0.60.$

SHG (superheated vapor/gas, $\Delta T_{sg} < 0$)

H_{ig} remains unchanged.

SCG (subcooled vapor/gas, $\Delta T_{sg} > 0$)

$$H_{ig} = H_{ig_{REG}}(1 - X_n)F_{41} \quad (4A\text{-}32)$$

where

REG = flow regime or transition regime in question

F_{41} = max [1.0, min (0.0, ΔT_{sg})].

Appendix 4B--Fuid Properties for Water and Steam for a Typical Reactor Operational Condition

Temperature = 315.56 °C (600 °F).

Pressure = 10.640 MPa (1,543.220 psia).

h_{fg} = 1.280 x 10^6 J/kg (550.501 Btu/lb_m).

Saturation Properties

Liquid Water

ρ_f = 677.7 kg/m^3 (42.309 lb_m/ft^3)

C_{pf} = 6,346.1 J/kg•K (1.5157 Btu/lb_m•°F)

k_f = 0.5175 W/m•K (0.299 Btu/hr•ft•°F)

μ_f = 7.996 x 10^{-5} kg/m•s (5.3731 x 10^{-5} lb_m/ft•s)

σ = 1.086 x 10^{-2} N/m (0.744 x 10^{-3} lb_f/ft).

Water Vapor (Steam)

ρ_g = 59.94 kg/m^3 (3.7417 lb_m/ft^3)

C_{pg} = 7,209 J/kg•K (1.7219 Btu/lb_m•°F)

k_g = 0.0796 W/m•K (0.04598 Btu/hr•ft•°F)

μ_g = 2.061 x 10^{-5} kg/m•s (1.3848 x 10^{-5} lb_m/ft•s).

5 Closure Relations Required by Fluid Mass Conservation Equations

The fluid mass conservation equations require only the mass transfer rate between the phases, Γ_g, for closure. The code calculation of Γ_g is directly tied to the energy partitioning relationships discussed in Section 4.7. Therefore, there is no new information to be added in this section. The entirety of the mass conservation closure relations is addressed in Section 4.7.

6 Momentum Equation Closure Relations

This section discusses the relations necessary for closure in the momentum equation. The relations covered are interphase friction and wall drag.

6.1 Interphase Friction

6.1.1 Basis

The semi-implicit scheme one-dimensional finite difference equation for the difference momentum equation, Equation (2.2-7), is

$$
\begin{aligned}
&\left(1+\frac{C\rho_m^2}{\rho_g\rho_f}\right)_j^n[(v_g^{n+1}-v_g^n)-(v_f^{n+1}-v_f^n)]_j\Delta x_j \\
&+\frac{1}{2}\left(\frac{\dot\alpha_g\dot\rho_g}{\alpha_g\rho_g}\right)_j^n[(v_g^2)_L^n-(v_g^2)_K^n]\Delta t-\frac{1}{2}\left(\frac{\dot\alpha_g\dot\rho_g}{\alpha_g\rho_g}\right)_j^n VISG_j^n\Delta t \\
&-\frac{1}{2}\left(\frac{\dot\alpha_f\dot\rho_f}{\alpha_f\rho_f}\right)_j^n[(v_f^2)_L^n-(v_f^2)_K^n]\Delta t+\frac{1}{2}\left(\frac{\dot\alpha_f\dot\rho_f}{\alpha_f\rho_f}\right)_j^n VISF_j^n\Delta t=-\left(\frac{\rho_f-\rho_g}{\rho_f\rho_g}\right)_j^n(P_L-P_K)^{n+1}\Delta t \\
&-\left(FWG_j^n(v_g)_j^{n+1}-FWF_j^n(v_f)_j^{n+1}-\left[\frac{\Gamma_g^n(\rho_m^n v_I^{n+1}-\alpha_f^n\rho_f^n v_g^{n+1}-\alpha_g^n\rho_g^n v_f^{n+1})}{(\alpha_g\rho_g\alpha_f\rho_f)^n}\right]_j\right. \\
&\left.-(f_x)_j^n\left(\frac{1}{\alpha_g\rho_g}+\frac{1}{\alpha_f\rho_f}\right)_j^n[(f_{wg})_j^n(v_g)_j^{n+1}-(f_{wf})_j^n(v_f)_j^{n+1}]\right. \\
&\left.+(\rho_m FI)_j^n\{[1+f_x(C_1-1)]_j^n(v_g)_j^{n+1}-[1+f_x(C_0-1)]_j^n(v_f)_j^{n+1}\}\right)\Delta x_j\Delta t \\
&-\left[\left(\frac{\dot\alpha_g\dot\rho_g}{\alpha_g\rho_g}\right)_j^n HLOSSG_j^n v_{g,j}^{n+1}-\left(\frac{\dot\alpha_f\dot\rho_f}{\alpha_f\rho_f}\right)_j^n HLOSSF_j^n v_{f,j}^{n+1}\right]\Delta t \\
&+\left(\frac{\rho_m}{\rho_g\rho_f}\right)_j^n(\rho_f-\rho_g)_j^n B_y(y_L^n-y_K^n)\Delta t
\end{aligned}
\tag{6.1-1}
$$

This equation contains the term

$$(\rho_m FI)_j^n\{[1+f_x(C_1-1)]_j^n(v_g)_j^{n+1}-[1+f_x(C_0-1)]_j^n(v_f)_j^{n+1}\}\Delta x_j\Delta t \tag{6.1-2}$$

which represents the interfacial friction force. This term is the product of a global interfacial friction coefficient and a relative velocity. The global interfacial friction coefficient FI is computed from

$$FI=\frac{\frac{F_i}{\alpha_g\rho_g}+\frac{F_i}{\alpha_f\rho_f}}{\rho_m v_R} \tag{6.1-3}$$

where the computation of the interfacial force F_i and the relative velocity between the phases v_R depends upon which of the two models for the interfacial force is being used. The derivation of this equation was shown in Volume I (Section 3.3.6) and will not be repeated here. The coefficients in this equation are computed from two different models, and the choice of which model to use depends upon the flow regime. The term f_x is used to specify which form of the relative velocity is used. The two models are the drift flux model and the drag coefficient model. These models will be summarized in the following sections.

6.1.1.1 Drift Flux Model. The drift flux approach is used only in the bubbly and slug-flow regimes for vertical flow. The method used is discussed in Volume I (Section 3.3.6) of this manual, and it will not be repeated here (see also Anderson[6.1-1] and Ishii[6.1-2, 6.1-3]). The final equations for the interphase friction force are

$$F_i = C_i |v_R| v_R \tag{6.1-4}$$

$$C_i = \frac{\alpha_g \alpha_f^3 (\rho_f - \rho_g) g \sin\phi_j}{|v_{gj}| v_{gj}} \tag{6.1-5}$$

$$v_R = C_1 v_g - C_0 v_f \tag{6.1-6}$$

where g is the gravitational acceleration, ϕ_j is the inclination (vertical) angle of the junction, and v_{gj} is the vapor/gas drift velocity. The vapor/gas drift velocity v_{gj} used in Equation (6.1-5) and the profile slip distribution coefficient C_0 used in Equation (6.1-6) are determined from a given geometry and flow condition. As discussed in Volume I, the term C_1 used in Equation (6.1-6) is given by

$$C_1 = \frac{1 - C_0 \alpha_g}{\alpha_f} \quad . \tag{6.1-7}$$

6.1.1.2 Drag Coefficient Model. The drag coefficient approach is used in all flow regimes other than vertical bubbly and slug-flow. This is also discussed in Volume I (Section 3.3.6) of this manual. For this case, $f_x = 0$. Thus Equations (6.1-4), (6.1-5), and (6.1-5) become

$$F_i = C_i |v_R| v_R \tag{6.1-8}$$

$$C_i = \frac{1}{8} \rho_c S_F a_{gf} C_D \tag{6.1-9}$$

$$v_R = v_g - v_f \tag{6.1-10}$$

where

ρ_c = density of the continuous phase

C_D = drag coefficient

a_{gf} = interfacial area per unit volume

S_F = shape factor, assumed to be unity (1.0), since rippling is assumed to not be a factor for interface drag.

The 1/8th factor in Equation (6.1-9) occurs as the result of the usual 1/2 factor being multiplied by 1/4. The 1/4th factor occurs because drag coefficients are based on projected area (i.e., πr^2) and a_{gf} is the surface area (i.e., $4\pi r^2$). To determine the interphase drag per unit volume, the combination of C_D and a_{gf} must be used.

6.1.2 Code Implementation

The interphase friction model is used to determine the interphase friction terms and the distribution parameters in the difference momentum equation. The interphase friction terms FIGJ and FIFJ, are calculated in subroutine VEXPLT, which calculates the sum and difference momentum equations. These terms, which are only used in the difference momentum equation, are of the form

$$FIGJ = \left(\frac{1}{\alpha_g\rho_g} + \frac{1}{\alpha_f\rho_f}\right) \bullet [FIJ \bullet (\left|C1 \bullet v^n_{g,j} - C0 \bullet v^n_{f,j}\right| C1 + 0.01)\Delta x_j + FIDXUP] \quad (6.1\text{-}11)$$

$$FIFJ = \left(\frac{1}{\alpha_g\rho_g} + \frac{1}{\alpha_f\rho_f}\right) \bullet [FIJ \bullet (\left|C1 \bullet v^n_{g,j} - C0 \bullet v^n_{f,j}\right| C0 + 0.01)\Delta x_j + FIDXUP] \quad (6.1\text{-}12)$$

The interphase friction terms, FIGJ and FIFJ, make use of the term FIJ, which is determined in subroutine FRICID. The term FIJ is set equal to the term FIJX, which is determined in subroutine PHANTJ. It can be shown that FIJ is equivalent to C_i, where C_i is determined from either Equation (6.1-5) or Equation (6.1-9). The term FIJ is determined for each junction from different models depending on what flow regimes are calculated for the junction (see Section 3).

The distribution terms C0 and C1 in Equations (6.1-11) and (6.1-12) are determined from the drift flux model distributions parameters C_0 and C_1 and the term f_x. They have the form

$$C0 = 1 + f_x(C_0 - 1) \quad (6.1\text{-}13)$$

and

$$C1 = 1 + f_x(C_1 - 1) \tag{6.1-14}$$

In subroutine VEXPLT, the terms FIGJ and FIFJ from Equations (6.1-11) and (6.1-12) are both multiplied by the time step size Δt. When the resulting terms are multiplied by the new time velocities v_{gj}^{n+1} and v_{fj}^{n+1}, respectively, it can be shown that the difference between the resulting terms is equal to (6.1-2) plus two extra terms, where FI is determined from Equation (6.1-3). The first extra term arises because Equations (6.1-11) and (6.1-12) contains the constant 0.01, which results in an extra term of the form

$$\left(\frac{1}{\alpha_g \rho_g} + \frac{1}{\alpha_f \rho_f}\right) FIJ(0.01)(v_{g,j}^{n+1} - v_{f,j}^{n+1})\Delta x_j \Delta t \tag{6.1-15}$$

This provides a friction force when the absolute value of the old time relative velocity $(C1 \bullet v_{g,j}^{n} - C0 \bullet v_{f,j}^{n})$ is small (i.e., less than 0.01 m/s)

The second extra term arises because Equations (6.1-11) and (6.1-12) contain the term FIDXUP. This term is a result of the extra interphase friction term $C_{i,extra}$ discussed in Section 7.1.1. This term is used in the abrupt area change model to add extra interphase friction to ensure more homogeneous flow when the flow becomes more increasingly cocurrent.

Some void fraction weighting is used between the two volumes to handle the case of countercurrent flow. This approach follows the method used in TRAC-B.[6.1-4,6.1-5] A junction void fraction $(\alpha_{g,j}^{*})$ is calculated from either of the volume void fractions of the neighboring volumes ($\alpha_{g,K}$ or $\alpha_{g,L}$) using a donor direction based on the mixture superficial velocity (j_m). A cubic spline weighting function is used to smooth the void fraction discontinuity across the junction when $|j_m| < 0.465$ m/s. The purpose of this method is to use a void fraction that more closely represents the real junction void fraction. This has the form

$$\alpha_{g,j}^{*} = w_j \bullet \alpha_{g,K} + (1 - w_j) \bullet \alpha_{g,L} \tag{6.1-16}$$

where

$$w_j = 1.0 \qquad j_m > 0.465 \text{ m/s}$$

$$= x_1^2(3 - 2x_1) \qquad -0.465 \text{ m/s} \le j_m \le 0.465 \text{ m/s}$$

$= \quad 0.0 \qquad j_m < -0.465$ m/s

$$x_1 = \frac{j_m + 0.465}{0.93}$$

$$j_m = \dot{\alpha}_{g,j} v_{g,j} + \dot{\alpha}_{f,j} v_{f,j} .$$

For horizontal stratified flow, the void fraction from the entrainment/pull through (or offtake) model is used. The case of vertical stratified flow is discussed in Section 6.1.3.8. The junction mass flux is then determined from

$$G_j = \dot{\alpha}_{g,j} \dot{\rho}_{g,j} |v_{g,j}| + \dot{\alpha}_{f,j} \dot{\rho}_{f,j} |v_{f,j}| \quad . \tag{6.1-17}$$

Then, depending on whether the volume is vertical or horizontal, the appropriate flow regime is determined. The flow regime is the same as the one used to determine the interfacial heat transfer coefficients, except that junction properties (usually based on the donor direction, except for $\alpha^*_{g,j}$) are used. The diameter used in these calculations is the junction diameter (D_j).

The physical junction diameter is used in many of the interphase drag models. This diameter, D_T, is calculated from the equation

$$D_T = D_j \left(\frac{A_T}{A_j} \right)^{1/2} \tag{6.1-18}$$

where

D_j = code junction diameter

A_T = physical junction area

A_j = code junction area.

For each ATHENA flow regime described, the model basis for either the drift flux C_i or the C_i from the combination of C_D and a_{gf} and the code implementation will be described next.

6.1.3 Individual Interphase Friction Models

The individual models for bubbly, slug, annular mist, inverted annular, inverted slug, and dispersed flow regimes are first discussed in the following sections. The models for stratified flows are then discussed, followed by a discussion of the models for transition regions between the flow regimes.

6.1.3.1 Bubbly Flow

6.1.3.1.1 Model--The bubbly and mist flow regimes are considered dispersed flow. For vertical bubbly flow, the drift flux model is used. For non-vertical bubbly flow and all droplet (mist) flow situations, the drag coefficient model is used.

The drag coefficient model will first be discussed. According to Wallis[6.1-6] and Shapiro,[6.1-7] the dispersed bubbles or droplets can be assumed to be spherical particles with a size distribution of the Nukiyama-Tanasawa form. The Nukiyama-Tanasawa distribution function in nondimensional form is (see Volume I, Section 3).

$$p^*(d^*) = 4d^{*2} e^{-2d^*} \tag{6.1-19}$$

where $d^* = \frac{d}{d'}$; d' is the most probable particle diameter, and p^* is the probability of particles with nondimensional diameter of d^*. With this distribution, it can be shown that the average particle diameter d_o = 1.5 d', and the surface area per unit volume is

$$a_{gf} = \frac{6\bar{\alpha}}{d'} \frac{\int d^{*2} p^* dd^*}{\int d^{*3} p^* dd^*} = \frac{2.4\bar{\alpha}}{d'} \tag{6.1-20}$$

where $\bar{\alpha} = \alpha_g$ for bubbles and $\bar{\alpha} = \alpha_f$ for droplets. In terms of the average diameter, d_o, the interfacial area per unit volume, a_{gf}, is

$$a_{gf} = \frac{3.6\bar{\alpha}}{d_o} \quad . \tag{6.1-21}$$

The average diameter d_o is obtained by assuming that $d_o = (1/2)\, d_{max}$. The maximum diameter, d_{max}, is related to the critical Weber number, We, by

$$We = \frac{d_{max}\rho_c (v_g - v_f)^2}{\sigma} \quad . \tag{6.1-22}$$

The values for We are presently taken as We = 10.0 for bubbles, We = 3.0 for pre-CHF droplets, and We = 12.0 for post-CHF droplets, these values being based on the maximum diameter, d_{max}.

The drag coefficient to be used in nonvertical bubbly flow and all droplet flow situations is given by Ishii and Chawla[6.1-8] as

$$C_D = \frac{24(1 + 0.1Re_p^{0.75})}{Re_p} \tag{6.1-23}$$

for the viscous regime where the particle Reynolds number Re_p is defined as

$$Re_p = \frac{\rho_c |v_g - v_f| d_o}{\mu_m} \quad . \tag{6.1-24}$$

The density, ρ_c, is for the continuous phase and is given by ρ_f for bubbles and ρ_g for drops. The mixture viscosity, μ_m, is $\mu_m = \frac{\mu_f}{\alpha_f}$ for bubbles and $\mu_m = \frac{\mu_g}{(\alpha_g)^{2.5}}$ for pre-CHF droplets. For post-CHF droplets, $\mu_m = \mu_g$ is used.

For vertical bubbly flow, the interphase friction terms are calculated using drift flux correlations from the literature based on Putney's work.[6.1-9,6.1-10,6.1-11,6.1-12,6.1-13] **Table 6.1-1** indicates which correlations are used for different geometry and flow conditions. The number in parenthesis is the value of the minor edit/plot variable IREGJ, the vertical bubbly/slug flow junction flow regime number. The name in parenthesis is the subroutine used to calculate the correlation. It should be noted that the EPRI correlation implementation has some differences between bundles and pipes; this is discussed later in the manual .

The correlation labeled EPRI is by Chexal and Lellouche.[6.1-14] The correlation has been recently modified[6.1-15,6.1-16] and many of the changes have been incorporated into ATHENA. The distribution coefficient C_0 is calculated from

$$C_0 = \frac{L}{K_0 + (1 - K_0)(\alpha_g)^r} \tag{6.1-25}$$

where

$$\alpha_g = \max(\alpha^*_{g,j}, 10^{-2})$$

$$\alpha_f = \min(1 - \alpha_g, 10^{-2})$$

$$L_n = 1 - \exp(-\alpha_g C_p) \qquad \text{if } \alpha_g C_p < 170$$

Table 6.1-1 Drift flux void fraction correlations for vertical bubbly-slug flow.

Flow rates	**Rod bundles**	**Narrow rectangular channels**	**Small pipes D ≤ 0.018m**	**Intermediate pipes 0.018m < D ≤ 0.08m**	**Large pipes 0.08m < D**
High upflow rates $G \geq 100$ kg/m^2•s	EPRI (2) (eprij)	Griffith (2) (griftj)	EPRI (3) (eprij)	EPRI (9) (eprij)	Churn-turbulent bubbly flow (14) transition (15) Kataoka-Ishii (16) (katokj)
Medium upflow rates 50 kg/m^2•s < G < 100 kg/m^2•s			Transition[1] (5)	Transition[a] (13)	
Low upflow, downflow, and countercurrent flow rates - 50 kg/m^2•s ≤ G ≤ 50 kg/m^2•s			Zuber-Findlay slug flow (4) (zfslgj)	Churn-turbulent bubbly flow (10) transition (11) Kataoka-Ishii (12) (katokj)	
Medium downflow rates - 100 kg/m^2•s < G <- 50 kg/m^2•s			Transition[a] (5)	Transition[a] (13)	
High downflow rates G ≤ -100 kg/m^2•s			EPRI (3) (eprij)	EPRI (9) (eprij)	

1. Interpolation is applied between different flow rates in pipes.

$$= \quad 1 \qquad \text{otherwise}$$

$$L_d = 1 - \exp(-C_p) \qquad \text{if } C_p < 170$$

$$= \quad 1 \qquad \text{otherwise}$$

$$L = \frac{L_n}{L_d}$$

$$C_p = \left| \frac{4P_{crit}^2}{P(P_{crit} - P)} \right|$$

P_{crit} = critical pressure

K_0 = $B_1 + (1 - B_1)\left(\frac{\rho_g}{\rho_f}\right)^{1/4}$

B_1 = $\min(0.8, A_1)$

A_1 = $\frac{1}{1 + \exp\left\{\max\left[-85, \min\left(85, -\frac{Re}{60{,}000}\right)\right]\right\}}$

Re = Re_g if $Re_g > Re_f$ or $Re_g < 0$

= Re_f otherwise

Re_f = $\frac{\rho_f j_f D_h}{\mu_f}$ (local liquid superficial Reynolds number)

Re_g = $\frac{\rho_g j_g D_h}{\mu_g}$ (local vapor/gas superficial Reynolds number)

j_f = $\alpha_f v_f$ (liquid superficial velocity)

j_g = $\alpha_g v_g$ (vapor/gas superficial velocity)

r = $\frac{1 + 1.57\left(\frac{\rho_g}{\rho_f}\right)}{1 - B_1}$.

The sign of j_k is positive if phase k flows upward and negative if it flows downward. This convention determines the sign of Re_g, Re_f, and Re.

The vapor/gas drift velocity, v_{gj}, for the Chexal-Lellouche correlation is calculated from

$$v_{gj} = 1.41\left[\frac{(\rho_f - \rho_g)\sigma g}{\rho_f^2}\right]^{1/4} C_1 C_2 C_3 C_4 \qquad (6.1\text{-}26)$$

where

$$C_1 = (1-\alpha_g)^{B_1} \quad \text{if } Re_g \geq 0$$

$$= (1-\alpha_g)^{0.5} \quad \text{if } Re_g < 0.$$

$$C_2 = 1 \quad \text{if } \frac{\rho_f}{\rho_g} \geq 18 \text{ and } C_5 \geq 1$$

$$= 1 \quad \text{if } \frac{\rho_f}{\rho_g} \geq 18 \text{ and } C_5 < 1 \text{ and } C_6 \geq 85$$

$$= \frac{1}{1-\exp(-C_6)} \quad \text{if } \frac{\rho_f}{\rho_g} \geq 18 \text{ and } C_5 < 1 \text{ and } C_6 < 85$$

$$= 0.4757\left\{\ln\left[\max\left(1.00001, \frac{\rho_f}{\rho_g}\right)\right]\right\}^{0.7} \quad \text{if } \frac{\rho_f}{\rho_g} < 18$$

$$C_5 = \left[150\left(\frac{\rho_g}{\rho_f}\right)\right]^{1/2}$$

$$C_6 = \frac{C_5}{1-C_5}$$

$$C_4 = 1 \quad \text{if } C_7 \geq 1$$

$$= \frac{1}{1-\exp(-C_8)} \quad \text{if } C_7 < 1$$

$$C_7 = \left(\frac{D_2}{D}\right)^{0.6}$$

D_2 = 0.09144 m (normalizing diameter)

$$C_8 = \frac{C_7}{1-C_7}$$

The parameter C_3 depends on the directions of the vapor/gas and liquid flows:

Upflow (both j_g and j_f are positive)

$$C_3 = \max\left[0.50, 2\exp\left(-\frac{|Re_f|}{300{,}000}\right)\right].$$

Downflow (both j_g and j_f are negative) or countercurrent flow (j_g is positive, j_f is negative)

$$C_3 = 2\left(\frac{C_{10}}{2}\right)^{B_2}$$

$$B_2 = \frac{1}{\left(1 + 0.05\left|\frac{Re_f}{350{,}000}\right|\right)^{0.4}}$$

$$C_{10} = 2\exp\left[\frac{(|Re_f|)^{0.4}}{350{,}000}\right] - 1.7|Re_f|^{0.035}\exp\left[\frac{-|Re_f|}{60{,}000}\left(\frac{D_1}{D}\right)^2\right] + \left(\frac{D_1}{D}\right)^{0.1}|Re_f|^{0.001}$$

D_1 = 0.0381 m (normalizing diameter).

The parameters C_1, C_2, C_3, C_4, ..., C_{10} are from the Chexal-Lellouche correlation.[6.1-14, 6.1-15,6.1-16]

The correlation labelled Griffith is for vertical narrow rectangular channels. The distribution parameter is given by Ishii[6.1-3]

$$C_0 = 1.35 - 0.35\sqrt{\frac{\rho_g}{\rho_f}} \tag{6.1-27}$$

and the drift velocity is given by Griffith[6.1-17]

$$v_{gj} = \left(0.23 + 0.13\frac{W}{S}\right)\left[\frac{(\rho_f - \rho_g)gS}{\rho_f}\right]^{1/2} \tag{6.1-28}$$

where W is the channel width (pitch, gap, short dimension) perpendicular to the flow and S is the channel length (span,long dimension) perperdiculat to the flow.

The correlation labeled Zuber-Findlay slug flow is by Zuber and Findlay.[6.1-18,6.1-19] The distribution parameter is given by

$$C_0 = 1.2 \tag{6.1-29}$$

and the drift velocity is given by

$$v_{gj} = 0.35\left[\frac{(\rho_f - \rho_g)gD}{\rho_f}\right]^{1/2} \quad . \tag{6.1-30}$$

The correlation labeled Kataoka-Ishii is by Kataoka and Ishii.[6.1-20] The distribution parameter is given by the modified Rouhani condition[6.1-21] used in TRAC-BF1[6.1-22]

$$C_0 = C_\infty - (C_\infty - 1)\left(\frac{\rho_g}{\rho_f}\right)^{1/2}$$

$$C_\infty = 1 + 0.2\left[\frac{\rho_f (gD)^{1/2}}{|G| + 0.001}\right]^{1/2} \tag{6.1-31}$$

and the drift velocity is given by

$$\begin{aligned} v_{gj} &= 0.0019(D^*)^{0.809}\left(\frac{\rho_g}{\rho_f}\right)^{-0.157} N_{\mu f}^{-0.562}\left[\frac{\sigma g(\rho_f - \rho_g)}{\rho_f^2}\right]^{1/4} \qquad \text{for } D^* \le 30 \\ &= 0.030\left(\frac{\rho_g}{\rho_f}\right)^{-0.157} N_{\mu f}^{-0.562}\left[\frac{\sigma g(\rho_f - \rho_g)}{\rho_f^2}\right]^{1/4} \qquad \text{for } D^* > 30 \end{aligned} \tag{6.1-32}$$

where the Bond number, D^*, is given by

$$D^* = D\left[\frac{g(\rho_f - \rho_g)}{\sigma}\right]^{1/2} \tag{6.1-33}$$

and the viscosity number, $N_{\mu f}$, is given by

$$N_{\mu f} = \frac{\mu_f}{\left\{\rho_f \sigma\left[\frac{\sigma}{g(\rho_f - \rho_g)}\right]^{1/2}\right\}^{1/2}} \quad . \tag{6.1-34}$$

The correlation labeled Churn Turbulent Bubbly Flow is by Zuber and Findlay.[6.1-18,6.1-19] The distribution parameter is given by the modified Rouhani correlation[6.1-21] used in TRAC-BF1[6.1-22]

$$C_0 = C_\infty - (C_\infty - 1)\left(\frac{\rho_g}{\rho_f}\right)^{1/2}$$

$$C_\infty = 1 + 0.2\left[\frac{\rho_f (gD)^{1/2}}{|G| + 0.001}\right]^{1/2}$$ [Equation (6.1-31)]

and the drift velocity is given by

$$v_{gj} = 1.41\left[\frac{\sigma g(\rho_f - \rho_g)}{\rho_f^2}\right]^{1/4} \quad . \tag{6.1-35}$$

For intermediate pipes (low upflow, downflow, and countercurrent flow rates) and large pipes (all cases), the churn turbulent bubbly flow correlation is applied when

$$j_g^+ = \frac{j_g}{\left[\frac{\sigma g(\rho_f - \rho_g)}{\rho_f^2}\right]^{1/4}} \le j_{g1}^+ = 0.5 \tag{6.1-36}$$

where $j_g = \alpha_g |v_g|$ is the vapor/gas superficial velocity. The Kataoka-Ishii correlation is applied when

$$j_g^+ \ge j_{g2}^+ \tag{6.1-37}$$

where $j_{g2}^+ = 2.5$. Linear interpolation is used between the two correlations.

Putney has also placed a countercurrent flow limitation (CCFL) on the drift flux parameters. The limitation is based on the Kutateladze condition

$$|Ku_g|^{1/2} + m|Ku_f|^{1/2} = Ku_{crit}^{1/2} \tag{6.1-38}$$

where

$$Ku_g = \frac{\alpha_g v_g \rho_g^{1/2}}{[\sigma g(\rho_f - \rho_g)]^{1/4}}$$

$$Ku_f = \frac{\alpha_f v_f \rho_f^{1/2}}{[\sigma g(\rho_f - \rho_g)]^{1/4}}$$

$$m = 1$$

and Ku_{crit} (using linear interpolation) is given by **Table 6.1-2**. This table for Ku_{crit} as a function of D^* is from Wallis and Makkenchery.[6.1-23] This has been used successfully in the RELAP-UK code.[6.1-24] The value of m = 1 was also used in the RELAP-UK code.

Table 6.1-2 Values of Ku_{crit}.

D*	**Ku_{crit}**
≤ 2	0
4	1.0
10	2.1
14	2.5
20	2.8
28	3.0
≥ 50	3.2

On the flooding curve, the drift flux parameters satisfy the relationship

$$v_{gj} = \frac{(1-\alpha_g C_0) C_0 Ku_{crit}\left[\frac{(\rho_f-\rho_g) g \sigma}{\rho_f^2}\right]^{1/4}}{\alpha_g C_0 \left(\frac{\rho_g}{\rho_f}\right)^{1/2} + m^2 (1-\alpha_g C_0)} \quad . \tag{6.1-39}$$

This flooding limit for v_{gj} is applied for mass fluxes (G) larger than 100 kg/m^2•s and for $\alpha_g \geq 0.5$. Linear interpolation is used down to a mass flux of 50 kg/m^2•s and to $\alpha_g = 0.3$, at which point the normal drift flux correlations are used.

The rationale for selecting which correlations are used for a given physical situation is presented by Putney in **Reference 6.1-9**, though some of Putney's original selections have been modified based on the developmental assessment. Putney first considers correlations for cocurrent upflow (both rod bundles and circular channels) and then considers down and countercurrent flows (both rod bundles and circular channels).

For cocurrent upflow in rod bundles, Putney's literature search, based on comparisons with experimental data, indicates that the Bestion correlation[6.1-25] and the EPRI correlation[6.1-14] were the best available void-fraction correlations for rod-bundle geometries. **Table 6.1-3** and **Table 6.1-4** are taken from Putney's report[6.1-9] and summarize the rod-bundle tests used in the validation of the two correlations reported in the literature. Putney concludes that the EPRI correlation appeared to have been validated

against a much wider range of conditions, whereas the Bestion correlation did not seem to have been tested against high-flow experiments.

Table 6.1-3 Separate-effects tests used in validation of EPRI drift flux model.

Type	Test	Geometry and hydraulic diameter (cm)	Flow conditions and rate ($kg/m^2 \cdot s$)	Pressure (bars)	Void fraction range
High pressure, high flow	FROJA; FRIGG; CISE; Kasai et al.	Rod bundle 1.0 to 4.7	956 to 1,853[1]	40 to 64[a]	0 to 1.0
	Kasai et al.	Boiling tube 1.5	278 to 1,667	68.7	0 to 0.8
High pressure, low flow	ORNL TLTA	Rod bundle 1.23	Level swell 3 to 30	40, 75	0 to 0.8
	GEC TLTA	Rod bundle	Boildown	13, 27, 54	0 to 0.8
Low pressure, low flow	Hall et al.	Rod bundle	Level swell	1, 2, 3, 4	0 to 0.3
		Pipe above bundle 10.5	Level swell	1, 2, 3, 4	0 to 0.5
	FLECHT SEASET	Rod bundle	Boildown	1, 3, 4	0 to 0.8
	THETIS	Rod bundle 0.91	Level swell	2, 5, 10, 20, 40	
Natural circulation	FIST	Rod bundle	Natural circulation	72	
Large pipe	Hughes	Pipe 16.8	5.7 to 33.4 114 to 341	82, 97, 124, 166	0 to 0.6
	Carrier	Pipe 45.6	Stagnant water	41, 55, 69, 83, 97, 138	0 to 0.8

1. Average values for a series of tests.

Table 6.1-4 Rod bundle tests used in validation of Bestion drift flux model.[1]

Test	Flow condition	Pressure (bars)
Pericles	Level swell	Low
Ersec	Boildown	6
G2	Boildown	3, 27, 55

1. Tests shown are those reported by Bestion and were carried out using the CATHARE code.

The two correlations were next compared against ORNL THTF level swell tests.[6.1-26] Predicted values of the level swell parameter for these tests are given in **Table 6.1-5** and compared with the measured values. Also shown are the errors (differences) in the predicted values and compared against the uncertainty in the measured value. The RELAP5/MOD2 results shown were obtained by applying Equations (2), (5), and (6) in **Reference 6.1-9** in conjunction with the code's models for wall and interphase friction (the resulting void fraction being found by iteration). A similar method was used to obtain the results with profile slip, except that Equation (23) was used to calculate the relative velocity in Putney's Equation (5) for the bubbly and slug regimes (but not the transition regime between the slug and annular-mist regimes). The EPRI drift flux correlation was used to provide the distribution coefficient for this calculation.

Table 6.1-5 Level swell results for ORNL THTF tests.

		Calculated level swell and error in calculated level swell (m)				
Test	**Measured level swell and tolerance (m)**	**EPRI**	**Bestion**	**Analytis-Bestion**	**ATHENA**	**ATHENA with profile slip**
3.09.10I	1.30 $\pm$ 0.08	1.40 + 0.10	0.98 - 0.32	1.25 - 0.05	2.62 + 1.32	1.83 + 0.53
3.09.10J	0.63 $\pm$ 0.05	0.70 + 0.07	0.56 - 0.07	0.76 + 0.13	1.47 + 0.84	1.00 + 0.37
3.09.10K	0.38 $\pm$ 0.24	0.20 - 0.18	0.17 - 0.21	0.25 - 0.13	0.46 + 0.08	0.38 + 0.00
3.09.10L	0.93 $\pm$ 0.12	0.94 + 0.01	0.81 - 0.12	1.04 + 0.11	1.64 + 0.71	1.22 + 0.29
3.09.10M	0.54 $\pm$ 0.05	0.49 - 0.05	0.48 - 0.06	0.65 + 0.11	0.97 + 0.43	0.74 + 0.20
3.09.10N	0.20 $\pm$ 0.24	0.18 - 0.02	0.19 - 0.01	0.28 + 0.08	0.38 + 0.18	0.34 + 0.14
3.09.10AA	0.98 $\pm$ 0.04	1.12 + 0.14	0.81 - 0.17	1.06 + 0.08	2.21 + 1.23	1.43 + 0.45

Table 6.1-5 Level swell results for ORNL THTF tests. (Continued)

		Calculated level swell and error in calculated level swell (m)				
Test	**Measured level swell and tolerance (m)**	**EPRI**	**Bestion**	**Analytis-Bestion**	**ATHENA**	**ATHENA with profile slip**
3.09.10BB	0.53 ± 0.03	0.56 + 0.03	0.45 - 0.08	0.62 + 0.09	1.23 + 0.70	0.85 + 0.32
3.09.10CC[1]	0.29 ± 0.02	0.46 + 0.17	0.37 + 0.08	0.52 + 0.23	1.05 + 0.76	0.74 + 0.45
3.09.10DD	0.57 ± 0.04	0.62 + 0.05	0.61 + 0.04	0.80 + 0.23	1.14 + 0.57	0.87 + 0.30
3.09.10EE	0.32 ± 0.03	0.37 + 0.05	0.39 + 0.07	0.54 + 0.22	0.75 + 0.43	0.60 + 0.28
3.09.10FF	0.16 ± 0.03	0.18 + 0.02	0.20 + 0.04	0.28 + 0.12	0.37 + 0.21	0.33 + 0.17

1. Posttest analysis shows the data from this test to be of poor quality. Significant emphasis should therefore not be placed on these results.

The results referred to as Analytis-Bestion were obtained by applying the Bestion correlation with a coefficient on v_{gj} equal to 0.124 rather than 0.188. This value was found by Analytis[6.1-27] to give better agreement with boildown tests on the NEPTUN facility, when the correlation was used to calculate interphase drag in TRAC-BD1/MOD1. Analytis and Richner[6.1-28] subsequently used this model in a version of RELAP5/MOD2 and obtained a dramatic improvement in the code's prediction of liquid carryover in low flooding rate reflood experiments in NEPTUN.

Examination of **Table 6.1-5** reveals that the EPRI correlation provides the most accurate prediction of level swell. In fact, if the results for Test 3.09.10CC are discounted for the reason given, the EPRI prediction can only be said to lie significantly outside the uncertainty in the measurement on one test (3.09.10AA). The Bestion correlation also performs quite well and leads to a better prediction than the Analytis-Bestion correlation in the majority of cases. In general, the ATHENA model provides a poor prediction of level swell. The results are a lot better when profile slip is included, but are still significantly worse than those from the drift flux models.

The correlations were next compared against THETIS level swell tests.[6.1-29] This was done for the EPRI, Bestion, Analytis-Bestion, and RELAP5/MOD2 models. As before, the RELAP5/MOD2 models

led to a significant overprediction of the mixture level, though an improvement was still obtained when profile slip effects were included. The results for the drift flux models are summarized in **Table 6.1-6**.

Table 6.1-6 Errors in calculated mixture levels for THETIS tests.

		Mean error in calculated mixture level (%)			RMS error in calculated mixture level (%)		
Pressure (bars)	**Collapsed liquid level (m)**	**EPRI**	**Bestion**	**Analytis-Bestion**	**EPRI**	**Bestion**	**Analytis-Bestion**
40	1.92	8.2	8.1	14.4	8.4	8.3	14.6
40	2.30	4.0	3.7	10.0	4.4	4.1	10.9
40	2.62	-1.2	-1.4	5.3	1.3	1.6	5.4
20	1.89	8.3	1.4	9.7	8.5	2.2	9.9
20	2.12	3.9	-3.2	5.0	5.9	4.0	6.3
20	2.62	0.8	-3.9	2.4	1.1	4.5	2.5
10	1.45	4.8	-5.0	0.8	5.5	5.4	1.0
10	2.07	21.3	-6.0	5.5	23.0	6.8	6.1
10	2.25	3.6	-8.7	-1.8	5.1	9.2	2.8
5	1.19	-1.9	-10.7	-6.8	4.5	12.6	8.7
5	1.48	12.0	-8.6	-0.7	14.7	9.0	2.5
5	1.92	12.8	-12.6	-3.5	15.4	13.3	4.4
2	1.18	4.2	-11.2	-3.4	6.3	12.0	4.3
2	1.56	-5.9	-24.3	-15.9	7.6	25.7	17.2
2	1.88	1.3	-14.8	-6.6	4.7	16.6	8.6
All	All	5.1	-6.4	1.1	9.6	10.7	8.2

In general, the mixture levels predicted by the three models are very good, and there is probably little to choose between them. Overall, the Analytis-Bestion correlation is slightly more accurate on the tests than the EPRI correlation, which is slightly more accurate than the Bestion correlation. The Analytis-Bestion correlation does particularly well for the tests carried out 10 bars, but tends to underpredict as the test pressure is reduced and overpredict as it is increased (hence, the very low mean error). A similar effect is evident with the Bestion correlation, except that the best results are obtained at a pressure of around 20 bars. The accuracy of the EPRI correlation, however, does not seem to be pressure dependent.

Finally, the correlations were compared at high-pressure, high-flow conditions that are typical of those prevailing in steam generators during normal operation. The EPRI correlation has been validated against a variety of bundle experiments (FROJA, FRIGG, CISE) in this area (see **Table 6.1-3**). The void fractions obtained by applying the RELAP5/MOD2 interphase drag model with profile slip effects included compare extremely well with those obtained from the EPRI correlation. This reflects the fact that profile slip is dominant for the conditions examined, as the distribution coefficient provided by the EPRI correlation was used to evaluate profile slip terms. This coefficient varied between 1.10 and 1.13, which is not very different from the value assumed in the ATHENA model without profile slip (i.e., unity), and explains why this model does not perform so badly. Although the distribution coefficient used in the Bestion and Analytis-Bestion correlations (1.2) is slightly closer to the EPRI value, these correlations do not perform well.

In summary, the EPRI correlation was selected for cocurrent upflow in rod bundles based on its wider range of validation, better accuracy when compared to ORNL THTF tests, and better performance against FROJA, FRIGG, and CISE high-pressure, high-flow tests.

For cocurrent upflow in circular channels, Putney first considered low flows in small tubes, intermediate pipes, and large pipes. For low flows in small tubes, the Zuber-Findlay slug flow correlation[6.1-18,6.1-19] was selected, based primarily on a good performance against a series of level swell tests carried out in a 1.25-cm tube at AERE Harwell. For low flows in intermediate pipes, the Kataoka-Ishii correlation[6.1-20] was selected, based primarily on the wide range of pool data used to validate the correlation. For low flows in large pipes, Putney originally selected the Gardner correlation[6.1-30] over the Kataoka-Ishii correlation[6.1-20] and the Wilson correlation,[6.1-31] although the selection was not conclusive. Putney later removed the Gardner correlation and replaced it with the Kataoka-Ishii correlation. This removed another discontinuity without significant loss of accuracy. Putney also found it was necessary to include the Zuber-Findlay churn turbulent bubbly flow correlation[6.1-18,6.1-19] at low vapor/gas fluxes for low flows in intermediate and large pipes in order to match the 1-foot GE level swell test,[6.1-32] which was used in RELAP5/MOD2's developmental assessment.[6.1-33] For high flows in small and intermediate circular pipes, Putney selected the EPRI correlation. For high upflow in large pipes, it was necessary to use the Zuber-Findlay churn turbulent bubbly flow correlation and the Kataoka-Ishii correlation to ensure that no discontinuities occur in the interphase drag model when a change in flow occurs.

For down and countercurrent flows in rod bundles, Putney selected the EPRI correlation in order to ensure that there will be no discontinuities in the interphase drag when a change in flow direction occurs. This was the best he could do, given that no void fraction data appropriate to this situation were available.

For high downflow in small and intermediate circular pipes, Putney selected the EPRI correlation based on the downflow validation using Petrick's data.[6.1-34] For low downflow and countercurrent flow in circular pipes, he selected the Zuber-Findlay slug flow correlation for small pipes and the churn turbulent bubbly and Kataoka-Ishii correlations for intermediate/large pipes in order to ensure that no discontinuities

occur in the interphase drag model when a change in flow occurs. For high down flow in large pipes, it was necessary to use the Zuber-Findlay churn turbulent bubbly flow correlation and the Kataoka-Ishii correlation to match the Marviken tests[6.1-35,6.1-36] that are also used in ATHENA developmental assessment. The EPRI correlation did not work well for these tests.

For the narrow rectangular channels in the Advanced Neutron Source (ANS) reactor, Ruggles[1] noted that Griffith's drift velocity correlation[6.1-17] worked well for data in channel cross sections of 3.3 mm x 45 mm (Griffith[6.1-17]) and 2.4 mm x 50 mm (Mishima[6.1-37]). Data in both of these experiments were taken at room temperature and atmospheric pressure. As a result, Ruggles recommended Griffith's drift velocity correlation, and it was incorporated into ATHENA (use volume flag b = 2 to activate it). For the distribution parameter, Ruggles recommended Ishii's distribution parameter[6.1-3], because it seemed to better correlate low pressure data (needed for the ANS reactor). This was also incorporated into ATHENA (also use volume flag b = 2 to activate it). Griffith's and Ishii's correlations have been applied to ANS preconceptual design calculations[6.1-38] using ATHENA.

6.1.3.1.2 Code Implementation--The coefficients for the bubbly regime interphase friction, as coded in the PHANTJ, FIDIS2, and FIDISJ subroutines, are tabulated in Appendix 6A. For non-vertical bubbly flow, Appendix 6A shows the interphase area per unit volume, a_{gf}, to have the same form and coefficient as Equation (6.1-21). The relationship for C_D also has the same form and coefficient as Equation (6.1-23). The manual mentions a critical Weber number of 10 for bubbles, while Appendix 6A shows the code using a value of 5. The difference is based on using an average diameter instead of a maximum diameter.

For vertical bubbly flow, the coding matches the equations for C_i, C_0, v_{gj} and v_R. Appendix 6A shows that the same equations are used, but limits are used to prevent computational problems. Subroutine FIDISJ is the driver subroutine for vertical bubbly flow. **Table 6.1-1**, in addition to indicating which correlations are used for different geometry and flow conditions, shows the names of the subroutines (in parentheses) used for particular correlations. The number indicated in each box is the number stored in the variable IREG in subroutine FIDISJ and eventually in the variable IREGJ in subroutine PHANTJ. The user can then minor edit/plot the variable IREGJ.

For rod bundles, subroutine EPRIJ is called for all flow rates, and the EPRI correlation is used. Various limits have been placed on variables to prevent computational problems that were not indicated by Chexal and Lellouche.[6.1-14,6.1-15,6.1-18] Examples are placing an upper bound of 85 and a lower bound of -85 on exponential functions.

1. A. Ruggles, "Review of RELAP5/MOD2 Two-Phase Thermal Hydraulic Models and Identification of Changes Needed for Application to Plate Fueled Reactor Cores," Letter Report, Oak Ridge National Laboratory, January 25, 1989.

For small pipes ($D \leq 0.018$ m) and low flow ($|G| < 50$ kg/m^2•s) or countercurrent flow, subroutine ZFSLGJ is called, and the Zuber-Findlay slug flow correlation is used. Appendix 6A shows that $C_0 = 1.2$ is modified by the factor $1 - e^{-18\alpha_g}$ when $\Gamma_w > 0$ (boiling due to wall effects). This factor is due to Ishii[6.1-3] and is also used in TRAC-BF1.[6.1-22] This factor correctly results in C_0 having a near-zero value at the beginning of the two-phase flow region (α_g near zero), matching developing flow data ($0 < \alpha_g < 0.25$), and matching the fully developed correlation from data ($\alpha_g \geq 0.25$). Finally, as $\alpha_g \rightarrow 1.0$, a ramp begins at $\alpha_g = 0.8$ such that $C_0 \rightarrow 1$ and $v_{gj} \rightarrow 0$. For small pipes and high flow ($|G| > 100$ kg/m^2·s), subroutine EPRIJ is called, and the EPRI correlation is used as discussed in the rod bundle section. For small pipes and medium flow (50 kg/m^2•s $\leq |G| \leq$ 100 kg/m^2•s), linear interpolation is used in this transition region (see Appendix 6A) in subroutine FIDISJ.

For intermediate pipes (0.018 m $< D \leq 0.08$ m) and low flow or countercurrent flow, subroutine KATOKJ is called. The following three possibilities can occur, based on the dimensionless vapor/gas flux j_g^+ Equation (6.1-36):

1. For $j_g^+ \leq 0.5$, the churn turbulent bubbly flow correlation is used. The correlation used for C_0 is the modified form of the Rouhani correlation that is used in TRAC-BF1.

2. For $j_g^+ \geq 2.5$, the Kataoka-Ishii correlation is used. Again, the correlation used for C_0 is the modified form of the Rouhani correlation that is used in TRAC-BF1.

3. For the region $0.5 < j_g^+ < 2.5$, linear interpolation is used (see Appendix 6A) to calculate v_{gj}. There is no need to interpolate C_0 since it is the same for both (modified Rouhani).

The scheme adopted is based on the statement by Kataoka and Ishii[6.1-20] that conventional drift flux correlations perform well for low vapor/gas fluxes satisfying $j_g^+ \leq 0.5$ and air-water data obtained by Baily et al.[6.1-39] for vessels with diameters of 15.3, 30.4, and 61.0 cm. Kataoka and Ishii present these data in the form of an α_g versus j_g^+ plot. For $j_g^+ < 0.5$, the data are consistent with the churn turbulent bubbly flow correlation; and for $j_g^+ > 1.0 - 2.5$, they are consistent with the Kataoka-Ishii correlation. The code uses 2.5. In the region in between, the void fraction is fairly constant with respect to j_g^+; thus, an interpolation based on j_g^+ can be used.

Originally, just the Kataoka-Ishii correlation was used; but Putney found it necessary to include the churn turbulent bubbly correlation at low vapor/gas fluxes to improve the comparison for the GE level swell tests.[6.1-32] As with the Zuber-Findlay slug flow correlation, C_0 is modified by the factor $1 - e^{-18\alpha_g}$ when $\Gamma_w > 0$, and as $\alpha_g \rightarrow 0$, a ramp begins at $\alpha_g = 0.8$ such that $C_0 \rightarrow 1$ and $v_{gj} \rightarrow 0$. For intermediate

pipes and high flow, subroutine EPRIJ is called and the EPRI correlation is used, as discussed in the rod bundle section. For intermediate pipes and medium flow, linear interpolation is used in this transition region, as discussed for small pipes.

For large pipes (0.08 m < D) at all flows, subroutine KATOKJ is called. The same three situations ($j_g^+ \le 0.5$, $j_g^+ \ge 2.5$, and $0.5 < j_g^+ < 2.5$) are used as in intermediate pipes. Originally, large pipes used the same correlations as intermediate pipes. During the developmental assessment of ATHENA using the Marviken test cases,[6.1-35,6.1-36] it was found necessary to not use the EPRI correlation (even with the modifications for downflow) for large pipes. Rather, the churn turbulent flow and Kataoka-Ishii correlations were extended to include all flows for large pipes, resulting in improved results. The value 0.08 m for the switch between intermediate and large pipes is based on Kataoka-Ishii.[6.1-20] It was also for these tests that the original C_0 formula was replaced by the modified Rouhani correlation that is used in TRAC-BF1. This is needed to give flat profiles at high mass fluxes, by decreasing C_0.

After the appropriate correlation has been determined, based on the geometry and flow conditions, the following limits on C_0 are applied:

1. Lower bound of zero.

2. Lower bound of 1 if $\Gamma_w \le 0$.

3. Upper bound of 1.33 if not a rod bundle.

4. Upper bound of $\frac{1}{\alpha_g}$.

Limits (2) and (3) were added when it was found that the EPRI correlation gave too high a slip for downflow conditions.

The next limit imposed is a CCFL limit, which was imposed by Putney. The limitation is based on the Kutateladze condition in Equation (6.1-38), which results in Equation (6.1-39) for v_{gj} being implemented (see Appendix 6A), using m = 1. **Table 6.1-2** is also the one used to obtain Ku_{crit}, and it allows the Kutateladze condition (originally obtained from data for large-diameter pipes) to be applied for small pipes. The reasons for using a CCFL limit are given below.

The drift flux models shown in **Table 6.1-1** were chosen on the basis of comparisons with void fraction data for cocurrent up and downflow. In the absence of suitable data for countercurrent flow, it was necessary to assume that the selected correlations would still be valid. While this is a reasonable assumption for low void fractions, it is not obvious that the correlations include an adequate representation of the flooding phenomenon at medium to high void fractions. To correct for such deficiencies, a CCFL is

placed on the drift flux parameters before they are used in the calculation of the interfacial friction coefficients.

The CCFL model adopted is intended to represent CCFL in a straight, uniform flow channel and has the effect of forcing the interfacial friction coefficients to yield phase velocities within or on an appropriate flooding curve. ATHENA also has a user-controlled junction CCFL model which, if invoked, may subsequently modify these velocities to account for flooding at a singularity in the channel geometry. Provided that the drift flux correlation selected does not grossly underpredict v_{gj}, this combined treatment should prove effective, as CCFL at a singularity in the channel geometry can be expected to be more severe than CCFL in a uniform channel.

Note that the countercurrent flow form of the EPRI drift flux correlation is not used by the new interfacial friction model. Instead, the upflow form is applied in conjunction with the CCFL model. The reasons for this are twofold:

1. The evaluation of the countercurrent flow form of the EPRI correlation presents considerable computational difficulties and could be extremely time-consuming. (An example was brought to Putney's attention where such a calculation slowed the code down by a factor of 12.)

2. The CCFL model in the EPRI correlation is derived from flooding data for geometries typical of a PWR core/upper plenum interface and a BWR inlet orifice, and thus may not be appropriate for flooding in a straight, uniform flow channel.

The flooding limit for v_{gj} [Equation (6.1-39)] is interpolated with the v_{gj} from the drift flux correlations, as follows:

1. Denoting the value of v_{gj} obtained from the drift flux correlation as v_{gj}^{DF} and the value obtained from Equation (6.1-39) as v_{gj}^{Ku}, a value corresponding to flooded conditions, v_{gj}^{FL}, is first determined from

$$
\begin{aligned}
v_{gj}^{FL} &= v_{gj}^{DF} && \text{for } |G| \le G_1 \\
&= v_{gj}^{DF} + \frac{|G| - G_1}{G_2 - G_1}[\min(v_{gj}^{DF}, v_{gj}^{Ku}) - v_{gj}^{DF}] && \text{for } G_1 < |G| < G_2 \\
&= \min(v_{gj}^{DF}, v_{gj}^{Ku}) && \text{for } |G| \ge G_2
\end{aligned}
\qquad (6.1\text{-}40)
$$

where $G_1 = 50$ kg/m^2•s and $G_2 = 100$ kg/m^2•s.

2. The value of v_{gj} used for the interfacial friction calculation is then determined from

$$
\begin{aligned}
v_{gj} &= v_{gj}^{DF} && \text{for } \alpha_g \le \alpha_1 \\
&= v_{gj}^{DF} + \frac{\alpha_g - \alpha_1}{\alpha_2 - \alpha_1}(v_{gj}^{FL} - v_{gj}^{DF}) && \text{for } \alpha_1 < \alpha_g < \alpha_2 \\
&= v_{gj}^{FL} && \text{for } \alpha_g \ge \alpha_2
\end{aligned}
\qquad (6.1\text{-}41)
$$

where $\alpha_1 = 0.3$ and $\alpha_2 = 0.5$. For $\alpha_g > \alpha_1$ and $|G| > G_1$, a lower bound is placed on v_{gj} of $0.01\ (1 - \alpha_g)$.

The values of G_1 and G_2 used in Equation (6.1-40) were chosen to prevent the CCFL model from being applied in conjunction with the low flow correlations shown in **Table 6.1-1** and to provide a smooth transition between nonflooding and flooding conditions. This approach was adopted because, provided that the flow regime is bubbly-slug, these low flow correlations should be valid in countercurrent flow. Also, when simulating stagnant liquid conditions, ATHENA may predict a very small liquid downflow. Consequently, if the CCFL model was applied for all countercurrent flow conditions, it could override the void fraction correlations in an area where they are at their most accurate.

After these limits have been placed on v_{gj}, the interphase drag term C_i is determined in subroutine FIDISJ, as indicated in Equation (6.1-5). Two protections are also used. If $v_{gj} = 0$, then C_i is set to 100. If for some reason subroutine FIDISJ was used for a horizontal pipe, then C_i is set to 0.

6.1.3.2 Slug Flow

6.1.3.2.1 Model--For vertical slug flow, the drift flux model is used. For non-vertical slug flow, the drag coefficient model is used.

The drag coefficient model will first be discussed. Slug flow for non-vertical geometry is modeled as series of Taylor bubbles separated by liquid slugs containing small bubbles. A sketch of a slug flow pattern is shown in **Figure 6.1-1**. The Taylor bubble has a diameter nearly equal to the pipe diameter and a length varying from one to one hundred pipe diameters.

Let α_{gs} be the average void fraction in the liquid film and slug region. The void fraction of a single Taylor bubble, α_b, in the total mixture is then

$$\alpha_b = \frac{\alpha_g - \alpha_{gs}}{1 - \alpha_{gs}} \quad . \qquad (6.1\text{-}42)$$

The Taylor bubble frontal area per unit volume is $\frac{\alpha_b}{L}$, where L is the cell length. Consequently, the interfacial area per unit volume, a_{gf}, for slug flow is

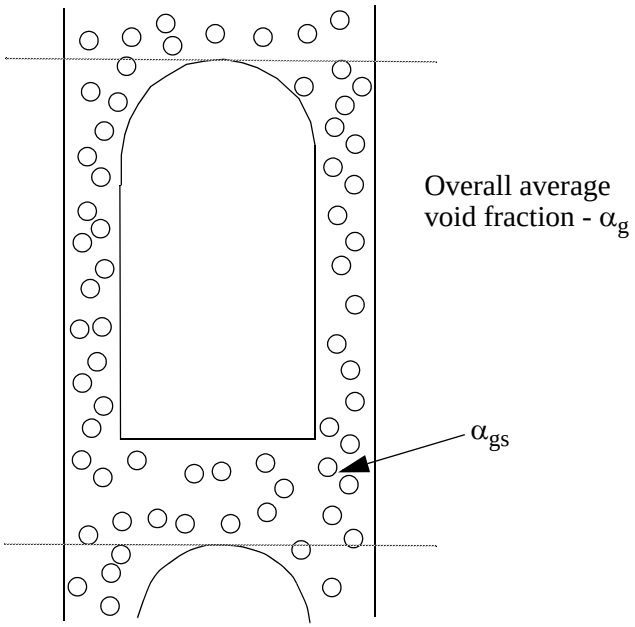

Figure 6.1-1 Slug flow pattern.

$$a_{gf} = \frac{\alpha_b}{L} + \frac{3.6\alpha_{gs}}{d_o}(1-\alpha_b) \quad . \tag{6.1-43}$$

To provide a smooth transition into and out of slug flow, α_{gs} [in Equation (6.1-42)] is considered as a free parameter varying from α_{BS} at the bubbly-to-slug flow regime transition to nearly zero at the slug-to-annular-mist flow regime transition. The variation is represented by the exponential expression

$$\alpha_{gs} = \alpha_{BS}\exp\left[-8\left(\frac{\alpha_g-\alpha_{BS}}{\alpha_{SA}-\alpha_{BS}}\right)\right] \quad . \tag{6.1-44}$$

The drag coefficient for Taylor bubbles in nonvertical slug flow is given by Ishii and Chawla[6.1-8] as

$$C_D = 10.9\frac{D'}{D}(1-\alpha_b)^3 \tag{6.1-45}$$

where D' is the Taylor bubble diameter, and α_b is given by combining Equations (6.1-42) and (6.1-44). From geometrical considerations, $\frac{D'}{D}$ is equal to the square root of α_b. This is discussed in Section 4.1.1.

The drag coefficient for the small bubbles in nonvertical slug flow is given by Ishii and Chawla[6.1-8] by Equation (6.1-23).

For vertical slug flow, the interphase drag and shear terms are calculated using the same drift flux conditions used in vertical bubbly flow.

6.1.3.2.2 Code Implementation--The coefficients for slug regime interphase drag as coded in the PHANTJ, FIDIS2, and FIDISJ subroutines are tabulated in Appendix 6A. For nonvertical slug flows, Appendix 6A shows the interphase area per unit volume, a_{gf}, to have the same form and coefficient as Equation (6.1-43). The first term for C_D is of the form of Equation (6.1-45) for the Taylor bubbles and uses α_{Tb} rather than α_b. The second term for C_D is of the form of the bubbly C_D in Equation (6.1-23).

For vertical slug flow, the coding matches the equations for C_i, C_0, v_{gj}, and v_R.

Code results were compared to General Electric level swell experiments (see Volume III of this manual). The code was shown to calculate void profiles similar to the experiments. Quantitative adequacy will depend on the application.

6.1.3.3 Annular Mist

6.1.3.3.1 Model--Annular mist flow is characterized by a liquid film along the wall and a vapor/gas core containing entrained liquid droplets. Let α_{ff} be the average liquid volume fraction of the liquid film along the wall. Then, from simple geometric considerations, the interfacial area per unit volume can be shown to be

$$a_{gf} = \left(\frac{4C_{ann}}{D}\right)(1-\alpha_{ff})^{1/2} + \left(\frac{3.6\alpha_{fd}}{d_o}\right)(1-\alpha_{ff}) \qquad (6.1\text{-}46)$$

where C_{ann} is a roughness parameter introduced to account for waves in the liquid wall film. Its form is

$$C_{ann} = (30\,\alpha_{ff})^{1/8} \ . \qquad (6.1\text{-}47)$$

This gives a value near unity for α_{ff} between 0.01 and 0.1, yet ensures that $C_{ann} \to 0$ as $\alpha_{ff} \to 0$.

The term α_{fd} is the average liquid volume fraction in the vapor/gas core, for which

$$\alpha_{fd} = \frac{\alpha_f - \alpha_{ff}}{1 - \alpha_{ff}}, \tag{6.1-48}$$

that is discussed in Section 4.1.1.

The term d_o is the average diameter of the drops.

A simple relation (see Section 6.3) based on the flow regime transition criterion and liquid Reynolds number is used to correlate the average liquid film volume fraction. For vertical flow regimes, the entrainment relation is

$$\alpha_{ff} = \alpha_f C_f \exp\left[7.5\times10^{-5}\left(\frac{\alpha_g v_g}{u_c}\right)^6\right] \tag{6.1-49}$$

where u_c is the entrainment critical velocity given by

$$u_c = \frac{3.2[\sigma g(\rho_f - \rho_g)]^{1/4}}{\rho_g^{1/2}} \quad . \tag{6.1-50}$$

For horizontal flow regimes, the entrainment relation is

$$\alpha_{ff} = \alpha_f C_f \exp\left[-4.0\times10^{-5}\left(\frac{|v_g - v_f|}{v_{gL}}\right)^6\right] \tag{6.1-51}$$

where v_{gL} is the horizontal stratification critical velocity given by Equation (3.1-2). The term C_f is expressed as

$$C_f = 1.0 - 10^{-4}\left(\alpha_f \rho_f |v_f| \frac{D}{\mu_f}\right)^{0.25} \quad . \tag{6.1-52}$$

The interfacial friction factor, f_i, for the liquid film takes the place of C_D in Equation (6.1-9), is described by a standard correlation in the laminar region, and is based on Wallis' correlation[6.1-6] in the turbulent region. In the turbulent region, the Wallis correlation was modified to use the factor 0.02 rather than 0.005. This is the value used in RELAP5/MOD1[6.1-40] and it was selected because of the MOD1 assessment. It is based on the interfacial Reynolds number defined as

$$Re_i = \frac{\rho |v_g - v_f| D_i}{\mu_g} \tag{6.1-53}$$

where

D_i = $\alpha_g^{1/2} D$ (D_i is the equivalent wetted diameter)

μ_g = viscosity of the vapor/gas phase.

The values of f_i are

$$\begin{aligned} f_i &= \frac{64}{Re_i} && \text{for } Re_i \le 500 \\ &= \left(\frac{1{,}500 - Re_i}{1{,}000}\right)\frac{64}{Re_i} + \left(\frac{Re_i - 500}{1{,}000}\right) 0.02\{1 + 150[1 - (1-\alpha_{ff})^{1/2}]\} && \text{for } 500 < Re_i < 1{,}500 \\ &= 0.02\left\{1 + 150\left[1 - (1-\alpha_{ff})^{\frac{1}{2}}\right]\right\} && \text{for } Re_i \ge 1{,}500 \end{aligned} \tag{6.1-54}$$

The interfacial drag coefficient C_D for the drops is given by Ishii and Chawla[6.1-8] by Equations (6.1-23) and (6.1-24), where d_o is the droplet diameter, ρ_c is the vapor/gas density (ρ_g), and $\mu_m = \frac{\mu_g}{(\alpha_g)^{2.5}}$ for droplets.

6.1.3.3.2 Code Implementation--The friction factor and interphase area per unit volume for annular-mist flow, as coded in subroutine PHANTJ, are tabulated in Appendix 6A. Appendix 6A shows the interphase area per unit volume, a_{gf} to have the same form and coefficient as Equation (6.1-46). The only difference is that the appendix uses d_d for the droplet diameter, whereas this section uses d_o for the droplet diameter. The expression for C_D shown in Appendix 6A has two terms. The first term for C_D is of the form of f_i in Equation (6.1-54) for the liquid film. The second term for C_D is of the form of the droplet C_D in Equation (6.1-23).

For an annulus component and a multid component (no drops option) in the annular mist regime, the code assumes that all the liquid is in the film and that there are no drops. Thus, $\alpha_{ff} = \alpha_f$ and $\alpha_{fd} = 0$ are used for an annulus. This was based on work by Schneider[6.1-41] on calculations for UPTF Test 6, who shows that this was necessary in order to get downcomer penetration following a cold leg break. In addition, the Bharathan[6.1-42] correlation used in RELAP5/MOD2 was replaced by a standard laminar correlation and the modified Wallis[6.1-6] correlation in the turbulent region for the interfacial drag when in the annular-mist flow regime (for either an annulus or any other component). Schneider found this was

also necessary in order to get downcomer penetration in UPTF Test 6 using RELAP5/MOD3. This interphase drag approach for an annulus component was also used in RELAP5/MOD1.

For bundles in vertical annular mist flow or in vertical slug/annular mist transition flow, the maximum of the interphase drag coefficient from the EPRI drift flux correlation (bubbly-slug flow) and the interface drag coefficient from annular mist flow (friction factor/drag coefficient previously discussed) is used. This was necessary to remove inaccurate low void fraction predictions in rod bundles. This was incorporated in the code as the result of developmental assessment cases using bundle experiments (FRIGG, THTF from ORNL, PERICLES, FLECHT SEASET, and ACHILLES).

6.1.3.4 Inverted Annular Flow Regime. Immediately downstream of a quench front or CHF position, there may be an inverted annular flow region if the combination of liquid flow and subcooling is high enough. The physical concept in the model is the presence of vapor/gas bubbles in the liquid core (just as there are liquid drops in the vapor/gas region for annular mist flow) and an annular vapor/gas layer between the walls and the core. Let α_{gb} be the volume of vapor/gas bubbles in the liquid core divided by the volume of the core. This is given by

$$\alpha_{gb} = \frac{V_{gas,\,core}}{V_{core}} = \frac{V_{gas,\,tot} - V_{gas,\,ann}}{V_{tot} - V_{gas,\,ann}} \quad . \tag{6.1-55}$$

Then, from simple geometric considerations, the interfacial area per unit volume can be shown to be

$$a_{gf} = \left(\frac{4C_{ann}}{D}\right)(1 - \alpha_{g,\,ann})^{1/2} + \frac{3.6\alpha_{gb}}{d_o}(1 - \alpha_{g,\,ann}) \tag{6.1-56}$$

where

$$\alpha_{g,\,ann} = \frac{V_{g,\,ann}}{V_{tot}} \quad . \tag{6.1-57}$$

The relation used to obtain $\alpha_{g,ann}$ is shown in Appendix 6A as α_B. C_{an} is obtained from Equation (6.1-47), where $\alpha_{g,ann}$ is used in place of α_{ff}.

The interfacial friction factor, f_i, for the vapor/gas film takes the place of C_D in Equation (6.1-9) and is described by a correlation obtained by Bharathan et al.,[6.1-42] for which

$$f_i = 4\,[0.005 + A(\delta^*)^B] \tag{6.1-58}$$

where

$$\log_{10} A = -0.56 + \frac{9.07}{D^*} \quad (6.1\text{-}59)$$

$$B = 1.63 + \frac{4.74}{D^*} \quad (6.1\text{-}60)$$

$$\delta^* = \delta\left[\frac{(\rho_f - \rho_g)g}{\sigma}\right]^{1/2} . \quad (6.1\text{-}61)$$

The term δ^* is the liquid wall film Deryagin number for which δ is the film thickness, and D^* is the dimensionless diameter Bond number [Equation (6.1-33)]. The film thickness δ is defined in Appendix 6A.

The drag coefficient for the bubbles is the Ishii-Chawla correlation given by Equation (6.1-23). Appendix 6A tabulates the equation.

6.1.3.5 Inverted Slug Flow. The inverted slug flow regime envisioned by DeJarlais and Ishii[6.1-43] consists of bubble-impregnated liquid slugs flowing in a pipe core surrounded by a vapor/gas blanket containing liquid droplets (see **Figure 3.2-3**). The coded interfacial friction coefficients recognize the liquid droplets, vapor/gas blanket, and liquid slugs but not the presence of bubbles in the slugs. Contributions to the interfacial friction are recognized, then, as coming from two sources: (a) the liquid droplet interfaces in the vapor/gas annulus and (b) the liquid slug/annulus interface. It is assumed, apparently, that the liquid slugs are so long that any contributions to interfacial friction at their ends are negligible.

The interfacial areas for the annulus/droplet portion and the slug/annulus portion are derived analogously to those for nonvertical slug flow, Section 6.1.3.2. The void fraction of the liquid slug, α_B, is analogous to that for a Taylor bubble, α_{Tb}, and the average droplet void fraction in the vapor/gas blanket, α_{drp}, is analogous to the average void fraction, α_{gs}, in the liquid annulus for slug flow. That is, the interfacial areas are computed for inverted slug flow by simply reversing the liquid and vapor/gas phases from slug flow. The droplet void fraction, α_{drp}, in the vapor/gas annulus is an expression that exponentially increases the portion of α_f due to droplets as α_g increases until the transition void fraction, α_{SA}, is reached, at which point all of the liquid is appropriately assumed to be in droplet form. The value for the Weber number used is 6.0.

The drag coefficients for the annulus/droplet portion and the slug/annulus portion are analogous to those for nonvertical slug flow, except that the liquid and vapor/gas phases are reversed. Appendix 6A tabulates the equation.

6.1.3.6 Dispersed (Droplet, Mist) Flow Regimes. The dispersed (droplet, mist) flow regime is discussed in Section 6.1.3.1, Bubbly Flow. For mist pre-CHF, We = 3.0, and for mist and mist post-CHF,

We = 12.0. For mist pre-CHF, mist, and mist post-CHF, $\mu_m = \frac{\mu_f}{(\alpha_g)^{2.5}}$. A lower limit of $C_D = 0.45$ is used[6.1-8] for the mist and mist post-CHF cases. In Appendix 6A this is shown as 0.05626 since the formula for $\frac{1}{8}C_D$ is shown. Appendix 6A tabulates the equations.

For bundles in vertical mist pre-CHF flow, the maximum of the interfase drag coefficient from the EPRI drift flux correlation (bubbly-slug flow) and the interfase drag coefficient from mist pre-CHF flow (friction factor/drag coefficient previously discussed) is used. This was necessary to remove inaccurate low flow void fraction preditions in rod bundles. This was incorporated in the code as the result of developmental assessment cases using bundle experiments (FRIGG, THTF from ORNL, PERICLES, FLECHT SEASET, and ACHILLES).

6.1.3.7 Horizontally Stratified Flow Regime

6.1.3.7.1 Model--By simple geometric consideration, one can show that the interfacial area per unit volume is

$$a_{gf} = \frac{4C_{st}\sin\theta}{\pi D} \tag{6.1-62}$$

where C_{st} is a roughness parameter introduced to account for surface waves and is set to one for the interphase surface area per unit volume. (See **Figure 3.1-2** for the definition of angle θ.)

The interface Reynolds number is defined with the vapor/gas properties and regarding liquid as the continuous phase for which

$$Re_i = \frac{\rho_g|v_g - v_f|D_i}{\mu_g} \tag{6.1–63}$$

where the equivalent wetted diameter, D_i, for the interface is

$$D_i = \frac{\alpha_g \pi D}{\theta + \sin\theta} \quad . \tag{6.1-64}$$

This can be derived from simple geometric considerations (see Section 4.1.1) using

$$\pi\alpha_g = \theta - \sin\theta\cos\theta \quad . \tag{6.1-65}$$

The interfacial friction factor, f_i, replaces C_D in Equation (6.1-9) and is obtained by assuming friction factor relationships for which

$$f_i = \max\left(\frac{64}{Re_i} , \frac{0.3164}{Re_i^{0.25}}\right) . \quad (6.1\text{-}66)$$

The term $\frac{64}{Re_i}$ is for laminar flow and $\frac{0.3164}{Re_i^{0.25}}$ is the Blasius formula for turbulent flow, which are friction factors based on the Darcy approach used in ATHENA. **Reference 6.1-44** presents these factors using the Fanning approach; one needs to multiply by four to get the Darcy approach factors used in Equation (6.1-66).

6.1.3.7.2 Code Implementation--The friction factor and interphase area per unit volume for horizontally stratified flow, as coded in subroutine PHANTJ, are tabulated in Appendix 6A. Appendix 6A shows the interphase drag area per unit volume, a_{gf}, to have the same form and coefficient as Equation (6.1-62) with $C_{st} = 1$. The expression for C_D in Appendix 6A is the same as Equation (6.1-66) for the friction factor f_i.

6.1.3.8 Vertically Stratified Flow

6.1.3.8.1 Model--For the junction above a vertically stratified volume, the interphase drag is set to a low number to help ensure that any drops donored up from the volume below will fall back down, thus maintaining the level in the vertically stratified volume. This is accomplished by using the void fraction in the volume above (mostly vapor/gas) for the junction void fraction needed to determine the junction interphase drag. Similarly, for the junction below a vertically stratified volume, the interphase drag is set low. This is accomplished by using the void fraction in the volume below (mostly liquid) for the junction void fraction needed to determine the junction interphase drag. The vertical stratification model is not intended to be a mixture level model.

6.1.3.8.2 Code Implementation--For the junction above the vertically stratified volume (junction j in **Figure 3.2-4**), the interphase drag for the volume above (volume L) is used. This is consistent with the junction-based interphase drag. This is obtained as follows: The void fraction $\alpha^*_{g,j}$ used in the junction j for the junction-based interphase drag is given by

$$\alpha^*_{g,j} = w_j \bullet \alpha^*_{g,K} + (1 - w_j) \bullet \alpha_{g,L} \quad (6.1\text{-}67)$$

and is similar to Equation (3.5-1), except that $\alpha_{g,K}$ is replaced by $\alpha^*_{g,K}$. The term w_j is given by Equation (3.5-2). This void fraction is given by

$$\alpha^*_{g,K} = \text{strat} \bullet \alpha_{g,L} + (1 - \text{strat}) \bullet \alpha_{g,K} \tag{6.1-68}$$

where strat takes on values from 0 to 1. For a vertically stratified volume, strat = 1, $\alpha^*_{g,K} = \alpha_{g,L}$, and $\alpha^*_{g,j} = \alpha_{g,L}$. For a nonvertically stratified volume, strat = 0, $\alpha^*_{g,K} = \alpha_{g,K}$, and $\alpha^*_{g,j}$ is given by Equation (3.5-1). The smoothing parameter strat is given by

$$\text{strat} = \text{strat1} \bullet \text{strat2} \tag{6.1-69}$$

where

$$\text{strat1} = 1 - e^{-0.5\alpha_{f,L}} \tag{6.1-70}$$

$$\text{strat2} = 2\left(1 - \frac{v_m}{v_{Tb}}\right) . \tag{6.1-71}$$

Both strat1 and strat2 are limited to values between 0 and 1. The variables v_m and v_{Tb} are the mixture velocity and Taylor bubble rise velocity, respectively. The variable strat1 exponentially turns off the stratification effect when the volume above (volume L) becomes empty of liquid. When $\alpha_{f,L} = 0.01$, strat1 = 0.005.

A different method is used at junction j-1 below the vertically stratified volume. Equations (6.1-67), (6.1-68), (6.1-69), and (6.1-71) are used, however, strat1 is given by

$$\text{strat1} = 20\,(\alpha_{level} - 0.05) \tag{6.1-72}$$

where

$$\alpha_{level} = \frac{\alpha_{g,L} - \alpha_{g,K}}{\alpha_{g,L} - \alpha_{g,I}} . \tag{6.1-73}$$

The variable α_{level} is an implied nondimensional mixture level position within volume K. The coding is generalized to handle the case where the volumes and junctions are oriented downward. The vertical

stratification model is not intended to be a mixture level model, and a more mechanistic level tracking model is discussed in Volume I.

If more than one junction is connected to the top, the volume above with the smallest void fraction will be treated as the "above volume;" if more than one junction is connected to the bottom, the volume below with the largest void fraction will be treated as the "below volume."

The primary developmental assessment for the vertically stratified interphase drag model is the MIT pressurizer test problem.[6.1-45] Some of the smoothing functions are required to ensure fast running as well as minimization of void fraction dips when the level appears in the next volume.

6.1.3.9 Transition Flow Regimes. A number of transitions between flow regimes are incorporated into ATHENA for interphase drag and shear. They are similar to the ones used for interfacial heat and mass transfer (Section 4.1.2) and are included to prevent numerical instability when abruptly switching from one flow regime to another. The full details of the transition logic used in the code are found in Appendix 6A.

6.1.4 Time Smoothing

Section 4.1.3 discusses the time smoothing of the interphase heat transfer coefficients H_{if} and H_{ig}. It indicates the rationale for using time smoothing as detailed in **Reference 6.1-46** and **Reference 6.1-47**. Using the notation established in Section 4.1.3, the following are used for the interphase drag coefficient, distribution coefficient, and interphase shear factor:

A logarithmic weighting process defined by

$$f_{weight}^{n+1} = f_{calculated}^{n+1}\left(\frac{f_{weight}^{n}}{f_{calculated}^{n+1}}\right)^{\eta} \tag{6.1-74}$$

is used for the interphase drag coefficient f_{gf} when the interphase drag coefficient is increasing. A linear weighting process defined by

$$f_{weight}^{n+1} = \eta f_{weight}^{n} + (1-\eta) f_{calculated}^{n+1} \tag{6.1-75}$$

is used for the interphase drag coefficient f_{gf} when the interphase drag coefficient is decreasing. The linear weighting process defined by Equation (6.1-75) is also used for the distribution coefficient C_0 and the interphase shear factor f_x. Linear time smoothing is used for these because they can have values of 0. The term f is the function to be smoothed and η is the weighting factor.

For f_{gf}, C_0, and f_x, the equation for η was developed by Chow and Bryce, is documented in Feinauer et al.,[6.1-48] and assumes the form

$$\eta = \min\left(0.90,\ e^{-\min\left\{0.693,\ \max\left[\frac{\Delta t}{\tau_c},\ \min\left(\frac{\Delta t}{\tau_f},\ \gamma_s\right)\right]\right\}}\right) \tag{6.1-76}$$

where

$$\tau_c = \frac{V_K + V_L}{\frac{0.7\min(|v_{g,K}|, |v_{f,K}|)}{\Delta x_K} V_K + \frac{0.7\min(|v_{g,L}|, |v_{f,L}|)}{\Delta x_L} V_L}$$

$$\tau_f = \frac{V_K + V_L}{\left[\frac{\max\left(g, \frac{gD_K^*}{19}\right)}{D_K}\right]^{1/2} V_K + \left[\frac{\max\left(g, \frac{gD_L^*}{19}\right)}{D_L}\right]^{1/2} V_L}$$

$$D_K^* = D_K\left[\frac{g(\rho_{f,K} - \rho_{g,K})}{\sigma_K}\right]^{1/2}$$

$$D_L^* = D_L\left[\frac{g(\rho_{f,L} - \rho_{g,L})}{\sigma_L}\right]^{1/2}$$

$$\gamma_s = \max\left\{0.0513,\ \frac{[\min(|v_{g,j}|, |v_{f,j}|) + 10^{-7}\text{m/s}]}{\max(|v_{g,j}|, |v_{f,j}|, 10^{-7}\text{m/s})} - 0.3\right\}.$$

The meaning of the terms τ_c, τ_f, and γ_s is the same as used for the interphase heat transfer coefficients, and these are discussed in Section 4.1.3.

As discussed in Section 4.1.3, Ransom[6.1-46] and Ransom and Weaver[6.1-47] indicated that a time step insensitive procedure is obtained if η is of the exponential form

$$\eta = e^{-\Delta t/\tau} \tag{6.1-77}$$

where τ is a time constant associated with the physical process. Equation (6.1-76) will produce an equation like Equation (6.1-77) when the min/max logic results in η being $\exp\left(\frac{-\Delta t}{\tau_c}\right)$ or $\exp\left(\frac{-\Delta t}{\tau_f}\right)$. Otherwise, it is time-step size dependent and nodalization dependent. Modifications are being tested so that the time-step size dependency and nodalization dependency will be removed in the future.

6.1.5 References

6.1-1. J. G. M. Anderson and K. H. Chu, *BWR Refill-Reflood Program, Task 4.7--Constitutive Correlations for Shear and Heat Transfer for the BWR Version of TRAC,* NUREG/CR-2134, EPRI NP-1582, 1981.

6.1-2. M. Ishhi, T. Chawla, and N. Zuber, "Constitutive Equation for Vapor Drift Velocity in Two-Phase Annular Flow," *AIChE Journal, 22,* 1976, pp. 283-289.

6.1-3. M. Ishii, *One-dimensional Drift-flux Model and Constitutive Equations for Relative Motion Between Phases in Various Two-phase Flow Regimes,* ANL-77-47, Argonne National Laboratory, September 1977.

6.1-4. D. D. Taylor et al., *TRAC-BD1/MOD1: An Advanced Best Estimate Computer Program for Boiling Water Reactor Transient Analysis, Volume I: Model Description,* NUREG/CR-3633, EGG-2294, Idaho National Engineering Laboratory, April 1984.

6.1-5. W. L. Weaver et al., *TRAC-BF1 Manual: Extensions to TRAC-BD1/MOD1,* NUREG/CR-4391, EGG-2417, Idaho National Engineering Laboratory, August 1986.

6.1-6. G. B. Wallis, *One-dimensional Two-phase Flow,* New York: McGraw-Hill, 1969.

6.1-7. A. H. Shapiro and A. J. Erickson, *Transactions of the ASME, 79,* 1957, p. 775.

6.1-8. M. Ishii and T. C. Chawla, *Local Drag Laws in Dispersed Two-Phase Flow*, NUREG/CR-1230, ANL-79-105, Argonne National Laboratory, December 1979.

6.1-9. J. M. Putney, *Proposals for Improving Interphase Drag Modeling for the Bubbly and Slug Regimes in RELAP5,* CERL Report RD/L/3306/R88, PWR/HTWG/P(88)622, June 1988.

6.1-10. J. M. Putney, *Implementation of a New Bubbly-Slug Interphase Drag Model in RELAP5/MOD2,* CERL Report RD/L/3369/R88, PWR/HTWG/P(88)597, November 1988.

6.1-11. J. M. Putney, *Equations for Calculating Interfacial Drag and Shear from Void Fraction Correlations,* CEGB Report RD/L/3429/R88, PWR/HTWG/P(88)630, December 1988.

6.1-12. J. M. Putney, *Development of a New Bubbly-Slug Interfacial Friction Model for RELAP5--Final Report,* National Power Report ESTD/L/0075/R89, PWR/HTWG/P(89)722, October 1989.

6.1-13. J. M. Putney, "Development of a New Bubbly-Slug Interfacial Friction Model for RELAP5," *Nuclear Engineering and Design, 131,* 1991, pp. 223-240.

6.1-14. B. Chexal and G. Lellouche, *A Full-Range Drift-Flux Correlation for Vertical Flows (Revision 1),* Electric Power Research Institute, EPRI NP-3989-SR, September 1986.

6.1-15. B. Chexal et al., *The Chexal-Lellouche Void Fraction Correlation for Generalized Applications,* Electric Power Research Institute, NSAC-139, April 1991.

6.1-16. B. Chexel et al., *Void Fraction Technology for Design and Analysis,* Electric Power Research Institute, TR-106326, March 1997.

6.1-17. P. Griffith, "The Prediction of Low-Quality Boiling Voids," *Transactions of the ASME, 86,* 1964, pp. 327-333.

6.1-18. N. Zuber and J. A. Findlay, "Average Volumetric Concentrations in Two-Phase Flow Systems," *Transactions of the ASME, Journal of Heat Transfer, 87,* 1965, pp. 453-568.

6.1-19. N. Zuber et al., *Steady-State and Transient Void Fraction in Two-Phase Flow Systems,* General Electric Company, GEAP-5417, 1967.

6.1-20. I. Kataoka and M. Ishii, "Drift Flux Model for Large Diameter Pipe and New Correlation for Pool Void Fraction," *International Journal of Heat and Mass Transfer, 30,* 1987, pp. 1927-1939.

6.1-21. S. Z. Rouhani, *Modified Correlations for Void and Pressure Drop,* AB Atomenergi, Sweden, Internal Report AE-RTC 841, March 1969.

6.1-22. S. Z. Rouhani et al., *TRAC-BF1/MOD1 Models and Correlations,* NUREG/CR-4391, EGG-2680, Idaho National Engineering Laboratory, August 1992.

6.1-23. G. B. Wallis and S. Makkenchey, "The Hanging Film Phenomenon in Vertical Annular Two-Phase Flow," *Transactions of the ASME, Journal of Fluids ENgineering, 96,* 1974, p. 297-298.

6.1-24. J. A. Holmes, "Description of the Drift Flux Model in the LOCA Code RELAP-UK," *I. Mech. E.*, C206/77, 1977.

6.1-25. D. Bestion, "Interfacial Friction Determination for the ID-6 Equations Two Fluid Model Used in the CATHARE Code," *European Two Phase Flow Group Meeting, Southampton, England, June 3-7, 1985.*

6.1-26. T. Anklam et al., *Experimental Investigations of Uncovered-Bundle Heat Transfer and Two-Phase Mixture-Level Swell under High Pressure, Low Heat Flux Conditions,* NUREG/CR-2456, ORNL-5848, Oak Ridge National Laboratory, March 1982.

6.1-27. G. Th. Analytis, "Assessment of a New Interfacial Function Correlation in TRAC-BD/MOD1," *Transactions of the American Nuclear Society, 52,* 1986, pp. 481-482.

6.1-28. G. Th. Analytis and G. Richner, "Effect of Bubbly/Slug Interfacial Shear on Liquid Carryover Predicted by RELAP5/MOD2 During Reflooding," *Transactions of the American Nuclear Society, 53,* 1986, pp. 540-541.

6.1-29. K. Pearson, *Full Length Cluster Level Swell Data at Pressures from 2 to 40 Bar,* AEEW-R2193, 1987.

6.1-30. G. Gardner, "Fractional Vapor Content of a Liquid Pool Through which Vapor is Bubbled," *International Journal of Multiphase Flow, 6,* 1980, pp. 399-410.

6.1-31. J. Wilson, *Primary Separation of Steam and Water by Natural Separation: Part 1,* ACNP-6500 2, 1965.

6.1-32. J. A. Findlay and G. L. Sozzi, *BWR Refill-Reflood Program--Model Qualification Task Plan,* NUREG/CR-1899, EPRI NP-1527, GEAP-24898, October 1981.

6.1-33. V. H. Ransom et al., *RELAP5/MOD2 Code Manual, Volume 3: Developmental Assessment Problems,* EGG-TFM-7952, Idaho National Engineering Laboratory, December 1987.

6.1-34. M. Petrick, *A Study of Vapor Carryunder and Associated Problems,* ANL-6581, Argonne National Laboratory, 1962.

6.1-35. L. Ericson et al., *The Marviken Full-Scale Critical Flow Tests Interim Report: Results from Test 24,* MXC-224, May 1979.

6.1-36. L. Ericson et al., *The Marviken Full-Scale Critical Flow Tests Interim Report: Results from Test 22,* MXC-222, March 1979.

6.1-37. K. Mishima et al., "A Study of Air-Water Flow in a Narrow Rectangular Duct Using Image Processing Technique," *Japan - U.S. Seminar on Two-Phase Flow Dynamics, Ohtsu, Japan, July 1988.*

6.1-38. C. D. Fletcher and L. H. Ghan, "Thermal-Hydraulic Systems Safety Analysis to Support the Design Process for the Advanced Neutron Source Reactor," *Nuclear Technology, 95,* 1991, pp. 228-246.

6.1-39. R. Baily et al., "Transport of Gases Through Liquid-Gas Mixture," *AIChE Meeting, New Orleans, LA, 1956.*

6.1-40. V. H. Ransom et al., *RELAP5/MOD1 Code Manual,* NUREG/CR-1826, EGG-2070, Idaho National Engineering Laboratory, March 1982.

6.1-41. K. Schneider, "Siemens Contributions to RCP Modeling and Evaluation of UPTF Test 6," *ICAP Meeting, Bethesda, MD, October 18-20, 1989.*

6.1-42. D. Bharathan, G. E. Wallis, and H. J. Richter, *Air-Water Counter-Current Annular Flow,* EPRI NP-1165, 1979.

6.1-43. G. DeJarlais and M. Ishii, *Inverted Annular Flow Experimental Study,* NUREG/CR-4277, ANL-85-31, Argonne National Laboratory, April 1985.

6.1-44. R.. B. Bird, W. E. Stewart, and E. M. Lightfoot, *Transport Phenomena,* New York: Wiley, 1960, p. 187.

6.1-45. H. Saedi and P. Griffith, "The Pressure Response of a PWR Pressurizer during an Insurge Transient," *Transactions of the American Nuclear Society, Detroit, MI, June 12-16, 1983.*

6.1-46. V. H. Ransom, *Course A-Numerical Modeling of Two-Phase Flows for Presentation at Ecole d'Ete d'Analyse Numerique*, EGG-EAST-8546, Idaho National Engineering Laboratory, May 1989.

6.1-47. V. H. Ransom and W. L. Weaver, "Selective Review of LWR Thermal-Hydraulic Simulation Methods," *Proceedings of the International Topical Meeting on Advances in Reactor Physics, Mathematics, and Computation, Paris, France, 1987,* pp. 1813-1829.

6.1-48. L. R. Feinauer, W. M. Bryce, D. M. Kiser, R. A. Riemke, and C. C. Tsai, *Post Release Improvements for RELAP5/MOD2,* EGG Internal Report, SE-CMD-001, Idaho National Engineering Laboratory, August 1984.

6.2 Wall Drag

6.2.1 Basis

The semi-implicit scheme, one-dimensional finite difference equations for the sum momentum equation, Equation (2.2-6), and the difference momentum equation, Equation (6.1-1) or Equation (2.2-7), contain the terms

$$FWG_j^n (v_g)_j^{n+1} \Delta x_j \Delta t \text{ and } FWF_j^n (v_f)_j^{n+1} \Delta x_j \Delta t \quad . \tag{6.2-1}$$

These terms represent the pressure loss due to wall shear from cell center to cell center of the cell volumes adjoining the particular junction that the momentum equation is considering. The wall drag or friction depends not only on the phase of the fluid but also on the flow regime characteristics.

The wall friction model is based on a two-phase multiplier approach in which the two-phase multiplier is calculated from the heat transfer and fluid flow service (HTFS) modified Baroczy correlation.[6.2-1] The individual phasic wall friction components are calculated by apportioning the

two-phase friction between the phases using a technique derived from the Lockhart-Martinelli[6.2-2] model. The model is based on the assumption that the frictional pressure drop may be calculated using a quasi-steady form of the momentum equation, as used by Chisholm.[6.2-3] As discussed in Volume I (Section 3.3.6, this wall friction partitioning model is used with the drag coefficient method of the interphase friction model. The drift flux method of the interphase friction model uses a wall friction model that partitions the total wall friction force to the phases based on the phasic volume fractions rather than using the Chisholm partition model.

6.2.1.1 ATHENA Wall Friction Coefficients. The ATHENA phasic Darcy-Weisbach wall friction coefficients are determined from the wall friction discussion in Volume I (Section 3.3.8) that apportion the overall wall frictional pressure gradient between the phases, to give,

$$FWF(\alpha_f\rho_f) = \alpha_{fw}\frac{\rho_f\lambda_f|v_f|}{2D} \bullet \frac{\left\{\lambda_f'\rho_f(\alpha_f v_f)^2 + C[\lambda_f'\rho_f(\alpha_f v_f)^2\lambda_g'\rho_g(\alpha_g v_g)^2]^{1/2} + \lambda_g'\rho_g(\alpha_g v_g)^2\right\}}{(\alpha_{gw}\lambda_g\rho_g v_g^2 + \alpha_{fw}\lambda_f\rho_f v_f^2)} \quad (6.2\text{-}2)$$

for the liquid, and

$$FWG(\alpha_g\rho_g) = \alpha_{gw}\frac{\rho_g\lambda_g|v_g|}{2D} \bullet \frac{\left\{\lambda_f'\rho_f(\alpha_f v_f)^2 + C[\lambda_f'\rho_f(\alpha_f v_f)^2\lambda_g'\rho_g(\alpha_g v_g)^2]^{1/2} + \lambda_g'\rho_g(\alpha_g v_g)^2\right\}}{(\alpha_{gw}\lambda_g\rho_g v_g^2 + \alpha_{fw}\lambda_f\rho_f v_f^2)} \quad (6.2\text{-}3)$$

for the vapor/gas, where the HTFS two-phase multiplier correlation coefficient C is found in Volume I, Section 3.

Because the Reynolds number in the friction factor correlation and the mass flux G in the two-phase friction multiplier were considered to be positive quantities by the correlation developers, the algorithm used in the ATHENA code to compute these quantities was implemented in such a way as to ensure that they are always computed as positive quantities. This means that the velocity used in the computation of the phasic mass flux used in computing the phasic Reynolds numbers is the magnitude of the volume velocity computed by ATHENA,

$$G_f = \alpha_f\rho_f|v_f| \quad (6.2\text{-}4)$$

for the liquid mass flux, and

$$G_g = \alpha_g \rho_g |v_g| \tag{6.2-5}$$

for the vapor/gas mass flux.

The equations used to calculate the magnitude of the phasic volume velocities are presented in Volume I of this manual.

The mixture mass flux G used in the computation of the correlation coefficient C for the HTFS two-phase multiplier is computed as

$$G = \alpha_f \rho_f |v_f| + \alpha_g \rho_g |v_g| \; . \tag{6.2-6}$$

To prevent a divide by zero in the denominator of the exponential in the term $T_1(\Lambda,G)$ defined in Volume I, the denominator $2.4 - G(10^{-4})$ is replaced by $\max[10^{-7}, 2.4 - G(10^{-4})]$ in the coding. It should be noted that from the definition of G, it follows that $G \geq 0$.

The HTFS correlation[6.2-1] was developed based on experiments from steam-water, air-oil, and air-water flows in horizontal and vertical pipes. The correlation is applicable over the following ranges: mixture mass flux (G) = 2.6 - 12,000 kg/m^2-s, static quality (X) = 0.0001 - 0.99, and Baroczy dimensionless property index $\left[\Lambda = \left(\frac{\rho_g}{\rho_f}\right)\left(\frac{\mu_f}{\mu_g}\right)^{0.2}\right] = 1.9\times10^{-3} - 0.11$.

The HTFS correlation coefficient C defined in Volume I is limited in the code to be ≥ 2. This is because in some limiting cases (i.e., no interphase drag or the pressure approaches the critical pressure), the coefficient C approaches 2. The equation for C was optimized to give the best fit to all the available data, however the resulting equation for C can produce values of C below 2 for high values of G and Λ (limited number of data points). Until a further study can be carried out, the HTFS recommended a minimum value of 2 for C should be applied when using the correlation.

6.2.1.2 ATHENA Friction Factor Model. The phasic friction factors used in the wall friction model in ATHENA are computed from the wall friction discussion in Volume I, where the Reynolds numbers used in the computation are computed as described above. One modification to the friction factor model as implemented in the ATHENA code is to limit the value of the phasic Reynolds number used in the computation of the laminar friction factor to be greater than or equal to a value 50. This prevents a divide by a small number or a potential divide by zero in low-speed flow. Another modification is to limit the ratio of the surface roughness to the hydraulic diameter in the computation of the turbulent friction factor to be greater than or equal to a value of $1.0\text{x}10^{-9}$. This prevents a potential logarithm of zero in high speed flow.

The Zigrang-Sylvester[6.2-4] approximation (used in ATHENA, see Volume I) to the Colebrook-White[6.2-5] correlation for turbulent flow, has a mean square error of 0.1% and a maximum deviation of 0.5% when compared to the Colebrook-White correlation over the ranges $10^{-5} \le \frac{\varepsilon}{D} \le 0.05$ and $2{,}500 \le Re \le 10^{7}$. **Figure 6.2-1** shows the friction factor computed from the ATHENA friction factor model for several values of the ratio of surface roughness to hydraulic diameter. Also shown as circular data points are several values of the turbulent friction factor computed from the Colebrook-White correlation. The friction factor model also has several user-input constants that allow the user to adjust the frictions factors if there are data for a particular test section or geometry. The shape factor can be used to adjust the laminar friction factor, an exponential function with users' input coefficients can

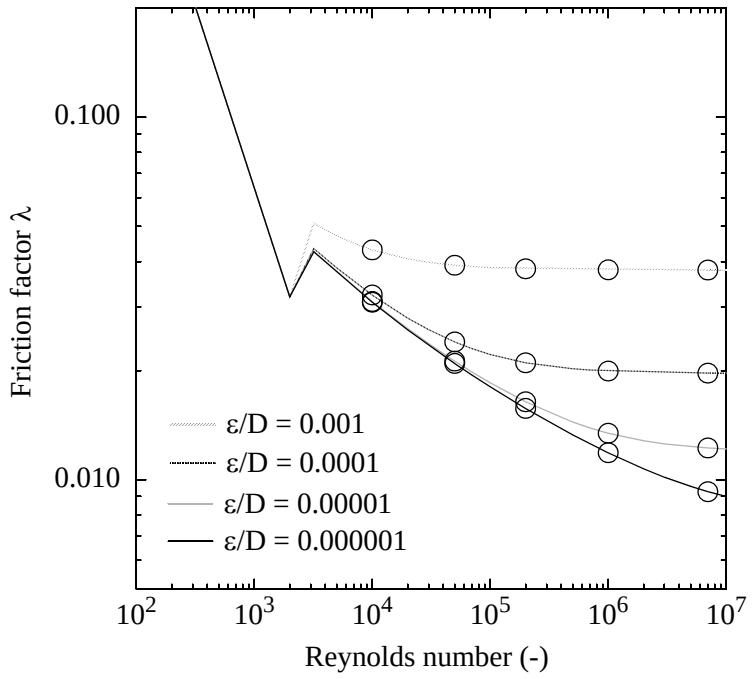

Figure 6.2-1 Comparison of Darcy-Weisbach friction factors for the Colebrook-White and the ATHENA friction factor correlations.

be used for the turbulent friction factor, and a viscosity ratio exponent can be used for the heated wall effect on both the laminar and turbulent friction factors.

6.2.2 Code Implementation

The wall drag model is used to determine the wall friction terms in the sum and difference momentum equations. The wall friction terms FRICGJ and FRICFJ, are calculated in subroutine VEXPLT, which calculates the sum and difference momentum equations, These terms, when used in the sum momentum equation, are of the form

FRICGJ = FRICGK + FRICGL (6.2-7)

FRICFJ = FRICFK + FRICFL (6.2-8)

The K and L terms indicate the "from" and "to" volumes relative to the junction orientation. These terms make use of the volume terms FWALF and FWALG, which have the form

$$FRICGK = \left(\frac{1}{\alpha_g \rho_g}\right) \bullet FWALG_K \bullet \frac{1}{2}\Delta x_K \quad (6.2\text{-}9)$$

$$FRICGL = \left(\frac{1}{\alpha_g \rho_g}\right) \bullet FWALG_L \bullet \frac{1}{2}\Delta x_L \quad (6.2\text{-}10)$$

$$FRICFK = \left(\frac{1}{\alpha_f \rho_f}\right) \bullet FWALF_K \bullet \frac{1}{2}\Delta x_K \quad (6.2\text{-}11)$$

$$FRICFL = \left(\frac{1}{\alpha_f \rho_f}\right) \bullet FWALF_L \bullet \frac{1}{2}\Delta x_L \quad (6.2\text{-}12)$$

The FWALG and FWALF terms contain the friction model information and are determined in subroutine FWDRAG with some necessary variables being calculated in earlier subroutines. For instance, flow regime effects are calculated in subroutine PHANTV.

The wall drag model in subroutine FWDRAG makes two loops over all volume cells. The first calculates the single-phase friction factors for wet wall and/or dry wall cases and interpolates if both cases are present. The second loop tests to see if the fluid is two-phase and, if so, calculates the H.T.F.S two-phase multiplier and, for either single- or two-phase, makes a final calculation of the FWALF and FWALG terms. In subroutine VEXPLT, the FWALG and FWALF terms are combined with other terms to form FRICGJ and FRICFJ, as shown previously. The $FWG_j \bullet \Delta x_j$ and $FWF_j \bullet \Delta x_j$ terms in Equations (6.2-2) and (6.2-3) are equal to the FRICGJ and FRICFJ terms.

For the difference momentum equation, the wall friction FRICGJ and FRICFJ terms in subroutine VEXPLT, used in the sum momentum equations, are modified to include wall friction changes discussed in Volume I (Section 3.3-6) when the drift flux method of the interphase friction model is used. The terms are modified as

$$FRICGJ = FRICGJ \bullet \left[1 - f_{xj} + f_{xj}\alpha_g\left(1 - \frac{\rho_g}{\rho_f}\right)\right] \quad (6.2\text{-}13)$$

and

$$FRICFJ = FRICFJ \bullet \left[1 - f_{xj} + f_{xj}\alpha_f\left(1 - \frac{\rho_f}{\rho_g}\right)\right] \quad (6.2\text{-}14)$$

These terms are multiplied by the time step size Δt. When the resulting terms involving f_{xj} are multiplied by the new time velocities v_{gj}^{n+1} and v_{fj}^{n+1}, respectively, it can be shown that the difference between the resulting terms is equal to the term

$$-f_{xj}^{n}\left(\frac{1}{\alpha_g\rho_g} + \frac{1}{\alpha_f\rho_f}\right)[(f_{wg})_j^n(v_g)_j^{n+1} - (f_{wf})_j^n(v_f)_j^{n+1}]\Delta x_j \Delta t \quad (6.2\text{-}15)$$

in Equation (6.1-1). As discussed in Volume I (Section 3.3.6, this is the additional wall friction term that appears when the drift flux method of the interphase friction model is used.

6.2.3 References

6.2-1. K. T. Claxton, J. G. Collier, and J. A. Ward, *H.T.F.S. Correlation for Two-Phase Pressure Drop and Void Fraction in Tubes,* HTFS Proprietary Report HTFS-DR-28, AERE-R7162, November 1972.

6.2-2. R. W. Lockhart and R. C. Martinelli, "Proposed Correlation of Data for Isothermal Two-Phase, Two-Component Flow in Pipes," *Chemical Engineering Progress, 45,* 1, 1949, pp. 39-48.

6.2-3. D. Chisholm, "A Theoretical Basis for the Lockhart-Martinelli Correlation for Two-Phase Flow," *International Journal of Heat and Mass Transfer, 10,* 1967, pp. 1767-1778.

6.2-4. D. J. Zigrang and N. D. Sylvester, "A Review of Explicit Friction Factor Equations," *Transactions of the ASME, Journal of Energy Resources Technology, 107,* 1985, pp. 280-283.

6.2-5. C. F. Colebrook, "Turbulent Flow in Pipes with Particular Reference to the Transition Region Between Smooth and Rough Pipe Laws," *Journal of Institute of Civil Engineers, 11,* 1939, pp. 133-156.

6.3 Entrainment Correlation

In the annular-mist flow regime, the calculation of wall-to-coolant heat transfer requires the proper apportioning of the liquid in the wall region as an annular film and in the vapor/gas region as droplets. The code uses the Ishii and Mishima[6.3-1,6.3-2] correlation for the entrainment fraction as a basis for calculating the liquid volume fraction in the film region and the liquid volume fraction in the vapor/gas region. The correlation determines the fraction of liquid flux flowing as droplets by the expression

$$E = \tanh\left(7.25 \times 10^{-7}\, We^{1.25}\, Re_f^{0.25}\right) \qquad (6.3\text{-}1)$$

where

We = effective Weber number for entrainment = $\dfrac{\rho_g(\alpha_g v_g)^2 D}{\sigma}\left(\dfrac{\rho_f - \rho_g}{\rho_g}\right)^{1/3}$

Re_f = total liquid Reynolds number = $\alpha_f \rho_f |v_f| \dfrac{D}{\mu_f}$.

The Ishii-Mishima entrainment correlation has been compared to air-water data over the ranges 1 atm < P < 4 atm, 0.95 cm < D < 3.2 cm, 370 < Re_f < 6,400, and j_g < 100 m/s, with satisfactory results. The correlation has also been developed to account for entrance effects and the development of entrainment.

The code, using the Ishii-Mishima correlation as a basis for determining entrainment, calculates the fraction of the total liquid volume residing in the annular film region (α_{ff}), by

$$\frac{\alpha_{ff}}{\alpha_f} = \max(0.0, F_{11}) \qquad (6.3\text{-}2)$$

where

F_{11} = $\gamma^* \max[0.0, (1 - G^*)] \exp(-C_e \times 10^{-5} \lambda^6)$

γ^* = factor accounting for entrance effects and ranges from 0.0 to 1.0 (defined in Appendix 4A, Annular Mist Flow)

G^* = $(10^{-4})(Re_f^{0.25})$

Re_f = $\dfrac{\alpha_f \rho_f |v_f| D}{\mu_f}$

C_e = 4.0 horizontal

= 7.5 vertical

λ = $\dfrac{\max(|v_f - v_g|, 10^{-15} m/s)}{v_{crit}}$ horizontal

$$= \frac{\alpha_g v_g}{v_{crit}} \quad \text{vertical}$$

$$v_{crit} = 0.5\left\{\frac{\max\left[(\rho_f - \rho_g), 10^{-7}\frac{kg}{m^3}\right] g \alpha_g A_{pipe}}{\rho_g D \sin\theta}\right\}^{1/2} (1 - \cos\theta) \quad \text{horizontal}$$

$$= \frac{3.2\left\{\sigma^* g \max\left[(\rho_f - \rho_g), 10^{-7}\frac{kg}{m^3}\right]\right\}^{1/4}}{\rho_g^{1/2}} \quad \text{vertical}$$

$$\sigma^* = \max(\sigma, 10^{-7}\ \text{N/m}).$$

From this expression, the fraction of liquid volume that exists as droplets α_{fg} in the vapor/gas phase can be calculated, since

$$\alpha_{ff} + \alpha_{fg} = \alpha_f \ . \tag{6.3-3}$$

Dividing by the total liquid volume fraction (α_f) and substituting Equation (6.3-2) yields

$$\frac{\alpha_{fg}}{\alpha_f} = \min(1.0, 1 - F_{11}) \ . \tag{6.3-4}$$

This relationship provides the entrainment volume fraction that is comparable to the Ishii-Mishima parameter calculated in Equation (6.3-1).

To demonstrate that the entrainment correlation in the code calculates the same entrainment fraction that the Ishii-Mishima correlation would predict, a set of conditions was taken from a small-break calculation for the Semiscale facility.[6.3-3] The code indicates that the annular-mist flow regime existed at the subject location. The conditions of the coolant are summarized as

ρ_g = 28.64 kg/m^3

ρ_f = 765.86 kg/m^3

v_g = 0.90463 m/s

v_f = 0.31068 m/s

D = 0.0127 m

α_g = 0.9980

α_f = 2.0×10^{-3}

μ_f = 9.689×10^{-5} kg/(m-s)

σ = 0.02 N/m.

The Ishii-Mishima correlation calculates a liquid volume fraction existing as droplets in the vapor/gas region of E = 0.0004978. The ATHENA code calculates the fraction to be 0.0004633, which suggests that the code representation of the correlation is relatively accurate.

6.3.1 References

6.3-1. I. Kataoka and M. Ishii, "Entrainment and Deposition Rates of Droplets in Annular Two-Phase Flow," CONF-830301-11, *ASME-JSME Thermal Engineering Joint Conference, Honolulu, HI, March 20, 1985.*

6.3-2. M. Ishii and K. Mishima, *Correlation for Liquid Entrainment in Annular Two-Phase Flow of Low Viscous Fluid,* ANL/RAS/LWR 81-2, Argonne National Laboratory, 1981.

6.3-3. M. Megahed, *RELAP5/MOD2 Assessment Simulation of Semiscale MOD-2C Test S-NH-3,* NUREG/CR-4799, EGG-2519, Idaho National Engineering Laboratory, October 1987.

Appendix 6A--Coefficients for Interfacial Drag/Shear and Wall Drag Models for ATHENA

Bubbly Flow

Interfacial Friction

For nonvertical bubbly flow,

$$C_i = \frac{1}{8}\rho_f a_{gf} C_D$$

$$C_0 = 1$$

$$f_x = 0$$

where

$\frac{1}{8}C_D$ = $\frac{3.0 + 0.3Re_b^{0.75}}{Re_b}$ (C_D is drag coefficient)

a_{gf} = $\frac{3.6\alpha_{bub}}{d_b}$, $\alpha_{bub} = \max(\alpha_g, 10^{-5})$

d_b = average bubble diameter

= $\frac{We\sigma}{\rho_f v_{fg}^2}$, $We = 5$, $We\sigma = \max(We\sigma, 10^{-10}\ N/m)$

v_{fg} = is as for bubbly flow SHL, Appendix 4A

Re_b = $\frac{(1-\alpha_{bub})\rho_f v_{fg} d_b}{\mu_f} = \frac{We\ \sigma(1-\alpha_{bub})}{\mu_f (v_{fg}^2)^{0.5}}$.

For vertical bubbly flow,

C_0 = profile slip distribution coefficient

C_i = $\frac{\alpha_g \alpha_f^3 \max\left[(\rho_f - \rho_g), 10^{-5}\frac{kg}{m^3}\right] g \sin\phi_j}{|v_{gj}| v_{gj}}$

α_g = $\max(\alpha^*_{g,j}, 10^{-2})$

α_f = $\max(1.0 - \alpha_g, 10^{-2})$

f_x = 1

where C_0 and v_{gj} are obtained for a given geometry and flow conditions, as seen in **Table 6.1-1**.

For the EPRI correlation,

$$C_0 = \frac{L}{K_0 + (1 - K_0)(\alpha_g)^r}$$

where

Ln = $1 - \exp(-C_p\alpha_g)$ if $C_p\alpha_g < 85$

= 1 otherwise

Ld = $1 - \exp(-C_p)$ if $C_p < 85$

= 1 otherwise

$$L = \frac{Ln}{Ld}$$

$$C_p = \left|\frac{4P_{crit}^2}{P(P_{crit} - P)}\right|$$

P_{crit} = critical pressure

$$K_0 = B_1 + (1 - B_1)\left(\frac{\rho_g}{\rho_f}\right)^{1/4}$$

B_1 = $\min(0.8, A_1)$

$$A_1 = \frac{1}{1 + \exp\left\{\max\left[-85, \min\left(85, -\frac{Re}{60{,}000}\right)\right]\right\}}$$

Re = Re_g if $Re_g > Re_f$ or $Re_g < 0$

$= \quad Re_f \quad$ otherwise

$Re_f = \frac{\rho_f j_f D_h}{\mu_f}$ (local liquid superficial Reynolds number)

$Re_g = \frac{\rho_g j_g D_h}{\mu_g}$ (local vapor/gas superficial Reynolds number)

$j_f = \alpha_f v_f$ (liquid superficial velocity)

$j_g = \alpha_g v_g$ (vapor/gas superficial velocity)

$r = \frac{1 + 1.57\left(\frac{\rho_g}{\rho_f}\right)}{1 - B_1}$.

The sign of j_k is taken as positive if phase k flows upward and negative if it flows downward. This convention determines the sign of Re_g, Re_f, and Re.

$$v_{gj} = 1.41\left\{\frac{\max\left[(\rho_f - \rho_g), 10^{-5}\frac{kg}{m^3}\right]\sigma g}{\rho_f^2}\right\}^{1/4} C_1C_2C_3C_4 \qquad \text{[see Equation (6.1-26)]}$$

where

$C_1 = (1 - \alpha_g)^{B_1}$ if $Re_g \geq 0$

$= (1 - \alpha_g)^{0.5}$ if $Re_g < 0$.

$C_2 = 1$ if $\frac{\rho_f}{\rho_g} \geq 18$ and $C_5 \geq 1$

$= 1$ if $\frac{\rho_f}{\rho_g} \geq 18$ and $C_5 < 1$ and $C_6 \geq 85$

$= \frac{1}{1 - \exp(-C_6)}$ if $\frac{\rho_f}{\rho_g} \geq 18$ and $C_5 < 1$ and $C_6 < 85$

$= 0.4757\left[\ln\left(\frac{\rho_f}{\rho_g}\right)\right]^{0.7}$ if $\frac{\rho_f}{\rho_g} < 18$

$$C_5 = \left[150\left(\frac{\rho_g}{\rho_f}\right)\right]^{1/2}$$

$$C_6 = \frac{C_5}{1 - C_5}$$

$$C_4 = 1 \quad \text{if } C_7 \geq 1$$

$$= \frac{1}{1 - \exp(-C_8)} \quad \text{if } C_7 < 1$$

$$C_7 = \left(\frac{D_2}{D}\right)^{0.6}$$

D_2 = 0.09144 m (normalizing diameter)

$$C_8 = \frac{C_7}{1 - C_7}$$

The parameter C_3 depends on the directions of the vapor/gas and liquid flows:

Upflow (both j_g and j_f are positive)

$$C_3 = \max\left[0.50, 2\exp\left(-\frac{|Re_f|}{60{,}000}\right)\right].$$

Downflow (both j_g and j_f are negative) or countercurrent flow (j_g is positive, j_f is negative)

$$C_3 = 2\left(\frac{C_{10}}{2}\right)^{B_2}$$

$$B_2 = \frac{1}{\left(1 + 0.05\left|\frac{Re_f}{350{,}000}\right|\right)^{0.4}}$$

$$C_{10} = 2\exp\left[\left(\frac{|Re_f|}{350{,}000}\right)^{0.4}\right] - 1.7|Re_f|^{0.035}$$

$$\bullet \exp\left[\frac{-|Re_f|}{60{,}000}\left(\frac{D_1}{D}\right)^2\right] + \left(\frac{D_1}{D}\right)^{0.1}|Re_f|^{0.001}$$

D_1 = 0.0381 m (normalizing diameter).

For the Griffith correlation,

$$C_0 = 1.35 - 0.35\sqrt{\frac{\rho_g}{\rho_f}}$$

$$v_{gj} = \left(0.23 + 0.13\frac{W}{S}\right)\left\{\frac{\max\left[(\rho_g - \rho_f),\ 10^{-5}\frac{kg}{m^3}\right]gS}{\rho_f}\right\}^{\frac{1}{2}}$$

For the Zuber-Findlay slug flow correlation,

$$C_0 = C_0^* \quad \text{for } \alpha_g \le 0.8$$

$$= 5(\alpha_g - 0.8) + (1 - \alpha_g)\, C_0^* \quad \text{for } \alpha_g > 0.8$$

$$v_{gj} = v_{gj}^* \quad \text{for } \alpha_g \le 0.8$$

$$= 5(1 - \alpha_g)\, v_{gj}^* \quad \text{for } \alpha_g > 0.8$$

$$C_0^* = 1.2(1 - e^{-18\alpha_g}) \quad \text{for } \Gamma_w > 0$$

$$= 1.2 \quad \text{for } \Gamma_w \le 0$$

$$v_{gj}^* = 0.35\left\{\frac{\max\left[(\rho_f - \rho_g),\ 10^{-5}\frac{kg}{m^3}\right]gD}{\rho_f}\right\}^{1/2}$$

For the Kataoka-Ishii correlation,

$$\left\{\text{used for the case } j_g^+ = \frac{j_g}{\left\{\frac{\max\left[(\rho_f - \rho_g),\ 10^{-5}\frac{kg}{m^3}\right]g\sigma}{\rho_f^2}\right\}^{1/4}} \ge j_{g2}^+ = 2.5\right\},$$

$$C_0 = C_0^* \quad \text{for } \alpha_g \le 0.8$$

$$= 5(\alpha_g - 0.8) + (1 - \alpha_g)C_0^* \quad \text{for } \alpha_g > 0.8$$

$$v_{gj} = v_{gj}^* \quad \text{for } \alpha_g \le 0.8$$

$$= 5(1 - \alpha_g)v_{gj}^* \quad \text{for } \alpha_g > 0.8$$

$$C_0^* = \left[C_\infty - (C_\infty - 1)\left(\frac{\rho_g}{\rho_f}\right)^{1/2}\right](1 - e^{-18\alpha_g}) \quad \text{for } \Gamma_w > 0$$

$$= C_\infty - (C_\infty - 1)\left(\frac{\rho_g}{\rho_f}\right)^{1/2} \quad \text{for } \Gamma_w \le 0$$

$$v_{gj}^* = 0.0019(D^*)^{0.809}\left(\frac{\rho_g}{\rho_f}\right)^{-0.157} N_{\mu f}^{-0.562}\left\{\frac{\sigma g \max\left[(\rho_f - \rho_g), 10^{-5}\frac{kg}{m^3}\right]}{\rho_f^2}\right\}^{1/4} \quad \text{for } D^* \le 30$$

$$= 0.030\left(\frac{\rho_g}{\rho_f}\right)^{-0.157} N_{\mu f}^{-0.562}\left\{\frac{\sigma g \max\left[(\rho_f - \rho_g), 10^{-5}\frac{kg}{m^3}\right]}{\rho_f^2}\right\}^{1/4} \quad \text{for } D^* > 30$$

where

$$D^* = D\left\{\frac{g \max\left[(\rho_f - \rho_g), 10^{-5}\frac{kg}{m^3}\right]}{\sigma}\right\}^{1/2}$$

$$N_{\mu f} = \frac{\mu_f}{\left(\rho_f \sigma\left\{\frac{\sigma}{g \max\left[(\rho_f - \rho_g), 10^{-5}\frac{kg}{m^3}\right]}\right\}^{1/2}\right)^{1/2}}$$

$$C_\infty = 1 + 0.2\left[\frac{\rho_f (gD)^{1/2}}{|G^*| + 0.001}\right]^{1/2}$$

$$G^* = \alpha_g\rho_g v_g + \alpha_f\rho_f v_f.$$

For the Churn-Turbulent Bubbly Flow correlation,

$$\left(\text{used for the case } j_g^+ = \frac{j_g}{\left\{ \frac{g\sigma \max\left[(\rho_f - \rho_g),\ 10^{-5}\frac{kg}{m^3}\right]}{\rho_f^2} \right\}^{1/4}} \le j_{g1}^+ = 0.5 \right),$$

$$C_0 = C_0^* \qquad \text{for } \alpha_g \le 0.8$$

$$= 5(\alpha_g - 0.8) + (1 - \alpha_g)C_0^* \qquad \text{for } \alpha_g > 0.8$$

$$v_{gj} = v_{gj}^* \qquad \text{for } \alpha_g \le 0.8$$

$$= 5(1 - \alpha_g)v_{gj}^* \qquad \text{for } \alpha_g > 0.8$$

$$C_0^* = \left[C_\infty - (C_\infty - 1)\left(\frac{\rho_g}{\rho_f}\right)^{1/2}\right](1 - e^{-18\alpha_g}) \qquad \text{for } \Gamma_w > 0$$

$$= C_\infty - (C_\infty - 1)\left(\frac{\rho_g}{\rho_f}\right)^{1/2} \qquad \text{for } \Gamma_w \le 0$$

$$v_{gj}^* = 1.41\left\{ \frac{\sigma g \max\left[(\rho_f - \rho_g),\ 10^{-5}\frac{kg}{m^3}\right]}{\rho_f^2} \right\}^{1/4}$$

where

$$C_\infty = 1 + 0.2\left[\frac{\rho_f (gD)^{1/2}}{|G^*| + 0.001}\right]^{1/2}$$

$$G^* = \alpha_g\rho_g v_g + \alpha_f\rho_f v_f.$$

For the CCFL,

C_0 is unchanged.

$$v_{gj} = \frac{(1-\alpha_g C_0) C_0 Ku_{crit} \left\{ \frac{\max\left[(\rho_f - \rho_g), 10^{-5}\frac{kg}{m^3}\right] g\sigma}{\rho_f^2} \right\}^{1/4}}{\alpha_g C_0 \left(\frac{\rho_g}{\rho_f}\right)^{1/2} + m^2(1-\alpha_g C_0)}$$

where Ku_{crit} is from **Table 6.1-2** and m = 1.

For the transition regions between low and high upflow rates and low and high downflow rates, the following method is used:

As indicated in the text near **Table 6.1-2**, the interfacial friction calculation is based on an interpolation of two drift flux correlations. In these regions, appropriate values of C_0 and v_{gj} are first calculated for both high and low flow conditions. Then, if GU_{low} and GU_{high} denote the boundaries of the low and high upflow ranges, and GD_{low} and GD_{high} denote the corresponding boundaries for downflow conditions, interpolated values are determined using the expressions

$$C_0 = XC_{0,low} + (1 - X)C_{0,high}$$

$$v_{gj} = Xv_{gj,low} + (1 - X)v_{gj,high}$$

where

$$X = \frac{GU_{high} - G^*}{GU_{high} - GU_{low}} \text{ for upflow conditions}$$

$$= \frac{GD_{high} - G^*}{GD_{high} - GD_{low}} \text{ for downflow conditions}$$

and an upward-directed channel has been assumed. The above interpolation scheme ensures that C_0 and v_{gj} vary continuously with G^*, though their first derivatives with respect to G^* are not continuous.

For the transition region between churn-turbulent bubbly flow and the Kataoka-Ishii correlation, the following is used:

C_0 is the same for both correlations.

$$v_{gj} = v_{gj}^{BUB} + \frac{j_g^+ - j_{g1}^+}{j_{g2}^+ - j_{g1}^+}(v_{gj}^{KI} - v_{gj}^{BUB})$$

where

$$j_g^+ = \frac{j_g}{\left\{\frac{g\sigma \max\left[(\rho_f - \rho_g), 10^{-5}\frac{kg}{m^3}\right]}{\rho_f^2}\right\}^{1/4}}$$

$j_{g1}^+ = 0.5$

$j_{g2}^+ = 1.768$

v_{gj}^{BUB} = v_{gj} for churn-turbulent bubbly flow

v_{gj}^{KI} = v_{gj} for Kataoka-Ishii correlation.

Wall Drag

$\alpha_{fw} = \alpha_f$

$\alpha_{gw} = \alpha_g$

Slug Flow

Interfacial Friction

For nonvertical slug flow,

$C_i = C_{i,Tb} + C_{i,bub}$

$C_0 = 1$

$f_x = 0$

where

$$C_{i,Tb} = \frac{1}{2}\rho_f a_{gf,TB} C_{D,Tb}$$

$a_{gf,Tb}$ is the frontal area per unit volume

$$a_{gf,Tb} = \frac{A_{Tb}}{V_{tot}} = \frac{A_{Tb}}{A_{tot}L} = \frac{\alpha_{Tb}}{L}$$

L = cell length

α_{Tb} is as for slug flow SHL, Appendix 4A

$$\frac{1}{2}C_{D,Tb} = 5.45\,(\alpha_{Tb})^{1/2}(1-\alpha_{Tb})^3$$

and

$$C_{i,bub} = \frac{1}{8}\rho_f a_{gf,bub} C_{D,bub}$$

where

$$a_{gf,bub} = \frac{3.6\alpha_{gs}}{d_b}(1-\alpha_{Tb})$$

$$\frac{1}{8}C_{D,bub} = \frac{3.0 + 0.3Re_s^{0.75}}{Re_s}$$

$$Re_s = \frac{(1-\alpha_{bub})\rho_f v_{fg} d_b}{\mu_f} = \frac{We\sigma(1-\alpha_{bub})}{\mu_f (v_{fg}^2)^{0.5}}$$

$$We = 5.0,\ We\sigma = \max(We\sigma,\ 10^{-10}\ N/m).$$

α_{bub}, α_{gs}, d_b, and v_{fg} are as for slug flow SHL, Appendix 4A.

For vertical slug flow, the same drift flux correlations that are used in bubbly flow are used.

Wall Drag

$$\alpha_{fw} = 1 - \alpha_{bub}$$

$\alpha_{gw} = \alpha_{bub}$

α_{bub} is as above.

Annular Mist Flow

Interfacial Friction

$C_i = C_{i,ann} + C_{i,drp}$

$C_0 = 1$

$f_x = 0$

where

$$C_{i,ann} = \left(\frac{1}{8}\right)\rho_g a_{gf,ann} C_{D,ann}$$

where

$$a_{gf,ann} = \left(\frac{4C_{ann}}{D}\right)(1-\alpha_{ff})^{0.5}$$

$$C_{ann} = (30\,\alpha_{ff})^{1/8}$$

α_{ff} is as for annular mist flow SHL, Appendix 4A

$$\left(\frac{1}{8}\right)C_{D,ann} = \frac{1}{8}\frac{64}{Re_i} \quad \text{for } Re_i \le 500$$

$$= \frac{1}{8}\left[\left(\frac{1{,}500 - Re_i}{1{,}000}\right)\frac{64}{Re_i} + \left(\frac{Re_i - 500}{1{,}000}\right)\,0.02\{1 + 150[1-(1-\alpha_{ff})^{1/2}]\}\right] \quad \text{for } 500 < Re_i < 1{,}500$$

$$= \frac{1}{8}0.02\{1 + 150[1-(1-\alpha_{ff})^{1/2}]\} \quad \text{for } Re_i \ge 1{,}500$$

$$Re_i = \frac{\rho_g |v_g - v_f| D_i}{\mu_g}$$

D_i = $\alpha_g^{1/2} D$ is the equivalent wetted diameter

μ_g = viscosity of the vapor/gas phase

and

$$C_{i,drp} = \left(\frac{1}{8}\right)\rho_g a_{gf,drp} C_{D,drp}$$

where

$$a_{gf,drp} = \frac{3.6\alpha_{fd}}{d_d}(1-\alpha_{ff})$$

α_{fd}, d_d are as for annular mist flow SHL, Appendix 4A

$$\left(\frac{1}{8}\right)C_{D,drp} = \frac{3.0 + 0.3Re_{drp}^{0.75}}{Re_{drp}}$$

$$Re_{drp} = \frac{(1-\alpha_{fd})^{2.5}\rho_g \hat{v}_{fg} d_d}{\mu_g} = \frac{We\ \sigma(1-\alpha_{fd})^{2.5}}{\mu_g \hat{v}_{fg}^{2\ 0.5}},\ We = 1.5,\ We\sigma = \max(We\sigma, 10^{-10}\text{N/m})$$

$\hat{v}_{fg}$ is as for annular mist flow SHL, Appendix 4A.

For bundles in vertical annular flow, a maximum of the interphase drag coefficient from the EPRI drift flux correlation (bubbly-slug flow) and the interphase drag coefficient from the annular mist flow (friction factor/drag coefficient previously discussed).

Wall Drag

α_{fw} = $\alpha_{ff}^{0.25}$

α_{gw} = $1 - \alpha_{ff}^{0.25}$.

Inverted Annular Flow

Interfacial Friction

$C_i = C_{i,bub} + C_{i,ann}$

$C_0 = 1$

$$f_x = 0$$

where

$$C_{i,bub} = \left(\frac{1}{8}\right)\rho_f a_{gf,\,bub} C_{D,\,bub}$$

where

$$a_{gf,bub} = \frac{3.6\alpha_{bub}}{d_b}(1-\alpha_B)$$

α_{bub}, d_b, α_B are as for inverted annular SHL, Appendix 4A

$$\left(\frac{1}{8}\right)C_{D,\,bub} = \frac{3.0 + 0.3Re_b^{0.75}}{Re_b}$$

$$Re_b = \frac{(1-\alpha_{bub})\rho_f v_{fg} d_{db}}{\mu_f} = \frac{We\sigma(1-\alpha_{bub})}{\mu_f(\hat{v}_{fg}^2)^{1/2}}\ ,\ We = 5.0,$$

$$We\,\sigma = \max(We\,\sigma,\ 10^{-10}\ N/m)$$

v_{fg} as for inverted annular flow SHL, Appendix 4A

and

$$C_{i,ann} = \left(\frac{1}{8}\right)\rho_f a_{gf,\,ann} C_{D,\,ann}$$

where

$$a_{gf,ann} = \frac{4}{D}(1-\alpha_B)^{0.5}$$

$$\frac{1}{8}C_{D,\,ann} = 0.0025 + 0.1375\,(10)^{9.07/D^*}\,(\delta^*)^{1.63 + 4.74/D^*}$$

$$D^* = D\left\{\frac{g\max\left[(\rho_f - \rho_g),\ 10^{-7}\frac{kg}{m^3}\right]}{\sigma}\right\}^{0.5},\ \frac{1}{D^*} = \min\left(30.0,\ \frac{1}{D^*}\right)$$

$$\delta^* = \delta\left\{\frac{g\max\left[(\rho_f-\rho_g), 10^{-7}\frac{kg}{m^3}\right]}{\sigma}\right\}^{0.5}, \delta^* = \max(10^{-8}, \delta^*)$$

where

δ = annular vapor/gas film thickness

= $\frac{1}{2}(D - D')$, D' = diameter of annulus

= $\frac{D}{2}\left(1-\frac{D'}{D}\right) = \frac{D}{2}[1-(1-\alpha_B)^{1/2}]$.

Wall Drag

$\alpha_{fw} = 1 - \alpha_B^{0.25}$

$\alpha_{gw} = \alpha_B^{0.25}$, α_B as for inverted annular interfacial drag.

Inverted Slug Flow

Interfacial Friction

$C_i = C_{i,ann} + C_{i,drp}$

$C_0 = 1$

$f_x = 0$

where

$C_{i,ann} = \frac{1}{2}\rho_g a_{gf,ann} C_{D,ann}$

where

$a_{gf,ann}$ is the frontal area per unit volume

$a_{gf,ann} = \frac{A_{ann}}{V_{tot}} = \frac{A_{ann}}{A_{tot}L} = \alpha_B$

L = cell length

α_B is as for inverted slug flow SHL, Appendix 4A

$$\left(\frac{1}{2}\right)C_{D,ann} = 5.45(\alpha_B)^{1/2}(1-\alpha_B)^3$$

and

$$C_{i,drp} = \left(\frac{1}{8}\right)\rho_g a_{gf,drp} C_{D,drp}$$

where

$$a_{gf,drp} = \frac{3.6\alpha_{drp}}{d_d}(1-\alpha_B)$$

α_{drp}, d_d are as for inverted slug SHL, Appendix 4A, with We = 6.0

$$\left(\frac{1}{8}\right)C_{D,drp} = \min\left[\frac{3.0 + 0.3Re_{drp}^{0.75}}{Re_{drp}}, 0.05625\right]$$

$$Re_{drp} = \rho_g v_{fg}\frac{d_d}{\mu_g}$$

v_{fg} is as for inverted slug SHL, Appendix 4A.

Wall Drag

$\alpha_{fw} = \alpha_{drp}$

$\alpha_{gw} = 1 - \alpha_{drp}$, α_{drp} as for inverted slug interfacial drag.

Dispersed (Droplet, Mist) Flow

Interfacial Friction

$$C_i = \left(\frac{1}{8}\right)\rho_g a_{gf} C_D$$

$C_0 = 1$

$$f_x = 0$$

where

$$a_{gf} = \frac{3.6\alpha_{drp}}{d_d}$$

$$\alpha_{drp} = \max(\alpha_f, 10^{-4})$$

d_d is as for dispersed flow SHL, Appendix 4A where We = 1.5 for pre-CHF and We = 6.0 for post-CHF.

$$\frac{1}{8}C_D = \frac{3.0 + 0.3Re_{drp}^{0.75}}{Re_{drp}} \quad \text{pre-CHF}$$

$$= \max\left[\frac{3.0 + 0.3Re_{drp}^{0.75}}{Re_{drp}}, 0.05626\right] \quad \text{post-CHF}$$

$$Re_{drp} = \frac{(1-\alpha_{drp})^{2.5}\rho_g v_{fg} d_d}{\mu_g} = \frac{We\sigma(1-\alpha_{drp})^{2.5}}{\mu_g v_{fg}} \quad \text{pre-CHF and post-CHF}$$

v_{fg} as for dispersed flow SHL, Appendix 4A.

Wall Drag

$$\alpha_{fw} = \alpha_f$$

$$\alpha_{gw} = \alpha_g.$$

Horizontally Stratified Flow

Interfacial Friction

$$C_i = \left(\frac{1}{8}\right)\rho_g a_{gf} C_D$$

$$C_0 = 1$$

$$f_x = 0$$

where

$$a_{gf} = \frac{4\sin\theta}{\pi D}$$

$$\frac{1}{8}C_D = \frac{1}{8}\max\left(\frac{64}{Re_i}, \frac{0.3164}{Re_i^{0.25}}\right)$$

$$Re_i = \frac{\rho_g(|v_g - v_f| + 0.01\,m/s)D_i}{\mu_g}$$

D_i = interphase hydraulic diameter

$$= \frac{\pi\alpha_g D}{\theta + \sin\theta}.$$

Wall Drag

$$\alpha_{fw} = 1 - \alpha_g^*$$

$$\alpha_{gw} = \alpha_g^*$$

$$\alpha_g^* = \frac{\theta}{\pi}.$$

Vertically Stratified Flow

Interfacial Friction

$C_0 = 1$, nonvertical bubbly/slug flow

= profile slip distribution coefficient, vertical bubbly/slug flow

$f_x = 0$, nonvertical bubbly/slug flow

= 1, vertical bubbly/slug flow.

The void fraction $\alpha_{g,j}^*$ used in the junction j above and below the vertically stratified volume for the interphase drag is

$$\alpha_{g,j}^* = w_j \bullet \alpha_{g,K}^* + (1 - w_j) \bullet \alpha_{g,L}$$

where

w_j is given by Equation (3.5-2)

$\alpha^*_{g,K}$ = strat • $\alpha_{g,L}$ + (1 - strat) • $\alpha_{g,K}$

strat = strat1 • strat2

$$\text{strat2} = 2\left(1 - \frac{v_m}{v_{Tb}}\right)$$

v_m and v_{Tb} are from Equation (3.2-29).

For the junction above,

$$\text{strat1} = 1 - e^{-0.5\alpha_{f,L}}.$$

For the junction below,

$$\text{strat1} = 20\,(\alpha_{level} - 0.05)$$

$$\alpha_{level} = \frac{\alpha_{g,L} - \alpha_{g,K}}{\alpha_{g,L} - \alpha_{g,I}}.$$

Wall Drag

$\alpha_{fw} = \alpha_f$

$\alpha_{gw} = \alpha_g$.

Transition Flow Regimes

The abbreviations for the flow regimes are defined in **Figure 3.1-1** and **Figure 3.2-1**.

In this section, FWF corresponds to α_{fw} and FWG corresponds to α_{gw}.

Horizontal Flow

Slug-Annular Mist Transition

$$C_{i_{SLG/ANM}} = [C_{i_{SLG}}]^{FSLUG}[C_{i_{ANM}}]^{FANM}$$

$$C_{0_{SLG/ANM}} = [C_{0_{SLG}}]^{FSLUG}[C_{0_{ANM}}]^{FANM}$$

$$f_{xSLG/ANM} = (f_{xSLG})FSLUG + (f_{xANM})\ FANM$$

$$FWF_{SLG/ANM} = (FWF_{SLG})FSLUG + (FWF_{ANM})\ FANM$$

$$FWG_{SLG/ANM} = (FWG_{SLG})FSLUG + (FWG_{ANM})\ FANM$$

where FSLUG and FANM are as for Transitions, Appendix 4A.

Transition to Horizontally Stratified Flow

$$C_{i_{REG-HS}} = C_{i_{REG}}\left[\frac{C_{i_{HS}}}{C_{i_{REG}}}\right]^{FSTRAT}$$

$$C_{0_{REG-HS}} = C_{0_{REG}}\left[\frac{C_{0_{HS}}}{C_{0_{REG}}}\right]^{FSTRAT}$$

$$f_{xREG\text{-}HS} = (f_{xHS})FSTRAT + (f_{xREG})(1\text{-}FSTRAT)$$

$$FWF_{REG\text{-}HS} = (FWF_{HS})FSTRAT + (FWF_{REG})(1\text{-}FSTRAT)$$

$$FWG_{REG\text{-}HS} = (FWG_{HS})FSTRAT + (FWG_{REG})(1\text{-}FSTRAT)$$

where FSTRAT is as for Transitions, Appendix 4A, and REG = BBY, SLG, SLG/ANM, ANM or MPR as appropriate.

Vertical Flow

Slug-Annular Mist Transition

The same formulas as for horizontal flow apply.

Inverted Annular-Inverted Slug Transition

$$C_{i_{IAN/ISL}}[C_{i_{IAN}}]^{FIAN}[C_{i_{ISL}}]^{FISLG}$$

$$C_{0_{IAN/ISL}} = 1$$

$$f_{xIAN/ISL} = 0$$

$FWF_{IAN/ISL} = (FWF_{IAN})FIAN + (FWF_{ISL})FISLG$

$FWG_{IAN/ISL} = (FWG_{IAN})FIAN + (FWG_{ISL})FISLG$

where FIAN and FISLG are as for Transitions, Appendix 4A.

Transition Boiling Regimes

$$C_{i_{REG1-REG2}} = C_{i_{REG1}} \bullet (1 - Z) + C_{i_{REG2}} \bullet Z$$

where REG1-REG2 can represent BBY-IAN, SLG-(IAN/ISL), SLG-ISL, (SLG/ANM)-ISL or ANM-MST. (see **Figure 3.2-1**).

$$Z = \max(0.0, \min\{1.0, 10.0[\min(1.0, T_{windo} \bullet T_{gsat})](0.4 - \alpha_{BS})\})$$

α_{BS} = transition from bubbly-to-slug flow (see **Figure 3.2-1**, and **Figure 3.2-2**)

$T_{gsat} = T_g - T^s - 1.0$

$$T_{windo} = 0.06666667 \qquad \frac{P}{P_{crit}} < 0.25$$

$$= \frac{1}{15 + 200\left[\left(\frac{P}{P_{crit}}\right) - 0.025\right]} \qquad 0.025 \le \frac{P}{P_{crit}} < 0.25$$

$$= 0.016666667 \qquad \frac{P}{P_{crit}} > 0.25$$

$$C_{0_{REG1-REG2}} = C_{0_{REG1}}\left(\frac{C_{0_{REG2}}}{C_{0_{REG1}}}\right)^Z$$

$f_{xREG1\text{-}REG2} = (f_{xREG1})(1 - Z)$

$FWF_{REG1\text{-}REG2} = (FWF_{REG1})(1 - Z) + (FWF_{REG2})Z$

$FWG_{REG1\text{-}REG2} = (FWG_{REG1})(1 - Z) + (FWG_{REG2})Z.$

High Mixing Map

Bubbly-Dispersed Transition

$$C_{i_{CTB-CTM}} = (C_{i_{CTB}})FBUB + (C_{i_{CTM}})FDIS$$

$$C_{0_{CTB-CTM}} = 1.0$$

$$f_{xCTB\text{-}CTM} = 0.0$$

$$FWF_{CTB\text{-}CTM} = (FWF_{CTB})FBUB + (FWF_{CTM})FDIS$$

$$FWG_{CTB\text{-}CTM} = (FWG_{CTB})FBUB + (FWG_{CTM})FDIS$$

where FBUB and FDIS are as for Transitions, Appendix 4A.

7 Flow Process Models

7.1 Abrupt Expansions and Contractions

In the sum and difference field equations (see Section 2.2), the HLOSSF and HLOSSG terms account for momentum losses due to abrupt expansions or contractions of flow areas. The abrupt area change model used to determine these terms is based on the Borda-Carnot[7.1-1,7.1-2,7.1-3,7.1-4] formulation for a sudden (i.e., sharp, blunt) enlargement and standard pipe flow relations, including the vena-contracta effect for a sudden (i.e., sharp, blunt) contraction or sharp-edge orifice or both. It does not include the case where an enlargement, contraction, or orifice is rounded or beveled. Quasi-steady continuity and momentum balances are employed at points of abrupt area change. The numerical implementation of these balances is such that hydrodynamic losses are independent of upstream and downstream nodalization. In effect, the quasi-steady balances are employed as jump conditions that couple fluid components having abrupt changes in cross-sectional area. This coupling process is achieved without change to the basic linear semi-implicit and nearly-implicit numerical time-advancement schemes.

7.1.1 Basis

The basic assumption used for the transient calculation of two-phase flow in flow passages with points of abrupt area change is that the transient flow process can be approximated as a quasi-steady flow process that is instantaneously satisfied by the upstream and downstream conditions (that is, transient inertia, mass, and energy storage are neglected at abrupt area changes). However, the upstream and downstream flows are treated as fully transient flows.

There are several bases for the above assumption. A primary consideration is that available loss correlations are based on data taken during steady flow processes; however, transient investigations[7.1-5] have verified the adequacy of the quasi-steady assumption. The volume of fluid and associated mass, energy, and inertia at points of abrupt area change is generally small compared with the volume of upstream and downstream fluid components. The transient mass, energy, and inertia effects are approximated by lumping them into upstream and downstream flow volumes. Finally, the quasi-steady approach is consistent with modeling other important phenomena in transient codes (heat transfer, pumps, and valves).

7.1.1.1 Single-Phase Abrupt Area Change Model. The modeling techniques used for dynamic pressure losses associated with abrupt area change in a single-phase flow are reviewed briefly before discussing the extension of these methods to two-phase flows. In a steady, incompressible flow, losses at an area change are modeled by the inclusion of an appropriate dynamic head loss term, h_L, in the one-dimensional modified Bernoulli equation

$$\left(\frac{v^2}{2}+\frac{P}{\rho}\right)_1 = \left(\frac{v^2}{2}+\frac{P}{\rho}\right)_2 + h_L \qquad (7.1\text{-}1)$$

where h_L is of the form $h_L = (1/2)\ Kv^2$. The particular form of the dynamic head loss is obtained by employing the Borda-Carnot[7.1-2,7.1-3,7.1-4]assumption for calculating losses associated with the expansion part of the flow process at points of abrupt area change.

For the case of a one-dimensional branch, apportioned volume areas are calculated. This is discussed in Volume I.

7.1.1.1.1 Expansion--Consider a steady and incompressible flow undergoing a sudden increase in cross-sectional area (expansion) as shown in **Figure 7.1-1**. Here the flow is assumed to be from left to right with the upstream conditions denoted by the subscript 1 and the downstream condition by 2. Here the upstream and downstream conditions are assumed to be far enough removed from the point of area change that flow is one-dimensional, i.e., none of the two-dimensional effects of the abrupt area change exist. These locations can range from several diameters upstream to as many as 30 diameters downstream. However, for purposes of modeling the overall dynamic pressure loss, the entire process is assumed to occur as a discontinuous jump in flow condition at the point of abrupt area change. In this context, the stations 1 and 2 refer to locations immediately upstream and downstream of the abrupt area change.

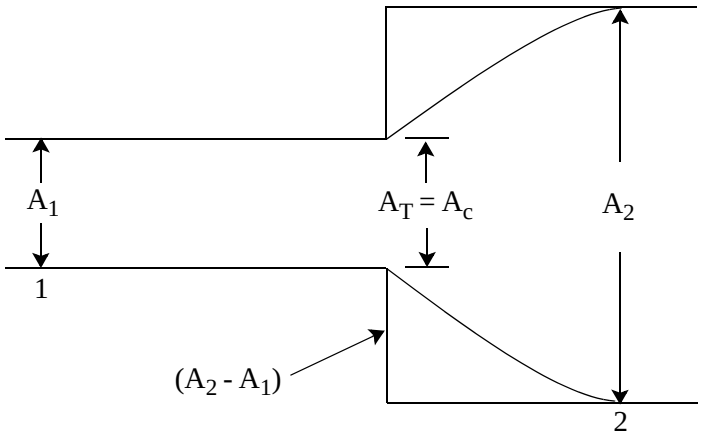

Figure 7.1-1 Abrupt expansion.

The dynamic head loss for the abrupt expansion shown in **Figure 7.1-1** can be obtained using the Borda-Carnot[7.1-2,7.1-3,7.1-4] assumption, i.e., the pressure acting on the "washer shaped" area, $A_2 - A_1$, is the upstream pressure, P_1. When this assumption is employed in an overall momentum balance, the head loss is

$$h_L = \frac{1}{2}\left(1 - \frac{A_1}{A_2}\right)^2 v_1^2 \quad . \tag{7.1-2}$$

The loss is the dynamic pressure associated with the area change and is related to the head loss by

$$\Delta P_f = \rho h_L = \frac{1}{2}\rho\left(1 - \frac{A_1}{A_2}\right)^2 v_1^2 \quad . \tag{7.1-3}$$

7.1.1.1.2 Contraction--The flow process at a point of abrupt reduction in flow area (contraction) is idealized in much the same manner as for the expansion, except that an additional process must be considered. The flow continues to contract beyond the point of abrupt area reduction and forms a vena contracta, see **Figure 7.1-2**. The point of vena contracta is designed by c. The far upstream and downstream conditions are designated by 1 and 2, respectively**.**

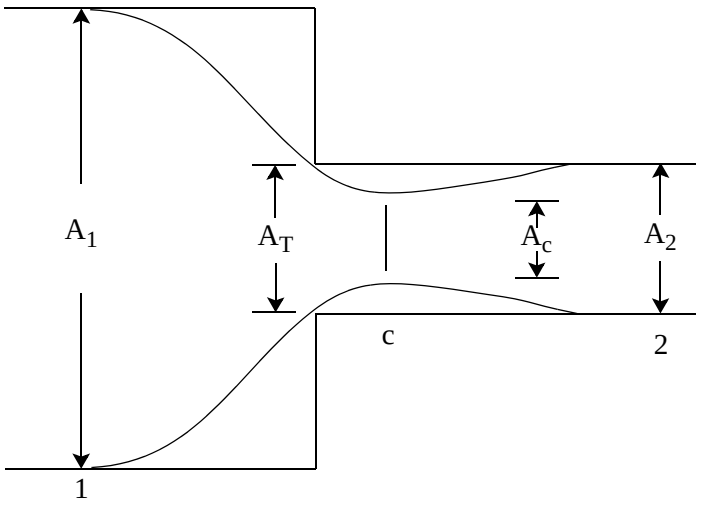

Figure 7.1-2 Abrupt contraction.

Consider a sudden contraction in a steady incompressible flow. The loss in dynamic pressure from the upstream station to the vena contracta is the smaller part of the total loss. Measurements[7.1-2] indicate that the contracting flow experiences a loss no larger than $\Delta P_f = 0.046\left(\frac{1}{2}\rho v_c^2\right) = 0.12\left(\frac{1}{2}\rho v_2^2\right)$, where v_c is the velocity at the vena contracta. This loss is at most 24% of the total loss and is neglected in ATHENA. The dynamic pressure loss associated with the expansion from the area at the vena contracta to the downstream area is modeled using the Borda-Carnot assumption with the condition at the vena contracta as the upstream condition, that is

$$\Delta P_f = \frac{1}{2}\rho\left(1 - \frac{A_c}{A_2}\right)^2 v_c^2 , \tag{7.1-4}$$

where from continuity considerations for incompressible flow

$$v_c = \frac{A_2 v_2}{A_c} \quad . \tag{7.1-5}$$

The contraction ratio, $\frac{A_c}{A_2}$, is a function of $\frac{A_2}{A_1}$. This is based on a synthesis of analytical approaches and generally accepted experimental information.[7.1-2,7.1-3] The function in **Reference 7.1-2** and **Reference 7.1-3** is in the form of a table and is shown in **Table 7.1-1**. The values in the table are referred to as Weisbach values, and **Reference 7.1-2** and **Reference 7.1-3** indicate they may be used as nominal values at high Reynolds numbers. The table has been approximated in ATHENA as the function equation $\frac{A_c}{A_2} = 0.62 + 0.38\left(\frac{A_2}{A_1}\right)^3$. A comparison between the table and the function used in ATHENA is shown in **Figure 7.1-3**.

Table 7.1-1 Contraction ratio $\frac{A_c}{A_2}$ as a function of area ratio $\frac{A_2}{A_1}$.

$\frac{A_2}{A_1}$	$\frac{A_c}{A_2}$
0.0	0.617
0.1	0.624
0.2	0.632
0.3	0.643
0.4	0.659
0.5	0.681
0.6	0.712
0.7	0.755
0.8	0.813
0.9	0.892
1.0	1.000

Combining Equations (7.1-4) and (7.1-5) leads to

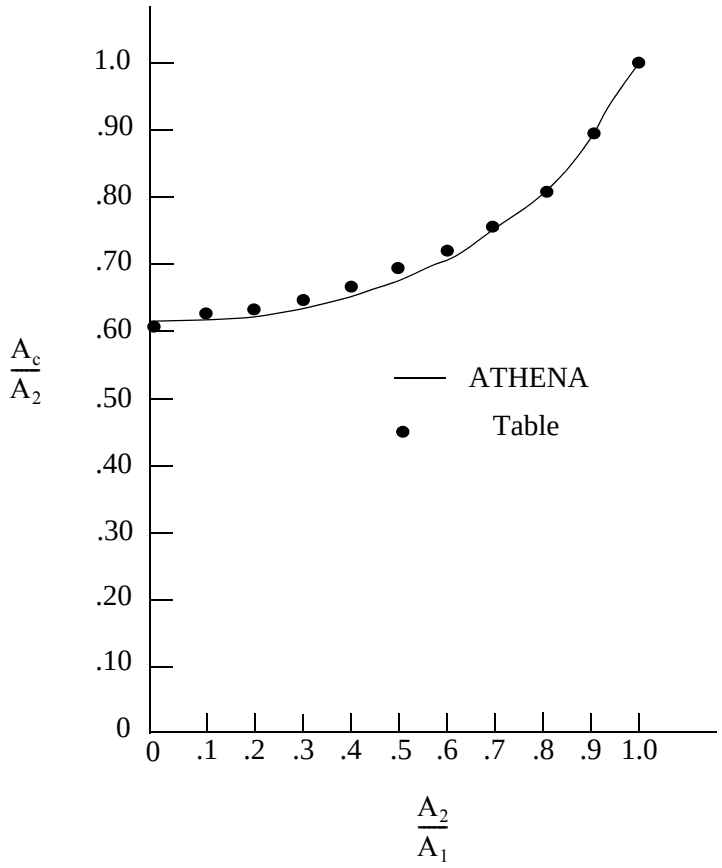

Figure 7.1-3 Comparison of ATHENA function equation and table for contraction ratio.

$$\Delta P_f = \frac{1}{2}\rho\left(1 - \frac{A_2}{A_c}\right)^2 v_2^2 \qquad (7.1\text{-}6)$$

as the dynamic pressure loss for a contraction.[7.1-3]

The total contraction K loss is a Weisbach value as is the contraction ratio. The K loss from the vena contracta to the downstream station (decelerating zone) (K_d) is from the Borda-Carnot result discussed previously (used in ATHENA), and the K loss from the upstream station to the vena contracta (accelerating zone) (K_a) as the difference between the total K loss (K) and the K loss from the decelerating zone K_d). As discussed previously, ATHENA neglects the loss from the upstream station to the vena contracta (accelerating zone) (K_a). **Table 7.1-2** from **Reference 7.1-2** and **Reference 7.1-3** shows the magnitude of this for different area ratios.

Table 7.1-2 Losses K_d, K_a, and K as a function of area ratio $\frac{A_2}{A_1}$

$\frac{A_2}{A_1}$	K_d	K_a	K
0	0.38	0.12	0.50
0.1	0.36	0.10	0.46
0.2	0.34	0.07	0.41
0.3	0.31	0.05	0.36
0.4	0.27	0.03	0.30
0.5	0.22	0.02	0.24
0.6	0.16	0.02	0.18
0.7	0.10	0.02	0.12
0.8	0.05	0.01	0.06
0.9	0.02	0	0.02
1.0	0	0	0

For a sudden contraction (i.e., inlet edge blunt), both Crane[7.1-6] and Idelchik[7.1-7] suggest a dynamic pressure loss of

$$\Delta P_f = \frac{1}{2}\rho\left[\frac{1}{2}\left(1-\frac{A_2}{A_1}\right)\right]v_2^2 \quad . \tag{7.1-7}$$

Table 7.1-3 shows both the ATHENA loss (K_{ATHENA}) used in Equation (7.1-6), which uses the function Equation $\frac{A_c}{A_2} = 0.62 + 0.38\left(\frac{A_2}{A_1}\right)^3$, and the loss from Crane and Idelchik (K_{ci}) used in Equation (7.1-7). The difference is 24.8% for $A_2/A_1 = 0$, decreasing to 1.7% at $A_2/A_1 = 0.3$, and then decreasing to 0% at $A_2/A_1 = 1$. The ATHENA loss in **Table 7.1-3** compares well to the deceleration loss in **Table 7.1-2**; the small difference is due to the contraction ratio difference shown in **Figure 7.1-3**. The Crane/Idelchik loss compares well to the total Weisbach loss shown in **Table 7.1-2** except at high area ratios.

Table 7.1-3 Losses K_{ATHENA} and K_{ci}.

$\frac{A_2}{A_1}$	K_{ATHENA}	K_{ci}
0	0.376	0.50
0.1	0.374	0.45
0.2	0.366	0.40
0.3	0.344	0.35
0.4	0.305	0.30
0.5	0.248	0.25
0.6	0.180	0.20
0.7	0.111	0.15
0.8	0.052	0.10
0.9	0.013	0.05
1.0	0	0

Figure 7.1-4 shows the ATHENA loss used in Equation (7.1-6), the loss from Crane and Idelchik used in Equation (7.1-7), and the total Weisbach loss shown in **Table 7.1-2**. At low area ratios, ATHENA loss underpredicts the Crane/Idelchik and the total Weisbach loss. At high area ratios, the ATHENA loss underpredicts the Crane/Idelchik loss, but compares well to the total Weisbach loss.

7.1.1.1.3 Abrupt Area Change With an Orifice--The most general case of an abrupt area change is a contraction with an orifice at the point of contraction. Such a configuration is shown in **Figure 7.1-5**. In this case, an additional flow area, the orifice flow area, must be specified. Conditions at the orifice throat station will be designated by a subscript T. Three area ratios are used throughout this development. The first is the contraction area ratio at the vena contracta relative to the minimum physical area, $\varepsilon_c = \frac{A_c}{A_T}$. The second is the ratio of the minimum physical area to the upstream flow area, $\varepsilon_T = \frac{A_T}{A_1}$. The third is the ratio of the downstream to upstream area, $\varepsilon = \frac{A_2}{A_1}$.

The dynamic pressure loss for an abrupt area contraction combined with an orifice is analyzed in a manner parallel to that for a simple contraction. The loss associated with the contracting fluid stream from Station 1 to c (the point of vena-contracta) is neglected. The dynamic pressure loss associated with the expansion from the vena contracta to the downstream section is given by

.

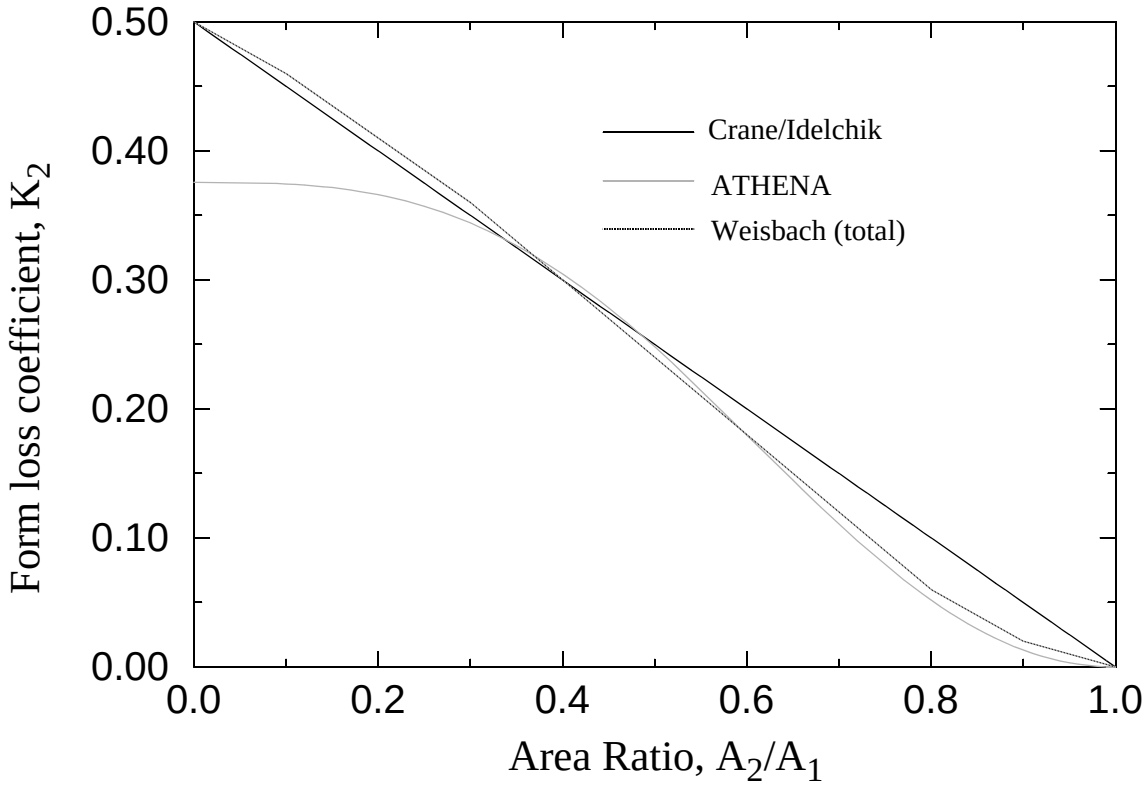

Figure 7.1-4 Loss coefficients for sudden contraction.

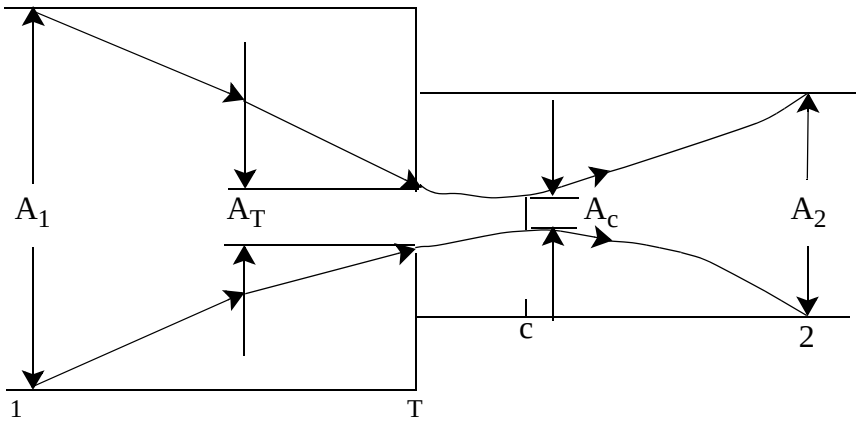

Figure 7.1-5 Orifice at abrupt area change.

$$\Delta P_f = \frac{1}{2}\rho\left(1 - \frac{A_c}{A_2}\right)^2 v_c^2 \quad . \tag{7.1–8}$$

The contraction ratio, $\varepsilon_c = \frac{A_c}{A_T}$, is a function of $\varepsilon_T = \frac{A_T}{A_1}$. The code uses the same function equation as is used for a contraction. The function equation ε_c has the form $\varepsilon_c = 0.62 + 0.38(\varepsilon_T)^3$. Using the continuity equations, $v_c = \frac{A_T v_T}{A_c} = \frac{v_T}{\varepsilon_c}$ and $v_T = \frac{A_2 v_2}{A_T} = \frac{\varepsilon}{\varepsilon_T} v_2$, Equation (7.1-8) can be written as

$$\Delta P_f = \frac{1}{2}\rho\left(1 - \frac{\varepsilon}{\varepsilon_c \varepsilon_T}\right)^2 v_2^2 \tag{7.1-9}$$

where $K_f = K_g = \left(1 - \frac{\varepsilon}{\varepsilon_c \varepsilon_T}\right)^2$.

Equation (7.1-9) is a generalization applicable to all the cases previously treated. For a pure expansion, $\varepsilon_T = 1$, $\varepsilon_c = 1$, and $\varepsilon > 1$; for a contraction, $\varepsilon_T = \varepsilon < 1$ and $\varepsilon_c < 1$. Each of these is a special case of Equation (7.1-9).

Using the continuity equation $v_2 = \frac{A_T v_T}{A_2} = \frac{\varepsilon_T}{\varepsilon} v_T$, Equation (7.1-9) can be written as

$$\Delta P_f = \frac{1}{2}\rho\left(\frac{A_T}{A_C} - \frac{A_T}{A_2}\right)^2 v_T \, . \tag{7.1-10}$$

For an orifice, Idelchik[7.1-7] suggests a dynamic pressure loss of

$$\Delta P_f = \frac{1}{2}\rho\left[1 + 0.707\left(1 - \frac{A_T}{A_1}\right)^{0.5} - \frac{A_T}{A_2}\right]^2 v_T^2 \, . \tag{7.1-11}$$

Table 7.1-4 shows both the ATHENA loss used in Equation (7.1-10) and the loss from Idelchik used in Equation (7.1-11). These comparisons are for the case $A_1 = A_2$. **Figure 7.1-6** shows the ATHENA loss

used in Equation (7.1-10) for the case $A_1 = A_2$ and the loss from Idelchik used in Equation (7.1-11) for the case $A_1 = A_2$. At low area ratios and high area ratios, the ATHENA loss underpredices the Idelchik loss.

Table 7.1-4 ATHENA loss (K_{ATHENA}) and Idelchik loss (K_i)

$\frac{A_T}{A_1}$	K_{ATHENA}	K_i
0	2.601	2.914
0.1	2.286	2.467
0.2	1.974	2.052
0.3	1.655	1.668
0.4	1.327	1.317
0.5	0.996	1.000
0.6	0.680	0.718
0.7	0.400	0.472
0.8	0.183	0.266
0.9	0.046	0.105
1.0	0.0	0.0

The two-phase dynamic pressure loss model is based on an adaptation of the general single-phase head loss given by Equation (7.1-9). It is given in the next section.

7.1.1.2 Two-Phase Abrupt Area Change Model. The two-phase flow through an abrupt area change is modeled in a manner very similar to that for single-phase flow by defining phasic flow areas. The two phases are coupled through the interphase drag, a common pressure gradient, and the requirement that the phases coexist in the flow passage. As with the single-phase case, apportioned volume areas are calculated for a one-dimensional branch. This is discussed in Volume I.

The one-dimensional phasic stream-tube momentum equations are given in Volume I. The flow at points of abrupt area change is assumed to be quasi-steady and incompressible. In addition, the terms in the momentum equations due to body force, wall friction, and mass transfer are assumed to be small in the region affected by the area change. The interphase drag terms are retained, since the gradient in relative velocity can be large at points of abrupt area changes.

The momentum equations can be integrated along a streamline approximately for a steady, incompressible, smoothly varying flow to obtain modified Bernoulli-type equations

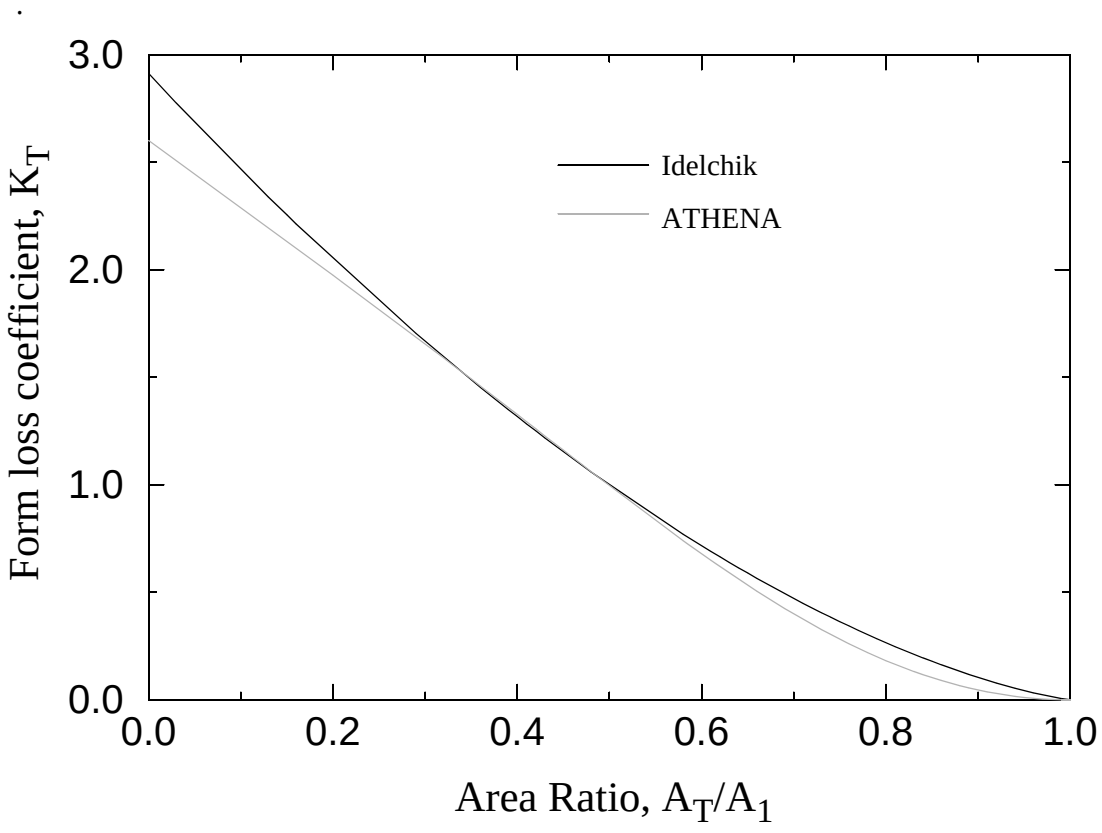

Figure 7.1-6 Loss coefficients for an orifice with $A_1 = A_2$

$$\left(\frac{1}{2}\rho_f v_f^2 + P\right)_1 = \left(\frac{1}{2}\rho_f v_f^2 + P\right)_2 + \left(\frac{FI'}{\alpha_f}\right)_1 (v_{f1} - v_{g1})L_1 + \left(\frac{FI'}{\alpha_f}\right)_2 (v_{f2} - v_{g2})L_2 \qquad (7.1\text{-}12)$$

and

$$\left(\frac{1}{2}\rho_g v_g^2 + P\right)_1 = \left(\frac{1}{2}\rho_g v_g^2 + P\right)_2 + \left(\frac{FI'}{\alpha_g}\right)_1 (v_{g1} - v_{f1})L_1 + \left(\frac{FI'}{\alpha_g}\right)_2 (v_{g2} - v_{f2})L_2 \quad , \qquad (7.1\text{-}13)$$

where FI' = $\alpha_f\alpha_g\rho_f\rho_g$FI and FI is obtained from Equation (6.1-3). The terms L_1 and L_2 are the lengths from the upstream condition to the throat and from the throat to the downstream condition, respectively. The interphase drag is divided into two parts, which are associated with the upstream and downstream parts of the co-current flow affected by the area change. The interphase drag is increased for horizontal stratified abrupt area changes in order to ensure more homogeneous flow when the flow becomes more increasingly cocurrent. **References 7.1-8, 7.1-9, and 7.1-10** discuss the observation of a strong mixing action as the flow contracts, so that the two-phase mixture is well homogenized at the vena contracta. The interphase drag is increased by adding an extra interphase drag term ($C_{i,extra}$) to the normal interphase drag (C_i) discussed in Section 6.1 of this volume of the manual. The extra interphase drag has the form

$$C_{i,\,extra} = C_{i,\,abrupt}^{scrah} \bullet C_i^{1-scrah} \tag{7.1-14}$$

where

$$C_{i,abrupt} = \max(C_i, C_a) \tag{7.1-15}$$

$$C_a = 8x10^5 Ns^2/m^5 \times \exp[-14(1-\alpha_{f,j})^2 + 2.5\ \max(0.0, \alpha_{f,j} - \alpha_{f,down})^{0.33}] \tag{7.1-16}$$

$$scrah = 1.0 - \frac{|v_{g,j} - v_{f,j}|}{\max(10^{-30} m/s, |v_{g,j} + v_{f,j}|)} \tag{7.1-17}$$

and $\alpha_{f,down}$ is the downstream volume liquid volume fraction. The term $C_{i,extra}$ is normally set to C_i, but when scrah > 0, then $C_{i,extra}$ is calculated from Equation (7.1-14). The form of this extra interphase drag was determined during the RELAP5/MOD2 development assessment[7.1-11] for the LOFT-Wyle small break test.

7.1.1.3 General Model. Consider the application of Equations (7.1-12) and (7.1-13) to the flow of a two-phase fluid through a passage having a generalized abrupt area change. The flow passage is shown in **Figure 7.1-7**.[1] Here, the area A_T is the throat or minimum area associated with an orifice located at the point of the abrupt area change. Since each phase is governed by a modified Bernoulli-type equation, it is reasonable to assume that losses associated with changes in the phasic flow area can be modeled by separate dynamic pressure loss terms for both the liquid and vapor/gas phases. Hence, it is assumed that the liquid sustains a loss as if it alone (except for interphase drag) were experiencing an area change from $\alpha_{f1}A_1$ to $\alpha_{fT}A_T$ to $\alpha_{f2}A_2$, and the vapor/gas phase experiences a loss as if it alone were flowing through an area change from $\alpha_{g1}A_1$ to $\alpha_{gT}A_T$ to $\alpha_{g2}A_2$. The area changes for each phase are the phasic area changes (see **Figure 7.1-7**). When the losses for these respective area changes [based on the Borda-Carnot model and given by Equation (7.1-9)] are added to Equations (7.1-12) and (7.1-13), the following phasic momentum equations are obtained:

1. In **Figure 7.1-7**, the flow is shown as a separated flow for clarity. The models developed are equally applicable to separated and dispersed flow regimes, as evidenced by the calculations performed when the abrupt area change model was incorporated into RELAP5.[7.1-1] The model was verified on single-phase expansions, contractions, and orifices. Three two-phase problems were also run: (1) expansion case with the interphase drag equal to zero, which simulates separated flow, (2) expansion case with the interphase drag appropriate for dispersed flow, and (3) contraction case with the interphase drag appropriate for dispersed flow.

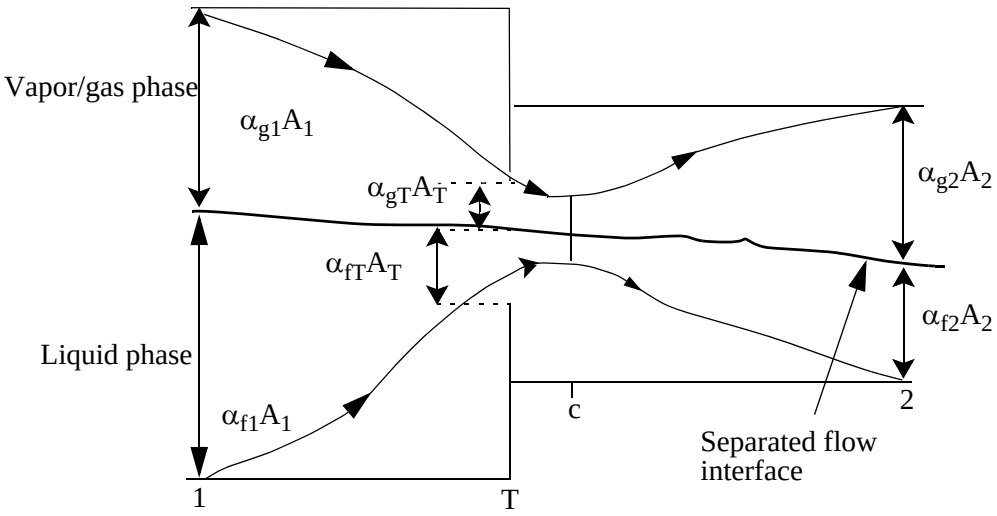

Figure 7.1-7 Schematic of flow of two-phase mixture at abrupt area change.

$$\left(\frac{1}{2}\rho_f v_f^2 + P\right)_1 = \left(\frac{1}{2}\rho_f v_f^2 + P\right)_2 + \frac{1}{2}\rho_f\left(1 - \frac{\alpha_{f2}\varepsilon}{\alpha_{fT}\varepsilon_{fc}\varepsilon_T}\right)^2 (v_{f2})^2 + \left(\frac{FI'}{\alpha_f}\right)_1 (v_{f1} - v_{g1})L_1 + \left(\frac{FI'}{\alpha_f}\right)_2 (v_{f2} - v_{g2})L_2 \quad (7.1\text{-}18)$$

and

$$\left(\frac{1}{2}\rho_g v_g^2 + P\right)_1 = \left(\frac{1}{2}\rho_g v_g^2 + P\right)_2 + \frac{1}{2}\rho_g\left(1 - \frac{\alpha_{g2}\varepsilon}{\alpha_{gT}\varepsilon_{gc}\varepsilon_T}\right)^2 (v_{g2})^2 + \left(\frac{FI'}{\alpha_g}\right)_1 (v_{g1} - v_{f1})L_1 + \left(\frac{FI'}{\alpha_g}\right)_2 (v_{g2} - v_{f2})L_2 \quad (7.1\text{-}19)$$

where

$$K_f = \left(1 - \frac{\alpha_{f2}\varepsilon}{\alpha_{fT}\alpha_{fc}\varepsilon_T}\right)^2$$

$$K_g = \left(1 - \frac{\alpha_{g2}\varepsilon}{\alpha_{gT}\alpha_{gc}\varepsilon_T}\right)^2 .$$

These phasic momentum equations are used across an abrupt area change. In Equations (7.1-18) and (7.1-19), ε_{fc} and ε_{gc} are the same tabular function of area ratio as in the single-phase case, except the area ratios used are the phasic area ratios, given by

$$\varepsilon_{fT} = \left(\frac{\alpha_{fT}}{\alpha_{f1}}\right)\varepsilon_T \tag{7.1–20}$$

and

$$\varepsilon_{gT} = \left(\frac{\alpha_{gT}}{\alpha_{g1}}\right)\varepsilon_T , \tag{7.1-21}$$

respectively. The area ratios, $\varepsilon = \frac{A_2}{A_1}$ and $\varepsilon_T = \frac{A_T}{A_1}$, are the same as for single-phase flow.

The interphase drag effects in Equations (7.1-18) and (7.1-19) are important. These terms govern the amount of slip induced by an abrupt area change; and, if they are omitted, the model will always predict a slip at the area change appropriate to a completely separated flow situation and give erroneous results for a dispersed flow.

7.1.2 Code Implementation

A few remarks concerning the way Equations (7.1-18) and (7.1-19) are applied to expansions and contractions, both with and without an orifice, are necessary. In a single-phase, steady-flow situation and given the upstream conditions, v_1 and P_1, one can solve for v_2 and P_2 using the continuity equation ($v_1A_1 = v_2A_2$) and Equation (7.1-1). Equations (7.1-18) and (7.1-19), along with the two-phasic continuity equations, can be used in a similar manner, except now the downstream void fraction is an additional unknown that must be determined.

7.1.2.1 Expansion. For the purpose of explanation, consider the case of an expansion ($\alpha_{fT} = \alpha_{f1}$, $\alpha_{gT} = \alpha_{g1}$, $\varepsilon > 1$, $\varepsilon_T = 1$, $\varepsilon_{fc} = \varepsilon_{gc} = 1$, $L_1 = 0$), for which Equations (7.1-18) and (7.1-19) reduce to

$$\left(\frac{1}{2}\rho_f v_f^2 + P\right)_1 = \left(\frac{1}{2}\rho_f v_f^2 + P\right)_2 + \frac{1}{2}\rho_f\left(1 - \frac{\alpha_{f2}\varepsilon}{\alpha_{f1}}\right)^2 (v_{f2})^2 + \left(\frac{FI'}{\alpha_f}\right)_2 (v_{f2} - v_{g2})L_2 \tag{7.1-22}$$

and

$$\left(\frac{1}{2}\rho_g v_g^2 + P\right)_1 = \left(\frac{1}{2}\rho_g v_g^2 + P\right)_2 + \frac{1}{2}\rho_g\left(1 - \frac{\alpha_{g2}\varepsilon}{\alpha_{g1}}\right)^2 (v_{g2})^2 + \left(\frac{FI'}{\alpha_g}\right)_2 (v_{g2} - v_{f2})L_2 \quad . \tag{7.1-23}$$

These two equations with the two incompressible continuity equations, given by

$$\alpha_{f1} v_{f1} A_1 = \alpha_{f2} v_{f2} A_2 \tag{7.1-24}$$

and

$$\alpha_{g1} v_{g1} A_1 = \alpha_{g2} v_{g2} A_2 \tag{7.1-25}$$

are a system of four equations having four unknowns, α_{f2} ($\alpha_{g2} = 1 - \alpha_{f2}$), v_{f2}, v_{g2}, and P_2, in terms of the upstream conditions, α_{f1} ($\alpha_{g1} = 1 - \alpha_{f1}$), v_{f1}, v_{g1}, and P_1. (The interphase drag, FI', is a known function of the flow properties.) It is important to note that the downstream value of the liquid fraction (α_{f2}) is an additional unknown compared with the single-phase case and is determined (with the downstream velocities and pressure) by simultaneous solution of Equations (7.1-22) through (7.1-25) without additional assumptions. It is reassuring that by taking a proper linear combination of Equations (7.1-18) and (7.1-19), the usual overall momentum balance obtained using the Borda-Carnot[7.1-2,7.1-3,7.1-4] assumption can be obtained.[7.1-12,7.1-13]

If, as in the cited literature,[7.1-12,7.1-13,7.1-14,7.1-15] only the overall momentum balance is used at an expansion, there will be an insufficient number of equations to determine all the downstream flow parameters, α_{f2}, v_{f2}, v_{g2}, and P_2. The indeterminacy has been overcome in cited works by means of several different assumptions concerning the downstream void fraction.[1] In the model developed here [Equations (7.1-22) and (7.1-23)], division of the overall loss into liquid and vapor/gas parts, respectively, results in sufficient conditions to determine all downstream flow variables, including α_{f2}. In addition, the present model includes force terms due to interphase drag in Equations (7.1-22) and (7.1-23), which are necessary to predict the proper amount of slip and void redistribution that occurs at points of area change.

7.1.2.2 Contraction. Consider the application of Equations (7.1-18) and (7.1-19) to a contraction. To determine both the downstream conditions and throat conditions from the upstream values of $\alpha_{f1}(\alpha_{g1})$, v_{f1}, v_{g1}, and P_1, an additional consideration must be made. To obtain the throat values, apply the

1. J. G. Collier[7.1-12] mentions three different assumptions that have been used: (a) $\alpha_{f2} = \alpha_{f1}$, (b) α_{f2} is given by a homogeneous model, and (c) α_{f2} is given by the Hughmark void fraction correlation.

momentum equations valid for the contracting section of flow (where the L_1 portion of the interphase force is associated with the contraction). This results in

$$\left(\frac{1}{2}\rho_f v_f^2 + P\right)_1 = \left(\frac{1}{2}\rho_f v_f^2 + P\right)_T + \left(\frac{FI'}{\alpha_f}\right)_1 (v_{f1} - v_{g1})L_1 \quad (7.1\text{-}26)$$

$$\left(\frac{1}{2}\rho_g v_g^2 + P\right)_1 = \left(\frac{1}{2}\rho_g v_g^2 + P\right)_T + \left(\frac{FI'}{\alpha_g}\right)_1 (v_{g1} - v_{f1})L_1 \quad (7.1\text{-}27)$$

The two incompressible continuity equations are

$$\alpha_{f1} v_{f1} A_1 = \alpha_{fT} v_{fT} A_T \quad (7.1\text{-}28)$$

$$\alpha_{g1} v_{g1} A_1 = \alpha_{gT} v_{gT} A_T \; . \quad (7.1\text{-}29)$$

These four equations are solved simultaneously for the values of $\alpha_{fT}(\alpha_{gT})$, v_{fT}, v_{gT}, and P_T at the throat section (the minimum physical area). No additional or special assumptions are made concerning the throat conditions, since they follow as a direct consequence of the unique head loss models for each phase. After the throat values have been obtained, the conditions at the point of vena contracta are established, assuming the void fraction is the same as at the throat. Thus, ε_{fc} and ε_{gc} are established using the single-phase contraction function equation and the throat area ratios, ε_{fT} and ε_{gT}, defined by Equations (7.1-20) and (7.1-21). The functions are $\varepsilon_{fc} = 0.62 + 0.38(\varepsilon_{fT})^3$ and $\varepsilon_{gc} = 0.62 + 0.38(\varepsilon_{gT})^3$. To determine the downstream values, Equations (7.1-18) and (7.1-19) can be applied directly from Stations 1 to 2 with the throat values known, or the expansion loss equations can be used from the throat section to Station 2. Both approaches produce identical downstream solutions. As in the case of an expansion, because the proper upstream and downstream interphase drag is included, this modeling approach establishes the phase slip and resulting void redistribution. An orifice at an abrupt area change is treated exactly as the contraction explained above (that is, with two separate calculations to establish first the throat and then the downstream flow variable).

7.1.2.3 Countercurrent Flow. The preceding development implicitly assumed a cocurrent flow. For countercurrent flow, Equations (7.1-18) and (7.1-19) are applied exactly as in cocurrent flow except the upstream sections for the respective phases are located on different sides of the abrupt area change. The difference appears in how the throat and downstream volume fractions are determined. To determine the throat properties, equations similar to Equations (7.1-26) through (7.1-29) are used with the upstream values appropriate for each phase. These four equations are then solved for $\alpha_{fT}(\alpha_{gT})$, v_{fT}, v_{gT}, and P_T. To determine the downstream values for each phase, only the head loss terms are needed for the downstream volume fractions. (The downstream v_f, v_g, and P do not appear.) For countercurrent flow, these volume fractions are set such that the downstream volume fraction of each phase plus the upstream volume fraction of the opposite phase adds to one. (Both phases together must fill the flow channel.) With the throat and

downstream volume fractions now known, Equations (7.1-18) and (7.1-19) can be used directly to determine the total loss for each phase at the abrupt area change.

7.1.2.4 Numerical Implementation. The numerical implementation will be described for the co-current expansion case only; the co-current contraction, countercurrent expansion, and countercurrent contraction cases are similar. Consider Equations (7.1-22) and (7.1-23) without the interphase drag term since it is not needed to show the implementation method. Using the incompressible continuity equations, Equations (7.1-24) and (7.1-25), in the second term on the right hand side of Equations (7.1-22) and (7.1-23) and neglecting the interphase drag yields,

$$\left(\frac{1}{2}\rho_f v_f^2 + P\right)_1 = \left(\frac{1}{2}\rho_f v_f^2 + P\right)_2 + \frac{1}{2}\rho_f\left(1 - \frac{\alpha_{f1}}{\alpha_{f2}\varepsilon}\right)v_{f1}^2 \tag{7.1-30}$$

and

$$\left(\frac{1}{2}\rho_g v_g^2 + P\right)_1 = \left(\frac{1}{2}\rho_g v_g^2 + P\right)_2 + \frac{1}{2}\rho_g\left(1 - \frac{\alpha_{g1}}{\alpha_{g2}\varepsilon}\right)v_{g1}^2 \ . \tag{7.1-31}$$

Subtracting Equations (7.1-30) and (7.1-31), solving Equations (7.1-24) and (7.1-25) for v_{f2} and v_{g2}, and substituting those expressions into the resulting equation yields,

$$\alpha_{f1}\rho_f v_{f1}^2\left(\frac{1}{\alpha_{f2}\varepsilon}\right)\left[\left(\frac{\alpha_{f1}}{\alpha_{f2}\varepsilon}\right) - 1\right] = \alpha_{g1}\rho_g v_{g1}^2\left(\frac{1}{\alpha_{g2}\varepsilon}\right)\left[\left(\frac{\alpha_{g1}}{\alpha_{g2}\varepsilon}\right) - 1\right] \tag{7.1-32}$$

where the assumption of incompressible flow implies $\rho_{g1} = \rho_{g2} = \rho_g$ and $\rho_{f1} = \rho_{f2} = \rho_f$. Multiplying by $\alpha_{f2}\alpha_{g2}\varepsilon^2$ and rearranging yields,

$$\alpha_{f1}\rho_f v_{f1}^2(\alpha_{f1} - \alpha_{f2}\varepsilon)(1 - 2\alpha_{f2} + \alpha_{f2}^2) = \alpha_{g1}\rho_g v_{g1}^2[\alpha_{g1} - (1 - \alpha_{f2})\varepsilon]\alpha_{f2}^2 \ . \tag{7.1-33}$$

This is a cubic equation which is solved for α_{f2} using donored phasic densities, Then Equations (7.1-24), (7.1-25), and (7.1-30) are used to obtain the remaining variables v_{f2}, v_{g2}, and P_2.

7.1.3 References

7.1-1. J. A. Trapp and V. H. Ransom, *RELAP5 Hydrodynamic Model Progress Summary-Abrupt Area Changes and Parallel Branching*, PG-R-77-92, Idaho National Engineering Laboratory, November 1977.

7.1-2. J. K. Vennard, "One-Dimensional Flow," in: V. L. Streeter (ed.), *Handbook of Fluid Dynamics*, 1st Edition, New York: McGraw-Hill, 1961.

7.1-3. J. K. Vennard and R. L. Street, *Elementary Fluid Mechanics*, 6th Edition, New York: Wiley, 1982.

7.1-4. R. B. Bird, W. E. Stewart, and E. M. Lightfoot, *Transport Phenomena*, New York: Wiley, 1960.

7.1-5. J. Weisman, T. Ake, and R. Knott, "Two-Phase Pressure Drop Across Abrupt Area Changes in Oscillatory Flow," *Nuclear Science and Engineering, 61*, 1976, pp. 297-309.

7.1-6. Crane Co., *Flow of Fluid Through Valves and Fittings*, 1980.

7.1-7. I. E. Idelchik, *Handbook of Hydraulic Resistance*, 3rd Edition, Boca Raton, FL: CRC Press, 1994.

7.1-8. E. Janssen and J. A. Kervinen, *Two-Phase Pressure Drop Across Contractions and Expansions; Water-Steam Mixtures at 600 to 1400 Psia*, GEAP-4622, General Electric Company, AEC Research and Development Report, June 1964.

7.1-9. P. B. Whalley, *Boiling, Condensation, and Gas-Liquid Flow*, Oxford: Clarendon Press, 1987.

7.1-10. K. W. McQuillan and P. B. Whalley, "The Effect of Orifices on the Liquid Distribution in Annular Two-Phase Flow," *International Journal of Multiphase Flow, 10*, 721-730, 1984.

7.1-11. V. H. Ransom et al., *RELAP5/MOD2 Code Manual, Volume 3: Developmental Assessment Problems*, EGG-TFM-7952, Idaho National Engineering Laboratory, December 1987.

7.1-12. J. G. Collier, "Advanced Study Institute on Two-Phase Flows and Heat Transfer," *ASI Proceedings, Istanbul, Turkey, August 1976.*

7.1-13. M. M. El-Wakil, *Nuclear Heat Transport*, Scranton, PA: International Textbook, 1971.

7.1-14. B. Harsch, A. Hussain, and J. Weisman, *Two-Phase Pressure Drop Across Restrictions and Other Abrupt Area Changes*, NUREG-0062, April 1976.

7.1-15. P. A. Lottes, "Expansion Losses in Two-Phase Flows," *Nuclear Science and Energy, 9*, 1961, pp. 26-31.

7.2 Choked Flow

In reactor blowdown transients, choked or critical flow will exist at the locale of the break. Furthermore, under certain circumstances, choked flow can exist at a point internal to the system or at multiple locations within the system. A one-dimensional choked flow model developed by Ransom and Trapp[7.2-1,7.2-2] is employed in ATHENA to predict the existence of choked flow at a break or internal

location and to establish the flow boundary condition if choking is predicted to occur. Since reactor blowdown transients can encompass single-phase and multi-phase flows, the choked flow model is designed to handle single phase liquid subcooled choked flow, two-phase choked flow (one-component and two-component), and single phase vapor/gas (one-component and two component) choked flow.

Choking is a condition where the mass discharge from a system or at an internal point in the system becomes independent of conditions downstream. In other words, for a given set of upstream conditions, the mass flow does not increase as the downstream pressure is decreased. Physically, choking occurs when acoustic signals can no longer propagate upstream. Such a situation exists when the fluid discharge velocity is equal to or exceeds the local propagation velocity. The following sections detail the basis for the choking criteria used in ATHENA and the implementation of the criteria described above for the various thermodynamic states that can occur during a blowdown transient.

7.2.1 Basis for Choking

As described above, various thermodynamic states and flow conditions can prevail during a reactor blowdown transient. The basis for the subcooled choking model and the two-phase choking model used in ATHENA are described below.

7.2.1.1 Subcooled Choking Model. The subcooled choking model employed in ATHENA is similar in concept to the model proposed by Burnell[7.2-3] and has been designed to reflect the physics occurring during the break flow process. Both models assume a Bernoulli expansion to the point of vapor inception at the choke plane. The ATHENA subcooled choking model (see Volume I) is somewhat different from the model proposed by Moody[7.2-4] in that the Moody model assumes that an isentropic process occurs up to the choke plane. In the early stage of a blowdown, the fluid approaching the break is a subcooled liquid. Because the downstream pressure (containment) is much lower than the upstream pressure, the fluid will undergo a phase change at the break. The phase change is accompanied by a large change in the fluid bulk modulus and hence sound speed. The sound speed change is most pronounced for the liquid-to-liquid/vapor/gas transition point, although there is also an abrupt change at the liquid/vapor/gas-to-pure-vapor/gas transition. The large change in sound speed mandates that extreme care be used in analyzing the choked flow process when upstream conditions are subcooled.

The physics involved during subcooled choking can be better appreciated by considering flow through a converging-diverging nozzle connected to a stagnation volume containing subcooled high pressure water, as shown in **Figure 7.2-1**. When the downstream pressure P_d is slightly less than the upstream pressure P_{up}, subcooled flow exists throughout the nozzle. The throat conditions for an idealized situation can be analyzed using the Bernoulli equation, i.e.,

$$v = \left[v_{up}^2 + \frac{2(P_{up} - P_t)}{\rho} \right]^{1/2} \quad . \tag{7.2-1}$$

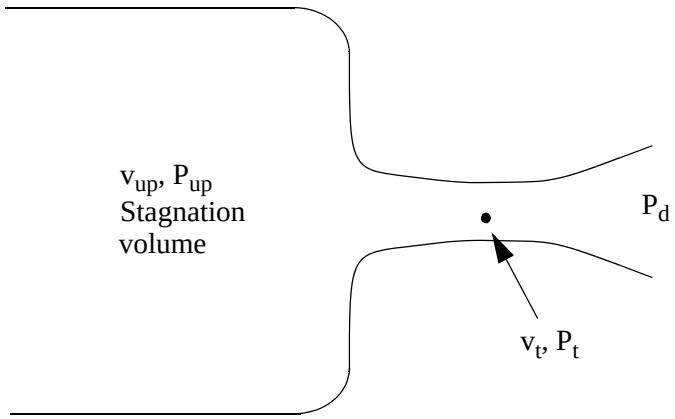

Figure 7.2-1 Converging-diverging nozzle.

As the downstream pressure is decreased, a point is eventually reached where the pressure at the throat is equal to the local saturation pressure, P_{sat}. Further reduction in the downstream pressure results in vaporization of fluid at the throat if homogeneous equilibrium assumptions are made. As discussed above, a slight amount of vapor/gas at the throat results in a significant reduction of the sound speed. Conservation of mass requires that the velocity of the two-phase mixture at the throat be equal to the velocity of the subcooled fluid just upstream of the throat. At this point, the velocity in the subcooled region is less than the subcooled fluid sound speed; but, in the two-phase region, the throat velocity can be larger than the two-phase sound speed. Under this condition, the flow is choked, since downstream pressure changes cannot be propagated upstream. Thus the supersonic two-phase flow at the throat must increase in velocity, and the pressure must decrease as the flow expands in the divergent section. In effect, there is no point in the flow stream where the Mach number is unity. This stems from the discontinuous sound speed change at the phase transition, although the fluid properties are continuous through the transition. **Figure 7.2-2**a shows this condition schematically; the flow rate can be established in ideal frictionless flow with Equation (7.2-1), where P_t is the local saturation pressure.

As the upstream pressure is decreased for the situation above, the throat pressure remains at P_{sat} and the subcooled fluid velocity at the throat decreases. As P_{up} is further decreased, a point is eventually reached where the throat velocity is equal to the homogeneous equilibrium sound speed a_{HE}, and the Mach number becomes unity on the two-phase side of the throat, while the Mach number in the subcooled side is much less than unity. Schematically, this is shown in **Figure 7.2-2**b.

With further decreases in P_{up}, the location where the pressure reaches P_{sat} moves upstream relative to the throat position. Upstream of the saturation point, the subcooled fluid velocity is less than the two-phase sound speed. Between the saturation point and the throat, the two-phase velocity is less than the two-phase

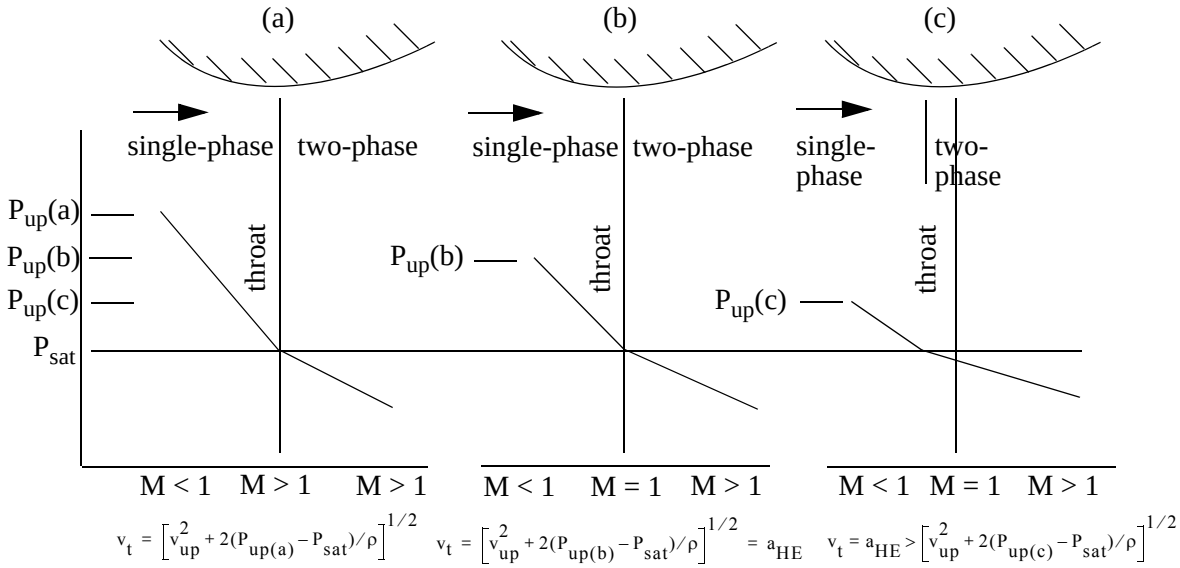

Figure 7.2-2 Subcooled choking process.

sound speed; and, at the throat, the fluid velocity is equal to the two-phase sound speed, as shown in **Figure 7.2-2**c. Ultimately, as P_{up} is decreased further, the saturation point moves farther and farther upstream until the flow is all two-phase.

The homogeneous process described above, although idealized, is an accurate representation when vapor is first formed. Nonequilibrium effects, however, can result in vapor formation at a pressure considerably less than the local saturation pressure. In other words, the existence of superheated liquid results in the onset of vaporization at P_t ($< P_{sat}$), rather than at local saturation pressure. A model described by Alamgir and Lienhard[7.2-5] and Jones[7.2-6,7.2-7] can be used to calculate the throat pressure at which vaporization first occurs. This model is

$$\Delta P = P_{sat} - P_t = 0.258 \frac{\sigma^{3/2} T_R^{13.76}}{\sqrt{k_B T_c}} \frac{V_g}{V_g - V_f} \left[1 + 2.078\times10^{-8}\left(\rho_f \frac{1}{A_t}\frac{dA_t}{dx} v_c^3\right)^{0.8}\right]^{1/2} - 6.9984\times10^{-2}\left(\frac{A_t}{A}\right)^2 \rho_f v_c^2 \quad (7.2\text{-}2)$$

where

σ = surface tension

T_R = temperature ratio, $\frac{T}{T_c}$

T = fluid temperature

T_c = critical temperature

k_B = Boltzmann constant

V_g = vapor/gas specific volume

V_f = liquid specific volume

ρ_f = liquid density

A = cell area

A_t = throat area

v_c = throat velocity.

In this equation, T, V_g, V_f, ρ_f, and A are upstream volume quantities. In the ATHENA implementation, $P_{sat} - P_t$ is taken to be the maximum of zero and the value from Equation (7.2-2), i.e.,

$$P_{sat} - P_t = \max(0.0, \Delta P) \quad . \tag{7.2-3}$$

For the situation shown in **Figure 7.2-2**a, the idealized choking criteria is

$$v_c = \left[v_{up}^2 + 2\frac{(P_{up} - P_t)}{\rho} \right]^{1/2} \tag{7.2-4}$$

where P_t is calculated from Equation (7.2-3). For the situations in **Figure 7.2-2**b and **Figure 7.2-2**c, the choking criterion is

$$v_c = a_{HE}, \tag{7.2-5}$$

and the two-phase choking criteria to be described in the next section applies. In the implementation of the model, both Equations (7.2-4) and (7.2-5) are evaluated; the larger of the two is used as the choking velocity at the throat. This velocity is then imposed numerically at the throat. The implementation is described in Section 7.2.2.

7.2.1.2 Two-Phase One-Component Choking Model. The two-phase choking model employed in ATHENA is based on the model described by Trapp and Ransom[7.2-1,7.2-2] for nonhomogeneous, nonequilibrium flow. Trapp and Ransom developed an analytic choking criteria using a characteristic analysis of a two-fluid model that included relative phasic acceleration terms and derivative-dependent mass transfer. During the original development and implementation of this model, both frozen flow and thermal equilibrium assumptions were employed to test the analytic criteria. Comparisons to existing data[7.2-1] indicated that the thermal equilibrium assumption was the more appropriate and is thus assumed in the following development.

The two-fluid model employed in the development of the ATHENA two-phase choking criteria includes an overall mass conservation equation, two-phasic momentum equations, and the mixture energy equation written in terms of entropy. The equation set is written without nondifferential terms, such as wall drag and heat transfer, since these terms do not enter into the characteristic analysis. The differential equations are

$$\frac{\partial}{\partial t}(\alpha_g\rho_g + \alpha_f\rho_f) + \frac{\partial}{\partial x}(\alpha_g\rho_g v_g + \alpha_f\rho_f v_f) = 0 \tag{7.2-6}$$

$$\alpha_g\rho_g\left(\frac{\partial v_g}{\partial t} + v_g\frac{\partial v_g}{\partial x}\right) + \alpha_g\frac{\partial P}{\partial x} + C\alpha_g\alpha_f\rho\left(\frac{\partial v_g}{\partial t} + v_f\frac{\partial v_g}{\partial x} - \frac{\partial v_f}{\partial t} - v_g\frac{\partial v_f}{\partial x}\right) = 0 \tag{7.2-7}$$

$$\alpha_f\rho_f\left(\frac{\partial v_f}{\partial t} + v_f\frac{\partial v_f}{\partial x}\right) + \alpha_f\frac{\partial P}{\partial x} + C\alpha_f\alpha_g\rho\left(\frac{\partial v_f}{\partial t} + v_g\frac{\partial v_f}{\partial x} - \frac{\partial v_g}{\partial t} - v_f\frac{\partial v_g}{\partial x}\right) = 0 \tag{7.2-8}$$

and

$$\frac{\partial}{\partial t}(\alpha_g\rho_g S_g + \alpha_f\rho_f S_f) + \frac{\partial}{\partial x}(\alpha_g\rho_g S_g v_g + \alpha_f\rho_f S_f v_f) = 0 \tag{7.2-9}$$

where

α_g = vapor/gas fraction

α_f = liquid fraction

ρ_g = vapor/gas density

ρ_f = liquid density

v_g = vapor/gas velocity

v_f = liquid velocity

C = virtual mass coefficient

ρ = density of mixture

S_g = vapor/gas specific entropy

S_f = liquid specific entropy.

This equation set includes interface force terms due to relative acceleration, since these terms have a significant effect on wave propagation.[7.2-2] Energy dissipation terms associated with interface mass transfer and relative phase acceleration have been neglected in the mixture entropy equation. Given the assumption of thermal equilibrium, ρ_g, ρ_f, S_g, and S_f are functions of pressure (i.e., saturation values). Using the chain rule and property derivatives for ρ_g, ρ_f, S_g, and S_f,

$$\rho_f^* = \frac{d\rho_f^s}{dP}, \qquad \rho_g^* = \frac{d\rho_g^s}{dP} \tag{7.2-10}$$

$$S_f^* = \frac{dS_f^s}{dP}, \qquad S_g^* = \frac{dS_g^s}{dP} \ . \tag{7.2-11}$$

Equations (7.2-6) through (7.2-9) can be written in terms of α_g, ρ, v_g, and v_f as four quasi-linear, first-order partial differential equations of the form

$$A(\bar{U})\frac{\partial \bar{U}}{\partial t} + B(\bar{U})\frac{\partial \bar{U}}{\partial x} + C(\bar{U}) = 0 \tag{7.2-12}$$

where A and B are fourth-order square coefficient matrices.

The characteristic velocities of the system of equations defined by Equation (7.2-12) are the roots[7.2-8,7.2-9] (λ_i, $i \leq 4$) of the characteristic polynomial

$$(A\lambda - B) = 0 \ . \tag{7.2-13}$$

The real part of any root λ_i gives the velocity of signal propagation along the corresponding path in the space/time plane. If the system of equations defined by Equation (7.2-12) is considered for a particular region defined by $0 \leq x \leq L$, the number of boundary conditions required at L equals the number of characteristic lines entering the solution region. At x = L, as long as any of the λ_i are less than zero, some

information is needed at the boundary to get a solution. If all λ_i are greater than or equal to zero, no boundary conditions are needed at L and the solution on $0 \leq x \leq L$ is not affected by conditions outside the boundary at L. This situation defines the choking criteria, i.e.,

$$\lambda_j = 0 \text{ for some } j \leq 4$$

$$\lambda_i \geq 0 \text{ for all } i \neq j \ . \tag{7.2-14}$$

Equation (7.2-13) corresponding to the system defined by Equation (7.2-12) and the A and B coefficient matrices is

$$\begin{aligned} &\rho C(\lambda - v_f)(\lambda - v_g) + \alpha_f\rho_g(\lambda - v_g)^2 + \alpha_g\rho_f(\lambda - v_f)^2 \\ &+ \left\{ \begin{array}{c} \dfrac{[\rho_g(\lambda - v_g) - \rho_f(\lambda - v_f)][\alpha_g\rho_g S_g^*(\lambda - v_g) + \alpha_f\rho_f S_f^*(\lambda - v_f)]}{S_g - S_f} \\ -(\alpha_f\rho_g\rho_f^* + \alpha_g\rho_f\rho_g^*)(\lambda - v_f)(\lambda - v_g) \end{array} \right\} \times \\ &\left[(\lambda - v_f)(\lambda - v_g) + \left(\frac{C\rho\alpha_f}{\rho_g}\right)(\lambda - v_f)^2 + \left(\frac{C\rho\alpha_g}{\rho_f}\right)(\lambda - v_g)^2\right] = 0 \ . \end{aligned} \tag{7.2-15}$$

Equation (7.2-15) is fourth-order in λ, and approximate factorization is possible. Details of the approximate factorization methodology are presented in **Reference 7.2-10**. The results for the first two roots are

$$\lambda_{1,2} = \frac{\left(\begin{array}{l} \left\{\alpha_f\rho_g + \dfrac{\rho C}{2} \pm \left[\left(\dfrac{\rho C}{2}\right)^2 - \alpha_g\alpha_f\rho_g\rho_f\right]^{1/2}\right\} v_g \\ + \left\{\alpha_g\rho_f + \dfrac{\rho C}{2} \mp \left[\left(\dfrac{\rho C}{2}\right)^2 - \alpha_g\alpha_f\rho_g\rho_f\right]^{1/2}\right\} v_f \end{array} \right)}{\left(\alpha_f\rho_g + \dfrac{\rho C}{2}\right) + \left(\alpha_g\rho_f + \dfrac{\rho C}{2}\right)} \ . \tag{7.2-16}$$

These two roots are obtained by neglecting the fourth-order factors relative to the second-order factors in $(\lambda - v_g)$ and $(\lambda - v_f)$. (There are no first- or third-order factors.) Inspection of Equation (7.2-16) shows that the $\lambda_{1,2}$ have values between v_g and v_f; thus, the fourth-order factors $(\lambda - v_g)$ and $(\lambda - v_f)$ are small (i.e., neglecting these terms is justified). The values for $\lambda_{1,2}$ may be real or complex depending on the sign of the quantity $\left[\left(\dfrac{\rho C}{2}\right)^2 - \alpha_g\alpha_f\rho_g\rho_f\right]$.

The remaining two roots are obtained by dividing out the quadratic factor containing $\lambda_{1,2}$, neglecting the remainder, and subsequent factorization of the remaining quadratic terms. [This procedure can be shown to be analogous to neglecting the second- and higher-order terms in the relative velocity, $(v_g - v_f)$.] The remaining roots are

$$\lambda_{3,4} = v + D\,(v_g - v_f) \pm a \tag{7.2-17}$$

where

$$v = \frac{\alpha_g\rho_g v_g + \alpha_f\rho_f v_f}{\rho}$$

$$a = a_{HE}\left[\frac{C\rho^2 + \rho(\alpha_g\rho_f + \alpha_f\rho_g)}{C\rho^2 + \rho_g\rho_f}\right]^{1/2} \tag{7.2-18}$$

and

$$D = \frac{1}{2}\left[\frac{(\alpha_g\rho_f - \alpha_f\rho_g)}{(\rho C + \alpha_f\rho_g + \alpha_g\rho_f)} + \frac{\rho_g\rho_f(\alpha_f\rho_f - \alpha_g\rho_g)}{\rho(\rho_g\rho_f + C\rho^2)} - a_{HE}^2\frac{\rho(\alpha_g\rho_g^2 S_g^* + \alpha_f\rho_f^2 S_f^*)}{\rho_g\rho_f(S_g - S_f)}\right] . \tag{7.2-19}$$

The quantity a_{HE} is the homogeneous equilibrium speed of sound (see Appendix 7A for development) and, for one component (vapor and liquid, no noncondensable), is defined as

$$a_{HE} = \frac{V\frac{dP^s}{dT}}{\left\{X\left[\frac{C_{pg}}{T_g} + V_g\frac{dP^s}{dT}\left(\kappa_g\frac{dP^s}{dT} - 2\beta_g\right)\right] + (1-X)\left[\frac{C_{pf}}{T_f} + V_f\frac{dP^s}{dT}\left(\kappa_f\frac{dP^s}{dT} - 2\beta_f\right)\right]\right\}^{1/2}} \tag{7.2-20}$$

where

$$\frac{dP^s}{dT} = \frac{h_g - h_f}{T^s(V_g - V_f)} \qquad \text{(Clausius-Clapeyron equation)} \tag{7.2-21}$$

V = specific volume

P^s = saturation pressure

X = mass quality of vapor

C_{pg} = saturated vapor specific heat

C_{pf} = saturated liquid specific heat

κ_g = isothermal compressibility for vapor

κ_f = isothermal compressibility for liquid

β_g = isobaric coefficient of thermal expansion for vapor

β_f = isobaric coefficient of thermal expansion for liquid.

This is also shown in Volume I. The homogeneous equilibrium speed of sound for two components is shown in Volume I, but it is not shown here.

Since the two roots $\lambda_{1,2}$ are between the phase velocities v_f and v_g, the choking criterion is established from the roots $\lambda_{3,4}$ and Equation (7.2-14). The choking criterion is

$$v + D(v_g - v_f) = \pm a \ . \tag{7.2-22}$$

The choking criterion can be rewritten in terms of the mass mean and relative Mach numbers

$$M = \frac{v}{a}, \qquad M_r = \frac{v_g - v_f}{a} \tag{7.2-23}$$

as

$$M_v + DM_r = \pm 1 \ . \tag{7.2-24}$$

This relation is very similar to the choking criterion for single-phase flow wherein only the mass average Mach number appears and choking also corresponds to a Mach number of unity.

Equation (7.2-24) forms the basis for the two-phase analytic choking criterion. In the actual implementation, the criterion is considerably simplified, and an approximation to Equation (7.2-24) is used. From Equation (7.2-24), it is clear that the choking criterion is a function of the D and a parameters. Trapp and Ransom[7.2-10] have investigated the impact of the virtual mass coefficient on the sound speed calculated using only Equation (7.2-18). Results of this calculation are shown in **Figure 7.2-3** (from Volume I) where values of C selected were 0 (stratified flow), 0.5 (dispersed flow), and ∞ (homogeneous

flow). As shown in the figure, the value of C has a significant effect on the sound speed. The effects of slip [through the D coefficient, Equation (7.2-19)] were also calculated. Equation (7.2-19) is plotted in **Figure 7.2-4** as a function of α_g, with the virtual mass coefficient as a third parameter. The results in **Figure 7.2-4** show that velocity nonequilibrium can have a substantial effect.

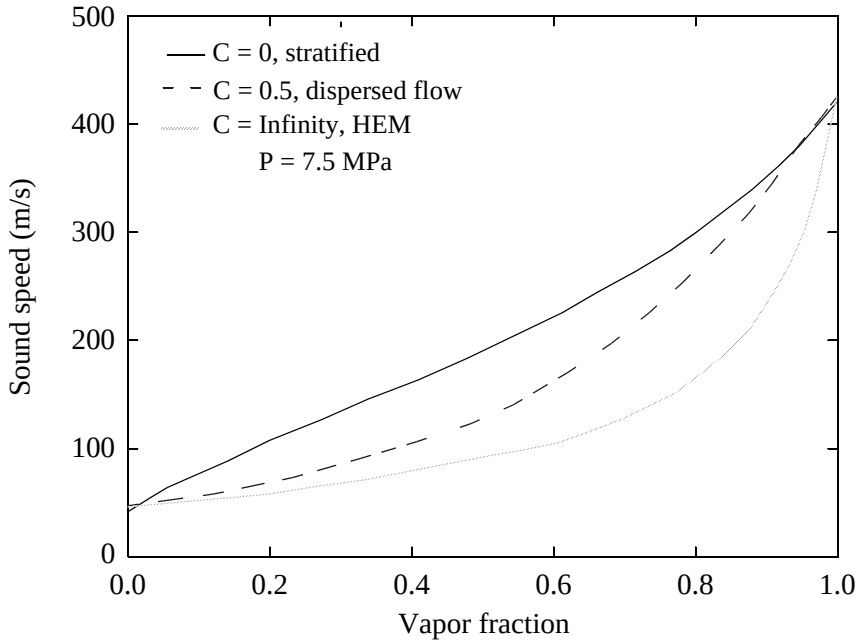

Figure 7.2-3 Equilibrium sound speed [from Equation (7.2-18)] as a function of virtual mass coefficient and void fraction.

As stated in **Reference 7.2-10**, the virtual mass coefficient is known for only a fairly narrow range. To preclude problems associated with the selection of C and the evaluation of the choking criteria, simplifications to the criterion are effected. This approximate criterion is

$$\frac{\alpha_g\rho_f v_g + \alpha_f\rho_g v_f}{\alpha_g\rho_f + \alpha_f\rho_g} = a_{HE} \quad . \tag{7.2-25}$$

Equation (7.2-25) can be obtained from Equation (7.2-22) as follows[7.1-11]. In Equation (7.2-18), the virtual mass coefficient C is taken to be infinity (the homogeneous equilibrium value). This results in an indeterminate form; and if L'Hopital's rule is used (twice), it can be shown that

$$a^2\big|_{C\to\infty} = \lim_{C\to\infty} a_{HE}^2\left[\frac{C\rho^2 + \rho(\alpha_g\rho_f + \alpha_f\rho_g)}{C\rho^2 + \rho_g\rho_f}\right] = a_{HE}^2 \quad . \tag{7.2-26}$$

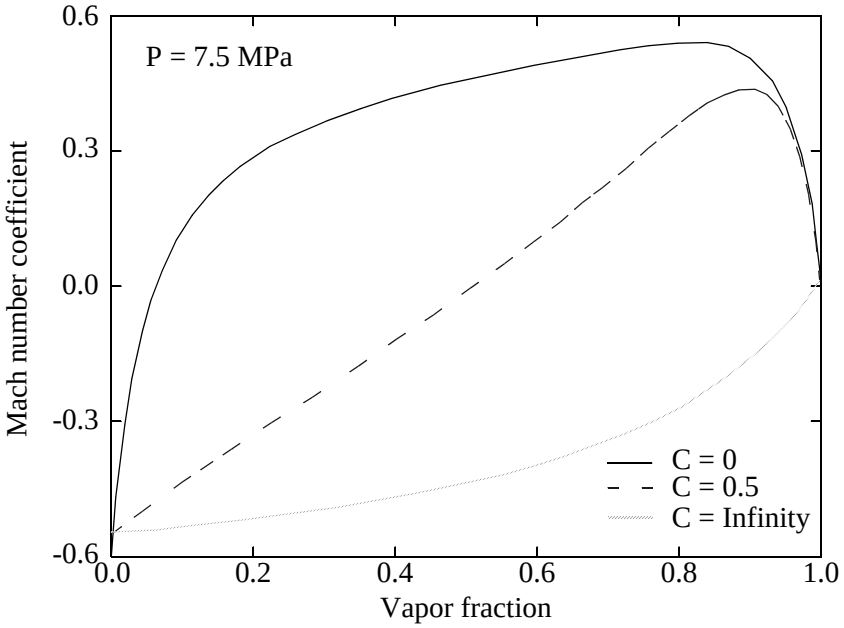

Figure 7.2-4 Relative Mach number coefficient [Equation (7.2-19)] as a function of virtual mass coefficient and void fraction.

In Equation (7.2-19), if the third term is neglected and the virtual mass coefficient C is taken as zero (stratified flow), the D coefficient becomes

$$D = \frac{1}{2}\left(\frac{\alpha_g\rho_f - \alpha_f\rho_g}{\alpha_f\rho_g + \alpha_g\rho_f} + \frac{\alpha_f\rho_f - \alpha_g\rho_g}{\rho}\right) \quad . \tag{7.2-27}$$

Substitution of Equations (7.2-26) and (7.2-27) into Equation (7.2-22) yields the expression given in Equation (7.2-25). Although there appears to be little justification for the assumptions regarding C in this derivation, the approximate criterion has been widely used and produces satisfactory results when compared to data.[7.2-1,7.2-12,7.2-13] Additional comparisons to data will be discussed in Section 7.2.7. Note that in the limit as α_g approaches unity, the choking criteria becomes

$$v_g = a_{HE}, \tag{7.2-28}$$

and the choking criterion applies for the vapor/gas phase alone. Furthermore, the expression given in Equation (7.2-25) retains some effects of velocity nonequilibrium. Bryce has noted,[1] however, that for a

1. Personal communication, W. M. Bryce to G. W. Johnsen, March 1988.

large section of the span of possible values of void fraction and virtual mass coefficients, the dependence of the mass flows implied by the two equations on the slip ratio is of opposite sign.

7.2.2 Implementation of Choking Criterion in ATHENA

In order to understand the implementation of the choking criterion described in the previous section, it is informative to briefly discuss the overall logic flow for the hydrodynamic advancement in the ATHENA code. This discussion will help describe the origin of various parameters (frictional parameters, state properties, etc.) that are used in the application of the choked flow criterion. Then the details of the numerical implementation of the choking criterion into the hydrodynamic scheme are described. Included, where appropriate, is a discussion of the calculation of state properties, including the homogeneous sound speed a_{HE} formulations utilized.

7.2.2.1 Hydrodynamic Advancement. The hydrodynamic advancement in ATHENA is controlled by subroutine HYDRO. Subroutine HYDRO is the driver that calls other subroutines to effect the calculations necessary to compute wall drag, interface heat transfer and drag, flow regimes, intermediate time velocities at cell edges, choking criterion discussed in Section 7.2.1, new-time pressure, phasic energies, vapor/gas void fraction, new-time state properties, and so forth. **Table 7.2-1** depicts this progression for the semi-implicit scheme, the subroutines called by subroutine HYDRO, and a brief verbal description of what each subroutine does. Volume I describes in detail the overall hydrodynamic numerical implementation. The purpose here is only to indicate how subroutine JCHOKE, the subroutine that does the choking computations, fits into the scheme.

Table 7.2-1 Hydrodynamic advancement for semi-implicit scheme.

Subroutine name	Purpose/description
HYDRO[1]	Time advancement for hydrodynamics.
VOLVEL	Calculates magnitude of phasic volume average velocities for use in wall friction subroutine FWDRAG.
VALVE	Computes valve characteristics.
PHANTV, PHANTJ	Computes interface drag, interface heat transfer, and some parameters for subroutine VEXPLT.
FWDRAG	Calculation of wall drag.
HLOSS	Calculates head loss, throat, void fraction, and downstream void fraction for abrupt area change model.
VEXPLT	Computes explicit liquid and vapor/gas velocities for junctions.
JCHOKE	Determines if a junction is choked. If choked, applies choking criterion.

Table 7.2-1 Hydrodynamic advancement for semi-implicit scheme. (Continued)

Subroutine name	Purpose/description
JPROP (1)	Recomputes junction properties if the junction velocity has changed sign.
VFINL	Calls subroutine PRESEQ to set up matrix elements and source vector for pressure equation by eliminating liquid and vapor/gas specific internal energy, vapor/gas void fraction, and noncondensable quality. Calls subroutine SYSSOL (sparse matrix solver) to solve for new-time pressure difference. Computes new-time junction velocities.
EQFINL	Computes new-time pressures and does back substitution to get new-time liquid and vapor/gas specific internal energies, vapor/gas void fraction, noncondensable quality, and boron density. Also computes vapor generation rate and mixture density.
STATE	Controls evaluation of equation of state and calls subroutine STATEP to determine thermodynamic properties and property derivatives for all components.
JPROP (0)	Computes junction phasic specific internal energies, liquid and vapor/gas volume fraction, and phasic densities.
VLVELA	Calculates phasic volume average velocities.

1. Subroutine HYDRO calls the subroutines below it in the order listed.

As shown in **Table 7.2-1**, the subroutine JCHOKE contains the coding for the implementation of the choking criterion. This implementation numerically imposes the choking criterion on the junctions determined to be in a choked state. Subroutine JCHOKE is self-contained and does not call any other routines except fluid property routines needed to establish thermodynamic conditions. Numerous parameters are passed into subroutine JCHOKE through common statements and data blocks for components and junctions.

7.2.2.2 Implementation of Choking Criterion. While the details of the coding for subroutine JCHOKE will be discussed in Section 7.2.4, it is instructive to illustrate the ultimate use of the two-phase choking criterion in the scheme of **Table 7.2-1**. Upon entry to subroutine JCHOKE, the criterion given in Equation (7.2-25) is checked using explicit velocities calculated in subroutine VEXPLT. If choking is predicted, Equation (7.2-25) is then written in terms of new-time phasic velocities and solved in conjunction with a difference momentum equation derived from the liquid and vapor/gas momentum equations. The difference momentum equation is derived by dividing the vapor/gas and liquid phasic momentum equations by $\alpha_g A$ and $\alpha_f A$ respectively, subtracting the resulting equations, utilizing the definitions of the interface velocity and drag (see Volume I) and keeping only the time derivative portion

of the relative acceleration terms. This subtraction results in elimination of pressure from the difference momentum differential equation to yield

$$\rho_g\left(\frac{\partial v_g}{\partial t}+\frac{1}{2}\frac{\partial v_g^2}{\partial x}\right)-\rho_f\left(\frac{\partial v_f}{\partial t}+\frac{1}{2}\frac{\partial v_f^2}{\partial x}\right) = (\rho_g-\rho_f)B_x - FWG\rho_g v_g + FWF\rho_f v_f + \Gamma_g\frac{(v_I-\alpha_f v_g-\alpha_g v_f)}{\alpha_g\alpha_f} - FI\rho_g\rho_f(v_g-v_f) - C\rho\frac{\partial(v_g-v_f)}{\partial t} \quad (7.2\text{-}29)$$

where

B_x = body force

FWG = wall drag on vapor/gas

FWF = wall drag on liquid

Γ_g = vapor generation rate per unit volume

FI = interface drag term

ρ = mixture density.

Equation (7.2-29) is then integrated from the upstream volume center to the junction to yield the following finite-difference equation:

$$
\begin{aligned}
&((\rho^n_{g,K} + \mathrm{VIRMAS})\frac{\Delta x_K}{2} + \left\{\rho^n_{g,K}\left[\mathrm{FRICGJ} + \frac{\mathrm{JCAT}^n}{(\mathrm{ATHROT}\bullet C_D)^2}\left(1 + \frac{\mathrm{JCAT}^{n+1}}{\mathrm{JCAT}^n}\right)\frac{1}{2}v^n_{g,j}\right]\right. \\
&\qquad \left. + \mathrm{FI}^n_j - \Gamma^n_{g,j}\right\}\Delta t)v^{n+1}_{g,j} + \left(-(\rho^n_{f,K} + \mathrm{VIRMAS})\frac{\Delta x_K}{2}\right. \\
&\qquad -\left\{\rho^n_{f,K}\left[\mathrm{FRICFJ} + \frac{\mathrm{JCAT}^n}{(\mathrm{ATHROT}\bullet C_D)^2}\left(1 + \frac{\mathrm{JCAT}^{n+1}}{\mathrm{JCAT}^n}\right)\frac{1}{2}v^n_{f,j}\right]\right. \\
&\qquad \left. + \mathrm{FI}^n_j - \Gamma^n_{g,j}\right\}\Delta t)v^{n+1}_{f,j} = (\rho^n_{g,K} + \mathrm{VIRMAS})\frac{\Delta x_K}{2}v^n_{g,j} \qquad (7.2\text{-}30) \\
&\qquad -(\rho_{f,K} + \mathrm{VIRMAS})\frac{\Delta x_K}{2}v^n_{f,j} - \left((\rho^n_{g,K} - \rho^n_{f,K})g\,\frac{\Delta z_K}{2}\right. \\
&\qquad + \rho^n_{g,K}\left\{-\frac{1}{2}\left[\frac{\mathrm{JCAT}^n}{(\mathrm{ATHROT}\bullet C_D)^2}(v^n_{g,j})^2 + (v^n_{g,K})^2\right]\right\} \\
&\qquad \left. -\rho^n_{f,K}\left\{-\frac{1}{2}\left[\frac{\mathrm{JCAT}^n}{(\mathrm{ATHROT}\bullet C_D)^2}(v^n_{f,j})^2 + (v^n_{f,K})^2\right]\right\}\right)\Delta t\ .
\end{aligned}
$$

The HLOSSGj and HLOSSFj terms (code-calculated abrupt area change loss terms and user-specified loss terms) are not present in this finite-difference equation, because these losses are primarily important downstream of the junction.

The finite difference form of Equation (7.2-25), written in terms of new-time phasic velocities and new-time sound speed, is

$$
\begin{aligned}
&(\dot\alpha^n_{g,j}\dot\rho^n_{f,j})v^{n+1}_{g,j} + (\dot\alpha^n_{f,j}\dot\rho^n_{g,j})v^{n+1}_{f,j} = (\dot\alpha^n_{g,j}\dot\rho^n_{f,j} + \dot\alpha^n_{f,j}\dot\rho^n_{g,j}) \\
&\bullet\ \left[a^n_{\mathrm{throat}}\left(\frac{\mathrm{ATHROT}\bullet C_D}{\mathrm{JCAT}^{n+1}}\right) + \frac{\partial\left(a^n_{\mathrm{throat}}\dfrac{\mathrm{ATHROT}\bullet C_D}{\mathrm{JCAT}^{n+1}}\right)}{\partial P}(P^{n+1}_K - P^n_K)\right]\ . \qquad (7.2\text{-}31)
\end{aligned}
$$

In these equations, the subscript K refers to the volume upstream of the junction determined to be choked, subscript j denotes the junction under consideration, subscript throat denotes throat values at the junction, the dot overscore implies a donored property, n+1 denotes new time, and n denotes old time. The Δx denotes the upwind volume length and Δz is the upwind volume elevation change. The velocity terms with subscript K are volume averaged velocities discussed in Volume I. VIRMAS is the virtual mass coefficient times the mixture average density at the junction, and FRICFJ is a wall friction parameter defined for the liquid as

$$\frac{\frac{\Delta x_K}{2}\phi^2 \rho_f \frac{\alpha_{f,w}}{\alpha_f}\frac{f}{D}\left|v^n_{f,j}\right|}{\alpha^n_{f,j}\rho^n_{f,j}} \tag{7.2-32}$$

and is similarly defined for the vapor/gas. In this equation, ϕ^2 is a two-phase friction multiplier, the subscript w indicates the phasic volume fraction at the wall, f is a Darcy friction factor, and D is the volume hydraulic diameter. The variable C_D is a user-specified discharge coefficient, and the parameters JCAT and ATHROT are density and area ratios that stem from continuity considerations at the choke plane and the manner in which the choke plane area is defined in ATHENA. With reference to **Figure 7.2-5** for the single-phase case, continuity requires

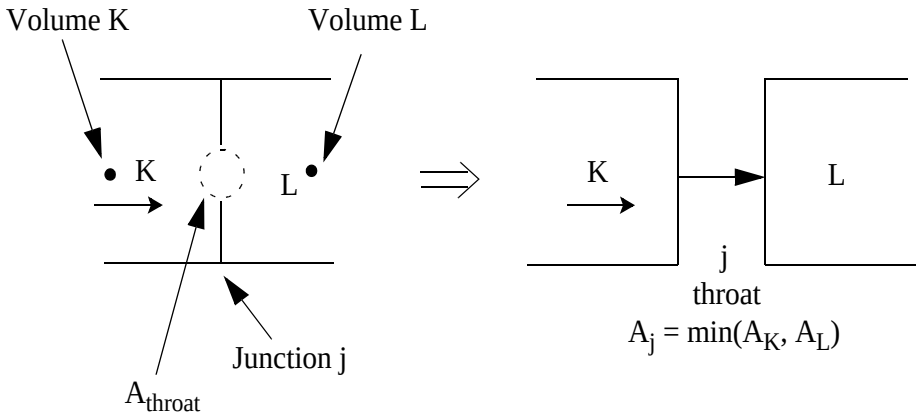

Figure 7.2-5 Control volume and junction relationship for subroutine JCHOKE.

$$\rho_{throat} v_{throat} A_{throat} = \dot{\rho}_j v_j A_j \quad . \tag{7.2-33}$$

Recalling that $\dot{\rho}_j$ is equal to ρ_K and solving for v_{throat} yields

$$v_{throat} = \frac{\rho_K}{\rho_{throat}}\frac{A_j}{A_{throat}} v_j = \frac{JCAT}{ATHROT} v_j \quad . \tag{7.2-34}$$

Bryce[1] points out that the continuity argument used to obtain Equation (7.2-34) ignores slip and any modifications of the standard junction properties donoring when the upstream volume is horizontal and stratified.

The single phase momentum equation can be simplified to obtain

1. Personal communication, W. M. Bryce to G. W. Johnsen, March 7, 1988.

$$
\begin{aligned}
P_{throat} &= P_K - \frac{1}{2}\rho_{throat} v_{throat}^2 + \frac{1}{2}\rho_K v_K^2 \\
&= P_K - \frac{1}{2}\rho_K \left(\frac{\rho_{throat}}{\rho_K} v_{throat}^2 - v_K^2 \right) \\
&= P_K - \frac{1}{2}\rho_K \left[\frac{\rho_{throat}}{\rho_K} \left(\frac{JCAT}{ATHROT} \right)^2 v_j^2 - v_K^2 \right] \\
&= P_K - \frac{1}{2}\rho_K \left[\frac{JCAT}{(ATHROT)^2} v_j^2 - v_K^2 \right]
\end{aligned}
\qquad (7.2\text{-}35)
$$

The density ratio is defined as JCAT, and the area ratio is ATHROT. Specifically, for the two-phase Equations (7.2-30) and (7.2-31),

$$
JCAT^n = \frac{\dot{\alpha}_{f,j}^n \dot{\rho}_{f,j}^n + \dot{\alpha}_{g,j}^n \dot{\rho}_{g,j}^n}{\rho_{throat}^n} \quad . \qquad (7.2\text{-}36)
$$

Note that the term in brackets on the right-hand side of Equation (7.2-31) represents the new-time throat sound speed approximated as a Taylor expansion in pressure. This approximation is made to increase the degree of the implicitness and numerical stability and to cast the solution in a form consistent for use in subroutine VFINL. With respect to Equation (7.2-30), it is written with the momentum flux terms in a form recommended by Bryce[7.2-14] to increase stability. Bryce suggested that the junction momentum flux terms should be kept as implicit as possible. Ultimately, one would desire that the flux term be written completely in new-time velocity. Since this is not possible in the present scheme, an approximation is used. Consider the new-time velocity squared written as

$$
\frac{1}{2} v_j^{n+1} v_j^{n+1} = \frac{1}{2}(v_j^{n+1} - v_j^n + v_j^n)(v_j^{n+1} - v_j^n + v_j^n) = \frac{1}{2}[(v_j^{n+1} - v_j^n) + v_j^n]^2 \quad . \qquad (7.2\text{-}37)
$$

Expanding the right-hand side gives

$$
RHS = \frac{1}{2}[(v_j^{n+1} - v_j^n)^2 + 2v_j^n(v_j^{n+1} - v_j^n) + (v_j^n)^2] \quad . \qquad (7.2\text{-}38)
$$

Neglecting the first term in Equation (7.2-38), then

$$
\frac{1}{2} v_j^{n+1} v_j^{n+1} \approx v_j^n(v_j^{n+1} - v_j^n) + \frac{1}{2}(v_j^n)^2 = v_j^n v_j^{n+1} - (v_j^n)^2 + \frac{1}{2}(v_j^n)^2 \quad . \qquad (7.2\text{-}39)
$$

This approximation is used for the junction momentum flux after integration of Equation (7.2-29) to produce the finite difference form shown in Equation (7.2-30).

Equations (7.2-30) and (7.2-31) form a 2 x 2 set of equations that can be put into the form

$$v_{f,j}^{n+1} = \tilde{v}_{f,j}^{n} + \frac{\partial \tilde{v}_{f,j}^{n}}{\partial P}(P_K^{n+1} - P_K^{n}) \qquad \text{and} \qquad v_{g,j}^{n+1} = \tilde{v}_{g,j}^{n} + \frac{\partial \tilde{v}_{g,j}^{n}}{\partial P}(P_K^{n+1} - P_K^{n}) \quad . \tag{7.2-40}$$

The JCHOKE subroutine computes the quantities

$$\tilde{v}_{f,j}^{n}, \tilde{v}_{g,j}^{n}, \frac{\partial \tilde{v}_{f,j}^{n}}{\partial P} \text{ and } \frac{\partial \tilde{v}_{g,j}^{n}}{\partial P} \quad .$$

In Equation (7.2-31), the throat sound speed and the throat sound speed derivative with respect to pressure are needed. While the upwind volume thermodynamic properties are provided to subroutine JCHOKE, values for the junction are calculated in subroutine JCHOKE. These parameters are dependent on the thermodynamic state present and will be discussed next.

7.2.2.3 Calculation of Junction Properties. Since the calculation of pressure, void fraction, specific internal energy, and density is made at volume centers and thermodynamic properties are needed at the cell edges (junctions), an approximation is made for the throat pressure and the throat specific internal energy. Upon entry to subroutine JCHOKE, Bernoulli's equation [Equation (7.2-1)] incorporating momentum flux and frictional effects is used to do a half-cell extrapolation to provide an estimate of the throat pressure. With reference to **Figure 7.2-5**, the Bernoulli balance from the center of volume K to the throat gives the throat pressure, which is given by

$$\begin{aligned} P_{throat}^{n} = P_K^{n} &- (\dot{\alpha}_{f,j}^{n}\dot{\rho}_{f,j}^{n} + \dot{\alpha}_{g,j}^{n}\dot{\rho}_{g,j}^{n})g\frac{\Delta z_K}{2} - \dot{\alpha}_{f,j}^{n}\dot{\rho}_{f,j}^{n}\frac{1}{2}\left[\frac{JCAT^{n}}{(ATHROT \bullet C_D)^2}(v_{f,j}^{n})^2 - (v_{f,K}^{n})^2\right] \\ &- \dot{\alpha}_{g,j}^{n}\dot{\rho}_{g,j}^{n}\frac{1}{2}\left[\frac{JCAT^{n}}{(ATHROT \bullet C_D)^2}(v_{g,j}^{n})^2 - (v_{g,K}^{n})^2\right] \\ &+ \frac{1}{2}\Delta P_{pump} - \dot{\alpha}_{f,j}^{n}\dot{\rho}_{f,j}^{n}FRICFJ \bullet v_{f,j}^{n} - \dot{\alpha}_{g,j}^{n}\dot{\rho}_{g,j}^{n}FRICGJ \bullet v_{g,j}^{n} \quad . \end{aligned} \tag{7.2-41}$$

The throat specific internal energy is computed from an energy balance approximation, which is given by

$$U^n_{throat} = \dot{U}^n_j + \frac{P^n_K - P^n_{throat} \bullet JCAT^n}{\left\{\frac{\dot{\rho}^n_{g,j}\dot{\rho}^n_{f,j}}{[\dot{X}^n_{s,j}\dot{\rho}^n_{f,j} + (1-\dot{X}^n_{s,j})\dot{\rho}^n_{g,j}]}\right\}} - g\frac{\Delta z_K}{2}$$

$$-\dot{X}^n_{s,j}\frac{1}{2}\left[\frac{JCAT^n}{(ATHROT \bullet C_D)^2}(v^n_{g,j})^2 - (v^n_{g,K})^2\right] \quad . \tag{7.2-42}$$

$$-(1-\dot{X}^n_{s,j})\frac{1}{2}\left[\frac{JCAT^n}{(ATHROT \bullet C_D)^2}(v^n_{f,j})^2 - (v^n_{f,K})^2\right] \quad .$$

The junction static quality is defined using the junction donor properties and is given by

$$\dot{X}^n_{s,j} = \frac{\dot{\alpha}^n_{g,j}\dot{\rho}^n_{g,j}}{\dot{\alpha}^n_{g,j}\dot{\rho}^n_{g,j} + \dot{\alpha}^n_{f,j}\dot{\rho}^n_{f,j}} \quad . \tag{7.2-43}$$

As discussed previously, to utilize Equation (7.2-31), the throat sound speed and the throat sound speed derivative with respect to pressure are needed. These quantities are calculated in subroutine JCHOKE. The method of calculating these parameters depends on whether the flow is subcooled liquid, the flow is two-phase, or the flow is pure vapor/gas.

In the subcooled region, the velocity is first calculated using Equation (7.2-4), Then the local homogeneous equilibrium sound speed based on saturation properties at the local temperature is calculated using standard relationships as

$$a_{HE} = \left(\frac{\partial P}{\partial \rho}\bigg|_S\right)^{1/2} = V_f\frac{dP}{dT}\left[\frac{T_{f,K}}{C_{pf} - T_{f,K}V_f\frac{dP}{dT}\left(2\beta_f - \kappa_f\frac{dP}{dT}\right)}\right]^{1/2} \tag{7.2-44}$$

where V, C_p, β (the isobaric thermal expansion), and κ (the isothermal compressibility) are evaluated using saturated liquid properties at $T_{f,K}$, the upwind volume liquid temperature. The term $\frac{dP}{dT}$ is evaluated using the Clapeyron equation

$$\frac{dP}{dT} = \frac{h_g - h_f}{T_{f,K}(V_g - V_f)} \tag{7.2-45}$$

where h_g (the vapor specific enthalpy), h_f (the liquid specific enthalpy), V_g (the vapor specific volume), and V_f (the liquid specific volume) are saturation values at temperature $T_{f,K}$. The choking velocity (v_c) is the larger of the velocities calculated from Equations (7.2-4) and (7.2-44). If the solution to Equation (7.2-4) produces a throat velocity (hereafter referred to as SONIC) larger than the value given by Equation (7.2-44) and the throat pressure is predicted to be less than the local saturation pressure [i.e., if Equation (7.2-2) yields a value of $\Delta P = P_{sat} - P_t > 0$], the sound speed derivative is calculated by differentiating Equation (7.2-4), which gives

$$\frac{\partial(v_c)}{\partial P} = \left[\rho_{f,K} v_c - \frac{\partial(\Delta P)}{\partial v_c}\right]^{-1} \quad . \tag{7.2-46}$$

Note that if the throat pressure is predicted to be saturation pressure, the second term in Equation (7.2-46) is zero and the derivative is given as the first term. The larger of the velocities calculated from Equations (7.2-4) and (7.2-44) is used for v_c in Equation (7.2-46).

If the junction vapor/gas void fraction indicates that two-phase conditions (i.e., $\dot{\alpha}_{g,j} > 1.0 \times 10^{-5}$) are present at the throat, Equations (7.2-20) and (7.2-21) are used to calculate the homogeneous equilibrium sound speed and $\frac{dP}{dT}$ using the thernodynamic property table routines with throat pressure and throat specific internal energy estimates from Equations (7.2-41) and (7.2-42) to provide junction thermodynamic properties. The variables T_f and T_g in this case are the saturation temperature and V is the specific volume, as calculated from the equilibrium quality and saturated vapor/gas and saturated liquid specific volumes. If the junction fluid conditions are determined to be liquid, an additional call to the thermodynamic property tables is made with saturation temperature (based on junction pressure and junction specific internal energy) and equilibrium quality set to zero. Equations (7.2-20) and (7.2-21) are then used to compute the homogeneous equilibrium sound speed using saturation conditions for the phasic V, κ, β, C_p, and h. The two-phase sound speed derivative is equilibrium quality weighted and has the form

$$\frac{(1 - X_{E,K})}{a_{j,SC}\rho_{f,K}} + \frac{X_{E,K}}{a_{HE,K}\rho_K}\frac{k-1}{2} \quad . \tag{7.2-47}$$

The first term is the liquid part. The second term is the vapor/gas part and is discussed in the derivation of Equation (7.2-51). If the contribution from the liquid is neglected in Equation (7.2-47) and the change in the sound speed is due to the compressibility of the vapor/gas, the derivative reduces to the same form as for single-phase vapor/gas

$$\left.\frac{\partial a}{\partial P}\right|_S = \frac{k-1}{2}\left(\frac{1}{a_{HE,K}\rho_K}\right) \quad . \tag{7.2-48}$$

If pure vapor/gas conditions exist at the throat, the choking velocity is set to the homogeneous frozen sound speed (see Appendix 7A for development) calculated as

$$a_{HF} = V\left[\frac{\frac{dP}{dT}}{V\left(\kappa \bullet \frac{dP}{dT} - \beta\right)}\right]^{1/2} \tag{7.2-49}$$

where

$$\frac{dP}{dT} = \frac{C_p}{T_{g,K} V \beta} \quad . \tag{7.2-50}$$

The sound speed derivative is computed by assuming that the vapor behaves as a perfect gas, i.e.,

$$\left.\frac{\partial a}{\partial P}\right|_S = \frac{k}{2a}\left.\frac{\partial (PV)}{\partial P}\right|_S = \frac{k-1}{2}\frac{1}{\rho_K a_{HF,K}} \tag{7.2-51}$$

where k is the specific heat ratio $\frac{C_p}{C_v}$.

Once the throat sound speed (a_{throat}) and throat sound speed derivative $\left(\frac{\partial a_{throat}}{\partial P}\right)$ have been computed, these values are multiplied by the $\frac{ATHROT}{JCAT}$ ratio per Equation (7.2-34).

Any user-input discharge coefficient C_D is also multiplied times the ATHROT parameter, so that the final junction sound speed expression becomes [see Equation (7.2-31)]

$$a_j = a_{throat}\frac{C_D \bullet ATHROT}{JCAT} \quad . \tag{7.2-52}$$

The ATHROT parameter in the sound speed derivative is likewise multiplied by the user input discharge coefficient C_D [see Equation (7.2-31)].

7.2.3 Constants Employed in the ATHENA Choked Flow Model

The only correlation used in the critical flow model other than the homogeneous sound speed expressions developed in Appendix 7A is the so-called pressure undershoot correlation described in

Section 7.2.1.1. The correlation used in the choking model is that described by Jones,[7.2-6,7.2-7] an extension to the original model proposed by Alamgir and Lienhard.[7.2-5]

The pressure undershoot model is used to determine the inception of net vaporization in flashing flows. According to Jones,[7.2-7] the flashing inception can be expressed by two additive effects, one due to static decompression described by Alamgir and Lienhard[7.2-5] and one due to turbulent fluctuations in the flowing liquid. As given by Jones, the static depressurization is

$$\Delta P_{static} = \Delta P^{o}_{stat}(1 + 13.25\Sigma'^{0.8})^{1/2} \tag{7.2-53}$$

where Σ' is a depressurization rate and

$$\Delta P^{o}_{stat} = 0.258\frac{\sigma^{3/2}T_R^{13.76}}{\sqrt{k_B T_c}\left(1 - \frac{V_f}{V_g}\right)} \tag{7.2-54}$$

and the terms are described in Section 7.2.1.1. Note that Σ' in this equation has units of Matm/s. Jones extended Equation (7.2-53) by including a turbulence term which, when written with the constant turbulent fluctuation intensity of 0.069984 he recommended, is

$$\Delta P_{turb} = 0.069984\left(\frac{A_t}{A}\right)^2 v_c^2 \quad . \tag{7.2-55}$$

For steady flow in a nozzle, the total expansion rate Σ' can be written as

$$\Sigma' = \rho\frac{v_c^3}{A_t}\frac{dA_t}{dx} \tag{7.2-56}$$

where the area is evaluated at the throat and the area derivative is also evaluated at the throat. When Equation (7.2-55) is subtracted from Equation (7.2-53), the result is Equation (7.2-2), which is the Alamgir-Lienhard-Jones model. Although none of the original constants have been altered, conversion to proper units has been effected so that, as coded, the model is

$$\Delta P_{FI} = \Delta P_{FIOC}\sqrt{1 + \Delta P_{rcon} \bullet v_c^{2.4}} - K_2 v_c^2 \tag{7.2-57}$$

where

$$\Delta P_{FIOC} = \frac{0.258}{\sqrt{k_B T_c}}\left(\frac{T_K}{T_c}\right)^{13.76}(\sigma_k)^{1.5}\frac{V_g}{V_g - V_f} = (2.72958 \times 10^{9})(T_K \bullet 1.5448787 \times 10^{-3})^{13.76} \bullet (\sigma_K)^{1.5}\frac{V_g}{V_g - V_f} \quad (7.2\text{-}58)$$

$$\Delta P_{rcon} = \left[\rho_{f,K}\frac{1}{A_t}\left(\frac{dA}{dx}\right)_t\right]^{0.8} 13.25 K_1 = \left[\rho_{f,K}\frac{1}{A_t}\left(\frac{dA}{dx}\right)_t\right]^{0.8} 2.078\times10^{-8} \quad (7.2\text{-}59)$$

$$K_2 = \rho_{f,K}\left(\frac{A_j}{A_K}\right)^2 6.9984\times10^{-2} \quad . \quad (7.2\text{-}60)$$

K_1 is a factor for converting Pa/s to Matm/s raised to the 0.8 power, and the term $\frac{1}{A_t}\left(\frac{dA}{dx}\right)_t$ is discussed in Section 7.2.6.

7.2.4 Model as Coded

The choking criterion described in the previous sections is a complex process. To aid in the understanding of the model and the implementation, a flow chart for subroutine JCHOKE is provided in **Figure 7.2-6**. A brief verbal description of the logic flow in the subroutine will help relate the implementation to the previous discussion, and this will help identify areas where weighting and averaging are used and where special cases exist.

Upon entry to subroutine JCHOKE in the hydrodynamic advancement, a loop over all junctions begins. A logical variable (TRANSR) is set to false for later use in testing whether or not the current conditions indicate transition between choked flow regimes. A user-set flag is then tested to determine if the user desires to apply the choking model at the junction in question. If the choking model is not to be applied, the calculation proceeds to the next junction. Likewise, a flag is tested to see if the junction is connected to an active accumulator and, if it is, the processing proceeds to the next junction. A flag is tested to determine if the junction was choked on the last time step and if the vapor/gas velocity is in the same direction as the last time step. If so, a logical variable (CHOKE) is set to true. Next, the junction vapor/gas and liquid velocities are tested for countercurrent flow and to see if the junction is connected to a time-dependent volume. If countercurrent flow exists or the junction "from volume" is a time-dependent volume, processing for the junction is terminated, since choking is not permitted for those circumstances. If cocurrent flow exists and the from volume is not a user-specified time-dependent volume, the logic proceeds to determine the upstream and downstream volumes based on the direction of the liquid velocity. Based on the flow direction, geometric properties such as cell half-length and junction-to-volume area ratios are set for the upwind (donor) volume. The denominator of Equation (7.2-25) is then calculated. Processing is terminated if the value of $\dot{\alpha}_{g,j}\dot{\rho}_{f,j} + \dot{\alpha}_{f,j}\dot{\rho}_{g,j}$ is less than 10^{-10}. Otherwise, Equation (7.2-25) is computed for the junction and set to the variable v_c, e.g.,

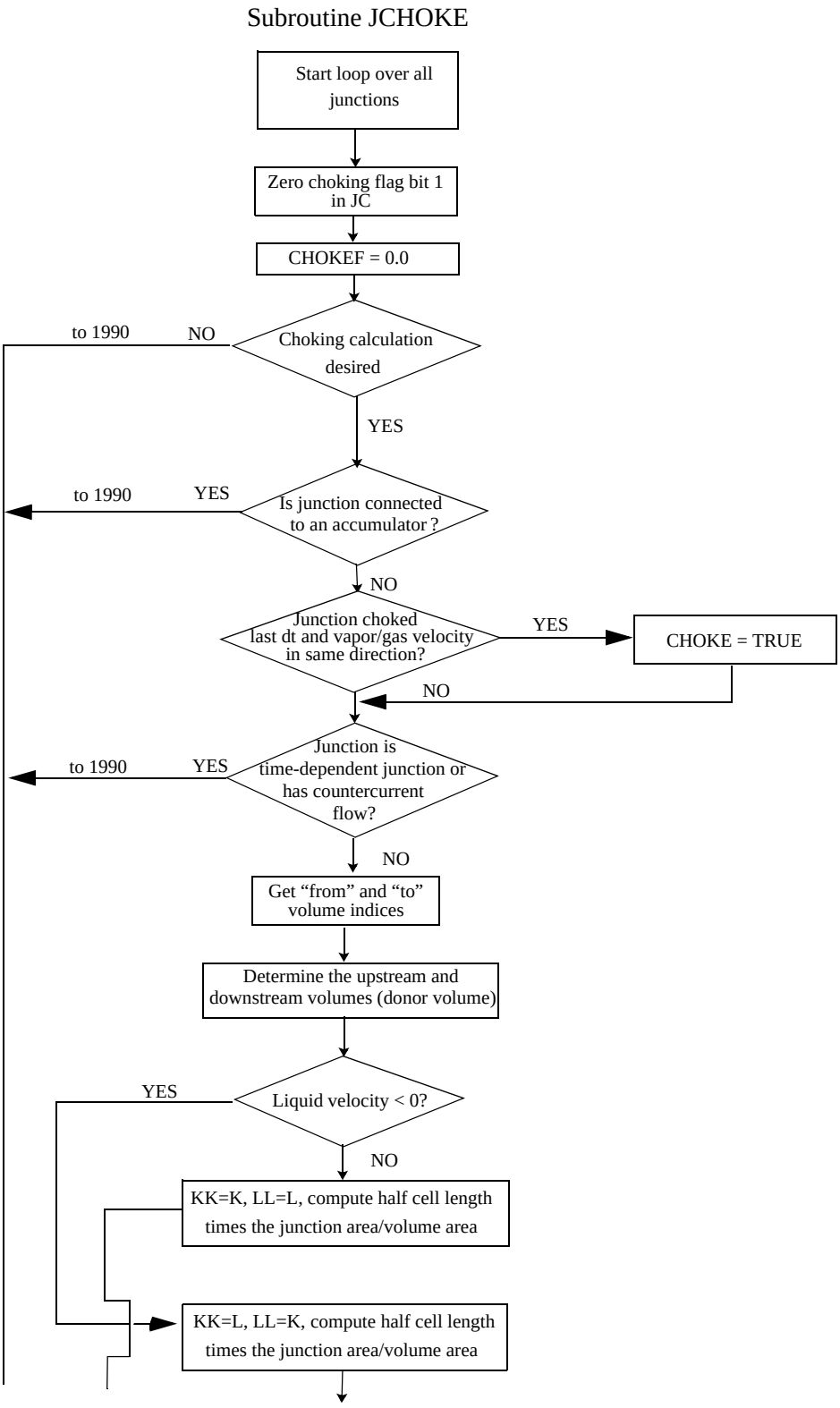

Figure 7.2-6 Subroutine JCHOKE flow logic.

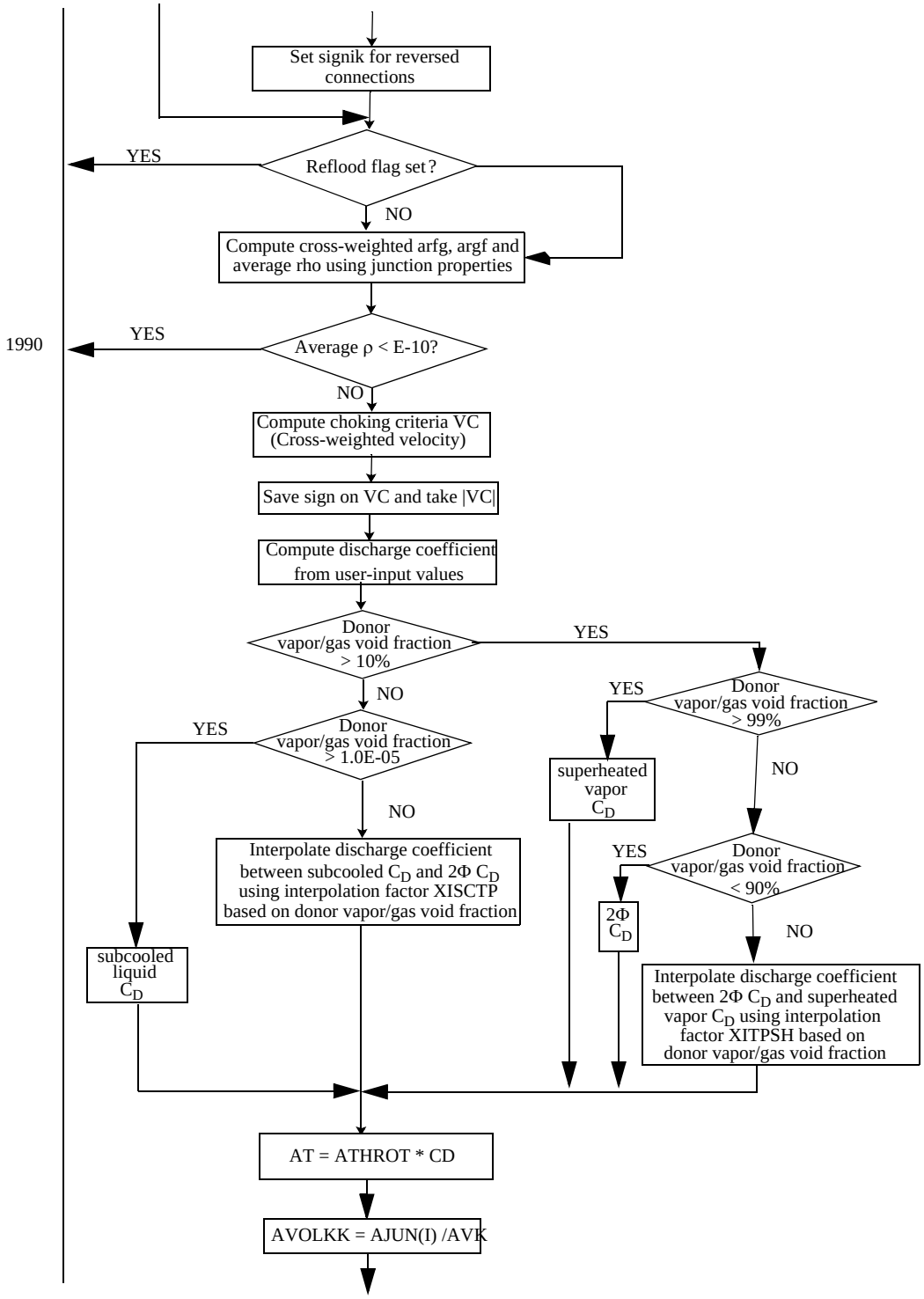

Figure 7.2-6 Subroutine JCHOKE flow logic. (Continued)

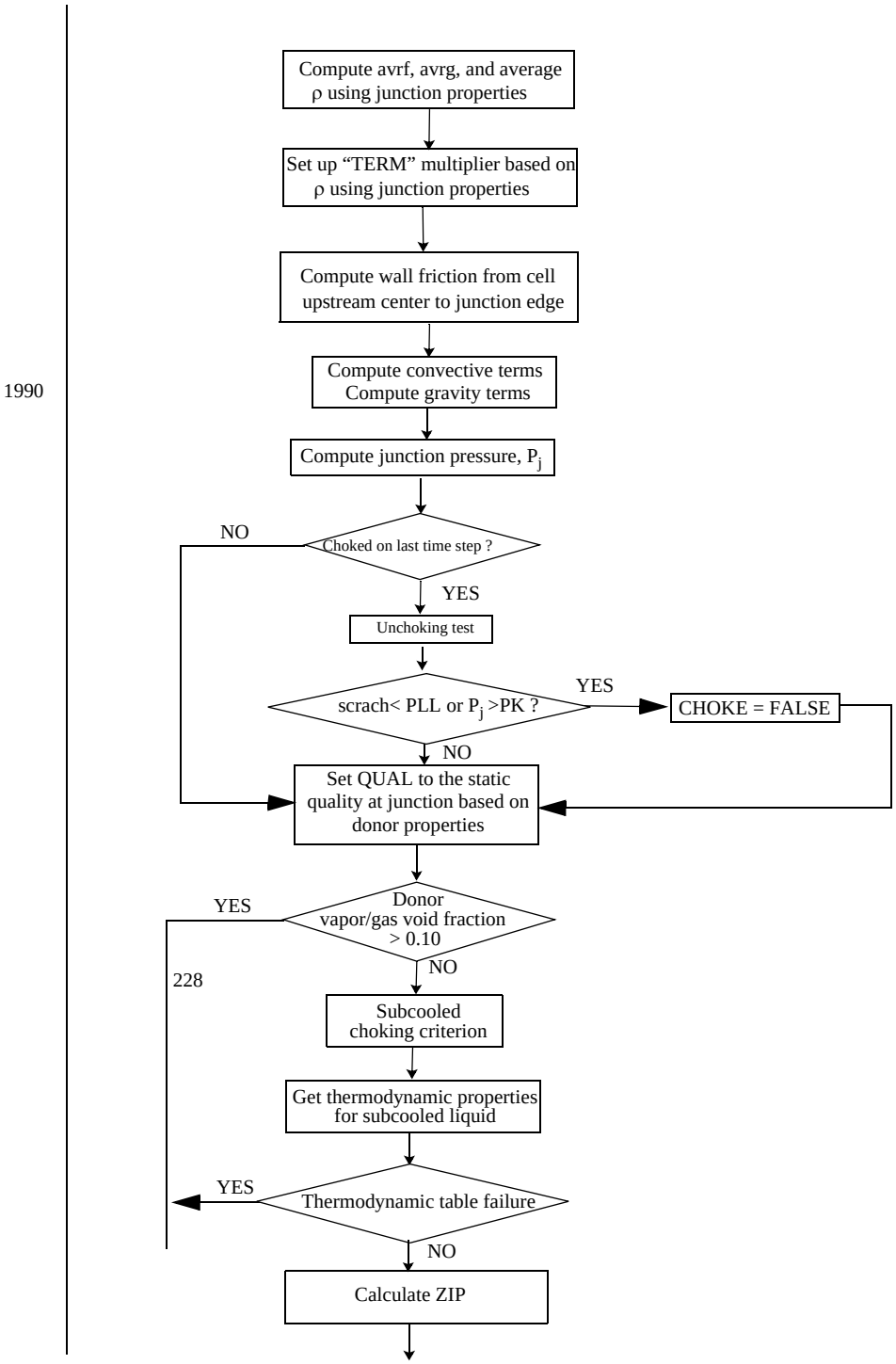

Figure 7.2-6 Subroutine JCHOKE flow logic. (Continued)

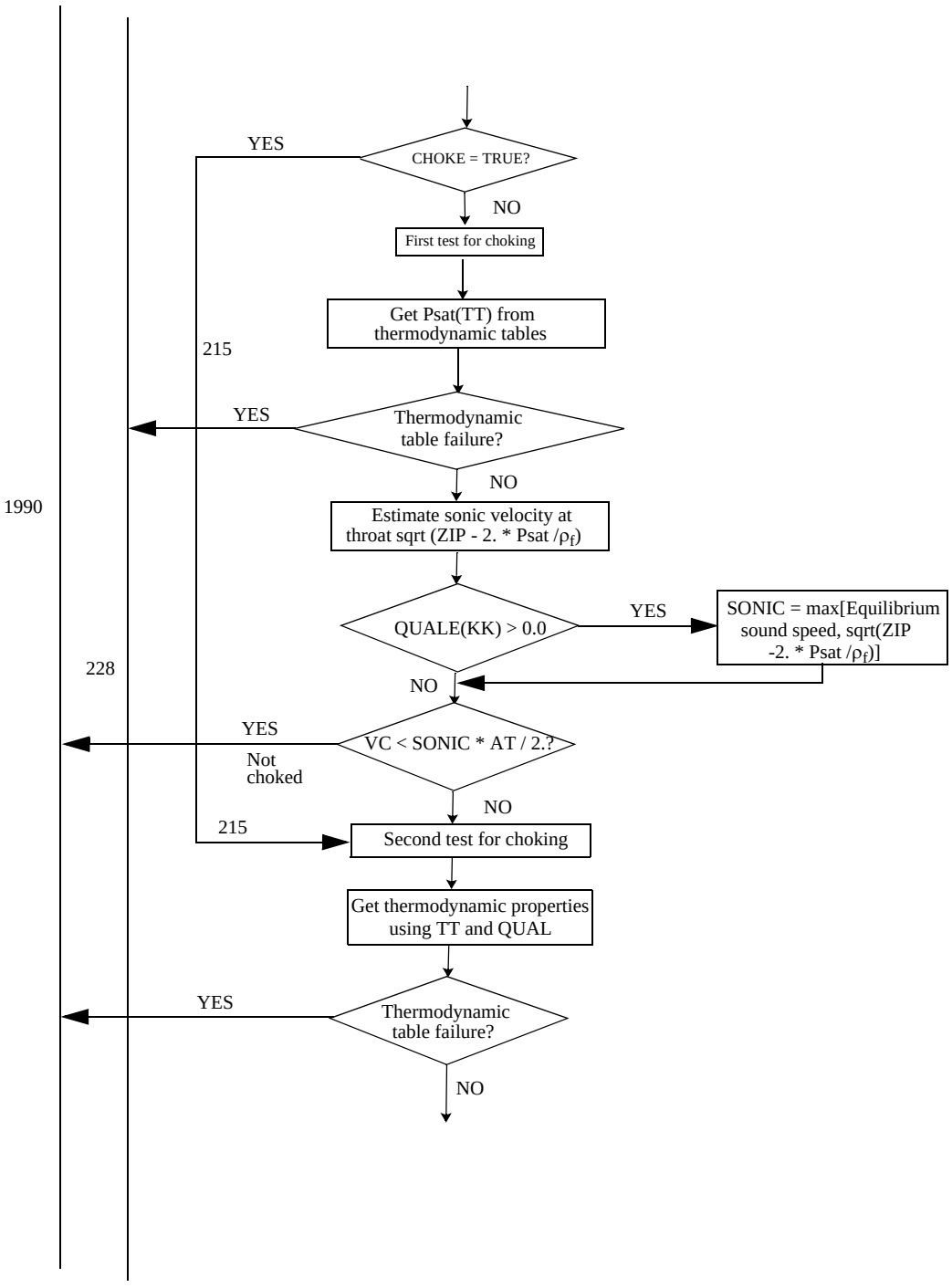

Figure 7.2-6 Subroutine JCHOKE flow logic. (Continued)

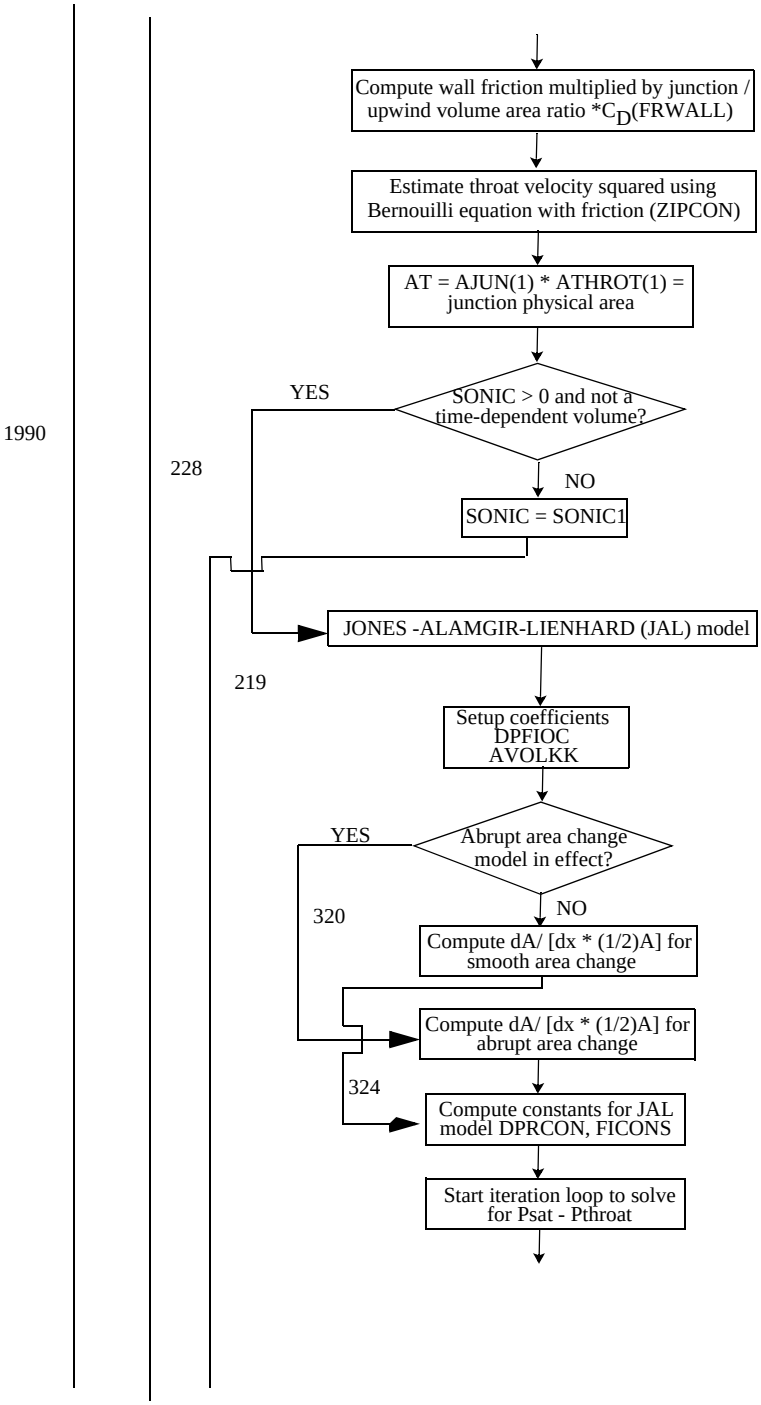

Figure 7.2-6 Subroutine JCHOKE flow logic. (Continued)

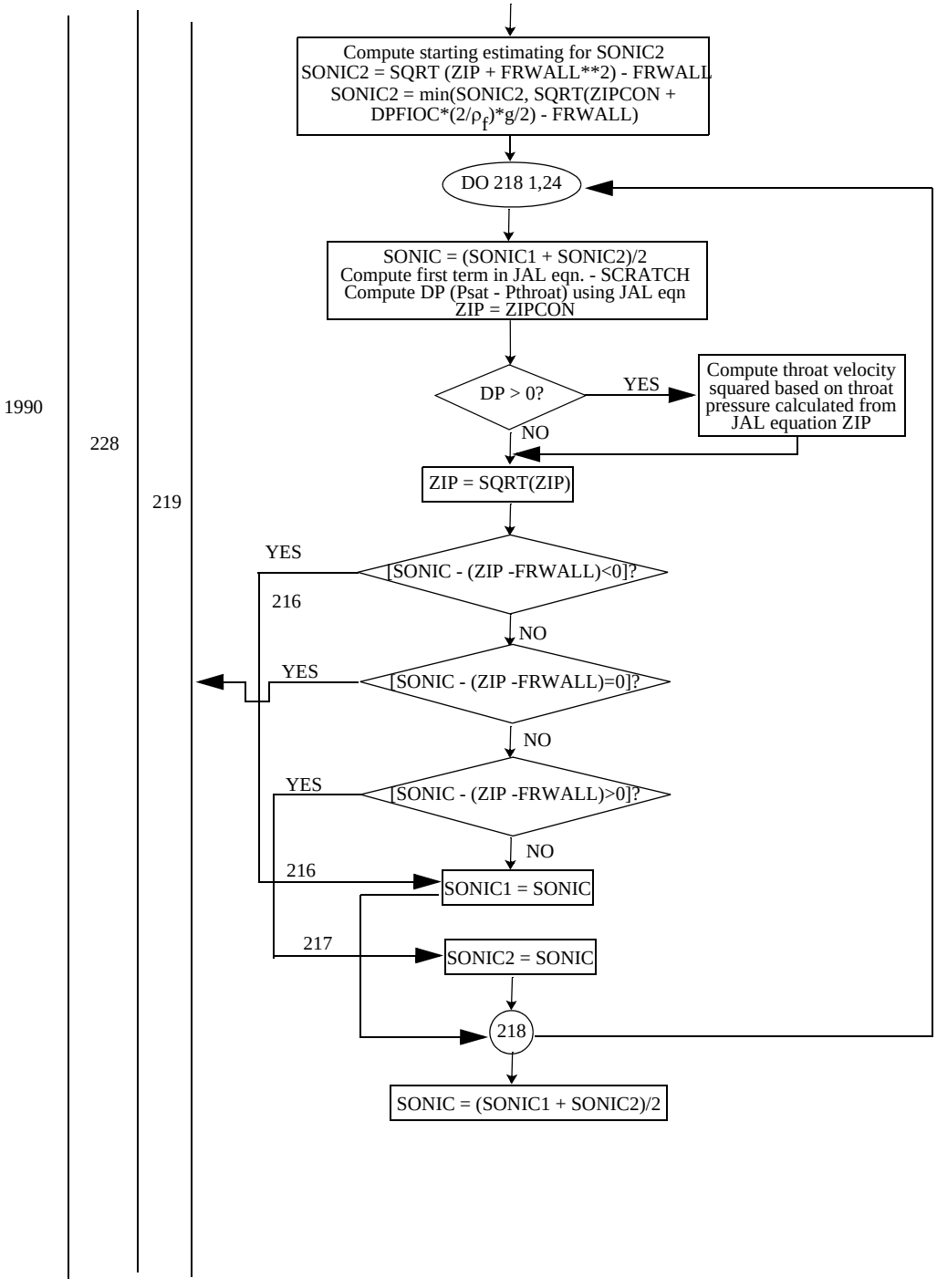

Figure 7.2-6 Subroutine JCHOKE flow logic. (Continued)

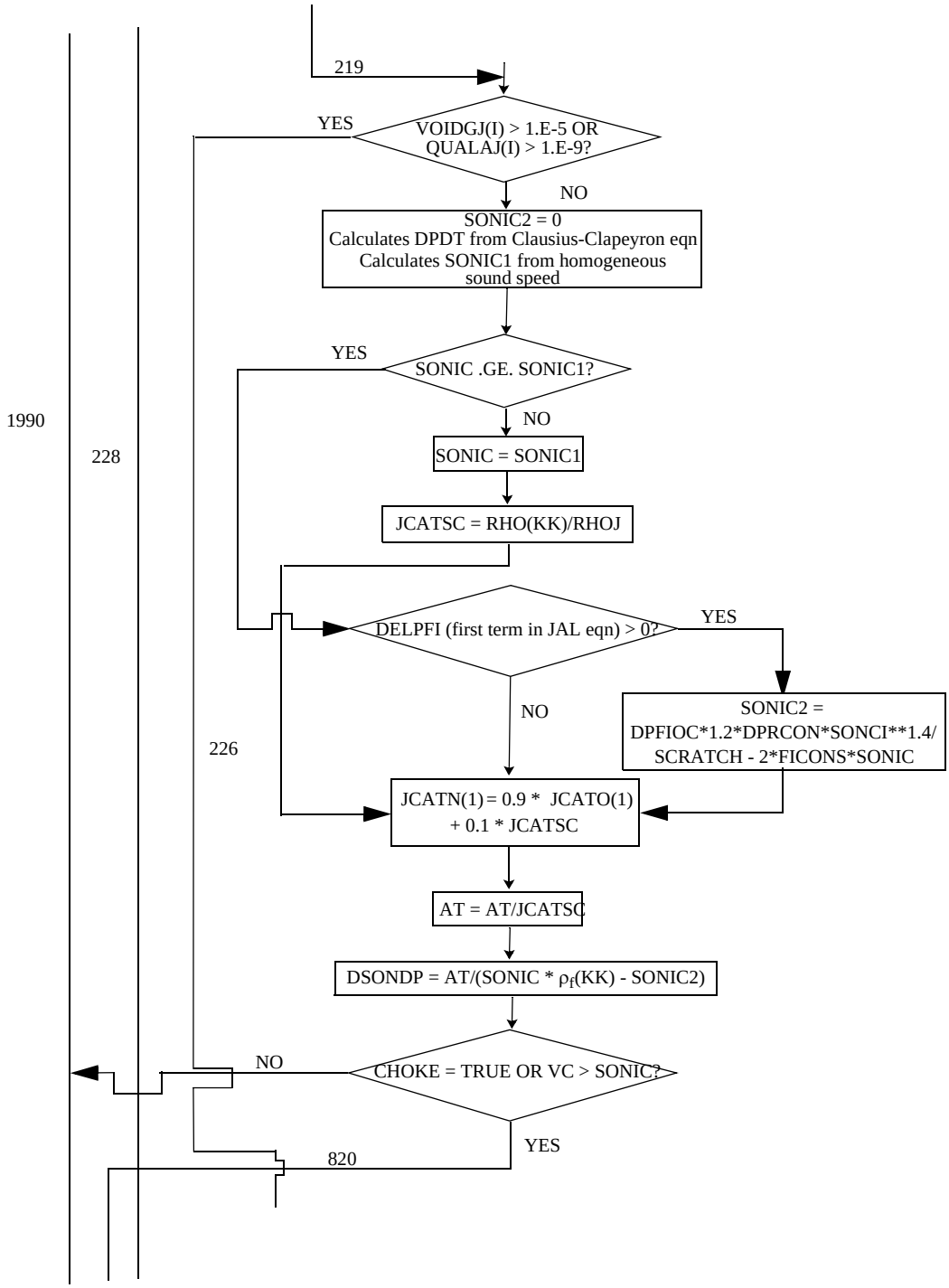

Figure 7.2-6 Subroutine JCHOKE flow logic. (Continued)

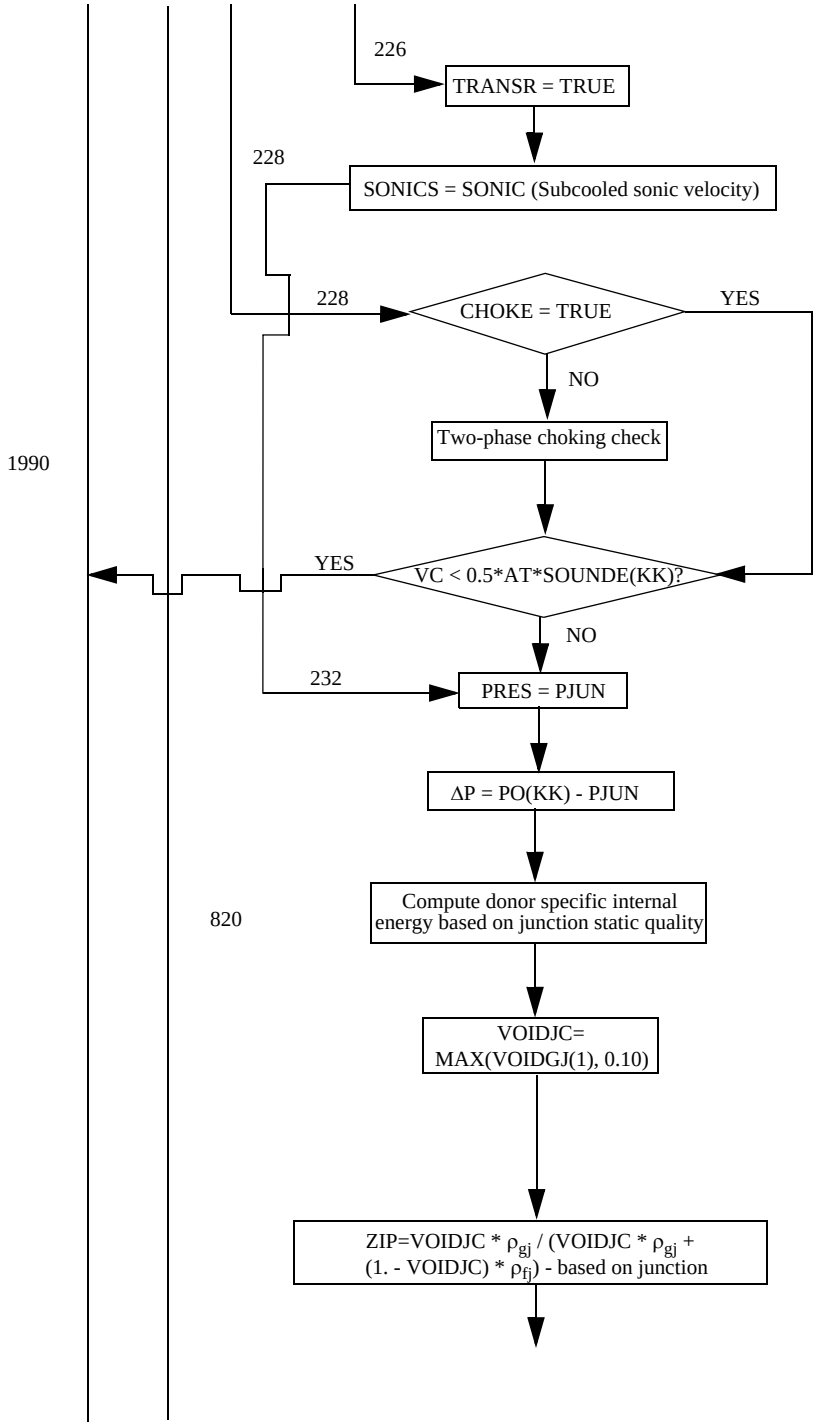

Figure 7.2-6 Subroutine JCHOKE flow logic. (Continued)

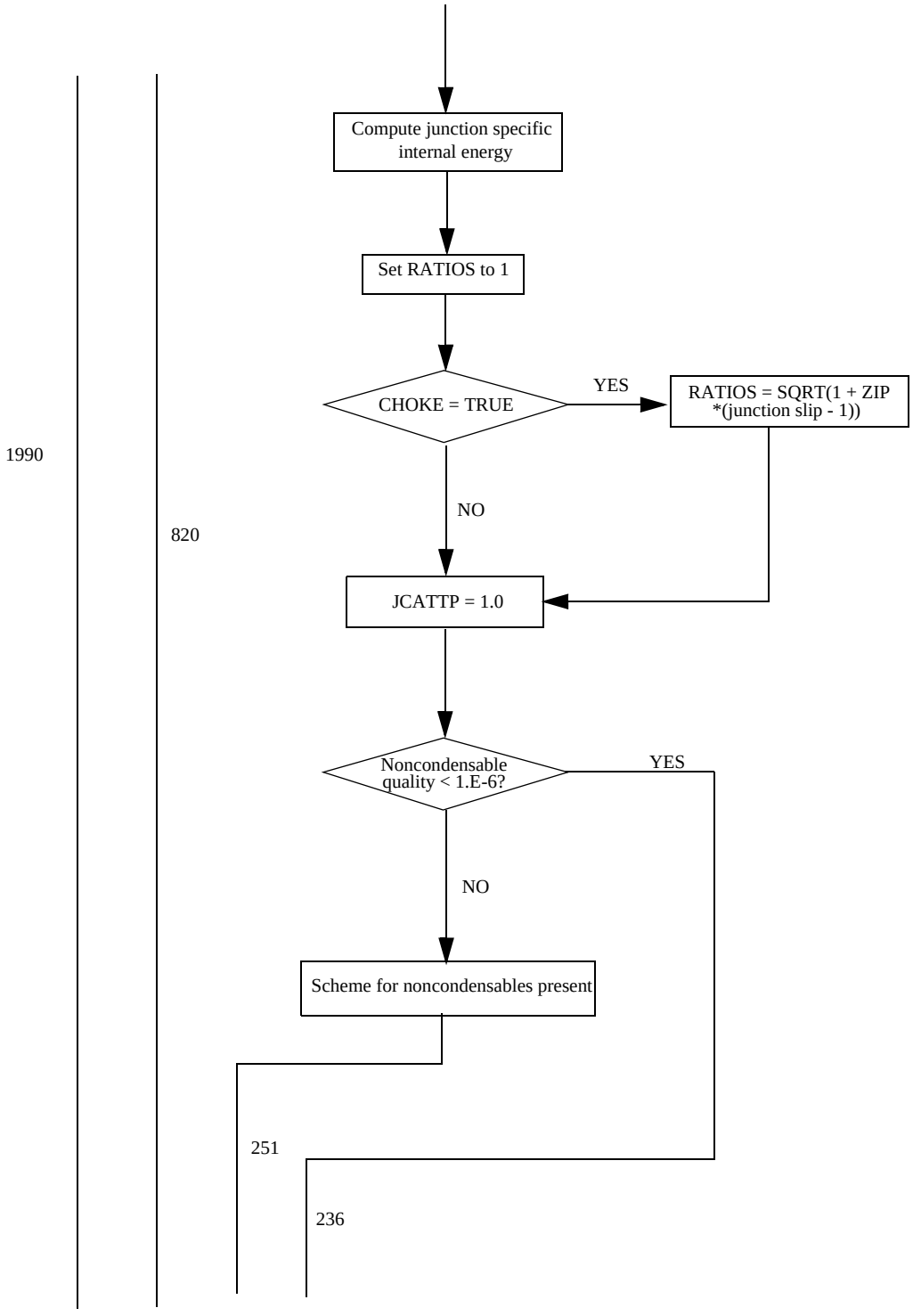

Figure 7.2-6 Subroutine JCHOKE flow logic. (Continued)

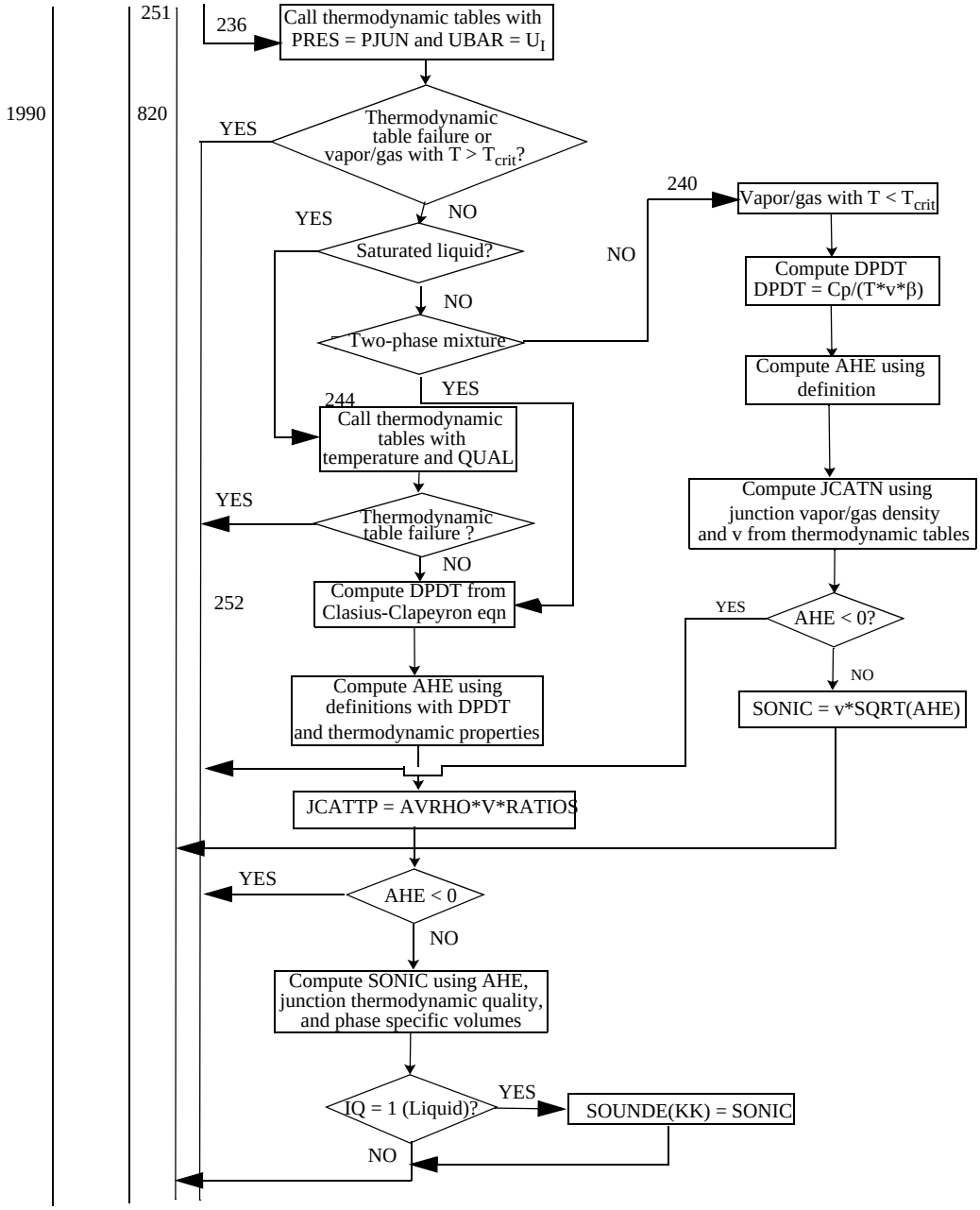

Figure 7.2-6 Subroutine JCHOKE flow logic. (Continued)

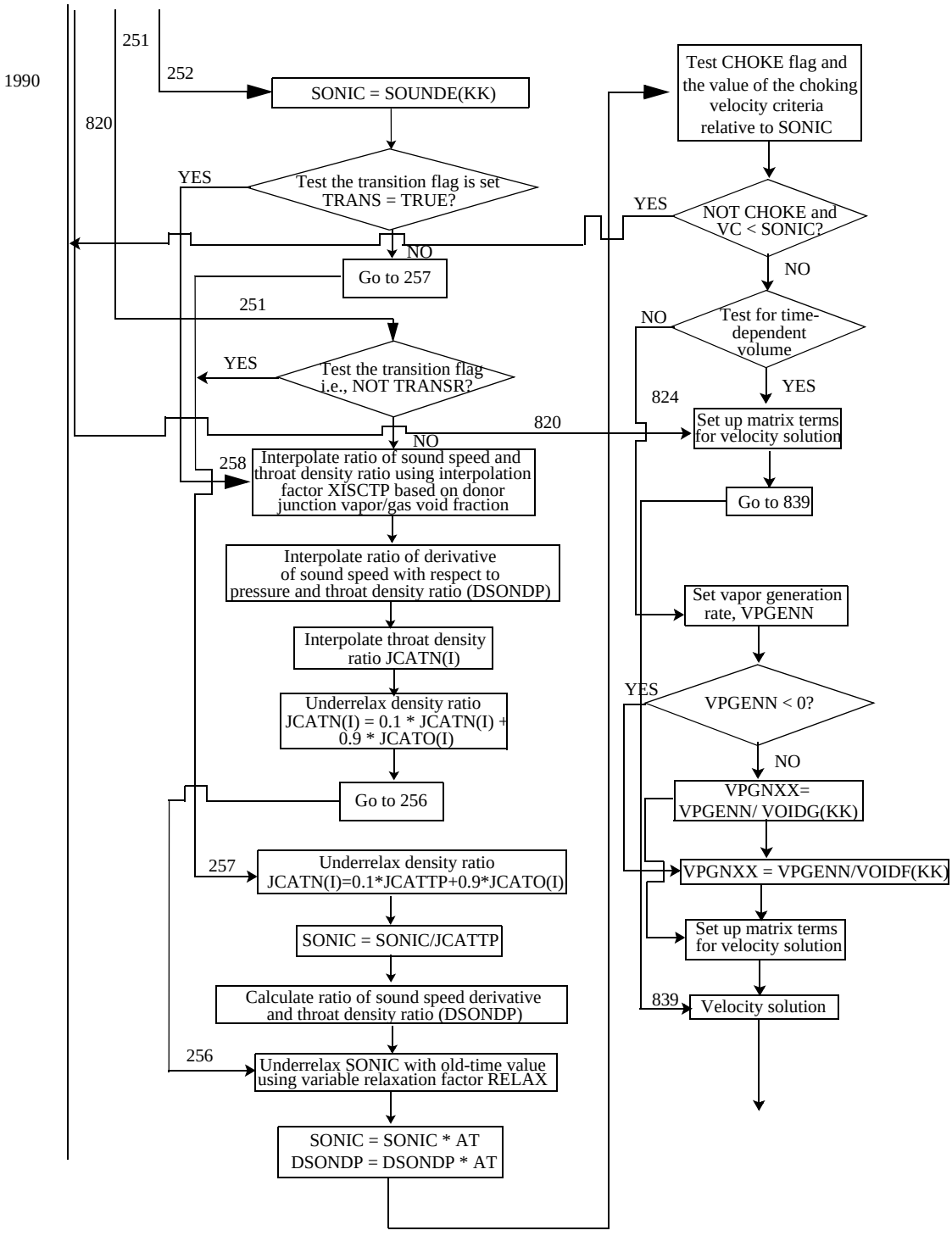

Figure 7.2-6 Subroutine JCHOKE flow logic. (Continued)

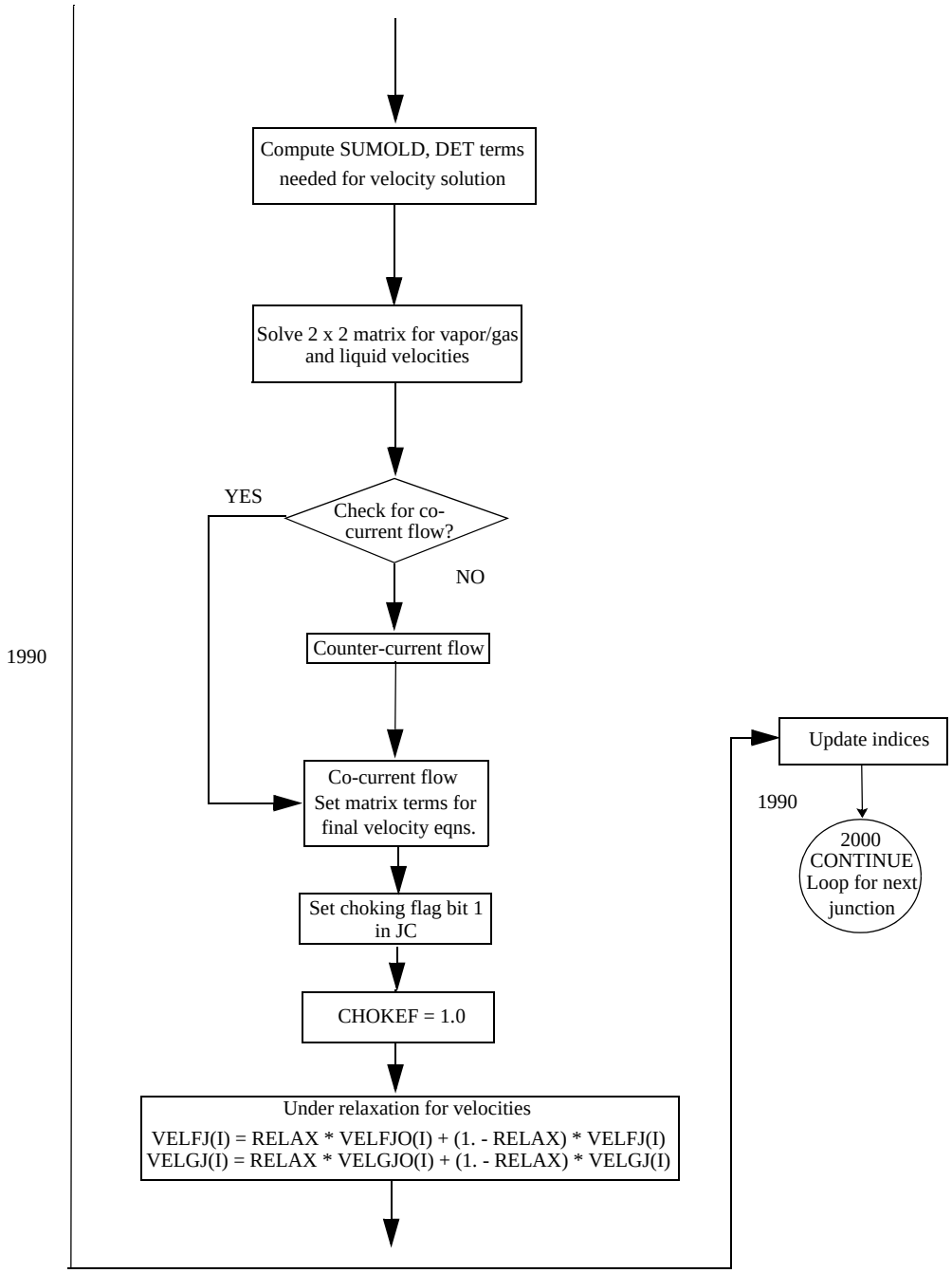

Figure 7.2-6 Subroutine JCHOKE flow logic. (Continued)

$$v_c = \frac{(\dot{\alpha}_g \dot{\rho}_f v_g)_j + (\dot{\alpha}_f \dot{\rho}_g v_f)_j}{(\dot{\alpha}_g \dot{\rho}_f)_j + (\dot{\alpha}_f \dot{\rho}_g)_j} \quad . \tag{7.2-61}$$

The discharge coefficient for the junction is computed from the user-input values based on the donor vapor/gas void fraction. Three transition regions are inserted between the three throat states, the first between the subcooled liquid and two-phase region ($1.0 \times 10^{-5} < \dot{\alpha}_{g,j} \leq 0.10$), the second is the first part of the two-phase region ($0.10 < \dot{\alpha}_{g,j} \leq 0.15$), and the third between the two-phase and single-phase vapor/gas region ($0.90 < \dot{\alpha}_{g,j} \leq 0.99$) (See **Figure 7.2-7**). The junction physical area-to-volume flow area ratio

.

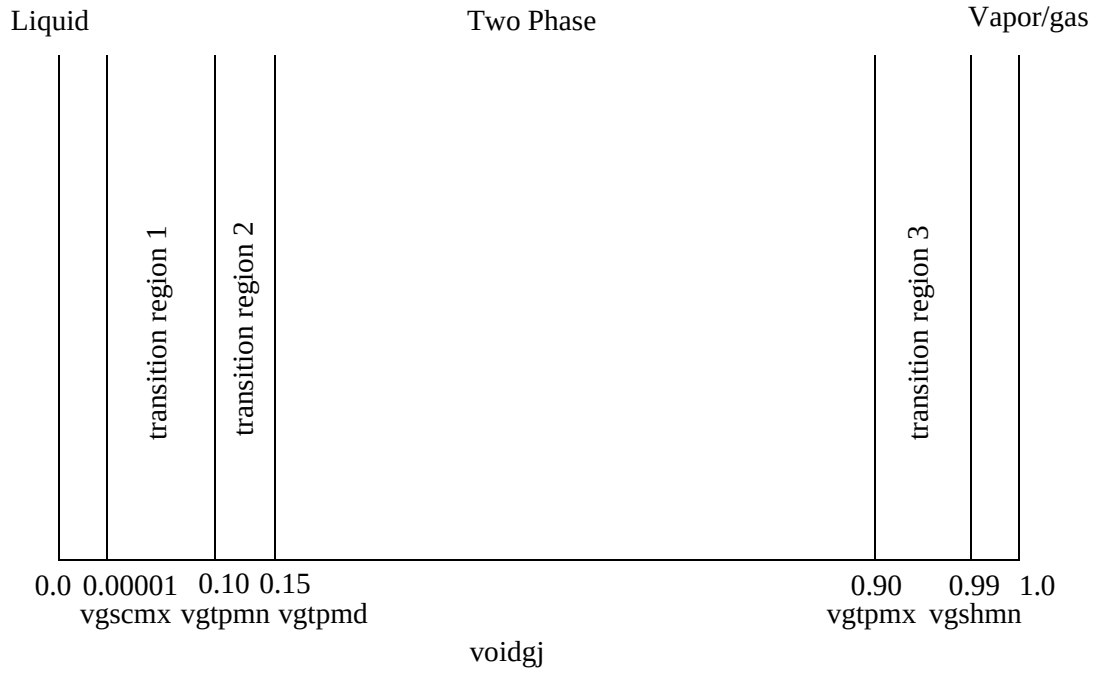

Figure 7.2-7 Choking model transition regions.

(ATHROT) is then multiplied by the discharge coefficient.

The junction average density $[(\dot{\alpha}_g \dot{\rho}_g)_j + (\dot{\alpha}_f \dot{\rho}_f)_j]$ and frictional, convective, and gravitational terms are then calculated for use in estimating the junction pressure via Equation (7.2-41). If the user turned off the momentum flux term in the “from” volume, a multiplier is set to zero out this term in this half cell extrapolation. If the junction was choked on the last time step, the newly calculated junction pressure is used in an unchoking test that checks to see if the junction pressure is greater than the upwind pressure or less than the downwind pressure. If the test is true, the logical variable CHOKE is set to false. If the junction was not choked on the last time step, the unchoking test is bypassed.

The junction vapor/gas void fraction $(\dot{\alpha}_{g,j})$ is then tested to determine whether the subcooled choking or two-phase choking criterion is to be applied. If $\dot{\alpha}_{g,j}$ is greater than 0.10, the flow is considered two-phase and the logic proceeds directly to the two-phase model.

7.2.4.1 Subcooled Criterion. On entry to the subcooled choking criterion logic in subroutine JCHOKE, an estimate of the throat velocity squared is made using the simplified momentum balance shown on **Figure 7.2-5** and assuming the throat pressure is saturation pressure based on the liquid temperature in the upwind volume. A throat velocity (SONIC) is then set to be the square root of the maximum of zero (to prevent errors associated with taking the square root of a negative number) or the value calculated. If the equilibrium quality in the upstream volume is greater than zero, the calculated value SONIC is also checked relative to the homogeneous equilibrium sound speed calculated for the upstream volume and the maximum of the two values is taken. The result is multiplied by ATHROT•C_D and compared relative to v_c, the value computed from Equation (7.2-61). If the value of v_c is less than 1/2 the calculated throat velocity times the discharge coefficient area ratio product, the junction is considered to be unchoked and processing is terminated. If v_c is larger, then a refined calculation is conducted using Equation (7.2-57) in the calculation of the throat pressure.

Equation (7.2-57) must be solved iteratively. To provide throat velocity estimates for use in the iteration, a throat velocity (SONIC1) is calculated by incorporating frictional effects into the Bernoulli balance assuming the throat pressure is P_{sat}. A second estimate of throat velocity, SONIC2, is computed by taking the minimum of a value calculated assuming the throat pressure is zero and a value calculated assuming the throat pressure is determined by $P_{sat} - \Delta P_{FI}$, where ΔP_{FI} is from Equation (7.2-57). Wall friction effects are incorporated in both estimates for SONIC2. Equation (7.2-57) is solved iteratively in conjunction with the Bernoulli equation by starting with an arithmetic average of SONIC1 and SONIC2 and updating either end point of the interval until the assumed throat velocity satisfies the pressure balance.

If the junction vapor/gas void fraction is greater than 1.0×10^{-5} and less than or equal to 0.10, the flow conditions are in transition region 1 (see **Figure 7.2-7**. The value of the throat velocity computed from the iterative solution is stored in a variable SONICS, the logical variable TRANSR is set to true, and the calculation proceeds to the two-phase criteria. If the junction vapor/gas void fraction is less than or equal to 1.0×10^{-5}, the value SONIC2 is reset to zero and the homogeneous equilibrium sound speed at the junction is computed using Equations (7.2-44) and (7.2-45) and saturated liquid properties. If the throat velocity computed from the Bernoulli equation coupled with the pressure undershoot model is larger than the homogeneous equilibrium sound speed, the density ratio JCAT is updated as

$$JCAT^{n+1} = 0.9\ JCAT^{n} + 0.1\frac{(\dot{\alpha}_g\dot{\rho}_g)_j + (\dot{\alpha}_f\dot{\rho}_f)_j}{\rho_K} \quad . \tag{7.2-62}$$

Equation (7.2-46) multiplied by $\frac{C_D \cdot ATHROT}{JCAT}$ is used to compute the final choking velocity derivative with pressure, and Equation (7.2-52) is used to compute the final junction sonic velocity.

If the saturated liquid homogeneous equilibrium sound speed is larger than the result of the iterative solution for the throat velocity, the throat velocity is reset to this saturated liquid homogeneous equilibrium value, $JCAT^{n+1}$ is computed as above, and Equation (7.2-46) multiplied by $\frac{C_D \cdot ATHROT}{JCAT}$ and Equation (7.2-52) are used for the final sound speed derivative and final sonic velocity, respectively. For this case, the second term in brackets in Equation (7.2-46) is set to zero.

At this point, the flow is determined to be subcooled. A final check is made to check that the flow is choked. If the variable CHOKE is true or the value of v_c is greater than or equal to the current value of SONIC, where

$$SONIC = \max (v_t, a_{HE}), \tag{7.2-63}$$

subcooled choked flow is verified, and the solution proceeds directly to the calculation of velocities. The variable v_t is from the iterative solution and a_{HE} is the saturated liquid homogeneous equilibrium sound speed. It should be noted that no underrelaxation is used on the intermediate velocities for the subcooled choking model ($\dot{\alpha}_g \le 10^{-5}$)

7.2.4.2 Two-Phase Criterion. On entry to subroutine JCHOKE, if the junction vapor/gas void fraction is greater than 1.0×10^{-5} and less than or equal to 0.10, the flow conditions are in the transition region 1 and the two-phase choking criterion and the subcooled choking criterion will be applied. If the junction vapor/gas void fraction is greater than 0.10, the flow is in the two-phase region and the two-phase choking criterion will be applied. The first part of the two-phase region (junction vapor/gas void fraction between 0.10 and 0.15) is transition region 2 (see **Figure 7.2-7**).

If the logic dictates that the two-phase criterion logic in subroutine JCHOKE is entered without first passing through the subcooled criterion, the value v_c is tested versus the homogeneous equilibrium sound speed based on the upstream volume conditions. If v_c is less than 1/2 of the homogeneous sound speed based on the upstream conditions, the junction is considered to be unchoked and processing is terminated. If this test is not true or if the choked flow is in the transition regime, the logic proceeds directly to calculate the junction specific internal energy using Equation (7.2-42). Note that the throat pressure was calculated previously. The term $\dot{U}_j$ in Equation (7.2-42) is defined as

$$\dot{U}_j = \dot{X}_{s,j}\dot{U}_{g,j} + (1 - \dot{X}_{s,j})\dot{U}_{f,j} \tag{7.2-64}$$

so that the correct upstream state will be used in the case of stratified flow in the junction. If the junction vapor/gas void fraction is in the transition region, the junction static quality, Equation (7.2-43), for use in the two-phase sound speed calculation is computed using a junction vapor/gas void fraction of 0.10.

After the throat specific internal energy is calculated, a smoothing function RATIOS is defined. If the flag CHOKE is set to true, RATIOS is given as

$$RATIOS = \left\{ 1 + \max\left[\dot{X}_{s,j} \left(\frac{v_{g,j}^{n}}{v_{f,j}^{n}} - 1 \right), 0 \right] \right\}^{1/2}; \tag{7.2-65}$$

otherwise, RATIOS is set to unity.

Once the throat specific internal energy is computed, the thermodynamic property tables are entered with throat pressure and throat specific internal energy to establish the fluid state. If pure vapor/gas exists, Equations (7.2-49) and (7.2-50) are used to calculate the homogeneous frozen sound speed and $\frac{dP}{dT}$, respectively. The density ratio JCAT is then defined as

$$JCAT^{n+1} = \dot{\rho}_{g,j} V_{throat} \tag{7.2-66}$$

where V_{throat} is the vapor/gas specific volume at the throat. If two-phase conditions are present, Equations (7.2-20) and (7.2-21) are used for the sound speed and $\frac{dP}{dT}$, respectively, where saturation conditions are used for the temperature and the phasic V, κ, β, C_p, and h. If liquid conditions are indicated, Equations (7.2-20) and (7.2-21) are also used, however an additional call to the thermodynamic property tables with temperature and quality as input is made to establish saturated liquid properties. In either case (liquid or two-phase), the density ratio JCAT is calculated as

$$JCAT = (\dot{\alpha}_{g,j}\dot{\rho}_{g,j} + \dot{\alpha}_{f,j}\dot{\rho}_{f,j}) \bullet V_{throat} \bullet RATIOS \tag{7.2-67}$$

where V_{throat} is the specific volume (for liquid or mixture) returned from the thermodynamic property table call. The function RATIOS converts the static quality at the junction, as computed by the calls to the thermodynamic property tables using the throat pressure and throat specific internal energy, into a flow quality at the throat by taking the slip ratio into account when computing the throat density ratio JCAT.

Because the value of the throat density ratio (JCAT) and sound speed are computed from extrapolated throat properties, and because the sound speed has a large discontinuity at the transition from single-phase liquid to two-phase choking, a combination of interpolation and time-averaging (i.e., underrelaxation) is used to determine the final value of the choking criterion to be used during a time step in order to eliminate code oscillations.

7.2.4.2.1 Transition Region 1 - - If the junction vapor/gas void fraction is in transition region 1 between single-phase liquid and two-phase flow ($1.0\text{x}10^{-5} < \dot{\alpha}_{g,j} \leq 0.10$), the ratio of the junction sound

speed and the throat density ratio is interpolated between the values for single-phase liquid (using a void fraction of 1.0×10^{-5}) and two-phase flow (using a void fraction of 0.10) as given by

$$\left(\frac{\tilde{a}_j}{JCAT}\right) = (1.0 - RX)\left(\frac{a_{j,SC}}{JCAT_{j,SC}}\right) + RX\left(\frac{a_{j,HE}}{JCAT_{j,TP}}\right) \tag{7.2-68}$$

where the subscripts SC and TP indicate values obtained from the single-phase liquid and two-phase models, respectively; the subscript HE indicates homogeneous equilibruim; ~ represents an intermediate value; and RX is an interpolation factor given by

$$RX = \begin{cases} 0 & \text{for } \dot{\alpha}_{g,j} < 1.0 \times 10^{-5} \\ \text{cubic spline interpolation function} & \text{for } 1.0 \times 10^{-5} \le \dot{\alpha}_{g,j} \le 0.10 \\ 1 & \text{for } \dot{\alpha}_{g,j} > 0.10 \end{cases} \tag{7.2-69}$$

Next, the ratio of the derivative of the sound speed with respect to pressure and the throat density ratio (variable DSONDP), the new time throat density ratio (variable JCATN), and the discharge coefficient are calculated in the same manner (interpolation using factor RX) as the ratio of the junction sound speed and the throat density ratio in Equation (7.2-68).

Next the variable JCATN is underrelaxed between the previously calculated intermediate value of the variable JCATN and the variable JCATO (old time throat density ratio) using the formula

$$JCATN = 0.1 \cdot JCATN + 0.9 \cdot JCATO \tag{7.2-70}$$

The variable JCATN is used in the next time step in the calculation of the throat pressure and the throat mixture specific internal energy.

Next, the ratio of the junction sound speed and the throat density ratio is underrelaxed between the previously calculated intermediate ratio [Equation (7.2-68), variable SONIC] and the old time step ratio (variable SONCJO). The resulting ratio is given by

$$\left(\frac{a_j}{JCAT}\right)^{n+1} = 0.1 \cdot \left(\frac{\tilde{a}}{JCAT}\right) + 0.9 \cdot \left(\frac{a_j}{JCAT}\right)^{n} \tag{7.2-71}$$

This ratio is stored in the variable SONIC and later in the variable SONICJ. The variables SONIC and DSONDP are multiplied by the variable AT (user-specified discharge coefficient C_D times the throat area ratio ATHROT). The variables SONIC and DSONDP are then used to limit the velocities computed from the momentum equations.

7.2.4.2.2 Transition Region 2- - If the junction vapor/gas void fraction is in transition region 2 ($0.10 < \dot{\alpha}_{g,j} \le 0.15$), the new time throat density ratio (variable JCATN) is first underralaxed between the original two-phase throat density ratio $JCAT_{j,TP}$ [Equation (7.2-67)] and the old time throat density ratio (variable JCATO) using the formula

$$JCATN = 0.1 \cdot JCAT_{j,TP} + 0.9 \cdot JCATO \tag{7.2-72}$$

This is used in the next time step to calculate the throat pressure and the throat mixture specific internal energy.

Next, the intermediate ratio $\frac{\tilde{a}}{JCAT}$ of the junction sound speed and the throat ratio ($JCAT_{j,TP}$) is calculated and stored in the variable SONIC. Then the ratio of the derivative of the sound speed with respect to pressure and the throat density ratio ($JCAT_{j,TP}$) is stored in the variable DSONDP.

Next the ratio of the junction sound speed and the throat density ratio is underrelaxed between the previously calculated intermediate ratio (variable SONIC) and the old time ratio (variable SONICO). The ratio is given by

$$\left(\frac{a_j}{JCAT}\right)^{n+1} = RZ\left(\frac{\tilde{a}_j}{JCAT}\right) + (1 - RZ)\left(\frac{a_j}{JCAT}\right)^{n} \tag{7.2-73}$$

where the underrelaxation factor is given by

$$RZ = \begin{cases} 0.1 & \text{for } \dot{\alpha}_{g,j} < 0.10 \\ \text{cubic spline interpolation function for } 0.10 \le \dot{\alpha}_{g,j} \le 0.15 \\ 0.9 & \text{for } \dot{\alpha}_{g,j} > 0.15 \end{cases} \tag{7.2-74}$$

The underrelaxation varies from heavy underrelaxation in transition region 1 to light underrelaxation in the full two-phase and single-phase vapor regions. This ratio is stored in the variable SONIC and later in the variable SONICJ. Then the variables SONIC and DSONDP are multiplied by the variable AT (user-specified discharge coefficient C_D times the throat area ratio ATHROT). The variables SONIC and DSONDP are then used to limit the velocities computed from the momentum equations.

7.2.4.2.3 Transition Region 3 -- If the junction vapor/gas fraction is in transition region 3 between two-phase flow and single phase vapor ($0.90 < \dot{\alpha}_{g,j} \le 0.99$), the calculation is the same as the two-phase transition regions except for the following:

The two-phase density ratio $JCAT_{j,TP}$ is underrelaxed between the original two-phase density ratio [Equation (7.2-67)] and the old time throat density ratio (variable JCATO) using the formula

$$JCAT_{j,TP} = (1 - RY) \cdot JCAT_{j,TP} + RY \cdot JCATO \tag{7.2-75}$$

where the underrelation factor is given by

$$RY = \begin{cases} 0 & \text{for } \dot{\alpha}_{g,j} < 0.9 \\ \text{cubic spline interpolation function} & \text{for } 0.9 \le \dot{\alpha}_{g,j} \le 0.99 \\ 0.9 & \text{for } \dot{\alpha}_{g,j} > 0.99 \end{cases}$$

The relaxation varies from no underrelaxation in the two-phase region to heavy underrelaxation in the vapor region.

As with two-phase transition region 2, the variables SONIC and DSONDP are then multiplied by the variable AT (user-specified discharge coefficient C_D times the throat area ratio ATHROT). The variables SONIC and DSONDP are then used to limit the velocities computed from the momentum equations.

7.2.4.2.4 Phasic Velocities -- The phasic velocity solution then proceeds as outlined in Section 7.2.2.2. Using Equations (7.2-30) and (7.2-31), the 2 x 2 system of equations shown as Equations (7.2-40) can be set up for the new-time phasic velocities in terms of the intermediate velocities, velocity derivatives with respect to pressure, old-time pressure, and new-time pressure.

For junction void fractions $\dot{\alpha}_{g,j}$ greater that or equal to 1.0×10^{-5}, the intermediate velocities computed in subroutine JCHOKE [$\tilde{v}^n_{f,j}$ and $\tilde{v}^n_{g,j}$ in Equation (7.2-40)] for use in the solution of the 2 x 2 system of equations are old-time weighted or underrelaxed with their values from the previous time step using the factor RZ [given by Equation (7.2-74)] used to obtain the final ratio of the junction sound speed and the throat density ratio [Equation (7.2-73)] . The equations are

$$\tilde{v}^n_{f,j} = v^n_{f,j} + RZ(\tilde{v}^n_{f,j} - v^n_{f,j}) \tag{7.2-76}$$

$$\tilde{v}^n_{g,j} = v^n_{g,j} + RZ(\tilde{v}^n_{g,j} - v^n_{g,j}) \tag{7.2-77}$$

where ~ on the right hand side denotes intermediate values from the initial 2 x 2 system of momentum equations and ~ on the left hand side denotes underrelaxed intermediate values used in the final 2 x 2 system of momentun equations. It should be noted that no underrelaxation is used on the intermediate velocities for the subcooled choking model ($\dot{\alpha}_g \le 10^{-5}$).

The procedure outlined above involves a complicated sequence of interpolations and underrelaxations. The net effect of all of these computations is to always underrelax the throat density ratio, underrelax the junction sound speed in the transition region between single-phase liquid and two-phase choking, and underrelax the phasic velocities in the two-phase region. The particular forms of the relaxation factors were chosen to ensure a smooth change from underrelaxation of the junction sound speed to underrelaxation of the phasic velocities.

7.2.5 Weighting, Magnitude Limits, and Averaging Techniques Used in the ATHENA Choking Model

Details of the weighting limits and averaging procedures used in subroutine JCHOKE were given in Section 7.2.4.

The constants in the relaxations were selected based on comparisons to data in which flow conditions passed through the subcooled to two-phase transition. The heavily old time-weighted formulation of Equations (7.2-70), (7.2-71), (7.2-72), (7.2-73), (7.2-76), and (7.2-77) is used to minimize velocity oscillations and time step reductions caused by large changes in the critical velocity that result during the transition.

The expression given in Equation (7.2-65) for RATIOS represents a static quality weighted slip factor. This expression is included to help account for the inaccuracies in the approximations used to establish junction properties [i.e., Equations (7.2-41) and (7.2-42)]. In particular, this term represents an additional correction factor for the junction density required for high vapor/gas quality conditions to approach homogeneous equilibrium conditions.

In many calculations performed in subroutine JCHOKE, great care is exercised to prevent divisions by zero or to prevent attempts to take the square root of negative numbers; for example, divisions by numbers that could possibly be zero (such as the product $\alpha_f\rho_f$). Likewise, square roots of the term VALUE are generally done as SQRT (MAX(0.0, VALUE)).

The derivative of the sound speed in the transition region is interpolated (using the same method as is done for the sound speed) between the single-phase liquid value given by Equation (7.2-46) and the two-phase value given by Equation (7.2-48). In the two-phase relation, vapor/gas is assumed to be a perfect gas with a specific heat ratio of 1.3.

7.2.6 Special Cases of Choking Application

The unique situations recognized by subroutine JCHOKE were addressed in Section 7.2.4 in the discussion of the model as coded. These special cases are summarized here.

If the junction in question is connected to a user-specified time-dependent volume that is specified as the from volume (volume K in **Figure 7.2-5**), the choking calculation is bypassed. The to volume (volume L in **Figure 7.2-5**) may be (and generally is) specified as a time-dependent volume. Also, if the from

volume is an active accumulator volume, the choking calculation is bypassed until the accumulator has emptied and becomes a normal volume.

As discussed in Section 7.2.4, it is possible through input to turn off the momentum flux in the from volume. In this case, the momentum flux in the from volume based on volume average velocity is zeroed out in the calculation of the junction pressure. If the flow reverses during the course of a calculation and the new upwind volume also has the momentum flux turned off through input, the choking model recognizes this and zeroes the momentum flux in the upwind volume based on volume averaged velocity accordingly.

The mixture specific internal energy, $\dot{U}_j$, used in the energy extrapolation is defined using the donor fluid properties to account for vapor/gas pullthrough and/or liquid entrainment through a small junction in a pipe wall when stratified flow exists in the main pipe. In the absence of pullthrough or entrainment, Equation (7.2-64) gives the upstream mixture specific internal energy.

If the abrupt area change model is in effect, the area change with spatial distance for use in the Jones pressure undershoot model [Equation (7.2-59)] is calculated differently than it is for a smooth area change. For a smooth area change,

$$\frac{1}{A_t}\frac{dA}{dx} = \frac{A'_K - A_t}{\left(\frac{\Delta x_K}{2}\right)A_t} \tag{7.2-78}$$

where A'_K is the minimum of the flow area in volume K (A_K) and $50A_t$, Δx_K is the length of volume K, and A_t is the physical area of the junction. If the abrupt area change model is in use, then

$$\frac{1}{A_t}\frac{dA}{dx} = \frac{A'_K - A_t}{D'_K A_t} \tag{7.2-79}$$

where A'_K is the minimum of A_K and $50A_t$, and D'_K is the length set to ten times the diameter of volume K. In the limit of increasing the volume to junction area, Equation (7.2-78) goes to $\frac{98m}{\Delta x_K}$, whereas Equation (7.2-79) goes to $\frac{4.9m}{D_K}$ where D_K is the volume diameter. When the abrupt change model is used at a branch, A'_K in Equation (7.2-79) is the minimum of $\frac{A_K Q_j}{Q_K}$ and $50A_t$, where Q_j is the junction volumetric flow rate and Q_K is the mixture volumetric flow rate for all the junctions on the same face as junction j.

In case choked flow has occurred at the previous time step, an unchoking test is used to determine whether choked flow persists at the current time step. The following notation is used: P_K is the upstream pressure, P_t is the throat pressure, and P_L is the downstream pressure. For choking, one has $P_K > P_t$. However, it may be that $P_t > P_L$ or $P_t < P_L$, depending on the nozzle geometry and the hydrodynamic conditions downstream of the throat. A quantity ΔP_{min} is calculated from the Bernoulli equation which includes the effects of the variation of flow area, wall friction, and form loss. In ATHENA, it is required that $P_K > P_t$ and either $P_t > P_L$ or $P_K - \Delta P_{min} > P_L$, in order to maintain choked flow; otherwise, the flow is considered to be unchoked.

A final special case is worthy of note. If the junction velocity solution computed in subroutine JCHOKE indicates that countercurrent flow exists, the liquid and vapor/gas velocities are both set to the sound speed.

7.2.7 Assessment of Choked Flow Model

The ATHENA critical flow model has been assessed using data from a standard model used to predict subcooled critical flow and using data from a number of different thermal-hydraulic facilities. A portion of this assessment is discussed below.

7.2.7.1 Comparison to Henry-Fauske Model. The small model shown in **Figure 7.2-8** was used to drive the ATHENA critical flow model to provide data for the purpose of comparison to critical flow models in the literature. Data for the Henry-Fauske subcooled critical flow model[7.2-15] were used for comparison to the ATHENA results.

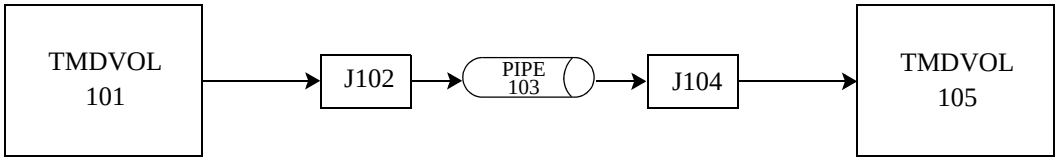

Figure 7.2-8 ATHENA nodalization used for subcooled critical flow investigation.

The model consists of a driver time-dependent volume (101) with specified thermodynamic conditions, a pipe component (103) containing four volumes, a time-dependent volume (105) representing atmospheric conditions, and two junctions (components 102 and 104) connecting the driver volume to the pipe and the pipe to the atmosphere, respectively. The choking model with discharge coefficients set to unity was applied at junction 104 and turned off at all other junctions in the model. Wall friction was turned off in all volumes and smooth area changes were used throughout. To compute subcooled choked flow values, the temperature in volume 101 was set to 557.7 K and the pressure was varied from approximately 7 to 18 MPa. For each pressure, the model was run to a steady-state to compute the

subcooled choked flow rate at junction 104. To compute saturated critical flow rates, the pressure in volume 101 was set to 8.1 MPa and the equilibrium quality was varied from 0 to 1. For each quality, the model was run to steady-state. Computations for the subcooled and saturated cases were run with the equilibrium option and with the nonequilibrium option. In all cases, the mass flux at junction 104 is plotted against the conditions in the volume at the end of pipe 103.

Figure 7.2-9 compares the subcooled critical mass flux calculated with ATHENA compared to the Henry-Fauske model. The homogeneous and nonhomogeneous options had no impact on the results, since the flow is single-phase. With the exception of pressures near saturation, the ATHENA results are consistently higher than the Henry-Fauske model. This result is consistent with other applications[7.2-16] where a discharge coefficient of 0.9 has been applied to bring the ATHENA results into better agreement with other subcooled choked flow models.

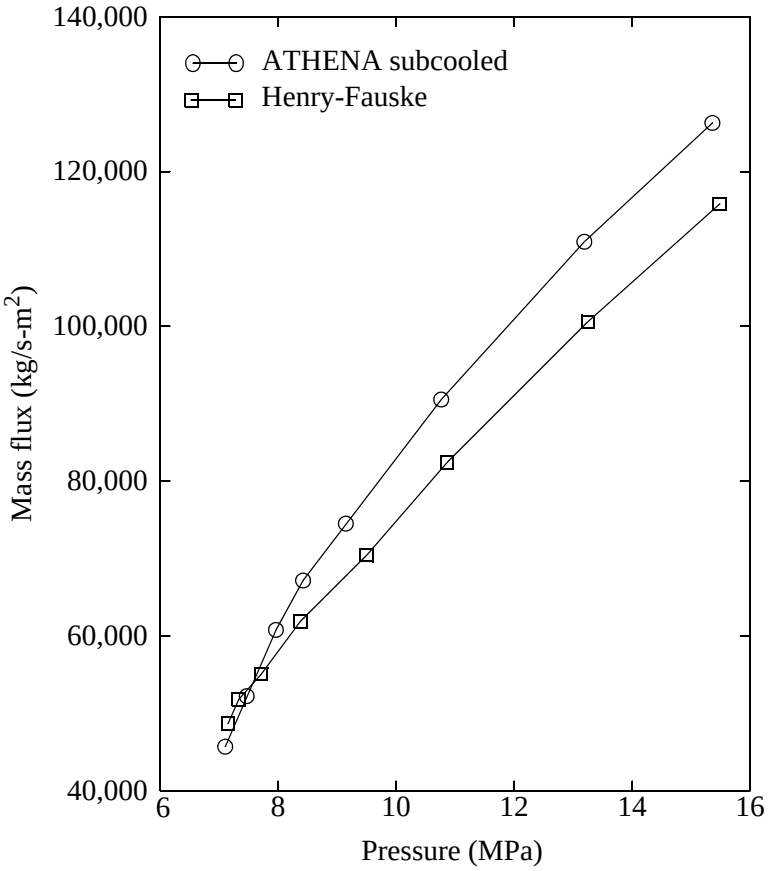

Figure 7.2-9 ATHENA subcooled critical flow compared with Henry-Fauske tabulated values (**Reference 7.2-15**), liquid temperature 557.7 K.

7.2.7.2 Assessment of ATHENA Critical Flow Model Using Facility Data. Numerous literature citations are available documenting comparisons of ATHENA critical flow calculations to

experimental data. Ransom and Trapp[7.2-1] used data from the Marviken Power Station Test 4.[7.2-17] Developmental assessment[7.2-12] was done using Marviken Tests 24[7.2-18] and 22.[7.2-13] Weaver[7.2-19] repeated the assessments of Rosdahl and Caraher[7.2-20] using ATHENA. Rosdahl and Caraher conducted an extensive assessment of the RELAP5/MOD2 choking model using Marviken Tests JIT-11 and CFT-21 data with various nodalizations. Most of the improvements to the ATHENA choking model which were implemented in ATHENA were motivated by the results of the Rosdahl and Caraher assessment study. Many other comparisons to integral test data from the LOFT and Semiscale test facilities can be found in **Reference 7.2-12** and Volume III of this code manual. The discussion below will concentrate on a summary of the comparisons of the ATHENA model results to Marviken results.

7.2.7.2.1 Marviken Facility Description--The Marviken facility in Sweden was used to conduct large-scale critical flow and jet impingement tests in 1978 - 1982. The pressure vessel from a full-scale BWR that was never commissioned was used to provide data for the critical discharge of subcooled liquid, low-quality two-phase mixtures, and steam. **Figure 7.2-10** (from **Reference 7.2-20**) shows the pressure vessel and associated instrumentation. The vessel ID and height are 5.22 m and 24.55 m, respectively. The total volume is approximately 420 m^3. For experiments producing saturated steam discharge, a standpipe (dotted line) was inserted in the vessel. In the subcooled liquid and two-phase mixture discharge experiments, no standpipe was used, and fluid entered the discharge piping directly from the bottom of the vessel. Nozzles of various length-to-diameter ratios (see **Figure 7.2-11**) could be attached to the bottom of the vessel. A rupture disk assembly containing two rupture disks was attached to the downstream end of the nozzle. Tests were initiated by overpressurizing the volume between the two disks, which then failed and were discharged from the nozzle region.

7.2.7.2.2 Calculation of Marviken Test 4--Ransom and Trapp[7.2-1] simulated Marviken Test 4 using ATHENA. The purpose of Test 4 was to establish critical flow rates with subcooled and low-quality fluid at the nozzle inlet. For this experiment, a nozzle with a 0.5-m diameter and a 3.6 length-to-diameter $\frac{L}{D}$ ratio was installed in the facility. **Figure 7.2-12** shows the ATHENA nodalization and initial temperature profile in the vessel. The water level was initially at 16.8 m above the bottom of the vessel, and the steam dome above the water level was saturated at 4.94 MPa. During the test, the subcooling at the nozzle inlet decreased from 60 to 35 K in the first 0.5 second and then decreased gradually until saturated conditions were established at 17 seconds. Two-phase flow persisted between 17 and 47 seconds.

Figure 7.2-13 compares the measured and predicted critical mass fluxes. Measured values were determined both from pitot-static measurements in the discharge pipe and from measurement of the vessel mass rate of change. The transition from subcooled flow to saturated flow at 17 seconds is clear on **Figure 7.2-13** The good agreement between the prediction and measurements lead to the conclusion that the thermal equilibrium assumption employed in the ATHENA critical flow model development was appropriate for the conditions encountered in Test 4, since with the large $\frac{L}{D}$ nozzle one would expect conditions approaching equilibrium. It should be noted that the break area in the ATHENA model was reduced by 5% to account for suspected separation effects.[7.2-1] In effect, then, a discharge coefficient of 0.95 has been applied.

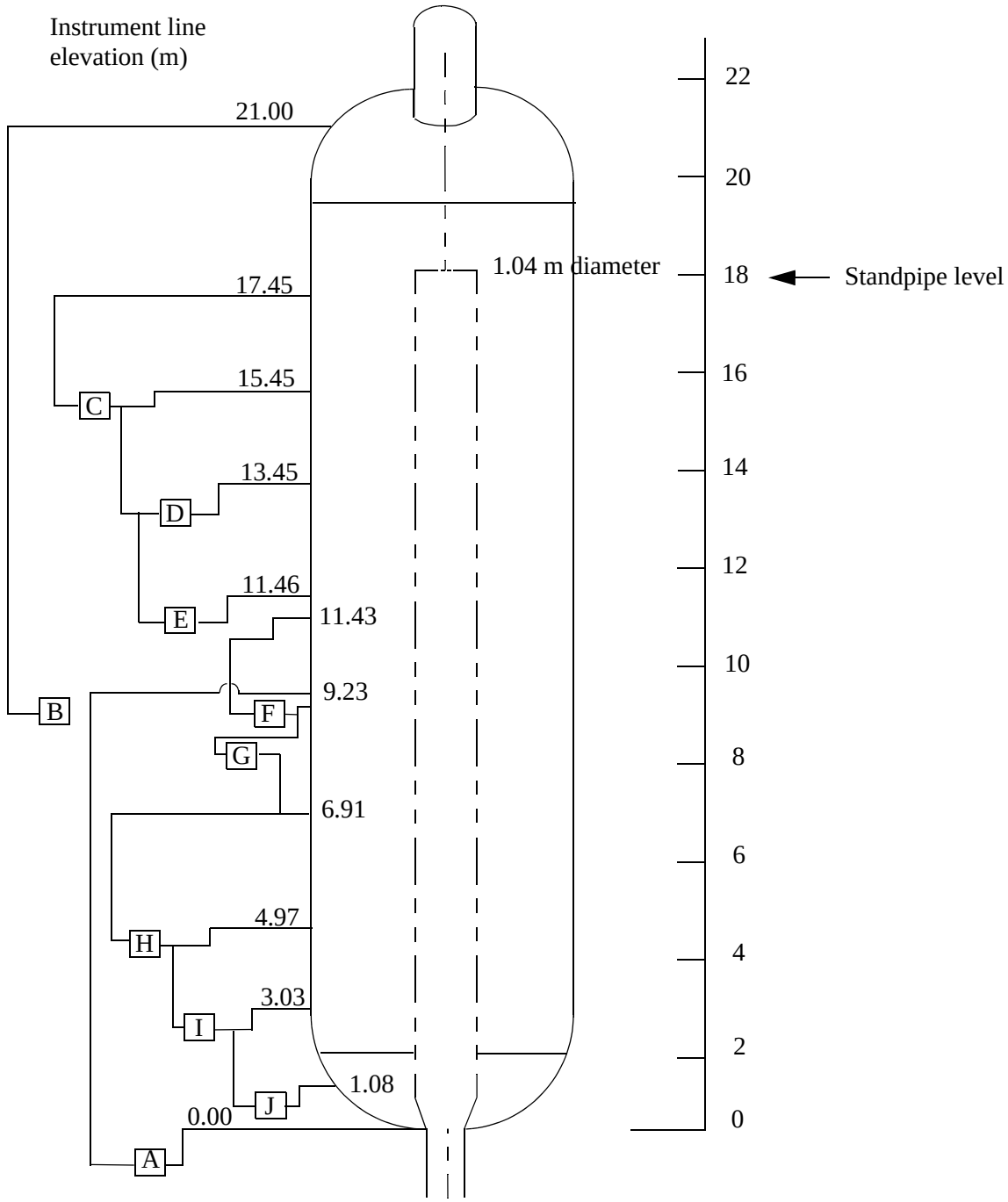

Figure 7.2-10 Marviken test vessel, showing differential pressure transducers A through J.

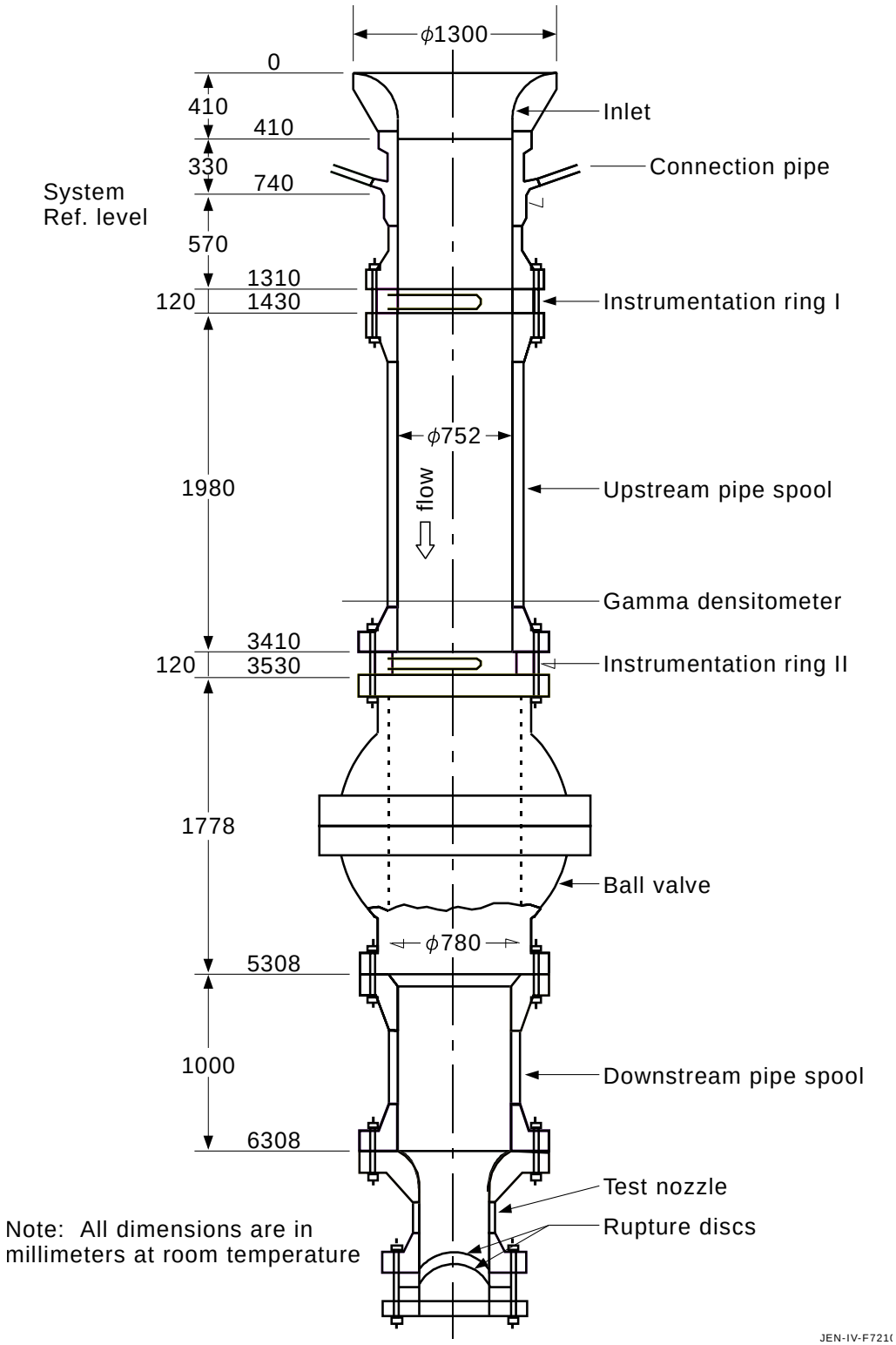

Figure 7.2-11 Arrangement of components in the discharge pipe for Critical Flow Test 21.

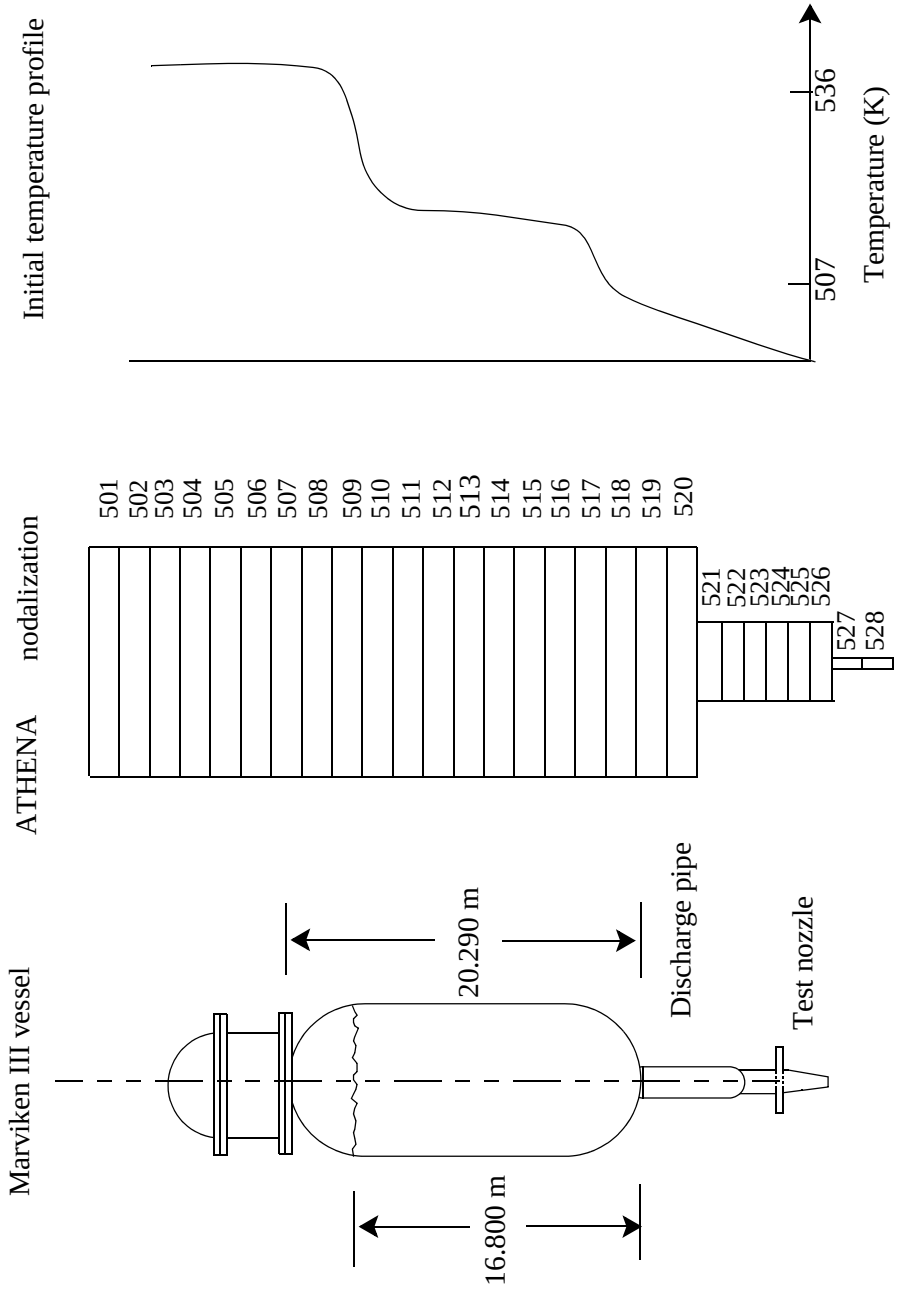

Figure 7.2-12 Marviken III Test 4 vessel schematic, ATHENA nodalization, and initial temperature profile.

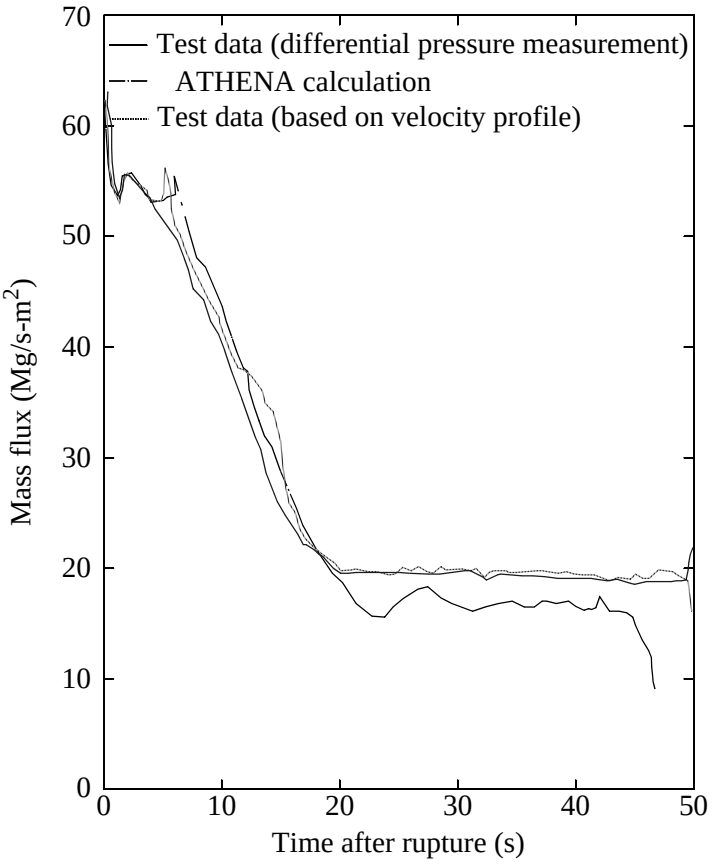

Figure 7.2-13 Calculated and measured mass flux at nozzle inlet (Volume 526 in ATHENA nodalization).

7.2.7.2.3 Calculation of Marviken Tests 22 and 24--Marviken Tests 22 and 24 were conducted in the same fashion as Test 4 described in the previous section. The major distinguishing features of Tests 22 and 24 relative to Test 4 concern the nozzle $\frac{L}{D}$ ratios. The nozzle $\frac{L}{D}$ ratios for these tests were 1.5 for Test 22 and 0.33 for Test 24. Data from these experiments are valuable for examining the subcooled choking criteria and in particular nonequilibrium effects. The same model as shown in **Figure 7.2-12** was used for the calculations of both tests. **Figure 7.2-14** and **Figure 7.2-15** show pressure and mass flow comparisons obtained for Test 24 $\left(\frac{L}{D} = 0.33\right)$. Results for Test 22 are similar.

Additional details for both tests can be found in **Reference 7.2-13** and **Reference 7.2-18**. For both tests, the vessel pressure was overpredicted for the first second, slightly underpredicted for the majority of the subcooled region, and then slightly overpredicted for the saturated flow region. The initial pressure overprediction has been attributed to the nucleation delay model used in ATHENA. Undoubtedly, this has an effect on the subsequent pressure and critical flow predictions. Given the differences in pressure, it is difficult to make judgments on the subcooled break flow model (the pressure undershoot model

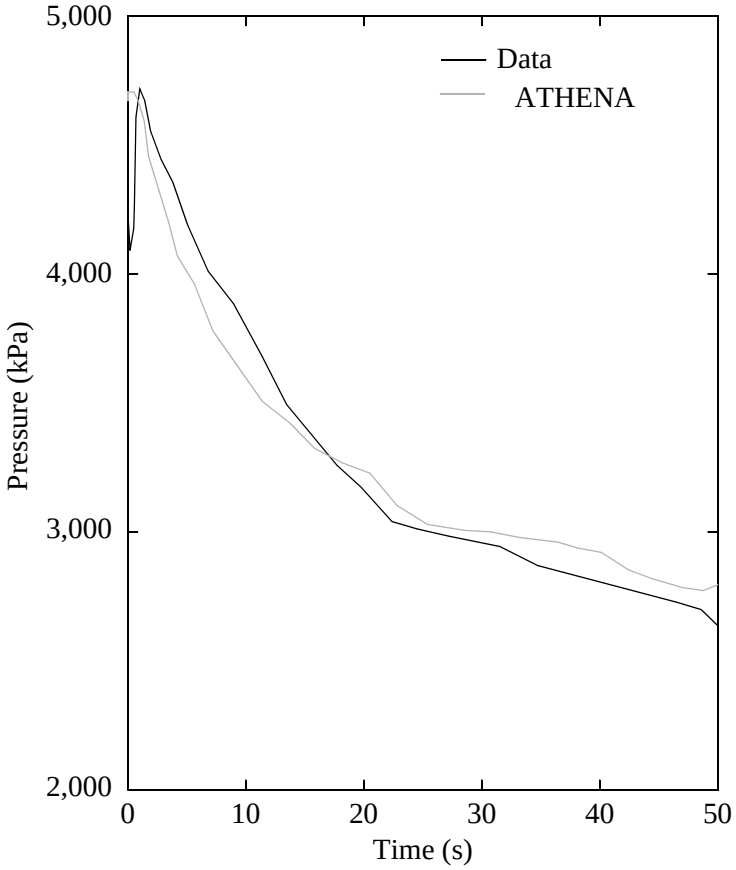

Figure 7.2-14 Measurement and ATHENA calculation of Marviken Test 24 pressure in the top of the vessel.

implementation), although the comparison for the first 20 seconds is very good. It was noted for both calculations that the transition to two-phase flow was too abrupt.

7.2.8 Model Application

Assessment of the ATHENA critical flow model was discussed in the previous section. These assessments, as well as the assessment study of Rosdahl and Caraher using RELAP5/MOD2, indicate that short nozzles or discharge pipes $\frac{L}{D} < 2$ should not be explicitly modeled and that a discharge coefficient of 0.85 should be used for subcooled flows. The assessment also showed that there was little benefit in explicitly modeling nozzles discharging saturated vapor/gas, and the conclusion was that there is little incentive to modeling discharge pipes of $\frac{L}{D} < 4$ when saturated vapor/gas is being discharged. Furthermore, a discharge coefficient of 0.82 was necessary to bring saturated steam flows into agreement with Marviken data.

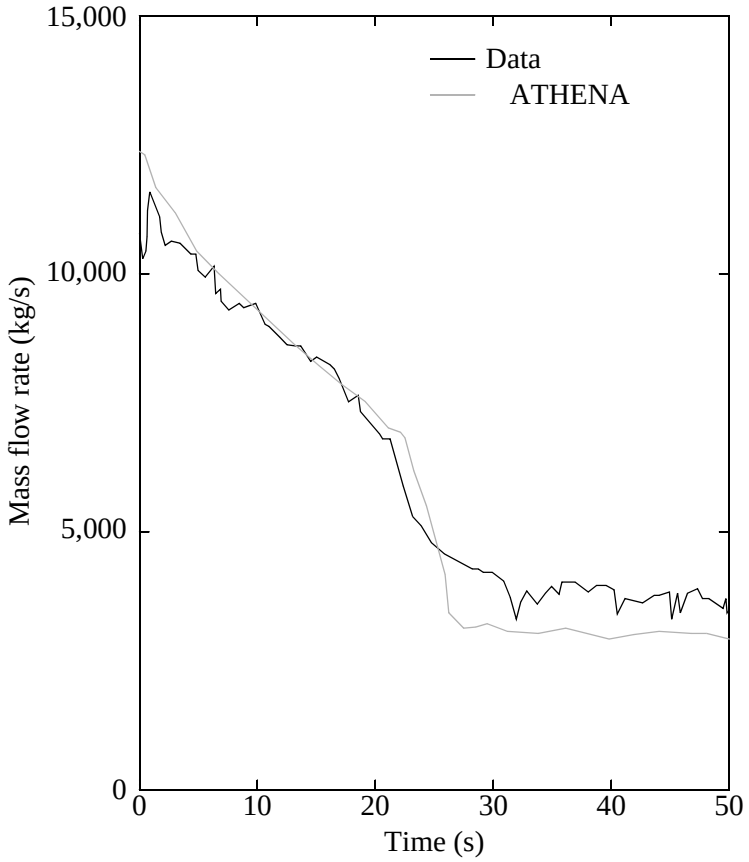

Figure 7.2-15 Measurement and ATHENA calculation of Marviken Test 24 mass flow rate at the nozzle.

In general, the use of discharge coefficients is required to account for multi-dimensional effects due to the break geometry being modeled. It is the code user's task, then, to determine the necessary discharge coefficient values for the specific geometry.

7.2.9 Scaling Considerations

The ATHENA break flow model was essentially developed from first principles. One-dimensional approximations are utilized in both the subcooled flow model and the two-phase mixture flow model. Empirical discharge coefficients are used to help account for multi-dimensional effects. One aspect of the model that involves scale considerations is in the implementation of the pressure undershoot correlation, as discussed in Sections 7.2.1.1 and 7.2.3, and the approximation of the spatial derivatives for the static depressurization term in the correlation described in Section 7.2.6.

As shown in Equations (7.2-78) and (7.2-79), the derivative terms depend on nodalization and have different limits depending on the area change option selected. The fact that the model predicts large-scale

critical flow data (given appropriate discharge coefficients) as discussed in Section 7.2.7 and small-scale data, given approximately the same discharge coefficients, lends support to the scaling ability of the subcooled critical flow model.

The two-phase critical flow model is analytically developed from a characteristic analysis of a four-equation, one-dimensional, two-fluid model assuming thermal equilibrium. The model development is scale-independent, although simplifications have been made to get a solution for roots in the characteristic analysis. The validity of these assumptions is not expected to be a function of scale. As discussed in the previous sections, the two-phase critical flow model predicts available large-scale critical flow data given the appropriate discharge coefficient. It should be noted that the discharge coefficient varies with scale due to the boundary layer effect. The velocities are not expected to depend on scale factors.

7.2.10 Summary and Conclusions

The ATHENA critical flow model represents a first-principle approach to the calculation of subcooled, two-phase mixtures and vapor/gas critical discharge. The model is based on a one-dimensional flow assumption, and discharge coefficients are generally necessary to account for geometry-specific, two-dimensional effects. For the subcooled flow regime, an empirical correlation is used to calculate pressure undershoot (liquid superheat) at the choke point for the estimation of the choke plane pressure. Thermal equilibrium assumptions were employed in the development of an analytic choking criterion for two-phase flow.

The model has been assessed against a wide variety of data from experimental facilities and against tabulated critical flow models, such as Henry-Fauske. Without application of discharge coefficients, the ATHENA model overpredicts Henry-Fauske tabulated data. Likewise, without the application of discharge coefficients, the ATHENA model overpredicts available large-scale critical discharge data from the Marviken facility.

Although not discussed in this report, the ATHENA critical flow model can accommodate a noncondensable gas. Although noncondensable gas is not expected to be present for many LBLOCA and SBLOCA analyses, if calculations are run with noncondensable present at the choke plane, critical flow results should be carefully analyzed since this aspect of the model has not had extensive application. Furthermore, if calculations are run that involve extensive deviation from the thermal equilibrium, the results should be carefully analyzed with respect to the choking criterion, since the criterion was based on thermal equilibrium assumptions.

7.2.11 References

7.2-1. V. H. Ransom and J. A. Trapp, “The RELAP5 Choked Flow Model and Application to a Large Scale Flow Test,” *Proceedings of the ANS/ASME/NRC International Topical Meeting on Nuclear Reactor Thermal-Hydraulics, Saratoga Springs, New York, October 5-8, 1980,* pp. 799-819.

7.2-2. J. A. Trapp and V. H. Ransom, "A Choked-Flow Calculation Criterion for Nonhomogeneous, Nonequilibrium, Two-Phase Flows," *International Journal of Multiphase Flow, 8,* 6, 1982, pp. 669-681.

7.2-3. J. W. Burnell, "Flow of Boiling Water Through Nozzles, Orifices, and Pipes," *Engineering,* 1947, pp. 572-576.

7.2-4. F. J. Moody, "Maximum Flow Rate of a Single-Component, Two-Phase Mixture," *Transactions of the ASME, Journal of Heat Transfer, 87,* 1965, pp. 134-142.

7.2-5. M. D. Alamgir and J. H. Lienhard, "Correlation of Pressure Undershoot During Hot Water Depressurization," *Transactions of the ASME, Journal of Heat Transfer, 103,* 1981, pp. 52-73.

7.2-6. N. Abuaf, O. C. Jones, Jr., and B. J. C. Wu, *Critical Flashing Flows in Nozzles with Subcooled Inlet Conditions,* BNL-NUREG-27512, Brookhaven National Laboratory, March 1980.

7.2-7. O. C. Jones, Jr., "Flashing Inception in Flowing Liquids," *Transactions of ASME, Journal of Heat Transfer, 102,* 1980, pp. 439-444.

7.2-8. P. R. Garabedian, *Partial Differential Equations,* New York: Wiley, 1964.

7.2-9. G. B. Whitham, *Linear and Nonlinear Waves,* New York: Wiley, 1974.

7.2-10. V. H. Ransom and J. A. Trapp, *RELAP5 Progress Summary, Analytical Choking Criterion for Two-Phase Flow,* CDAP-TR-013, Idaho National Engineering Laboratory, April 1978.

7.2-11. V. H. Ransom and J. A. Trapp, *RELAP5 Progress Summary-PILOT Code Hydrodynamics and Numerical Scheme,* CDAP-TR-005, Idaho National Engineering Laboratory, January 1978.

7.2-12. V. H. Ransom et al., *RELAP5/MOD2 Code Manual, Volume 3: Developmental Assessment Problems,* EGG-TFM-7952, Idaho National Engineering Laboratory, December 1987.

7.2-13. L. Ericson et al., *The Marviken Full-Scale Critical Flow Tests Interim Report: Results from Test 22,* A. B. Atomenergi Sweden, Report MCX-222, March 1979.

7.2-14. W. M. Bryce, *Improvements to the RELAP5/MOD1/014 LOCA Code: The RELAP5/MOD1/WIN001 Code,* AEEW-R-1649, Atomic Energy Establishment Winfrith, May 1983, pp. 64-65.

7.2-15. R. E. Henry and H. K. Fauske, "The Two-Phase Critical Flow of One-Component Mixtures in Nozzles, Orifices, and Short Tubes," *Transactions of the ASME, Journal of Heat Transfer, 93,* 1971, pp. 179-187.

7.2-16. M. T. Leonard, *Post-Test RELAP5 Simulation of the Semiscale S-UT Series of Experiments,* EGG-SEMI-5622, Idaho National Engineering Laboratory, October 1982.

7.2-17. L. Ericson et al., *The Marviken Full-Scale Critical Flow Tests Interim Report: Results from Test 4*, A. B. Atomenergi Sweden, Report MXC-204, May 1979.

7.2-18. L. Ericson et al., *The Marviken Full-Scale Critical Flow Tests Interim Report: Results from Test 24*, A. B. Atomenergi Sweden, Report MXC-224, May 1979.

7.2-19. W. L. Weaver, *Improvements to the RELAP5/MOD3 Choking Model*, EGG-EAST-8822, Idaho National Engineering Laboratory, December 1989.

7.2-20. O. Rosdahl and D. Caraher, *Assessment of RELAP5/MOD2 Against Critical Flow Data from Marviken Tests JIT-11 and CFT-21*, NUREG/IA-0007, September 1986.

7.3 Countercurrent Flow Limitation Model

A completely deterministic physical model to specify the start of flow-limiting situations for all geometrical conditions is impossible, given the state of the art of two-phase flow modeling. Without a countercurrent flow limitation (CCFL) or flow limitation model, coolant distribution cannot be adequately predicted for certain situations (e.g., LOCA flooding at the core tie plate, small-break flooding at the steam generator inlet plenum, flooding at tube support plates in once-through steam generators). This can result in an improper distribution of liquid and vapor/gas in the RCS and, therefore, an unacceptable uncertainty regarding the maintenance of core coolability during a LOCA.

Loomis and Streit[7.3-1] and Fineman[7.3-2] reported that RELAP5/MOD2 incorrectly predicted the core liquid inventory in Semiscale small-break LOCA test S-LH-1, and this subsequently resulted in the lack of a core heat-up in the code calculation when compared to data. They attributed this to the inability of the code to limit the delivery of liquid from the upper plenum through the upper core tie plate. The Semiscale core contains an upper tie plate, and the downward liquid flow penetrating through this upper tie plate needs to be correct in order to obtain the proper void profile. Kolesar, Stitt, and Chow[1] reported that incorporation of a CCFL model into RELAP5/MOD2 similar to the one used in TRAC-B[7.3-3,7.3-4] resulted in the proper heatup in a similar Semiscale test (S-UT-8). Kukita[7.3-5] observed that flooding at the steam generator inlet plenum in the ROSA-IV Program's Large Scale Test Facility (LSTF) controlled drainage of the steam generators and hot leg in small-break LOCA tests.

There are several structures internal to RCSs where gravity drainage of liquid can be impeded by upward flowing vapor/gas. These include the upper core tie plate, downcomer annulus, steam generator tube support plates, and the entrance to the tube sheet in the steam generator inlet plenum. A completely mechanistic approach to determine the onset of flow limiting for all structural configurations is impractical. Both the Wallis and Kutateladze forms of the general flooding limit equation have been found to provide acceptable results when constants applicable to specific geometries are used in conjunction with

1. D. C. Kolesar, B. D. Stitt, and H. Chow, *Exxon Nuclear Company Evaluation Model, EXEN PWR Small Break Model,* Proprietary Report XN-NF-82-49(P), Revision 1, June 1986.

them. Wallis[7.3-6] discusses the phenomenon of flooding, which can occur when liquid is falling in a vertical structure and vapor/gas is moving upward. For a specified liquid downflow rate, there is a certain vapor/gas upward flow rate at which very large waves appear on the interface, the flow becomes chaotic, vapor/gas pressure drop increases, and liquid flows upward. **Figure 7.3-1** is a reproduction of Wallis' Figure 11.11 and shows this phenomena for water and gas. Wallis points out that the flooding point is not approached as the limit of a continuous process (which occurs in drops or bubbles), but it is the result of a marked instability.

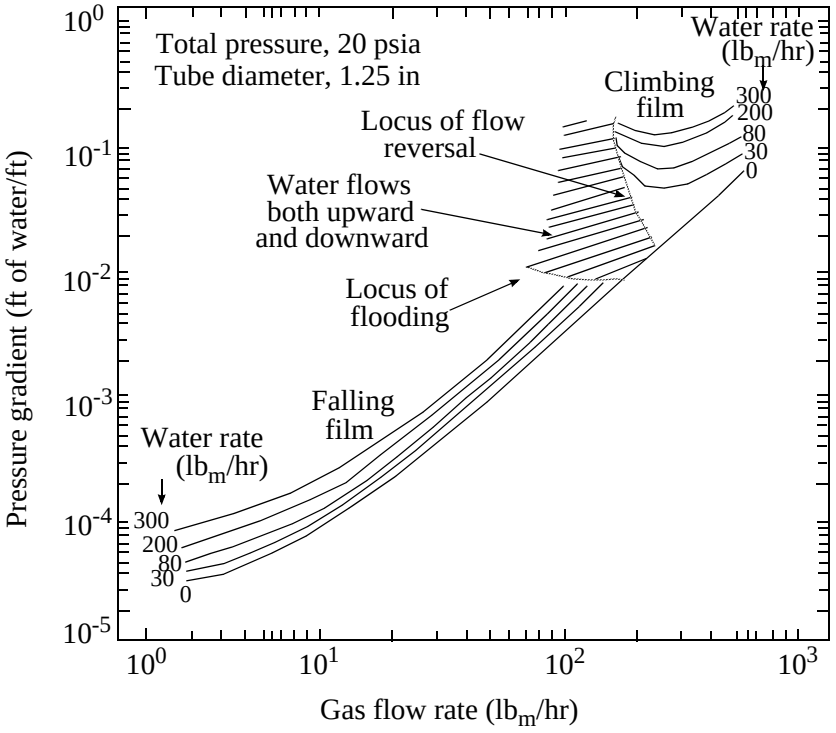

Figure 7.3-1 Pressure-drop characteristics near the boundary between countercurrent and cocurrent flow (from Wallis,[7.3-6] p. 337).

7.3.1 Code Modeling

A general countercurrent flow limitation (CCFL) model[7.3-7] is used that allows the user to select the Wallis form, the Kutateladze form, or a form in between the Wallis and Kutateladze forms. This general form was proposed by Bankoff et al.[7.3-8] and is used in the TRAC-PF1 code.[7.3-9] It has the structure

$$H_g^{1/2} + mH_f^{1/2} = c \qquad (7.3\text{-}1)$$

where H_g is the dimensionless vapor/gas flux, H_f is the dimensionless liquid flux, c is the vapor/gas intercept (value of $H_g^{1/2}$ when $H_f = 0$, i.e., complete flooding), and m is the "slope", that is the vapor/gas intercept divided by the liquid intercept (the value of $H_f^{1/2}$ when $H_g = 0$). A typical plot of $H_g^{1/2}$ versus $H_f^{1/2}$ is shown in **Figure 7.3-2**. Quotes are used around the word "slope" because in a strict mathematical sense, the slope is negative for Equation (7.3-1) and m = -slope. The constant m will be called the slope in this section of the manual and in the input cards and output edit, but one should think of this as -slope. The dimensionless fluxes have the form

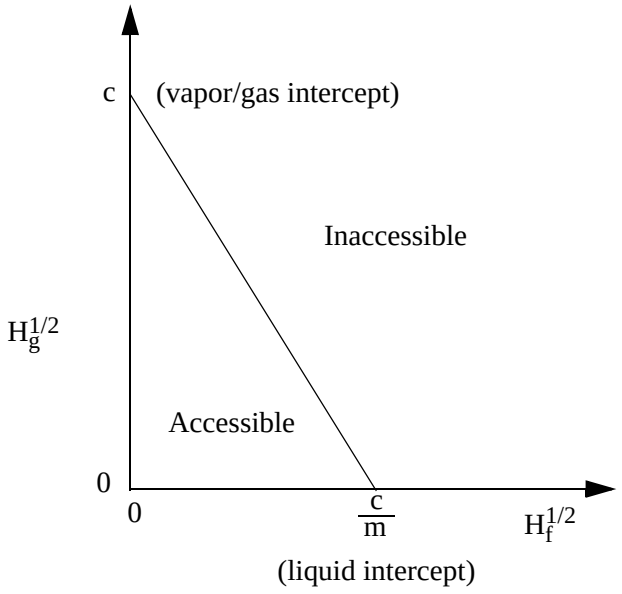

Figure 7.3-2 Plot of $H_g^{1/2}$ versus $H_f^{1/2}$ for a typical CCFL correlation.

$$H_g = j_g \left[\frac{\rho_g}{gw \cdot \max(\rho_f - \rho_g, 10^{-7} kg/m^3)} \right]^{1/2} \tag{7.3-2}$$

$$H_f = j_f \left[\frac{\rho_f}{gw \cdot \max(\rho_f - \rho_g, 10^{-7} kg/m^3)} \right]^{1/2} \tag{7.3-3}$$

where j_g is the vapor/gas superficial velocity ($\alpha_g v_g$), j_f is the liquid superficial velocity ($\alpha_f v_f$), ρ_g is the vapor/gas density, ρ_f is the liquid density, α_g is the vapor/gas volume fraction, α_f is the liquid volume fraction, g is the gravitational acceleration, and w is given by the expression

$$w = D_j^{1-\beta} L^{\beta} \quad . \tag{7.3-4}$$

In Equation (7.3-4), D_j is the junction hydraulic diameter and L is the Laplace capillary length constant, given by

$$L = \left[\frac{\sigma}{g \cdot \max(\rho_f - \rho_g, 10^{-7} kg/m^3)} \right]^{1/2} \tag{7.3-5}$$

where σ is the surface tension. In Equation (7.3-4), β can be a number from 0 to 1. For $\beta = 0$, the Wallis form of the CCFL equation is obtained; and for $\beta = 1$, the Kutateladze form of the CCFL equation is obtained. For $0 < \beta < 1$, a form in between the Wallis and Kutateladze forms is obtained; and Bankoff[7.3-8] suggests that β be correlated to data for the particular geometry of interest. He has included a possible function for β, although it is somewhat restrictive. The form of Equations (7.3-1) through (7.3-4) is general enough to allow the Wallis or Kutateladze form to appear at either small or large diameters. Other approaches (e.g., Tien, et. al.[7.3-10]) appear to be more restrictive by defaulting to the Wallis form at small diameters and the Kutateladze form at large diameters.

7.3.2 Code Implementation

With regard to the solution method, if the CCFL model is requested by the user, the coding checks if countercurrent flow exists and if the liquid downflow exceeds the limit imposed by Equation (7.3-1). If this is true, the sum momentum equation and the flooding limit equation are applied. This approach was suggested by Trapp,[1] who observed that the CCFL model is similar to the choking model in that both place limits on the momentum equations. He observed that since the flooding phenomenon can be incorporated by altering the interphase friction (as is done in TRAC-PF1), it can also be incorporated by replacing the code's difference momentum equation with the flooding limit equation. The difference equation contains the interphase friction, whereas the sum equation does not. (In the choking model, the sum momentum equation is replaced with the choking limit equation.) This method is advantageous in that the phasic velocities still must satisfy the sum momentum equation, which contains gravity and pressure terms. The numerical form of Equation (7.3-1) needed by the code is obtained by letting $c_g = \frac{H_g}{v_g}$ and $c_f = \frac{H_f}{v_f}$, solving for $mH_f^{1/2}$, and squaring the equation, which results in

$$m^2 c_{f,j}^n v_{f,j}^{n+1} = c^2 - 2c(c_{g,j}^n)^{1/2}(v_{g,j}^{n+1})^{1/2} + c_{g,j}^n v_{g,j}^{n+1} \quad . \tag{7.3-6}$$

1. Personal communication, J. A. Trapp to R. A. Riemke, January 1987.

Linearization of $(v_{g,j}^{n+1})^{1/2}$ gives

$$(v_{g,j}^{n+1})^{1/2} = (v_{g,j}^{n})^{1/2} + \frac{1}{2}(v_{g,j}^{n})^{-1/2}(v_{g,j}^{n+1} - v_{g,j}^{n}) \tag{7.3-7}$$

and substitution into Equation (7.3-6) gives

$$m^2 c_{f,j}^{n} v_{f,j}^{n+1} + [c(c_{g,j}^{n})^{1/2}(v_{g,j}^{n})^{-1/2} - c_{g,j}^{n}]v_{g,j}^{n+1} = c^2 - c(c_{g,j}^{n})^{1/2}(v_{g,j}^{n})^{1/2} \quad . \tag{7.3-8}$$

In keeping with the philosophy of considering the CCFL model as a limit model similar to the choking model, the subroutine CCFL contains the CCFL model and is structurally similar to the choking model subroutine JCHOKE. This subroutine is called following the call to subroutine JCHOKE in subroutine HYDRO (if the semi-implicit scheme is requested) and following the call to subroutine JCHOKE in subroutine VIMPLT (if the nearly-implicit scheme is requested). If the semi-implicit scheme is requested, the three coefficients for the sum momentum equation (variables SUMF, SUMG, and SUMOLD) are stored in the scratch variables FWFXAF, FWFXAG, and PFINRG in subroutine VEXPLT for use in subroutine CCFL. If the nearly-implicit scheme is requested, the three coefficients for the sum momentum equation are already stored in the variables COEFV(ISF), COEFV(ISF+1), and SOURCV(IS) in the first part of subroutine VIMPLT, so no change is required.

Regarding the subroutine CCFL, a flow chart describing the main features of this subroutine is shown in **Figure 7.3-3** and a glossary defining the FORTRAN names for important variables in this subroutine is shown in **Table 7.3-1**. After the preliminary calculations, the terms needed for the Wallis-Kutateladze flooding correlation are determined. Following the same philosophy as the choking model, the explicit liquid velocity from subroutine VEXPLT (or VIMPLT) is checked against the liquid velocity allowed by the flooding correlation equation [based on the explicit vapor/gas velocity from subroutine VEXPLT (or VIMPLT)]. If the subroutine VEXPLT (or VIMPLT) liquid velocity is larger, the correlation is used to determine the actual final velocities using the sum momentum equation and the flooding limit equation. Depending on which scheme (semi-implicit or nearly-implicit) is requested, different terms are computed.

As shown in **Figure 7.3-3**, there is some logic in subroutine CCFL to restrict the calculation to be on one of the two axes above the intercepts when the ccfl option in on. The coding relies on the calculation of the phasic velocities at the intercepts (VELGJC and VELFJC). When a phasic velocity is predicted to be on the axis above the intercept, the other phase velocity is calculated to be zero (except for the new-time pressure effects). When this occurs, the ccfl calculation is not used. Thus, changing the ccfl correlation via

input (i.e., changing β, m, c, etc.) may have no effect on the calculation, especially if the phasic velocity is significantly larger than the phasic velocity at the intercept.

Table 7.3-1 Glossary of important FORTRAN variables in subroutine CCFL.

Variable	Description
SIGMA	Junction surface tension, obtained by length-averaging the adjacent volumes' surface tension (used in variable CLPLAC)
CLPLAC	Laplace capillary length constant $L = \{\sigma/[\ g \cdot \max(\rho_f - \rho_g, 10^{-7}\text{kg/m}^3)\ ]\}^{1/2}$
BETACC(I)	Form of the CCFL equation input by the user (β)
DIAMJ(I)	Junction hydraulic diameter (D_j) input by the user
W	Expression used in nondimensional fluxes that determines the length used ($= D_j^{1-\beta}L^{\beta}$)
RDENOM	Inverse of the denominator in the nondimensional fluxes $\{= 1/[gw \cdot \max(\rho_f - \rho_g, 10^{-7}\text{kg/m}^3)\ ]^{1/2}\}$
CG	Coefficient of the velocity in the nondimensional vapor/gas flux $(= H_g/v_g = \alpha_g\{\rho_g/[gw \cdot \max(\rho_f - \rho_g, 10^{-7}\text{kg/m}^3)\ ]\}^{1/2})$
CF	Coefficient of the velocity in the nondimensional liquid flux $(= H_f/v_f = \alpha_f\{\rho_f/[gw \cdot \max(\rho_f - \rho_g, 10^{-7}\text{kg/m}^3)\ ]\}^{1/2})$
CONSTC(I)	Constant c input by the user for the flooding correlation equation (vapor/gas intercept)
CONSTM(I)	Constant m input by the user for the flooding correlation equation (slope)
VLFJMX	Maximum liquid velocity allowed by the correlation equation using the explicit vapor/gas velocity from subroutine VEXPLT
DIFF	Coefficient of new-time liquid velocity in linearized flooding correlation Equation (7.3-8) $(= m^2 c_f)$
DIFG	Coefficient of new-time vapor/gas velocity in linearized flooding correlation Equation (7.3-8) $\left[= c\left(\frac{c_g}{v_g}\right)^{1/2} - c_g \right]$
DIFOLD	Right-hand side in linearized flooding correlation Equation (7.3-8) $\left[= c^2 - c\left(\frac{c_g}{c_g}\right)^{1/2} \right]$
DET	Inverse of determinant for the two-phasic velocity equations (later multiplied by dt). Similar to that used in subroutines VEXPLT, VIMPLT, and JCHOKE
VELGJC	Vapor/gas velocity at the vapor/gas intercept (where liquid velocity is zero)

Table 7.3-1 Glossary of important FORTRAN variables in subroutine CCFL. (Continued)

Variable	Description
VLEFJC	Liquid velocity at the liquid intercept (where vapor/gas velocity is zero)
VELFJ(I)	New explicit liquid velocity using flooding limit equation for the semi-implicit scheme
VELGJ(I)	New explicit vapor/gas velocity using flooding limit equation for the semi-implicit scheme
VFDPK(IX), VFDPL(IX)	New liquid velocity pressure derivatives using flooding limit equation for the semi-implicit scheme
VGDPK(IX), VGDPL(IX)	New vapor/gas velocity pressure derivatives using flooding limit equation for the semi-implicit scheme
COEFV(IDG-1)	Coefficient of new-time liquid velocity in linearized flooding correlation for the nearly-implicit scheme (=DIFF)
COEFV(IDG)	Coefficient of new-time vapor/gas velocity in linearized flooding correlation for the nearly-implicit scheme (=DIFG)
SOURCV(IS+1)	Right-hand side in linearized flooding correlation equation for nearly-implicit scheme (=DIFOLD)
DIFDPK(IX), DIFDPL(IX)	Limit flooding correlation equation pressure coefficients for nearly-implicit scheme

7.3.3 Assessment of Model

An assessment of the implementation of the CCFL model into ATHENA was carried out using both the semi-implicit and nearly-implicit schemes. In subroutine CCFL, we set $H_g = v_g$, $H_f = v_f$, m = 1, and c = 3.9316. Thus, Equation (7.3-1) has the form

$$v_g^{1/2} + v_f^{1/2} = 3.9316 \quad . \tag{7.3-9}$$

The ATHENA input deck used to model Dukler's air/water flooding test[7.3-11] for the code's developmental assessment was modified to simulate a gradual approach to the flooding limit, and the end-time used was 2.0 seconds. **Figure 7.3-4** shows the nodalization for this experiment. The junction between Components 105 and 104 was flagged to use Equation (7.3-9) if CCFL conditions were met. Runs were made with this junction oriented up and down, and the results were the same. **Figure 7.3-5** shows the vapor/gas and liquid velocities at this junction, with complete flooding (where the liquid velocity switches from downflow to upflow) occurring at approximately 1.26 seconds. **Figure 7.3-6** shows a plot for the square root of the liquid velocity versus the square root of the vapor/gas velocity. The plot shows that when the test problem calculation reached the flooding curve given by Equation (7.3-9), it followed it as desired.

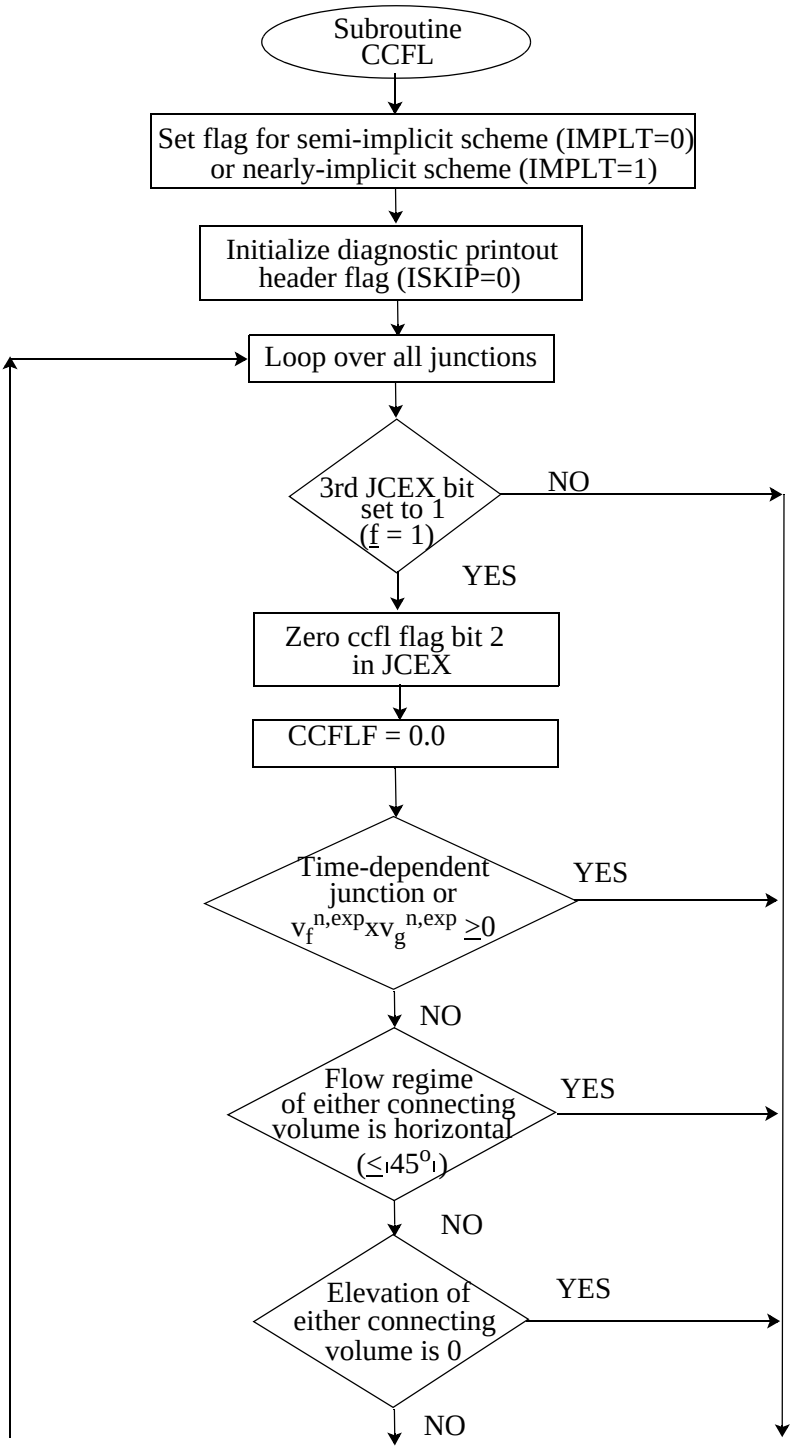

Figure 7.3-3 Flow chart for subroutine CCFL.

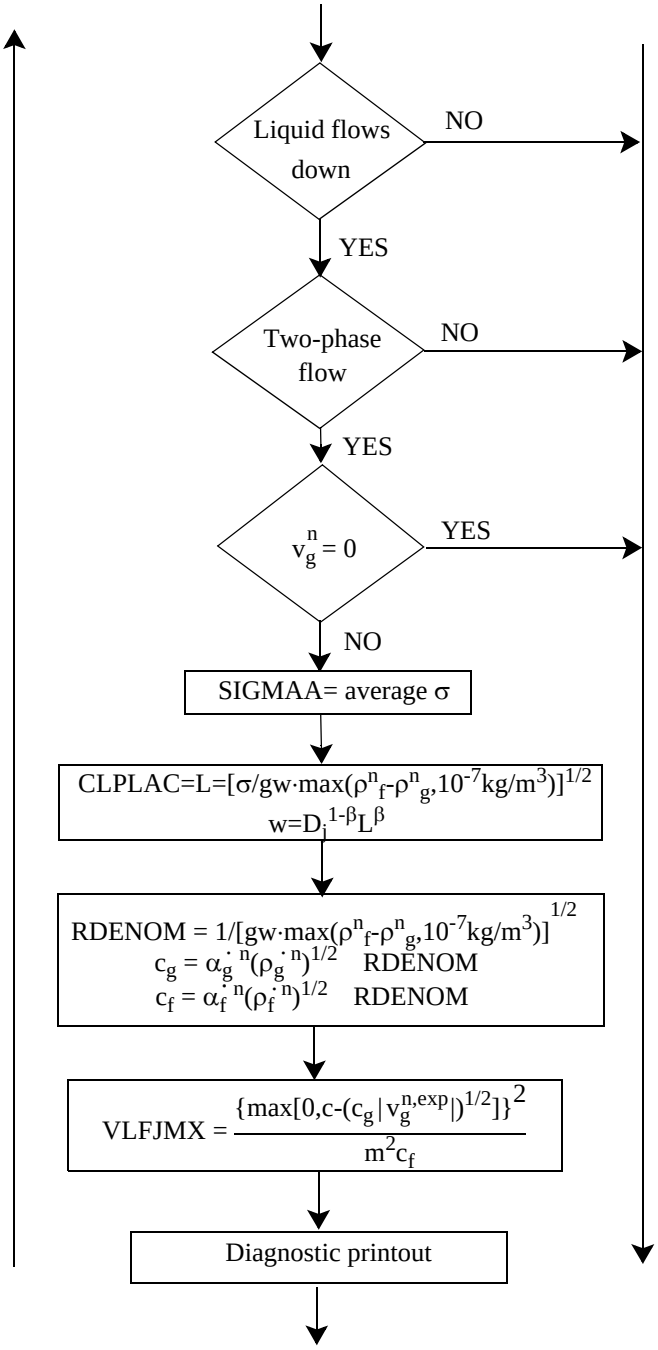

Figure 7.3-3 Flow chart for subroutine CCFL. (Continued)

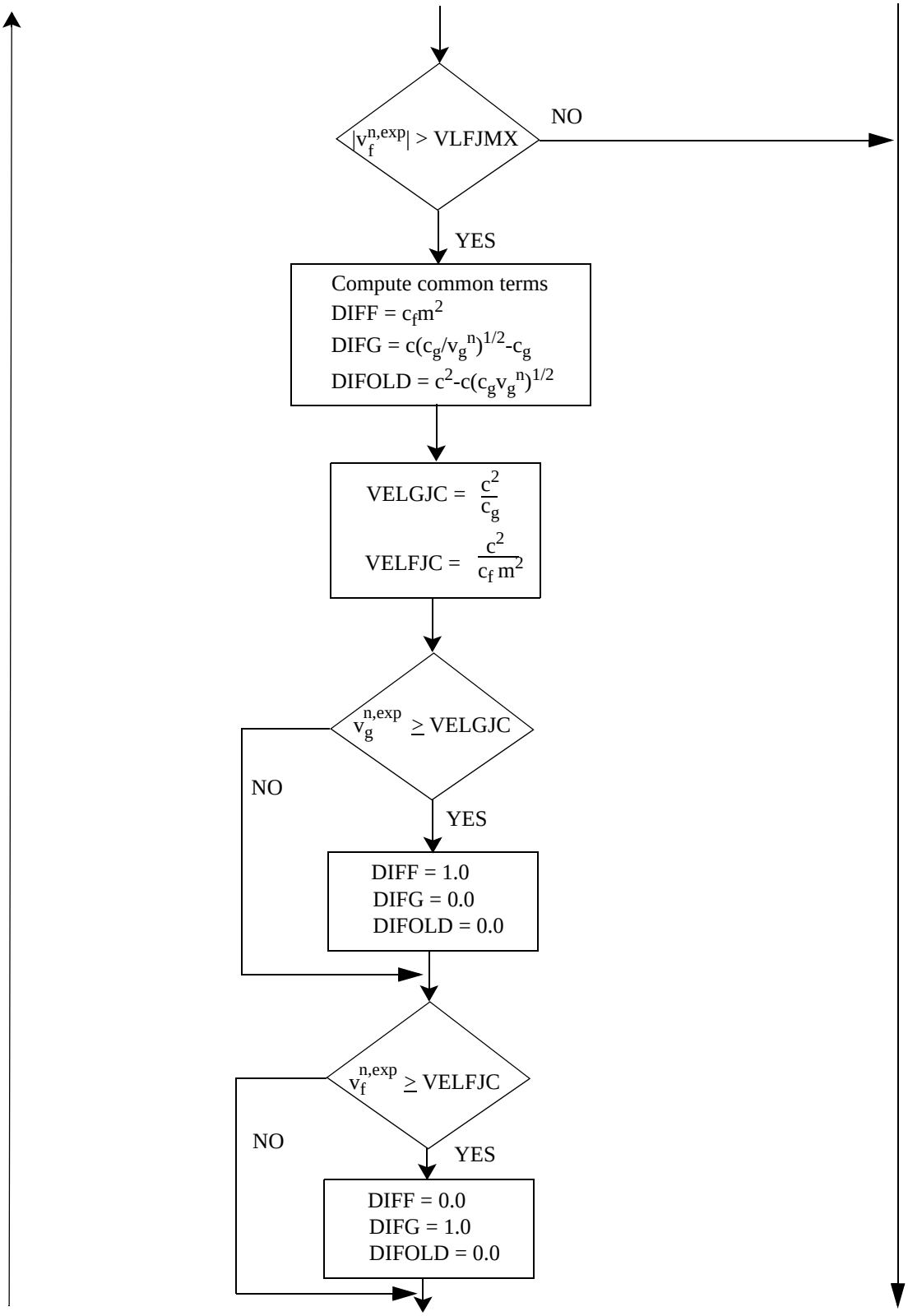

Figure 7.3-3 Flow chart for subroutine CCFL. (Continued)

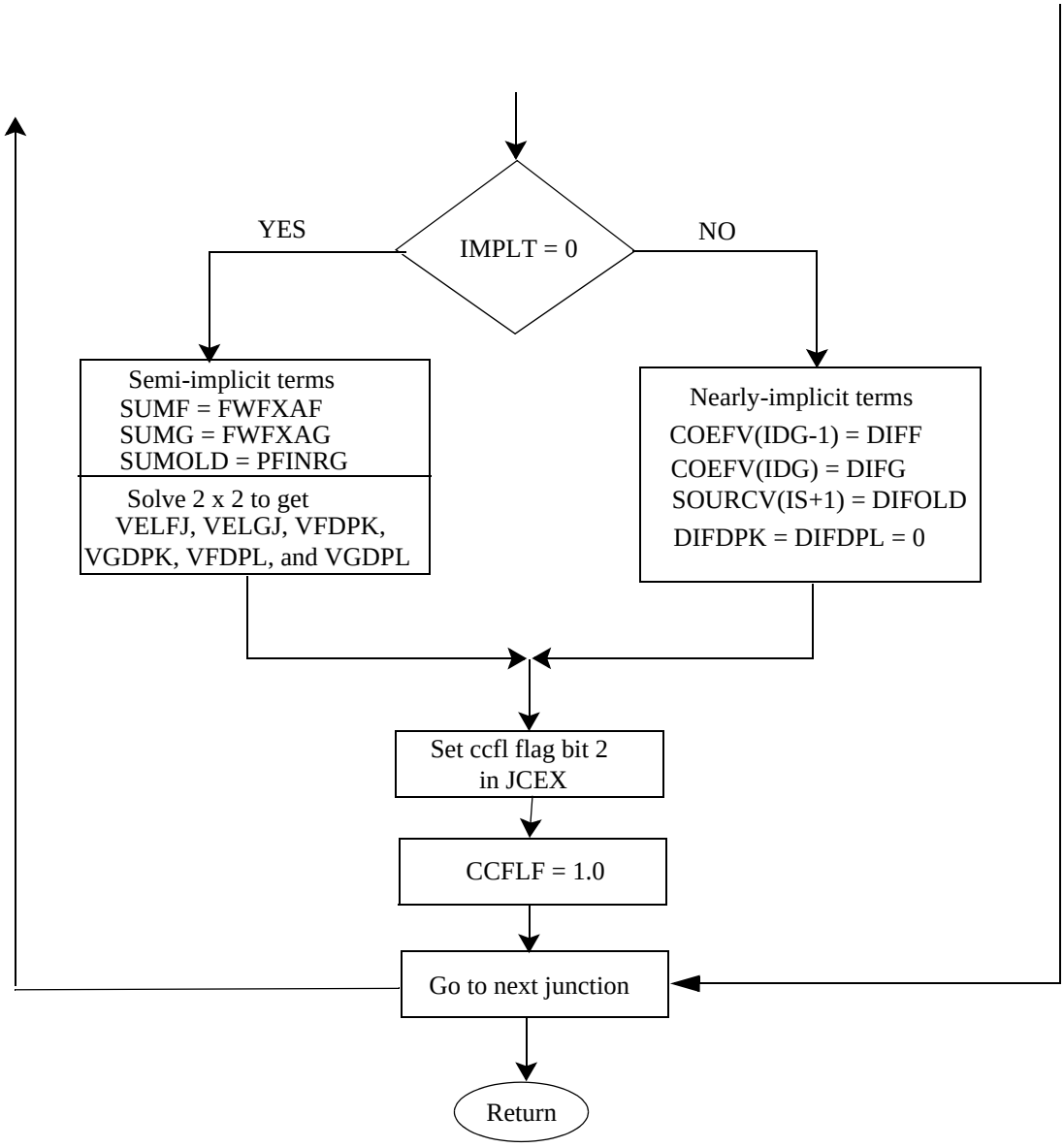

Figure 7.3-3 Flow chart for subroutine CCFL. (Continued)

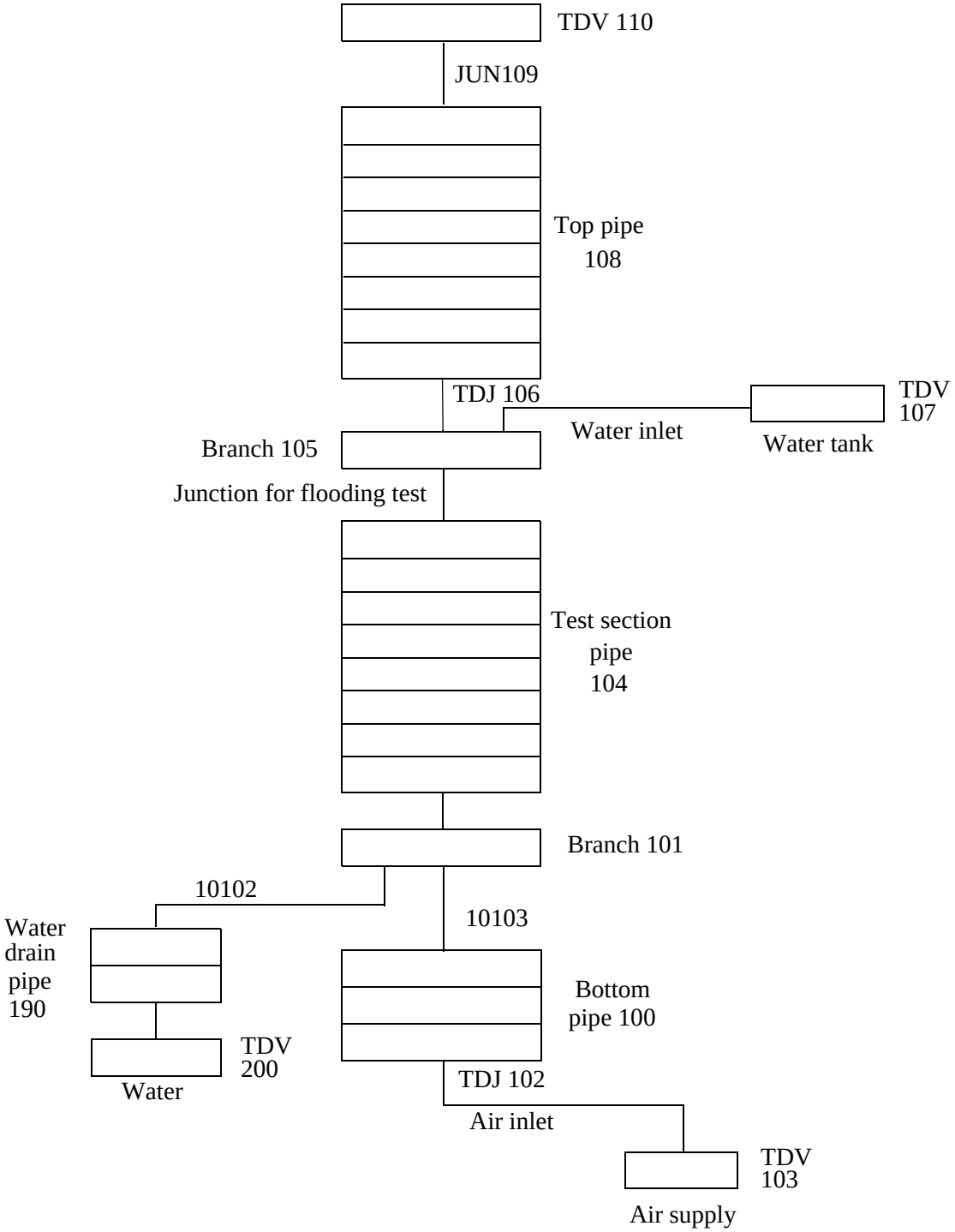

Figure 7.3-4 Nodalization for modified and original (unmodified) Dukler's air/water test problem.

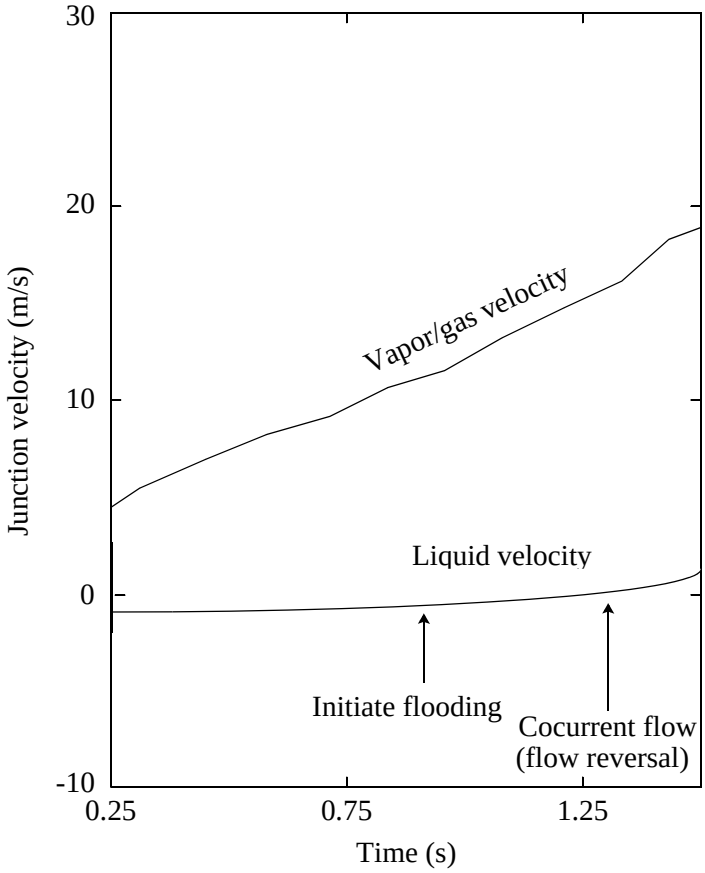

Figure 7.3-5 Liquid and vapor/gas velocities for modified Dukler's air/water test problem.

The results of modeling Dukler's actual air/water flooding test[7.3-11] are presented in Volume III of this code manual. The code results are quite close to the data when the CCFL model is used.

Wallis,[7.3-6] Bankoff,[7.3-8] and Tien[7.3-10] discuss the effects of viscosity, surface tension, and subcooling on the correlations. At the present time, these effects have not been directly incorporated into the form of the CCFL correlation used in ATHENA. It is anticipated that these, particularly the subcooling effects, will be addressed in future modifications to the code.

7.3.4 References

7.3-1. G. G. Loomis and J. E. Streit, *Results of Semiscale Mod-2C Small Break (5%) Loss-of-Coolant Accident Experiments S-LH-1 and S-LH-2*, NUREG/CR-4438, EGG-2424, Idaho National Engineering Laboratory, November 1985.

7.3-2. C. P. Fineman, "RELAP5/MOD2 Code Assessment for the Semiscale Mod-2C Test S-LH-1," *International ANS/ENS Topical Meeting on Thermal Reactor Safety, San Diego, California, February 2-6, 1986.*

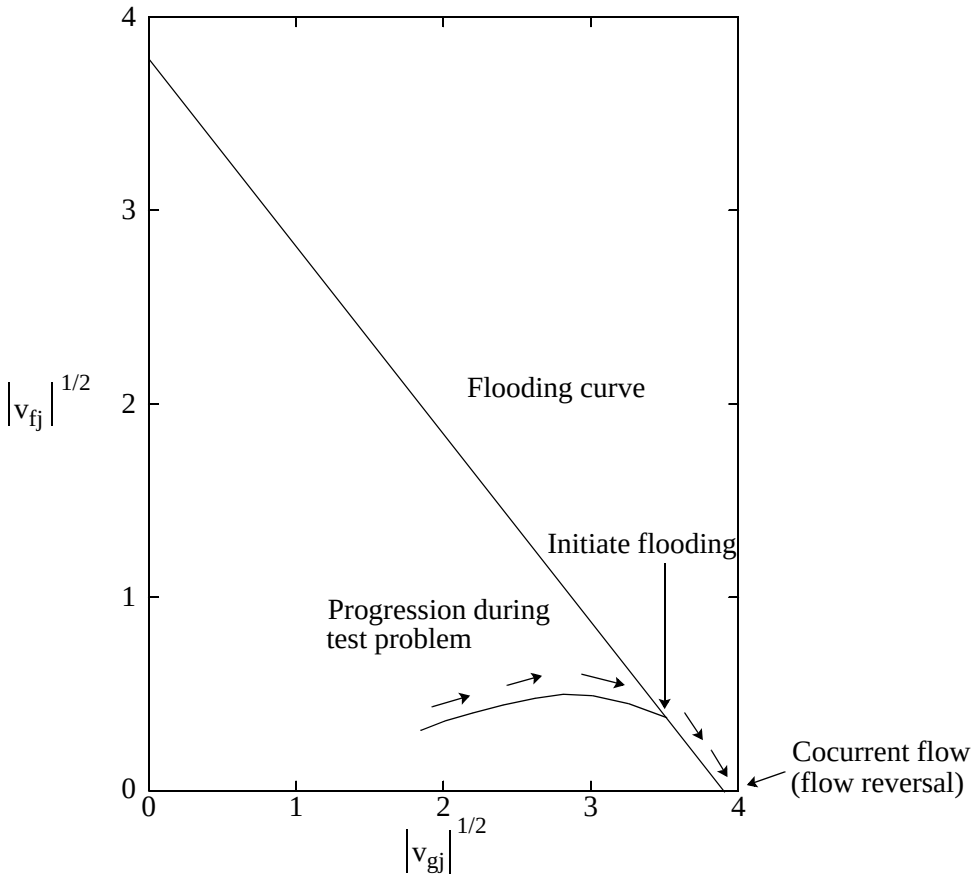

Figure 7.3-6 Overlay of velocities on flooding curve for modified Dukler's air/water test problem.

7.3-3. W. L. Weaver et al., *TRAC-BF1 Manual: Extensions to TRAC-BD1/MOD1*, NUREG/CR-4391, EGG-2417, Idaho National Engineering Laboratory, August 1986.

7.3-4. D. D. Taylor et al., *TRAC-BD1/MOD1: An Advanced Best Estimate Computer Program for Boiling Water Reactor Transient Analysis, Volume 1: Model Description,* NUREG/CR-3633, EGG-2294, Idaho National Engineering Laboratory, April 1984.

7.3-5. Y. Kukita et al., "Flooding at Steam Generator Inlets and Its Impacts on Simulated PWR Natural Circulation," *International Symposium on Natural Circulation, ASME Winter Annual Meeting, Boston, Massachusetts, December 13-18, 1987.*

7.3-6. G. B. Wallis, *One-dimensional Two-phase Flow,* New York: McGraw-Hill, 1969, pp. 336-341.

7.3-7. R. A. Riemke, "Countercurrent Flow Limitation Model for RELAP5/MOD3," *Nuclear Technology, 93,* 1991, pp. 166-173.

7.3-8. S. G. Bankoff, R. S. Tankin, M. C. Yuen, and C. L. Hsieh, "Countercurrent Flow of Air/Water and Steam/Water Through a Horizontal Perforated Plate," *International Journal of Heat and Mass Transfer, 24,* 1981, pp. 1381-1385.

7.3-9. M. W. Cappiello, *A Description of the TRAC-PF1/MOD1 CCFL Model,* LA-UR-87-294, Los Alamos National Laboratory, 1987.

7.3-10. C. L. Tien, K. S. Chung, and C. P. Liu, *Flooding in Two-Phase Countercurrent Flows,* EPRI NP-1283, December 1979.

7.3-11. A. E. Dukler and L. Smith, *Two Phase Interactions in Countercurrent Flow: Studies of the Flooding Mechanism,* NUREG/CR-0617, January 1979.

7.4 Stratification Entrainment/Pullthrough Model

7.4.1 Background

One of the assumptions used in ATHENA to convert the partial differential equations describing the evolution of two-phase flow into a set of ordinary differential equations that can be solved numerically is that the fluid within a given control volume is homogeneously mixed. This assumption implies that the fluid that is convected from one volume to the next has the same properties (void fraction, phasic temperatures, phasic densities, etc.) as the average properties in the volume from which the fluid originates. The numerical procedure based on this assumption is called donor or upwind differencing and is a standard technique in the modeling of flows of all types. One consequence of the assumption is numerical diffusion, which smears out the spatial gradient of the fluid properties within the flow passage being modeled. Another undesired property of this assumption is that the flux of mass and energy between volumes may be incorrectly computed if significant phase separation occurs in the donor volume. The homogeneously mixed assumption ignores such phase separation and causes additional computational errors.

Phase separation usually occurs due to gravitational forces (ignoring phase separation in specialized equipment designed to produce it using centrifugal forces), which cause the liquid phase to pool at the bottom of a vertical volume or on the bottom of a large horizontal pipe. This can occur if the flow rates of the phases in the volume are low enough so that gravitational forces overcome the frictional force between the phases that tends to keep the phases well mixed. The phase separation caused by gravitational forces is called flow stratification in ATHENA, and there are stratification regions in both the vertical and horizontal flow regime maps described in Section 3.

7.4.1.1 Horizontal Volumes. One consequence of stratification in a large horizontal pipe is that the properties of the fluid convected through a small flow path in the pipe wall (i.e., a small break), called an offtake, depend on the location of the stratified liquid level in the large pipe relative to the location of the flow path in the pipe wall. If the offtake is located in the bottom of the horizontal pipe, liquid will flow through the offtake until the liquid level starts to approach (but not reach) the bottom of the pipe, at which time some vapor/gas will be pulled through the liquid layer and the fluid quality in the offtake will

increase. If the phase separation phenomenon is ignored, vapor/gas will be passed through the offtake regardless of the liquid level in the pipe. Likewise, if the offtake is located at the top of the pipe, vapor/gas will be convected through the offtake until the liquid level rises high enough so that liquid can be entrained from the stratified surface. The flow quality in the offtake will decrease as the liquid level rises. If the phase separation phenomenon is ignored, liquid will pass through the offtake for all stratified liquid levels regardless of their height relative to the offtake. Lastly, if the offtake is located in the side of the large horizontal pipe, the same phenomenon of vapor/gas pullthrough or liquid entrainment will occur, depending on the elevation of the stratified liquid level in the pipe relative to the location of the offtake in the wall of the pipe. These several situations are shown in **Figure 7.4-1.**

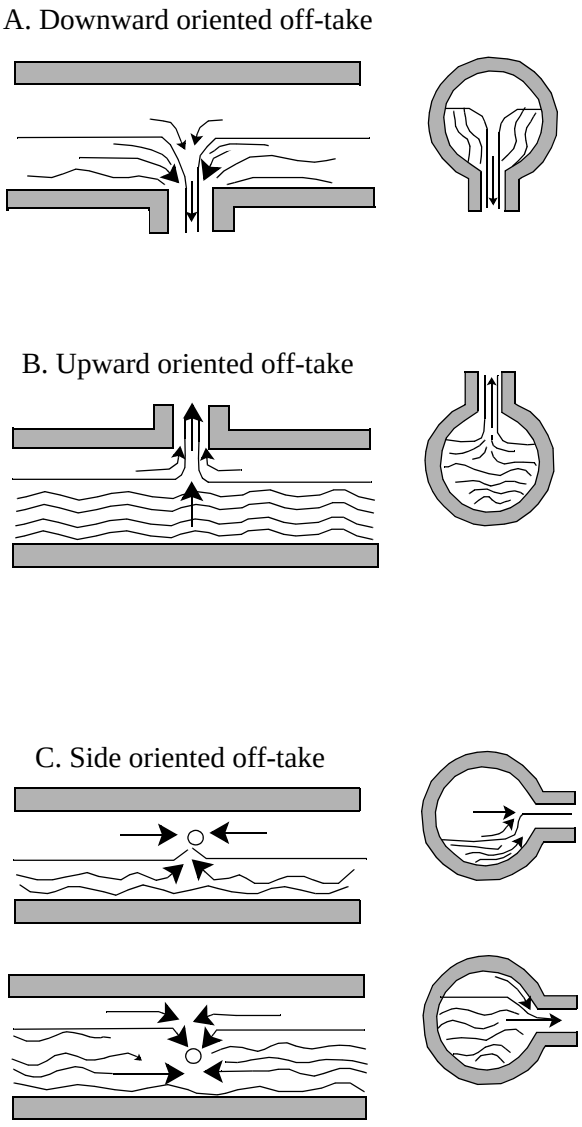

Figure 7.4-1 Phase separation phenomena in various offtakes.

The ATHENA stratification entrainment/pullthrough model[7.4-1,7.4-2] for horizontal volumes accounts for the phase separation phenomena and computes the flux of mass and energy through an offtake attached to a horizontal pipe when stratified conditions occur in the horizontal pipe. This model is sometimes refered to as the offtake model. The importance of predicting the fluid conditions through an offtake in a small-break LOCA has been discussed in detail by Zuber.[7.4-3]

7.4.1.2 Vertical Volumes. With the development of a mechanistic two-phase level tracking model, the code is able to model stratified flow in vertical volumes. If a junction is attached to the side of a vertical volume, the fluid properties convected through the junction depend upon the position of the two-phase mixture level relative to the offtake in a manner analogous to the dependence of the properties convected through a junction attached to the side of a horizontal volume. The original implementation of the entrainment/pullthrough model for horizontal volumes has been modified to consider the case of a junction attached to the side of a vertical volume. A vertical volume is a one-dimensional volume in which the primary flow direction (i.e., the 'x' direction) is oriented in the vertical direction or a volume in the multi-dimensional component in which the 'z' direction is oriented vertically. If a junction is attached to the 'side' of a vertically oriented volume, i.e., attached to the 'y' or' 'z' faces of a vertically oriented one-dimensional volume or to the 'x' or 'y' faces of a volume in the multi-dimensional component, the user may activate the 'side offtake' section of the entrainment/pullthrough model. The computation for the 'side offtake' is the same regardless of whether the main volume is oriented horizontally or vertically. The only difference between the two computations is the determination of the height of the stratified liquid interface relative to the offtake.

7.4.2 Model Description

There have been several recent experimental studies of the phase separation phenomena that are relevant for PWR small break LOCA analysis.[7.4-4,7.4-5,7.4-6,7.4-7] The range of pressure in these studies was 0.2 to 6.2 MPa, and either air-water or steam-water fluids were utilized.

The offtake pipe was located at the top, bottom, or side of the large horizontal pipe. Experiments were conducted by establishing a steady-state in which known flow rates of liquid and vapor/gas were introduced into the main pipe. The mass flow rate and the flow quality in the offtake pipe were measured by either separating the phases or by using calorimetric methods. The liquid depth in the main pipe was measured visually or with a gamma densitometer. In all the experimental studies, the critical depth for the onset of vapor/gas pullthrough or liquid entrainment was measured.

7.4.2.1 Inception Height. The results of the experiments showed that in most cases the depth or height (i.e., the distance between the stratified liquid level and the elevation of the offtake) for the onset of liquid entrainment or vapor/gas pullthrough could be defined by an equation of the form

$$h_b = \frac{C W_k^{0.4}}{[g\rho_k(\rho_f - \rho_g)]^{0.2}} \qquad (7.4\text{-}1)$$

where subscript k refers to the continuous phase in the offtake, which is the phase flowing through the offtake before the onset of pullthrough or entrainment of the other phase. For an upward offtake, the vapor/gas phase is the continuous phase. For a downward offtake, the liquid phase is the continuous phase. For a side offtake, the vapor/gas phase is the continuous phase when the liquid level is below the offtake center and the liquid phase is the continuous phase when the liquid level is above the offtake center. The variable W_k is the mass flow rate of the continuous phase in the offtake. This correlation is based on the work of Smoglie,[7.4-4] who derived an equation of this form for the case of liquid entrainment into a side or top offtake by considering the force exerted on the liquid by the accelerating vapor/gas flow. A similar equation was derived in **Reference 7.4-8** and **Reference 7.4-9** for the onset of vapor/gas pullthrough in the draining of a tank through an orifice in the bottom of the tank by using surface instability arguments. The constant C for the various arrangements of offtake and liquid level is discussed next.

7.4.2.1.1 Top Offtake--The onset of liquid entrainment through a top offtake was correlated by a value of C in the range of 1.2 to 2.2 for the high-pressure steam-water data of **Reference 7.4-5**, with the tendency of C to decrease as the diameter of the offtake increased. The air-water and steam-water data of **Reference 7.4-6** were correlated by C equal to 1.60, while the air-water data of **Reference 7.4-4** was correlated by a value of 1.67. A value of 1.67 was chosen to characterize the experimental data for the onset of liquid entrainment through a top offtake.

7.4.2.1.2 Bottom Offtake--The value of C for the onset of vapor/gas pullthrough in a bottom offtake was found to be strongly influenced by the liquid flow rate in the main pipe. Smoglie[7.4-4] found that a value of C = 2 was appropriate for stagnant or low-flow conditions in which a vortex was formed at the offtake. A value of C = 1.17 was appropriate if there was significant liquid flow in the main pipe and the vortex was suppressed. The results of several steam-water experiments[7.4-5,7.4-7] suggest values in the range of 0.95 to 1.1. In the air-water and steam-water experiments of **Reference 7.4-6**, C was found to depend on the liquid depth and the diameter of the offtake pipe; these data were correlated by values of C in the range of 1.25 to 1.9. A value of 1.5 was chosen to characterize the experimental data for the onset of vapor/gas pullthrough.

7.4.2.1.3 Side Offtake--For the side offtake geometry, there is good consistency among the results of the various experimental studies. **Reference 7.4-4** suggests a value of C = 0.75 for the onset of vapor/gas pullthrough and a value of C = 0.69 for the onset of liquid entrainment through a side offtake. The air-water and steam-water data in **Reference 7.4-6** suggest the value of 0.69 for the onset of liquid entrainment, while the steam-water data in **Reference 7.4-5** suggest a value of 0.62 for the onset of both vapor/gas pullthrough and liquid entrainment. The INEEL data in **Reference 7.4-7** suggests C = 0.82 for vapor/gas pullthrough and C = 0.62 for liquid entrainment. In all of these experiments, the liquid flow rate in the main pipe had only a weak effect on the onset of pullthrough or entrainment. A value of 0.75 was chosen to characterize the data for the onset of vapor/gas pullthrough in a side offtake, and a value of 0.69 was chosen to characterize the data for the onset of liquid entrainment through a side offtake.

Based on the experimental studies, it may be concluded that the use of Equation (7.4-1) should give a reasonable representation of the test data if the following values are adopted for the correlation constant C:

C = 1.67 for top offtake liquid entrainment;

= 1.50 for bottom offtake vapor/gas pullthrough;

= 0.75 for side offtake vapor/gas pullthrough; and

= 0.69 for side offtake liquid entrainment.

7.4.2.2 Offtake Flow Quality. Once the inception criterion for the given geometry of offtake location and liquid level has been exceeded, pullthrough or entrainment will begin. Correlations for the rate of minor-phase pullthrough or entrainment have been developed that describe the flow quality in the offtake as a function of the nondimensional distance between the offtake and the stratified liquid level. The reference height or depth is the inception height or depth. Separate correlations have been developed for the several geometric arrangements and are discussed below.

7.4.2.2.1 Top Offtake--The flow quality through a top offtake is given by[7.4-6]

$$X = R^{3.25(1-R)^2} \tag{7.4-2}$$

where

$$R = \frac{h}{h_b} \tag{7.4-3}$$

and h is the distance from the stratified liquid level to the junction.

7.4.2.2.2 Bottom Offtake--The flow quality through a bottom offtake is given by[7.4-6]

$$X = e^{-3.1R}(1-R^2)^{3.5} \tag{7.4-4}$$

where R is given by Equation (7.4-3).

7.4.2.2.3 Side Offtake--The correlation for the flow quality through a side offtake has the form[7.4-4]

$$X = X_o^{1+CR}\,[1 - 0.5R\,(1+R)X_o^{(1-R)}]^{0.5} \tag{7.4-5}$$

where

C = 1.09 for vapor/gas pullthrough

= 1.00 for liquid entrainment

$$X_o = \frac{1.15}{1 + \left(\frac{\rho_f}{\rho_g}\right)^{1/2}} ,$$

and the other variables have been defined previously.

These correlations are plotted in **Figure 7.4-2**, **Figure 7.4-3**, and **Figure 7.4-4** for steam-water flow at pressures of 0.70 and 7.0 MPa. Note that the saturated steam and water at a pressure of 0.7 MPa has a density ratio approximately equal to that of air-water at 20°C and a pressure of 0.35 MPa. The experimental data of **Reference 7.4-4**, **Reference 7.4-5**, **Reference 7.4-6**, and **Reference 7.4-7** are also shown on the figures. For each experimental point, the appropriate value of the inception height has been computed using Equation (7.4-1). It can be seen that the correlations give a reasonable overall representation of the test data. However, some detailed trends are apparent that are not captured by the correlations.

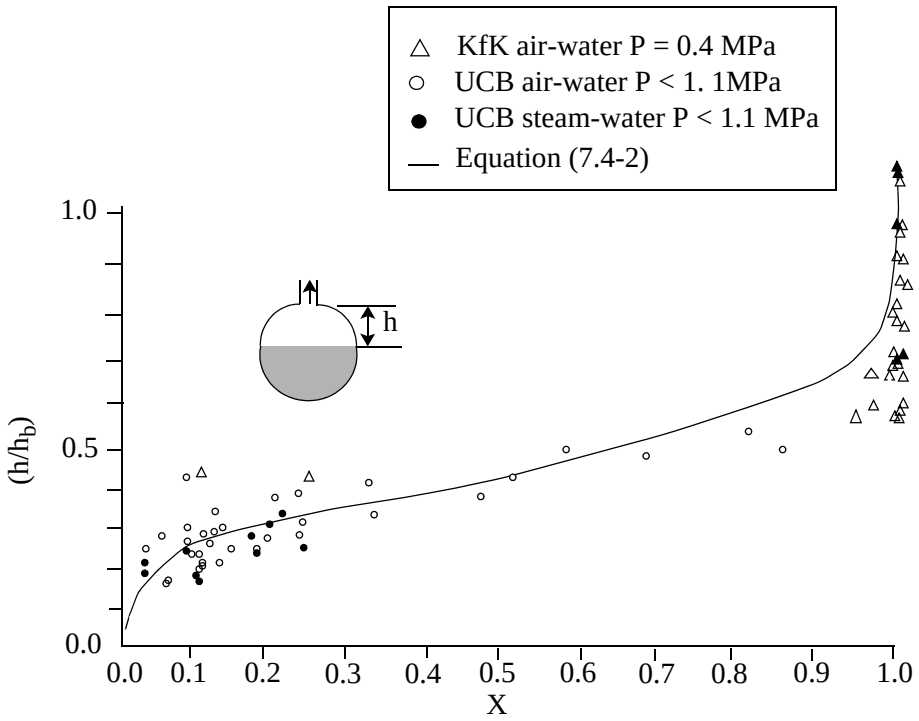

Figure 7.4-2 Discharge flow quality versus liquid depth for an upward offtake branch.

7.4.3 Model As Coded

The correlations for the critical offtake height and the offtake discharge quality described in the previous section were developed from data taken in well-controlled experimental situations. The

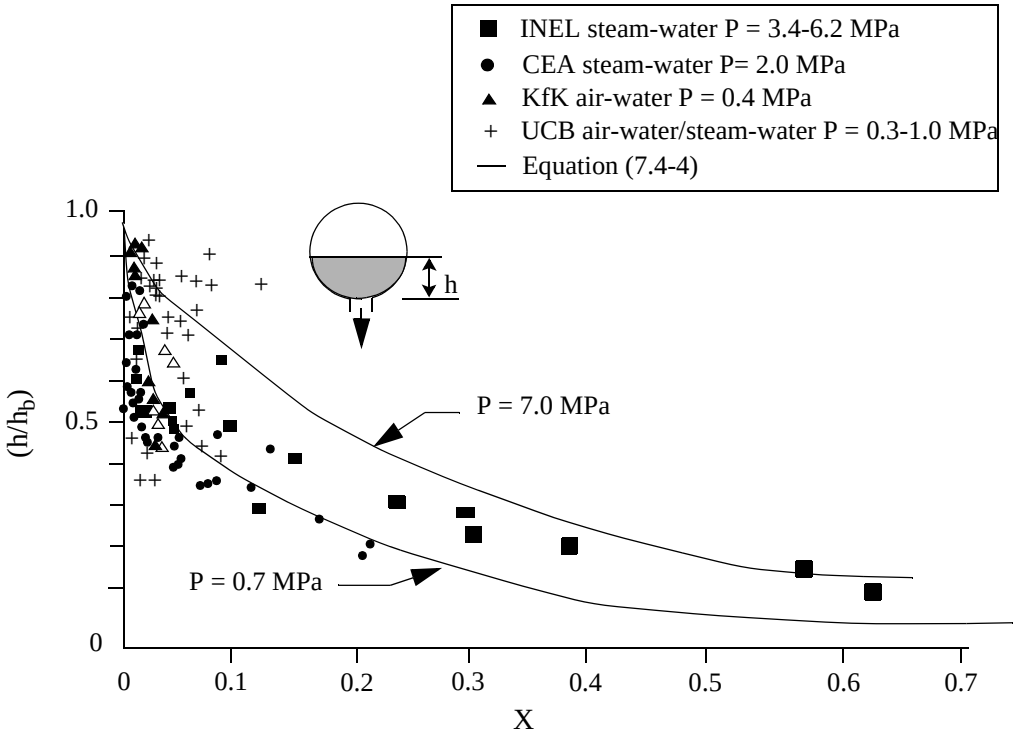

Figure 7.4-3 Discharge flow quality versus liquid depth for a downward offtake branch.

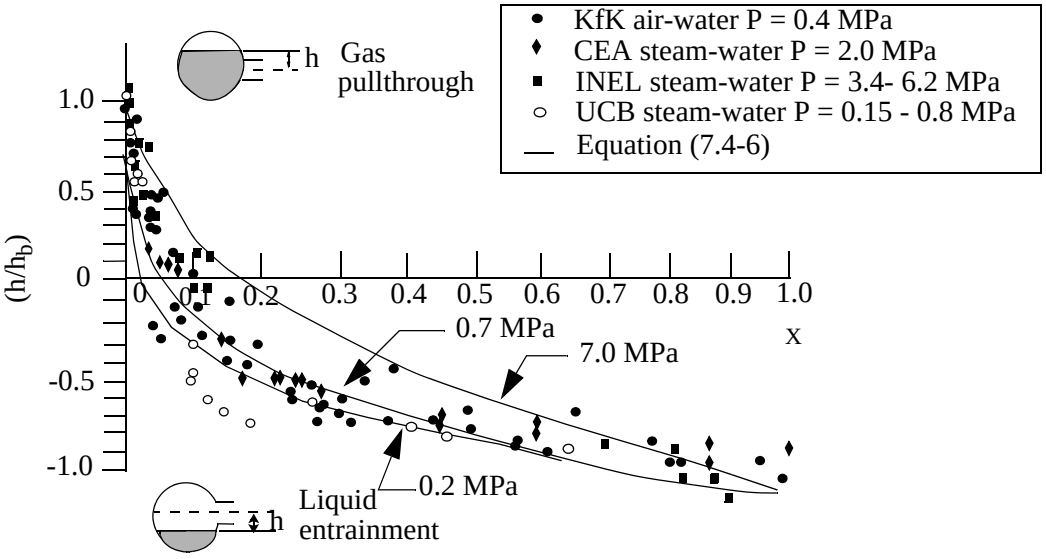

Figure 7.4-4 Discharge flow quality versus liquid depth for a horizontal offtake branch.

correlations were developed for cocurrent flow in the offtake and horizontally stratified flow in the main pipe. ATHENA is a general-purpose code, and the conditions under which the offtake model may be applied may not have been covered in the experiments from which the correlations were developed. For example, the flow in the main pipe may not be low enough for horizontally stratified flow according to the flow regime map or the flow in the offtake may be countercurrent flow. In addition, there are other physical restrictions on the applicability of the correlations, such as applying the pullthrough correlations when the flow in the main pipe is entirely liquid with no vapor/gas and, conversely, trying to apply the liquid entrainment correlation when the flow in the main pipe is entirely vapor/gas. Finally, there are numerical implementation questions such as the effect of the model on the stability of the numerical solution procedure used in ATHENA. The resolution of these questions and others has affected the implementation of the stratification entrainment/pullthrough model.

The stratification entrainment/pullthrough model is implemented in subroutine HZFLOW, which computes the phasic void fractions to be used for the computation of the mass and energy convected through a junction if the user has activated the model at that junction. The following sections first describe general considerations for the implementation of the stratification entrainment/pullthrough model in ATHENA and then discuss several limitations and restrictions placed on the model.

7.4.3.1 General Considerations. All of the modifications that are made to the model originate from attempts to generalize the correlations as described above to cover all geometries and flow conditions, to make the model computationally robust (i.e., to prevent code failures due to dividing by zero), and to make the model more computationally efficient by implementing the model in such a way that larger time steps can be taken without oscillations in the code results. The limits that are placed on intermediate results to make the model computationally robust and prevent code failures are obvious and will not be discussed further. The modifications that attempt to expand the range of applicability of the model to all geometries and flow conditions are discussed in Section 7.4.3.2, and modifications used to enhance the numerical efficiency of the model are discussed in Section 7.4.3.3. No attempt has been made to follow the actual subroutine logic in the discussions that follow, although modifications that expand the applicability of the model are made before modifications concerning numerical stability.

7.4.3.2 Model Applicability. The correlation for the critical height at the onset of minor-phase pullthrough or entrainment, as well as the correlations for the flow quality in the offtake, was developed from data generated under well-controlled conditions in specific geometries. The correlations developed are applicable for (a) cocurrent outflow in the offtake, (b) horizontally stratified flow in the main pipe, and (c) offtakes whose diameter is small relative to the diameter of the main pipe. Some or all of these conditions may be violated for a junction to which the horizontal stratification entrainment/pullthrough model is to be applied in the ATHENA code.

7.4.3.2.1 Countercurrent Flow in the Offtake--In ATHENA, the phasic area fractions (i.e., void fraction for the vapor/gas phase and liquid fraction for the liquid phase) used to compute the phasic fluxes of mass and energy through a junction are the phasic area fractions in the upstream volume, where upstream is based on the phasic velocity direction. If the flow in the junction is cocurrent, the phasic area fractions will sum to a value of one, since they are computed from the conditions in the same upstream volume. If the flow at the junction is counter-current, the phasic area fractions in the junction will not necessarily sum to a value of one, since they are computed from conditions in different volumes. If the

phasic area fractions in the junction were rescaled so they sum to a value of one, it can be shown that this will lead to a numerical instability. The same logic is used if the horizontal stratification entrainment/pullthrough model has been activated by the user at a junction. If the flow in the junction is cocurrent, the stratification entrainment/pullthrough model is used to compute the phasic area fraction of the minor (other) phase if the upstream volume is horizontal; the other area fraction is computed so that they sum to a value of one. If the flow in the offtake junction is counter-current, the stratification entrainment/pullthrough model is used to compute the area fraction of a phase if the upstream volume for that phase is horizontal and the area fractions will not necessarily sum to a value of one. However, there are four combinations of phasic velocity direction that will cause problems and must be handled differently. These situations are:

1. A vapor/gas outflow from above a liquid level that could cause liquid entrainment except that the liquid flow is into instead of out of the offtake.

2. A liquid outflow through an offtake from below a liquid level that could cause vapor/gas pullthrough except that the vapor/gas flow is into instead of out of the offtake.

3. A vapor/gas outflow from below a liquid level that would be pulled through the liquid except that the liquid flow is into instead of out of the offtake.

4. A liquid outflow from above a liquid level which would be entrained by the vapor/gas flow except that the vapor/gas flow is into instead of out of the offtake where outflow means flow out of the large horizontal pipe and inflow means flow into the large horizontal pipe.

Figure 7.4-5 shows these situations for a side junction. Cases 1 and 2 are situations in which the major phase velocity direction would indicate that the minor phase would be entrained (case 1) or pulled through (case 2) except that the upstream volume for the minor phase is not a large horizontal pipe, as required by the model. In these situations, the reversed flow of the minor phase is ignored, since the flow rate of the minor phase does not appear in the critical depth correlation. The junction quality correlation is used to compute the area fraction of the major phase, and the area fraction of the minor phase is computed from conditions in its upstream volume.

Cases 3 and 4 are situations in which the minor phase velocity indicates that pullthrough (case 3) or entrainment (case 4) are possible except that the major phase velocity indicates that the upstream volume for the major phase is not the large horizontal volume, as required by the stratification entrainment/pullthrough model. In these situations, a fix-up is required that will not introduce large discontinuities in the phasic area fractions during velocity reversals or when the level crosses a side offtake. For the situation in which the major phase velocity is reversed, the minor phase area fraction is computed from the correlations as if the major phase velocity is outward at the limit of zero. The area fraction of the major phase is computed for conditions in its upstream volume. This prevents discontinuities at phase reversals. Since the offtake quality correlation is independent of phase velocity as the level reaches the center of a side offtake, no problems are encountered for this situation.

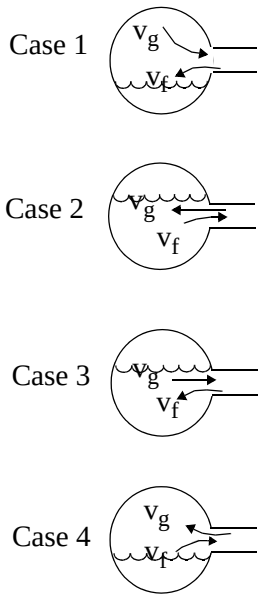

Figure 7.4-5 Four cases of countercurrent flow in a side offtake.

7.4.3.2.2 Offtakes of Non-Negligible Area--The model correlations were developed from data sets in which the offtake diameter was small relative to the diameter of the main pipe. However, in ATHENA, the user may specify a geometry in which the offtake diameter is not small with respect to the diameter in the horizontal pipe. The phasic area fractions are modified to take the offtake diameter into account in order to make the model more robust by smoothing the phasic area fractions at the junctions as the liquid level approaches the elevation of the offtake. The smoothing procedure for side offtakes is different than the procedure for top and bottom offtakes. The two procedures will be discussed separately.

Top or Bottom Offtake of Non-Negligible Area

The purpose of the modifications of the phasic area fractions in top or bottom junctions is to smooth the area fractions so that they will not have a large discontinuity as the main horizontal pipe fills up or empties completely. The smoothing is based on the physical picture. Looking into the main pipe through the offtake, if the liquid level is near the offtake and the edge of the interface between the liquid and vapor/gas space is in the field of view, smoothing is applied (see **Figure 7.4-6**). The phasic area fraction is interpolated to the donor value based on the fraction of the field of view not occupied by liquid for a bottom offtake and according to that occupied by liquid for a top offtake. For a bottom offtake, the relevant equations are

$$\begin{aligned} \alpha_f &= 1 - \alpha_g^c && \text{for } \alpha_{gK} \geq 0.5 \text{ or } \sin\phi > 1 \\ &= 1 - \frac{2}{\pi}(\sin\phi\cos\phi + \phi) && \text{otherwise} \end{aligned} \qquad (7.4\text{-}6)$$

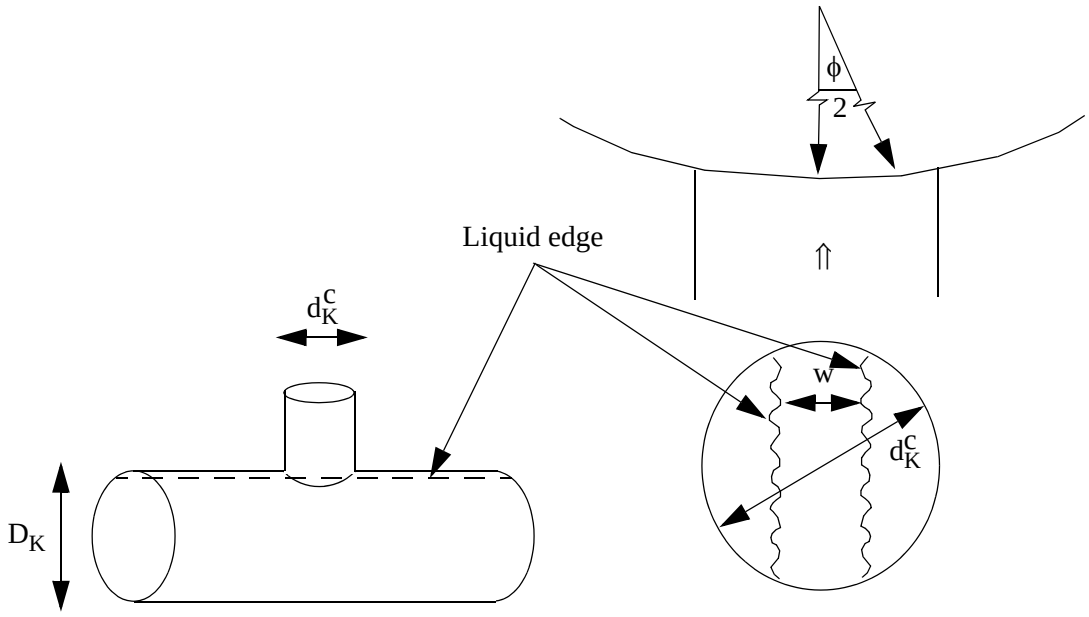

Figure 7.4-6 Smoothing to avoid discontinuities in top or bottom offtake of non-negligible area.

where

$$\sin\phi = \frac{w}{\min(D_K, d_K^c)}$$

$$d_K^c = D_K\left(\frac{A_j}{A_K}\right)^{\frac{1}{2}}$$

α_g^c = void fraction from pullthrough correlation

K = value in the main pipe

where the diameter of the offtake is computed from the diameter of the main pipe and the square root of the ratio of the flow areas in the main pipe and offtake.

Side Offtake of Non-Negligible Area

ATHENA contains coding for treating the case where the liquid level in the main pipe is between the elevations of the top and bottom of the side branch entrance. The procedure used ensures that the phasic area fractions in the offtake junction tends to the phasic area fractions in the main pipe as the flow area in the offtake junction approaches the area of the main pipe. The diameter of the offtake junction is checked against the diameter of the main pipe for the case of a horizontal main pipe during the initialization phase

of the computation and an error message issued if the offtake junction is larger than the main pipe. For the case of a side junction attached to a vertical volume, the diameter of the offtake junction is checked against the dimensions of the volume face to which it is attached to ensure that the offtake junction fits entirely within the face to which it is attached.

Consider the case where the liquid level in the main pipe is above the center of the side offtake. Let α_g^* be the vapor/gas area fraction at which the liquid level would be at the elevation of the top of the side offtake and let α_g^c be the vapor/gas area fraction computed from the pullthrough correlations. The subscript K is the value in the main pipe. Then, the interpolated vapor/gas area fraction would be given by

$$\alpha_f = 1 - \alpha_g^c \qquad \text{for } \alpha_g^* \geq \alpha_{gK}$$

$$= 1 - \left[\left(\frac{\alpha_g^*}{\alpha_{gK}} \right) \alpha_g^c + \left(1 - \frac{\alpha_g^*}{\alpha_{gK}} \right) \alpha_{gK} \right] \qquad \text{for } \alpha_g^* < \alpha_{gK} \tag{7.4-7}$$

where

$$\alpha_g^* = \min (\alpha_g^*, 0.49) \; . \tag{7.4-8}$$

There is an additional modification that limits the minimum value of the vapor/gas area fraction at which the liquid level reaches the elevation of the top of the offtake. This modification ensures that the width of the interpolation window is sufficiently wide that the code takes several advancements to traverse the interpolation zone. If this were not done, the code could traverse the interpolation zone in one advancement and no smoothing would be used.

7.4.3.2.3 High Flow or Extreme Voids in Main Pipe--The stratification entrainment/pullthrough model correlations were developed from data in which the flow rates in the main pipe were low enough that horizontally stratified flow was obtained. In the implementation of the stratification entrainment/pullthrough model for horizontal volumes in ATHENA, the same criteria used in horizontal stratification (see Volume I, Section 3 and Section 3.1.1 of this manual) are used. This uses mass flux G and relative velocity $|v_g - v_f|$. The same interpolation zone is defined in which the junction phasic area fractions are linearly interpolated between the values computed from the stratification entrainment/pullthrough model for horizontal volumes and the donor values.

Another requirement is that the maximum of the upstream volume mass flux and the junction mass flow (upstream area) must be less than 3,000 kg/m^2•s. This choice should suppress the horizontal stratification entrainment/pullthrough model for horizontal volumes if there is high flow anywhere in the upstream volume.

The stratification entrainment/pullthrough model for horizontal volumes must also recognize that there is a sufficient amount of the minor phase in its upstream volume before trying to pull it through or entrain it. Two interpolation regions are defined, and the junction phasic area fraction is linearly interpolated to the donor value as the area fraction goes to zero. The vapor/gas interpolation region is defined as

$$0 \leq \alpha_{gK} \leq 10^{-5} \tag{7.4-9}$$

in which the vapor/gas pullthrough is suppressed as the main pipe completely fills with liquid. The liquid interpolation region is defined as

$$0 < \alpha_{fK} \leq \max\left[2\times10^{-7}, \min\left(2\times10^{-4}, 2\times10^{-3}\frac{\rho_{gK}}{\rho_{fK}}\right)\right] \tag{7.4-10}$$

where the interpolation function suppresses the liquid entrainment as the main pipe completely fills with vapor/gas. The interpolation function based on the mass flux is multiplied by the interpolation function based on the minor phase content of the main pipe to define an overall interpolation function, which is used to interpolate the offtake junction phasic area fractions between the value obtained from the stratification entrainment/pullthrough model for horizontal volumes and the donor value. This combined interpolation smooths out the phasic area fraction used in the time advancement of the conservation equations as the horizontal stratification entrainment/pullthrough model for horizontal volumes is activated and deactivated.

7.4.3.2.4 Large Critical Heights--It is conceivable that the critical height computed from the model correlations could be larger than the diameter of the main pipe, in the case of a top or bottom offtake, or larger than the radius of the main pipe, in the case of a side offtake. In this case, the offtake quality correlations would predict vapor/gas pullthrough when the main pipe was full of liquid or liquid entrainment when the main pipe was full of vapor/gas. Such extreme values of the critical height take the correlations out of the range of their applicability. In the implementation of the stratification entrainment/pullthrough model for horizontal volumes in ATHENA, the range of the critical height is limited to lie within the span of the main pipe. This implies that there will be less pullthrough or entrainment when the critical height is limited because the height ratio R will be smaller than it would have been if the critical height had not been limited.

7.4.3.3 Numerics of Implementation. The straightforward implementation of the correlations and extensions described above using beginning of time advancement values for all the required properties could lead to code instability, since the offtake phasic area fractions implied by the quality correlations are implicit functions. The junction flow quality is a function of the height ratio R, which is a function of the phasic flow rate, which is a function of the phasic area fraction. Several improvements on an explicit evaluation of the model have been implemented to improve the numerical stability of the model so that larger time steps can be taken without oscillations appearing in the solution.

7.4.3.3.1 Time Level of Properties--The beginning of time advancement values of almost all of the property variables are used. The exceptions are the phasic area fractions, which are used to evaluate the major phase flow rate W_k in Equation (7.4-1). The junction values used for the previous time step are used rather than the current donor values, since they would most likely have been computed from the stratification entrainment/pullthrough model for horizontal volumes in the previous time step and the same values would be used if the time step should have to be repeated. The second exception occurs if the flow rate computed using the phasic area fraction from the previous time step predicts that there would be no pullthrough or entrainment for this time step. Then, the computation is repeated using a flow rate calculated assuming no pullthrough or entrainment in the previous time step. This helps to avoid large perturbations as pullthrough or entrainment starts or stops.

7.4.3.3.2 Conditioning the Correlations--Some of the offtake quality correlations contain terms of the form

$$[1 - 0.5R\,(1 + R)X_o^{(1-R)}]^{0.5}$$

which changes rapidly in the region of R = 1. To avoid numerical instabilities due to this behavior, the correlations are conditioned by replacing this term by a linear variation between its value at R = 0.9 and R = 1.0. This term is used in Equation (7.4-5), and it is prevented from being negative. The quantity $(\rho_f - \rho_g)$ is prevented from being less than 10^{-7} to prevent a divide by zero in Equation (7.4-1).

The nondimensional height R involves a division by the critical height. To avoid division by zero as the major phase flow rate goes to zero, the critical height is given a minimum value of 1.0×10^{-6} m. The value of the major phase flow rate is back-calculated from the minimum critical height to ensure that the relation between critical height and major phase flow rate implied by Equation (7.4-1) is maintained.

To avoid other singularities, the slip ratio used to convert the flow quality into a phasic area fraction is limited, as is the phase density difference. The slip ratio used to convert the offtake flow quality into phasic area fraction is given by

$$S = \max\left\{1.0, \min\left[\max\left(\frac{\rho_{fj}}{\rho_{gj}}, 10^{-7}\right)^{0.5}, \frac{|v_{gj}|}{|v_{fj}|}\right]\right\} \quad . \tag{7.4-11}$$

This expression restricts the range of the slip ratio and uses absolute velocities to give phasic area fractions in the range of zero to one, even when the flow in the offtake junction is counter-current. The square root of the density ratio gives a slip ratio consistent with the non-homogeneous Henry-Fauske critical flow model and is a reasonable upper limit to the slip ratio. In most cases, the slip ratio used in the computation will be the actual slip ratio.

7.4.3.3.3 Numerics--The explicit formulation described above is an invitation for instability. Consider the case of liquid entrainment for unchoked, cocurrent flow in the offtake junction. The vapor/gas area fraction is evaluated from the correlation for the offtake quality as a function of the nondimensional

liquid level. The scaling factor for the nondimensional liquid depth is the critical liquid depth. The critical liquid depth is a function of the vapor/gas flow rate in the offtake. The critical depth may have been modified if it was less than the minimum critical depth and the offtake vapor/gas flow rate recomputed to be consistent with the critical depth. The appropriate offtake flow quality correlation gives a flow quality that was converted to a vapor/gas area fraction using the offtake slip ratio. This vapor/gas area fraction may, in turn, have been modified for the finite area of the offtake and for high flow or extreme voids in the upstream horizontal pipe. This final offtake vapor/gas area fraction is unlikely to be the same as that used to compute the vapor/gas mass flow rate in the offtake junction used to compute the critical depth. This is the source of the instability. To overcome the explicit nature of the computation of the offtake phasic area fractions, a predictor-corrector technique is used. The correlations are evaluated explicitly, as described above, to give a predicted value of the phasic area fractions. Then, a first-order Taylor expansion of the model correlations is used to adjust the values of the phasic area fractions to make them consistent with the phasic flow rates in the offtake. The procedure is somewhat different for choked flow than unchoked flow, and the two procedures will be discussed separately.

Numerics for Unchoked Flow

Consider the case of liquid entrainment for cocurrent, unchoked flow in the offtake. The model correlations are evaluated explicitly as described above, using the beginning of time step values for the properties to give a predicted value of the vapor/gas area fraction in the offtake, α_{gj}^{p}, where the superscript p indicates a value predicted from the stratification entrainment/pullthrough correlations. The vapor/gas area fraction in the offtake is expanded in terms of the vapor/gas flow rate (W_g) in the offtake, and the vapor/gas flow rate in the offtake is expanded in terms of the vapor/gas area fraction in the offtake to give the following set of equations:

$$\alpha_{gj} = \alpha_{gj}^{p} + \frac{\partial \alpha_{gj}^{p}}{\partial W_g}(W_g^{*} - W_g^{p}) \tag{7.4-12}$$

where

$$W_g^{*} = W_g + \frac{\partial W_g}{\partial \alpha_{gj}}(\alpha_{gj} - \alpha_{gj}^{n}) \tag{7.4-13}$$

and where the derivatives of the flow rate in terms of the area fraction and the derivative of the area fraction in terms of the flow rate are evaluated using the beginning of time step conditions. The extrapolated offtake flow rate can be eliminated from these two equations to give an extrapolated value of the vapor/gas area fraction in terms of the beginning of time step conditions and derivative of the vapor/gas area fraction in terms of the vapor/gas flow rate and the slip ratio. The various interpolation factors, such as the interpolation between the model value of vapor/gas area fraction and the donor value of the offtake vapor/gas area fraction due to the finite area of the offtake, are held constant. The resultant vapor/gas area fraction is

$$\alpha_{gj} = \frac{\alpha_{gj}^{p} + \frac{\partial \alpha_{gj}^{p}}{\partial W_g}\left(W_g - W_g^{p} - \alpha_{gj}^{n}\frac{\partial W_g}{\partial \alpha_{gj}}\right)}{1 - \frac{\partial W_g}{\partial \alpha_{gj}}\frac{\partial \alpha_{gj}^{p}}{\partial W_g}} \tag{7.4-14}$$

where the derivative of the vapor/gas flow rate in the offtake in terms of the offtake vapor/gas area fraction is given by

$$\frac{\partial W_g}{\partial \alpha_{gj}} = \rho_{gj} v_{gj} A_j \tag{7.4-15}$$

and the derivative of the offtake vapor/gas fraction with respect to the offtake vapor/gas flow rate is negative. If the derivative of the vapor/gas area fraction with respect to the vapor/gas flow rate is not negative, the extrapolation procedure is not used; and the predicted value of the offtake vapor/gas area fraction is used for the time step.

The partial derivative of the offtake vapor/gas area fraction with respect to the vapor/gas flow rate is set to zero under the following conditions:

- The large critical depth modification is activated.
- The flow is in countercurrent flow (cases 3 or 4).
- The predicted value of the vapor/gas area fraction is one and the vapor/gas area fraction used during the last time step is one. (If the vapor/gas area fraction used during the last time step is one and a nonzero derivative is computed, the extrapolation is used.)
- The predicted value of the offtake vapor/gas area fraction is zero.

Exactly the same procedure is used for the case of vapor/gas pullthrough except that the roles of liquid and vapor/gas are reversed. In this case, the extrapolation equation for the liquid fraction is given by

$$\alpha_{fj} = \frac{\alpha_{fj}^{p} + \frac{\partial \alpha_{fj}^{p}}{\partial W_f}\left(W_f - W_f^{p} - \alpha_{fj}^{n}\frac{\partial W_f}{\partial \alpha_{fj}}\right)}{1 - \frac{\partial W_f}{\partial \alpha_{fj}}\frac{\partial \alpha_{fj}^{p}}{\partial W_f}} \tag{7.4-16}$$

where W_f is the liquid flow rate in the offtake and where the derivative of the offtake liquid area fraction is set to zero under the following circumstances:

- The large critical depth modification is activated.
- The flow in the offtake is countercurrent flow (cases 3 or 4).
- Both the predicted value of the liquid area fraction in the offtake and the value of the liquid area fraction in the offtake used during the previous time step are one. (If the value of the liquid fraction used during the previous time step is less than one and the derivative of the liquid area fraction with respect to the liquid flow rate is nonzero, the extrapolation procedure is used to reduce perturbations as entrainment starts or stops.)
- Both the predicted value of the liquid fraction in the offtake and the value of the liquid area fraction in the offtake used during the previous time step are zero. (If the liquid fraction in the offtake used during the previous time step is greater than zero and a nonzero derivative is computed, the extrapolation procedure is used to reduce perturbations as liquid first appears in the offtake.)

Choked Flow in the Offtake

If the flow in the offtake is choked, a different extrapolation procedure is used because of the way in which the individual phase velocities are computed at the choked junction. The choking model computes the critical mass flux as the product of the mixture density at the critical plane and the critical velocity at the critical plane. The critical velocity is defined in terms of the phase velocities, the phase densities, and the phase area fractions. The extrapolation procedure for the choked flow situation assumes that the critical mass flux remains constant as extrapolation is performed, rather than assuming that the individual phase velocities remain constant as the extrapolation is performed. The assumption of constant mass flow accounts for the effect of the phasic area fractions on the phasic velocities. This effect is small for unchoked flow and is neglected but can become large for critical flow and must be taken into account. The net effect on the extrapolation procedure is a change in the way the derivative of offtake flow rate with respect to offtake area fraction is computed. The procedure is slightly different for the cases of liquid entrainment and vapor/gas pullthrough, so each will be discussed separately.

Liquid Entrainment in Choked Offtake

As stated above, the effect of the change in the choked flow vapor/gas velocity due to changes in the vapor/gas area fraction in the offtake cannot be neglected. Over a wide range of vapor/gas area fractions, an increase in the junction vapor/gas area fraction results in an increase in the offtake vapor/gas velocity. This would lead to increased entrainment in the next time step, reducing the vapor/gas area fraction. This negative feedback process can cause oscillations. The approximation used to account for the change in the choked vapor/gas velocity is to assume that the critical mixture mass flux remains constant during the extrapolation procedure, as well as assuming that the phase densities and slip ratio remain constant as is assumed for the case of unchoked flow. The critical mass flux is computed from the offtake vapor/gas fraction used during the previous time step and the current values of the phase velocities, which have been set by the critical flow model for this time step as

$$G_c = \rho_j v_c \tag{7.4-17}$$

where

$$v_c = \frac{\alpha^n_{gj}\rho^n_{fj}v_{gj} + \alpha^n_{fj}\rho^n_{gj}v_{fj}}{\alpha^n_{gj}\rho^n_{fj} + \alpha^n_{fj}\rho^n_{gj}} \tag{7.4-18}$$

$$\rho_j = \alpha^n_{gj}\rho^n_{gj} + \alpha^n_{fj}\rho^n_{fj}\,. \tag{7.4-19}$$

The vapor/gas velocity is then written as

$$v_g = \frac{v_c(\alpha^n_{gj}\rho^n_{fj} + \alpha^n_{fj}\rho^n_{gj})S}{\alpha^n_{gj}\rho^n_{fj}S + \alpha^n_{fj}\rho^n_{gj}} \tag{7.4-20}$$

and the vapor/gas mass flow rate expressed in terms of the vapor/gas velocity is expressed as

$$W_g = \alpha_{gj}\rho_{gj}v_g A_j \quad . \tag{7.4-21}$$

These equations can be combined to give an expression for the vapor/gas flow rate as a function of the vapor/gas area fraction. This expression can then be used to compute the derivative of the vapor/gas flow rate with respect to the vapor/gas area fraction in the offtake. The derivative is then used in the extrapolation equation to compute an adjusted vapor/gas area fraction in the offtake for use during the current time step [Equation (7.4-14)].

Vapor/Gas Pullthrough in Choked Flow

The situation is different for vapor/gas pullthrough. The negative feedback process described for liquid entrainment becomes a positive feedback process. An increase in the offtake liquid area fraction results, for a wide range of liquid area fractions, in a decrease in offtake choked flow liquid velocity. The next time step would then have less vapor/gas pullthrough (ignoring the countering effect of the increased liquid area fraction on the liquid mass flow rate); hence, there would be an increase in offtake liquid area fraction. This may or may not give rise to instability. Using a procedure like that described above for liquid entrainment is likely to exacerbate any potential positive feedback instability because it could result in a reduced or negative denominator in the extrapolation expression for vapor/gas area fraction due to a small or negative derivative of the offtake liquid mass flow rate with respect to offtake liquid area fraction.

Another problem is associated with the transition in the choked flow model between the subcooled and two-phase choking models. This problem can be illustrated by considering a horizontal volume

containing stratified vapor/gas and liquid with the liquid being subcooled. Consider a side offtake below the liquid level with the choked outflow liquid causing vapor/gas pullthrough. As the liquid level falls, the equilibrium quality of the flow from the side offtake can change from subcooled to two-phase (the actual quality being two-phase throughout). As this happens, the choked flow rate drops. This causes a drop in pullthrough, resulting in a drop in offtake equilibrium quality to a subcooled value. The next time step will use the subcooled choking model, giving an increase in the offtake flow. This cycle can continue, causing oscillations with a period linked to the time step. In order to reduce such oscillations, a kind of damping is introduced by replacing the derivative of the liquid flow rate with respect to the liquid area fraction by an artificially large negative value.

Let X^n be the static quality based on the liquid area fraction used during the last time step and X^p be the static quality based on the predicted liquid area fraction. The damping is applied if X^n or $X^p < 2.5 \times 10^{-3}$.

In the case of damping, the liquid flow rate is assumed to depend on the static quality as

$$W_f^p = C(5 \times 10^{-3} - X^p) \qquad (7.4\text{-}22)$$

where the constant C is chosen such that at a static quality X^d, the liquid flow rate using the current liquid velocity matches that given by the flow rate as a function of static quality. The static quality X^d is the minimum of 2.5×10^{-3} and the static quality used during the previous time step. The derivative of the liquid flow rate with respect to the liquid area fraction is obtained from the assumed flow rate dependence on static quality. This derivative is then used in the previously described extrapolation equation for choked flow.

The procedure for vapor/gas pullthrough in cocurrent choked flow was developed for use with the RELAP5/MOD2 choked flow model, which used the equilibrium quality at the offtake junction to determine whether to use the subcooled or two-phase choking model at the offtake. The choking model in ATHENA has been modified to use the vapor/gas area fraction in the offtake to make the determination as to which critical flow model to use in a given time step. The effect of the inconsistency between the choked flow model and the stratification entrainment/pullthrough model for horizontal volumes with respect to the transition between single-phase liquid flow and two-phase flow at the initiation of vapor/gas pullthrough is not known at this time and should be investigated as part of the independent assessment of ATHENA.

7.4.4 Assessment

The performance of the stratification entrainment/pullthrough model for horizontal volumes was assessed using a simple test case to confirm that the implementation of the stratification entrainment/pullthrough correlations was performed correctly and that the correlations gave an adequate representation of the stratification entrainment/pullthrough data base. The test case consisted of a horizontal pipe of 206-mm inner diameter into which steam and water were introduced by time-dependent

junctions. A 20.0-mm-diameter offtake branch discharging into a time-dependent volume at a fixed pressure of 0.1 MPa was connected to the main pipe at the mid-length position. To help promote a stable condition, the phasic flow rates in the time-dependent junctions were set equal to the phasic flow rates in the offtake branch using the ATHENA control logic.

The computations were performed by setting the pressure and vapor/gas fraction in the main pipe and allowing a steady-state to develop. The pressure and the vapor/gas area fraction in the main pipe changed very little from their initial values in their approach to a steady-state. Computations were done for a side, bottom, and top offtake branch. In all cases, the offtake volume was assumed to be horizontal.

Calculated steady-state conditions obtained with RELAP5/MOD2 cycle 36.04 are plotted in **Figure 7.4-7** through **Figure 7.4-9** as broken lines. The curves are drawn through a large number of individual steady-state operating points. For each operating point, the liquid depth in the main pipe was computed from the vapor/gas area fraction using the appropriate geometric relations. The critical height for the onset of entrainment or pullthrough was computed from Equation (7.4-1). It is seen that the RELAP5/MOD2 stratification entrainment/pullthrough model for horizontal volumes underpredicts the experimental data (discharge flow quality); the new model, shown as a solid line, does a much better job of describing the experimental data. The results for the new model were generated using RELAP5/MOD2 with a set of code updates that implemented the new model. The computed curves also overlay the hand-computed curves shown in **Figure 7.4-2** through **Figure 7.4-4**, showing that the various modifications and extensions made to the model as part of its implementation have not degraded the model's predictive ability. The RELAP5/MOD2 and modified RELAP5/MOD2 assessment results are from Ardron and Bryce.[7.4-1] The assessment was repeated with RELAP5/MOD3,[7.4-2] and the results are similar to the modified RELAP5/MOD2 results.

To demonstrate the performance of the revised stratification entrainment/pullthrough model for horizontal volumes in a small-break LOCA in a PWR, calculations were performed of test LP-SB-02 in the LOFT experimental facility.[7.4-10] Test LP-SB-02 simulated a break in the hot leg of area equal to 1% of the hot leg flow area. The break line consisted of a 29.4-mm-diameter side offtake connected to the 286-mm-diameter hot leg. The test exhibited a long period of stratified two-phase flow in the hot leg, during which pullthrough/entrainment effects were evident. A detailed description of the RELAP5/MOD2 analysis is given in **Reference 7.4-10**. **Figure 7.4-10** and **Figure 7.4-11** show the hot leg and break line densities calculated using the standard and modified versions of RELAP5/MOD2 Cycle 36.04. The standard code predicted a transition to stratified flow in the hot leg at 2,250 seconds, after which time the stratification entrainment/pullthrough model for horizontal volumes was used to calculate break line density. It is seen that the break line density continues to be overpredicted after 2,250 seconds, apparently due to the tendency of the standard stratification entrainment/pullthrough model for horizontal volumes to underpredict flow quality in a side offtake (see **Figure 7.4-8**). The standard model also fails to describe effects of flow stratification evident before 2,250 seconds.

The modified code version gives a better agreement after 850 seconds, when the hot leg mass velocity falls below the threshold value of 3,000 $kg/m^2 \cdot s$, allowing the new stratification

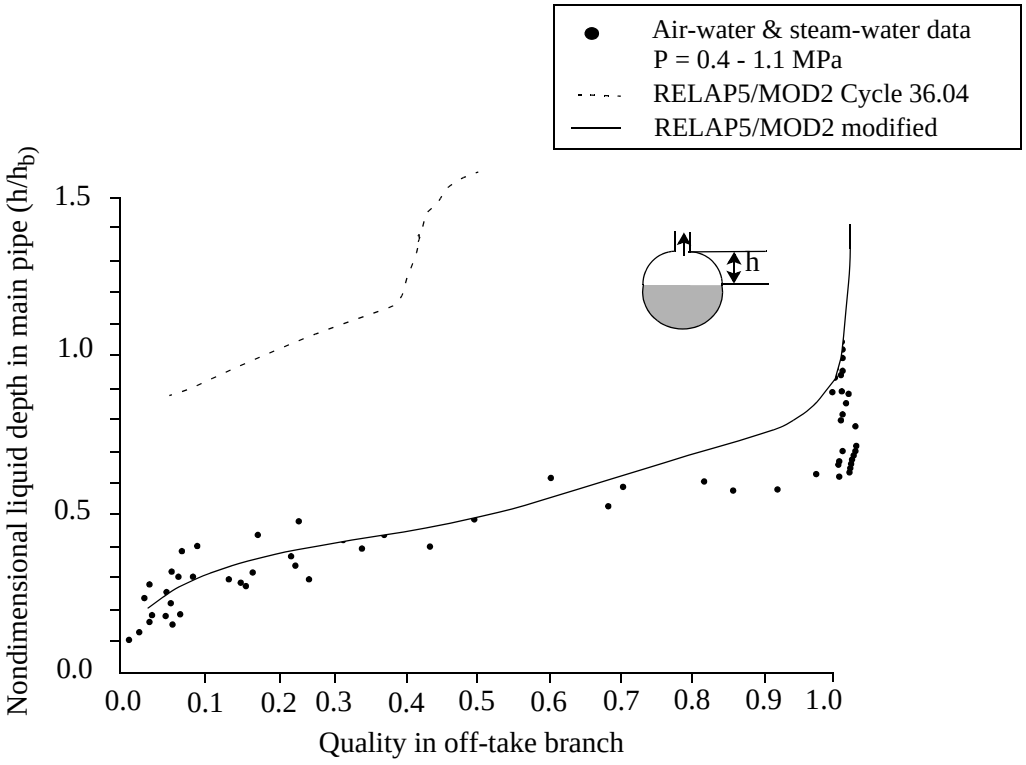

Figure 7.4-7 A comparison of discharge flow quality versus liquid depth for the upward offtake branch as calculated using the old and new stratification entrainment/pullthrough models for horizontal volumes.

entrainment/pullthrough model for horizontal volumes to be invoked. The calculation of break line density after 850 seconds gives an improved prediction of the mass inventory, leading to a more accurate calculation of the liquid level in the hot leg after 2,000 seconds (see **Figure 7.4-10**). In the period before 850 seconds, normal donoring is used, and the break line density is seen to be overpredicted. The reason for preferential discharge of vapor/gas under these highly mixed flow conditions is unknown. A possible mechanism is that the curved streamlines in the nozzle entrance produce inertial separation in the manner of a centrifugal separator. In general, the modified stratification entrainment/pullthrough model for horizontal volumes gives a much better simulation of the phase separation phenomena in this experiment.

7.4.5 Scalability and Applicability

The correlations used in the improved stratification entrainment/pullthrough model for horizontal volumes were developed from data obtained under conditions representative of small leaks in large horizontal pipes at low pressure and stratified flow conditions. The experiments cover a range of diameters of the main horizontal pipe, of operating pressure, and of offtake diameter and orientation. There were no scale effects observed in the data due to the ratio of the diameters of the offtake and the main pipe. (The smallest diameter ratio was for the INEEL data, which were obtained at a diameter ratio of approximately 8.5.) Since the horizontal pipes in a PWR system are several times larger than the experimental test sections, there should be no restriction as to the applicability of the stratification entrainment/pullthrough

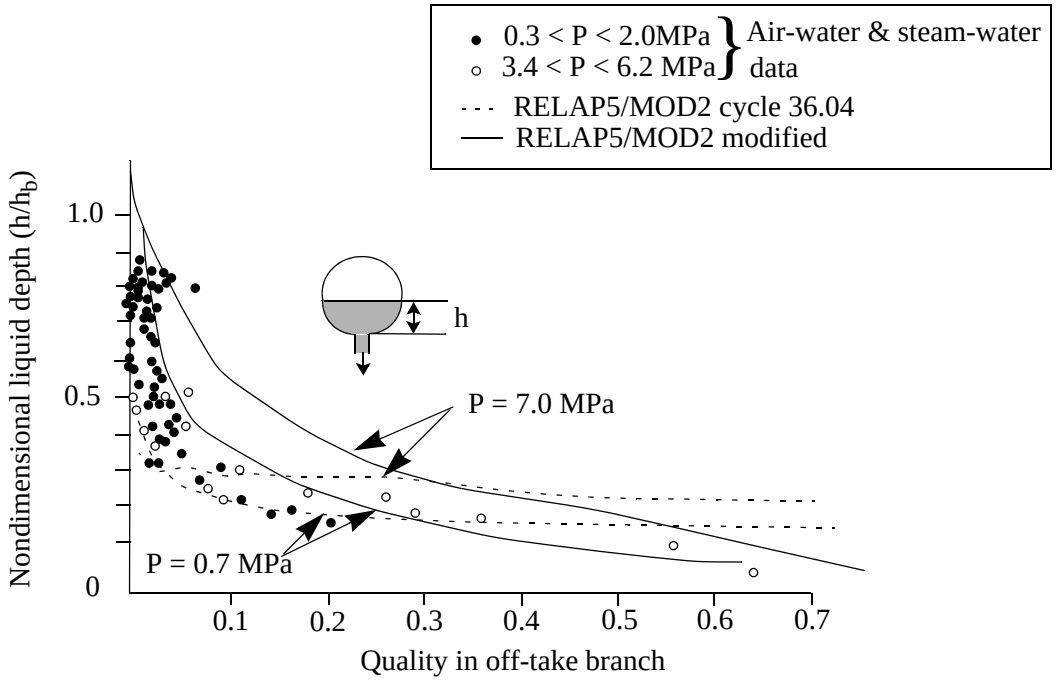

Figure 7.4-8 A comparison of discharge flow quality versus liquid depth for the downward offtake branch as calculated using the old and new stratification entrainment/pullthrough models for horizontal volumes.

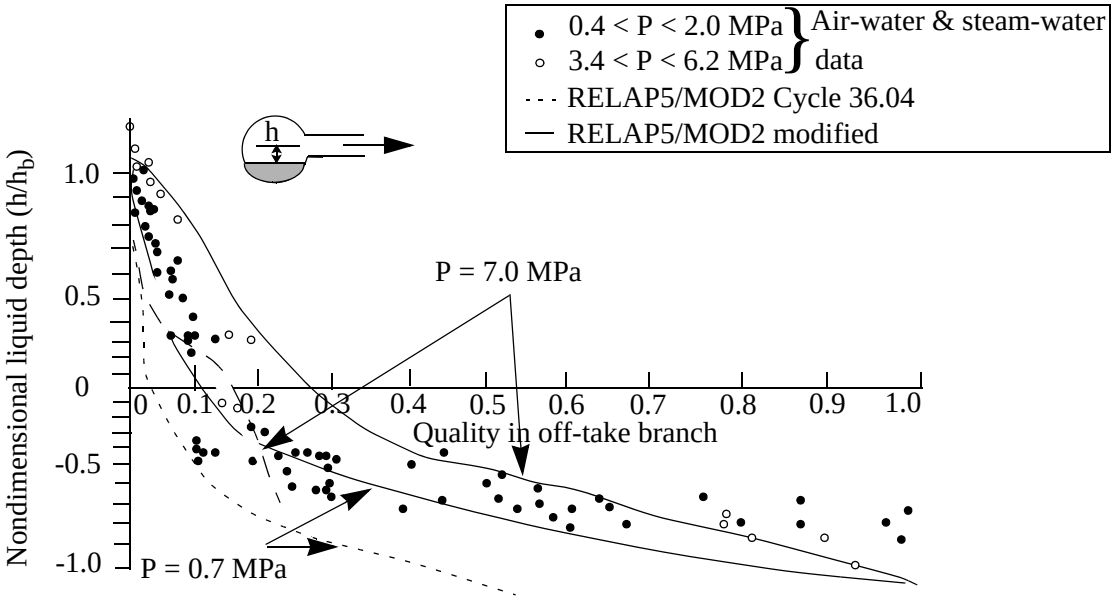

Figure 7.4-9 A comparison of discharge flow quality versus liquid depth for the horizontal offtake branch as calculated using the old and new stratification entrainment/pullthrough models for horizontal volumes.

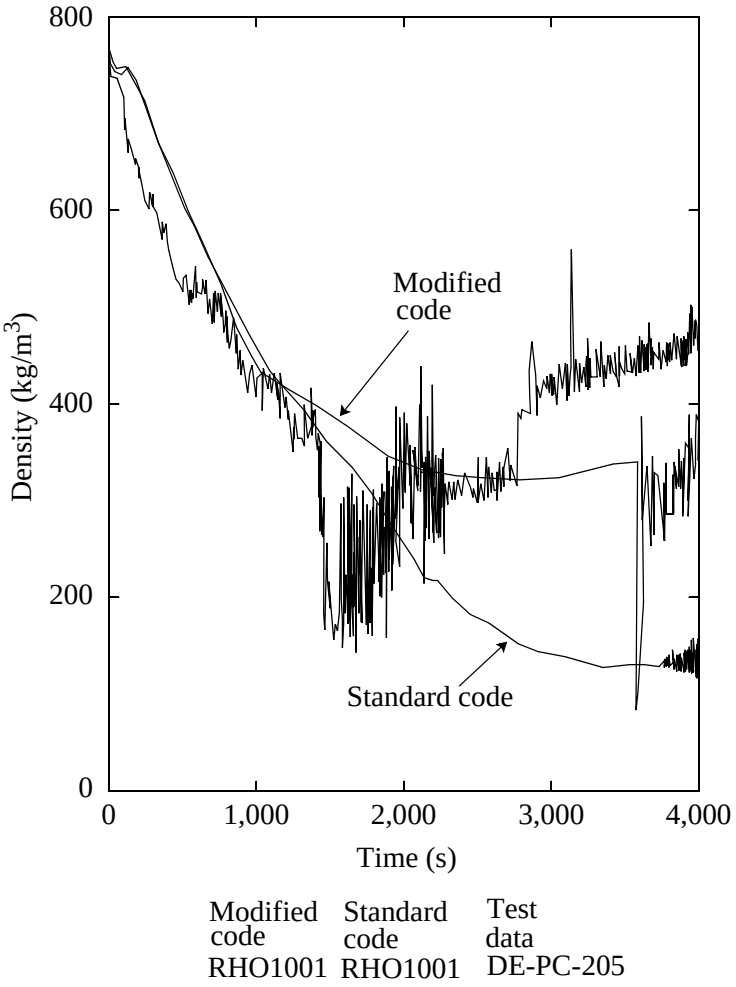

Figure 7.4-10 Measured and calculated hot leg densities using the old and new stratification entrainment/pullthrough models for horizontal volumes.

model for horizontal volumes to reactor system analysis for the large-diameter pipes in real reactor systems. The only major restriction for the stratification entrainment/pullthrough model for horizontal volumes is the orientation of the offtake. Since individual correlations are needed for top, bottom, and side offtakes, the model must be restricted to these orientations.

7.4.6 Summary and Conclusions

A new model describing the phase separation phenomena for flow through a small flow passage in the wall of a large horizontal pipe has been developed and implemented in ATHENA. The model was developed from data obtained under prototypical conditions and describes the conditions under which the minor phase will be entrained or pulled through the continuous phase and the flow quality in the offtake after the initiation of entrainment or pullthrough. Correlations were developed for offtakes situated in the

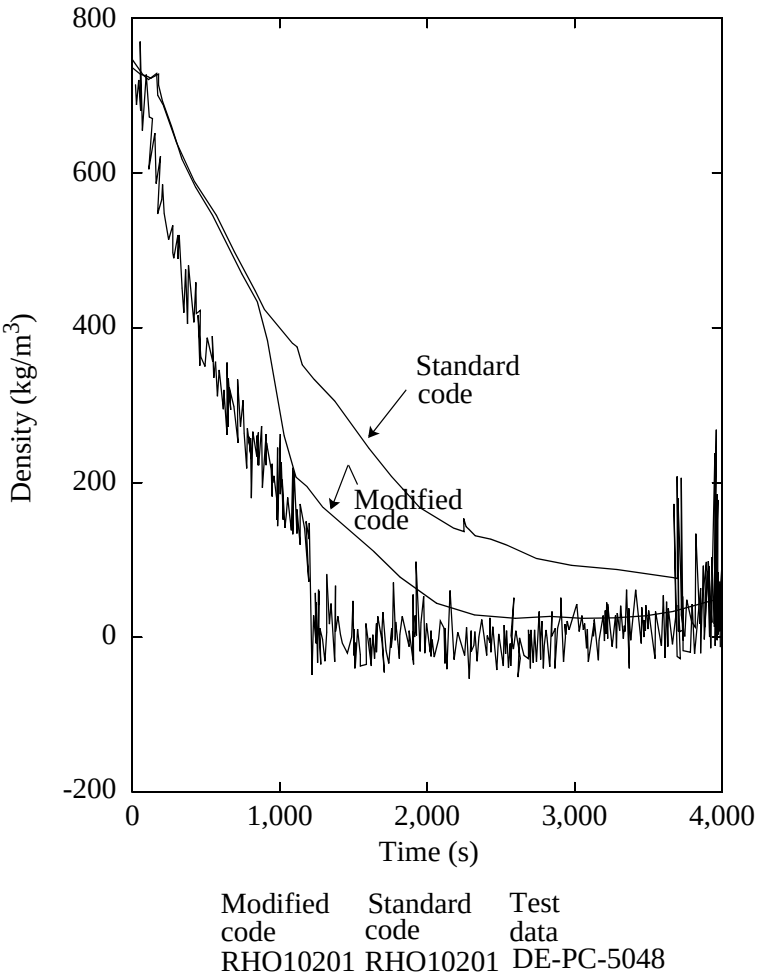

Figure 7.4-11 Measured and calculated break line densities using the old and new stratification entrainment/pullthrough models for horizontal volumes.

top, bottom, and side of the horizontal pipe. The model was modified and extended for implementation into the ATHENA code, and the extensions and modifications were shown not to affect its predictive capability. The model as implemented was tested against the data used in its derivation as well as in the simulation of a small-break loss-of-coolant LOFT experiment. The results of the assessments performed show that the new model provides a good representation of the data from which it was developed and leads to a better prediction LOFT experimental results.

7.4.7 References

7.4-1. K. Ardron and W. Bryce, *Assessment of Horizontal Entrainment Model in RELAP5/MOD2,* AEEW-R 2345, Atomic Energy Establishment Winfrith, April 1988.

7.4-2. W. Bryce, *Numerics and Implementation of the UK Horizontal Stratification Entrainment Off-Take Model into RELAP5/MOD3*, AEA-TRS-1050, AEEW-R 2501, Atomic Energy Establishment Winfrith, March 1991.

7.4-3. N. Zuber, *Problems in Modeling of Small Break LOCA*, NUREG-0724, U. S. Nuclear Regulatory Commission, October 1980.

7.4-4. C. Smoglie, *Two-Phase Flow Through Small Branches in a Horizontal Pipe with Stratified Flow*, KfK 3861, Kernforschungszentrum Karlsruhe GmbH (KfK), Karlsruhe, FRG, December 1984.

7.4-5. T. Maciaszek and A. Menponteil, "Experimental Study on Phase Separation in a Tee Junction for Steam-Water Stratified Inlet Flow," Paper C2, *European Two-Phase Flow Working Group Meeting, Munich, FRG, June 10-13, 1986.*

7.4-6. V. E. Schrock, S. T. Revankar, R. Mannheiner, and C. H. Wang, *Small Break Critical Discharge - The Role of Vapor and Liquid Entrainment in a Stratified Two-Phase Region Upstream of the Break*, NUREG/CR-4761, LBL-22024, Lawrence Berkeley Laboratory, December 1986.

7.4-7. J. L. Anderson and R. L. Benedetti, *Critical Flow Through Small Pipe Breaks*, EPRI NP-4532, Idaho National Engineering Laboratory, May 1986.

7.4-8. D. R. L. Harleman, R. L. Morgan, and R. A. Purple, "Selective Withdrawal from a Vertically Stratified Fluid," *Proceedings of the 8th Congress of the International Association for Hydraulic Research, Montreal, Canada, August 24-29, 1959*, p. 10-C-1 ff.

7.4-9. B. T. Lubin and G. S. Springer, "The Formation of a Dip on the Surface of a Liquid Draining from a Tank," *Journal of Fluid Mechanics, 29*, 1967, pp. 385-390.

7.4-10. P. C. Hall, *RELAP5/MOD2 Calculation of OECD LOFT Test LP-SB-02*, CEGB Report GD/PE-N/606.

Appendix 7A--Development of Sound Speed Expressions

The generalized homogenous sound speed formulation (for 1 component) presented here was developed by V. H. Ransom and is internally documented.[1]

The propagation velocity for a small disturbance in a homogenous medium (thermal equilibrium) is

$$a^2 = \left(\frac{\partial P}{\partial \rho}\right)_S = -\frac{V^2}{\left(\frac{\partial V}{\partial P}\right)_S} \quad . \tag{7A-1}$$

For a two-phase homogeneous mixture, the specific volume is

$$V = XV_g + (1 - X)V_f, \tag{7A-2}$$

where X is the quality.

The partial derivative of specific volume with respect to pressure is

$$\left(\frac{\partial V}{\partial P}\right)_S = X\left(\frac{\partial V_g}{\partial P}\right)_S + (1 - X)\left(\frac{\partial V_f}{\partial P}\right)_S + \varepsilon(V_g - V_f)\left(\frac{\partial X}{\partial P}\right)_S \tag{7A-3}$$

where $\varepsilon = 0$ for a frozen composition system, and $\varepsilon = 1$ for equilibrium mass exchange between phases.

The derivatives of specific volume can be expressed in terms of the isothermal compressibility, κ, and the isobaric coefficient of thermal expansion, β, to obtain

$$\left(\frac{\partial V_g}{\partial P}\right)_S = V_g\left[\beta_g\left(\frac{\partial T}{\partial P}\right)_S - \kappa_g\right] \tag{7A-4}$$

$$\left(\frac{\partial V_f}{\partial P}\right)_S = V_f\left[\beta_f\left(\frac{\partial T}{\partial P}\right)_S - \kappa_f\right] \tag{7A-5}$$

where

1. EG&G Idaho, Inc., Idaho National Engineering Laboratory, Interoffice Correspondence, “Sound Speed Behavior at Phase Boundaries,” RANS-4-77, May 19, 1977.

$$\beta = \frac{1}{V}\left(\frac{\partial V}{\partial T}\right)_P \quad (7A\text{-}6)$$

$$\kappa = -\frac{1}{V}\left(\frac{\partial V}{\partial P}\right)_T \quad . \quad (7A\text{-}7)$$

The quality derivative in Equation (7A-3) is expanded in terms of the individual phase properties by starting with the definition of system entropy.

$$S = XS_g + (1 - X)S_f \quad . \quad (7A\text{-}8)$$

Differentiating Equation (7A-8) with respect to pressure at constant total entropy yields

$$\left(\frac{\partial S}{\partial P}\right)_S = 0 = X\left(\frac{\partial S_g}{\partial P}\right)_S + (1 - X)\left(\frac{\partial S_f}{\partial P}\right)_S + (S_g - S_f)\left(\frac{\partial X}{\partial P}\right)_S \quad . \quad (7A\text{-}9)$$

If S_g and S_f are taken to be functions of P and T, then

$$\left(\frac{\partial S_g}{\partial P}\right)_S = \left(\frac{\partial S_g}{\partial P}\right)_T \left(\frac{\partial P}{\partial P}\right)_S + \left(\frac{\partial S_g}{\partial T}\right)_P \left(\frac{\partial T}{\partial P}\right)_S \quad (7A\text{-}10)$$

$$\left(\frac{\partial S_f}{\partial P}\right)_S = \left(\frac{\partial S_f}{\partial P}\right)_T \left(\frac{\partial P}{\partial P}\right)_S + \left(\frac{\partial S_f}{\partial T}\right)_P \left(\frac{\partial T}{\partial P}\right)_S \quad . \quad (7A\text{-}11)$$

From Maxwell's second relation,

$$\left.\frac{\partial S}{\partial P}\right|_T = -\left.\frac{\partial V}{\partial T}\right|_P \quad (7A\text{-}12)$$

which, from Equation (7A-6), is $-\beta V$ and, from the definition of specific heat at constant pressure,

$$C_p = T\left(\frac{\partial S}{\partial T}\right)_P \quad . \quad (7A\text{-}13)$$

Using Equations (7A-12) and (7A-13), Equations (7A-10) and (7A-11) become

$$\left(\frac{\partial S_g}{\partial P}\right)_s = -V_g\beta_g + \frac{C_{pg}}{T}\left(\frac{\partial T}{\partial P}\right)_s \tag{7A-14}$$

$$\left(\frac{\partial S_f}{\partial P}\right)_s = -V_f\beta_f + \frac{C_{pf}}{T}\left(\frac{\partial T}{\partial P}\right)_s \quad . \tag{7A-15}$$

Substituting Equations (7A-14) and (7A-15) into Equation (7A-9) gives a relation for $\left(\frac{\partial X}{\partial P}\right)_s$ in terms of $\left(\frac{\partial T}{\partial P}\right)_s$,

$$\left(\frac{\partial X}{\partial P}\right)_s = \frac{-1}{(S_g - S_f)}\left\{X\left[\frac{C_{pg}}{T}\left(\frac{\partial T}{\partial P}\right)_s - V_g\beta_g\right] + (1-X)\left[\frac{C_{pf}}{T}\left(\frac{\partial T}{\partial P}\right)_s - V_f\beta_f\right]\right\} \quad . \tag{7A-16}$$

The behavior of the temperature with pressure must be evaluated before the sound speed can be established. For the two-phase system in equilibrium, the temperature is only a function of pressure, and the Clausius-Clapeyron relation can be used to obtain the derivative of temperature, i.e.,

$$\left(\frac{\partial T}{\partial P}\right)_s = \left(\frac{dT}{dP}\right) = \frac{V_g - V_f}{S_g - S_f} \tag{7A-17}$$

or, since $S_g - S_f = \frac{h_g - h_f}{T}$,

$$\left(\frac{\partial P}{\partial T}\right)_s = \frac{h_g - h_f}{T(V_g - V_f)} \quad . \tag{7A-18}$$

If a system having frozen composition is considered, the behavior of temperature with pressure is obtained from Equation (7A-16) with $\left(\frac{\partial X}{\partial P}\right)_s = 0$, i.e.,

$$\left(\frac{\partial T}{\partial P}\right)_s = \frac{T[XV_g\beta_g + (1-X)V_f\beta_f]}{XC_{pg} + (1-X)C_{pf}} \quad . \tag{7A-19}$$

We next define P'_ε to be $\left(\frac{\partial P}{\partial T}\right)_s$. Thus, P'_ε is given by Equation (7A-18) for $\varepsilon = 1$ (homogeneous equilibrium flow) and by the inverse of Equation (7A-19)

$$P'_{\varepsilon} = \frac{XC_{pg} + (1-X)C_{pf}}{T[X\beta_g V_g + (1-X)\beta_f V_f]} \tag{7A-20}$$

for ε = 0 (frozen flow). Equations (7A-1), (7A-3), (7A-4), (7A-5), (7A-16), (7A-18), and (7A-20) can be combined to yield a generalized expression for the homogeneous sound speed

$$a^2 = \frac{[XV_g + (1-X)V_f]^2 T(P'_{\varepsilon})^2}{X\{\varepsilon C_{pg} - TV_g P'_{\varepsilon}[(1+\varepsilon)\beta_g - \kappa_g P'_{\varepsilon}]\} + (1-X)\{\varepsilon C_{pf} - TV_f P'_{\varepsilon}[(1+\varepsilon)\beta_f - \kappa_f P'_{\varepsilon}]\}} . \tag{7A-21}$$

For ε = 1, the homogeneous equilibrium speed of sound is obtained and, for ε = 0, the homogeneous frozen speed of sound is obtained. The pure component sound speed (without phase change) is obtained from the expression for the frozen sound speed expression with X = 0 or 1 for liquid and vapor, respectively. For example, the pure vapor sound speed is obtained from Equation (7A-21) with X = 1 and ε = 0,

$$a_V^2 = \frac{V_g^2\left(\frac{\partial P}{\partial T}\right)_S^2}{V_g\left[\kappa_g\left(\frac{\partial P}{\partial T}\right)_S - \beta_g\right]\left(\frac{\partial P}{\partial T}\right)_S} \tag{7A-22}$$

where $\left(\frac{\partial P}{\partial T}\right)_S$ is from Equation (7A-20) with X = 1

$$\left(\frac{\partial P}{\partial T}\right)_S = \frac{C_{pg}}{T\beta_g V_g} . \tag{7A-23}$$

The behavior of the homogeneous speed of sound at phase boundaries is of interest in development of numerical schemes since the system bulk modulus depends directly on $\left(\frac{\partial \rho}{\partial P}\right)_S$, i.e., $1/a_H^2$, where H indicates homogeneous.

The ratio of pure phase to two-phase equilibrium speeds of sound is obtained by taking the ratio of Equation (7A-21) with ε = 0 to Equation (7A-21) with ε = 1 and evaluating the resulting expression at X = 0 and 1 to obtain the ratios for pure liquid and pure vapor, respectively. This is given by

$$a_F^2/a_E^2 = (P'_0/P'_1)[P'_0/P'_1 + \kappa P'_1/\beta - 2]/([\kappa P'_0/\beta] - 1) \tag{7A-24}$$

where F indicates frozen, E indicates equilibrium, P'_0 (frozen) is given by Equation (7A-20), and P'_1 (equilibrium) is given by Equation (7A-18).

The properties appearing in Equation (7A-24) are evaluated at the conditions of saturated vapor or saturated liquid, depending upon which phase boundary is being investigated.

As an example, the ratio is evaluated at $6x10^5$ Pa for liquid water and steam. The following fluid properties apply:

V_f = 0.001101 m^3/kg

Vg = 0.315474 m^3/kg

β_f = 0.001765 K^{-1}

β_g = 0.002931 K^{-1}

κ_f = $6.74345x10^{-10}$ Pa^{-1}

κ_g = $1.76503x10^{-6}$ Pa^{-1}

C_{pf} = 4335.01 J/(kg·K)

C_{pg} = 2387.27 J/(kg·K)

T = 431.987 K

$(P'_0)_f$ = $5.1641x10^6$ Pa/K

$(P'_0)_g$ = $5.97659x10^3$ Pa/K

P'_1 = $1.53572x10^3$ Pa/K

At the liquid - two-phase boundary

a_F = 1821.7 m/s

a_E = 5.37 m/s

a_F/a_E = 339.4

At the vapor - two-phase boundary

a_F = 497.5 m/s

a_E = 465.2 m/s

a_F/a_E = 1.0695

With the exception of the vapor state, Equations (7A-18) and (7A-21) with $\varepsilon = 1$ are used in ATHENA to compute the homogeneous sound speed. **Table 7.4-1** summarizes the homogeneous sound speed formulas used in the two-phase choking model. For the pure liquid case, the saturation values of V_f^s, κ_f^s, β_f^s, C_{pf}^s, h_f^s, and h_g^s are determined with the saturation temperature being the liquid temperature.

Table 7.4-1 Homogeneous sound speed formulas used in ATHENA.

Pure Vapor (homogeneous frozen sound speed, $\varepsilon = 0$, X = 1)
$a = V_g\left\{\dfrac{\left(\dfrac{\partial P}{\partial T}\right)_S}{V_g\left[\kappa_g\left(\dfrac{\partial P}{\partial T}\right)_S - \beta_g\right]}\right\}^{1/2}$; $\left(\dfrac{\partial P}{\partial T}\right)_S = \dfrac{C_{pg}}{T_g V_g \beta_g}$
Pure liquid (homogeneous equilibrium sound speed, $\varepsilon = 1$, X = 0)
$a = V_f^s\left(\dfrac{\partial P}{\partial T}\right)_S\left\{\dfrac{T_f}{C_{pf}^s - T_f V_f^s\left(\dfrac{\partial P}{\partial T}\right)_S\left[2\beta_f^s - \kappa_f^s\left(\dfrac{\partial P}{\partial T}\right)_S\right]}\right\}^{1/2}$; $\left(\dfrac{\partial P}{\partial T}\right)_S = \dfrac{h_g^s - h_f^s}{T_f(V_g^s - V_f^s)}$
Two-Phase (homogeneous equilibrium sound speed, $\varepsilon = 1$, $0 < X < 1$)
$a = [XV_g^s + (1-X)V_f^s]\left(\dfrac{\partial P}{\partial T}\right)_S\left(\dfrac{T^s}{A+B}\right)^{1/2}$
$A = X\left\{C_{pg}^s - T^s V_g^s\left(\dfrac{\partial P}{\partial T}\right)_S\left[2\beta_g^s - \kappa_g^s\left(\dfrac{\partial P}{\partial T}\right)_S\right]\right\}$
$B = (1-X)\left\{C_{pf}^s - T^s V_f^s\left(\dfrac{\partial P}{\partial T}\right)_S\left[2\beta_f^s - \kappa_f^s\left(\dfrac{\partial P}{\partial T}\right)_S\right]\right\}$
$\left(\dfrac{\partial P}{\partial T}\right)_S = \dfrac{h_g^s - h_f^s}{T^s(V_g^s - V_f^s)}$

8 Special Component Models

8.1 Pump Component

The PUMP component model in ATHENA is a special component model composed for simulating centrifugal pumps in both single- and two-phase conditions. The model and the required input are described in detail in Volumes I and II and is not repeated in this section. However, some general comments about the underlying assumptions and applicability of the model are presented.

The pump model is implemented in the one-dimensional fluid field equations by using a dimensionless-homologous pump model to compute the pump head as a function of fluid flow rate and pump speed. The head developed by the pump is apportioned equally between the suction and discharge junctions that connect the pump volume to the system. The pump model is interfaced with the two-fluid hydrodynamic model by assuming the head developed by the pump is similar to a body force. Thus, the head term appears in the mixture momentum equation, but, like the gravity body force, it does not appear in the difference-of-momentum equation.

In ATHENA, one of two numerical schemes can be used to perform calculations. One is referred to as the semi-implicit scheme; the other is referred to as the nearly-implicit scheme. The pump model is implemented in each scheme in a somewhat different way. In the semi-implicit scheme, the pump head term is coupled implicitly only for the junction for which the new-time velocity is calculated. In the nearly-implicit scheme, the pump head term is coupled implicitly for both junction velocities.

To account for two-phase effects on pump performance, an option is provided to model two-phase degradation effects. To use the model, the user must provide a separate set of two-phase homologous curves in the form of difference curves. These curves were developed from the 1-1/2 loop model Semiscale and Westinghouse Canada Limited (WCL) experiments. Assumptions inherent in the pump model for two-phase flow include the following:

1. The head multiplier, $M_H(\alpha_g)$, determined empirically for the normal operating region of the pump, is also valid as an interpolating factor in all other operating regions.

2. The relationship of the two-phase to the single-phase behavior of the Semiscale pump is applicable to large reactor pumps. This assumes that the pump model of two-phase flow is independent of pump specific speed.

8.1.1 Pump Head and Torque Calculations

The average mixture density in the pump control volume is used to convert the total pump head H to the pressure rise through the pump ΔP by the definition $\Delta P = \rho_m H$. The pump ΔP thus determined is applied to the momentum equation by adding (1/2) ΔP to the momentum mixture equation for the pump suction junction and (1/2) ΔP to the momentum mixture equation at the pump outlet junction. To compute

the pump hydraulic torque τ_{hy}, the single- and two-phase torque components must be computed. The single-phase torque, $\tau_{1\phi}$, depends on the fluid density and is calculated from

$$\tau_{1\phi} = \beta_1 \tau_R \left(\frac{\rho_m}{\rho_R} \right) \tag{8.1-1}$$

where β_1 is the dimensionless hydraulic torque from the single-phase homologous torque curves, ρ_m is the average pump mixture density, and ρ_R is the rated pump density. The density ratio is needed to correct for the density difference between the pumped fluid and the rated condition. Similarly, the fully degraded torque, $\tau_{2\phi}$, is obtained from

$$\tau_{2\phi} = \beta_2 \tau_R \left(\frac{\rho_m}{\rho_R} \right) \tag{8.1-2}$$

where β_2 is the dimensionless hydraulic torque from the fully degraded homologous torque curves.

Total pump torque is used for two purposes in the pump model. First, it is used to calculate the pump speed if the electric motor drive or the pump coastdown with trip options are used. Second, the product of pump torque and speed is the pump energy dissipation included in the one-dimensional fluid field energy equation. Total pump torque is the sum of the pump hydraulic, frictional, and pump motor drive torques.

If the electric motor drive model is not used, the total pump torque is calculated by considering the hydraulic torque from the single- and two-phase homologous curves and the pump frictional torque, i.e.,

$$\tau = \tau_{hy} + \tau_{fr} \tag{8.1-3}$$

where

τ_{hy} = hydraulic torque

τ_{fr} = frictional torque.

The frictional torque is in the form of a constant or in the form of a four-term equation, that depends on the speed ratio. The value of the frictional torque is also dependent on the sign of the pump speed. The user must also input the coefficients for the four-term friction equation.

If the electric motor drive model is used, the motor torque τ_m is included in the total torque as

$$\tau = \tau_{hy} + \tau_{fr} - \tau_m \quad (8.1\text{-}4)$$

where the sign convention for τ_m is such that at steady flow operating conditions total torque is zero.

Using the total torque, then, the pump speed ω can be calculated from the deceleration equation as

$$\tau = I\frac{d\omega}{dt} \quad (8.1\text{-}5)$$

where I is the rotational moment of inertia of the pump-motor assembly.

Note that the electric motor pump drive model assumes an induction motor. Other drive models can be used, however, depending on the options selected by the user. For example, pump speed tables can be used that are governed by user-defined control variables, or the SHAFT component can be used to couple the PUMP component to a TURBINE component or to a GENERATOR component (i.e., the GENERATOR component can be used to simulate a motor). Excellent examples are presented for these cases in Volume II of this code manual.

The total pump power added to the fluid by the pump ($\tau\omega$) is separated into a hydraulic term $gH[(\alpha_f\rho_f v_f + \alpha_g\rho_g v_g)A]$ and a dissipation term (DISS). The dissipation term arises from turbulence in the pump and is added to the pump volume as heat. In a closed system, the hydraulic head from the pump is balanced by the sum of wall friction losses and form losses in the momentum equation. These losses should also appear as energy source terms in the energy equation, but only the wall friction terms are implemented in the default code. The default code should also add the form loss (code calculated abrupt area change loss and user-supplied loss) dissipation to the energy equation. This dissipation was removed in RELAP5/MOD2 because of temperature problems (i.e., overheating), and thus it is not present in ATHENA. The dissipation can be activated by the user in the input deck, however the user is cautioned that temperature problems may occur.

8.1.2 Pump Conclusions

The accuracy of the model highly depends on the specific pump performance data supplied by the user. The ATHENA pump head degradation model is an empirical model based largely on Semiscale data[8.1-1] and has little theoretical or mechanistic basis. Also, the Semiscale pump on which the model is based is not hydrodynamically similar to full-size reactor pumps. Therefore, data for the specific pump being simulated should be supplied.

Although the pump head degradation model has not been fully validated for calculating the two-phase performance of large nuclear reactor coolant pumps, it has performed well on a variety of integral tests. For most transients of interest, low void fractions at the pump inlet does not persist for long periods of time. As a result, the accuracy of the pump degradation model has little effect on the overall

transient since the head developed by centrifugal pumps degrades quickly and significantly at moderate to high void fractions.

For very small break accidents where the void fractions may be at low values for long periods of time, the effect of the pump model may be more important. In order to analyze these postulated accidents with confidence, accurate pump performance data under two-phase conditions may be important.

In summary, the accuracy of the model highly depends on the specific pump performance data supplied by the user. Ideally, data for the specific pump being simulated should be supplied. However, these data are not always available. Two-phase pump performance data are especially difficult to obtain. As a consequence, performance data from other pumps must often be used. Volume II provides the theory and criteria for evaluating the applicability of pump data to a pump other than on which the data were obtained. The built-in curves should be reviewed for applicability and used with caution.

8.1.3 Reference

8.1-1. D. J. Olson, *Single- and Two-Phase Performance Characteristics of the MOD-1 Semiscale Pump Under Steady-State and Transient Conditions,* Aerojet Nuclear Company, ANCR 1165, Idaho National Engineering Laboratory, October 1974.

8.2 Separator/Dryer Model

The mechanistic separator/dryer option of the separator component in ATHENA is intended for modeling of the separator and dryer hardware in a Boiling Water Reactor (BWR) system. These models were developed by The General Electric Company as part of the USNRC - General Electric - EPRI BWR Refill-Reflood Program. The models were originally developed for and implemented in the TRAC-BWR codes. The theory underlying the models is presented in Volume I of this manual. This section of Volume IV documents the interface between the mechanistic separator and the dryer models and the ATHENA hydrodynamic algorithm. The interface for each of the models comprises two sections, the input interface and the output interface. Each of these two interfaces are explained in the following sections.

8.2.1 Separator Model Input Interface

The input interface for the separator model comprises two sections. The first section describes the time-varying fluid state at the inlet of the separator; the second section provides time-invariant geometric and model parameter data. The geometric and model parametric data are specified in the user-input data deck, though default data are provided for these data items. The fluid state at the inlet of the separator is specified as the total fluid mass flow rate, the fluid quality, the phasic densities and viscosities, and the liquid level outside the separator barrel. Since the inlet to the separator is attached to a junction, the total mass flow rate, phasic densities and phasic viscosities are those in the inlet junction. The fluid quality at the inlet to the separator is computed from the inlet junction phasic densities, the inlet junction phasic velocities, and the phasic void fractions in the separator volume. The void fraction in the separator volume is used instead of the junction void fraction in the computation of the inlet quality, so that the separator

model will respond to the amount of fluid in the separator volume. The separator model computes the thickness of the liquid film on the inside of the separator barrel in order to compute the fluid carryover and carryunder qualities. The model equations represent a quasi-static description of the separating process which can respond instantaneously to changes in inlet flow rate and quality. The ATHENA hydrodynamic model includes fluid storage in each of the fluid volumes. The separator volume void fraction is used in the definition of the fluid inlet quality, so that the model will respond to the amount of liquid available in the volume with which to determine the liquid film used in the separating process. This ensures that if the amount of liquid stored in the separator volume increases such that the film thickness exceeds the critical film thickness, the separator performance degrades, and the liquid carryover increases. Conversely, if the void fraction in the separator volume increases, the film thickness decreases, and more vapor/gas is carried out of the separator discharge passages.

The last input parameter needed by the separator model is the liquid level surrounding the separator barrel. This liquid level is variable H_{12} in the discharge passage momentum equation. A liquid level model was not available when the separator model was originally developed, so the discharge momentum equation was changed to use the hydrostatic head from the separator outlet to the first-stage liquid discharge passage outlet as the input parameter. This is actually no change to the model because the term in which the liquid level was used represents the hydrostatic head at the exit of the separator discharge passage. The modified model uses the head directly rather that computing it from the liquid level and the fluid properties outside the separator. The head is computed as the difference in the pressures in the two volumes attached to the separator discharge junctions. The pressure in each volume is adjusted by the hydrostatic head in the volume between the volume center and the elevation of the separator connection.

8.2.2 Separator Model Output Interface

The separator model is incorporated in a subroutine that computes phasic flow rates in the vapor/gas outlet and liquid outlet passages given the fluid properties at the inlet to the separator. The liquid and vapor/gas outlets are represented in the ATHENA separator model as junctions, and the separator model flow rates must be converted into ATHENA junction variables. The separator junction flow qualities are computed from the separator model phasic flow rates and are then converted into junction volume fractions using the ATHENA junction phasic velocities and densities. The use of junction volume fraction to represent phase separation is the basis of the liquid level, and the same technique is used in the separator model interface.

8.2.3 Dryer Model Input Interface

The dryer model input interface comprises the same two sections as the separator model interface, though the dryer model is much simpler than the separator model. The dryer model performance parameters are contained in the user-input data for the dryer component though default data are provided. The input fluid properties are the inlet vapor/gas velocity and the dryer inlet moisture. The inlet vapor/gas velocity is obtained from the vapor/gas velocity in the dryer inlet junction. The dryer inlet moisture is computed as the liquid static quality in the dryer volume. This definition of the inlet property is used so

that the dryer model will respond to the amount of moisture stored in the dryer, rather than to the amount of moisture in the inlet junction.

8.2.4 Dryer Model Output Interface

The dryer model computes the “dryer capacity” using the dryer model parameters, the vapor/gas velocity at the inlet to the dryer, and the dryer inlet moisture. The computed dryer capacity is used to compute the void fraction in the dryer vapor/gas outlet junction. The junction void fraction is interpolated between a value of one for a dryer capacity of one (i.e., perfect drying) and the regular donor value at a dryer capacity of zero (no drying at all). This void fraction is limited so that no more than 90% of the available vapor/gas will be removed during the time step. This limitation is used to prevent the overextraction of vapor/gas during the time step. The void fraction in the liquid discharge junction is set to zero subject to the limitation that the liquid discharge junction remove no more than 90% of the available liquid during the time step. This is to prevent the overextraction of liquid out of the liquid discharge junction. In the physical dryer, the separated liquid flows back under the force of gravity to the downcomer from trays located under the dryer chevrons. The discharge pipes extend below the liquid level in the downcomer so that a liquid level is created in the discharge pipe, which prevents vapor/gas from being discharged from the interior of the dryer to the downcomer through the liquid discharge pipes at normal operating conditions and downcomer liquid levels. Establishing the correct liquid flow rate at steady-state conditions can be accomplished by adjusting the liquid discharge junction form loss coefficient by trial and error.

9 Heat Structure Process Models

The heat structures in ATHENA permit the calculation of heat across the solid boundaries of the hydrodynamic volumes. Heat transfer can be modeled from and/or through structures, including fuel pins or plates (with nuclear or electrical heating), steam generator tubes, and pipe and vessel walls. Temperatures and heat transfer rates are computed from the one-dimensional form of the transient heat conduction equation for non-reflood and from the two-dimensional form of the transient heat conduction equation for reflood. The one-dimensional form is discussed first. The two-dimensional form is discussed in Section 9.2.

One-dimensional heat conduction in rectangular, cylindrical, and spherical geometry can be represented by the heat structures in ATHENA. Surface multipliers are used to convert the unit surface of the one-dimensional calculation to the actual surface of the heat structure. Thermal conductivities and volumetric heat capacities as functions of temperature can be input in tables, or built-in values can be used.

Finite differences are used to advance the heat conduction solutions. Each mesh interval may contain a different mesh spacing, a different material, or both. The spatial dependence of the internal heat source, if any, may vary over each mesh interval. The time-dependence of the heat source can be obtained from the reactor kinetics, a table, or a control system. Energy from a metal-water reaction is added to the source term of inner and outer fuel cladding mesh intervals when this reaction occurs during a transient. Boundary conditions can be simulated by using tables of surface temperature versus time, heat transfer rate versus time, heat transfer coefficient versus time, or heat transfer coefficient versus surface temperature. Symmetrical or insulated boundary conditions can also be simulated. For heat structure surfaces connected to hydrodynamic volumes, a heat transfer package containing correlations for convective, nucleate boiling, transition boiling, and film heat transfer from the wall-to-fluid and reverse transfer from fluid-to-wall is provided. These correlations are discussed in Section 4.2 of this volume of the manual.

9.1 Heat Conduction for Components

One-dimensional heat conduction in rectangular, cylindrical, and spherical geometry can be used to represent the heat structures in any of the components in ATHENA. It is assumed in one-dimensional heat conduction that the temperature distribution in the axial or radial direction is the same throughout the structure being modeled and that the linear heat flow is negligible. The equations governing one-dimensional heat conduction are

$$\rho C_p \frac{\partial T}{\partial t} = \frac{\partial}{\partial x}\left(k \frac{\partial T}{\partial x}\right) + S \qquad \text{for rectangular geometry} \tag{9.1-1}$$

$$\rho C_p \frac{\partial T}{\partial t} = \frac{1}{r}\left[\frac{\partial}{\partial r}\left(rk \frac{\partial T}{\partial r}\right)\right] + S \qquad \text{for cylindrical geometry} \tag{9.1-2}$$

and

$$\rho C_p \frac{\partial T}{\partial t} = \frac{1}{r^2}\left[\frac{\partial}{\partial r}\left(r^2 k \frac{\partial T}{\partial r}\right)\right] + S \qquad \text{for spherical geometry} \qquad (9.1\text{-}3)$$

where T is the temperature, t is the time, x is the length, r is the radius, S is the internal volumetric heat source, ρC_p is the volumetric heat capacity, and k is the thermal conductivity.

In order to model a heat structure in ATHENA, a mesh is set up beginning at the left boundary of the structure being modeled and continuing to the right boundary. The mesh point spacing (**Figure 9.1-1**) is taken as positive as x or r increases from left to right. Mesh points must be placed on the external boundaries of the structure unless a symmetrical or adiabatic boundary condition is to be used. Mesh points may also be placed at any desired intervals within the structure and should be placed at the interfaces between the different materials. The spacing of the mesh points may vary from material to material and may vary within the material as the user desires. If the structure being modeled is symmetrical, such as a core heater rod, the left boundary must be the center of the rod and the right boundary the outside surface of the rod. This symmetry is simulated by an adiabatic boundary across which no heat may flow (this can also be used to simulate a perfectly insulated boundary). The thermal conductivities (k) and volumetric heat capacities (ρC_p) of the materials between the mesh points are required to complete the description of the heat structure in ATHENA. These material properties can be input in tabular form as functions of temperature or the user may choose to use the built-in values.

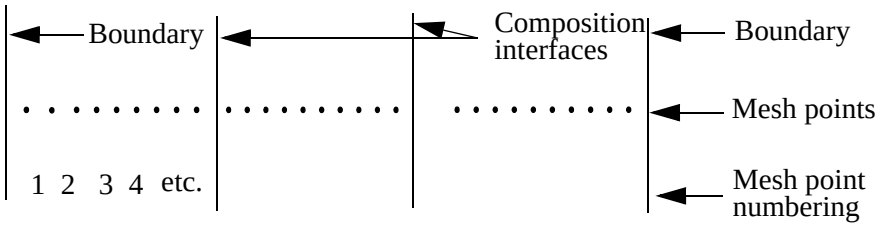

Figure 9.1-1 Mesh point layout.

Heat may flow across the external heat structure boundaries to either the environment or to the reactor coolant. For heat structure surfaces connected to hydrodynamic volumes containing reactor coolant, a heat transfer package is provided containing correlations for convective, nucleate boiling, transition boiling, and film heat transfer from wall-to-liquid and reverse heat transfer from liquid-to-wall. These correlations are discussed in Section 4.2 and will not be discussed here. Any number of heat structures may be connected to each hydrodynamic volume. These heat structures may vary in geometry type, mesh spacing, internal heat source distribution, etc. This flexibility allows the user to accurately model any type of structure. For heat structure surfaces connected to volumes simulating the environment, tables can be used to simulate the desired boundary conditions. Tables of surface temperature versus time, heat transfer rate versus time, heat transfer coefficient versus time, or heat transfer coefficient versus surface temperature can be used to simulate the boundary conditions. Usually, heat losses are modeled

using the heat transfer coefficient versus surface temperature boundary condition and combining the radiative and natural convection heat transfer coefficients in the table.

A contact-resistance interface condition cannot be specified directly, since the temperature, instead of being continuous at the interface, is given by $q = k_c \Delta T$, where q is the heat transfer rate across the interface, k_c is the contact thermal conductivity, and ΔT is the temperature change across the interface. This condition can be specified by defining a small mesh interval with thermal properties of $k = k_c$ and $\rho C_p = 0$. The size of the mesh interval is arbitrary except that in the cylindrical and spherical geometries the surface and volume depend on the radius. The mesh interval is usually chosen very small with respect to the dimensions of the problem.

Internal heat sources can be placed into any heat structure in ATHENA, whether it represents a fuel rod or a pipe wall. The spatial dependence of the heat source can be simulated using weighting factors that partition the heat source to various portions of the heat structure. The time-dependence of the heat source can be obtained from the reactor kinetics solution, a table, or a control system.

In ATHENA, various subroutines are used in solving the one-dimensional heat conduction equations. HTCOND returns left and right boundary conditions for a heat structure. HTCSOL finds temperature solution by back substitution. HTRC1 computes heat transfer coefficients from correlations. HT1SST solves the one-dimensional steady-state heat problem. HT1TDP advances one heat structure one time step by advancing the transient one-dimensional heat conduction equation. HTADV controls the advancement of heat structures and computes heat added to the hydrodynamic volumes. Subroutines HT1SST and HT1TDP are the same except that HT1SST is used when the heat structure steady-state option is specified by the user. HT1SST differs from HT1TDP in that the time-dependence in the difference equations is removed.

The heat conduction equation is not a correlation and can be solved by various numerical techniques. ATHENA uses the Crank-Nicolson[9.1-1] method for solving this equation. The actual coding will not be shown or discussed here. The discussion in Volume I of this code manual represents what is actually in the code, except for the separation of the steady-state and transient solutions into the two subroutines HT1SST and HT1TDP. For the derivation of the finite difference equations from the one-dimensional heat conduction equations, see Volume I of this manual. Several heat conduction test problems were run to illustrate how well calculates heat conduction. All of the cases have closed-form solutions as given in **Reference 9.1-2**. These comparisons were done for the RELAP5/MOD2 models and correlations report[9.1-3]. These same RELAP5/MOD2 comparisons are shown here in this volume of the ATHENA manual (**Figure 9.1-2** through **Figure 9.1-8**). Since the heat conduction model has not changed, it is expected that the ATHENA comparisons would be the same as these RELAP5/MOD2 comparisons. (note: As discussed next, Case 3 has been run on ATHENA).

Case 1. Steady-state heat conduction in a composite wall, $0 < x < l$, with surface temperatures held constant at T_o and T_l. A 0.24-inch wall was modeled consisting of Inconel 718, constantan, stainless steel, and Inconel 600, and with

surface temperatures of T_o = 80 °F and T_l = 70 °F. This is the basic and simplest case for heat conduction in rectangular geometry. **Figure 9.1-2** compares the solution and the textbook solution.

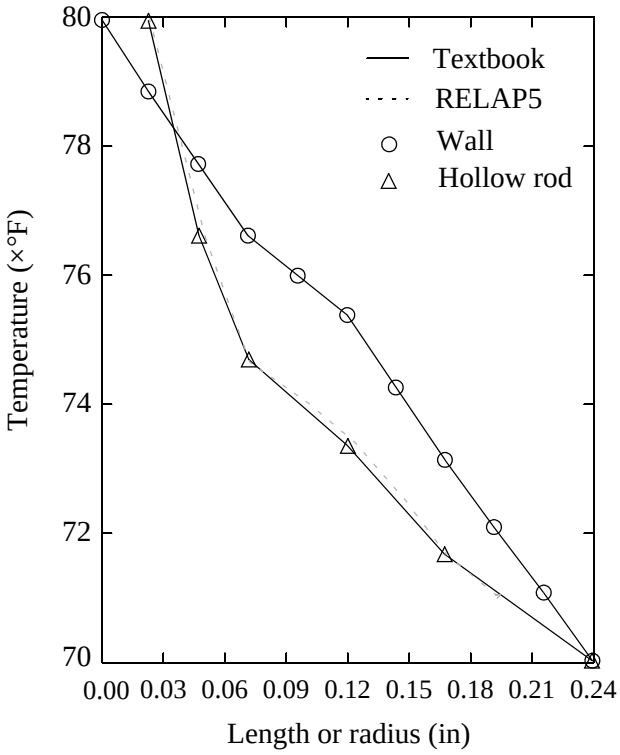

Figure 9.1-2 Cases 1 and 2, temperature versus length or radius.

Case 2. Steady-state heat conduction in a composite hollow cylinder, $R_i < r < R_o$, with surface temperatures held constant at T_i and T_o. A hollow cylinder was modeled with an inside radius of 0.024 inch and an outside radius of 0.24 inch, consisting of Inconel 718, constantan, stainless steel, and Inconel 600, and with surface temperatures of T_i = 80 °F and T_o = 70 °F. This is the basic and simplest case for heat conduction in cylindrical geometry. **Figure 9.1-2** compares the solution and the textbook solution.

Case 3. Transient heat conduction in a uniform wall, -l < x < l, with an initial temperature distribution of $\Delta T \cos\left(\frac{\pi x}{21}\right) + T_o$ and surface temperatures held constant at T_o. A 0.48-inch wall was modeled consisting of stainless steel with a surface temperature of T_o = 70 °F and with ΔT = 10 °F. The resulting time-dependent temperature distribution is given by

$$T = \Delta T \bullet \cos\left(\frac{\pi x}{2l}\right) \bullet e^{-\kappa\pi^2 t/4l^2} + T_o \qquad (9.1\text{-}4)$$

where κ is $\frac{k}{\rho C_p}$. **Figure 9.1-3** compares the solution to the closed-form solution for various times. This problem is run on every new version of ATHENAto test the conduction model before the new version is released.

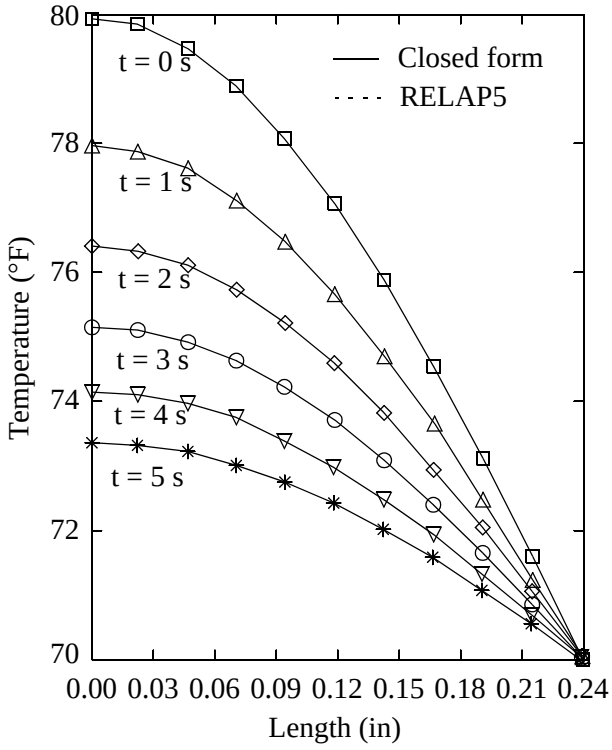

Figure 9.1-3 Case 3, temperature versus length.

Case 4. Transient heat conduction in a uniform rod, $0 < r < R_o$, with an initial parabolic temperature distribution of $T_i - ar^2$ and surface temperatures held constant at T_o. A 0.48-inch outside diameter rod was modeled consisting of stainless steel with a surface temperature of T_o = 70 °F, and with T_i = 80°F and a = 25,000 °F/ft^2. This gives similar results to Case 3, but for cylindrical geometry. The resulting time-dependent temperature distribution is given by

$$T = \frac{2}{R_o} \bullet \sum_{n=1}^{\infty} \{ e^{-\kappa\alpha_n^2 t} \bullet \frac{J_o(r\alpha_n)}{\alpha_n^2 \bullet J_1^2(R_o\alpha_n)} \bullet \alpha_n \bullet [(T_i - T_o - kR_o^2) \bullet J_1(R_o\alpha_n) + 2kR_o \bullet J_2(R_o\alpha_n)] \} T_o \qquad (9.1\text{-}5)$$

where κ is $\frac{k}{\rho C_p}$ and α_n are the positive roots of $J_o(\alpha R_o) = 0$. **Figure 9.1-4** compares the solution to the closed form solution for various times.

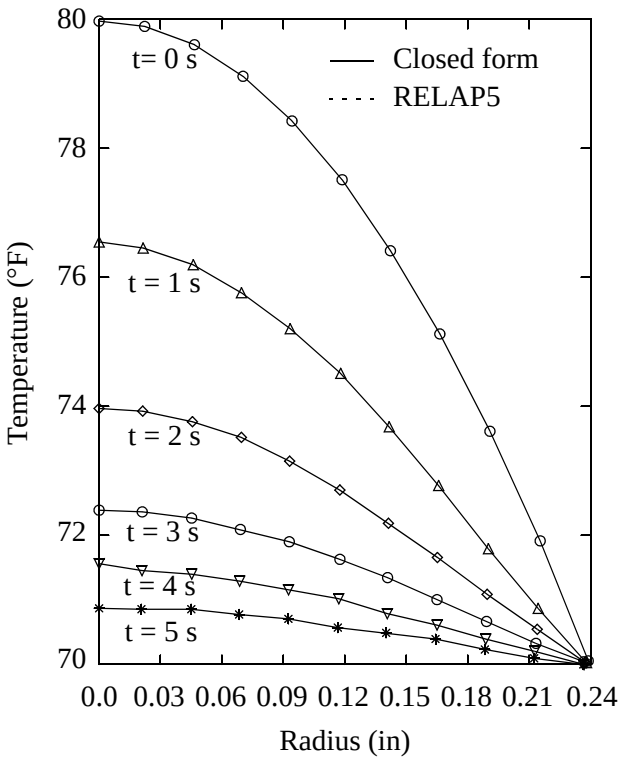

Figure 9.1-4 Case 4, temperature versus radius.

Case 5. Transient heat conduction in a uniform wall, $-l < x < l$, with a uniform initial temperature distribution at T_i and surface temperatures maintained at $\Delta T \sin(\omega t) + T_i$ for $t > 0$. A 0.48-inch wall was modeled consisting of stainless steel with a uniform initial temperature of $T_i = 75$ °F and with $\Delta T = 5$ °F and $\omega = \frac{\pi}{2}$ s^{-1}. The resulting time-dependent temperature distribution is given by

$$T = \Delta T \bullet A \bullet \sin(\omega t + \phi) + T_1 + 4\pi\kappa \bullet \sum_{n=0}^{\infty} \left\{ \frac{(-1)^n (2n+1)(41^2\omega)}{161^4\omega^2 + \kappa^2\pi^4 \bullet (2n+1)^4} \right. \\ \left. \bullet e^{-\kappa(2n+1)^2\pi^2 t/4l^2} \bullet \cos\left[\frac{(2n+1)\pi x}{2l}\right] \right\} \quad (9.1\text{-}6)$$

where κ is $\frac{k}{\rho C_p}$ and

$$A = \left|\frac{\cosh[\nu x(1+i)]}{\cosh[\nu l(1+i)]}\right| = \left[\frac{\cosh(2\nu x)+\cos(2\nu x)}{\cosh(2\nu l)+\cos(2\nu l)}\right]^{1/2}$$

$$\phi = \arg\left\{\frac{[\cosh \nu x(1+i)]}{[\cosh \nu l(1+i)]}\right\}, \qquad \nu = \left(\frac{\omega}{2\kappa}\right)^{1/2} .$$

Figure 9.1-5 compares the solution to the closed form solution for various times.

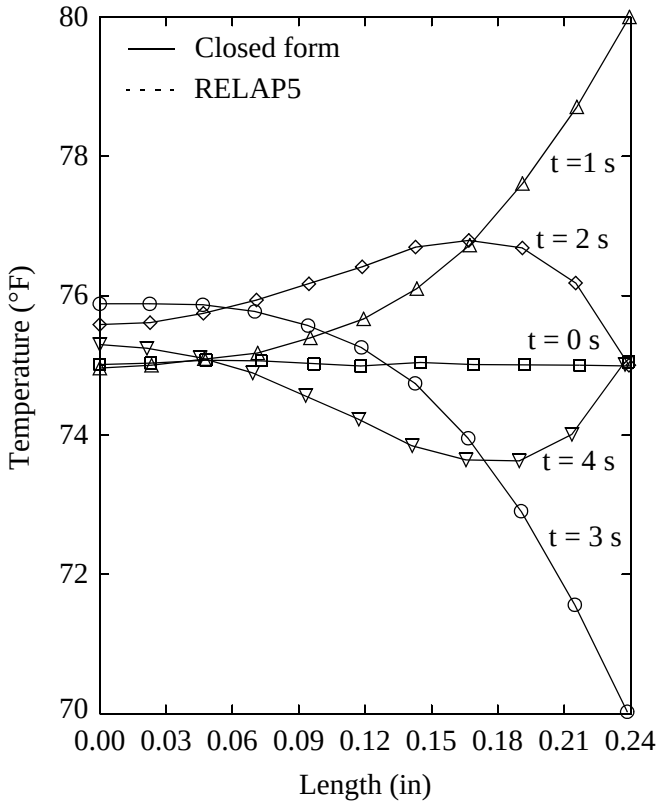

Figure 9.1-5 Case 5, temperature versus length.

Case 6. Transient heat conduction in a uniform rod, $0 < r < R_o$, with a uniform initial temperature distribution at T_i and surface temperatures maintained at $\Delta T \sin(\omega t) + T_i$ for $t > 0$. A 0.48-inch outside diameter rod was modeled consisting of stainless steel with a uniform initial temperature of T_i = 75 °F and with ΔT = 5 °F and $\omega = \frac{\pi}{2}$ s^{-1}. The resulting time-dependent temperature distribution is given by

$$T = \Delta T \bullet \mathrm{Real}\left\{\frac{I_o\left[r \bullet \left(\frac{i\omega}{\kappa}\right)^{1/2}\right]}{iI_o\left[R_o \bullet \left(\frac{i\omega}{\kappa}\right)^{1/2}\right]}\right\} \bullet e^{i\omega t} + \frac{2\kappa \bullet \Delta T}{R_o} \bullet \sum_{n=1}^{\infty}\left[e^{-\kappa\alpha_n^2 t} \bullet \frac{\alpha_n \bullet \omega \bullet J_o(r\alpha_n)}{(\kappa^2\alpha_n^4 + \omega^2) \bullet J_1(R_o\alpha_n)}\right] + T_i \quad (9.1\text{-}7)$$

where κ is $\frac{k}{\rho C_p}$ and α_n are the positive roots of $J_0(aR_o) = 0$. **Figure 9.1-6** compares the solution to the closed-form solution for various times. This is the same as Case 5 but for cylindrical geometry.

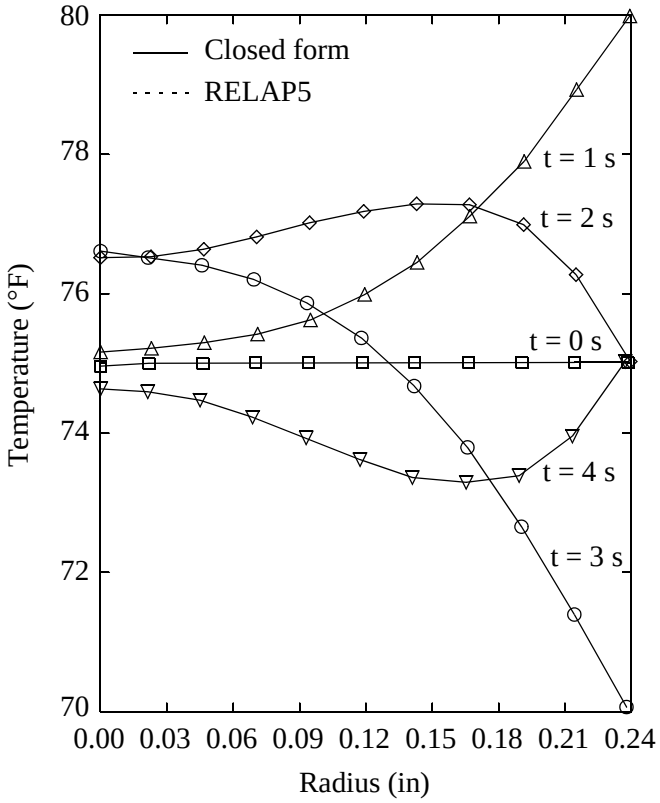

Figure 9.1-6 Case 6, temperature versus radius.

Case 7. Transient heat conduction in a uniform rod, $0 < r < R_o$, with a uniform initial temperature distribution of T_i and with uniform heat production at the rate of $Q_o e^{-\lambda t}$ per unit time per unit volume for $t > 0$. A 0.48-inch outside diameter rod was modeled consisting of stainless steel with a uniform initial temperature of

T_i = 70 °F and with Q_o = 709.5 Btu/s-ft^3 and $\lambda = \ln(2) = 0.693147\ s^{-1}$. The resulting time-dependent temperature distribution is given by

$$T = \frac{\kappa Q_o}{kg} \bullet e^{-\lambda t} \bullet \left\{ \frac{J_o\left[r \bullet \left(\frac{\lambda}{\kappa}\right)^{1/2} \right]}{J_O\left[R_0 \bullet \left(\frac{\lambda}{\kappa}\right)^{1/2} \right]} - 1 \right\} - \frac{2Q_o\kappa}{R_o k} \bullet \sum_{n=1}^{\infty} \left[\frac{e^{-\kappa\alpha_n^2 t} \bullet J_o(r\alpha_n)}{\alpha_n \bullet (\kappa\alpha_n^2 - \lambda) \bullet J_1(R_o\alpha_n)} \right] + T_i \qquad (9.1\text{-}8)$$

where κ is $\frac{k}{\rho C_p}$ and α_n are the positive roots of $J_o(\alpha R_o) = 0$. **Figure 9.1-7** compares the solution to the closed form solution for various times. The exponential decay modeled in this case is similar to the decay experienced in a core heater rod.

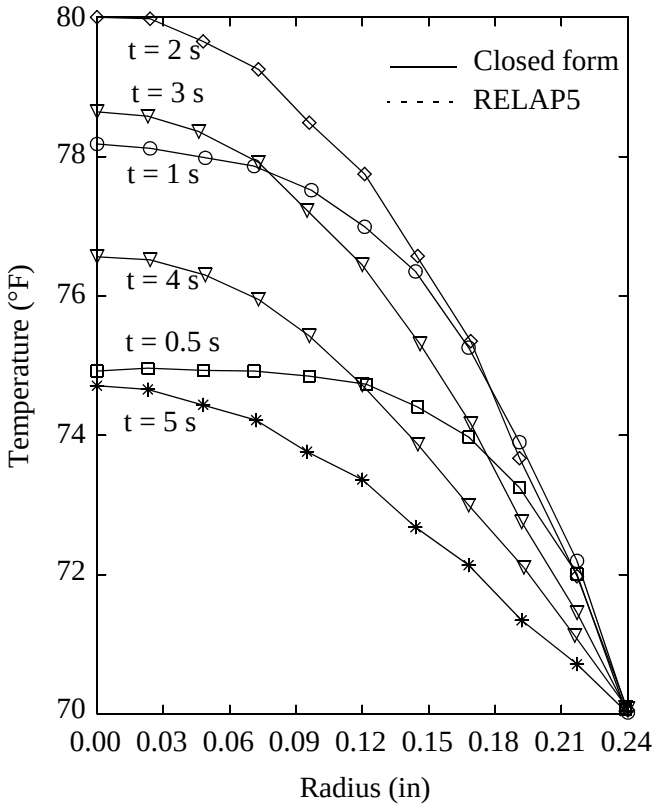

Figure 9.1-7 Case 7, temperature versus radius.

All seven cases were run with different time step sizes of 0.01, 0.1, 0.5, 1.0, and 2.0 seconds to test the stability of the solution. The Crank-Nicolson method is designed to be stable for all conditions, and the

solution was stable for all the time steps tested. However, calculational inaccuracies did occur as the time step size was increased. These inaccuracies did not result because of instabilities in the solution technique of the heat conduction equation in , but resulted from making the time step larger than the time-constant for the particular problem and changing the boundary conditions. The time-constant for any particular problem is difficult to define, and only in Cases 3 and 4 did the boundary conditions remain constant as the time step size was increased. (For steady-state Cases 1 and 2, the choice of time step size made no difference.) No significant inaccuracies were seen in these two cases until the time step was increased to 1.0 second, and then only in Case 4 with the cylindrical geometry (**Figure 9.1-8**). In these two cases, the temperature variation was fairly benign, but inaccuracies were calculated. The time step size is the choice of the user, and the user should be aware that the larger the time step chosen the greater the possibility that inaccuracies will be calculated. Unless the transient being calculated is at a quasi-steady-state, using a time step of 1.0 second is bordering on recklessness and is not recommended. A larger time step size may also change the boundary conditions, because the boundary conditions are assumed to vary linearly between time step values. The boundary conditions input to can change only as fast as the time step. If the boundary conditions vary faster than one time step, the change is not input to . The boundary conditions between the time steps are not actually changed by R; they are never put in. If, for example, a sine wave with a period of 4 seconds (as in Cases 5 and 6) is used as a boundary condition and a time step of 1 second is used, the resulting boundary condition would be a saw tooth curve; if a time step of 2 seconds is used, the resulting boundary condition would be a straight line. This obviously leads to inaccuracies that are not associated with the solution technique.

In all seven cases, when the time step size was 0.01 second the calculated temperature distribution agreed very well with the temperature distribution calculated from the closed-form solution. The closed-form solutions involve summations to infinity and had to be approximated. In addition, for cylindrical geometry, the closed-form solutions involve Bessel functions; and approximations were used in calculating these functions. As a result, the closed-form solutions are not exact. No significant differences between and the closed-form solutions were found for the small time steps, so the conduction model in is judged to work very well. As indicated earlier, since the heat conduction model has not changed, it is expected ATHENA comparisons would be the same as these RELAP5/MOD2 comparisons. (Note: As discussed before, Case 3 has been run on ATHENA).

9.1.1 References

9.1-1. J. Crank and P. Nicolson, “A Practical Method for Numerical Evaluation of Solutions to Partial Differential Equations of the Heat-Conduction Type,” *Proceedings of the Cambridge Philosophical Society, 43,* 1947, pp. 50-67.

9.1-2. H. S. Carslaw and J. C. Jeager, *Conduction of Heat in Solids,* 2nd Edition, Oxford: Oxford University Press, 1959.

9.1-3. R. A. Dimmena et al., *RELAP5/MOD2 Models and Correlations,* NUREG/CR-5194, EGG-2531, Idaho National Engineering Laboratory, August 1988.

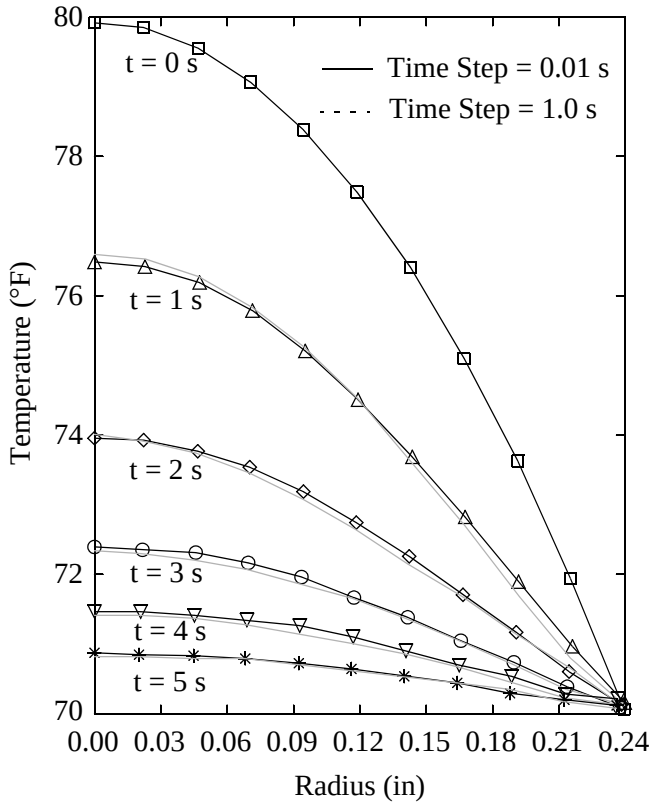

Figure 9.1-8 Temperature versus radius, varying time steps.

9.2 Reflood Heat Conduction

A two-dimensional heat conduction scheme is used in the reflood model for cylindrical and rectangular heat structures. This scheme is an extension of the one-dimensional heat conduction scheme and is found in subroutine HT2TDP. Included with the two-dimensional heat conduction scheme is a fine mesh-rezoning scheme. The fine mesh-rezoning scheme is implemented to efficiently use the two-dimensional conduction solution for reflood calculations. The scheme is similar to the one used in COBRA-TF[9.2-1] and is intended to resolve the large axial variation of wall temperatures and heat fluxes during core reflood. The number of axial nodes in the heat structures is varied in such a way that the fine nodes exist only in the nucleate boiling and transition boiling regions. Volume I of this code manual discusses in detail the two-dimensional heat conduction solution and the fine mesh-rezoning scheme.

Reflood becomes important during a LOCA after the core has been voided and liquid begins to refill the core as a result of the ECCS. As the core liquid level rises, liquid contacts the hot core rods and vapor is formed. Eventually, the rods cool down sufficiently so that they can no longer form vapor. The core rods, however, do not cool down uniformly, and there exists a transition region above which the core rods

have not been rewet and below which they have. It is this transition region that the reflood model and fine mesh rezoning scheme were designed to calculate. In this transition region, there is a large axial variation in wall temperatures and heat fluxes that require a finer noding than is necessary for the normal temperature and heat flux calculations. At the initiation of the reflood model, each heat structure is subdivided into two axial intervals (**Figure 9.2-1**). A two-dimensional array of mesh points is thus formed. Thereafter, the number of axial intervals may be doubled, halved, or remain unchanged at each time step as the transition region moves up the core.

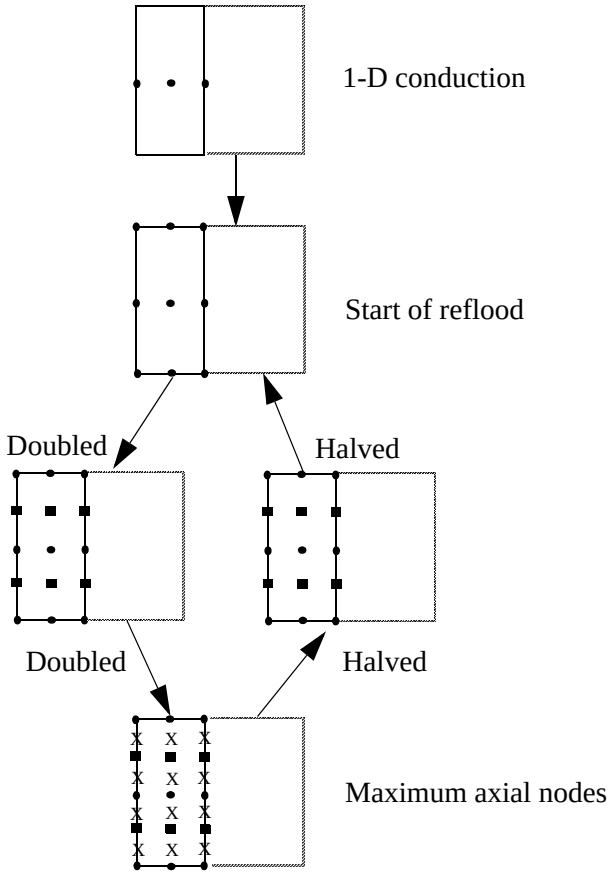

Figure 9.2-1 An example of fine mesh-rezoning process.

The number of axial mesh intervals in a heat structure depends on the heat transfer regimes in the heat structures. At each time step, all heat structures in a heat-structure geometry are searched to find the positions of T_{CHF}, the wall temperature where CHF occurs, of T_Q, the quench or rewetting temperature, and of T_{IB}, the wall temperature at the incipience of boiling. As the transition region moves up through the core, so do the points where T_{CHF}, T_Q, and T_{IB} occur. For heat structures where the transition region has not yet been reached (void fraction greater than 0.999), the number of axial mesh points remains subdivided into two. For heat structures where the transition region has past (void fraction equals 0.0), the number of axial mesh points is halved, but not less than two. For heat structures at the beginning and at the

end of the transition region (where T_Q and T_{IB} occur), the number of axial mesh points is doubled, but not to more than half the maximum specified by the user. For the heat structures between those containing T_Q and T_{IB} (which includes the heat structure containing T_Q), the number of axial mesh points is doubled up to the maximum specified by the user. This rezoning of the axial mesh points is shown in **Figure 9.2-1**. As a result of this rezoning, the largest number of mesh points is always around the transition region as it moves up through the core.

The reflood heat transfer correlations used in the nucleate boiling and transition boiling regions are specialized for the low-pressure and low-flow cases typical of reflood situations. As a result, the reflood model should only be used for pressures less than 1 MPa and mass fluxes less than 200 kg/s•m^2. In general, the time when the reflood model is activated need not coincide with the time the liquid enters the core. In fact, the most appropriate time to activate the reflood model is when the pressure is less than 1 MPa and the core is nearly empty.

The reflood model in ATHENA has shown good agreement with nonuniform heated rod bundle data with respect to time to maximum temperature, maximum temperature, and quench temperature, but predicted a longer time to quench.[9.2-2,9.2-3] This predicted time to quench could be larger than the actual time by a factor of 1.1 to 1.5, depending upon the position within the core. Generally, the greatest discrepancy in the time to quench has been observed above the point of maximum power at slow reflood rates. The reason for this is suspected to be overprediction of the liquid entrainment above the quench front so that the liquid inventory in the core is progressively underpredicted. For LBLOCAs, the time to quench may not be as important as the maximum temperature. Comparison to test data has shown that the reflood model in ATHENA yields a good simulation for a high flow rate, but only a fair simulation for a low flow rate. The problem with the low flow rate simulation is probably due to water-packing.

9.2.1 References

9.2-1. J. M. Kelly, "Quench Front Modeling and Reflood Heat Transfer in COBRA-TF," *ASME Winter Annual Meeting, New York, New York, 1979,* 79-WA/HT-63.

9.2-2. V. H. Ransom et al., *RELAP5/MOD2 Code Manual, Volume 3: Developmental Assessment Problems,* EGG-TFM-7952, Idaho National Engineering Laboratory, December 1987.

9.2-3. H. Chow and V. H. Ransom, "A Simple Interphase Drag Model for Numerical Two-Fluid Modeling of Two-Phase Flow Systems," *ANS Topical Meeting on Nuclear Reactor Thermal Hydraulics, New Orleans, LA, June 1984.*

9.3 Gap Conductance Model

The gap conductance between the fuel and the cladding depends strongly on the gap width and has a significant influence on the fuel temperatures. The actual gap width of a LWR fuel rod can be substantially different from the as-fabricated fuel-cladding gap width even during normal reactor operation and especially during a postulated LOCA transient. The change in the fuel-cladding gap is due to differential

thermal expansion of the fuel and cladding, elastic and plastic deformation of the fuel and the cladding, and other effects.

The ATHENA gap conductance model accounts for the first-order effects of material deformations under normal reactor operating conditions and most postulated LOCA conditions. The model is based on a simplified material deformation condensed from FRAP-T6[9.3-1] and is contained in subroutine GAPCON. The material properties are taken from MATPRO-11 (Revision 1).[9.3-2] The model considers, among other things, the thermal expansion of the fuel and the cladding, and the elastic deformation of cladding under the differential pressure between the gas internal to the gap and the fluid outside the cladding.

The dynamic gap conductance model in subroutine GAPCON defines an effective gap conductivity and employs the following assumptions. First, the fuel-to-cladding radiation heat transfer, which only contributes significantly to the gap conductivity under the conditions of cladding ballooning, is neglected. This is appropriate, since cladding ballooning is not included in this simple model. Second, the minimum gap size is limited such that the maximum effective gap conductivity is about the same order as that of metals. Third, the direct contact of the fuel pellet and the cladding is not explicitly considered. Again, a detailed discussion of the numerical techniques employed in this model is given in Volume I of this code manual and will not be repeated here.

Steady-state average centerline temperature data from the Power Burst Facility (PBF) Test LOC-11c[9.3-3] were used to evaluate the dynamic gap conductance model. The test system consists of four nearly identical fuel rods with their own individual flow shroud. Only a single rod along with its flow channel was modeled. The model consists of nine volumes and nine heat structures in the length of the active fuel stack. The top volume has a length of 0.1159 mm, and the rest each have a length of 0.1 m. Some other input specifications are listed in **Table 9.3-1**. **Table 9.3-2** lists the axial power profile. An earlier cycle of ATHENA was used in these calculations, but the gap conductance model has remained unchanged.

Table 9.3-1 Fuel rod geometry characteristics and conditions for PBF Test LOC-11C.

Pellet diameter	9.30 mm
Cladding outside diameter	10.72 mm
Cladding inside diameter	9.50 mm
Diametrical gap	0.20 mm
Helium prepressurization	2.41 MPa (Rod 611-3)
Flow channel area	2.257×10^{-4} m^2
Hydraulic diameter	2.68×10^{-2} m
Flow rate	0.643 kg/s

Table 9.3-1 Fuel rod geometry characteristics and conditions for PBF Test LOC-11C. (Continued)

Lower plenum pressure	15.3 MPa
Lower plenum temperature	596.0 K

Table 9.3-2 Axial power profile of PBF Test LOC-11C.

Distance From Bottom of Fuel Stack (m)	Normalized Axial Power[1]
0.0	0.163
0.0254	0.326
0.0762	0.620
0.1270	0.862
0.1778	1.047
0.2286	1.184
0.2794	1.285
0.3302	1.355
0.3810	1.296
0.4318	1.400
0.4826	1.368
0.5334	1.304
0.5842	1.221
0.6350	1.128
0.6858	1.028
0.7366	0.910
0.7874	0.754
0.8382	0.548
0.8890	0.290
0.9159	0.256

1. Local power/average power.

Figure 9.3-1 shows the comparison of the data and the calculated results. The data are centerline temperatures averaged over four fuel rods. Two ATHENA-calculated results are given, one with and one without the gap deformation model. The calculated values using the gap conductance model are about 0 to

100 K higher than the data. However, the calculation without using the gap conductance model yields temperatures much higher than the data. In particular, the differences are about 500 to 700 K in the high-power region. The reduction of centerline temperatures with the gap conductance model is primarily due to thermal expansion of UO_2, which reduced the gap size and increased the gap conductance. The dynamic gap conductance model in ATHENA can significantly improve the simulation of nuclear reactor transients where the gap size has a significant effect on the transient.

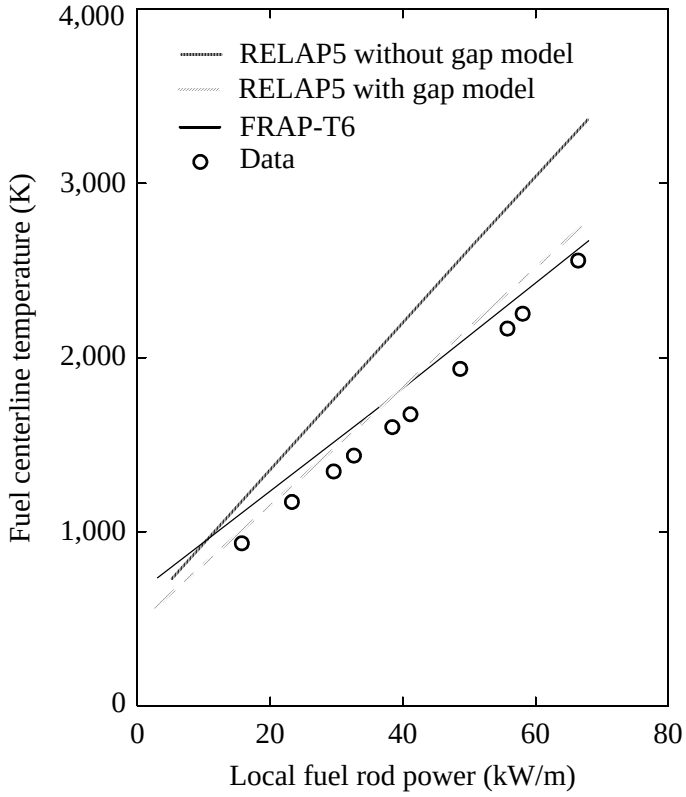

Figure 9.3-1 Comparison of measured and calculated steady-state fuel centerline temperature for PBF Test LOC-11C.

9.3.1 References

9.3-1. L. J. Siefken, C. M. Allison, M. P. Bohn, and S. O. Peck, *FRAP-T6: A Computer Code for the Transient Analysis of Oxide Fuel Rods*, EGG-CDAP-5410, Idaho National Engineering Laboratory, April 1981.

9.3-2. D. L. Hagrman, G. A. Reymann, and R. E. Mason, *MATPRO-Version 11 (Revision 1)*, NUREG/CR-0479, TREE-1280, Rev. 1, Idaho National Engineering Laboratory, February 1980.

9.3-3. J. R. Larson et al., *PBF-LOCA Test Series Test LOC-11 Test Results Report*, NUREG/CR-0618, TREE-1329, Idaho National Engineering Laboratory, April 1979.

9.4 Reactor Kinetics

The primary energy source for a nuclear reactor is the reactor core. ATHENA allows the user to model the power generated in the reactor core as specified from a table, or as determined by point-reactor kinetics with reactivity feedback. This power is modeled as an internal heat source in user-defined heat structures and can be partitioned by inputting weighting factors to distribute the energy to the various portions of the core as the user desires. The point reactor or space-independent kinetics approximation is adequate for cases in which the spatial power distribution remains nearly constant.

The point reactor kinetics model in ATHENA computes both the immediate (prompt and delayed) fission power and the power from decay of fission fragments. The immediate (prompt and delayed) power is released at the time of fission and includes fission fragment kinetic energy and neutron moderation. Decay power is generated as the fission products undergo radioactive decay. The user can select the decay power model based on an approximation to the 1973 ANS Proposed Standard[9.4-1], the exact 1979 ANSI/ANS Standard[9.4-2,9.4-3,9.4-4], or the exact 1994 ANSI/ANS Standard[9.4-5]. The ATHENAimplementation of the 1973 Proposed Standard uses one isotope (^{235}U) for the fission source and 11 groups for fission product decay. The 1979 Standard lists data for three isotopes (^{235}U,^{238}U,^{239}Pu) and uses 23 groups for each isotope. A user option also allows only the 1979 Standard data for ^{235}U to be used. The 1994 Standard lists data for four isotopes (^{235}U, ^{238}U, ^{239}Pu, ^{241}Pu) and uses 23 groups for each isotope. A user option also allows only the 1994 Standard data for ^{235}U to be used. The data for all standards are built into ATHENA as default data, but the user may enter different data. In addition, ATHENA contains an actinide decay model that may be switched on by the user. Two isotopes, ^{239}U and ^{239}Np, are used in the ATHENA model. ^{239}U is produced by neutron capture in ^{238}U and forms ^{239}Np by beta decay. ^{239}Np then forms ^{239}Pu by beta decay. The actinide model gives the result quoted in the 1979 Standard and the 1994 Standard.

The point reactor kinetics equations are (see Glasstone and Sesonske[9.4-6])

$$\frac{dn(t)}{dt} = \frac{[\rho(t) - \beta]}{\Lambda} n(t) + \sum_{i=1}^{N_d} \lambda_i C_i(t) + S \qquad (9.4\text{-}1)$$

$$\frac{dC_i(t)}{dt} = \frac{\beta f_i}{\Lambda} n(t) - \lambda_i C_i(t) \qquad i = 1, 2, ..., N_d \qquad (9.4\text{-}2)$$

$$\varphi(t) = n(t)v \qquad (9.4\text{-}3)$$

$$\psi(t) = V\Sigma_f\varphi\ (t) \tag{9.4-4}$$

$$P_f(t) = Q_f\ \psi(t) \tag{9.4-5}$$

where

t	=	time (s)
n	=	neutron density (neutrons/m^3)
φ	=	neutron flux (neutrons/m^2·s)
v	=	neutron velocity (m/s)
C_i	=	delayed neutron precursor concentration in group i (nuclei/m^3)
β	=	effective delayed neutron fraction
	=	$\sum_{i=1}^{N_d} \beta_i$
Λ	=	prompt neutron generation time (s)
ρ	=	reactivity (only the time-dependence has been indicated; however, the reactivity is dependent on other variables)
f_i	=	fraction of delayed neutrons of group i
	=	β_i/β
β_i	=	effective delayed neutron precursor yield of group i
λ_i	=	decay constant of group i (1/s)
S	=	source rate density (neutrons/m^3·s)
ψ	=	fission rate (fissions/s)
Σ_f	=	macroscopic fission cross-section (1/m)
P_f	=	immediate (prompt and delayed) fission power (MeV/s)

Q_f = immediate (prompt and delayed) fission energy per fission (MeV/fission)

V = volume (m^3)

N_d = number of delayed neutron precursor groups.

After some modifications and variable substitutions, these equations are solved in subroutine RKIN by the modified Runge-Kutta method of Cohen[9.4-7] used in the AIREK II Reactor Kinetics Code.[9.4-8] These equations are not correlations, so was run to test the point-reactor kinetics model without reactivity feedback against textbook data. These comparisons were done for the RELAP5/MOD2 models and correlations report[9.4-9]. These same RELAP5/MOD2 comparisons are shown here in this volume of the ATHENA manual (**Figure 9.4-1** through **Figure 9.4-4**). Since the point reactor kinetics model has not changed, it is expected that the ATHENA comparisons would be the same as these RELAP5/MOD2 comparisons. The textbook solutions were not programmed into the computer to determine the textbook results, as this would just compare the different solution techniques. The technique in is more complex than any that could be quickly programmed for comparison. Instead, points were scaled from curves in textbooks that showed the results from various reactivity perturbations.

Figure 9.4-1 shows a comparison for various positive step insertions of reactivity from initial equilibrium in ^{235}U and ^{239}Pu systems with neutron lifetimes of 10^{-4} seconds. **Figure 9.4-2** shows a comparison for various linear time variations of reactivity from initial equilibrium in ^{235}U systems with neutron lifetimes of 10^{-4} seconds. **Figure 9.4-3** shows a comparison for various quadratic time variations of reactivity from initial equilibrium in ^{235}U systems with neutron lifetimes of 10^{-4} seconds. **Figure 9.4-4** shows a comparison for various negative step changes of reactivity from initial equilibrium in ^{235}U systems with neutron lifetimes of 10^{-4} seconds. The data for **Figure 9.4-1**, **Figure 9.4-2**, and **Figure 9.4-3** were obtained from **Reference 9.4-10**. Kinetics calculations using the RTS (Reactor Transient Solution) computer code were performed to produce the curves shown in **Reference 9.4-10**. The data for **Figure 9.4-4** were obtained from **Reference 9.4-11**. Unlike the other figures, only the immediate (prompt and delayed neutron) fission power was normalized in **Figure 9.4-4** and not the total power. Also, a slightly larger delayed neutron fraction (β) was used in determining **Figure 9.4-4**. This slightly larger delayed neutron fraction is typical of ^{235}U reactors with reflectors.

The solutions agreed well with the textbook solutions. Differences between the and textbook solutions can be attributed partly to the scaling of a curve from a textbook that may have been distorted as a result of printing or to show a specific trait. The curve from which the data for **Figure 9.4-4** were obtained was one-fourth the size of the curves from which the data for the other figures were obtained. As a result, the data points obtained for **Figure 9.4-4** are not as accurate as those obtained for the other figures. The difference at the larger power levels seen in **Figure 9.4-1** cannot, however, be a result of inaccurate scaling as the difference is too consistent. However, experience with calculations of reactivity-induced accident transients indicates that the power would unlikely go higher than 1,000 times the initial power if reactivity feedback was included in the power determination. In this range, the and textbook solutions

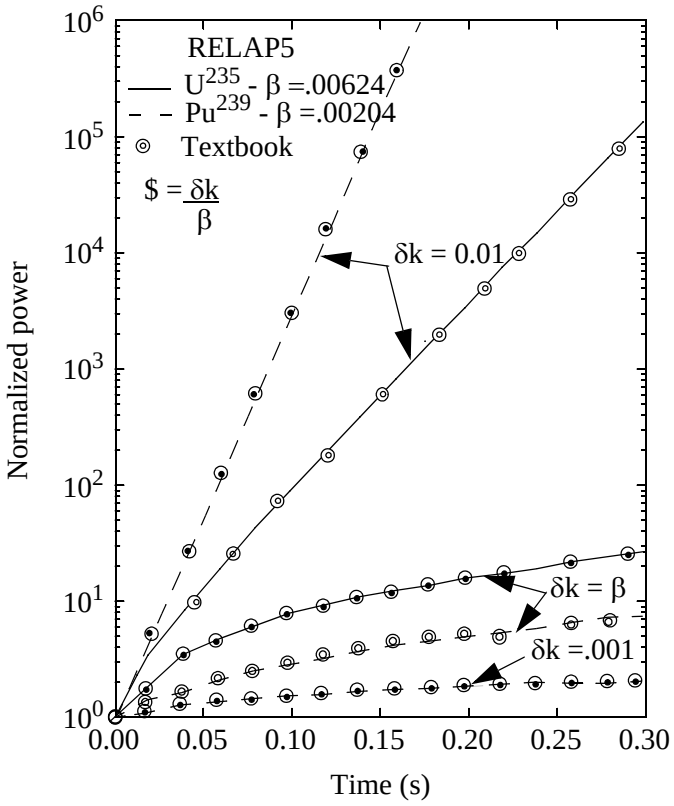

Figure 9.4-1 A comparison for various positive step insertions of reactivity from initial equilibrium in ^{235}U and ^{239}Pu systems with neutron lifetimes of 10^{-4} seconds.

show much better agreement. As indicated earlier, since the point kinetics model has not changed, it is expected ATHENA comparisons would be the same as these RELAP5/MOD2 comparisons.

Reactivity feedback can be input into ATHENA in one of two models: a separable model and a tabular model. In addition, two different sets of variables (standard and alternate) are allowed for the tabular model. The separable model is so defined that it assumes that each effect is independent of the other effects. This model also assumes nonlinear feedback effects from moderator density and fuel temperature changes and linear feedback from moderator temperature changes. The separable model does not provide for boron reactivity feedback, though user-defined boron feedback can be implemented with a control system. The separable model can, however, be used if boron changes are small and the reactor is near critical about only one state point. For those reactor transients where the assumption of no interactions among the different feedback mechanisms cannot be justified, the tabular model can be used. All feedback mechanisms can be nonlinear, and interactions among the mechanisms are included in the tabular model. However, the expanded modeling capability greatly increases the input data requirements.

The separable model is defined by

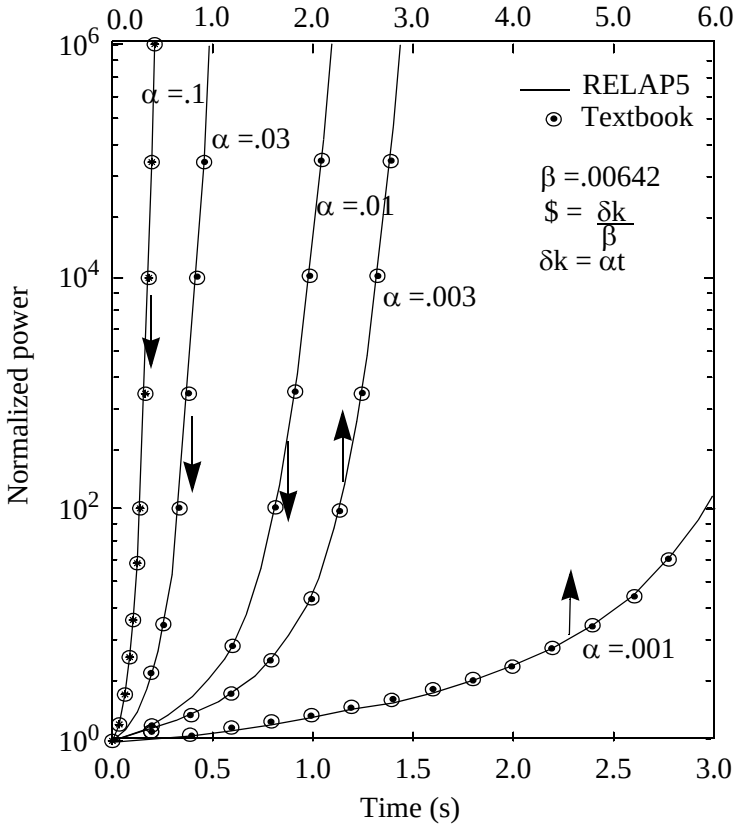

Figure 9.4-2 A comparison for various linear time variations of reactivity from initial equilibrium in ^{235}U systems with neutron lifetimes of 10^{-4} seconds.

$$r(t) = r_o - r_B + \sum_{i=1}^{n_s} r_{si}(t) + \sum_{i=1}^{n_c} V_{ci} + \sum_{i=1}^{n_\rho} [W_{\rho i} \bullet R_\rho(\rho_i(t)) + a_{Wi} \bullet T_{Wi}(t)] + \sum_{i=1}^{n_F} [W_{Fi} \bullet R_F(T_{Fi}(t)) + a_{Fi} \bullet T_{Fi}(t)] \quad . \tag{9.4-6}$$

The quantity r_o is an input quantity and represents the reactivity corresponding to assumed steady-state reactor power at time equal zero. The quantity r_B is a bias reactivity calculated during input processing such that the reactivity at time equal zero is r_o. The purpose of the bias reactivity is to ensure that the initial reactivity is equal to the input reactivity after including the feedback effects. Without this quantity, the user would have to manually adjust a scram curve or control variable to obtain the input value of initial reactivity or have a step input of reactivity as the transient starts.

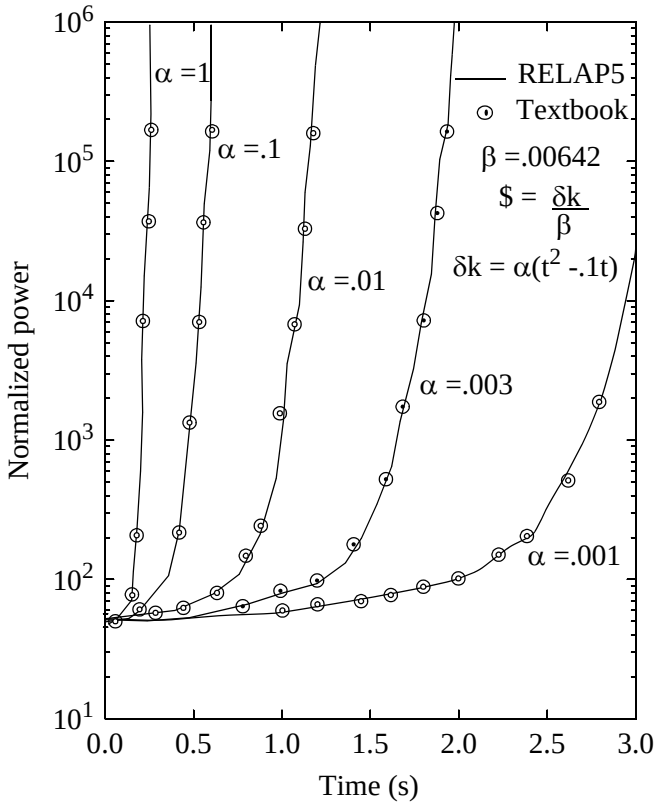

Figure 9.4-3 A comparison for various quadratic time variations of reactivity from initial equilibrium in ^{235}U systems with neutron lifetimes of 10^{-4} seconds.

The quantities r_{si} are obtained from input tables defining n_s reactivity curves as functions of time. The quantities V_{ci} are n_c control variables that can be user-defined as reactivity contributions. The value R_ρ is a table defining reactivity as a function of the moderator fluid density, $\rho_i(t)$, in the hydrodynamic volume i; $W_{\rho i}$ is density weighting factor for volume i; T_{Wi} is the spatial density averaged moderator fluid temperature of volume i; a_{Wi} is the temperature coefficient (not including density changes) for volume i; and n_ρ is the number of hydrodynamic volumes in the reactor core. The value R_F is a table defining reactivity as a function of the heat structure volume average fuel temperature T_{Fi} in heat structure i; W_{Fi} and a_{Fi} are the fuel temperature weighting factor and the fuel temperature coefficient, respectively for heat structure i; and n_F is the number of heat structures in the reactor core.

The tabular model using the standard variables defines reactivity as

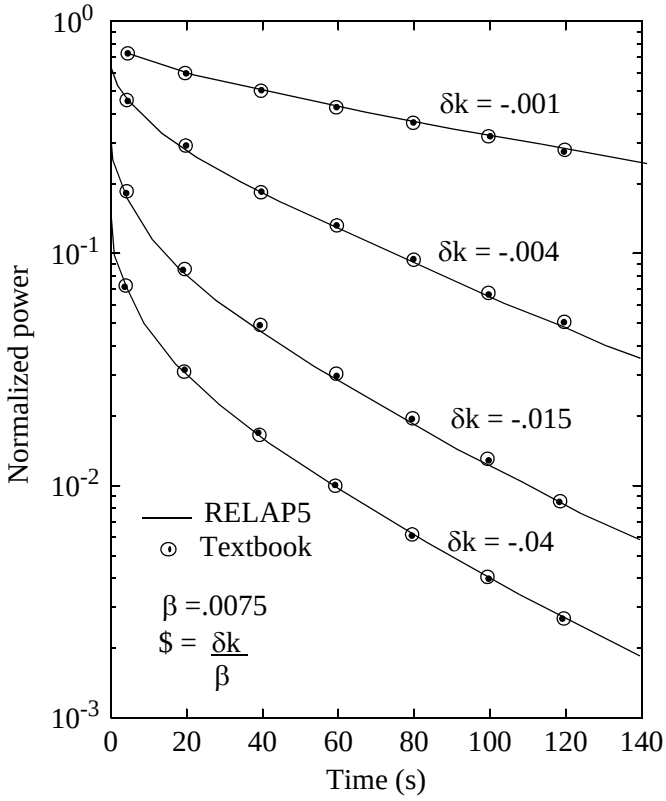

Figure 9.4-4 A comparison for various negative step changes of reactivity from initial equilibrium in ^{235}U systems with neutron lifetimes of 10^{-4} seconds.

$$r(t) = r_o - r_B + \sum_{i=1}^{n_s} r_{si}(t) + \sum_{i=1}^{n_c} V_{ci} + R(\bar{\rho}(t), \bar{T}_W(t), \bar{T}_F(t), \rho_b(t)) \quad (9.4\text{-}7)$$

$$\bar{\rho}(t) = \sum_{i=1}^{n_\rho} W_{\rho i}\rho_i(t) \quad (9.4\text{-}8)$$

$$\bar{T}_W(t) = \sum_{i=1}^{n_\rho} W_{\rho i}T_{Wi}(t) \quad (9.4\text{-}9)$$

$$\bar{T}_F(t) = \sum_{i=1}^{n_F} W_{Fi}T_{Fi}(t) \quad (9.4\text{-}10)$$

$$\bar{\rho}_b(t) = \sum_{i=1}^{n_\rho} W_{\rho i}\rho_{bi}(t) \tag{9.4-11}$$

where ρ_b is spatial boron density. The following are used:

1. The average quantities are obtained with the use of one weighting factor for each hydrodynamic volume and each heat structure contributing to reactivity feedback.

2. The reactivity function R is defined by a table input by the user.

3. The four-dimensional table lookup and interpolation option computes reactivity as a function of moderator fluid density (ρ), moderator fluid temperature (T_W), heat structure volume average fuel temperature (T_F), and spatial boron density (ρ_b). The three-dimensional option does not include spatial boron density.

The tabular model using the alternate variables defines reactivity as

$$r(t) = r_o - r_B + \sum_{i=1}^{n_s} r_{si}(t) + \sum_{i=1}^{n_c} V_{ci} + R(\bar{\alpha}_g(t), \bar{T}_f(t), \bar{T}_F(t), \bar{C}_b(t)) \tag{9.4-12}$$

$$\bar{\alpha}_g(t) = \sum_{i=1}^{n_\rho} W_{\rho i}\alpha_{gi}(t) \tag{9.4-13}$$

$$\bar{T}_f(t) = \sum_{i=1}^{n_\rho} W_{\rho i}T_{fi}(t) \tag{9.4-14}$$

$$\bar{T}_F(t) = \sum_{i=1}^{n_F} W_{Fi}T_{Fi}(t) \tag{9.4-15}$$

$$\bar{C}_b(t) = \sum_{i=1}^{n_\rho} W_{\rho i}\frac{\rho_{bi}}{\alpha_{fi}\rho_{fi}}(t) \tag{9.4-16}$$

where C_b is the boron concentration in mass of boron per mass of liquid, and the other quantities are the same as for the standard variables. As with the standard variables, the following are used:

1. The average quantities are obtained with the use of one weighting factor for each hydrodynamic volume and each heat structure contributing to reactivity feedback.

2. The reactivity function R is defined by a table input by the user.

3. The four-dimensional table lookup and interpolation option computes reactivity as a function of void fraction (α_g), liquid moderator temperature (T_f), fuel temperature (T_F), and boron concentration (C_b). The three-dimensional option does not include boron concentration.

The reactivity function R is evaluated by a direct extension of the one-dimensional table lookup and linear interpolation scheme to multiple dimensions. One-dimensional table lookup and interpolation of the function V = F(X) uses an ordered set of N_X independent variable values X_i, with the corresponding values of the dependent variable V_i, to determine the value of V corresponding to the search argument X. The independent variable is searched such that X_i and X_{i+1} bracket X. An equation for a straight line is fitted to the points X_i, V_i, and X_{i+1}, V_{i+1}, and the straight line equation is evaluated for the given X.

For one-dimension, the value of V is bracketed between X_i and X_{i+1}. For two-dimensions, the value of V is within the quadrilateral defined by the points X_i, Y_j and X_{i+1}, Y_j and X_i, Y_{j+1} and X_{i+1}, Y_{j+1}. For three-dimensions, the value of V lies within the box defined by the points X_i, Y_j, Z_k and X_{i+1}, Y_j, Z_k and X_i, Y_{j+1}, Z_k and X_{i+1}, Y_{j+1}, Z_k and X_i, Y_j, Z_{k+1} and X_{i+1}, Y_j, Z_{k+1} and X_i, Y_{j+1}, Z_{k+1} and X_{i+1}, Y_{j+1}, Z_{k+1}. This process continues for more dimensions. Using the appropriate weighting factors for each dimension, the value of V can be determined by linear interpolation in each dimension, one at a time.

Using N_X, N_Y, N_Z, and N_W as the number of values in the four sets of independent variables, the number of data points for a three-dimensional table is $N_X \cdot N_Y \cdot N_Z$ and is $N_X \cdot N_Y \cdot N_Z \cdot N_W$ for a four-dimensional table. Using only four values for each independent variable, a four-dimensional table requires 256 data points.

9.4.1 References

9.4-1. *American Nuclear Society Proposed Standard ANS 5.1, Decay Energy Release Rates Following Shutdown of Uranium-Fueled Thermal Reactors*, October 1971, revised October 1973.

9.4-2. *American National Standard for Decay Heat Power in Light Water Reactors*, ANSI/ANS-5.1-1979, August 1979.

9.4-3. V. E. Schrock, "A Revised ANS Standard for Decay Heat from Fission Products," *Nuclear Technology*, 46, 1979, pp. 323-331.

9.4-4. V. E. Schrock, "Evaluation of Decay Heating in Shutdown Reactors," *Progress in Nuclear Energy*, 3, 1979, pp. 125-156.

9.4-5. *American National Standard for Decay Heat Power in Light Water Reactors*, ANSI/ANS-5.1-94, August 1994.

9.4-6. S. Glasstone and A. Sesonske, *Nuclear Reactor Engineering*, New York: Von Nostrand Reinhold, 1981.

9.4-7. E. M. Cohen, "Some Topics in Reactor Kinetics," *A/CONF, 15*, 1958, p. 629.

9.4-8. A. Schwartz, *Generalized Reactor Kinetics Code AIREK II*, NAA-SR-Memo-4980, 1960.

9.4-9. R. A. Dimenna et al., *RELAP5/MOD2 Models and Correlations*, NUREG/CR-5194, EGG-2531, Idaho National Engineering Laboratory, August 1988.

9.4-10. G. R. Keepin, *Physics of Nuclear Kinetics*, Reading, MA: Addison-Wesley, 1965, pp. 287-293.

9.4-11. M. A. Schultz, *Control of Nuclear Reactors and Power Plants*, 2nd Edition, New York: McGraw-Hill, 1961, p. 91.

10 Closure Relations Required by Extra Mass Conservation Fields

The effects of the noncondensables on the heat transfer and mass transfer processes are discussed elsewhere in the manual in conjunction with the vapor-liquid processes and are not repeated in this section.

The only solute in the liquid field (solvent) that is explicitly treated in the code is boron. The assumption is made that the boron concentration is sufficiently dilute that the following assumptions are valid:

- Liquid (solvent) properties are not altered by the presence of the solute.
- Solute is transported only in the liquid phase (solvent) and at the velocity of the liquid phase (solvent).
- Energy transported by the solute is negligible.
- Inertia of the solute is negligible.

With these assumptions, only an additional equation for the conservation of the solute (i.e., boron) is required.

11 Steady-State

11.1 Basis for the Model

The model for steady-state analyses using ATHENA was originally implemented in RELAP5/MOD1.5,[11.1-1] which was a version of RELAP5/MOD1[11.1-2] extended to provide reflood heat transfer. The steady-state model was subsequently modified for use in RELAP5/MOD2[11.1-3] and, except for debugging, has remained essentially unchanged since RELAP5/MOD2 was released.

The basic modeling technique used by the steady-state model is that the user must set up the input database to perform a null transient, so that the problem being simulated will undergo a transient progressing from input initial conditions to the steady-state conditions defined by the user. To achieve this, the algorithm does not solve a set of steady-state formulations of the field equations. Instead, the algorithm uses the full transient algorithm and simply provides an automated method of monitoring the calculated results to detect when an average steady-state is achieved and maintained for a reasonable time interval. Upon achievement of steady-state, the algorithm automatically stops the calculational process, provides a final "restart-plot" file, and provides the printed and plotted output requested by the user. The user can then examine the results and, if desired, the problem can be either restarted as a continuation of the steady-state problem or restarted as a transient problem.

In performing the transient calculations, the steady-state algorithm uses only one special model in the solution of the thermal-hydraulic field equation. The special model used ignores the heat structure heat capacity data input by the user and replaces its value with a small value computed to be just large enough to maintain stability for the calculations. This technique reduces the thermal inertia of the bounding heat structures, allowing them to respond quickly and closely follow the hydraulic transient as it approaches steady-state.

The basis of the algorithm to detect steady-state is an original technique using least-squares curve fitting and smoothing methods to measure the time-rates of change in state of the calculational cells and the average linear rate of change of the modeled system. The scheme also considers calculational precision in determining the steady-state convergence criteria. This scheme often terminates a calculation prematurely so most users deactivate the scheme using input on the time step cards. In versions of the code after code version 2.2, the checking for steady-state is bypassed by default but can be reactivated by the user through additional input data. The purpose of the following discussion is to summarize the basic methodology described in the code manual, summarize differences between the manual and the code formulations, and summarize deficiencies noted by the users of the technique.

11.1.1 References

11.1-1. V. H. Ransom et al., *RELAP5/MOD1.5: Models, Developmental Assessment, and User Information,* EGG-NSMD-6035, Idaho National Engineering Laboratory, October 1982.

11.1-2. V. H. Ransom et al., *RELAP5/MOD1 Code Manual*, NUREG/CR-1826, EGG-2070, Idaho National Engineering Laboratory, March 1982.

11.1-3. V. H. Ransom et al., *RELAP5/MOD2 Code Manual*, NUREG/CR-4312, EGG-2396, Idaho National Engineering Laboratory, August 1985 and December 1985, revised March 1987.

11.2 Summary of the Steady-State Model

11.2.1 Model Description

In Volume I of this code manual, the steady-state model is described and is divided into five subsections discussing the fundamental concepts, the steady-state convergence criteria, the steady-state test time interval control, the heat structure heat conductance scheme, and the interrelationship of steady-state and transient restart-plot records.

The discussion concerning fundamental concepts states that it is only necessary to monitor three terms whose "variation in time include the variations of all the other terms." These three terms are the thermodynamic density, internal energy, and pressure, and these three terms can be combined into a single term, *enthalpy*. The enthalpy of each volume cell is then formulated. Furthermore, it is expressed that an absolute steady-state occurs when the time-rate of change in enthalpy approaches zero for all of the volume cells in the model, and that this is monitored by fitting the time-rate of change in enthalpy to an exponential smoothing function giving a least squares approximation of the root mean square (RMS) of the time-rate of change in enthalpy for the modeled system. A means of monitoring the system average enthalpy is also discussed, for which a straight line is fitted by least-squares to the average system enthalpy results over a time interval. Time-average steady-state then occurs when the linear average rate of change is zero within a convergence criterion related to the calculational precision.

The formulations presented are statistical equations expressing the difference between the state calculated by the transient numerical algorithm and the state calculated by the thermodynamic equation of state algorithm. This difference in state properties is then shown to be the difference in two-phase mixture densities computed by the two algorithms. This difference has been called the "mass error" in the code manual. A second source of density uncertainty is also discussed. It is the uncertainty of the thermodynamic equation of state itself. Since a steam table computed from the 1967 ASME formulation for steam water properties[11.2-1] is used as the default thermodynamic equation of state, and since these tables have five-significant-figure accuracy, the approximate uncertainty in thermodynamic is $\pm$ 5 in the density sixth significant figure. The resultant net uncertainty in the system mean enthalpy is then expressed as the statistical variance, summing the squares of the calculational precision and the steam table standard precision. The uncertainty in the rate of change in state is then written as the net uncertainty divided by the calculational time step.

Volume I also discusses the steady-state test time interval control and separates the scheme into two basic tasks, which are

1. To monitor the behavior of the time-smoothed RMS rate of change in system enthalpy.

2. To monitor the behavior of the linear average rate of change in the system enthalpy.

It also discusses the terms printed in the steady-state printed edit.

In performing a steady-state calculation, the full transient algorithm is solved at each time step; and, after each successful solution, the steady-state monitoring algorithm is entered. Tests for the preceding two tasks are performed as outlined in the following discussion.

In the test time interval control scheme, the first calculations performed are those evaluating the system mean enthalpy, the system mean rate of change in enthalpy, and the system mean square rate of change in enthalpy at each time step for ten successive successful time steps. At the end of this first time interval, the equation for time-smoothed root mean square rate of change in enthalpy is determined using the method of least squares. Its first two derivatives are evaluated at the current time step; and, if the rate of change is increasing, the progression to steady-state is divergent. If the rate of change is decreasing or zero, the progression to steady-state is convergent. If the divergent condition is determined, the next time at which the test will be performed is estimated by either maintaining, halving, or doubling the current test time interval based on a projected estimate of the current time-smoothed convergence function. This test procedure is then successively repeated until a convergent condition is calculated. The discussion explains the formulation of this process. If a convergent condition is determined, then testing for linear time-average steady-state is begun.

After the RMS rate of change test indicates a convergent condition, the linear average rate of change tests are begun. These tests are conducted by curve fitting three overlapping straight line equations to the system mean enthalpy results accumulated over two successive test time intervals. For example, if the two successive test time intervals are over the range in time from t_1 to t_2 to t_3, then three straight lines can be fitted to the results, such that line A is a line fitted from t_1 to t_2, Line B is a line fitted from t_2 to t_3, and Line C is a line fitted from t_1 to t_3. The implication of the manual is that if the slopes of these three straight lines both agree and approach zero within the calculational uncertainty, then the system is approaching a time-average steady-state. Of course, if the slopes of the three lines disagree and are not approaching zero, then the solution is diverging from steady-state.

If the solution is diverging, then the accumulated line results are discarded, and the testing scheme is reset to continue the RMS rate of change scheme until it again indicates convergence, at which time the linear time-average scheme is reinitiated.

It has been noted that the full transient algorithm is solved at each time step for the system being modeled, and that only thermal-hydraulic parameters are monitored to detect steady-state, with no mention of how the state of heat structures is monitored as they achieve steady-state. In the steady-state algorithm, the heat structure response is forced to closely follow the thermal-hydraulic response by ignoring the heat structure heat capacity data input by the user and replacing it with a small value just large enough to ensure

calculational stability. This technique artificially reduces the thermal inertia of the heat structures, allowing them to rapidly store or reject heat, and thereby closely follow the thermal-hydraulic state as it approaches steady-state. The formula used to calculate the minimal heat capacity term is the explicit stability criterion for numerical heat conduction analyses.

Finally, to allow a high degree of utility in using the steady-state technique, the ability is provided to restart problems as continuations of steady-state problems or as transients using the steady-state restart-plot records as initial conditions. Capability is also included to restart steady-state problems using transient restart-plot records as initial conditions. Of course, the fundamental capability of running a new problem as a steady-state is also included.

11.2.2 Code Implementation

Comparing the steady-state scheme discussed in the manual to the scheme as coded in the subroutine SSTCHK shows that all of the formulations have been implemented as described except two. The first exception is that the standard uncertainty is coded as

$$\varepsilon_{std,\rho,1}^{n+1} \approx \pm (6x10^{-6})\rho_i^{n+1} \qquad (11.2\text{-}1)$$

which gives a better approximation to $\pm$ 5 in the sixth significant figure for density of saturated liquid. The second exception is that if upon testing the three straight lines to determine if time-average steady-state has been achieved, it is determined that steady-state has not been achieved, the first test line (i.e., Line A) is not simply reset to the second test line (i.e., Line B). Instead, the straight line results for both Lines A and B are discarded, and Line A is replaced by a least-squares fit to the transient algorithm results over the Line B test time interval. The remainder of the time-average steady-state testing scheme remains as discussed in the manual.

11.2.3 Reported Deficiencies

Very few users have reported deficiencies to the ATHENA code development personnel. However, the deficiencies that have been reported have all been for models simulating full-size power plants or integral test facilities simulating power plants. The deficiencies fall into three categories:

1. The modeled system undergoes a significant transient from user-input initial conditions and begins to steady out, but the code terminates the calculation too early, with the statement printed that the system has achieved steady-state.

2. The modeled system undergoes a significant transient from user-input initial conditions to a good steady-state, but the algorithm allows calculations to proceed at steady-state for too long a time.

3. The modeled system achieved a good steady-state in a reasonable simulation time, but, for the secondary side, if the steam generator heat transfer conditions are matched, the

secondary pressure does not agree with the data. If the secondary pressure is matched, then the steam generator heat transfer conditions do not agree with the data.

4. The default code contains an energy discrepancy.

The first deficiency definitely shows a weakness in the time-average steady-state testing scheme. The deficiency occurs, however, when the user inputs very crude or approximate initial conditions. The transient problem simulated is then quite extreme, resulting in a high calculational uncertainty. This uncertainty is monitored by the code time step control routine as mass error; and, as a result, the time step taken is usually reduced to the minimum value input by the user. Once the minimum time step is reached, the code is then forced to run at that time step and forced to accept the high error. Since this mass error is used by the steady-state algorithm to define the time-average steady-state convergence criteria, the resultant convergence criterion is large. Hence, since the criterion for time-average steady-state is that the slope of the time-average straight line be zero plus or minus the convergence criterion, the large convergence criterion allows the algorithm to prematurely estimate achievement of time-average steady-state. The user can generally work around this problem by simply restating the run as a continuation of the steady-state problem.

The second deficiency is usually a direct function of the steady-state scheme and not really a deficiency. Roughly, the first 25% of the total time simulated is the transient approach to steady-state. The test time interval for the first achievement of steady-state will be of the same approximate duration as this transient time interval. This is, if it takes approximately 100 seconds simulated time to undergo the transient approach to steady-state, then the first test time interval showing the achievement of time-average steady-state will also be approximately 100 seconds. The algorithm then repeats the testing scheme for two additional intervals of the same duration, and if this average steady-state is successively maintained for all three time intervals, then the algorithm terminates the calculation with the statement that steady-state has been achieved. The time needed to achieve steady-state can usually be shortened by improving the modeled control variables that drive the system to steady-state.

The third deficiency noted is also not a deficiency in the steady-state algorithm. It is a heat transfer modeling problem typical of PWR steam generator models. Users should refer to previous sections in this document describing these models for more detailed recommendations (see Volume I).

The fourth deficiency that the default code contains is a discrepancy when checking the steady-state by means of an energy balance, The default code should add the form loss (code calculated abrupt area change loss and user-specified loss) dissipation to the phasic energies. This dissipation was removed in RELAP5/MOD2 because of temperature problems (i.e., overheating), and thus is not present in ATHENA. The dissipation can be activated by the user in the input deck, however the user is cautioned that temperature problems may occur.

Note that the user can define a plant controller such as a steam generator feedwater control operating between high and low set points that will force the modeled system to a steady oscillating state or an oscillating state with slowly decreasing amplitude. For these circumstances, the steady-state algorithm will

determine that a time-average steady-state has been achieved, and within the steady-state edit the mean RMS amplitude of these oscillations is printed as the term FLUCTUATION. If the user desires to remove these oscillations, a revised controller must be used that will drive the system to a precise set point.

11.2.4 Conclusions

The steady-state algorithm provides an adequate automated method of performing a null transient solution for steady-state conditions. However, the experienced ATHENA user will undoubtedly have better success than the inexperienced user. ATHENA personnel have included a new modeling capability for self-initialization of PWR plant system models.[11.2-2] Two examples are included that demonstrate how a good steady-state can be achieved.

It is also concluded that the steady-state algorithm can be improved by delaying the initiation of testing for steady-state until the initial calculational mass error has begun to decrease. This would prevent premature estimates of the achievement of steady-state.

11.2.5 References

11.2-1. C. A. Meyer, R. G. McClintock, G. J. Silvertri, and R. C. Spencer, Jr., *1967 ASME Steam Tables -- Thermodynamic and Transport Properties of Steam*, New York: The American Society of Mechanical Engineers, 1967.

11.2-2. G. W. Johnsen et al., *Self Initialization Option for RELAP5/MOD2*, EGG-RTH-7381, Idaho National Engineering Laboratory, September 1986.